

Ch. Enss

# Cryogenic Particle Detection



Springer

# Topics in Applied Physics

## Volume 99

Available online at  
**SpringerLink.com**

Topics in Applied Physics is part of the SpringerLink service. For all customers with standing orders for Topics in Applied Physics we offer the full text in electronic form via SpringerLink free of charge. Please contact your librarian who can receive a password for free access to the full articles by registration at:

[springerlink.com](http://springerlink.com) → Orders

If you do not have a standing order you can nevertheless browse through the table of contents of the volumes and the abstracts of each article at:

[springerlink.com](http://springerlink.com) → Browse Publications

# Topics in Applied Physics

---

Topics in Applied Physics is a well-established series of review books, each of which presents a comprehensive survey of a selected topic within the broad area of applied physics. Edited and written by leading research scientists in the field concerned, each volume contains review contributions covering the various aspects of the topic. Together these provide an overview of the state of the art in the respective field, extending from an introduction to the subject right up to the frontiers of contemporary research.

Topics in Applied Physics is addressed to all scientists at universities and in industry who wish to obtain an overview and to keep abreast of advances in applied physics. The series also provides easy but comprehensive access to the fields for newcomers starting research.

Contributions are specially commissioned. The Managing Editors are open to any suggestions for topics coming from the community of applied physicists no matter what the field and encourage prospective editors to approach them with ideas.

## Managing Editors

Dr. Claus E. Ascheron

Springer-Verlag GmbH  
Tiergartenstr. 17  
69121 Heidelberg  
Germany  
Email: claus.ascheron@springer-sbm.com

Dr. Hans J. Koelsch

Springer-Verlag New York, LLC  
233, Spring Street  
New York, NY 10013  
USA  
Email: hans.koelsch@springer-sbm.com

## Assistant Editor

Dr. Werner Skolaut

Springer-Verlag GmbH  
Tiergartenstr. 17  
69121 Heidelberg  
Germany  
Email: werner.skolaut@springer-sbm.com

Christian Enss (Ed.)

# Cryogenic Particle Detection

With 238 Figures and 23 Tables

**Prof. Dr. Christian Enss**

Kirchhoff-Institut der Physik  
Universität Heidelberg  
Im Neuenheimer Feld 227  
69120 Heidelberg, Germany  
[christian.enss@physik.uni-heidelberg.de](mailto:christian.enss@physik.uni-heidelberg.de)

Library of Congress Control Number: 2005921508

**Physics and Astronomy Classification Scheme (PACS):**

**29.40.Vj, 85.25.-j, 85.60.Gz, 87.64Gb**

**ISSN print edition: 0303-4216**

**ISSN electronic edition: 1437-0859**

**ISBN-10 3-540-20113-0 Springer Berlin Heidelberg New York**

**ISBN-13 978-3-540-20113-7 Springer Berlin Heidelberg New York**

This work is subject to copyright. All rights are reserved, whether the whole or part of the material is concerned, specifically the rights of translation, reprinting, reuse of illustrations, recitation, broadcasting, reproduction on microfilm or in any other way, and storage in data banks. Duplication of this publication or parts thereof is permitted only under the provisions of the German Copyright Law of September 9, 1965, in its current version, and permission for use must always be obtained from Springer. Violations are liable for prosecution under the German Copyright Law.

Springer is a part of Springer Science+Business Media

[springeronline.com](http://springeronline.com)

© Springer-Verlag Berlin Heidelberg 2005

Printed in Germany

The use of general descriptive names, registered names, trademarks, etc. in this publication does not imply, even in the absence of a specific statement, that such names are exempt from the relevant protective laws and regulations and therefore free for general use.

Typesetting: DA-T<sub>E</sub>X · Gerd Blumenstein · [www.da-tex.de](http://www.da-tex.de)  
Production: LE-T<sub>E</sub>X Jelonek, Schmidt & Vöckler GbR, Leipzig  
Cover design: *design & production* GmbH, Heidelberg

Printed on acid-free paper 57/3141/YL 5 4 3 2 1 0

# Preface

In 1800 Friedrich Wilhelm Herschel (better known as Sir William Herschel) discovered infrared radiation by passing sunlight through a prism and holding a thermometer just beyond the red end of the visible spectrum. The thermometer indicated a temperature rise, which led Herschel to the conclusion that there must be an invisible form of light. This was perhaps the first time that a previously unknown form of radiation was observed by a thermal measurement. More than a century later, in 1903, Pierre Curie and Albert Laborde demonstrated that the radioactive decay of radium led to the production of heat.

These early experiments summed the heat produced by a large number of particles. An important milestone in the calorimetric detection of individual particles was the observation in 1935 by Franz Eugen Simon (later Sir Francis Simon) that calorimetric detectors, operated at low temperatures, would have enhanced sensitivity. Since then, many advances have been made in the development of cryogenic detectors. Today, more than two hundred years after Herschel's discovery, the calorimetric detection of individual elementary particles with cryogenic detectors has become routine in many laboratories.

Over the last twenty years, the strongest driving force for the development of cryogenic detectors has come from the need for more sensitive and versatile instruments in astrophysics, astronomy and nuclear physics. The field as we know it today really began back in 1984 when several groups independently proposed new types of particle detectors to investigate fundamental problems in nuclear and astro-particle physics. From that point on, the new field of cryogenic detectors has experienced a very rapid growth, resulting in devices with fascinating capabilities. Applications range from basic research to industrial quality control.

Although this frontier in science and technology is developing rapidly, it seemed a good time to assemble a comprehensive overview of cryogenic particle detection. The present book contains a collection of review articles written by leading scientists in the field, describing major techniques for cryogenic particle detection, their developmental status and a number of applications. Despite the considerable size of the book it was impossible to cover all the different types of cryogenic detectors that have been investigated or are now under study. We have tried to include the main branches of this field to give

a picture as balanced as possible of the current science and technological status of cryogenic detectors. Of course, the selection of topics is somewhat subjective and possible short comings should be blamed on me.

The book is directed mainly to students and researchers working in the field of cryogenic particle detection, but it should also be useful as a reference for those interested in applying the technology to particular problems. The first chapter gives an introduction into the general aspects of calorimetric particle detection. The following four chapters describe the detection technologies presently at the forefront of the field and the current status of their development. Applications including X-ray fluorescence analysis, dark matter searches, astronomy, nuclear and heavy ion physics are discussed in the remaining part of the book.

I believe that progress in this field will continue to be very rapid and that cryogenic detectors will ultimately aid in answering a number of fundamental questions that will deepen our understanding of nature. At the same time, there is a good chance that such detectors will become standard tools in several industrial applications. The commercialization of cryogenic detectors already has started.

In conclusion, I would like to thank the authors of our common book for committing so much of their time to writing their contributions and for their constructive collaboration throughout the editing process. They responded enthusiastically to my invitation to join in this effort and have produced extremely interesting state-of-the-art reviews.

Heidelberg, February 2005

*Christian Enss*

# Contents

## Thermal Equilibrium Calorimeters – An Introduction

D. McCammon	1
1 Introduction .....	1
2 Basic Linear Theory of Calorimeters .....	2
2.1 Limits on Energy Resolution: A First Look.....	3
2.2 Power Responsivity as Function of Frequency .....	7
2.2.1 D.C. Response .....	7
2.2.2 A.C. Response .....	8
2.2.3 Electrothermal Feedback .....	9
2.3 Major Noise Terms .....	11
2.3.1 Thermodynamic Fluctuation Noise .....	11
2.3.2 Thermometer Johnson Noise .....	12
2.3.3 Load Resistor Johnson Noise.....	13
2.3.4 Amplifier Noise .....	14
2.3.5 Photon Background Noise .....	15
2.3.6 Additional Thermometer Noise.....	15
2.4 Optimal Filtering and Energy Resolution .....	15
2.5 Optimization of Detector and Operating Conditions .....	18
2.6 Complex Load Impedance .....	22
2.7 External Electrothermal Feedback .....	22
2.8 Thermometer Nonlinearities .....	23
2.9 Voltage Output versus Current Output .....	25
2.10 Complications .....	26
2.10.1 Internal Time Constants and Internal Fluctuation Noise	26
2.10.2 Thermalization Noise .....	28
3 Limitations of Linear Theory .....	29
4 Other Thermometer Types .....	31
4.1 Kinetic Inductance .....	32
4.2 Magnetic .....	32
4.3 NIS Junctions .....	33
4.4 Pyro-electric .....	33
References .....	34

<b>Semiconductor Thermistors</b>	
D. McCammon	35
1 Introduction . . . . .	35
2 Hopping Conduction . . . . .	36
2.1 Deviations from Coulomb Gap Behavior . . . . .	37
2.2 Doping and Device Fabrication . . . . .	40
2.2.1 Neutron Transmutation Doped Germanium . . . . .	40
2.2.2 Ion-implanted Silicon . . . . .	42
3 Electrical Nonlinearities . . . . .	44
3.1 Electric-Field Effects . . . . .	45
3.2 “Hot Electron” Effects . . . . .	46
3.2.1 Time Constants and Heat Capacity . . . . .	50
3.2.2 Internal Thermodynamic Fluctuation Noise . . . . .	50
4 Excess Noise . . . . .	52
5 Fundamental Limitations and Ultimate Performance . . . . .	55
5.1 Optimization . . . . .	56
5.2 Germanium versus Silicon . . . . .	57
5.3 Expected Performance . . . . .	58
References . . . . .	59

**Transition-Edge Sensors**

K. D. Irwin and G. C. Hilton	63
1 Introduction . . . . .	63
2 Superconducting Transition-Edge Sensor Theory . . . . .	65
2.1 The Superconducting Transition . . . . .	65
2.2 TES Small Signal Theory Summary . . . . .	70
2.3 TES Electrical and Thermal Response . . . . .	71
2.4 TES Stability . . . . .	83
2.5 Negative Electrothermal Feedback . . . . .	85
2.6 Thermodynamic Noise . . . . .	88
2.7 Excess Noise . . . . .	98
2.8 Large Signals . . . . .	104
3 Single-Pixel Implementation . . . . .	105
3.1 TES Thermometers . . . . .	106
3.1.1 Elemental Superconductors . . . . .	107
3.1.2 Bilayers and Multilayers . . . . .	108
3.1.3 Magnetically Doped Superconductors . . . . .	109
3.2 Thermal Isolation . . . . .	110
3.2.1 Micromachined Thermal Supports . . . . .	110
3.2.2 Phonon Decoupling . . . . .	111
3.3 Absorbers . . . . .	112
3.4 Useful Formulas . . . . .	115
3.4.1 Electrical Conductivity of Normal-Metal Thin Films . . . . .	115
3.4.2 Heat Capacity . . . . .	117
3.5 Thermal Conductance . . . . .	117

3.6	Example Devices and Results .....	118
3.6.1	Optical-Photon Calorimeters.....	118
3.6.2	X-ray Calorimeters .....	119
4	Arrays .....	121
4.1	Array Fabrication and Micromachining .....	122
4.1.1	Bulk Micromachining .....	123
4.1.2	Surface Micromachining .....	127
4.2	Multiplexed Readout .....	128
4.2.1	The Nyquist Theorem and Multiplexing .....	130
4.2.2	SQUID Noise and Multiplexing .....	131
4.2.3	Low-Frequency TDM .....	132
4.2.4	Low-Frequency FDM .....	135
4.2.5	Microwave SQUID Multiplexer .....	137
5	Future Outlook .....	141
	References .....	142

## Metallic Magnetic Calorimeters

A.	Fleischmann, C. Enss, G.M. Seidel .....	151
1	Introduction .....	151
2	Theoretical and Experimental Background.....	153
2.1	Detection Scheme .....	153
2.2	Sensor Materials .....	153
2.2.1	Au:Er .....	155
2.3	Scaling .....	163
2.4	Optimization of Signal-to-SQUID-Noise Ratio .....	165
2.4.1	Basic Ideas .....	165
2.4.2	SQUID-based sensor readout .....	168
2.4.3	Cylindrical Sensors .....	174
2.4.4	Meander Geometry .....	179
2.5	Magnetic Johnson Noise .....	186
2.6	Energy Resolution .....	190
2.6.1	First Approach – A Canonical Ensemble .....	191
2.6.2	Canonical Ensemble Consisting of Two Subsystems .....	192
3	Status of Development .....	199
3.1	Experimental Setup .....	199
3.1.1	Cryogenics .....	200
3.1.2	SQUID Magnetometer .....	201
3.2	High Resolution X-ray Spectroscopy .....	202
3.3	Self-Inductance Magnetic Calorimeter .....	207
3.4	Activity Measurements in Metrology .....	209
3.5	Gamma-Ray Spectroscopy .....	211
4	Summary and Outlook .....	214
	References .....	214

**Quantum Giaever Detectors**

P. Lerch, A. Zehnder	217
1 Introduction . . . . .	217
2 Theoretical Background . . . . .	221
2.1 Charge Creation . . . . .	221
2.2 Quasi-Particles and Phonons in the <i>Operational Stage</i> . . . . .	224
2.3 Quasi-Particle Losses . . . . .	226
2.4 Tunneling . . . . .	227
2.5 Diffusion . . . . .	229
2.6 Quasi-Particle Trapping . . . . .	229
2.7 Proximity Effects and Band-Gap Engineering . . . . .	230
3 Statistical Fluctuations . . . . .	235
4 Experimental . . . . .	237
4.1 Devices . . . . .	237
4.2 Readout Schemes . . . . .	239
4.3 Single Pixel . . . . .	241
4.3.1 Nb-Based Devices . . . . .	241
4.3.2 Nb-Based Devices and Trapping . . . . .	242
4.3.3 Improvement with Ta-Based Devices . . . . .	243
4.3.4 Al-Based Devices . . . . .	243
4.3.5 Charge Gain and Linearity . . . . .	243
4.3.6 Energy Resolution . . . . .	246
4.4 Charge Division Approach . . . . .	247
5 Outlook . . . . .	251
6 Appendix . . . . .	256
6.1 Readout Circuit and Electronics Noise . . . . .	256
References . . . . .	257

**Electron Probe Microanalysis  
with Cryogenic Detectors**

D. E. Newbury, K. D. Irwin, G. C. Hilton, D. A. Wollman, J. A. Small, J. M. Martinis	267
1 Introduction . . . . .	267
1.1 Low Temperature X-ray Detectors for Analytical Applications	267
1.2 Electron Probe X-ray Microanalysis . . . . .	268
2 EPMA with Si-EDS . . . . .	271
3 EPMA with Wavelength Dispersive X-ray Spectrometry . . . . .	274
4 EPMA with Si-EDS and WDS: The Complementarity of WDS and Si-EDS . . . . .	275
5 EPMA with Low-temperature X-ray Detectors . . . . .	276
5.1 Prototype Microcalorimeter EDS in an SEM/EPMA Environment . . . . .	278
5.2 Characteristics of an Ideal X-ray Spectrometer for EPMA Compared with the Microcalorimeter-EDS . . . . .	281
5.2.1 Energy Dispersive Character . . . . .	282

5.2.2 Resolution . . . . .	282
5.2.3 Energy Efficiency . . . . .	283
5.2.4 Geometric Efficiency . . . . .	284
5.2.5 High Count Rate . . . . .	287
5.2.6 Linearity . . . . .	289
5.2.7 Lack of Spectral Artifacts . . . . .	290
5.3 Performance of the Microcalorimeter EDS in Classic EPMA Applications . . . . .	291
5.3.1 Resolving Peaks in an EDS Mode . . . . .	291
5.3.2 Limits of Detection . . . . .	292
5.3.3 Detecting “Chemical Shifts” with the Microcalorimeter EDS . . . . .	297
5.3.4 Application of the Microcalorimeter-EDS to Low Voltage Microanalysis . . . . .	298
5.4 Future Prospects, Further Developments, and Commercialization . . . . .	306
5.4.1 Commercialization . . . . .	306
5.4.2 Anticipated Future Developments . . . . .	308
6 Summary . . . . .	311
References . . . . .	311

## Dark Matter Direct Detection

G. Chardin	313
1 Motivations for Non-Baryonic Dark Matter . . . . .	313
1.1 Searching for Baryonic Dark Matter . . . . .	314
1.2 Cosmological Constraints . . . . .	315
2 Weakly Interacting Massive Particles (WIMPs) . . . . .	317
2.1 Phenomenology . . . . .	317
2.2 Experimental Signatures . . . . .	319
3 WIMP Direct Detection: Initial Results and the DAMA Candidate . . . . .	320
3.1 The DAMA Annual Modulation Candidate . . . . .	321
4 Cryogenic Detectors: Motivations . . . . .	323
5 Charge-Phonon Detectors . . . . .	326
5.1 Charge-Phonon Detectors with MIT Sensors . . . . .	327
5.1.1 Solving the Problem of Surface Events . . . . .	327
5.2 Charge-Phonon Detectors with TES Sensors . . . . .	328
5.3 Thin Film Sensors in the Metal-Insulator Transition . . . . .	330
5.4 Charge Regeneration . . . . .	331
5.5 Developments and Perspectives . . . . .	332
6 Event Categories . . . . .	335
7 Light-Phonon Detectors . . . . .	337
7.1 Introduction . . . . .	337
7.2 Schematics of a Light-Phonon Detector . . . . .	337
7.3 Discussion . . . . .	339

7.4	First Results . . . . .	339
7.5	Conclusions . . . . .	341
8	Other Cryogenic Detectors . . . . .	342
8.1	MACHE3: $^3\text{He}$ , the Purest of All Materials . . . . .	342
8.2	ORPHEUS: Superconducting Superheated Granules . . . . .	343
8.3	The Tokyo LiF Bolometer Experiment . . . . .	343
8.4	Detecting the recoil direction . . . . .	344
9	Towards Ton-Scale Dark Matter Experiments . . . . .	345
9.1	Ton-Scale Experiments without Background Discrimination . . . . .	345
9.1.1	The DAMA/LIBRA Experiment . . . . .	346
9.1.2	The GENIUS-TF/GENIUS Experiment . . . . .	346
9.1.3	The CUORICINO/CUORE Experiment . . . . .	347
9.2	Large-Scale Cryogenic Discriminating Experiments . . . . .	348
9.3	Strategy For Ton-Scale Dark Matter Cryogenic Experiments . . . . .	349
9.3.1	The Neutron Background . . . . .	349
9.3.2	Detector Mass and Resolution . . . . .	351
10	Conclusions . . . . .	352
	References . . . . .	353

## X-Ray Astronomy and Astrophysics

F.S. Porter, G.V. Brown, J. Cottam	359	
1	The Wealth and Breadth of the X-Ray Universe . . . . .	359
2	High-Resolution X-Ray Spectroscopy . . . . .	360
2.1	Ionization Mechanism . . . . .	361
2.2	Temperature Structure . . . . .	362
2.3	Density Structure . . . . .	363
2.4	Velocity Structure . . . . .	364
2.5	Optical Depth . . . . .	364
2.6	Fluorescence Emission . . . . .	365
2.7	Instrument Requirements . . . . .	366
3	Instrumentation for X-Ray Spectroscopy . . . . .	366
3.1	Dispersive Spectrometers . . . . .	367
3.1.1	Chandra . . . . .	368
3.1.2	XMM-Newton . . . . .	368
3.2	Non-Dispersive Spectrometers . . . . .	369
3.3	The Niche for Low Temperature Detectors . . . . .	371
4	Ground Rules for Low Temperature Detectors in X-Ray Astronomy . . . . .	372
4.1	Cryogenics . . . . .	372
4.1.1	Adiabatic Demagnetization Refrigerators . . . . .	373
4.1.2	Cryogens, Cryo-coolers, and Lifetime . . . . .	374
4.2	Mass and Power . . . . .	376
4.3	Survivability: Mechanical Design and Analysis, Radiation Damage . . . . .	377
4.4	Electronics . . . . .	378

4.5	Risk .....	380
5	Current and Near-Term Missions .....	381
5.1	The X-Ray Quantum Calorimeter: The First LTD X-Ray Mission .....	381
5.1.1	Introduction to the XQC .....	381
5.1.2	The XQC Instrument .....	382
5.1.3	XQC Results and Future Plans .....	384
5.2	The XRS on Astro-E2 .....	386
5.2.1	Introduction to the XRS .....	386
5.2.2	The XRS Cryogenic System .....	388
5.2.3	The XRS Detector System .....	389
5.3	Future Missions .....	393
6	Laboratory Astrophysics and LTDs .....	395
6.1	Instruments for Laboratory Astrophysics: LTDs and Electron Beam Ion Traps .....	396
6.1.1	The Electron Beam Ion Trap .....	397
6.1.2	The GSFC Microcalorimeter Detector For Laboratory Astrophysics .....	399
6.2	Measurements Using the XRS/EBIT at the LLNL EBIT Facility .....	401
6.2.1	Measuring Electron Impact Excitation Cross Sections of X-ray Transitions .....	401
6.2.2	The Study of X-ray Emission Following Charge Exchange Recombination for Diagnosing Cometary Plasmas .....	403
7	Future Challenges .....	406
7.1	Scaling Limits in Current LTD Technologies .....	407
7.2	Where Do We Go From Here? Future Missions, Dreams, and Challenges .....	410
	References .....	411

## Optical/UV Astrophysics Applications of Cryogenic Detectors

B.	Cabrera and R. W. Romani	417
1	Introduction .....	417
2	Optical STJ and TES Sensors .....	419
2.1	The Superconducting Transition Edge Sensor .....	422
2.2	Optimal Filter Analysis for Nonlinear TES Response .....	425
3	Fiber-Optic-Coupled TES Spectrophotometer .....	428
3.1	Operation of Four-Pixel Fiber-Optic TES Spectrophotometer .....	428
3.2	Crab Pulsar and Other Observations at McDonald 2.7 m .....	431
4	Imaging STJ and TES Arrays .....	434
4.1	ESA S-Cam Instruments and Observations .....	434
4.2	Imaging Array with TESs .....	437
4.3	Reflection Masking .....	438

4.4	Anti-reflection Coatings .....	439
4.5	IR Blocking Filters.....	440
4.6	The Path to Larger Arrays and Multiplexing .....	441
5	Development Goals for Cryogenic Spectrophotometers .....	443
5.1	Optical Configurations .....	443
5.2	Astrophysics Science Goals .....	444
5.3	Design of Future Missions .....	447
6	Conclusions.....	448
	References .....	449
	References .....	449

## Beta Decay Experiments

E.	Fiorini	453
1	Introduction .....	453
2	The Neutrino Mass .....	454
3	Single Beta Decay .....	455
3.1	Determination of the Antineutrino Mass .....	455
3.2	The BEFS Effect .....	456
3.3	Measurements of the Antineutrino Mass .....	457
3.4	Searches for Rare Beta Decays.....	458
3.5	Cryogenic Detectors and Solar Neutrinos .....	459
4	Double Beta Decay .....	460
4.1	Experimental Approaches and Present Experimental Status ..	462
4.2	The Future .....	463
4.2.1	Future Experiments to Search for Neutrinoless Double Beta Decay .....	466
	References .....	468

## Heavy Ion Physics

P.	Egelhof, S. Kraft-Bermuth	469
1	Introduction .....	469
2	Experimental Conditions and Specific Requirements for Cryogenic Heavy Ion Detectors .....	473
3	Design and Performance of Calorimetric Low Temperature Detectors for Energetic Heavy Ions .....	475
3.1	Detector Design .....	475
3.1.1	Calorimetric Detectors Based on Semiconductor Thermistors .....	475
3.1.2	Calorimetric Detectors Based on Aluminum Transition Edge Sensors .....	476
3.2	Detector Performance .....	478
4	Applications of Calorimetric Low Temperature Detectors for Heavy Ions and First Results .....	484
4.1	High Resolution Nuclear Spectroscopy .....	484

4.2	High Resolution Mass Determination for Identification of Superheavy Elements and Reaction Products from Direct Reactions with Radioactive Beams .....	485
4.3	Accelerator Mass Spectrometry .....	489
4.3.1	Cryogenic Detectors in Accelerator Mass Spectrometry .	489
4.3.2	First Application of Cryogenic Detectors in AMS for Trace Analysis of $^{236}\text{U}$ .....	490
5	Cryogenic Detectors for Hard X-rays and their Application in Atomic Physics with Highly Charged Heavy Ions .....	494
5.1	Lamb Shift Measurements on Hydrogen-like Heavy Ions .....	494
5.2	Development of Calorimetric Low Temperature Detectors for Hard X-rays and First Results .....	496
	References .....	498
	<b>Index</b> .....	501

# Thermal Equilibrium Calorimeters – An Introduction

D. McCammon

Physics Department, University of Wisconsin, Madison, WI 53706, USA  
[mccammon@wisp.physics.wisc.edu](mailto:mccammon@wisp.physics.wisc.edu)

**Abstract.** Near-equilibrium thermal detectors operate as classical calorimeters, with energy deposition and internal equilibration times short compared to the thermal time constant of the device. Advances in fabrication techniques, cryogenics, and electronics have made it practical to measure deposited energy with unprecedented sensitivity and precision. In this chapter we discuss performance considerations for these devices, including optimal filtering and energy resolution calculations. We begin with the basic theory of simple equilibrium calorimeters with ideal resistive thermometers. This provides a starting point for a brief discussion of electrothermal feedback, other noise sources, various non-ideal effects, and nonlinearity. We then describe other types of thermometers and show how they fit into this theoretical framework and why they may require different optimizations and figures of merit. Most of this discussion is applicable also to power detectors, or bolometers, where the detector time constants may be short compared to variations in the incident signal power.

## 1 Introduction

Thermal detectors in general have a number of characteristics that make them more attractive than ionization detectors for many applications. Some of these are directly related to the lack of a requirement for efficient charge transport: if it is not necessary to collect electrons, large amounts impurities can be tolerated, and a radioactive source or specialized target material could be embedded within the detector. This also opens up a wide range of materials options, so the detector might in fact be made of the source. Other useful characteristics are sensitivity to exotic interactions that produce no ionization, and energy thresholds that can be made almost arbitrarily small.

Most detectors, including all ionization detectors, are non-equilibrium devices. In such a detector the idea is to get a substantial fraction of the deposited energy into a detection channel, and then to collect it as completely as possible before it decays into an undetectable channel. Here “channels” are the various forms that the internal energy of the detector can take, and the “detection channel” might for example be free charge (for an ionization detector), photons, phonons, or quasi-particles. To get good energy resolution, conditions must be made very uniform throughout the detection volume so

that the branching ratio into the desired channel, channel lifetime, and collection efficiency are the same for all events. Even if this were done perfectly, however, statistical fluctuations in the branching still limit the energy resolution. In a typical ionization detector the charge channel gets only about 1/3 of the event energy, and statistical fluctuations in this fraction from event to event produce a fundamental constraint, or “Fano limit”, on resolution [1]. For silicon, this is about 118 eV FWHM (full width at half maximum) at 6 keV.

Some thermal detectors also operate in a non-equilibrium mode, collecting only quasi-ballistic phonons or using sensors sensitive only to excitation energies  $\gg \tau_B^{-1}$ . These can be fast relative to equilibrium devices, since thermal equilibrium often takes a very long time to establish at low temperatures, and with no restrictions on equilibration time they offer even more flexibility in choice of materials. Such detectors may suffer greatly from position dependence in the branching ratio into the detection channel and/or the lifetime and detection efficiency of the relevant excitations. They are also subject to branching statistics that are qualitatively the same as for ionization detectors. But for applications that require large volumes of dielectric material and do not need exceptionally good energy resolution, the speed advantage may outweigh other considerations.

Equilibrium detectors in principle offer the ultimate in energy resolution. With all channels in equilibrium, there are still fluctuations, but now many independent samples can be taken on a single event. For example, consider a thermometer embedded in a copper block. The energy content in the thermometer is the detection channel, while the electrons and phonons in the rest of the block contain most of the total energy. The energy content of the thermometer fluctuates, and the fluctuations can be fractionally large if the thermometer is very small and contains few excitations. However, if all the channels are well-coupled a very large number of independent samples are taken in a short time, and there is no fundamental limit on how accurately the total energy can be determined from the average energy density in the thermometer. In this chapter we will develop a quantitative statement of this argument and discuss the limits on resolution introduced by real thermometers and other departures from the ideal case. At this writing, the best resolution for thermal detectors is  $\sim 3$  eV FWHM at 6 keV, so it is a worthwhile exercise to try to understand how far we can go with these devices.

## 2 Basic Linear Theory of Calorimeters

A simple calorimeter or bolometer has only three parts. As shown in Fig. 1, these are an absorber or thermal mass that contains the event or absorbs the incident power and thermalizes the energy, a perfectly coupled thermometer that measures the temperature increase of the absorber, and a weak thermal link to a heat sink that returns the absorber temperature to some defined

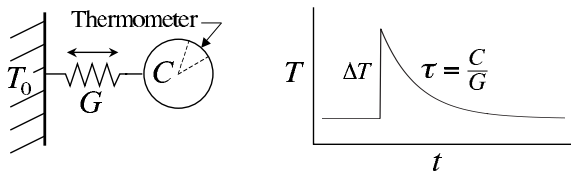


**Fig. 1.** The ideal calorimeter. An instantaneous energy input  $E_0$  will raise the temperature by an amount  $\Delta T = E_0/C$ , and it will then decay back to its starting point with a time constant  $\tau = C/G$

value in the absence of a signal. The absorber can be characterized by its heat capacity  $C$ , the thermal link by its conductivity  $G$ , and the heat sink by its temperature  $T_0$ .

The same configuration can be used to measure a steady power input,  $\Delta P$ , with  $\Delta T = \Delta P/C$ . In this case the device is usually referred to as a bolometer. Such detectors have been used for many years to measure infrared radiation, and their theory is well-developed [2, 3, 4]. In particular, Mather has presented a complete linear theory for simple bolometers with ideal resistive thermometers [4] and made the straightforward extension to adapt these results to energy detectors [5]. These papers are somewhat terse. We will use a slightly different approach to arrive at the same results, and will keep much of the discussion of this section as general as possible so that it can be applied to detectors with all types of thermometers.

Section 2.1 contains a qualitative discussion of the most basic factors that influence energy resolution in any thermal equilibrium detector. It then uses thermometer Johnson noise as a basic example of resolution limited by a white noise source. Section 2.3 analyzes several major noise sources, of which only thermometer and load resistor Johnson noise are specific to resistive thermometers. The derivation in Sect. 2.4 of optimal filtering for energy detection should be entirely general for any linear system. Sect. 2.9 on the symmetry of equations for voltage and current output and Sect. 2.10 on common deviations from the simple detector of Fig. 1 are also quite general. The detailed derivation for resistive thermometers begins in Sect. 2.2. Optimization of the detector and bias power discussed in Sect. 2.5, which also contrasts the optimization of bolometers, or power detectors. Section 2.6 introduces circuit capacitance and inductance, Sect. 2.7 external feedback, and Sect. 2.8 the modifications necessary for thermometers where the resistance depends on voltage or current as well as temperature.

## 2.1 Limits on Energy Resolution: A First Look

One irreducible source of noise comes from the random exchange of energy between the absorber and the heat sink over the thermal link. It is an elementary result of classical statistical mechanics that the magnitude of the

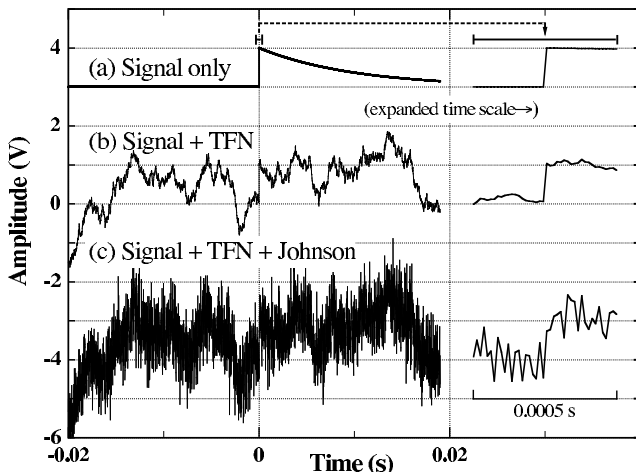


**Fig. 2.** Simulation of an event in an ideal calorimeter – time domain. Expanded views are shown at *right*. (a) Signal only, shows 10 ms thermal decay time constant. (b) Signal plus thermodynamic fluctuations as measured with a noiseless thermometer. The event energy can in principle be measured quite precisely, even though it is here just equal to the r.m.s. magnitude of the fluctuations. (c) Includes Johnson noise from a thermometer of sensitivity  $\alpha = 250$  near optimum bias. The 50 kHz Nyquist frequency of the simulation was used as the noise bandwidth. This is  $\sim 3200 \tau_{\text{sig}}^{-1}$

resulting fluctuations in the energy content of the calorimeter is given by  $\langle \Delta^2 \rangle = B^2$ , independent of the conductance of the link [6]. If the energy carriers in the calorimeter have a mean energy  $B$ , this can be thought of as Poisson fluctuations in their number.

These thermodynamic fluctuations represent a background against which the temperature increase due to an event must be measured, but they do not in themselves limit the accuracy of the measurement. The reason for this can be seen most easily in the time domain, as shown in Fig. 2b. This shows a simulation of a signal in the presence of thermodynamic fluctuation noise (TFN), and it is clear that the sudden increase in temperature due to the event can be measured quite precisely despite the large fluctuations if one looks closely enough at the “corners”. This can be made quantitative in the frequency domain. Figure 3 shows the power spectrum of the exponential signal pulse and the noise power spectrum of the thermodynamic fluctuations. These have the same shape, with a single-pole roll off at  $c = (2)$ , so the signal-to-noise ratio is the same in all frequency bins. Each bin provides an estimate of the signal amplitude, and under rather general assumptions the noise in different bins is uncorrelated, so the signal to noise ratio will improve as the square root of the number of bins averaged. Averaging a bandwidth  $\Delta = \Delta_c = 2 c$  will give a mean error just equal to the thermodynamic

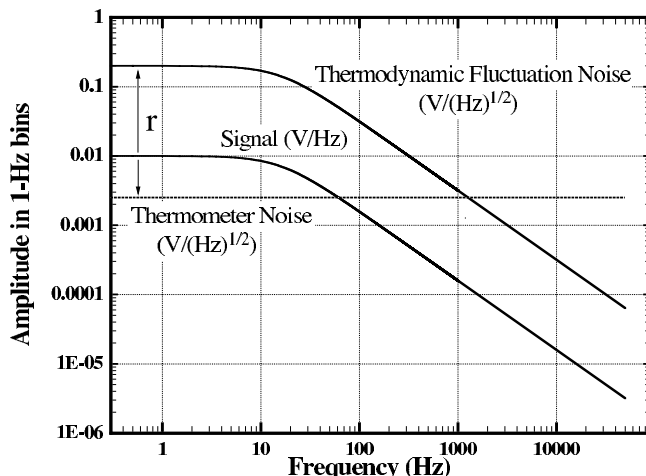


**Fig. 3.** Frequency domain. Note that the signal spectrum has different dimensions than the noise spectra

fluctuations,  $\sqrt{B^2}$ , while  $8\text{ }_c$  will halve this value. By going to arbitrarily high frequencies, the signal can be measured to arbitrary accuracy.

There are a number of things that keep us from reaching this goal. Anything that makes the signal start falling faster than  $1/\omega$  or makes the noise fall more slowly than this will produce a reduction in signal to noise ratio above the frequency – call it  $\omega_{\text{bad}}$  – where this occurs. The resolution improves as the square root of the bandwidth as long as the s/n ratio is constant, but little more is gained once it starts dropping rapidly, so the “useful bandwidth” will be proportional to  $\omega_{\text{bad}}$ . If energy is deposited or thermalized over a finite time, or if the absorber is imperfectly coupled to the thermometer, the signal will have a finite risetime and its power spectrum will have an additional pole above which it falls off as  $1/\omega^2$ . This limitation is discussed in more detail in Sect. 2.10. Alternatively, there might be some additional noise source, such as amplifier noise, that is independent of frequency. Since the thermodynamic fluctuation noise is dropping as  $1/f$ , it will at some point reach this “noise floor,” and the total noise spectrum will flatten out. The energy uncertainty is proportional to  $(\omega_{\text{bad}})^{1/2}$  and to the magnitude of the TFN,  $\sqrt{B^2}$ , so for a high-resolution detector one would like to minimize both.

In the sections below, we analyze in detail the operation of detectors with an ideal resistive thermometer, or thermistor. This important class includes both the standard doped semiconductor thermometer and the promising superconducting transition edge sensor (TES). A thermistor might seem to be a poor choice for a calorimeter, first because it has an irreducible Johnson noise and second because it transduces temperature changes as resistance changes which then require power dissipation to read out. This readout power will warm the detector and increase the energy fluctuations. We will see that

the very high sensitivity of available thermistors does much to mitigate these drawbacks, and they are currently the most common thermometer type. Here we use the Johnson noise of such a thermometer as a concrete example of how a white noise source limits the useful bandwidth, and of the optimal operation of a detector where the thermometer signal to noise ratio increases with readout power.

The effect of the Johnson noise is shown in Fig. 2c. At frequencies above the point where it crosses the thermodynamic fluctuation noise, the signal-to-noise ratio per frequency bin starts dropping linearly with  $\omega$  as can be seen in Fig. 3, and there is less and less gain from including higher-frequency bins in the total. The useful bandwidth is proportional to  $\omega_c$ , the ratio of the low-frequency TFN to the Johnson noise, since the TFN  $\propto 1/\omega$  above  $\omega_c$ , making the crossing point  $\omega_c$ . The Johnson noise is fixed in voltage spectral density, while the TFN is a temperature spectral density, so  $r$  depends on both the thermometer sensitivity in converting temperature to resistance changes and on the readout current that converts these to voltage changes. It is convenient to define a dimensionless local sensitivity for the thermometer

$$\equiv \frac{d\log}{d\log} = -\frac{d}{d} \quad (1)$$

and the readout current can be parameterized by the temperature rise  $\Delta_{\text{Bias}}$  it causes when the dissipated power flows to the sink over the thermal link. For a very small temperature rise, one then gets the simple result that  $r \approx (\Delta_{\text{Bias}}/T_0)^{1/2}$ , where  $T_0$  is the heat sink temperature.

The temperature increase clearly has an optimum value. If the bias current and  $\Delta_{\text{Bias}}$  are very small, then the signal and transduced TFN are also very small in terms of voltage and will be completely dominated by the Johnson noise. On the other hand, a large  $\Delta_{\text{Bias}}$  significantly increases both  $r$  and  $\Delta_{\text{TFN}}$ , greatly increasing the TFN. The optimum value of  $\Delta_{\text{Bias}}$  depends on the temperature coefficients of  $r$  and  $\Delta_{\text{TFN}}$ , and on  $\omega_c$  for  $\omega_c \lesssim 5$ . For practical devices this value is between 0.11 and 0.20 [5].

We can anticipate some results below and express the minimum energy uncertainty due to these two noise sources alone as  $\Delta_E = \sqrt{\Delta_{\text{TFN}}^2 + \Delta_{\text{Johnson}}^2}/T_0$ , where  $T_0$  is the heat capacity at the heat sink temperature [see (37)]. With  $\Delta_{\text{Bias}}$  optimized, the only strong dependence of  $\Delta_E$  is on  $\omega_c$ . Since the signal-to-noise ratio scales with the square root of the usable bandwidth, which is in turn proportional to  $\omega_c$  and  $r$ , we expect  $\Delta_E$  to scale as  $\omega_c^{-1/2}$  for large values of  $\omega_c$ . In fact,  $\Delta_E \approx 5\omega_c^{-1/2}$ , so the energy resolution can be much better than the magnitude of the thermodynamic fluctuations for very high thermometer sensitivities. Inspection of Fig. 3 shows that achieving this result depends on meeting the stringent requirement that there not be another pole in the signal response (due to thermalization time or internal time constants in the detector) at a frequency below about  $\omega_c$ . This is discussed further in Sect. 2.10. Figure 3 also shows that for a very sensitive thermometer, the

Johnson noise will appear negligible compared to the TFN at low frequencies, yet the energy resolution is still entirely dependent on its level.

We will now look more quantitatively at the detector response and noise, both to justify the assertions above and to include additional effects. These are first derived in terms of voltage output, but see Sect. 2.9 for conversion to current output.

## 2.2 Power Responsivity as Function of Frequency

This derivation is done in steps in an attempt to keep it as transparent as possible. I have also introduced several definitions that are more or less commonly used to keep later equations from becoming too dense. These are by no means standardized, and they have been borrowed without attribution from a number of sources based variously on a) breadth of use, b) logical consistency, or c) earliest definition. For those new to thermal calculations, note that most of the familiar solutions to electrical circuits can be taken over using the analogies for thermal variables shown in Table 1.

For historical reasons, the derivations of this section are done with the assumption that the output signal is the voltage across the thermistor. As explained in Sect. 2.9, however, the symmetry of Kirchhoff's circuit equations results in a very simple transformation that will convert these to the current-output form. As a result, for example, the current output of a voltage-biased positive temperature coefficient detector is identical to the voltage output of a current-biased negative temperature coefficient detector. Table 5 gives the current-out form for all of the equations derived in this section. If you have been working primarily with current output (as is usual for TES detectors), you are encouraged to skip ahead and read Sect. 2.9 before continuing.

**Table 1.** Thermal-electrical analogies

Basic quantities	Equivalent equations		
Temperature:	$T \rightarrow V$	(voltage)	$T = P/G \rightarrow V = IR$
Thermal power:	$P \rightarrow I$	(current)	$dT/dt = P/C \rightarrow dV/dt = I/C$
Thermal conductivity:	$G \rightarrow 1/R$	(conductance)	
Thermal energy:	$E \rightarrow Q$	(charge)	
Heat capacity:	$C \rightarrow C$	(capacitance)	

### 2.2.1 D.C. Response

We can write the change in voltage across a resistive thermometer for a given power input as

$$\frac{d}{d_{in}} = \frac{d}{d_{in}} \frac{d}{d} \frac{d}{d} \quad (2)$$

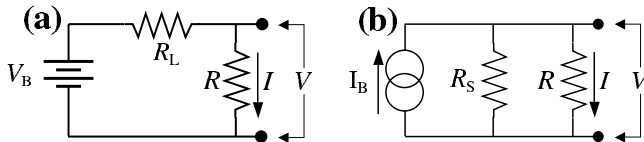


**Fig. 4.** Common detector bias circuits: (a) bias with series load impedance,  $R_L$ , and (b) a circuit often used when  $R_L$  is small. Since (b) is readily converted to (a) by Thevenin's theorem ( $V_B = I_B R_S$ ,  $R_L = R_S$ ), we will consider only (a)

A steady energy input  $\dot{q}_{in}$  will produce a temperature rise in the absorber  $\Delta T = \dot{q}_{in}/\rho C_p$  as it flows through the thermal link to the head sink, so  $d\Delta T/d\dot{q}_{in} = 1/\rho C_p$ . Using the definition (1) for thermometer sensitivity  $\beta$ ,  $dT/d\Delta T = \beta$ . For the bias circuit shown in Fig. 4a,  $d\Delta T/d\dot{q}_{in} = -\beta R_L$  and we can write for the voltage across the thermistor

$$= \dots \Rightarrow \frac{d}{d\dot{q}_{in}} = \dots + \frac{d}{d\Delta T} \frac{d\Delta T}{d\dot{q}_{in}} \Rightarrow \frac{d}{d\dot{q}_{in}} = \frac{-\beta R_L}{1 + \beta R_L} = \beta R_L \quad (3)$$

where for future convenience we define  $\beta_L \equiv \beta R_L / (1 + \beta R_L)$ . For  $\beta L \gg 1$ ,  $\beta_L = 1$ . For lower values of  $\beta L$ ,  $\beta_L$  represents the “loading factor” of the load resistance. Substituting these quantities into (2) and writing the bias power dissipated in the thermometer as  $P = \dot{q}_{in}^2 / R_L$ , we get

$$\frac{d}{d\dot{q}_{in}} = \frac{1}{\beta_L} \quad \beta_L = \frac{1}{1 + \beta R_L} = \frac{\mathcal{L}_0}{R_L} \quad (4)$$

The quantity  $\mathcal{L}_0 \equiv \beta / (1 + \beta)$  appears often in calorimeter calculations, and can be regarded as the dimensionless D.C. “gain”.

### 2.2.2 A.C. Response

Figure 5 shows the thermal circuit equivalent of the calorimeter of Fig. 1. The net current onto the capacitor is  $\dot{q}_{in} - \dot{q}_{out}$ , so we can write

$$\frac{d}{dt} = \frac{1}{C} (\dot{q}_{in} - \dot{q}_{out}) \quad (5)$$

For  $\dot{q}_{in}$  a delta-function, the solution to (5) is clearly just the exponentially decaying pulse shown in Fig. 1. If we assume  $\dot{q}_{in}(t) = q_0 e^{i\omega t}$ , then the solution is

$$q(t) = \frac{q_0 e^{i\omega t}}{(1 + i\omega C)} \quad (6)$$

where  $\omega \equiv 1/C$ . We can then write

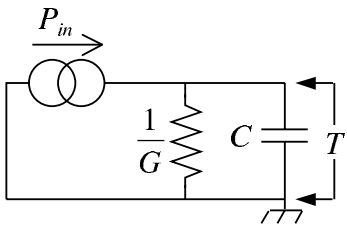


Fig. 5. Thermal equivalent circuit

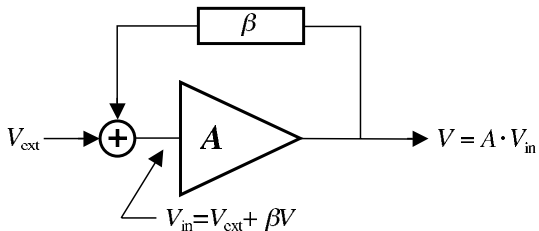


Fig. 6. Feedback circuit

$$\frac{d}{d_{in}} = \frac{1}{(1+i)} \quad (7)$$

and using this in (2) makes (4) become

$$\frac{d}{d_{in}} = \frac{\mathcal{L}_0}{(1+i)} \quad L \equiv ( ) \text{ (V/W)}. \quad (8)$$

### 2.2.3 Electrothermal Feedback

Up to this point we have been ignoring the fact that the bias power  $=^2 =^2$  is part of  $_{in}$ . We can regard the bolometer as an “amplifier” with a thermal power input and an electrical voltage output. The “gain” of this circuit is then given by (8). The contribution to  $_{in}$  due to  $$  can be regarded as “feedback”. Going back to the purely electrical case as shown in Fig. 6, if  $\equiv _{in} |_{V_{ext}}$ , then  $_{in} = _{ext} + _{in}$ , and  $= _{in} = ( _{ext} + _{in})$ . This leads to the standard result for the “closed-loop gain”:

$$_{CL} \equiv \frac{1}{1 -} \quad (9)$$

where the product  $$  is called the “loop gain”.

For our bolometer, the input to  $\mathbf{A}$  is thermal power, and  $_{ext}$  becomes  $_{ext}$ . The output is still voltage, so  $$  and  $$  now have dimensions, although their product necessarily does not. Now  $$  is given by (8) and  $= d/d$  is the change in bias power into the detector caused by a change in voltage at the output, or “electrothermal feedback” (ETF). With  $=$ , we have  $d = d + d$ . From the bias circuit in Fig. 4a,  $d/d = -1/L$  and

$$= \frac{d}{d} = + \left( \frac{-1}{L} \right) = \left( 1 - \frac{1}{L} \right) \quad (10)$$

Taking the gain from (8), the loop gain is then

$$= \left( \frac{L^-}{L^+} \right) \frac{\mathcal{L}_0}{(1+i^-)} \quad L = \left( \frac{L^-}{L^+} \right) \frac{\mathcal{L}_0}{(1+i^-)} = \frac{\mathcal{L}_0}{(1+i^-)} \quad (11)$$

where we have defined

$$\equiv \frac{L^-}{L^+} = 2 \quad L - 1 \quad (12)$$

Our responsivity including electrothermal feedback (the “closed loop gain”) is now

$$v(\ ) \equiv \frac{d}{d_{ext}} = CL = \frac{1}{1 -} = F \quad (13)$$

where  $F$  is the “feedback factor” giving the change in gain introduced by ETF. Therefore

$$F \equiv \frac{1}{1 -} = \frac{1}{1 - \mathcal{L}_0 (1+i^-)} = \frac{1}{1 - \mathcal{L}_0} \frac{1+i^-}{(1-\mathcal{L}_0)} \quad (14)$$

and

$$v(\ ) = \frac{\mathcal{L}_0}{1+i^-} \quad L \quad F = \frac{\mathcal{L}_0}{(1-\mathcal{L}_0)} \frac{1}{1+i^-_e} \quad L \quad (V/W), \quad (15)$$

where  $e \equiv (1 - \mathcal{L}_0)$ . Note that (12) shows the ETF is controlled entirely by the load resistance, since and the resulting feedback depend on the value of  $L$  relative to . For a negative temperature coefficient thermometer ( and  $\mathcal{L}_0 < 0$ ), one gets negative feedback for  $L < 1$  and positive feedback for  $L > 1$ . For a positive temperature coefficient, the reverse is true. In both cases, there is *no* electrothermal feedback when  $L = 1$ .

We will point out in Sect. 2.5 that in the idealized linear case we are considering here electrothermal feedback has no effect on the NEP, energy resolution, or count rate capability. However, for real detector systems there can be large practical benefits. Positive ETF has been used to boost signal levels to reduce the effect of amplifier noise, but the biggest benefits come from exploiting the large negative ETF available with very high sensitivity thermistors. This can stabilize gain and reduce nonlinearity effects, as first discussed extensively by Irwin [7]. One can get some idea of the importance of this for high- detectors by trying to imagine using a high gain operational amplifier without negative feedback. Flattening the gain over a wide bandwidth and stabilizing the operating point are two major benefits, although

there are differences of degree from the op-amp case. The nonlinearities are worse, the loop gain usually does not have the very large values needed to stabilize the gain at 1 to the desired accuracy, and itself depends on a varying and on for finite values of  $L$ . Section 3 discusses consequences of large signals, where single events heat the detector enough to change its properties and alter the response to additional events that occur before the detector has returned to its equilibrium temperature. Negative ETF shortens the cooling time by a factor of 1 ( $1 - \mathcal{L}_0$ ), and can greatly reduce response variability between events at high count rates when such large signals are present.

## 2.3 Major Noise Terms

Now that we have the voltage responsivity of the detector to an arbitrary signal power input, we need to find the noise voltage at the output in order to determine how precisely signals can be measured. We calculate the output noise voltage below for the most important noise terms. These are generally uncorrelated, so the total output noise can be found by simply adding their squares. A common figure of merit for power detectors is the r.m.s. power required at the input at a given frequency to produce an output voltage equal to the r.m.s. noise voltage in a unit bandwidth at that frequency. This noise equivalent power, or NEP, is given by  $n(\lambda) v(\lambda)$ .

### 2.3.1 Thermodynamic Fluctuation Noise

One unavoidable source of noise is the statistical fluctuations in the energy content of the detector produced as it exchanges energy with the heat sink. One can derive directly from fundamental assumptions and definitions of statistical mechanics that

$$\langle \Delta^2 \rangle = B^2 \quad (16)$$

where  $B$  is the detector heat capacity [6]. This, however, says nothing about their frequency spectrum. The fluctuations are produced by a noise power flow over the thermal link  $G$ , and the power in a unit bandwidth at frequency could be represented by the  $\omega$  in of Fig. 5, resulting in temperature fluctuations given by (6). If we assume for now that this power spectrum is a shot noise and therefore independent of frequency, then  $\omega_0$  is constant. As shown, for example, by Richards [8] this can be integrated over all frequencies to give the total energy fluctuation (16), which requires the spectral density of  $\omega$  to be

$$\frac{2}{TFN} = 4 B^2 \quad (W^2 Hz) \quad (17)$$

A white spectrum is the only fixed spectrum that will give the correct result (16) for an arbitrary choice of  $\omega$ , and is also the result of detailed

calculations of the power flow on the link for cases with simple physics. Equations (16) and (17) are valid only in thermal equilibrium, where the temperature  $T_0$  of the detector is equal to the heat sink temperature  $T_0$ . In general, the detector will be at some higher temperature, most usually due to the bias power  $P_B$  used to read out the thermometer. The power spectral density in the link will then depend on details of the nature of the link. Two limiting cases have been worked out. When the mean free path of the energy carriers is large compared to the length of the link (the radiative or specular limit), Boyle and Rogers [9] find

$$\frac{P_{TFN}}{2} = 4 \cdot P_B \cdot T_0^2 \cdot \frac{\beta+2 + 1}{2} \quad (\text{W}^2 \text{ Hz}) \quad (18)$$

while for mean free path small compared to the length (diffusive limit) Mather [4] gets

$$\frac{P_{TFN}}{2} = 4 \cdot P_B \cdot T_0^2 \cdot \frac{+1}{2 + 3} \cdot \frac{2\beta+3 - 1}{\beta+1 - 1} \quad (\text{W}^2 \text{ Hz}) \quad (19)$$

where  $\beta \equiv \beta_0$  (here and for the remainder of the chapter), and  $\beta$  is the assumed temperature dependence of  $G$ . Note that we are using the most conventional definition for the link thermal conductivity,  $\kappa_{END} \equiv$

INTO LINK  $\kappa_{END}$ , which is different at the two ends of a link with a temperature gradient, but is always positive. How this  $\kappa$  is related to the thermal conductivity constant is shown nicely in [4]. In this Chapter, without a subscript refers to the detector or hot end. Equations (18) and (19) have been normalized to  $P_B$  and  $T_0$  at the heat sink temperature for later convenience in optimizing the value of  $\beta$ . We also collect the thus-normalized link properties into functions  $\text{LINK}(\cdot, \text{link physics})$  such that (18) and (19) can both be written as

$$\frac{P_{TFN}}{2} = 4 \cdot P_B \cdot T_0^2 \cdot \text{LINK}(\cdot, \text{link physics}) \quad (20)$$

Since  $P_{TFN}$  is equivalent to an external power input  $P_{ext}(\cdot)$  in each frequency interval, we can use (14) to write the output noise spectral density as

$$\begin{aligned} n(\cdot)_{TFN} &= P_{TFN} \cdot V(\cdot) \\ &= \sqrt{4 \cdot P_B \cdot T_0^2 \cdot \text{LINK}(\cdot, \text{link physics})} \cdot \frac{\mathcal{L}_0}{1+i} \cdot L_F(V \sqrt{\text{Hz}}) \end{aligned} \quad (21)$$

### 2.3.2 Thermometer Johnson Noise

Another irreducible noise source for detectors with resistive thermometers is the Johnson or Nyquist noise in the thermometer. This can be modeled as

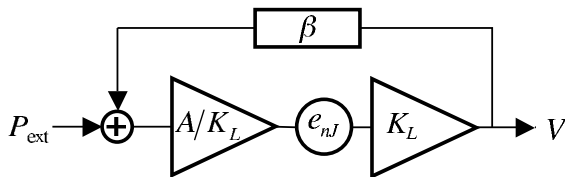


**Fig. 7.** Johnson noise source equivalent circuit

a voltage source with spectral density  $n_{J,ext}$  V  $\sqrt{\text{Hz}}$  in series with a noiseless (but temperature sensitive) resistance  $R$ , where  $n_{J,ext} = (4 \pi k_B T)^{1/2}$ . In the bias circuit of Fig. 4a, the output voltage in a unit bandwidth would be  $d = n_{J,ext} R / (R + L) = n_{J,ext} R / L$  if there were no thermal effects. However, the bias current  $I$  does work  $n_{J,ext} I$  on the Johnson noise source. This is physically located in the detector and therefore heats it and changes the resistance. The total power is  $IV$ , so the expression for  $d$  in (10) is still correct to first order in  $n_{J,ext}$ , and we can use the equivalent circuit shown in Fig. 7. We can then write  $d = n_{J,ext} R / L + d_{\text{noise}}$ , which can be solved for the output noise spectral density due to the Johnson noise:

$$n_{J,\text{Therm}}(f) = d_{\text{noise}} = n_{J,ext} \frac{L}{1 - f^2} = n_{J,ext} R F \sqrt{4 \pi k_B T} \quad (22)$$

The same result can be obtained by direct differentiation of  $d = d_{\text{noise}} + n_{J,ext}$ , noting that  $d_{\text{noise}} = (d_{\text{noise}} - d_{\text{noise}})(d_{\text{noise}} + d_{\text{noise}})(d_{\text{noise}} - d_{\text{noise}})$ , with  $d_{\text{noise}} = 0$  and  $d_{\text{noise}} = -d_{\text{noise}}$ , and retaining only first-order terms in  $n_{J,ext}$ .

### 2.3.3 Load Resistor Johnson Noise

Referring to Fig. 4a, we can model the load resistor Johnson noise as a voltage source with spectral density  $n_{JRL} = \sqrt{4 \pi k_B T L}$ , where  $L$  is the physical temperature of the load resistor. Following the same approach used above for detector Johnson noise, we first assume no thermal effects. We then have a simple voltage divider, and the change in detector voltage  $d$  produced by  $n_{JRL}$  is  $d = n_{JRL} (1 + L/R)$ . We write this as  $n_{JRL}(1 + L/R) L$ , so we can simply substitute  $n_{JRL} L$  for  $n_{J,ext}$  in the circuit of Fig. 7.

Now, however, the expression for  $d$  in (10) must be modified to  $d = (R + n_{JRL} L) L$ . This gives rise to an extra term in  $d$ , which becomes  $d = d_{\text{noise}} + n_{JRL} L$ . The  $d_{\text{noise}}$  term is still taken care of by the feedback loop, and we can represent the new term as  $d_{\text{noise}} = n_{JRL} L$  in Fig. 7. The circuit equation is then  $d = n_{JRL} (1 + L/R) L + (1 + n_{JRL} L) L$ . Solving for  $d$  and using  $F = 1/(1 + i)$ :

$$\begin{aligned} n_{J,\text{Load}}(f) &= d_{\text{noise}} = \frac{L + n_{JRL} L}{1 - f^2} \left( \frac{1}{L} \right) n_{JRL} \\ &= \frac{n_{JRL}}{L} \left( 1 + \frac{\mathcal{L}_0}{1 + i} \right) L F \sqrt{4 \pi k_B T L} \end{aligned} \quad (23)$$

At the cost of considerably more algebra, this can also be obtained by direct evaluation of the derivatives in  $d \frac{d}{d} n_{JRL} = (d \frac{d}{d}) (d \frac{d}{d} n_{JRL})$ . It is worthwhile to calculate the first of these, since  $d \frac{d}{d}$  is the dynamic impedance  $(\omega)$  of the detector, a function that is easily measured and provides a valuable experimental diagnostic of detector characteristics [10]. The usual approach is to differentiate  $\frac{d}{d} = \frac{d}{d}$ , writing  $d \frac{d}{d} = (d \frac{d}{d}) (d \frac{d}{d}) (d \frac{d}{d})$  with  $d \frac{d}{d}$  from (7) and differentiating  $\frac{d}{d} = \frac{d}{d}^2$  to get  $d \frac{d}{d} d$ . Substituting and solving for  $d \frac{d}{d}$  gives

$$( ) \equiv \frac{d}{d} = \frac{1 + \mathcal{L}_0 + i}{1 - \mathcal{L}_0 + i} \quad (24)$$

The response to load resistor noise is then just the voltage-divider formed by  $L$  and  $( )$ :  $n( ) = n_{JRL} ( ) [ ( ) + L]$ . With some manipulation, this gives the result (23). The load resistor Johnson noise can normally be made negligible by choosing  $L \gg 1$ , but care must be taken to choose a resistor type that does not produce large amounts of “excess noise” when the bias current flows through it.

### 2.3.4 Amplifier Noise

Amplifier noise is normally specified as a voltage noise source  $n_A$  in series with the amplifier input and a current noise source  $n_A$  in parallel with the input as shown in Fig. 8. The voltage noise then simply adds to the noise at the detector. If we had modeled the load resistor Johnson noise as its Thevenin-equivalent current source in parallel with  $L$ , we would see that the amplifier current noise source occupies effectively the same position (the battery can be shorted as far as changing signals are concerned). So we use the responsivity from (23) for this, and the total noise from the amplifier referred to the voltages at its input is

$$n_{-AMP}( ) = \sqrt{\frac{n_A^2}{n_A}( ) + \frac{n_A^2}{n_A}( ) \left[ \left( 1 + \frac{\mathcal{L}_0}{1+i} \right) - L_F \right]^2} \quad (25)$$

This assumes that the amplifier current and voltage noises are uncorrelated, which may not be the case.

It is usually possible to make the amplifier noise negligible for the commonly-used thermistor types. Doped semiconductor thermometers are easily made with resistances of tens of megohms. At this source resistance, silicon junction field effect transistors (JFETs) operated at  $\sim 120$  K have noise temperatures less than 5 mK, far below the operating point of today’s detectors. Superconducting transition edge sensors (TESs) typically have resistances of less than one ohm, where superconducting quantum interference device (SQUID) amplifiers are even better than JFETs at high impedance. Multiplexing multiple detectors onto an amplifier eats into this margin however, and amplifier noise can become a major consideration for such schemes.

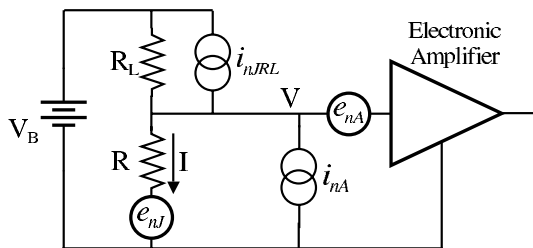


**Fig. 8.** Equivalent circuit showing definitions of amplifier noise and Johnson noise sources

### 2.3.5 Photon Background Noise

Photon background absorbed by a detector has two effects. First, it is a power source that raises the temperature of the detector while adding no readout power. This degrades the detector performance and requires a different optimization, as discussed for example in [11]. Second, the quantized photon energy produces shot noise, which appears as a noise power at the input to the detector in the same way that TFN does. The input noise power can be calculated by integrating the shot noise over the photon spectrum. For high-efficiency systems and  $\ll B$  it is necessary to take into account the Bose statistics that greatly increase the fluctuation level. A useful form of this calculation is given in [4], while a more extensive treatment can be found in [12]. This background is often very important for infrared detectors, but for calorimeters detecting higher energy photons it is generally assumed that it can be made negligible through proper optical filtering. In practice, it is much more difficult than it seems to actually achieve this, and “light leaks” should be one of the suspects when unexpected noise is observed.

### 2.3.6 Additional Thermometer Noise

All resistive thermometers must have Johnson noise, but they may have additional noise sources as well. These are specific to the thermometer type, and are discussed in the following chapters. Their contribution to the output voltage can usually be treated in the same way that the Johnson noise was above. For instance, thermometer resistance fluctuations  $n$  can be multiplied by  $F$  to give a voltage fluctuation that is substituted for  $n_J$  in (22). This gives

$$n - \Delta R = F L n \quad \text{or} \quad \left\langle \frac{\Delta^2}{2} \right\rangle = (F L)^2 \left\langle \frac{\Delta^2}{2} \right\rangle \quad (26)$$

## 2.4 Optimal Filtering and Energy Resolution

We assume the signal is of the form  $s(t) = s_0(t)$ , where  $s_0(t)$  is known and independent of  $s(t)$ .<sup>1</sup> The problem is to extract the best estimate of  $s_0(t)$

<sup>1</sup> In this section,  $t$  is time

in the presence of a known random noise of spectral density  $n(\ )$ . This problem can be solved rather generally for a linear system, which we have assumed in the analysis of this section. The calculation is difficult in the time domain because the noise in different time bins is correlated if its spectrum is frequency dependent. In the frequency domain, however, the noise in different bins is uncorrelated on the condition that it is stationary, which means that its statistical properties do not change during the signal pulse. This seems likely to hold for almost any system in the linear small-signal limit. (Filtering of large signals is discussed in Sect. 3).

We take the discrete Fourier transform of  $(\ )$  to obtain the values of  $i$ , which is the signal amplitude in the  $^{\text{th}}$  frequency bin. The root mean square value of the noise voltage in a bin is given by  $i$ . Each  $i$  is proportional to  $0$ , so if the noise is uncorrelated, every bin provides an independent estimate of its magnitude. We can choose a set of weights  $i$  and combine all the bins to get an expected value for the signal of  $= \sum_{i=1}^{\infty} i i$ , and a corresponding noise fluctuation

$$\Delta_{\text{rms}} = \left[ \sum_{i=1}^{\infty} (i i)^2 \right]^{1/2}$$

We want choose  $i$  to maximize  $\Delta_{\text{rms}}$ , so we take the derivative of this ratio with respect to an arbitrary  $k$  and set it equal to zero, giving

$$k = \frac{k}{2} \left[ \sum_{i=1}^{\infty} (i i)^2 \Big/ \sum_{i=1}^{\infty} i i \right] \quad (27)$$

The ratio  $\Delta_{\text{rms}}$  is clearly independent of any common scale factor on the  $i$ , so we simply drop the constant term in brackets. The  $i$  are in general complex. The denominator of  $\Delta_{\text{rms}}$  depends only on the absolute value of the  $i$ , so we are free to choose their phases to maximize the numerator. This is accomplished by making each term entirely real, with

$$i = \frac{\hat{i}}{2} \quad (28)$$

where  $\hat{i}$  is the complex conjugate of  $i$ . This will make  $a$  pure cosine sum, and in the time domain the filtered signal  $(\ )$  will always peak at  $t = 0$ .

To get the resulting energy resolution, we must be careful with the normalization of the Fourier transforms. We will use the pair

$$(\ ) = \int_{-\infty}^{\infty} (\ ) e^{-i2\pi f t} dt \quad \text{and} \quad (\ ) = \int_{-\infty}^{\infty} (\ ) e^{i2\pi f t} dt \quad (29)$$

We assume a power input to the detector  $0(\ )$ , with Fourier transform

$$\int_{-\infty}^{\infty} \text{v}_0(\omega) e^{i2\pi f t} d\omega = \text{v}_0(f) \quad (30)$$

Using the detector responsivity (15), gives the detector output voltage spectrum  $\text{v}(f) = \text{v}_0 \text{v}(\omega)(f) = \text{v}_0(\omega)$ . The optimal filter in (28) is  $\hat{n}^2(f)$ , so the filtered signal becomes  $\text{FILT}(f) = \text{v}_0 \hat{n}^2(f) \text{v}(f)$ . Transforming this to the time domain,

$$\begin{aligned} \text{FILT}(f) &= \text{v}_0 \int_{-\infty}^{\infty} \frac{\hat{n}^2(\omega)}{\hat{n}^2(\omega)} e^{-i2\pi f t} d\omega \quad \text{and} \\ \text{FILT}(0) &= 2 \text{v}_0 \int_0^{\infty} \frac{|\hat{n}(\omega)|^2}{\hat{n}^2(\omega)} d\omega \end{aligned} \quad (31)$$

where in the second integral we have made use of the fact that  $\hat{n}(\omega)$  is the transform of a real function of  $\omega$ , so  $|\hat{n}(-\omega)|^2 = |\hat{n}(\omega)|^2$ .  $\text{FILT}(0)$  is our best estimate of the input signal amplitude. (In practice, the filter coefficients might have an arbitrary normalization, and the energy scale would be determined empirically from events of known energy.)

The filtered noise is  $\text{n-FILT}(f) = \hat{n}^2(f) \text{v}(f) = \hat{n}^2(f) \text{v}_n(f)$ . This is uncorrelated at different frequencies, so we can sum its absolute square and get

$$\langle \text{n-FILT}^2 \rangle = \int_0^{\infty} \frac{|\hat{n}(\omega)|^2}{\hat{n}^2(\omega)} d\omega \quad (32)$$

the mean square fluctuation expected at any time, including  $f = 0$ . We can normalize it to energy units by dividing by  $\text{FILT}(0)$  from (31) with  $\text{v}_0$  equal to one energy unit:

$$\langle \Delta^2 \rangle = \frac{\int_0^{\infty} \frac{|s(f)|^2}{e_n^2(f)} d\omega}{\left( 2 \int_0^{\infty} \frac{|s(f)|^2}{e_n^2(f)} d\omega \right)^2} = \frac{1}{4 \int_0^{\infty} \frac{|s(f)|^2}{e_n^2(f)} d\omega} = \frac{1}{4 \int_0^{\infty} \frac{|S_V(f)|^2 |p(f)|^2}{e_n^2(f)} d\omega} \quad (33)$$

Assuming the energy in an event is deposited all at once,  $s(f)$  is a delta function at  $f = 0$ , and  $|s(f)| = 1$ . Using the definition of noise equivalent power as  $\text{NEP}(f) \equiv \text{v}_n(f) / \text{v}(f)$ , the right-most expression in (33) then gives:

$$\Delta_{\text{rms}} = \left( \int_0^{\infty} \frac{4 d\omega}{\text{NEP}^2} \right)^{-1/2} \quad (34)$$

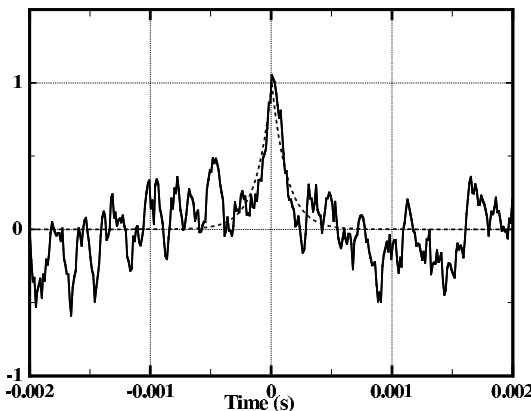


**Fig. 9.** Optimally filtered pulse of Fig. 2c. The r.m.s. noise at the filter output is about 0.22. A noise-free pulse from the same filter is shown by the *dashed line*

The assumption of instantaneous energy input is often not a good one, so the more general form in (33) is also useful.

Figure 9 shows the pulse in Fig. 2c after application of the optimal filter. Note that this output pulse is a factor of  $\sqrt{2^2 + 1}$  faster than the pulse from the detector in Fig. 2, where  $\gamma$  is the ratio of TFN to Johnson noise at low frequencies discussed in Sect. 2.1. If negative electrothermal feedback were used, the pulse from the detector would be much faster, and the noise spectrum would look quite different, but the output of the optimal filter would be unchanged.

## 2.5 Optimization of Detector and Operating Conditions

Since (34) shows that the energy resolution depends only on NEP, we will first calculate the contributions to this by dividing the noise voltage spectral densities derived in Sect. 2.3 by the responsivity  $v$  from (15). The results are summarized in Table 2.

We first notice that the electrothermal feedback and load resistor loading terms  $F$  and  $L$  have dropped out of the NEP for both TFN and thermometer Johnson noise. This is as expected, since any noise sources that appear inside a feedback loop or ahead of it will be affected by the feedback in exactly the same way as the signal, leaving the signal to noise ratio and NEP unchanged. The output of the optimal filter is  $\sigma_o |( )|^2 \frac{2}{n}( )$ , which is proportional to the square of the signal to noise ratio, so the shape of the pulses is also unchanged by feedback. This means that if  $L$  is made greater than  $\gamma$  to “turn on” negative electrothermal feedback, the pulses at the detector will decay faster because  $\tau_e$  is shortened, but the pulses at the output of the optimal filter will be unchanged. On the other hand, if there is a “knob” that allows  $\gamma$  to be increased with no electrothermal feedback,

the pulses from the detector simply get higher, while at the output of the optimal filter they will get faster.

**Table 2.** NEP from major noise sources

Definitions:

$$\begin{aligned}\alpha &\equiv \frac{d\log R}{d\log T} & \mathcal{L}_0 &\equiv \frac{\alpha P}{GT} & K_L &\equiv \frac{R_L}{R_L + R} \\ b &\equiv \frac{R_L - R}{R_L + R} = 2K_L - 1 & K_F &\equiv \frac{1}{1 - b\mathcal{L}_0} \frac{1 + i\omega\tau}{1 + i\omega\tau/(1 - b\mathcal{L}_0)}\end{aligned}$$

Responsivity (15):

$$S(\omega) = \frac{\mathcal{L}_0}{I} \frac{1}{1 + i\omega\tau} K_L K_F \quad (\text{V/W})$$

Thermodynamic fluctuation noise from (21):

$$e_{n-TFN}(\omega) = \sqrt{4k_B T_0^2 G_0 F_{\text{LINK}}(t, \beta)} \frac{\mathcal{L}_0}{I} \frac{1}{1 + i\omega\tau} K_L K_F \quad (\text{V}/\sqrt{\text{Hz}})$$

$$\text{NEP}_{TFN}^2(\omega) \equiv e_{n-TFN}^2(\omega) / S^2(\omega) = 4k_B T_0^2 G_0 F_{\text{LINK}}(t, \beta) \quad (\text{W}^2/\text{Hz})$$

Thermistor Johnson noise from (22):

$$e_{nJ-Therm}(\omega) = \sqrt{4k_B T R} K_L K_F$$

$$\text{NEP}_{J-Therm}^2(\omega) = 4k_B T P (1 + \omega^2 \tau^2) / \mathcal{L}_0^2$$

Load resistor Johnson noise from (23):

$$e_{nJ-Load}(\omega) = \sqrt{4k_B T_L R_L} \frac{R}{R_L} \left(1 + \frac{\mathcal{L}_0}{1 + i\omega\tau}\right) K_L K_F$$

$$\text{NEP}_{J-Load}^2(\omega) = 4k_B T_L P \frac{R}{R_L} \frac{(1 + \mathcal{L}_0)^2 + \omega^2 \tau^2}{\mathcal{L}_0^2}$$

Amplifier noise from (25):

$$e_{n-AMP}(\omega) = \sqrt{e_{nA}^2(\omega) + i_{nA}^2(\omega) \left[ R \left(1 + \frac{\mathcal{L}_0}{1 + i\omega\tau}\right) K_L K_F \right]^2}$$

$$\text{NEP}_{AMP}^2(\omega) = e_{nA}^2 I^2 \frac{(1 + \omega^2 \tau^2)}{\mathcal{L}_0^2 K_L^2 K_F^2} + i_{nA}^2 R P \frac{(1 + \mathcal{L}_0^2) + \omega^2 \tau^2}{\mathcal{L}_0^2}$$

The amplifier voltage noise however comes in after the feedback loop and so is unaffected by it. The NEP from this then depends inversely on the signal, and so is improved by positive electrothermal feedback ( $F > 1$ ) and made worse by negative electrothermal feedback ( $F < 1$ ) and load resistor loading ( $L < 1$ ). The amplifier current noise goes in ahead of the loop and

is modulated by the feedback, so the  $s$  again cancel out in the NEP. The same is true of load resistor Johnson noise, which when taken as a current noise  $\frac{2}{n_{JRL}} = 4 \frac{B}{L} \frac{L}{L}$  is entirely equivalent to  $\frac{2}{n_A}$ . The only dependence on  $L$  is in  $\frac{2}{n_{JRL}}$  itself.

Optimization depends on its starting assumptions. We will assume that there is some minimum heat sink temperature  $o$  it is practical to provide, that the detector, due to constraints on desired volume, available materials, and construction methods has some minimum heat capacity  $o$  at this temperature, and that we have a thermometer technology that offers some maximum sensitivity  $.$  In this case, our optimization problem is how to get the best energy resolution for given values of  $o$ ,  $o$ , and  $.$  The remaining adjustable parameters are  $,$ ,  $L$ , and  $,$  the bias power. The noise sources are independent, making the total  $NEP^2$  simply the sum of the individual contributions.  $NEP_{TFN}^2$  and  $NEP_{J-Therm}^2$  do not depend on  $o$  and  $L$ , so we are free to choose these to minimize the other contributions. We assume that making  $a$  sufficiently good match to the noise resistance of the amplifier will make this term negligible, and then choose  $L$  large enough relative to  $o$  that we can ignore  $NEP_{J-Load}^2$ . This leaves  $NEP_{Total}^2 \approx NEP_{TFN}^2 + NEP_{J-Therm}^2$ , and  $o$  and  $L$  as our free parameters.

While we have been assuming a small-signal limit, the temperature increase  $\equiv o - o_0$  produced by the bias power is not necessarily small, and can cause significant changes in the heat capacity of the detector and thermal conductivity of the link. We therefore need a model for these changes. We will assume power-law temperature dependencies:  $(o) = o_0^\beta$ , where  $\beta = (o_0)$ , and  $(o) = o_0^\gamma$ . Fortunately these are fairly accurate representations for most materials over the required temperature range, with  $\beta = 1$  for metals, 3 for insulators, 4 for electron–phonon coupling in metals, and  $\sim 5$  (at least empirically) for electron–phonon coupling in semiconductors. Heat capacity scaling is  $\gamma = 1$  for metals, 3 for insulators, and 0–1 for doped semiconductors. Magnetic materials and superconductors have more complicated behavior, but can usually be approximated by some power law over the range from  $o_0$  to  $o$ . It will be convenient to use  $\beta$  as a parameter rather than  $\gamma$ , which can now be expressed in terms of  $\beta$  as:

$$\begin{aligned} (\beta) &= \frac{d}{d\beta} \implies \beta = \int_0^P d\beta = \int_{T_0}^T (\beta) d\beta \\ &= \int_1^t o_0^\beta o_0 d\beta = \frac{o_0^{t+1} - o_0}{t+1} \quad (35) \end{aligned}$$

We use this expression for  $\beta$  to write  $\mathcal{L}_0 \equiv (\beta) = (1 - \frac{o_0^{t+1}}{t+1}) (t+1)$ . Substituting the above and  $\beta \equiv \gamma = o_0^{-\gamma-\beta} o_0$  into the expressions for  $NEP_{TFN}^2$  and  $NEP_{J-Therm}^2$  from Table 2, we get

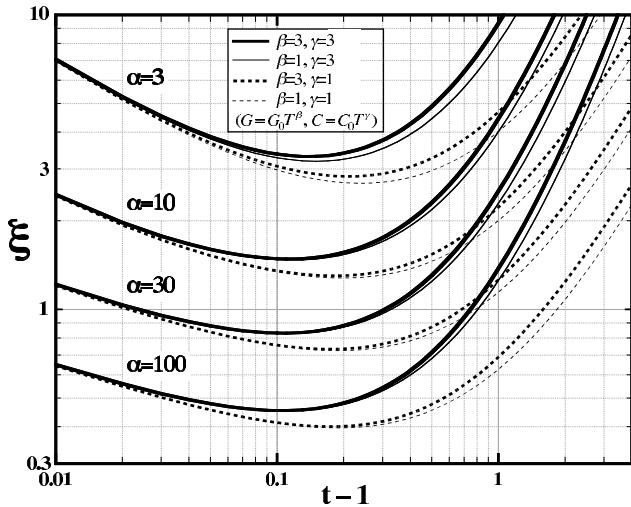


**Fig. 10.** Normalized energy resolution as a function of the temperature increase  $t - 1 = \Delta T_{\text{Bias}}/T_0$  produced by bias power. The effective link temperature function  $\text{FLINK}$  appropriate for radiative transfer was used, but the result is not appreciably different for the diffuse scattering case

$$\text{NEP}_{\text{Total}}^2(\alpha) = 4 \frac{B}{B_0} \frac{2}{\alpha} \left\{ \text{LINK}(\alpha) + \frac{(\alpha+1)^{-2\beta+3}}{2(\beta+1-1)} [1 + (\alpha)^2] \right\} \quad (36)$$

This is readily integrated in (34) to give the expected energy resolution:

$$\Delta_{\text{RMS}} = \left[ \left( \frac{B}{B_0} \right)^2 \frac{4(\alpha+1)^{\gamma+2}}{2(1-(\beta+1))} \sqrt{1 + \frac{2(\beta+1-1)}{(\alpha+1)^{2\beta+3}} \text{LINK}(\alpha)} \right]^{1/2} \quad (37)$$

Note that  $B$ , the thermal conductivity of the link, does not appear in this expression, although its temperature dependence does. This means that we are free to choose  $\alpha$  to give any desired time constant (but see Sect. 2.8 and Sect. 2.10 for limits to the validity of this statement for real detectors and thermometers). We can see that for  $\alpha$  sufficiently large to neglect the 1 under the radical,  $\Delta_{\text{RMS}} \propto \sqrt{\frac{B}{B_0}}$ .

We have only the bias power available for optimization, so we insert the appropriate function for  $\text{LINK}$ , which would be from (18) for a hot-electron device or one with a very specular conducting link and from (19) for a perfectly diffusive link, and adjust  $\alpha$  to minimize  $\Delta_{\text{RMS}}$ . Figure 10 shows the variation of  $\Delta_{\text{RMS}}$  with  $\alpha$  for various values of  $\beta$ ,  $\gamma$ , and  $\text{LINK}$ . The dependence of  $\Delta_{\text{RMS}}$  on  $\beta$  and  $\gamma$  is weak, although  $\gamma$  significantly affects the optimum value of  $\alpha$ . Figure 2 of [5] gives  $\alpha_{\text{opt}}$  and  $\Delta_{\text{RMS, min}}$  as functions of  $\beta$  for some values of  $\gamma$  and  $\text{LINK}$ .

For power detectors, the figure of merit is rather than  $\Delta$ , and the form of (36) makes it appear that this depends on rather than . Mather, however, argues in [11] that the proper figure of merit is always the NEP at some chosen frequency , and writes  $\text{NEP}^2(\omega) = (4 B_0^2 \sigma_0) \cdot (L^2 + R^2)$ , where and are respectively the normalized link conductivity and background power. Conductivity is assumed to be a free parameter, so can be minimized with respect to both and . The NEP optimized for any given frequency then has qualitatively the same dependencies as  $\Delta$ , with  $\propto \omega^{-1/2}$  for sufficiently large .

## 2.6 Complex Load Impedance

The derivations above do not require that the load resistance,  $L$ , be real and we are free to include intentional or stray capacitive and inductive effects in its value. With the bias circuit of Fig. 4a, the high end of the load resistor is fixed, and capacitance in parallel with the detector is equivalent to a parallel capacitance on the load resistor and can be accounted for in this fashion. This is not true when a time varying signal is applied to the top of the load resistor (as in Sect. 2.7 below). In this case, and to handle an inductor in series with the detector, it would be necessary to redo the analysis to explicitly include these components (but see Sect. 2.9). For high impedance thermometers, such as doped semiconductors, stray capacitance effects usually dominate, while for very low impedance thermometers such as superconducting TES, only stray inductance is normally important.

## 2.7 External Electrothermal Feedback

The practical advantages of electrothermal feedback, and particularly of large amounts of negative ETF, were discussed above and will come up again in Sect. 3. Large feedback effects require the absolute value of the loop gain,  $\mathcal{L} = \mathcal{L}_0 (1 + i \omega)$ , to be  $\gg 1$  at low frequencies. For  $L \neq 0$ ,  $\mathcal{L} \equiv (L - R) / (L + R)$  will always lie between  $-1$  and  $+1$ , so this would normally require  $|\mathcal{L}_0| \gg 1$ , which can only be obtained with extremely sensitive thermometers.

It is possible however to get arbitrarily large feedback effects with low-thermometers by using the gain of the electronic amplifier. Suppose the thermometer voltage  $V_{\text{Th}}$  is amplified by a factor  $d$  and then added to the bias supply voltage  $V_{\text{Bias}}$  at the top of  $L$ . We can then write the current as  $I = (V_{\text{Bias}} + V_{\text{Th}} - V_{\text{Feedback}}) / L$ , and  $dV_{\text{Feedback}}/dV_{\text{Th}} = (d - 1) / L$ . All of the equations derived in Sect. 2 depend on  $L$  only through  $dV_{\text{Feedback}}/dV_{\text{Th}}$ , so we take this external feedback into account simply by substituting an effective value of  $L$  equal to  $L(1 - d)$  for all occurrences of  $L$  in  $F$  and  $L$  (the explicit appearance of  $L$  in the expression for load resistor Johnson noise is only to give the magnitude of the Johnson noise current source  $I_{\text{nJRL}} = \sqrt{4 k_B T_L L}$ , which

is not affected by feedback). In particular the expression for  $\frac{d}{dV}$  will have a zero in the denominator for  $\frac{d}{dV} = \frac{L}{L + \frac{1}{\mathcal{L}_0}}$ , so  $\mathcal{L}_0$  and  $L$  can become arbitrarily large positive or negative with  $V$  sufficiently close to this critical value.

All of the equations derived above are then valid for this situation with the exception of the one for amplifier voltage noise. Since the amplifier noise is now inside the feedback loop, it is also modified by the feedback, and in principle one can get the benefits of negative ETF without the potentially adverse effect on  $\text{NEP}_{\text{AMP}}$  produced by intrinsic negative ETF. Of course, improvements in  $\text{NEP}_{\text{J-Therm}}$  and energy resolution depend on  $\mathcal{L}_0$  and not on the feedback, and come only from increasing the thermometer sensitivity. Also, when  $\mathcal{L}_0$  is large it becomes very sensitive to changes in  $V$ , so problems with stability in the face of large signals or changing background power will limit the practical amount of external feedback.

## 2.8 Thermometer Nonlinearities

Up to this point we have assumed that the thermometer resistance depends only on  $V$ , i.e.  $R = R(V)$ . More generally,  $R = R(V, T)$ . This behavior is normally referred to as “nonlinearity”, since it makes ohm’s law a nonlinear equation. For small signals, however, it can be linearized around the operating point and characterized by the two partial derivatives

$$\frac{\partial R}{\partial V} \Big|_T \quad \text{and} \quad \frac{\partial R}{\partial T} \Big|_V \quad (38)$$

The following chapters discuss specifics of the nonlinear behavior for the most common types of resistive thermometers. It is straightforward however to incorporate the linearized form into the relations derived so far. This was first done for  $\frac{dR}{dV}(V)$  and  $\frac{dR}{dT}(T)$  by Mather [13].

For example, to re-derive the D.C. response in (8) from (2), we must find  $\frac{dR}{dV}$  when  $R = R(V, T)$ . We can write

$$\frac{dR}{dV} = \left. \frac{\partial R}{\partial V} \right|_T + \left. \frac{\partial R}{\partial T} \right|_V \quad \Rightarrow \quad \frac{dR}{dV} = \left. \frac{dR}{dV} \right|_T + \left. \frac{dR}{dT} \right|_V \frac{dV}{dT} \quad (39)$$

Using  $\frac{dR}{dV}$  from (39), this can be solved for  $\frac{dR}{dV}$ :

$$\frac{dR}{dV} = \left. \frac{dR}{dV} \right|_T \left( 1 - \left. \frac{dR}{dT} \right|_V \frac{V}{L} \right)^{-1} \quad (40)$$

Substituting this into (2) with the other terms the same as for (8) gives

$$\frac{dR}{dV} = \frac{\mathcal{L}_V}{(1 + i_V) \left( 1 - \frac{L}{L + \frac{1}{\mathcal{L}_0}} V \right)} \quad (41)$$

where we have changed the subscript on  $\mathcal{L}_0$  as a reminder that it is now  $\mathcal{L}_V \equiv \frac{dR}{dV}$ . Next, we can easily compute the changes to the loop gain

that controls feedback effects, since from (10) remains the same, and the gain in (41) differs from (8) only by the additional term  $1/(1 - K_{L-}V)$ . (Note that the feedback factor is unrelated to  $V$ .) If we still want to write  $\mathcal{L}$  as  $V\mathcal{L}_V$ , then  $\mathcal{L}$  must be modified to  $\mathcal{L} = V/(1 - K_{L-}V)$ . As  $V$  is usually negative, the new term is degenerative and can significantly reduce both gain and the effects of feedback.

**Table 3.** Response with thermometer nonlinearity:  $R = R(T, V)$

Definitions:

$$\begin{aligned}\alpha &\equiv \left. \frac{\partial \log R}{\partial \log T} \right|_V & \beta &\equiv \left. \frac{\partial \log R}{\partial \log V} \right|_T & \mathcal{L} &\equiv \frac{\alpha P}{GT} & K_{L-} &\equiv \frac{R_L}{R_L + R} \\ b &\equiv \frac{R_L - R}{R_L(1 - \beta) + R} & K_{F-} &\equiv \frac{1}{1 - b \mathcal{L}} \frac{1 + i\omega\tau}{1 + i\omega\tau/(1 - b \mathcal{L})}\end{aligned}$$

Responsivity:

$$S(\omega) = \frac{\mathcal{L}}{I(1 - K_{L-}\beta)} \frac{1}{1 + i\omega\tau} K_{L-} K_{F-} \quad (42)$$

Impedance:

$$Z(\omega) \equiv \frac{dV}{dI} = \frac{(1 + i\omega\tau) + \mathcal{L}}{(1 + i\omega\tau)(1 - \beta) - \mathcal{L}} R \quad (43)$$

Thermodynamic fluctuation noise:

$$e_{n-TFN}(\omega) = \sqrt{4k_B T_0^2 G_0 F_{LINK}(t, \beta)} \frac{\mathcal{L}}{I(1 - K_{L-}\beta)} \frac{1}{1 + i\omega\tau} K_{L-} K_{F-} \quad (44)$$

Thermistor Johnson noise:

$$e_{nJ-Therm}(\omega) = \sqrt{4k_B T R} \frac{1}{(1 - K_{L-}\beta)} K_{L-} K_{F-} \quad (45)$$

Load resistor Johnson noise:

$$e_{nJ-Load}(\omega) = \sqrt{4k_B T_L R_L} \frac{R}{R_L} \left(1 + \frac{\mathcal{L}}{1 + i\omega\tau}\right) \frac{1}{(1 - K_{L-}\beta)} K_{L-} K_{F-} \quad (46)$$

Amplifier noise:

$$e_{n-AMP}(\omega) = \sqrt{e_{nA}^2(\omega) + i_{nA}^2(\omega) \left[ \frac{R}{(1 - K_{L-}\beta)} \left(1 + \frac{\mathcal{L}}{1 + i\omega\tau}\right) K_{L-} K_{F-} \right]^2} \quad (47)$$

This process can be continued for the response to major noise sources with the results shown in Table 3. Note that the responsivity and major noise terms all include the added factor of  $1/(1 - \frac{L}{V} \cdot V)$  and the modified  $F_V$ . These will therefore cancel out in the NEP calculation, leaving this and the energy resolution unchanged. A reservation must be made about this regarding thermistor Johnson noise. Johnson noise and the nonlinearity are both internal to the thermistor. The result in (45) was derived assuming that the Johnson noise voltage modulated its own resistance, but the physics behind the nonlinearity is unspecified and it is not obvious that this should always be the case.

## 2.9 Voltage Output versus Current Output

We have pointed several advantages of negative electrothermal feedback, and one often wishes to maximize it. Since the feedback factor is  $1/(1 + \mathcal{L}_0)$ , we then want  $\mathcal{L}_0$  negative and as large as possible. For  $\mathcal{L}_0 = 0$ ,  $\mathcal{L}_0$  is negative, so we need  $\mathcal{L}_0 = (L - ) / (L + )$  close to  $+1$ . This is readily done by making  $L \gg R$ , since this also minimizes its loading effects ( $L \approx 1$ ) and its Johnson noise contribution to the NEP. However, for positive temperature coefficient thermometers, we want  $\mathcal{L}_0$  close to  $-1$ , and this requires  $L \ll R$ . We would then have significant load resistor Johnson noise, and the signal level would be reduced to a point where amplifier noise is important.

The obvious solution in the latter situation is to switch to using the current through the thermistor rather than the voltage across it as the output signal. Signal loading effects are then minimized for  $L \ll R$ , and it is easily shown that this condition also makes load resistor Johnson noise insignificant.

**Table 4.** Dual circuit transformations

$V$ (across a component)	$\longrightarrow$	$I$ (through transformed component)
$I$ (through a component)	$\longrightarrow$	$V$ (across transformed component)
$R$ (resistance)	$\longrightarrow$	$1/R$ (conductance)
$C$ (parallel)	$\longrightarrow$	$L$ (series)
$L$ (series)	$\longrightarrow$	$C$ (parallel)

Rather than re-derive all of the relations in Sect. 2 for current output, we can make use of the simple dual circuit transformation to change them to this form. This allows us to switch all of the ‘ $V$ ’s for ‘ $I$ ’s (and ‘ $I$ ’s for ‘ $V$ ’s) if accompanied by the other substitutions given in Table 4. It will also work for more complicated circuits that incorporate stray capacitance and inductance. The circuit transformation is usually obvious in our simple cases. If the effects of voltage amplifier parallel input capacitance have been included, for instance, this would just become the series inductance of the current

amplifier input in the transformed equation. For more complex circuits, one should consult the full algorithm for the transformation under “Duality” in a suitable textbook [14].

The results for all the formulae of this section are given in Table 5. Only the versions including thermistor nonlinearity are given; to recover the linear form, set  $I = 0$ . Nonlinear thermistors are characterized by partial derivatives of  $(\cdot)$  rather than  $(\cdot)$ . The NEP contributions from TFN and thermistor Johnson noise are unchanged. Those from the load resistor and amplifier are given in the table. These and other useful current-output formulae are derived directly in [15].

## 2.10 Complications

The detector of Fig. 1, where the absorber, thermometer, and structure are regarded as a single isothermal entity, is clearly an idealization, as is the supposition that deposited energy in an event is instantaneously in equilibrium in all available channels. In this section we discuss the effects of some of the more important complications.

### 2.10.1 Internal Time Constants and Internal Fluctuation Noise

A detector can more reasonably be modeled as separate components: a thermometer, an absorber, and perhaps some structure, connected by thermal resistances. In addition, any component with more than one channel for energy content, such as a metal with both lattice phonons and conduction electrons, should be modeled as two or more parts with their own heat capacities connected by appropriate thermal conductances. This has two potentially major effects, which we illustrate by a simple (but realistic) example where the energy-absorbing part of the detector has a finite thermal conductivity,

$\lambda_A$ , to the rest of the detector, including the thermometer. When an event deposits energy in the absorber, the thermometer temperature will have a finite risetime, limited by  $\lambda_A$  and the heat capacities of the absorber and thermometer. The qualitative effect of this is apparent by looking at Fig. 2b. A better quantitative impression can be obtained from Fig. 3, where  $\lambda_A$  introduces another pole in the signal response. Above the frequency of this second pole, the signal to TFN ratio, which is otherwise completely independent of frequency, will start to drop as  $1/\omega$ . This is the same effect that otherwise occurs above the frequency where the TFN drops below the level of the Johnson noise, so it will not seriously impact the energy resolution if the new pole is at a considerably higher frequency than this crossing point. The crossing, where (21) and (22) are equal, is at  $\sim 4$  times frequency of the main pole of the signal, so this is an increasingly stringent requirement as the thermometer sensitivity becomes very high. Put another way, to get the improvement in energy resolution expected from an increase in thermometer

**Table 5.** Equations for current output with  $R = R(T, I)$ 

Dual Transformations and Definitions:

$$\begin{aligned} \alpha &\rightarrow -\alpha, \quad \alpha \equiv \frac{\partial \log R}{\partial \log T} \Big| \\ \beta &\rightarrow -\beta, \quad \beta \equiv \frac{\partial \log R}{\partial \log I} \Big| \\ K_{L^-} &\rightarrow 1 - K_{L^-} = K_{L^-} \equiv \frac{R}{R_L + R} \quad \mathcal{L} \rightarrow -\mathcal{L}, \quad \mathcal{L} \equiv \frac{\alpha P}{GT} \\ b &\equiv \frac{b}{(1 - K_{L^-}) \beta} \rightarrow -b, \quad b \equiv \frac{b}{(1 + K_{L^-}) \beta}; \quad b \equiv \frac{R - R}{R + R} \\ K_{F^-} &\equiv \frac{1}{1 - b} \frac{1 + i\omega\tau}{\mathcal{L}} \frac{1 + i\omega\tau/[1 - b] \mathcal{L}}{1 + i\omega\tau/[1 - b] \mathcal{L}} \rightarrow \frac{1}{1 - b} \frac{1 + i\omega\tau}{\mathcal{L}} \frac{1 + i\omega\tau/[1 - b] \mathcal{L}}{1 + i\omega\tau/[1 - b] \mathcal{L}} \equiv K_{F^-} \end{aligned}$$

Responsivity – from (42):

$$S(\omega) = \frac{-\mathcal{L}}{V(1 + K_{L^-}) \beta} \frac{1}{1 + i\omega\tau} K_{L^-} K_{F^-} \quad (48)$$

Admittance – from (43):

$$A(\omega) \equiv \frac{dI}{dV} = \frac{(1 + i\omega\tau) - \mathcal{L}}{(1 + i\omega\tau)(1 + \beta) + \mathcal{L}} \frac{1}{R} \quad (49)$$

Thermodynamic fluctuation noise – from (44):

$$i_{n-TFN}(\omega) = \sqrt{4k_B T_0^2 G_{LINK}(t, \beta)} \frac{\mathcal{L}}{V(1 + K_{L^-}) \beta} \frac{1}{1 + i\omega\tau} K_{L^-} K_{F^-} \quad (50)$$

Thermistor Johnson noise – from (45):

$$i_{nJ-Therm}(\omega) = \sqrt{4k_B T / R} \frac{1}{(1 + K_{L^-}) \beta} K_{L^-} K_{F^-} \quad (51)$$

Load resistor Johnson noise – from (46):

$$i_{nJ-Load}(\omega) = \sqrt{4k_B T_L / R_L} \frac{R_L}{R} \left(1 - \frac{\mathcal{L}}{1 + i\omega\tau}\right) \frac{1}{(1 - K_{L^-}) \beta} K_{L^-} K_{F^-} \quad (52)$$

$$NEP_{J-Load}^2(\omega) = 4k_B T_L P \frac{R_L}{R} \frac{(1 - \mathcal{L})^2 + \omega^2 \tau^2}{\mathcal{L}^2} \quad (53)$$

Amplifier noise – from (47):

$$i_{n-AMP}(\omega) = \sqrt{i_{nA}^2(\omega) + e_{nA}^2(\omega) \left[ \frac{1}{R(1 + K_{L^-}) \beta} \left(1 - \frac{\mathcal{L}}{1 + i\omega\tau}\right) K_{L^-} K_{F^-} \right]^2} \quad (54)$$

$$NEP_{AMP}^2(\omega) = i_{nA}^2 V^2 \frac{(1 + K_{L^-})^2 (1 + \omega^2 \tau^2)}{\mathcal{L}^2 K_{L^-}^2 K_{F^-}^2} + e_{nA}^2 P \frac{(1 + \mathcal{L}^2) + \omega^2 \tau^2}{\mathcal{L}^2} \quad (55)$$

sensitivity, you must ensure that internal time constants in the detector are of order times shorter than the main detector time constant.

The second detrimental effect is that random exchange of energy between parts of the detector can produce additional thermodynamic fluctuation noise. This “internal TFN” is another term that must be added to the total NEP. Reference [10] derives the proper equations for a few models of detector internal structure that are reasonable representations of some real detectors. These include both the altered frequency response to signals and the internal TFN. A general approach is outlined that allows algebraic equations to be derived for other internal structures, but these quickly become unwieldy. A general matrix method is demonstrated in [15] that allows numerical solutions to be obtained for very complex structures.

There is one additional effect of internal thermal resistances. If the thermometer itself is isolated from the rest of the detector, as for instance by the electron–phonon coupling in a thermistor where the resistance depends on the electron temperature, then the bias power dissipated in the thermistor will create a temperature drop across the coupling resistance. If the temperature coefficient is large, and it is 4–5 for electron-lattice coupling, then as this temperature drop increases the thermometer temperature quickly becomes insensitive to the external temperature. This loss of effective thermometer sensitivity is a particularly severe problem for doped semiconductor thermistors, as discussed in the next chapter. Models worked out in [10] include this effect, as well as the increased Johnson noise, additional internal TFN, and loss of high frequency signal response that go with it.

### 2.10.2 Thermalization Noise

We have been assuming that all of the event energy comes instantaneously into equilibrium with at least the absorber portion of the detector. It is possible however for part of the energy to go into a channel that is so weakly coupled with the others that it takes a significant length of time to come into equilibrium with them. For example, when an X-ray photon is absorbed in a semiconductor about one-third of the energy initially goes into producing electron–hole pairs. At low temperatures, these are mostly trapped on impurity sites, and recombinations that return this energy to the phonon system can be very long. If the equilibration time is not short compared with , then it will have an effect on detector performance. There are three forms of such effects. The first is simply due to part of the energy being completely lost, or slowed in delivery relative to the main thermal time constant so that it is measured with poorer signal to noise ratio. These change the optimal filter and the energy scale to make the resolution worse, but are still independent of event energy. This would not usually be regarded as thermalization “noise”, although it involves a loss of resolution related to thermalization processes. To some extent it is completely unavoidable: thermalization in a

phonon system cannot be faster than the sound crossing time of the detector, for instance. For effects like this where the time is not too long, the solution is to slow the detector by making it smaller, increasing until it is at least comparable to the thermalization time. *Twerenbold* [16] includes a basic discussion of the physics involved in this process.

The other forms of thermalization effects are ones that vary from one event to the next. The variations can be either statistical, such as the Fano fluctuations in the fraction of energy going into ionization, or position-dependent. Position dependence can come from detector geometry or from local variations in a parameter like defect density. This kind of “noise” generally causes a loss of energy resolution that is proportional to the event energy. Position dependence produced by variations in the energy collection time can be reduced by making the detector slower if the application allows it, or by altering the filtering to compromise between signal-to-noise ratio and insensitivity to risetime.

### 3 Limitations of Linear Theory

The linear theory of Sect. 2 is simple and allows many useful generalizations, but the unfortunate truth is that many thermal detectors, particularly the small ones applied to high-resolution X-ray measurements, are often run well into the nonlinear regime. As shown in (37), the fundamental parameters determining energy resolution are the bath temperature and detector heat capacity, and it is technologically practical to make detectors for soft X-rays with such small heat capacities that  $\Delta$  is a substantial fraction of  $\theta_0$  when a photon is absorbed. (Detectors for higher energy photons and other things with small cross sections usually require such a massive absorber that nonlinearity is not a problem.) All the thermodynamic parameters tend to change rapidly with temperature, and thermometer characteristics can be the worst offender. The very sensitive and promising superconducting transition edge sensor (TES) represents the extreme case. Its resistance can go from zero to the full normal value with less than 1% temperature change. Within this range,  $\Delta$  is changing rapidly, and outside of it the thermometer is completely saturated. Modest amounts of nonlinearity can be handled simply by careful calibration of the pulse height vs. energy relation. However, significant increases in temperature will change the noise characteristics during the pulse, leading to correlations between the noise at different frequencies and invalidating the optimal filter as calculated in Sect. 2.4.

One standard way of handling this is to increase the heat capacity of the detector until the nonlinearity is acceptable for the highest event energy of interest,  $\theta_{\text{Max}}$ . This has the interesting consequence that the energy resolution becomes independent of thermometer sensitivity. If the width of the superconducting-to-normal transition is narrowed,  $\Delta$  is approximately proportional to the inverse of the width, and the heat capacity must be similarly

increased to keep the event within the same part of the transition. The energy resolution, which scales approximately as  $(\dots)^{1/2}$ , is unchanged by this, but is now proportional to  $\frac{1}{\text{Max}}^{1/2}$ . There is still a major benefit to increasing  $\dots$ , however. Since  $\dots$  is to be increased above the minimum technologically feasible value, this extra “budget” allows a wider choice of materials to be used for constructing the detector that can provide faster and more complete thermalization or better thermal contact. This makes the detector a better approximation of an ideal device, particularly if short time constants are desired.

*Fixsen et al. [17, 18]* have taken another approach and developed an optimal filtering algorithm that properly accounts for the noise correlations between frequencies. They find that for any amount of nonlinearity, including complete saturation of the TES, the resulting resolution is no worse than it would have been had  $\dots$  been increased to lessen the nonlinear effects. This is a very important result, since it means that much better resolution can be obtained at all lower energies with the same detector. The signal processing is more complex, but could be worthwhile for an application that covers a wide range of event energies. Some of these authors have proposed that the best design would be to choose a  $\dots$  that just starts to saturate completely at  $\text{Max}$ . This is at least a factor of three lower heat capacity than would normally be required to keep nonlinearity to a moderate level, and results in a significant resolution improvement at low energies. Heat capacity could be reduced still further without hurting the resolution at  $\text{Max}$ , but with the detector fully saturated there is no way to detect an accidental additional event that adds to the total energy. Somewhat below saturation, the pulse shape distortion produced by the pileup can still be detected and used to reject the event. For applications where the best energy resolution over a very wide dynamic range is important, it might also be practical to include a second thermometer with lower sensitivity for the sole purpose of detecting pileup while the main thermometer is saturated.

Up to this point, we have been considering isolated events, but the large nonlinearities of thermal detectors can make pileup a much more severe problem than it is in the usually rather linear ionization detectors. For the small-signal linear case, pileup considerations are the same as they are for charge detectors. The only thing that matters is the output of the filter, and with a sensitive thermometer the signal-to-noise ratio is good at frequencies far above the thermal corner at  $c = \dots (2 \dots)$ . Therefore even the optimal filter can show little pileup at event separations much smaller than the thermal time constant, and other filters can be used that allow even higher rates with some compromise in energy resolution.

For pulses big enough to show nonlinear effects, however, a second event that arrives before the detector has actually cooled sufficiently will show a different response than the first event. For large events, this could require several thermal time constants. Here negative electrothermal feedback, ei-

ther intrinsic or external, can make a big difference. As can be seen in (15), feedback will speed the actual cooling rate by a factor of  $(1 - \mathcal{L}_0)$ , allowing counting rates to increase by a similar amount before pileup effects become important. This points out a drawback of the scheme proposed above where large events are allowed to completely saturate the thermometer, since feedback then quits operating and thermal recovery times become much longer. How serious this is depends on the application. For many astronomical observations, for instance, the rate of high energy events is very small compared to that at lower energies, so the increased deadtime from these might be a small price to pay for significantly improved resolution at low energies.

## 4 Other Thermometer Types

There are many other potential thermometer systems. Besides the reactive analogs of thermistors [ ( ) and ( )], we have pyro-electric [ ( )] and paramagnetic [ ( )] devices. Any temperature-dependent physical parameter that can be measured is a potential thermometer, but the only one I know of in addition to the above list that has been used for low temperature detectors is the tunneling current of an NIS junction. It would be handy to make some grand synthesis of all thermometer types so they could be compared directly, but in practice qualitative and quantitative differences in the operation change the approximations that can be used and often require entirely different figures of merit. The only universal quantity is the thermodynamic fluctuation noise. As we have seen, this does not itself limit the energy resolution, but it does set a scale where the resolution is proportional to the square root of the bandwidth over which the signal to noise ratio is approximately constant. This frequency range is where TFN is the dominant noise source and the signal frequency response is dominated by the same thermal time constant that determines the TFN spectrum. For resistive thermometers, the Johnson noise provided a fundamental and in most cases attainable limit to how large this bandwidth could be. For other thermometer types, the Johnson noise may be negligible, and some other noise source or attenuation of the signal frequency response will become the limiting factor.

The reactive thermometers appear to be much like thermistors. They have an output that depends on both their sensitivity  $\equiv d\log \frac{dI}{dV}$  and the bias current, but the dissipation is only  $\frac{1}{2}$  of an equivalent resistive element. Here  $\mathcal{Q}$  is the standard “Quality Factor” for a reactive element, among whose equivalent definitions is  $\mathcal{Q} \equiv (\text{energy stored energy per cycle}) / (\text{energy dissipated per cycle})$ . The optimum bias current is therefore increased by  $\mathcal{Q}^{1/2}$  and the Johnson noise is reduced by  $\mathcal{Q}^{-1/2}$ . This improves the TFN to Johnson noise ratio by a factor of  $\mathcal{Q}$ , so we should be able to define an effective sensitivity  $\mathcal{E}_{\text{eff}} \equiv \dots$  and take over most of the thermistor results. Although most of these devices have relatively low  $\mathcal{Q}$ 's, available  $\mathcal{Q}$ 's can be very high (often  $10^5 - 10^6$ ). Unfortunately, something else usually dominates

the noise or the signal has another pole before the TFN drops below the level of the Johnson noise. In these cases  $\text{Eff}$  is not a good figure of merit, and the optimization will probably look quite different than it does for a resistive thermometer. So each of these new thermometer types must be analyzed individually, at least until it is determined whether it is amplifier noise, internal time constants, or both, or something entirely different, that dominates the behavior. The result for the optimal filter, at least in the form of (33), should be generally applicable for any detector in the small-signal limit.

## 4.1 Kinetic Inductance

The kinetic inductance thermometer uses the steep temperature variation in magnetic penetration depth in a superconductor just below its transition temperature to modulate the inductance of a nearby coil [19, 20]. Usually an insulating film is deposited on top of a thin superconducting plane, and the coil is deposited on top of that. The detector is well matched to a SQUID amplifier, and in principle could be very sensitive, with  $Q$  values close to  $10^6$ . Versions have recently been proposed that construct an array of pixels with resonators of different frequencies, allowing the entire array to be read out in parallel with multi-frequency microwave excitation. This requires no physical connections to the detector array, and puts almost all of the readout electronics at room temperature [21]. Detectors of this type developed thus far operate far from equilibrium.

## 4.2 Magnetic

The net magnetization of a system of spins of moment  $\mathbf{m}$  in a magnetic field depends on temperature as  $\tanh(-\beta B)$ . The spin system must be made dilute enough to avoid strong spin-spin interactions, which severely limits the sensitivity per unit volume. However, tiny changes in magnetization can be sensed with a pickup coil and SQUID amplifier, and no excitation is required. This means that only third-order effects produce dissipation from the readout system, and the power input can be tiny [22]. The system has almost no intrinsic Johnson noise, so the useful bandwidth is limited instead by some combination of the amplifier noise, internal thermodynamic fluctuation noise, and internal coupling times that drop off the signal relative to the TFN at high frequencies.

With a magnetic thermometer, the signal amplitude is approximately proportional to the thermometer volume. When the amplifier noise dominates, an optimum design will then enlarge the thermometer until its heat capacity is equal to that of the rest of the detector. This changes the scaling of energy resolution vs. absorber  $V$ , and makes signal level per unit heat capacity an important figure of merit for the thermometer. If the amplifier and its coupling to the field are good enough, the limiting factor will be the internal

TFN and signal roll-off due to internal time constants. The most fundamental of these is the coupling time between the spin system and the lattice, which for high resolution should be much smaller than the detector time constant. The very small power dissipation would allow small values for  $G$  and large thermal time constants, but application requirements and technical feasibility put a limit on this, so another fundamental figure of merit for magnetic thermometers is the spin-lattice relaxation time. This is normally quite long in dielectric materials, so metallic systems are favored. As different aspects of these detectors are improved, the optimization and figures of merit will change.

Magnetic thermometers have received much less attention than thermistors up to this point, but they have recently attained resolution levels comparable to the best thermistor results [23]. Since their different optimization gives them additional advantages in certain applications, they now appear very promising and are discussed in much more detail in a subsequent chapter in this volume.

### 4.3 NIS Junctions

These are tunnel junctions with a superconductor on one side and a normal metal on the other. They are biased so that only electrons in the high-energy tail of the thermal distribution in the normal metal can tunnel, making the tunneling current extremely sensitive to temperature [24]. These devices can also be designed to refrigerate themselves, and there is some interest in using them as “microcoolers” for other detectors [25].

### 4.4 Pyro-electric

Like the magnetic thermometer, this sensor requires no excitation. For an all-metallic system, it should be possible to make an extremely fast detector. The figures of merit and optimization are quite different from most other sensors, which leads to the possibility that there are applications for which it might have an advantage. However its basic properties do not seem to favor it for very high energy resolution [26].

### Acknowledgements

A number of people read early drafts of this manuscript and made helpful comments. I thank in particular Kent Irwin, Lindsay Rocks, Yoh Takei, and John Vaillancourt for their thorough reviews and thoughtful suggestions that have greatly improved the final version. This work was supported in part by NASA grant NAG5-5404.

## References

- [1] G.W. Fraser: *X-ray Detectors in Astronomy* (Cambridge Univ. Press, Cambridge 1989). [2](#)
- [2] R.C. Jones: J. Opt. Soc. Am. **37**, 879 (1947). [3](#)
- [3] F.J. Low: J. Opt. Soc. Am. **51**, 1300 (1961). [3](#)
- [4] J.C. Mather: Appl. Opt. **21**, 1125 (1982). [3, 12, 15](#)
- [5] S.H. Moseley, J.C. Mather, D. McCammon: J. Appl. Phys. **56**, 1257 (1984). [3, 6, 21](#)
- [6] F. Mandl: *Statistical Physics* (Wiley; New York 1971) p 58. [4, 11](#)
- [7] K.D. Irwin: Appl. Phys. Lett. **66**, 1998 (1995). [10](#)
- [8] P.L. Richards: J Appl. Phys. **76**, 1 (1994). [11](#)
- [9] W.S. Boyle, K.F. Rodgers, Jr.: J. Opt. Soc. Am. **49**, 66 (1959). [12](#)
- [10] M. Galeazzi, D. McCammon: J. Appl. Phys. **93**, 4856 (2003). [14, 28](#)
- [11] J.C. Mather: Appl. Opt. **23**, 584 (1984). [15, 22](#)
- [12] J. Zmudrias: Appl. Opt. **42**, 4989 (2003). [15](#)
- [13] J.C. Mather: Appl. Opt. **23**, 3181 (1984). [23](#)
- [14] B. Friedland, O. Wing, R. Ash: *Principles of Linear Networks* (McGraw-Hill, New York 1961) pp113–117. [26](#)
- [15] E. Figueroa-Feliciano: Ph.D. thesis, Stanford University (2001). [26, 28](#)
- [16] D. Twerenbold: Rep. Prog. Phys. **59**, 349 (1996). [29](#)
- [17] D.J. Fixsen, S.H. Moseley, B. Cabrera, E. Figueroa-Feliciano: in *Low Temperature Detectors*, F.S. Porter, D. McCammon, M. Galeazzi, C.K. Stahle (Eds.), Proc. 9th Int'l Workshop on Low Temperature Detectors in Madison, Wisconsin, July 2001 (AIP, New York 2002), p 339. [30](#)
- [18] D.J. Fixsen: Nucl. Instrum. Methods A**520**, 555 (2004). [30](#)
- [19] D.B. McDonald: Appl. Phys. Lett. **50**, 775 (1987) [32](#)
- [20] L. Hao, J.C. Macfarlane, P. Josephs-Franks: J.C. Gallop, IEEE Trans. Appl. Supercond. **1**, 622 (2003). [32](#)
- [21] P.K. Day, H.G. LeDuc, B.A. Mazin, A. Vayonakis, J. Zmuidzinas: Nature **425**, 817 (2003). [32](#)
- [22] C. Enss, A. Fleischmann, K. Horst, J. Schönefeld, J. Sollner, J.S. Adams, Y.H. Huang, Y.H. Kim, G.M. Seidel: J Low Temp. Phys. **121**, 137 (2000) [32](#)
- [23] A. Fleischman, M. Link, T. Daniyarov, H. Rotzinger, C. Enss, G.M. Seidel: Nucl. Instrum. Methods A**520**, 27 (2004) [33](#)
- [24] R. Leoni, B. Buonomo, M.G. Castellano, F. Mattioli, G. Torrioli, L. Di-Gaspere, F. Evangelisti: Nucl. Instrum. Methods A**520**, 44 (2004) [33](#)
- [25] M. Nahum, T.M. Eiles, J.M. Martinis: Appl. Phys. Lett. **65**, 3123 (1994) [33](#)
- [26] A. Gulian, K. Wood, G. Fritz, A. Gyulamiryan, V. Nikogosyan, N. Giordano, T. Jacobs, D. Van Vechten: Nucl. Instrum. Methods A **444**, 232 (2000) [33](#)

# Index

- absorber, 3
- amplifier noise, 14
- bias circuit, 8
- bias power, 20
- bolometer, 3
- branching ratio, 2
- calorimeter
  - basic linear theory, 2–7, 29
  - ideal, 3
- capacitance, 22
- closed-loop gain, 9
- current output, 25, 27
- current-biased, 7
- detector response, 7
- dual circuit transformation, 25
- duality, 26
- electrothermal feedback, 9–11, 19, 30
  - external, 22
- energy resolution, 21
  - first look, 3
  - optimal filtering, 15
- ETF, 9
- $F_{\text{LINK}}$ , 12
- feedback
  - external, 22
- feedback factor, 10
- Fourier transforms, 16
- gain, 9
- heat sink, 2
- inductance, 22
- internal fluctuation noise, 26
- internal time constant, 26
- Johnson noise, 12
- kinetic inductance thermometer, 32
- load impedance, 22
- load resistor noise, 13
- loop gain, 9
- magnetic calorimeters, 32
- NEP, 11, 18
- NIS junctions, 33
- noise, 11–15
  - amplifier noise, 14
  - Johnson noise, 12–13
  - load resistor noise, 13–14
  - photon noise, 15
  - thermodynamic fluctuations, 11–12
  - thermometer noise, 15
- noise correlations, 30
- noise equivalent power, 11
- noise sources, 18
- nonlinear regime, 29
- nonlinearity, 23
- optimal filtering, 15–18
  - energy resolution, 15
- optimization, 18
- paramagnetic thermometer, 32
- photon noise, 15
- pileup, 30
- power responsivity, 7–11
- pyro-electric thermometer, 33
- saturation, 30
- spectral density, 11

- stray capacitance, 22  
stray inductance, 22  
thermal circuit, 8  
thermal conductivity, 12  
thermal link, 2  
thermal-electrical analogies, 7  
thermalization noise, 28  
thermistor, 5  
thermodynamic fluctuation noise, 4, 11  
thermometer noise, 15  
useful bandwidth, 5  
voltage output, 25  
voltage-biased, 7

# Semiconductor Thermistors

D. McCammon

Physics Department, University of Wisconsin, Madison, WI 53706, USA

[mccammon@wisp.physics.wisc.edu](mailto:mccammon@wisp.physics.wisc.edu)

**Abstract.** Semiconductor thermistors operating in the variable range hopping conduction regime have been used in thermal detectors of all kinds for more than fifty years. Their use in sensitive bolometers for infrared astronomy was a highly developed empirical art even before the basic physics of the conduction mechanism was understood. Today we are gradually obtaining a better understanding of these devices, and with improvements in fabrication technologies thermometers can now be designed and built with predictable characteristics. There are still surprises, however, and it is clear that the theory of their operation is not complete. In this chapter we give an overview of the basic operation of doped semiconductor thermometers, outline performance considerations, give references for empirical design and performance data, and discuss fabrication issues.

## 1 Introduction

Early thermal detectors were hampered by the lack of practical thermometers with good sensitivity at low temperatures. Thermocouples and metallic resistance thermometers rapidly lose sensitivity below room temperature. Semiconductor thermistors were in use at high temperatures, but the readily available semiconductors – mostly metal oxides – became much too resistive when cooled. All of the most sensitive devices discussed in *Jones'* classic 1947 paper on the ultimate sensitivity of thermal detectors operated at room temperature [1].

By 1950 there were conference reports indicating that doped germanium could be a suitable thermometer at temperatures as low as 1 K [2], but reproducibility was elusive. Material purity and characterization were difficult issues, and providing low-noise electrical contacts was a poorly understood black art. By 1961, *Frank Low* had developed practical gallium-doped germanium devices operating at liquid helium temperature with noise equivalent power (NEP) below  $10^{-12} \text{ W/Hz}^{1/2}$  [3]. The radio frequency resistivity of this material made it a reasonable match to free space, so the sensing element could also be used as an efficient radiation absorber, and these “germanium bolometers” were soon applied to the burgeoning field of infrared astronomy.

Today, developments by the semiconductor electronics industry have solved many of the materials and fabrication issues. Germanium and silicon are readily available with more than adequate purity, essentially noise-free

contacts are easily formed by ion-implanted doping, and a host of techniques and machines are available that facilitate the fabrication of the thermistors, thermal isolation structures, and large arrays of detectors and their electrical interconnections. There have been considerable advances in theoretical understanding of the conduction mechanism. As we will see below, this understanding is far from complete, but empirical characterizations should be adequate for optimizing the design of low temperature detectors, and for predicting their ultimate performance with thermometers of this type.

## 2 Hopping Conduction

Shallow impurities in germanium and silicon have binding energies typically tens of milli-electron volts and are almost completely ionized at room temperature. As the temperature is lowered, the ionized fraction drops rapidly. This produces an increase in the resistance of lightly-doped material, but for most low temperature thermometry applications this is not the regime nor mechanism of interest. Instead, we are normally working at temperatures where thermal ionization of impurities is negligible. While the crystal structure is perfectly regular, the random substitution of dopant atoms at a small fraction of the lattice sites produces a disordered system that has, at sufficiently low temperatures, the electron transport properties of an amorphous material. The basic properties of such systems were determined by *Anderson* [4] and *Mott* [5]. They find that there is a critical doping density below which the conductivity goes to zero at zero temperature, and above which there is always a finite conductivity. We are interested in materials doped below this “metal-insulator transition”, where charge transport takes place by phonon-assisted tunneling between impurity sites. The energy levels of these sites are effectively randomized by the long-range Coulomb potential of charges distributed over distant sites, and the energy difference required in a given tunneling event or “hop” is made up by absorption or emission of a phonon of the required energy.

At sufficiently high temperatures, the distance barrier wins and hops take place to the nearest unoccupied site. This is referred to as “nearest neighbor hopping”. At lower temperatures, the scarcity of high energy phonons favors longer hops as necessary to find an unoccupied site sufficiently close to the same energy that a phonon is more readily available. This is usually the regime of interest for low temperature thermometry, and the process is called “variable range hopping” (vrh). An extensive development of the theory can be found in the text by *Shklovskii* and *Efros* [6]. For vrh, the conduction is expected to behave as

$$( \ ) = \sigma_0 \exp \left( -\frac{E}{kT} \right)^p \quad (1)$$

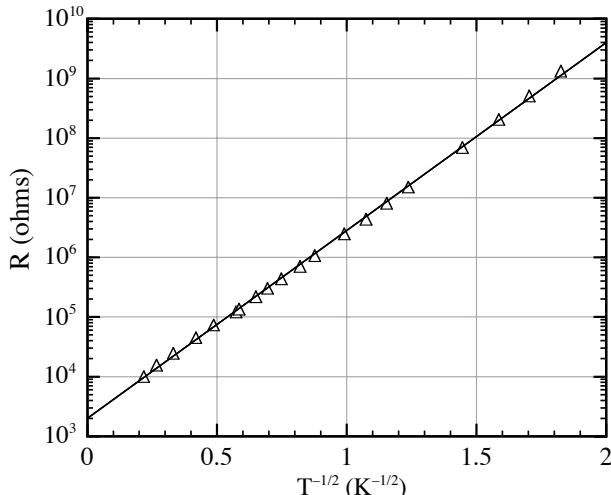


**Fig. 1.** Measured  $R(T)$  for ion-implanted silicon. The linear dependence of  $\log R$  on  $T^{-1/2}$  predicted by the variable range hopping model with a Coulomb gap is observed over several orders of magnitude in resistance

where Mott found  $\gamma = 1/4$  for the approximately constant density of states he expected at the Fermi level. Efros and Shklovskii later showed that the changing Coulomb interactions accompanying a hop should guarantee the existence of a parabolic gap in the density of states centered at the Fermi level [7]. This modifies the result to make  $\gamma = 1/2$ .

Measurements at the time, particularly on germanium and silicon, usually did not look much like this. Experiments gave a variety of  $\gamma$  curves that were not reproducible from one sample to the next. However, data from samples doped by nuclear transmutation (NTD) or by careful ion implantation *do* show the expected behavior. This can be seen in Fig. 1, where the  $\gamma = 1/2$  behavior predicted by VRH with a “Coulomb gap” is quite accurately followed over several orders of magnitude in resistance.

Even modern melt-doped material seldom shows this clear Coulomb gap behavior. The resistance usually flattens as the temperature is reduced, and the power-density effects discussed below become apparent at lower than expected power levels. Both of these observations are consistent with the existence of small-scale nonuniformities in the doping density, but it is not clear that this is the correct explanation.

## 2.1 Deviations from Coulomb Gap Behavior

At sufficiently low temperatures, when  $\theta_0 \gtrsim 24$ , systematic deviations from this Coulomb gap behavior are observed [8, 9]. This is shown in Fig. 2, where  $\gamma$  is plotted for ion-implanted silicon samples with several different doping

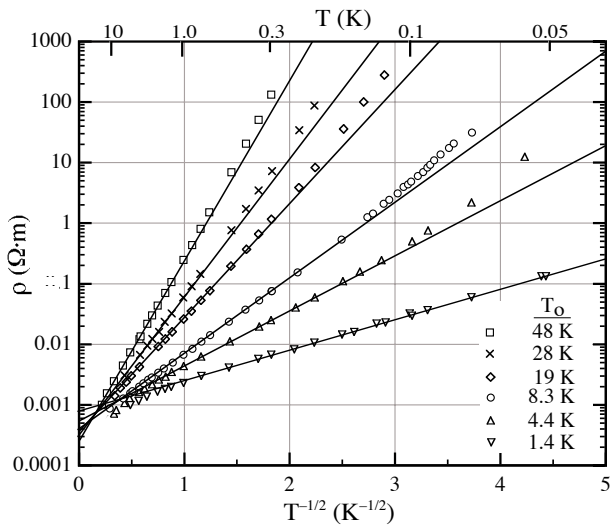


**Fig. 2.** Resistivity vs.  $T^{-1/2}$  for six ion-implanted Si:P,B samples. The straight lines are fits to the Coulomb gap model over a temperature range  $6.5 < T_0/T < 24$ . The different samples have different doping densities, which determines the value of  $T_0$  in (1). (From [8])

densities. It is clear that many of these curve upwards, but it is difficult to see a pattern in the deviations and in fact would be difficult to detect them at all had the lowest temperatures been included in the straight line fits. However, if we divide out the Coulomb gap model fits, where  $\log \rho \propto T^{-1/2}$ , and plot the ratio as a function of the temperature normalized by  $T_0$  for each sample as shown in Fig. 3, it can be seen that the deviations are quite systematic.

*Shlimak* observed similar behavior in arsenic-doped germanium, and suggested that a magnetic hard gap due to spin-spin interactions might be responsible [10]. There is evidence that ( ) reverts to Coulomb gap behavior with applied magnetic fields  $> 1$  T, which supports the idea that the deviations are some kind of magnetic effect [11].

From an experimental standpoint, this low-temperature rise can easily be masked by light leaks, RF pickup, or other extraneous heating effects, all of which tend to make measurements turn down below the intrinsic ( ) curve. It is useful to have an analytic expression that can be fit to measurements at higher temperatures, where these effects are usually negligible, and extrapolated to compare with the lowest temperature measurements to determine the extent of any heating problems. Of course, it is also convenient for thermometric purposes to have such a function, since only a small number of calibration points are then required to fix the entire ( ) dependence. *Bergmann-Tiest* has fit the deviations with a purely empirical function, which is reproduced here [12]:

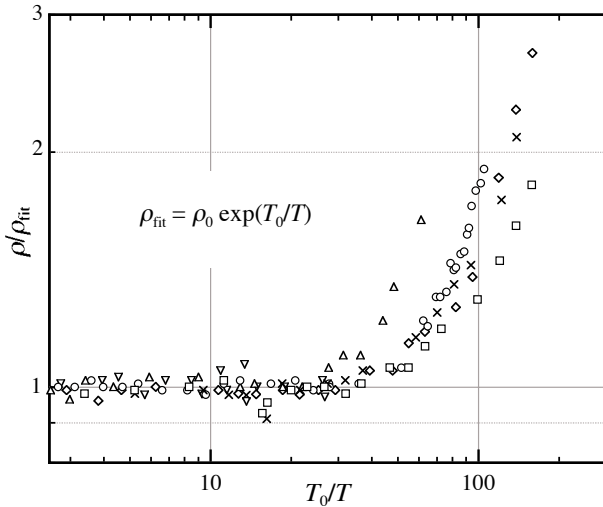


**Fig. 3.** Resistivity of samples in Fig. 2 divided by the best-fit Coulomb gap model vs. the normalized inverse temperature  $T_0/T$ . (From [8])

$$\rho(\tau) = \rho_0 \exp\left(-\frac{\tau}{\tau_0}\right)^{1/2} + \rho'_0 \exp\left(-\frac{\tau}{\tau'_0}\right)^{1/2} \quad (2)$$

where  $\tau'_0 = \tau_0 \exp(2522 \tau_0^{-0.25} - 8733)$  and  $\tau'_0 = 27148 \tau_0 + 12328$ .

This is not pretty, but it introduces no additional free parameters, and considerably increases the temperature range over which a good fit can be made. (In principle, there should be only one free parameter to the fit, which is  $\tau_0$  and corresponds to the doping density. The quantity  $\tau_0$  should be calculable from this and the sample geometry. In practice however this cannot be done with the required precision, so  $\tau_0$  is normally fit simultaneously). The function is designed to give the same values for  $\tau_0$  and  $\tau'_0$  as the Coulomb gap model if the latter is fit only to the higher temperature data.

The generality of whatever effect is producing this low-temperature deviation is illustrated in Fig. 4, which shows  $\rho(\tau)$  for an NTD germanium sample, fit by both the simple Coulomb gap model and by the “Wouter function” given above. Each has the same two free parameters. The Wouter function was derived from the behavior of very thin ( $0.3 \mu\text{m}$ ) ion-implanted silicon samples, but it provides a good fit for this relatively thick ( $200 \mu\text{m}$ ) NTD germanium device.

This function works reasonably well, but its additive term offers little help with physical significance. *Semo-Sharfman* has made another fit to similar data, and chose to represent the correction as a multiplicative term [13]:

$$\rho(\tau) = \rho_0 \exp\left(-\frac{\tau}{\tau_0}\right)^{1/2} \left[ 1 + \left(\frac{\tau}{\tau_0}\right)^B \right] \quad (3)$$

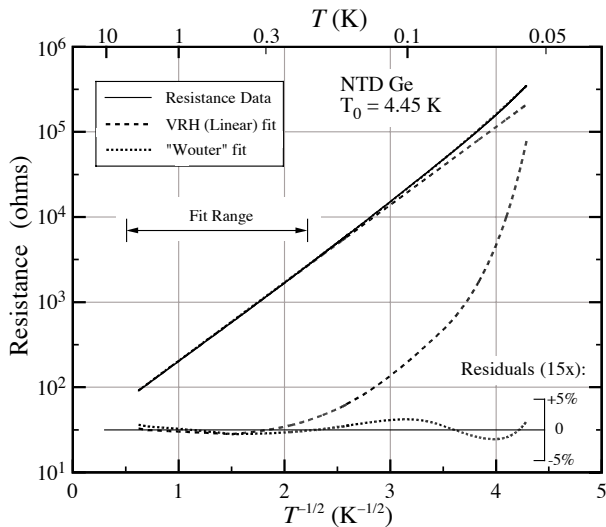


**Fig. 4.** Resistance of a  $200 \times 1000 \times 2000 \mu\text{m}^3$  NTD germanium thermometer, showing the best-fit Coulomb gap model and a fit using the “Wouter function” given in (2). This function and its fixed parameters were derived from a set of thin ion-implanted silicon samples. Both functions were fit only to data for  $4 \text{ K} < T < 0.2 \text{ K}$

where  $B = (0.1884 - 0.01241 \ln \rho_0)60^{-B}$  and  $\rho = 2.074 + 3.179 \exp(-\rho_0/8.81)$ . This actually doesn’t fit quite as well as (2), but it is well within the systematic accuracy of the data. *Woodcraft et al.* [14] use a variable value of  $\rho$  in (1) instead, but this gives poor fits to the data in [8].

## 2.2 Doping and Device Fabrication

This section contains quantitative information on doping germanium and silicon for device thermometers, and some examples of construction techniques.

### 2.2.1 Neutron Transmutation Doped Germanium

Extremely reproducible thermometers can be produced by irradiating germanium with reactor neutrons [15]. Natural germanium has four stable isotopes with substantial abundances, and the neutron cross sections and abundances of two of these conspire to produce gallium-doped (p-type) material that is 32% compensated with arsenic. Since the isotopes are chemically identical, they are presumably distributed perfectly randomly in the lattice, and the moderate neutron cross section makes the neutron flux uniform throughout even quite large blocks of germanium. These can then be cut up to make large numbers of very uniform thermometers. Plots of the resistivity ( $\rho$ ) for

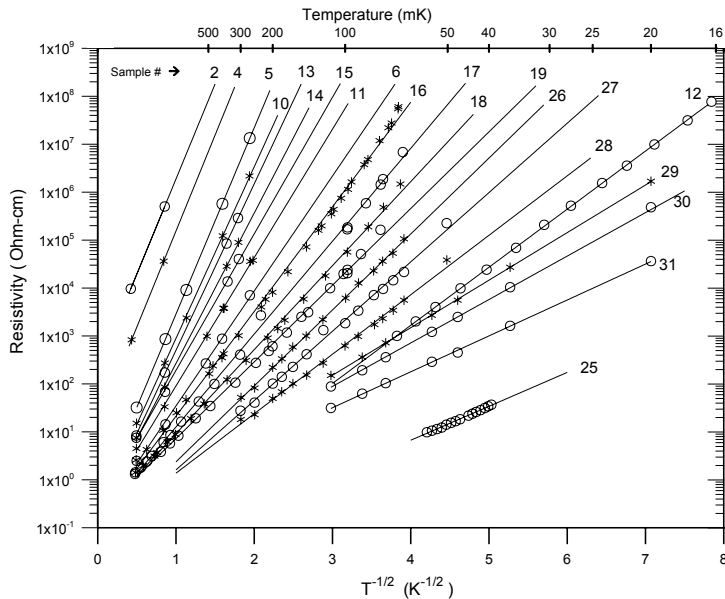


**Fig. 5.** Resistivity vs. temperature for a number of samples of transmutation doped germanium exposed to different neutron fluences [17]

a number of different neutron doses are shown in Fig. 5, and the fit  $\rho_0$  vs. net doping density is given in Fig. 6. The value of  $\rho_0$  should also be a simple function of doping density, and a plot of this is given in [16]. However, the derived value is highly correlated with the  $\rho_0$  fit, small systematic problems with the data make large differences, and there is little agreement in published values. Inspection of Fig. 5 shows that over a wide range of intermediate values of  $\rho_0$ ,  $\rho_0$  is within a factor of  $\sim 2$  of 0.1  $\Omega\text{cm}$ , while samples with extreme values of  $\rho_0$  can be a factor of 100 or more different.

The uniformity and predictability of NTD Ge thermometers is particularly valuable in the construction of large arrays of detectors. However, the penetrating power of the neutrons that helped provide the very uniform doping also means that it is impractical to mask the process and dope only selected areas in a crystal. So the thermometers must be cut to the optimum dimensions, and then individually attached to the detector elements. This is not a drawback, however, when the elements are very large and individually mounted, as in the CUORE project [18]. For arrays of small detectors, clever use of hybrid circuit mounting techniques that treat the thermistors as components to be “bump-bonded” can allow the use of integrated wiring and somewhat automated assembly [19].

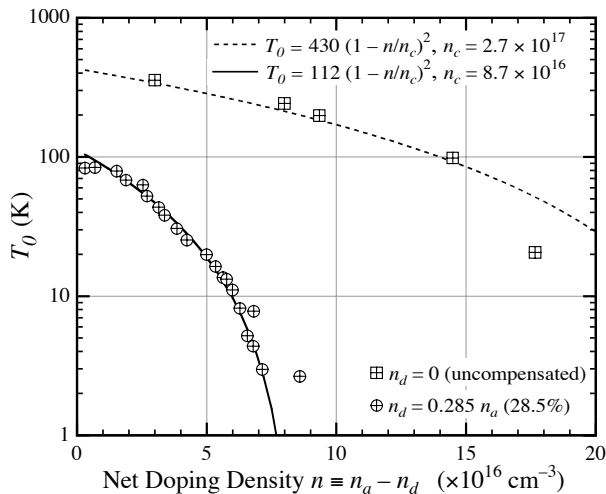


**Fig. 6.** Doping density parameter  $T_0$  vs. net density ( $n_{\text{acceptor}} - n_{\text{donor}}$ ) for neutron transmutation doped germanium. Data provided by [17]

### 2.2.2 Ion-implanted Silicon

Silicon requires very large neutron doses to dope by transmutation, and this is seldom attempted. However, doping by implanting ions from a beam with kinetic energies from tens of keV to a few MeV is a well-developed technique in the semiconductor electronics industry. This allows penetration depths of up to  $\approx 1 \mu\text{m}$ , but results in an approximately Gaussian density profile with depth. Uniform densities can be obtained by superimposing implants with several different energies and carefully designed doses to produce a flat-top profile [8, 9], or by implanting a single dose of each ion into a thin piece of silicon, preferably capped with  $\text{SiO}_2$  on both sides, and then treating it at high temperature to allow the implanted ions to diffuse completely and uniformly throughout the thickness [20]. The diffusion times and temperatures are practical up to a thickness of a few microns.

The great advantage of this doping method is that it can be masked by standard photolithographic techniques, allowing the simultaneous fabrication of large numbers of thermistors than can have almost arbitrarily small dimensions, and have fully integrated electrical connections [21, 22]. Silicon also has excellent mechanical and thermal properties, and many techniques exist for fabricating mechanical structures from it that can be used, for instance, for thermal isolation of the individual detector elements. Figure 7 shows a sketch of the structure for a single pixel of an X-ray detector array, where a limited region is doped to form the thermometer and undoped silicon is used for the mechanical structure, including the thermal isolation beam supports.

Figure 8 shows a photograph of the pixel, and of the entire  $6 \times 6$  array after the X-ray absorbers have been attached. Techniques exist that should make

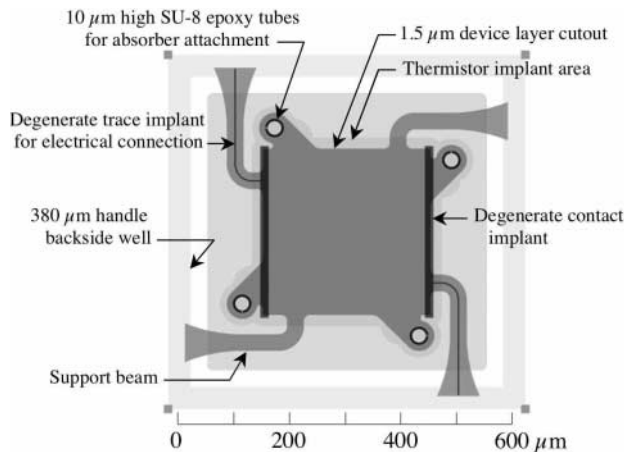


**Fig. 7.** Structure of one pixel of a monolithic X-ray detector array with ion-implanted thermistors

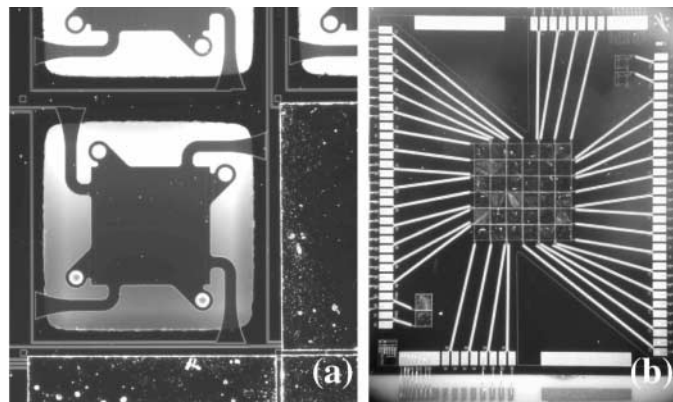


**Fig. 8.** (a) One pixel of a monolithic silicon array for the XRS instrument on Astro-E2. The small cylinders on the short curved arms are attachment points for the HgTe X-ray absorbers. (b) Full view of the  $6 \times 6$  array chip after the absorbers are attached with epoxy

it possible to fabricate the absorbers monolithically, rather than attaching them by hand, but these have not yet been perfected.

Ion implanted thermistors of the stacked-implant variety have been plagued by a lack of reproducibility that is not understood. Both doses and energies can be measured with more than adequate precision, but the run-to-run repeatability is poor enough that it is common to implant a series of wafers with slightly different doses, and then pick the one that comes closest to the desired resistivity. Fortunately, uniformity across a wafer is generally

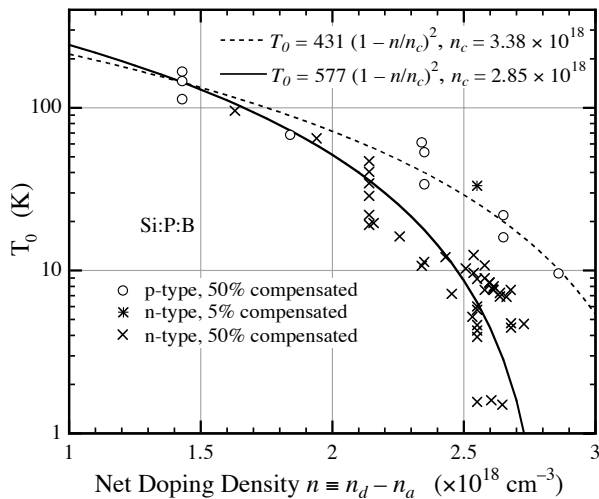


**Fig. 9.**  $T_0$  vs. net doping density for ion-implanted silicon. Data are from [8] but the estimated thickness of these stacked implants has been normalized to results from a small number of diffused samples with accurately determined thicknesses, resulting in a 60% increase in thickness and a corresponding reduction in the derived doping densities

good, and the steps in implant density within a single processing run give a monotonic sequence. Figure 9 shows  $T_0$  vs. doping density for silicon, but it should not be taken too seriously, as the scatter among the data points shows. Diffused thermistors seem more repeatable, although there is not much experience with them yet. Reference [8] has a figure showing  $T_0$  as a function of  $n$  for implanted silicon. The difficulties are the same as for germanium, and this should be regarded as a rough guide only. The variation seems even smaller than for germanium, however, and  $T_0 \approx 0.05 \Omega\text{cm}$  over a wide range of  $n$ .

### 3 Electrical Nonlinearities

It might seem that doped semiconductors should make almost ideal thermometers. The figure of merit  $\alpha \equiv d(\log \sigma) / d(\log V)$  from the Introduction to this volume (Chap. 1) is just  $\alpha = 0.5 (\tau_0 / \tau)^{1/2}$  for Coulomb gap ( $\tau$ ). One can make  $\alpha$  arbitrarily high by doping lightly, so it should be possible to make  $\alpha$  as large as desired. At the same time, it is easy to fabricate ion-implanted sensors with such small volumes that the heat capacity contribution of the thermometer could be negligible, despite the relatively high specific heat of the doped material.

However, the effects described in this section introduce severe and in most cases fundamental limits to the extent that small volume and high

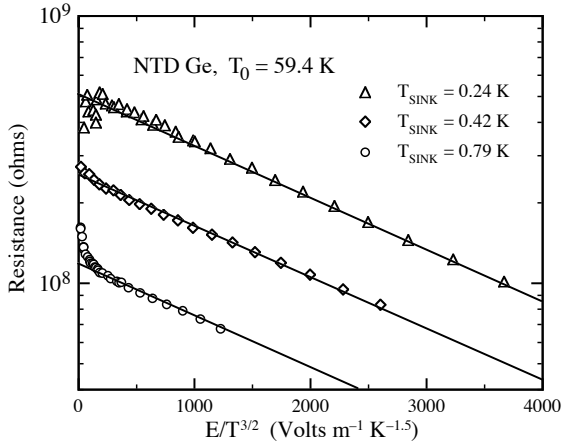


**Fig. 10.** Effect of electric field on resistance for a NTD Ge sample with  $T_0 = 59.4$  K at three different heat sink temperatures. The sample was fixed to the sink with a high thermal conductivity. According to (4) with  $\lambda \propto T^{-1/2}$ , the data should follow parallel straight lines (from [24]).

sensitivity can be pursued. None of them is entirely understood theoretically, but empirical data are available (at least in principle) that allow optimum values for thermistor size and  $\tau_0$  to be determined for a given application. These effects also introduce intrinsic limits to the speed of semiconductor thermometers.

### 3.1 Electric-Field Effects

Phonon-assisted tunneling is an inherently non-linear process, and is expected to appear linear only in the limit of small electric fields. There are several models that differ in detail, but most can be approximated by

$$(R) = (R_0) \exp\left(-\frac{eE}{k_B T}\right) \quad (4)$$

where  $E$  is the electric field,  $(R_0)$  is the resistance in the limit of low fields – the Coulomb gap function in this case –  $k_B$  is a constant of order unity,  $e$  is the electronic charge, and  $\tau_0$  is a characteristic hopping length that in most models scales as  $\tau_0 \sim E^{-1/2}$  [23]. See also discussion and references in [24]. This type of behavior is observed in doped germanium and silicon under certain conditions [24, 25, 26], as shown in Fig. 10.

In the linear theory of Chap. 1, this behavior is represented by a local slope  $\equiv (R/E)_T$  evaluated at the operating point. This is negative, and always acts to reduce thermometer sensitivity. Raising  $\tau_0$  by decreasing the doping concentration makes  $\tau_0$  larger and increases the magnitude of this term. To

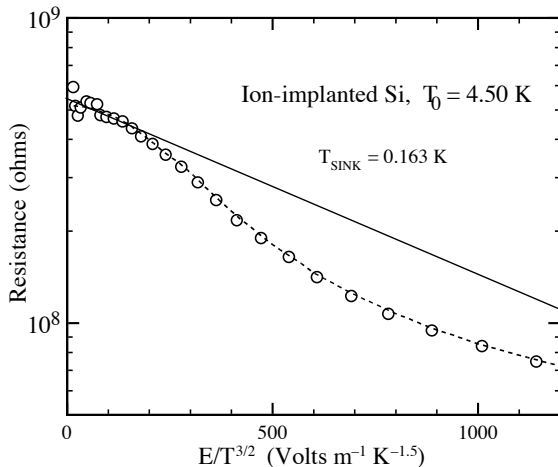


**Fig. 11.** As in Fig. 10, but for an ion-implanted Si sample with  $T_0 = 4.5$  K, operated at 0.163 K. The *solid line* is a field-effect model. The *dashed line* is the hot electron model described in the text

optimize thermometer design, it would be nice to know  $\sigma_0$  as a function of  $T_0$  and  $T_{SINK}$ , particularly for NTD Ge, as we will see below. References [24, 25, 26] and [27] have modest amounts of data for Ge, and less modest amounts of disagreement. This is clearly an area where there is a shortage of needed engineering data.

### 3.2 “Hot Electron” Effects

As can be seen in Fig. 11, the standard electric field effect form given in (4) does not always describe the observed behavior very well. Over most of the parameter range of interest for low temperature detectors, field-dependence can be better fit by an analog of the hot electron effect in metals [24, 28, 29]. If the bias power is dissipated in the conduction electron system and sunk through the crystal lattice, one can envision an effective thermal conductivity between the electrons and phonons. Again by analogy to other thermal conductivities, this is assumed to have the form  $\sigma_0 \propto e^\beta$ , making the power transfer

$$= \frac{\sigma_0}{e + 1} \left( e^{\beta+1} - e^{\beta+1}_{\text{lattice}} \right) \quad (5)$$

In such a model, one further assumes that the resistance is a function of  $e$  only. (Note that this  $e$  is unrelated to one used for thermistor voltage dependence.) The  $(\cdot)$  function can be calibrated in the limit of small bias power, where  $e \approx e_{\text{lattice}}$ . Then  $\sigma_0$  and  $\beta$  are fit to resistance data taken with a range of bias powers. Figure 12 shows that this form fits well over

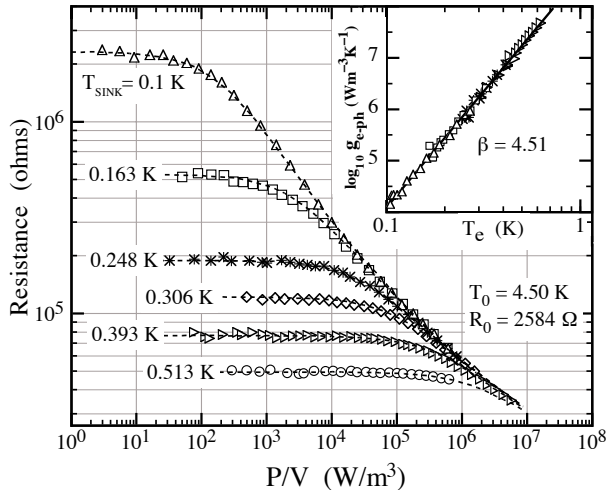


**Fig. 12.** Resistance vs. bias power for an ion-implanted Si device. Data series are labeled by lattice temperature. The *dashed lines* show the hot electron model, with electron temperature derived from (5) and resistance from this  $T_e$  and (2). The parameters  $T_0$  and  $R_0$  are fit to measured values of  $R$  in the limit of low power. All data series are fit simultaneously with the same values of  $G_0$  and  $\beta$ . The *inset* plots  $G_{e\text{-ph}} \equiv d(P/V)/dT_e$  vs.  $T_e$ , showing a single power-law dependence over four orders of magnitude in  $G$  (from [24])

a wide range of electron and lattice temperatures, although  $\beta$  is generally found to be  $\sim 5$ , rather than the 4 expected and measured for metals.

Zhang et al. [24] investigated a variety of ion-implanted Si and NTD Ge thermistors with a wide range of doping densities. They found that the difference between the behaviors of Figs. 10 and 12 is not that one is Ge and the other Si, but is rather the combination of operating temperature and doping density. Devices with high  $\rho_0$ 's operated at low temperatures had behavior well described by the field effect model of (4), while low  $\rho_0$ 's and high operating temperatures gave results better represented by the hot electron model of (5). Thermistors operating near the borderline, roughly described by  $\rho_0 \approx 100$ , didn't fit either model well.

They suggested that both effects are always operative, with one or the other dominating in most parts of  $\rho_0 - T$  space, but with both required to explain the behavior in the boundary region, as evidenced by the data shown in Fig. 13 for an Si detector. Piat et al. [27] found it essential to use a combined model to fit high quality data on NTD Ge thermometers intended for temperature control on the Planck-HFI instrument. The combined model simply substitutes  $T_e$  from (5) for  $T$  in the field effect model (4). The mean hopping length  $a$  is assumed to scale as  $a^{-1/2}$ , which is observed to be an

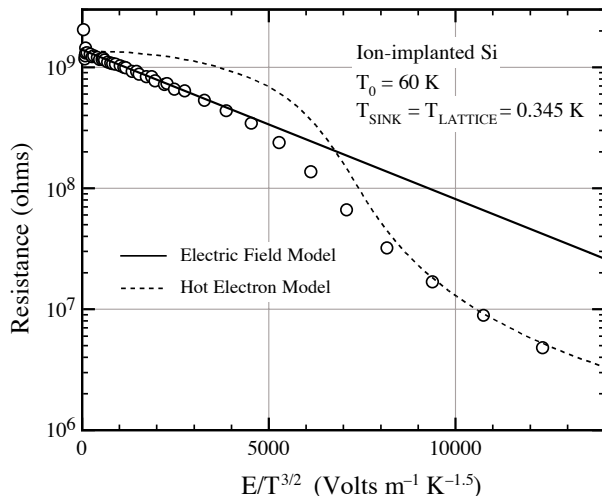


**Fig. 13.** Data for an ion-implanted Si sample operated near the  $T_0 - T$  borderline that separates good fits to the field effect and hot electron models. The *solid line* shows an electric field effect model (4), while the *dashed line* is for a hot electron model

approximation at best [24, 25, 26] (and [26] finds  $\sim -1$ ), but is adequate for fitting over a limited temperature range.

Like the field effect, hot electron behavior is an important limitation on detector performance, and its parameters are needed to optimize detector design. Zhang et al. [24] characterized a large number of ion-implanted Si devices with a wide range of doping densities. They used the hot electron model to determine values for the electron–phonon thermal conductivity parameters  $\sigma_0$  and  $\sigma$  in (5) as a function of doping density, as shown in Fig. 14. Zhang et al. were measuring thin stacked-implant devices, where the effective thickness is somewhat ambiguous. We have used measurements on a small number of diffused implant thermometers, where the thickness is precisely known, to normalize the volumes used for computing  $\sigma_0$  in Fig. 14b. The devices used for normalization had  $\sigma_0$  near 7 K, and the correction was about 40%. It is possible that the correction should really be a function of  $\sigma_0$ . Also, no corrections were made for electric field effect, which could be a significant contributor at the higher  $\sigma_0$ 's. This would tend to reduce  $\sigma$  and increase  $\sigma_0$  in this region.

While it is relatively easy to ensure that the lattice temperature remains constant as bias power is increased with the implanted Si samples, for practical reasons related to the generally quite different sample geometry and mounting, this is more difficult for NTD Ge. Again because of differences in the usual thermometer geometry, NTD Ge seldom has useful resistance values where hot electron effects are entirely dominant. Partly due to these

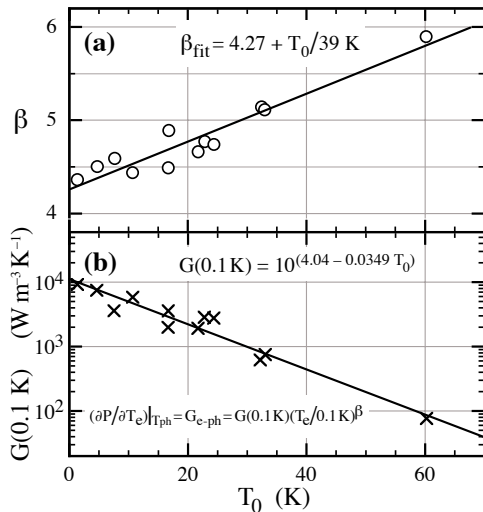


**Fig. 14.** Parameters fit to the hot electron model for a number of ion-implanted Si devices. (a) Best-fit power law exponent  $\beta$  as a function of  $T_0$ . (b)  $G_{e-ph}$  at 0.1 K as a function of  $T_0$

factors, there is less quantitative data available on  $\beta_0$  and  $G_{e-ph}$  for Ge. References [27, 28] and [29] have modest amounts of data on this, and again it is not in good agreement. Piat et al. [26] were the only ones to make a simultaneous fit of the hot electron and electric field effects, so their results are probably the most reliable.

The difficulty with this “hot electron” model is that it has no basis in current theory of variable range hopping conduction. The doping of these devices is far on the insulating side of the critical density, and the electrons should be strongly localized. The electrons can change their energy distribution by tunneling from site to site, with emission or absorption of phonons making up the energy difference. But for the electrons to set up a thermal distribution of their own independent of the phonons would require that their energy be somehow delocalized while the electrons themselves are not [30]. It is interesting that  $\beta = 5$  is expected for three-dimensional phonons in semiconductors doped on the metallic side of the metal-insulator transition, although this appears to have been verified only for the two-dimensional case, where  $\beta = 4$  [31]. It is also true that the thin implants measured in [24] should be close to two-dimensional.

Since a real electron heating effect would depend on power density, while normal electric field effects depend on  $E$ , it might at first seem that we could distinguish between these models by varying the sample geometry. However, a simple algebraic exercise shows that the shape drops out and  $\beta = E^2 / \rho$ , so there is no way to distinguish an electric field effect from a power density effect without theoretical guidance. We therefore might consider the hot electron

model simply a convenient if accidental analytic description of  $(\quad)$  in a range of parameters where (4), for whatever reason, does not apply.

### 3.2.1 Time Constants and Heat Capacity

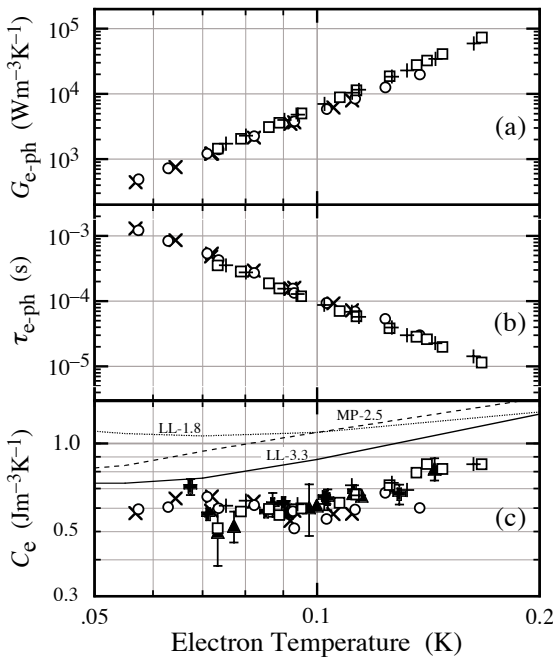
However, the hot electron picture has consequences that go beyond a particular  $(\quad)$  relation. Since the electron system should have some heat capacity  $c_e$ , and we have already determined an electron–phonon thermal conductivity  $\kappa_{e-ph}$ , then there should be a characteristic time  $\tau = c_e / \kappa_{e-ph}$  for changes in the electron temperature  $T_e$ . This has been investigated for NTD Ge [28, 29], for ion implanted Si [32, 33], and for other disordered systems [34, 35]. A thermometer directly attached to the heat sink so that its lattice temperature does not change should look like a simple bolometer as shown in Chap. 1, with the thermal link provided by  $\kappa_{e-ph}$  and the bolometer heat capacity equal to  $c_e$ . This is clearly observed, and the thermal time constant  $\tau$  can be determined quite precisely by measuring the A.C. impedance of the device as a function of frequency and fitting the  $(\quad)$  function given in Chap. 1. Details of this procedure and an example of a measurement of a “tied down” thermometer can be found in [36].

Figure 15 shows  $\kappa_{e-ph}(T_e)$  as determined from D.C.  $\tau$  curves,  $c_e(T_e)$  as determined from A.C. impedance measurements, and their product, which in this hot electron picture should represent the heat capacity of the conduction electron system,  $c_e$ . Remarkably, while the independently-measured  $\kappa_{e-ph}$  and  $c_e$  both vary by almost three orders of magnitude over this temperature range, their product is almost constant. Even more remarkable, if one chooses to regard the hot electron model as simply an empirical description of  $(\quad)$ , is that a conventional measurement of the total heat capacity of the implanted impurity system, also shown in Fig. 15c, agrees almost perfectly with the derived  $c_e$  [33]. This indicates that essentially all of the heat capacity of the impurity system is effectively coupled to the part of the system directly involved in conduction.

The electronic heat capacity, both derived and measured, is considerably flatter than the linear temperature dependence expected for a metallic system. It is almost constant below 0.1 K, then steepens at higher temperatures, approaching  $c_e = 1$  at 0.2 K. This is in good qualitative agreement with other measurements [37, 38], and the small shift in absolute value could be due to the difference in compensation (50% vs.  $\sim 0\%$ ). The flat temperature dependence (which becomes negative at sufficiently low doping densities) was predicted and is ascribed to the formation of spin-exchange clusters [39].

### 3.2.2 Internal Thermodynamic Fluctuation Noise

Another consequence of the literal interpretation of the hot electron model is that additional noise should be observed in the biased thermometer output



**Fig. 15.** Measurements of ion implanted and diffused Si:P:B devices, with net doping densities near  $2.5 \times 10^{18} \text{ cm}^{-3}$  and 50% compensation ( $T_0 \simeq 6\text{--}11 \text{ K}$ ). (a) Coupling constant  $G_{e\text{-ph}}$  as a function of  $T_e$  determined from D.C. resistance as a function of bias power. (b) Characteristic time constant  $\tau$  as a function of  $T_e$ , determined from A.C. impedance measurements. (c) *Open symbols* are the product of (a) and (b); electronic heat capacity  $C_e = G_{e\text{-ph}}\tau$ . The *filled symbols* are the heat capacity of the implanted silicon measured conventionally by attaching a piece of this material to a thermally isolated platform. The *lines* show published heat capacity measurements of uncompensated doped Si:P with similar net donor densities from [37] and [38] (data from [32])

due to transduced temperature fluctuations of the electron system caused by random energy transport between the electron and phonon systems. Figure 16 shows the measured noise in a “tied down” implant, after the Johnson noise of the resistance is subtracted. The noise and its temperature and bias dependence are readily calculated from the simple bolometer theory outlined in Chap. 1, and the agreement is very good.

This means that when a doped semiconductor thermometer is used in a bolometer or calorimeter structure with a separate absorber and thermal isolation link, the effective “thermal circuit” must include at least two thermal links and two heat capacities. Internal thermodynamic fluctuations and internal time constants may become important. The simple detector theory of Chap. 1 can be used only if  $\tau_{e\text{-ph}} \gg \tau_{\text{sink}}$ . In general, it will be necessary

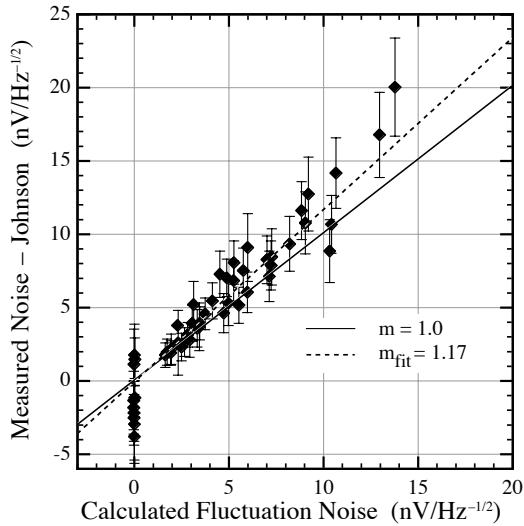


**Fig. 16.** Excess noise observed in an ion implanted Si detector tied down to the heat sink. The observed excess is in good agreement with the predictions of standard bolometer theory for thermodynamic fluctuations over a thermal link with the measured value of  $G_{e\text{-ph}}$  (from [32])

to use more complicated thermal models, such as those derived in [40], that can explicitly include  $G_{e\text{-ph}}$  and  $G_e$ .

## 4 Excess Noise

Additional noise has been observed, primarily in ion-implanted silicon, that appears as an unexpected low-frequency component and has had a significant impact on detector performance. Ion implanted Si detectors made in three different labs according to somewhat different recipes all show similar behavior [41]. Characterization of the noise of these thin ( $\approx 200$  nm) stacked-implant devices over a wide range of doping density, lattice temperature, and bias current shows a complicated dependence on all of these factors (including the load resistor value) [42]. When interpreted in terms of the hot electron model described above, however, the behavior after correcting for bias power heating of the electrons and electrothermal feedback effects is greatly simplified and can be characterized as relative resistance fluctuations with a  $1/f$  spectral density that depend only on the electron temperature and doping density. Figure 17 shows the resistance fluctuations as a function of  $T_e$  for different lattice temperatures and bias currents. Combinations of these that result in the same  $T_e$  also give the same derived values for  $\langle (\Delta R)^2 \rangle$ .

The resistance fluctuations are independent of the shape of the device going from 36:1 to 1:36 length to width ratios, which virtually rules out

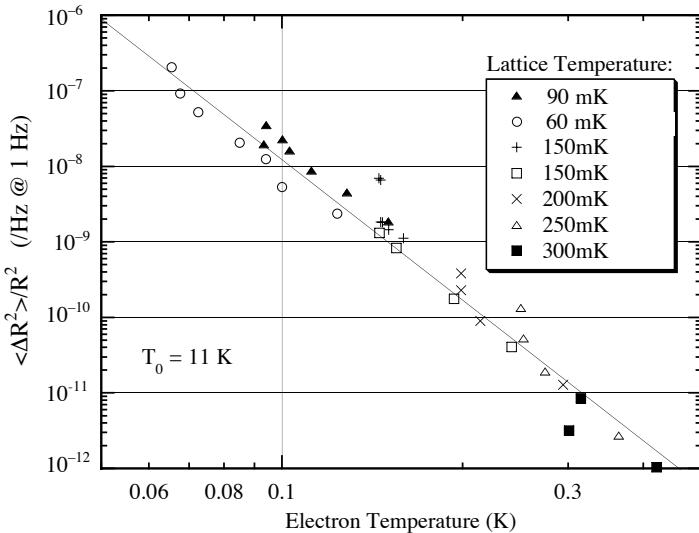


**Fig. 17.** Resistance fluctuations in a thin ion-implanted Si thermometer as a function of the electron temperature  $T_e$  for several values of  $T_{\text{lattice}}$  and bias. The fluctuations appear to depend only on  $T_e$ , which increases with bias power for a given  $T_{\text{lattice}}$  (from [42])

the ohmic contacts as a significant contributor. They scale quite precisely with  $(\text{thermistor volume})^{-1/2}$ , as expected for any random fluctuation that is uncorrelated in different parts of the volume. Since the thickness of these devices is limited by the acceleration energy of standard commercial ion implanters, they all have approximately the same thickness. So it is actually only the  $(\text{area})^{-1/2}$  dependence that has been verified. The conventional parameterization for 1 noise is the Hooge alpha:

$$\left\langle \left( \frac{\Delta R}{R} \right)^2 \right\rangle \equiv \frac{\text{Hooge}}{V} \quad (6)$$

where  $V$  is a stand-in for the volume, and  $N$  is conventionally the number of “carriers”. Han et al. [42] arbitrarily use the net number of donors for  $N$ . Since the doping density does not change very much over the practical range of  $N_0$ , this is nearly equivalent to volume. Figure 18 shows measurements of Hooge as a function of  $T_e$  for a range of doping densities ( $N_0$ ). These were reasonably well-fit by the empirical function

$$\text{Hooge} = 0.034 \left( \frac{N_0}{1 \text{K}} \right)^{2.453} \left( \frac{T_e}{0.153 \text{K}} \right)^{-[5.2 + 0.9 \log_{10}(T_0/1 \text{K})]} \quad (7)$$

There has been only a little theoretical work on fluctuations in hopping conductivity [43, 44], and it is not clear that what has been done is applicable

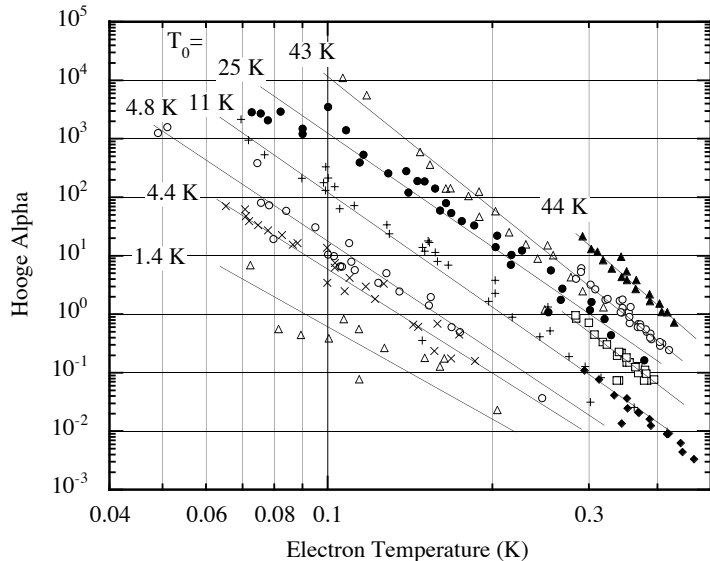


**Fig. 18.** Excess noise parameter  $\alpha_{\text{Hooge}}$  for thermistors with different doping densities

to the usual conditions for low-temperature thermometers. It can be seen from Fig. 18 that the  $1/f$  noise increases rapidly as  $T_e$  decreases, going approximately as  $T_e^{-6}$ . Perhaps coincidentally, the size of the percolation network at these temperatures is becoming comparable to the device thickness and is increasing exponentially as the temperature drops, making the conduction rapidly more two-dimensional [6]. Thus the strong temperature dependence offers a hint that the  $1/f$  noise is a 2-d or surface effect. NTD Ge thermometers generally do not show significant  $1/f$  noise, but most Ge devices are at least  $100\mu\text{m}$  thick, and there are at least anecdotal reports of it showing up in unusually thin Ge.

The ready availability of good quality silicon-on-insulator wafers with almost any desired device thickness now makes it straightforward to fabricate thicker doped Si thermometers. As described in [20], these have been made by implanting the phosphorus and boron dopants at approximately the middle of a  $1.5\mu\text{m}$  silicon layer, then annealing at high temperature for a long time so that the impurity atoms diffuse uniformly through the entire thickness. The  $1/f$  noise in these devices is reduced by at least a factor of six, as shown in Fig. 19.

An alternative explanation for the  $1/f$  noise is that while it is a surface effect, it is caused by the proximity of the lightly-doped wings of the stacked-implant profile [46]. Slow tunneling of electrons between sites that are not part of the conduction network could modulate the main conduction path, in analogy to the standard McWhorter theory of low frequency noise in Metal-

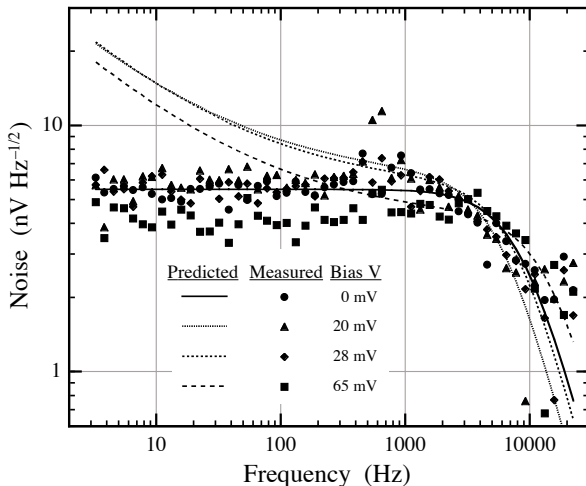


**Fig. 19.** Noise spectra from a 1500 nm thick diffused implant in Si. The *lines* show the predictions from (7). In the absence of  $1/f$  noise, the white noise level falls with increasing bias due to the drop in resistance from bias power heating of the electrons (from [45])

Oxide-Semiconductor Field Effect Transistors. The improvement is then due less to the increased thickness than to the very abrupt cutoff in the doping density profile. There are obvious experiments that could distinguish between these possibilities, but they have not been done.

## 5 Fundamental Limitations and Ultimate Performance

The “non-ideal” effects described above all limit the performance of detectors with semiconductor thermometers. The linear analysis of Chap. 1 gives the logarithmic sensitivity as the only significant thermometer parameter. Hot electron and field effects limit practical values of to 10 or less in most cases – far less than the sensitivity currently available with superconducting transition edge thermistors. So why use semiconductors at all? The answer to this is certainly application-dependent. The most obvious consideration is large signals, where the saturation characteristics of transition edge sensors are best described as “less than graceful.” Semiconductor thermometers become more nonlinear and less sensitive with increasing signal size, but have no hard saturation limits. They are easier to characterize and can also be easier to fabricate and simpler to use. The ideal amplifier for semiconductor thermometers is a simple Junction Field Effect Transistor (JFET) costing less than 1\$. On the other hand, for large numbers of detectors practical advantage can swing strongly in favor of the SQUID amplifiers used with superconducting thermometers.

One perhaps fundamental advantage of semiconductors is that they are relatively insensitive to magnetic fields. They have been operated without degradation in fields as large as 10 T [47]. The characteristics shift considerably, but the thermometer can be optimized for a given field. Conversely, a single thermometer can be made to perform over a wide range of temperatures by “tuning” it with a variable magnetic field.

Even the shortcomings can occasionally be put to good use. The hot electron effect allows a simple thermometer to be used as a complete detector, with an absolute minimum of addenda. The electron system is both the absorber and the thermometer, and the thermal isolation suspension is provided by the electron–phonon coupling. The usual drawback of these hot electron bolometers is that they have few adjustable parameters and cannot be optimized for a particular situation. However, the built-in characteristics of thin silicon implants are almost ideal for the requirements of some infrared detector applications [48, 49]. The R.F. sheet resistance is a good match to free space or a simple transmission line, so the absorber is highly efficient. Time constants cover a reasonable range at temperatures where the thermodynamic performance is good, and the low-frequency resistance for a square detector is a good match to the noise resistance of a JFET amplifier. It appears that very simple detectors could be made with outstanding performance.

## 5.1 Optimization

Getting the best possible performance requires optimizing the thermometer design. To do this, one needs both an understanding of how the thermometer works and quantitative data on the behavior of key parameters. We now seem to have an adequate phenomenological understanding of how semiconductor thermometers work, even if the underlying theory is a little murky. The hot electron model should be taken at face value and modeled as a separate thermal conductance and heat capacity. This complicates the thermal circuit (aside from the happy case of the hot electron bolometer) but appears to account correctly for the additional time constants and noise sources that are observed, and formalisms exist for handling arbitrary thermal models [40, 50]. The field effect can be included simultaneously. In the linearized performance theory of Chap. 1 it shows up as the parameter  $\equiv (\log \log)_T$ . For the field effect model (4),  $\equiv$  is simply  $-B$ . Of course, to perform the optimization, one has to know how  $\equiv$ ,  $e_{ph}$ , and  $e$  depend on other parameters.

We are not so well off with the necessary engineering data. The data for silicon are barely adequate for low  $T_0$  material operated at not too low temperatures where electric field effects are negligible. For NTD germanium both field effect and electron heating are usually important, and there is a surprising scarcity data on either. Part of the problem is that little analysis has been done that takes both effects into account, and this has confused the results. Now that the situation is better understood, it is relatively easy to separate

parameters and evaluate both effects simultaneously. It is straightforward to measure the A.C. impedance  $(\omega)$ , and since  $\omega = 1 - \frac{1}{T} (\infty)$ , and with it the local value of  $\tau_{e-ph}$  can be extracted immediately from its high frequency limit. This can be used to separate heating and field effects at the bias point, giving a value for  $\tau_{e-ph}$ , which along with  $\tau_e$  can then be put into the fit of  $(\omega)$  to get  $\tau_e$  and  $\tau_{e-ph}$ .

## 5.2 Germanium versus Silicon

The choice of Si or Ge depends very much on the application, and is usually decided by non-performance characteristics such as the excellent reproducibility of NTD Ge or the ease of fabricating large numbers of small integrated thermometers with ion-implanted Si. However, it is still interesting to consider whether there is some universal figure of merit that favors one or the other. The beneficial thermometer parameter is its sensitivity, while its heat capacity has a negative impact on detector performance. Both electric field and hot electron effects reduce the effective sensitivity as the power density goes up and a rough figure of merit would be sensitivity at a given power per unit heat capacity and temperature. This is a complex quantity, since field effect and electron heating affect the sensitivity in different ways.

Field effect (non-zero  $\tau_e$ ) reduces both signal and thermodynamic fluctuation noise by the same amount, so if amplifier noise is not significant, the only change in signal to noise ratio comes from Johnson noise. Johnson noise in biased nonlinear resistances is a difficult theoretical subject [51, 52] that we will avoid here, since hot electrons generally have more impact on detector performance than field effect. (The opposite is the case for superconducting transition edge thermometers, so see the next chapter for more discussion.) In the usual case where the signal comes in through the phonon system, the sensitivity to phonon temperature is rapidly degraded by electron heating. This can be seen from (5), remembering that the exponent is  $\approx 6$ . The thermodynamic fluctuations between the electron and phonon baths can create additional noise, and the  $\tau_e \tau_{e-ph}$  time constant rolls off the signal spectrum with respect to the thermometer Johnson noise and will degrade the overall signal to noise ratio unless it is shorter than the primary thermal time constant of the detector by a factor of  $\sim 10$ . For all of these hot electron effects, the figure of merit is  $\tau_{e-ph} / \tau_e$  at a given thermometer sensitivity  $\approx 0.5(\tau_0 \tau_e)^{1/2}$ . This quantity is independent of thermometer volume, and is plotted in Fig. 20 as  $\tau_{e-ph} \equiv \tau_e / \tau_{e-ph}$ . Data for NTD Ge are very sparse and inconsistent by a factor of ten or more. On the average, however, it appears that the intrinsic time constants may be faster by a factor of about six for the same  $\tau_0$  and  $\tau_e$ . Much better data are needed for design optimization and predictions of ultimate performance, and it should be straightforward to make the necessary measurements.

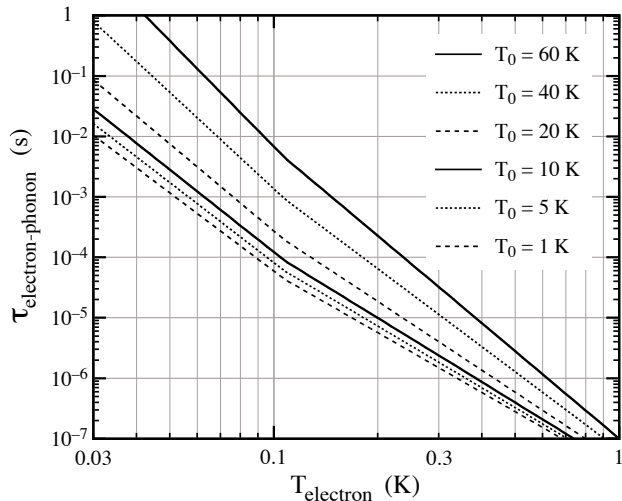


**Fig. 20.** The electron–phonon time constant  $C_e/G_{e\text{-}ph}$  vs. electron temperature. The solid lines are for Si with doping density given by the indicated  $T_0$  using fits to  $G_{e\text{-}ph}$  data from [24] with normalization and  $C_e$  from [33]

### 5.3 Expected Performance

We are at a point where performance can be predicted with reasonable accuracy when thermal data are available. A 32-detector array, identical to the XRS-2 array shown in Fig. 8, was built for an atomic physics experiment and operated at 60 mK. It had measured resolution within 10% of the calculated 4.8 eV FWHM for 6 keV X-rays on almost all of the detectors. Given the particular X-ray absorber used, the main avenue for improving the resolution would be to improve the thermal coupling between the absorber and thermistors. With perfect coupling, the predicted resolution would be 3.4 eV, but problems with “thermalization noise”, where variable numbers of super-thermal phonons reaching the thermometer produce pulse-to-pulse variations in the response, would actually make the resolution worse. The optimum solution for this is unknown, and the phonon physics is complex, so progress requires experimenting with different absorber couplings. Lowering the operating temperature could improve the resolution further, and germanium thermometers might be better, but we don’t have the data to say by how much or under what conditions.

One of the better X-ray detector results obtained so far with a semiconductor thermometer is shown in Fig. 21. There is some room for improvement: one might expect that if everything could be optimized, a 2 eV detector with these parameters is feasible. But for a detector of this heat capacity operating at  $\sim 50$  mK, some other thermometer technology will be necessary to reach 1 eV.

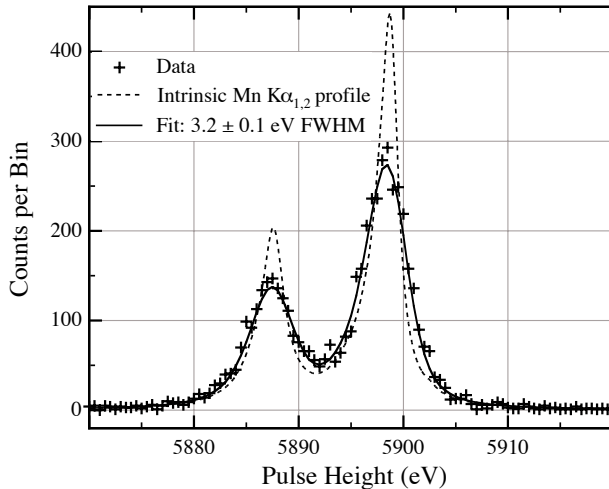


**Fig. 21.** Pulse height spectrum of the  $^{55}\text{Mn}$  K $\alpha_1$  and K $\alpha_2$  lines at 5.9 keV, showing a resolution of  $3.2 \pm 0.1$  eV FWHM. This device had a uniformly illuminated  $0.41 \times 0.41\text{ mm}^2$  HgTe absorber  $8\text{ }\mu\text{m}$  thick, which gives better than 95% X-ray stopping efficiency up to 7 keV and 50% up to 17 keV. It was operated at a detector temperature of 60 mK

## Acknowledgements

I would like to thank E.E. Haller and J.W. Beeman for providing their data on NTD Ge prior to publication. Many members of the Wisconsin and NASA/Goddard X-ray groups contributed heavily to this Chapter. I thank in particular Massimiliano Galleazzi, Mike Juda, Jiahong Zhang, Regis Brekosky, Richard Kelley, Caroline Kilbourne, Scott Porter, and Andy Szymkowiak. This work was supported in part by NASA grant NAG5-5404.

## References

- [1] R.C. Jones: J. Opt. Soc. Am. **37**, 879 (1947) [35](#)
- [2] I. Esterman: Phys. Rev. **78**, 83 (1950) [35](#)
- [3] F.J. Low: J. Opt. Soc. Am. **51**, 1300 (1961) [35](#)
- [4] P.W. Anderson: Phys. Rev. **109**, 1492 (1958) [36](#)
- [5] N.F. Mott, W.D. Twose: Adv. Phys. **10**, 107 (1961) [36](#)
- [6] B.I. Shklovskii, A.L. Efros: *Electronic Properties of Doped Semiconductors*, (Springer, Berlin, Heidelberg 1984) [36](#), [54](#)
- [7] A.L. Efros, B.I. Shklovskii: J. Phys. C **8**, L49 (1975) [37](#)
- [8] J. Zhang, W. Cui, M. Juda, D. McCammon, R.L. Kelley, S.H. Moseley, C.K. Stahle, A.E. Szymkowiak: Phys. Rev. B**48**, 2312 (1993) [37](#), [38](#), [39](#), [40](#), [42](#), [44](#), [60](#)

- [9] J. Zhang, W. Cui, M. Juda, D. McCammon, R.L. Kelley, S.H. Moseley, C.K. Stahle, A.E. Szymkowiak: Phys. Rev B **57**, 4950 (1998; erratum to [8]) **37**, 42
- [10] I.S. Shlimak: in *Hopping and Related Phenomena*, eds. H. Fritzsch, M. Pollak (World Scientific, Singapore 1990) p. 49 **38**
- [11] P. Dai, Y. Zhang, M.P. Sarachik: Phys. Rev. Lett. **69**, 1804 (1992) **38**
- [12] W. Bergmann-Tiest: personal communication (1998) **38**
- [13] L.R. Semo-Scharfman: personal communication (2003) **39**
- [14] A.L. Woodcraft, R.V. Sudiwala, E. Wakui, C. Paine: J. Low Temp. Phys. **134**, 925 (2004) **40**
- [15] E.E. Haller, N.P. Palaio, M. Rodder, W.L. Hansen, E. Kreysa: in *Neutron Transmutation Doping of Semiconductor Materials*, (Ed.)R.D. Larrabee, (Plenum, New York 1984) p 21 **40**
- [16] Itoh, J.W. Beeman, E.E. Haller, J.W. Farmer, V.I. Ozhigin: J. Low Temp. Phys. **93**, 307 (1993) **41**
- [17] E.E. Haller, J.W. Beeman: personal communication (2004) **41**, **42**
- [18] C. Arnaboldi, F.T. Avignone III, J. Beeman, M. Barucci, M. Balata, C. Brofferio, C. Bucci, S. Cebrian, R. J. Creswick, S. Capelli, , L. Carbone, O. Cremonesi, A. de Ward, E. Fiorini, H.A. Farach, G. Frossati, A. Giuliani, D. Giugni, P. Gorla, E.E. Haller, I.G. Irastorza, R.J. McDonald, A. Morales, E.B. Norman, P. Negri, A. Nucciotti, M. Pedretti, C. Pobes, V. Palmierii, M. Pavani, G. Pessina, S. Pirro, E. Previtali, C. Rosenfeld, A.R. Smith, M. Sisti, G. Venturad, M. Vanzini, L. Zanotti: Nucl. Instrum. Methods A **518**, 775 (2004) **41**
- [19] A.D. Turner, J.J. Bock, J.W. Beeman, J. Glenn, P.C. Hargrave, V.V. Hristov, H.T. Nguyen, F. Rahman, S. Sethuraman, A.L. Woodcraft: Appl. Opt. **40**, 4921 (2001) **41**
- [20] R.P. Brekosky, C.A. Allen, M. Galeazzi, J.D. Gygax, H. Isenburg, R.L. Kelley, D. McCammon, R.A. McClanahan, F.S. Porter, C.K. Stahle, A.E. Szymkowiak: Nucl. Instrum. Methods A **520**, 439 (2004) **42**, **54**
- [21] P.M. Downey, A.D. Jeffries, S.S. Meyer, R. Weiss, F.J. Bachner, J.P. Donnelly, W.T. Lindley, R.W. Mountain, D.J. Silversmith: Appl. Opt. **23**, 910 (1984) **42**
- [22] S.H. Moseley, J.C. Mather, D. Mc Cammon: J. Appl. Phys. **56**, 1257 (1984) **42**
- [23] R.M. Hill: Philos. Mag. **24**, 1307 (1971) **45**
- [24] J. Zhang, W. Cui, M. Juda, D. McCammon, R.L. Kelley, S.H. Moseley, C.K. Stahle, A.E. Szymkowiak: Phys. Rev. B **57**, 4472 (1998) **45**, **46**, **47**, **48**, **49**, **58**
- [25] T.W. Kenny, P.L. Richards, I.S. Park, E. E. Haller, J.W. Beeman: Phys. Rev. B **39**, 8476 (1989) **45**, **46**, **48**
- [26] S.M. Grannan, A.E. Lange, E.E. Haller, J.W. Beeman: Phys. Rev. B **45**, 4516 (1992) **45**, **46**, **48**, **49**
- [27] M. Piat, J.P. Torre, J.W. Beeman, J.M. Lamarre, R. S. Bhatia: J. Low Temp. Phys. **125**, 189 (2001) **46**, **47**, **49**
- [28] N. Wang, F.C. Wellstood, B. Sadoulet, E. E. Haller, J. Beeman: Phys. Rev. B **41**, 3761 (1990) **46**, **49**, **50**
- [29] E. Auberg et al.: J. Low Temp. Phys. **93**, 289 (1993) **46**, **49**, **50**
- [30] B.I. Shklovskii: personal communication (2004) **49**
- [31] M. Prunnila, J. Ahopelto, A.M. Savin, P.P. Kivinen, J.P. Pekola, A.J. Manninen: Physica E **13**, 773 (2002)

49

- [32] D. Liu, D. McCammon, W.T. Sanders, B. Smith, P. Tan, K.R. Boyce, R. Brekosky, J.D. Gygax, R. Kelley, D.B. Mott, F.S. Porter, C.K. Stahle, C.M. Stahle, A.E. Szymkowiak: in *Low Temperature Detectors*, F.S. Porter, D. McCammon, M. Galeazzi, C.K. Stahle (Eds.), Proc. 9th Int'l Workshop on Low Temperature Detectors in Madison, Wisconsin, July 2001 (AIP, New York 2002) p 87. (see also M. Galeazzi et al., Nucl. Instr. Methods A **520**, 469 (2004)) 50, 51, 52
- [33] M. Galeazzi, D. Liu, D. McCammon, L.E. Rocks, W.T. Sanders, B. Smith, P. Tan, J.E. Vaillancourt, K.R. Boyce, R. Brekosky, J.D. Gygax, R.L. Kelley, F.S. Porter, C.K. Stahle, C.M. Stahle, A.E. Szymkowiak: Phys. Rev. B (submitted) 50, 58
- [34] M.A. LaMadrid, W. Contrata, J.M. Mochel: Phys. Rev. B **45**, 3870 (1992) 50
- [35] S. Marnieros, L. Bergé, A. Juillard, L. Dumoulin: Phys. Rev. Lett. **84**, 2469 (2000) 50
- [36] J.E. Vaillancourt, D. Mc Cammon: Rev. Sci. Instrum. (submitted) 50
- [37] M.A. Paalanen, J.E. Graebner, R.N. Bhatt: Phys. Rev. Lett. **61**, 597 (1988) 50, 51
- [38] M. Lakner, H.v. Löhneysen: Phys. Rev. Lett. **63**, 648 (1989) 50, 51
- [39] R.N. Bhatt, P.A. Lee: Phys. Rev. Lett. **48**, 344 (1982) 50
- [40] M. Galeazzi, D. McCammon: J. Appl. Phys. **93**, 4856 (2003) 52, 56
- [41] A. Nucciotti: personal communication (1998) 52
- [42] S-I Han et al.: in *EUV, X-Ray and Gamma-Ray Instrumentation for Astronomy IX*, O.H. Siegmund, M.A. Gummin, (Eds.), Proc. SPIE **3445**, 640 (1998) 52, 53
- [43] B.I. Shklovskii: Solid State Commun. **33**, 273 (1980) 53
- [44] Sh.M. Kogan, B.I. Shklovskii: Fiz. Tekh. Poluprovodn. **15**, 1049 (1981) [Sov. Phys. Semicond. **15**, 605 (1981)] 53
- [45] D. Mc Cammon et al.: in *Low Temperature Detectors*, F.S. Porter et al. (Eds.), Proc. 9th Int'l Workshop on Low Temperature Detectors in Madison, Wisconsin, July 2001 (AIP, New York 2002) p. 91 55
- [46] S.H. Moseley: personal communication (2001) 54
- [47] P. De Moor et al.: J Low Temp. Phys. **93**, 295 (1993) 56
- [48] H. Moseley, D. Mc Cammon: in *Low Temperature Detectors*, F.S. Porter et al. (Eds.), Proc. 9th Int'l Workshop on Low Temperature Detectors in Madison, Wisconsin, July 2001 (AIP, New York 2002) p. 103 56
- [49] T.R. Stevenson et al.: in *Millimeter and Submillimeter Detectors for Astronomy II*, J. Zmuidzinas, W.S. Holland (Eds.), Proc. SPIE **5498** (in press) 56
- [50] E. Figueiroa-Feliciano: Ph.D. thesis, Stanford University (2001) 56
- [51] H.B. Callen, T.A. Welton: Phys. Rev. **83**, 34 (1951) 57
- [52] L. Weiss, W. Mathis: IEEE Electron Dev. Lett. **20**, 402 (1999) 57

# Index

- contacts, 36
- Coulomb gap, 37
- critical density, 36
- disordered system, 36
- doping, 40
  - ion-implanting, 42
  - neutron transmutation doping (NTD), 40
- electric field effects, 45
- electrical nonlinearities, 44–52
- electron–phonon
  - time constant, 50
- electronic heat capacity, 50
- excess noise
  - thermistors, 52
- germanium, 48, 57
- hopping conduction, 36–40
  - nearest neighbor hopping, 36
  - variable range hopping, 36
- hot electron bolometer, 56
- hot electron model, 46, 49
  - ion-implanting, 42
- magnetic field sensitivity, 56
- metal oxides, 35
- metal-insulator transition, 36
- nearest neighbor hopping, 36
- neutron transmutation doping (NTD), 40
  - 1/f noise, 52
- optimization, 56
- silicon, 48, 57
- spin-exchange, 50
- spin–spin interaction, 38
- thermal conductivity
  - electron–phonon, 46
- thermal ionization, 36
- thermocouples, 35
- time constant, 50
- variable range hopping, 36

# Transition-Edge Sensors

K. D. Irwin and G. C. Hilton

National Institute of Standards and Technology, Boulder, CO 80305-3328, USA  
[irvin@boulder.nist.gov](mailto:irvin@boulder.nist.gov)

**Abstract.** In recent years, superconducting transition-edge sensors (TES) have emerged as powerful, energy-resolving detectors of single photons from the near infrared through gamma rays and sensitive detectors of photon fluxes out to millimeter wavelengths. The TES is a thermal sensor that measures an energy deposition by the increase of resistance of a superconducting film biased within the superconducting-to-normal transition. Small arrays of TES sensors have been demonstrated, and kilopixel arrays are under development. In this Chapter, we describe the theory of the superconducting phase transition, derive the TES calorimeter response and noise theory, discuss the state of understanding of excess noise, and describe practical implementation issues including materials choice, pixel design, array fabrication, and cryogenic SQUID multiplexing.

## 1 Introduction

In 1911, *Kammerlingh Onnes* cooled a sample of mercury in liquid helium, and made the dramatic discovery that its electrical resistance drops abruptly to zero as it cools through its superconducting transition temperature,  $T_c = 4.2\text{ K}$  [1]. A large number of materials have since been found to have phase transitions into a zero-resistance state at various transition temperatures. The superconducting phase transition can be extremely sharp, suggesting its use as a sensitive thermometer (Fig. 1). In fact, the logarithmic sensitivity (the Chapter “Thermal Equilibrium Calorimeters – An Introduction” by *McCammon* in this book) of a superconducting transition,  $\alpha = d \log R / d \log T$ , can be two orders of magnitude more sensitive than that of the semiconductor thermistor thermometer that has been used so successfully in cryogenic calorimeters (the Chapter “Semiconductor Thermistors” also by *McCammon*).

A superconducting transition-edge sensor (TES), also called a superconducting phase-transition thermometer (SPT), consists of a superconducting film operated in the narrow temperature region between the normal and superconducting state, where the electrical resistance varies between zero and its normal value. A TES thermometer can be used in a bolometer (to measure power) or in a calorimeter (to measure a pulse of energy). The sensitivity of a TES makes it possible in principle to develop thermal detectors with faster

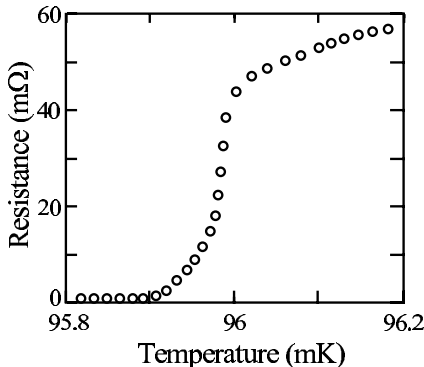


**Fig. 1.** The transition of a superconducting film (a Mo/Cu proximity bilayer) from the normal to the superconducting state near 96 mK. The sharp phase transition suggests its use as a sensitive thermometer

response, larger heat capacity, and smaller detectable energy input than thermal detectors made using conventional semiconductor thermistors. However, the sharp transition leads to a greater tendency for instability and lower saturation energy, so that careful design is required.

In 1941, Andrews et al. applied a current to a fine tantalum wire operating in its superconducting transition region at 3.2 K and measured the change in resistance caused by an infrared signal [2]. This was the first demonstration of a TES bolometer. In 1949, the same researcher applied a current to a niobium nitride strip within its superconducting transition at 15 K and measured the voltage pulses when it was bombarded by alpha particles [3] – the first reported demonstration of a TES calorimeter. This work followed on earlier suggestions by Andrews himself in 1938 [4] and Goetz in 1939 [5].

During the first half century after their invention, TES detectors were seldom used in practical applications. One of the principal barriers to their adoption was the difficulty of matching their noise to FET amplifiers (the TES normal resistance is typically a few ohms or less). In order to noise match, the TES was sometimes read out using a cross-correlation circuit to cancel noise [6], ac biased in conjunction with a step-up transformer [7], or fabricated in long meander lines with high normal resistance [8, 9]. In recent years, this problem has been largely eliminated by the use of superconducting quantum interference device (SQUID) current amplifiers [10], which are easily impedance-matched to low-resistance TES detectors [11, 12]. In addition to their many other advantages, SQUID amplifiers make it possible to multiplex the readout of TES detectors (Sect. 4.2), so that large arrays of detectors can be instrumented with a manageable number of wires to room temperature. Large arrays of TES detectors are now being deployed for a number of different applications.

Another barrier to the practical use of TES detectors has been that it is difficult to operate them within the extremely narrow superconducting transition region. When they are current-biased, Joule heating of the TES by the current can lead to thermal runaway, and small fluctuations in bath temperature significantly degrade performance. Furthermore, variations in the transition temperature between multiple devices in an array of TES detectors can make it impossible to bias them all at the same bath temperature. As will be explained in Sect. 2.5, when the TES is instead voltage-biased and read out with a current amplifier, the devices can easily be stably biased and they self-regulate in temperature within the transition with much less sensitivity to fluctuations in the bath temperature [13]. The introduction of voltage-biased operation with SQUID current readout has led to an explosive growth in the development of TES detectors in the past decade.

The potential of TES detectors is now being realized. TES detectors are being developed for measurements across the electromagnetic spectrum from millimeter [14, 15, 16] through gamma rays [17, 18] as well as with weakly interacting particles [19] and biomolecules [20, 21, 22]. They have contributed to the study of dark matter and supersymmetry [23, 24], the chemical composition of materials [25], and the new field of quantum information [26]. They have extended the usefulness of the single-photon calorimeter all the way to the near infrared [27], with possible extension to the far infrared. They are being used in the first multiplexed submillimeter, millimeter-wave, and X-ray detectors for spectroscopy and astronomical imaging [15, 16, 28, 29, 30].

## 2 Superconducting Transition-Edge Sensor Theory

We now describe the theory of a superconducting transition-edge sensor. We describe the physics of the superconducting transition (Sect. 2.1), summarize the equations for TES small-signal theory (Sect. 2.2), and analyze the bias circuit for a TES and its electrical and thermal response (Sect. 2.3), the conditions for the stability of a TES (Sect. 2.4), the consequences of negative electrothermal feedback (Sect. 2.5), thermodynamic noise (Sect. 2.6), unexplained noise (Sect. 2.7), and the effects of operation outside of the small-signal limit (Sect. 2.8). Particular implementations of both TES single pixels and arrays, including performance results, will be described in Sect. 3 and Sect. 4.

### 2.1 The Superconducting Transition

In this work, we discuss sensors based on traditional “low- $T_c$ ” superconductors (often those with transition temperatures below 1 K). Other classes of superconductors, including the cuprates such as yttrium-barium-copper-oxide, are also used in thermal detectors. Transition-edge sensors based on these

“high- $T_c$ ” materials have much lower sensitivity and much higher saturation levels than those that are discussed here.

In low- $T_c$  materials, the phenomenon of superconductivity has been fairly well understood since the 1950s, when detailed microscopic and macroscopic theories were developed. Superconductivity in low- $T_c$  materials occurs when two electrons are bound together in “Cooper” pairs, acting as one particle. The energy binding Cooper pairs prevents them from scattering, allowing them to flow without resistance. *Bardeen, Cooper, and Schrieffer* first explained the formation of Cooper pairs in 1957 in the landmark microscopic BCS theory [31].

The energy binding the two electrons in a Cooper pair is due to interactions with positive ions in the lattice mediated by phonons (quantized lattice vibrations). When a negatively charged electron flows in a superconductor, positive ions in the lattice are drawn towards it, creating a cloud of positive charge. A second electron is attracted to this cloud. The energy binding the two electrons is referred to as the “superconducting energy gap” of the material. In the BCS theory, the size of the Cooper pair wave function is determined by the temperature-dependent coherence length  $\xi(T)$ , which has the zero-temperature value  $\xi_0 \equiv \xi(0) \approx 0.18v_F/(k_B T_c)$ . Here  $v_F$  is the Fermi velocity of the material,  $k_B$  is the Boltzmann constant, and  $T_c$  is the superconducting transition temperature. At temperatures above the transition temperature, thermal energies of order  $k_B T$  spontaneously break Cooper pairs and superconductivity vanishes. In a BCS superconductor, the transition temperature  $T_c$  is related to the superconducting energy gap  $E_{\text{gap}}$  of the material by  $E_{\text{gap}} = 2\Delta(0) \approx 3.5k_B T_c$ . In addition to perfect dc conductivity below  $T_c$ , a second hallmark of superconductivity is the Meissner effect: the free energy of the system is minimized when an external magnetic field is excluded from the interior of a superconducting sample. An applied magnetic field is exponentially screened by an induced Cooper-pair supercurrent with an effective temperature-dependent penetration depth,  $\lambda_{\text{eff}}(T)$ . The approximate zero-temperature value of the penetration depth is the London penetration depth,  $\lambda_L(0)$ .

Near the transition temperature, the physics of a superconductor is well described by the macroscopic Ginzburg–Landau theory [32], which was derived by a Taylor expansion of a phenomenological order parameter  $\Psi$ .  $\Psi$  was later shown to be proportional to the density of superconducting pairs [33]. One result of the Ginzburg–Landau theory is that the characteristics of a superconductor with penetrating magnetic flux (such as a superconductor on its transition) are strongly dependent on its dimensionless Ginzburg–Landau parameter,  $\kappa \equiv \lambda_{\text{eff}}(T)/\xi(T)$ . If  $\kappa < 1/\sqrt{2}$ , the superconductor is of Type I, and the free energy is minimized when magnetic flux that has penetrated the material clumps together. If  $\kappa > 1/\sqrt{2}$ , the superconductor is of Type II, and magnetic flux that has penetrated the material preferentially separates into individual flux quanta that repel each other. The size of the flux quantum is

$\Phi_0 = h/2e = 2.0678 \times 10^{-15}$  Wb. Whether a film is of Type I or II influences the physics of the transition, its noise behavior, current-carrying capability, and sensitivity to magnetic field. Transition-edge sensors with  $T_c < 1$  K can be either Type I or II.

The superconducting films considered in this section are usually in the dirty limit (the coherence length is typically  $> 1$   $\mu\text{m}$  for  $T_c < 1$  K, and mean free paths are usually a few tens or hundreds of nanometers.) See Table 2 in Sect. 3 for a list of coherence lengths of typical TES superconductors. A film in the dirty limit at  $T_c$  has an approximate Ginzburg–Landau Parameter ([34] p. 120),

$$\kappa \approx 0.715 \lambda_L(0)/\ell(d) , \quad (1)$$

where  $\ell(d)$  is the electron mean free path, which is a function of the film thickness  $d$ . See Table 2 for a list of London penetration depths, and Sect. 3.4 for a discussion of the electron mean free path. As can be shown by (1), TES detectors with a high mean free path, such as many TES X-ray detectors, have a low  $\kappa$  and are typically Type I. TES detectors with a shorter mean free path, including optical TES detectors fabricated using thin tungsten films, have a higher  $\kappa$  and are typically Type II.

The physics of a BCS superconductor well below  $T_c$  is largely understood. However, the situation is more complicated in the transition region. In a typical TES, the measured transition width in the presence of a very small bias current (e.g. the current from a sensitive resistance bridge) is 0.1 mK to  $\sim 1$  mK. In the presence of typical operational bias currents, the transition width is usually a few mK. The variation of resistance with temperature can be caused by nonuniformities in  $T_c$ , by an external field, by transport current densities approaching the critical current density, by magnetic fields induced by transport current, or by variations in temperature within the TES due to Joule heating or other sources of power. The transition is strongly influenced by the geometry and by imperfections in the boundaries of the film and in the film itself. However, the transition width is finite even for a uniform film with near-zero applied current and no external field, which is the case that we consider first.

In a Type II superconductor, a current exerts a Lorentz force on flux quanta at pinning sites in the film. When the current is near zero, the Lorentz force is insufficient to overcome the pinning force, and the superconductor does not exhibit dc electrical resistance. However, as the temperature approaches the transition temperature, thermal energy of order  $k_B T$  allow flux lines to jump between pinning sites, creating a voltage and a finite transition width. The number of vortices present is a function of the magnetic field. Even at zero field, vortex–antivortex pairs can be thermally generated in the interior of the film. At the Kosterlitz–Thouless transition temperature of the film,  $T_{\text{KT}}$  [35, 36], thermal energies are sufficient to generate and unbind vortex–antivortex pairs, creating a thermally excited distribution of vortices

that can move in response to a transport current.  $T_{KT}$  is typically slightly below  $T_c$ , leading to a finite transition width even in a perfect Type II film at zero field and transport current approaching zero.

A finite transition width must also occur in Type I superconductors, because thermodynamic fluctuations cause the system to statistically sample any states that raise the free energy by about  $k_B T$ . In a thin, one-dimensional superconducting wire, as the transition is approached, fluctuations periodically cause the order parameter to reach zero at some point, allowing a phase slip of  $2\pi$  [37]. These phase slips lead to a finite transition width. The onset of resistance occurs when  $k_B T$  approaches the energy required to drive a segment of the wire as long as  $\xi(T)$  normal. Quantitative predictions of the phase-slip-driven width of the transition of tin wires have been experimentally verified [38, 39].

At the bottom of the transition (near  $R = 0$ ) in a perfect two-dimensional Type I thin film (wider than  $\xi(T)$ ) at zero current bias, it is energetically unfavorable for thermal fluctuations to drive a segment that is the entire width of the film normal. The transition is thus more complicated in a two-dimensional Type I film than in a one-dimensional Type I film. Any flux that penetrates a Type I film tends to clump together, producing larger superconducting and normal regions – a situation referred to as the “mixed state.” As in Type II materials, flux can be generated either by magnetic fields or by thermal effects near  $T_c$ . Smaller normal regions in Type I materials can move in response to a transport current. Higher in the transition, normal regions that span the entire width of the superconducting film lead to resistance even when they do not move. Both of these phenomena lead to a finite transition width at zero field and near-zero applied current.

The transition widths predicted by flux motion in perfect superconducting films at near-zero current bias are typically much smaller than the transition widths measured under bias in a practical TES. In a TES, the approximations of near-zero applied current and film uniformity are not valid. It is obvious that nonuniformity of  $T_c$  or applied magnetic field can lead to finite transition widths. Large bias currents can also lead to transition broadening through Joule heating, critical current effects and self-induced magnetic fields. We now discuss the effect of large transport currents.

Joule heating in the film can lead to variations in temperature across the film, resulting in apparently larger transition widths, and to instability against phase separation into two or more normal and superconducting regions [40]. The effects of self-heating depend on the thermal conductances and geometry of the detector and the form of the superconducting transition. In the general case, the effects of self-heating must be analyzed numerically. However, a simple analysis shows how the effect of self-heating on the transition scales.

At temperatures below 1 K, conductance in a normal-metal film is dominated by Wiedemann–Franz thermal conductance of the normal electrons,

$G_{WF} = L_0 T / R$ , where  $R$  is the resistance of the film and  $L_0$  is the Lorenz number (see Sect. 3.5). The temperature variation caused by the Joule power dissipation depends on the geometry of the detector and the geometry of its link to the heat sink, but is of order  $\Delta T \sim P_J / G_{WF}$ , where  $P_J$  is the Joule power dissipation in the film.

Self-heating can also lead to detector instability and geometrical separation of parts of the device into superconducting and normal phases. If parallel segments of a TES have a temperature differential, the hotter segment has a higher temperature and resistance, and the current preferentially flows to the low-resistance segment, leading to stability. However, if series segments of a TES have a temperature differential, the hottest segment has the highest resistance and receive the highest Joule power, which can lead to thermal runaway and separation into superconducting and normal-phase regions. The condition for thermal runaway depends on the geometry of the TES and its link to the heat sink. In the case where the heat flows uniformly from the TES to the heat bath (for instance, in the case where electron-phonon decoupling is the dominant thermal conductance), the condition for stability against phase separation in a rectangular film can be solved in closed form by expansion of the temperature profile in a two-dimensional Fourier series [40]:

$$R_N < \pi^2 \frac{L_0 T_c n}{G \alpha}, \quad (2)$$

where  $R_N$  is the normal resistance of the film,  $n$  is the exponent of power flow to the heat bath (see Sect. 2.3),  $G$  is the thermal conductance to the heat bath, and  $\alpha = d\log R / d\log T$  is the logarithmic sensitivity of the superconducting transition. At normal resistance above this value, the Wiedemann–Franz thermal conductance is insufficient to prevent separation into superconducting and normal phases.

Even if the Wiedemann–Franz thermal conductance is large enough to minimize temperature gradients in the TES, large transport currents can lead to broadening of the transition width. In Type II films, this broadening occurs as the Lorentz force becomes large enough to overcome the forces binding flux quanta to pinning sites in the material, leading to flux flow and dissipation further below  $T_c$ . In Type I films, the process is even more complicated. A solution of the Ginzburg–Landau equations shows that well below  $T_c$  and  $I_c$ , most of the current flows along the edges of the film. As the bias current approaches the critical current, or the temperature approaches the transition temperature, normal regions are created at the edges that grow across the full width of the film in a phase-slip line (PSL) with a normal core of width  $\xi_{\text{eff}}(T)$  [41]. As the transport current crosses a PSL, it is carried predominantly by the quasiparticles. After crossing the PSL, a fraction of the current is converted to supercurrent by Andreev reflection, but a fraction continues to be carried in the quasiparticle branch. The quasiparticle current relaxes back to a supercurrent over a timescale  $\tau_{Q^*}$ , the quasiparticle branch-imbalance relaxation time. This time corresponds to an effective

normal length scale  $\Lambda_{Q^*} = \sqrt{D\tau_{Q^*}}$ , where  $D$  is the diffusion coefficient of the film. As  $T \rightarrow T_c$ , the Andreev reflected component goes to zero and  $\Lambda_{Q^*}$  diverges, leading to a broadened transition width in the presence of a large current.

The situation is complicated by the fact that new PSLs can be nucleated and denucleated either as a function of the current and temperature, or due to fluctuations. The nucleation of new PSLs leads to steps in the differential resistance of the film. Steps in the differential resistance can in some cases be measured in the complex impedance of a TES, and may be due to the nucleation of new PSLs. Also, the telegraph noise sometimes seen in TES devices may be due to the nucleation of new PSLs. Attempts have been made to derive approximate limits on the  $\alpha$  of a TES due to variations in  $\Lambda_{Q^*}$  [40].

The transition temperature of the TES must be chosen to achieve the needed energy resolution and response time, and to match the available cryogenic system for a particular application. The energy resolution and response time of a TES depend strongly on the temperature because of the temperature dependence of the heat capacity, thermal conductance, thermal noise, and other parameters. Fortunately, the transition temperature can be tuned to the desired value by choosing an element with an appropriate superconducting transition temperature, by the use of the proximity effect in a normal/superconductor bilayer, or by the use of magnetic dopants to suppress the  $T_c$  of a superconductor (see Sect. 3). The most commonly chosen transition temperatures are  $\sim 100$  mK (above the bath temperature in an adiabatic demagnetization refrigerator or dilution refrigerator), and  $\sim 400$  mK (above the bath temperature of a  ${}^3\text{He}$  refrigerator).

## 2.2 TES Small Signal Theory Summary

In Table 1, we summarize the equations for the ideal small-signal performance of a TES. These equations are similar to those derived in the Chapter “Thermal Equilibrium Calorimeters – An Introduction” by *McCammon*, but are specialized for a TES calorimeter. Most importantly, they explicitly include the inductance in the bias circuit, which strongly influences the detector response and noise performance. Because of interactions between the electrical and thermal poles, a consideration of the inductance in the bias circuit is required even to compute the response time of the TES. The explicit inclusion of inductance also allows a computation of the conditions for stability. The results in this section reduce to the results in the Chapter “Thermal Equilibrium Calorimeters – An Introduction” by *McCammon* when the inductance is taken to zero, to the extent that there are comparable equations. In these summary tables, we present the equations for the response of a TES to a delta-function energy impulse, the response to an incident power load (the power responsivity), the response of a TES to a signal on the bias line

(the complex impedance), the stability criteria, the equations for electrothermal feedback (ETF) self-calibration, and the noise performance and energy resolution. The derivation of these equations follows in Sects. 2.3–2.6, but they are gathered here for convenience, with terms defined in the following sections. These equations do not include the effects of excess noise or large signals, which are described in Sects. 2.7 and 2.8.

The derivation of the equations is complicated, but full understanding of all of the mathematical steps is not necessary to make use of the equations. If a detailed understanding of the derivations is not desired, Sects. 2.3–2.6 can be skipped.

### 2.3 TES Electrical and Thermal Response

In this section, we discuss the electrical and thermal bias circuit of the TES and derive the differential equations describing the TES response. In the small signal limit, we solve the equations for response to a pulse of energy (as in a calorimeter), response to an input power (as in a bolometer), and response to a voltage signal on the bias line (the complex impedance of the TES). In later sections, we use these equations to derive the conditions for stability, fluctuations due to noise, and the achievable energy resolution and noise equivalent power.

A TES can be biased with real source impedance ranging from zero (constant voltage bias) to infinite (constant current bias). When a voltage amplifier is used, the chosen bias condition is typically close to a constant-current bias, so as to minimize loading effects that increase the relative amplifier noise and minimize the Johnson noise contribution of the load resistor. When a SQUID current amplifier [10] is used, the bias condition is typically close to a constant-voltage bias for the same reasons. The bias circuit also has reactive elements. For the low-impedance, voltage-bias case, this reactance principally consists of parasitic inductance in the leads and inductance from the SQUID input coil. For a high impedance, current bias case, this reactance principally consists of parasitic capacitance and capacitance from the voltage amplifier. In most cases, TES detectors are now low-impedance devices coupled to SQUID amplifiers. This is the configuration that we consider in this section.

SQUID amplifiers are operated at low temperatures, but they are biased and read out with room-temperature electronics. Wires are run from room temperature to the operating temperature of the SQUID to provide a bias current, to measure the voltage across the SQUID, and to provide a feedback flux to the SQUID to linearize its output.

The output voltage of a typical SQUID is too low to couple directly to a room-temperature amplifier without significant degradation in noise performance, so a variety of techniques are used to improve the match. These include modulating the SQUID and transforming its impedance with a wire-wound transformer, the use of “additional positive feedback” to increase the

**Table 1.** Summary of important equations for TES small-signal performance

Definitions (Sect. 2.3):

$$\alpha \equiv \frac{T_0}{R_0} \frac{\partial R}{\partial T} \Big|_0 \quad \beta \equiv \frac{I_0}{R_0} \frac{\partial R}{\partial I} \Big|_0 \quad \mathcal{L} \equiv \frac{P_0 \alpha}{G T_0}, \text{ where } P_0 = I_0^2 R_0$$

Time constants:

Natural (no feedback)	Constant-current
$\tau = \frac{C}{G}$	$\tau = \frac{\tau}{1 - \mathcal{L}}$
Zero-inductance effective thermal	Electrical
$\tau_{\text{eff}} = \tau \frac{1 + \beta + R_L/R_0}{1 + \beta + R_L/R_0 + (1 - R_L/R_0)\mathcal{L}}$	$\tau_{\text{el}} = \frac{L}{R + R_0(1 + \beta)}$
Delta-function response	Low-inductance limit of $\tau_{\pm}$
$\frac{1}{\tau_{\pm}} = \frac{1}{2\tau_{\text{el}}} + \frac{1}{2\tau} \pm \frac{1}{2} \sqrt{\left(\frac{1}{\tau_{\text{el}}} - \frac{1}{\tau}\right)^2 - 4 \frac{R_0}{L} \frac{\mathcal{L}(2 + \beta)}{\tau}}$	$\tau_+ \rightarrow \tau_{\text{el}}$ and $\tau_- \rightarrow \tau_{\text{eff}}$

Current response to an energy impulse: ( $t > 0$ )

$$\delta I(t) = \begin{cases} \left(\frac{\tau}{\tau_+} - 1\right) \left(\frac{\tau}{\tau_-} - 1\right) \frac{1}{(2 + \beta)} \frac{C \Delta T}{I_0 R_0 \tau^2} \frac{(e^{-\tau/\tau_+} - e^{-\tau/\tau_-})}{(1/\tau_+ - 1/\tau_-)} & \tau_+ \neq \tau_- \\ \left(\frac{\tau}{\tau_{\pm}} - 1\right)^2 \frac{1}{(2 + \beta)} \frac{C \Delta T}{I_0 R_0 \tau^2} (-t e^{-\tau/\tau_{\pm}}) & \tau_+ = \tau_- \end{cases}$$

Power to current responsivity: ( $\omega = 2\pi f$ )

$$s(\omega) = -\frac{1}{I_0 R_0} \frac{1}{(2 + \beta)} \frac{(1 - \tau_+/\tau)}{(1 + i\omega\tau_+)} \frac{(1 - \tau_-/\tau)}{(1 + i\omega\tau_-)} = -\frac{1}{I_0 R_0} \left[ \frac{L}{\tau_{\text{el}} R_0 \mathcal{L}} + \left(1 - \frac{R}{R_0}\right) + i\omega \frac{L\tau}{R_0 \mathcal{L}} \left(\frac{1}{\tau} + \frac{1}{\tau_{\text{el}}}\right) - \frac{\omega^2 \tau}{\mathcal{L}} \frac{L}{R_0} \right]^{-1}$$

Complex impedance: ( $\omega = 2\pi f$ )

$$Z(\omega) = R_L + i\omega L + Z_{\text{TES}}(\omega),$$

where

$$Z_{\text{TES}}(\omega) = R_0(1 + \beta) + \frac{R_0 \mathcal{L}}{1 - \mathcal{L}} \frac{2 + \beta}{1 + i\omega\tau}$$

Stability (Sect. 2.4):

$$L_{\text{crit}\pm} = \left\{ \mathcal{L} \left(3 + \beta - \frac{R_L}{R_0}\right) + \left(1 + \beta + \frac{R_L}{R_0}\right) \pm 2 \sqrt{\mathcal{L}(2 + \beta) \left[\mathcal{L} \left(1 - \frac{R_L}{R_0}\right) + \left(1 + \beta + \frac{R_L}{R_0}\right)\right]} \right\} \frac{R_0 \tau}{(\mathcal{L} - 1)^2}$$

Table 1 (continued)

$\tau_+ = \tau_-$ , or $L = L_{\text{crit}\pm}$	Critical damping ( $L_{\text{crit}-}$ most important)
$L < L_{\text{crit}-}$ or $L > L_{\text{crit}+}$	Overdamping
$\frac{L_{\text{crit}\pm}}{R_0} = (3 + \beta \pm 2\sqrt{2 + \beta}) \frac{\tau}{\mathcal{L}}$	In the limit $R_L = 0$ , $\mathcal{L}_I \gg 1$
$R_0 > \frac{(\mathcal{L} - 1)}{(\mathcal{L} + 1 + \beta)} R_L$	Stability condition, overdamped
$\tau > (\mathcal{L} - 1) \tau_{\text{el}}$	Stability condition, underdamped
ETF self-calibration (Sect. 2.5):	
$\Delta P_{\text{ETF}} = -I_0(R_0 - R_L)\delta I$	ETF power
$E_{\text{ETF}} = (I_0 R_L - V) \int_0^\infty \delta I(t) dt + R_L \int_0^\infty \delta I(t)^2 dt$	ETF energy
Noise (Sect. 2.6): (linear approx. $\xi(I_0) = 1$ , quadratic approx. $\xi(I_0) = 1 + 2\beta_I$ )	
$S_{\text{TES}} = 4k_B T_0 R_0 \xi(I_0)$	TES voltage noise
$S_{\text{TES}}(\omega) = 4k_B T_0 I_0^2 R_0 \xi(I_0)(1 + \omega^2 \tau^2)  s(\omega) ^2 / \mathcal{L}^2$	TES current noise
$S_L = 4k_B T_0 R_L$	Load voltage noise
$S_L(\omega) = 4k_B T_0 I_0^2 R_L (\mathcal{L} - 1)^2 (1 + \omega^2 \tau^2)  s(\omega) ^2 / \mathcal{L}^2$	Load current noise
$S_{\text{TFN}} = 4k_B T_0^2 G F(T_0, T_{\text{bath}})$	TFN power noise
$S_{\text{TFN}}(\omega) = 4k_B T_0^2 G F(T_0, T_{\text{bath}})  s(\omega) ^2$	TFN current noise
Total power-referred noise: ( $S_{\text{amp}}(\omega)$ is the SQUID noise current)	
$S_{\text{tot}}(f) = S_{\text{TFN}} + S_{\text{TES}} I_0^2 \frac{1}{\mathcal{L}^2} (1 + \omega^2 \tau^2) + S_L I_0^2 \frac{(\mathcal{L} - 1)^2}{\mathcal{L}^2} (1 + \omega^2 \tau^2) + \frac{S_{\text{amp}}(\omega)}{ s(\omega) ^2}$	
Energy resolution: (for $S_{\text{amp}} = 0$ )	
$\Delta E_{\text{FWHM}} = 2\sqrt{2 \ln 2} \left( \frac{\tau}{\mathcal{L}^2} \left\{ [ \mathcal{L}^2 S_{\text{TFN}} + I_0^2 S_{\text{TES}} + (\mathcal{L} - 1)^2 I_0^2 S_L ] \right. \right.$	
$\times \left. \left( I_0^2 S_{\text{TES}} + I_0^2 S_L \right) \right\}^{1/2} \right)^{1/2}$	
In the limit $R_L = 0$ , $\mathcal{L}_I \gg 1$ :	
$\Delta E_{\text{FWHM}} = 2\sqrt{2 \ln 2} \sqrt{\frac{\tau I_0}{\mathcal{L}}} \sqrt{(S_{\text{TFN}})(S_{\text{TES}})}$	
$= 2\sqrt{2 \ln 2} \sqrt{\frac{4k_B T_0^2 C}{\alpha}} \sqrt{\frac{n F(T_0, T_{\text{bath}}) \xi(I_0)}{1 - (T_{\text{bath}}/T_0)}}$	

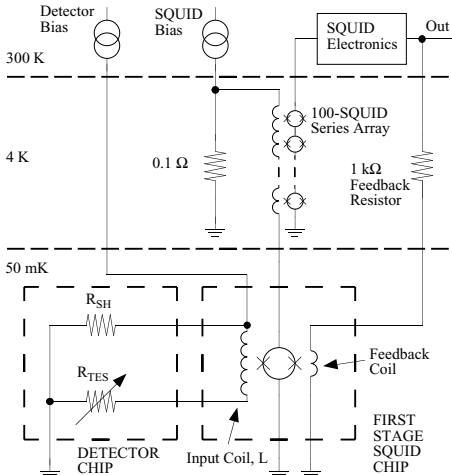


**Fig. 2.** An example of a SQUID readout circuit for a TES. A TES is voltage-biased by applying a current to a small shunt resistor  $R_{SH}$  in parallel with the TES resistance  $R_{TES} \gg R_{SH}$ . The current through the TES is measured by a first-stage SQUID, which is in turn voltage-biased by a current through a small shunt resistor with resistance  $\approx 0.1\Omega$ . The output current of the first-stage SQUID is measured by a series-array SQUID. A feedback flux is applied to linearize the first-stage SQUID

transimpedance of the SQUID (at the cost of reduced dynamic range)[42], the use of “noise cancellation,” [43] and the use of a series array of SQUIDS to increase the output voltage swing [44, 45, 46].

One example implementation of a SQUID circuit to read out a TES is shown in Fig. 2. In this circuit, the stray inductance is kept small by mounting the first-stage SQUID chip at the base temperature of the cryostat, adjacent to a chip with the TES. The shunt resistor is fabricated on the TES chip, and the TES chip is connected to the first-stage SQUID chip by wirebonds. The first-stage SQUID is voltage-biased in series with the input coil of a series-array-SQUID second-stage amplifier. The series-array SQUID amplifies the signal sufficiently to couple to room-temperature electronics.

In addition to the shunt resistance  $R_{SH}$  and the TES resistance shown in Fig. 2, the bias circuit of the TES can also have a parasitic resistance  $R_{PAR}$  in series with the SQUID input coil (Fig. 3a). The TES bias circuit can be represented by a Thevenin-equivalent circuit consisting of a bias circuit with a voltage  $V = I_{BIAS}R_{SH}$  applied to a series combination of a load resistor  $R_L = R_{SH} + R_{PAR}$ , the SQUID input inductance  $L$ , and the TES (Fig. 3b). It is this Thevenin-equivalent circuit that we analyze in this work.

The response of the TES is governed by two coupled differential equations describing the electrical and thermal circuits. Each differential equation governs the evolution of a state variable: the electrical equation determines the current  $I$ , and the thermal equation determines the temperature  $T$ . Ignoring

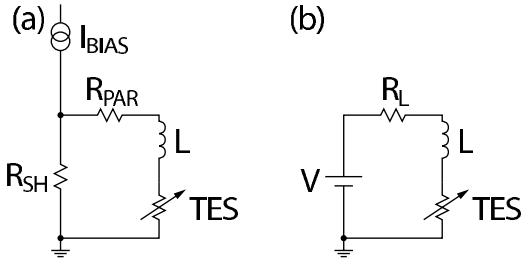


**Fig. 3.** The TES input circuit and a Thevenin-equivalent representation. (a) A bias current  $I_{BIAS}$  is applied to a shunt resistor  $R_{SH}$  in parallel with a parasitic resistance  $R_{PAR}$ , an inductance  $L$  (including both SQUID and stray inductance), and a TES. (b) The circuit model used in this section, the Thevenin equivalent of the circuit in 3(a). A bias voltage  $V = I_{BIAS}R_{SH}$  is applied to a load resistor  $R_L = R_{SH} + R_{PAR}$ , the inductance  $L$ , and the TES

noise terms for the present, the *thermal differential equation* is:

$$C \frac{dT}{dt} = -P_{\text{bath}} + P_J + P , \quad (3)$$

where  $C$  is the heat capacity (of both the TES and any absorber),  $T$  is the temperature of the TES (the state variable),  $P_{\text{bath}}$  is the power flowing from the TES to the heat bath,  $P_J$  is the Joule power dissipation and  $P$  is the signal power.

Once again ignoring noise terms, the *electrical differential equation* is:

$$L \frac{dI}{dt} = V - IR_L - IR(T, I) , \quad (4)$$

where  $L$  is the inductance,  $V$  is the Thevenin-equivalent bias voltage,  $I$  is the electrical current through the TES (the state variable) and  $R(T, I)$  is the electrical resistance of the TES, which is generally a function of both temperature and current. One subtlety is that, depending on the design, a feedback flux applied to the SQUID can reduce the effective value of  $L$  within the bandwidth of the feedback. The feedback bandwidth can be (but is not always) larger than the signal bandwidth. If feedback changes the inductance, the physical  $L$  should be used in signal-to-noise ratio calculations, and the effective  $L$  (including any reduction due to feedback) should be used in calculations of signal level and stability.

These differential equations can be solved in this form [13, 47, 48], or they can be converted to the electrical circuit analogues of the Chapter “Thermal Equilibrium Calorimeters – An Introduction” by *McCammon* – the powerful approach used in Mather’s classic papers [49, 50, 51]. In this Chapter, we keep the thermal–electrical differential equation formalism.

The two differential equations are complicated by several nonlinear terms. These nonlinear terms can be linearized in a small-signal limit around the

steady-state values of resistance, temperature, and current:  $R_0, T_0, I_0$ . In the small-signal limit, we use steady-state values of heat capacity and thermal conductance. We describe the linearization of the power flow to the heat bath, the nonlinear TES resistance, and the Joule power dissipation, and then derive the linearized differential equations for current and temperature.

For the power flow to the heat bath, we assume a power-law dependence, which can be written as

$$P_{\text{bath}} = K (T^n - T_{\text{bath}}^n) , \quad (5)$$

where  $n = \beta + 1$ ,  $\beta$  is the thermal conductance exponent defined in the Chapter “Thermal Equilibrium Calorimeters – An Introduction” by *McCammon*, and the prefactor  $K = G/n(T^{n-1})$ , where the differential thermal conductance  $G \equiv dP_{\text{bath}}/dT$ . Equation (5) can be expanded for small signals around  $T_0$  as:

$$P_{\text{bath}} \approx P_{\text{bath}_0} + G\delta T , \quad (6)$$

where  $G = nKT^{n-1}$  and  $\delta T \equiv T - T_0$ . The values of  $K$  and  $n$  are determined by the nature of the thermal weak link to the heat bath. Four experimentally relevant cases for TES detectors are described in detail in Sect. 3 (insulators such as silicon nitride, electron–phonon coupling, normal-metal links, and acoustic crystal mismatch). The steady-state power flow to the heat bath  $P_{\text{bath}_0} = P_{\text{J}_0} + P_0$ , where the steady-state Joule power is  $P_{\text{J}_0} = I_0^2 R_0$  and the steady-state signal power is  $P_0$ .

Similarly, for small signals, the resistance of the TES can be expanded around  $R_0, T_0, I_0$  to first order as

$$R(T, I) \approx R_0 + \left. \frac{\partial R}{\partial T} \right|_{I_0} \delta T + \left. \frac{\partial R}{\partial I} \right|_{T_0} \delta I , \quad (7)$$

where  $\delta I \equiv I - I_0$ . Substituting the unitless logarithmic temperature sensitivity used in the Chapter “Thermal Equilibrium Calorimeters – An Introduction” by *McCammon*,

$$\alpha_I \equiv \left. \frac{\partial \log R}{\partial \log T} \right|_{I_0} = \frac{T_0}{R_0} \left. \frac{\partial R}{\partial T} \right|_{I_0} , \quad (8)$$

and the current sensitivity

$$\beta_I \equiv \left. \frac{\partial \log R}{\partial \log I} \right|_{T_0} = \frac{I_0}{R_0} \left. \frac{\partial R}{\partial I} \right|_{T_0} , \quad (9)$$

the expression for the resistance is

$$R(T, I) \approx R_0 + \alpha_I \frac{R_0}{T_0} \delta T + \beta_I \frac{R_0}{I_0} \delta I . \quad (10)$$

This equation includes the dependence of the resistance of the TES on both the temperature and the electrical current (the Chapter “Thermal Equilibrium Calorimeters – An Introduction” by *McCammon*). Some authors have defined  $\alpha$  as a total derivative, incorporating the effect on the resistance when the current changes with temperature [40]. In that definition,  $\alpha$  incorporates both temperature and current dependence. Here we use the partial derivative definition, and divide the temperature and current dependence into  $\alpha_I$  and  $\beta_I$ .

It is useful to note that, from (10), the constant-temperature dynamic resistance of the TES is

$$R_{\text{dyn}} \equiv \left. \frac{\partial V}{\partial I} \right|_{T_0} = R_0 (1 + \beta_I) . \quad (11)$$

The Joule power can also be expanded to first order around  $R_0, T_0, I_0$  as

$$P_J = I^2 R \approx P_{J_0} + 2I_0 R_0 \delta I + \alpha_I \frac{P_{J_0}}{T_0} \delta T + \beta_I \frac{P_{J_0}}{I_0} \delta I . \quad (12)$$

We also define the low-frequency loop gain under constant current,

$$\mathcal{L}_I \equiv \frac{P_{J_0} \alpha_I}{G T_0} , \quad (13)$$

and the natural thermal time constant (in the absence of electrothermal feedback),

$$\tau \equiv \frac{C}{G} . \quad (14)$$

We substitute (6), (10), (12), (13), and (14) into (3) and (4), substitute in the small-signal values for the state variables,  $\delta T \equiv T - T_0$  and  $\delta I \equiv I - I_0$ , and drop second-order terms. The dc terms cancel and we arrive at the linearized differential equations:

$$\frac{d\delta I}{dt} = -\frac{R_L + R_0 (1 + \beta_I)}{L} \delta I - \frac{\mathcal{L}_I G}{I_0 L} \delta T + \frac{\delta V}{L} , \quad (15)$$

$$\frac{d\delta T}{dt} = \frac{I_0 R_0 (2 + \beta_I)}{C} \delta I - \frac{(1 - \mathcal{L}_I)}{\tau} \delta T + \frac{\delta P}{C} . \quad (16)$$

Here  $\delta P \equiv P - P_0$  represents small-power signals around a steady-state power load  $P_0$ , and  $\delta V \equiv V_{\text{bias}} - V_0$  represents small changes in the voltage bias around the steady-state value  $V_0$ .

Two limiting cases of these equations can be directly integrated to give results that are used in the full solutions derived later. In the limit of  $\mathcal{L}_I = 0$ , (15) is independent of  $\delta T$  and can be integrated to give an exponential

decay of current to steady state with the bias circuit electrical time constant

$$\tau_{\text{el}} = \frac{L}{R_L + R_0(1 + \beta_I)} = \frac{L}{R_L + R_{\text{dyn}}} . \quad (17)$$

In the limit of  $\delta I = 0$  (hard current bias), (16) can be integrated to give an exponential decay of temperature to steady state with the current-biased thermal time constant

$$\tau_I = \frac{\tau}{1 - \mathcal{L}_I} . \quad (18)$$

When  $\mathcal{L}_I$  is larger than one, the current-biased thermal time constant  $\tau_I$  is negative. As will be seen later, the negative time constant is indicative of instability due to thermal runaway.

These coupled differential equations have been solved both by using harmonic expansion [47, 49, 50, 51] and by using a change of variables by matrix diagonalization to uncouple the two equations. The harmonic expansion approach is necessary to evaluate the spectral dependence of the noise (Sect. 2.5). However, the change of variables approach, which has been used by *Lindeman* to study the TES differential equations [48], provides superior insight into the TES response. We adopt Lindeman's approach to calculating the current response. Substituting in (17), (15), (16) can be represented in a matrix format as

$$\frac{d}{dt} \begin{pmatrix} \delta I \\ \delta T \end{pmatrix} = - \begin{pmatrix} \frac{1}{\tau_{\text{el}}} & \frac{\mathcal{L}_I G}{I_0 L} \\ -\frac{I_0 R_0 (2 + \beta_I)}{C} & \frac{1}{\tau_I} \end{pmatrix} \begin{pmatrix} \delta I \\ \delta T \end{pmatrix} + \begin{pmatrix} \frac{\delta V}{L} \\ \frac{\delta P}{C} \end{pmatrix} . \quad (19)$$

The homogeneous form of (19) is found by taking  $\delta V$  and  $\delta P$  to zero. An appropriate change of variables decouples the two equations. Then, the differential equations can be directly integrated to find solutions in the form of exponentials. The solutions can be converted back to functions of  $T$  and  $I$  by an inverse change of variables. A conventional technique to accomplish this change of variables for coupled linear differential equations is to represent them in a matrix format and to diagonalize the matrix using its eigenvectors. The matrix has two eigenvectors,  $\mathbf{v}_{\pm}$ , with eigenvalues  $\lambda_{\pm}$ .

Consider two functions proportional to the two eigenvectors,  $f_{\pm}(t) = f_{\pm}(t)\mathbf{v}_{\pm}$ . When these functions are substituted into the homogeneous form of (19), the equation reduces to

$$\frac{d}{dt} f_{\pm}(t) = -\lambda_{\pm} f_{\pm}(t) , \quad (20)$$

which can be directly integrated to give a full homogeneous solution

$$\begin{pmatrix} \delta I \\ \delta T \end{pmatrix} = A_+ e^{-\lambda_+ t} \mathbf{v}_+ + A_- e^{-\lambda_- t} \mathbf{v}_-, \quad (21)$$

where the prefactors  $A_{\pm}$  are unitless constants.

The two eigenvalues of the  $2 \times 2$  matrix in (19) are

$$\frac{1}{\tau_{\pm}} \equiv \lambda_{\pm} = \frac{1}{2\tau_{\text{el}}} + \frac{1}{2\tau_I} \pm \frac{1}{2} \sqrt{\left( \frac{1}{\tau_{\text{el}}} - \frac{1}{\tau_I} \right)^2 - 4 \frac{R_0 \mathcal{L}_I (2 + \beta_I)}{L} \frac{\tau}{\tau}}, \quad (22)$$

where we define two time constants  $\tau_{\pm}$  as the inverse eigenvalues. The two eigenvectors are

$$\mathbf{v}_{\pm} = \begin{pmatrix} \frac{1 - \mathcal{L}_I - \lambda_{\pm} \tau}{2 + \beta_I} & G \\ I_0 R_0 \\ 1 \end{pmatrix}. \quad (23)$$

We now present specific solutions of these equations for two important cases: a small delta-function impulse of energy, and a small sinusoidal power load at a given frequency.

In the case of a delta-function impulse (such as the absorption of a photon with instantaneous thermalization), the homogenous solution in (21) can be used with the values of the prefactors determined by the initial value of temperature change from the impulse  $\delta T(0) = \Delta T = E/C$  and initial quiescent current  $\delta I(0) = 0$ :

$$\begin{pmatrix} 0 \\ \Delta T \end{pmatrix} = A_+ e^{-\lambda_+ t} \mathbf{v}_+ + A_- e^{-\lambda_- t} \mathbf{v}_-, \quad (24)$$

which makes it possible, using (23), to solve for the prefactors

$$A_{\pm} = \pm \Delta T \frac{\frac{1}{\tau_I} - \lambda_{\mp}}{\lambda_+ - \lambda_-}. \quad (25)$$

Substituting (25) into (21) and (23) and using the time constants  $1/\tau_{\pm} \equiv \lambda_{\pm}$  in place of the eigenvalues yields equations for the current and temperature for times  $t > 0$ ,

$$\delta I(t) = \left( \frac{\tau_I}{\tau_+} - 1 \right) \left( \frac{\tau_I}{\tau_-} - 1 \right) \frac{1}{(2 + \beta_I)} \frac{C \Delta T}{I_0 R_0 \tau_I^2} \frac{\left( e^{-t/\tau_+} - e^{-t/\tau_-} \right)}{\left( 1/\tau_+ - 1/\tau_- \right)}, \quad (26)$$

$$\delta T(t) = \left( \left( \frac{1}{\tau_I} - \frac{1}{\tau_+} \right) e^{-t/\tau_-} + \left( \frac{1}{\tau_I} - \frac{1}{\tau_-} \right) e^{-t/\tau_+} \right) \frac{\Delta T}{\left( 1/\tau_+ - 1/\tau_- \right)} \quad (27)$$

which are valid for  $t \geq 0$ .

From the form of the current response  $\delta I(t) \propto (e^{-t/\tau_+} - e^{-t/\tau_-})$  in (26), we identify the time constants as the “rise time”  $\tau_+$  and “fall time”  $\tau_-$  (relaxation to steady state) after a delta-function temperature impulse. Equations (26) and (27) are a complete solution for the response of a TES calorimeter to a small delta-function temperature impulse at time  $t = 0$ .

It is interesting to note that, when  $L$  is small so that  $\tau_+ \ll \tau_-$ , (22) reduces to

$$\tau_+ \rightarrow \tau_{\text{el}}, \quad (28)$$

$$\tau_- \rightarrow \tau \frac{1 + \beta_I + R_L/R_0}{1 + \beta_I + R_L/R_0 + (1 - R_L/R_0)\mathcal{L}_I} = \tau_{\text{eff}} \quad (29)$$

which are the electrical time constant  $\tau_{\text{el}}$  of (17), and the effective thermal time constant of the bolometer in the case of zero bias-circuit inductance,  $\tau_{\text{eff}}$ . As the two time constants approach each other, the poles interact, causing the rise and fall times of (22) to differ significantly from  $\tau_{\text{el}}$  and  $\tau_{\text{eff}}$ .

A useful form of (26) is for the case where  $\tau_+ = \tau_-$ . Then, taking the limiting form of (26), the current reduces to

$$\delta I(t) = \left( \frac{\tau_I}{\tau_{\pm}} - 1 \right)^2 \frac{1}{(2 + \beta_I)} \frac{C \Delta T}{I_0 R_0 \tau_I^2} \left( -te^{-t/\tau_{\pm}} \right). \quad (30)$$

As will be seen later, this solution is “critically damped,” and is often chosen to optimize a tradeoff between energy resolution or noise-equivalent power and the required slew rate in the readout electronics.

We now proceed to determine the power-to-current responsivity of the TES. Usually, this is done by means of a harmonic expansion of (19) in a Fourier series [14, 47, 50]. Instead, we find these parameters by direct solution of the differential equation including an inhomogeneous sinusoidal drive term. This approach yields a useful and simple expression that clearly illustrates the dependence of the power-to-current responsivity on the rise and fall times of a delta-function pulse.

In the case of a small, sinusoidal power load  $\delta P = \text{Re}(\delta P_0 e^{i\omega t})$ , the full solution to (19) can be found in the conventional manner of finding a particular solution including the inhomogeneous terms, and adding the homogenous solution (21). The particular solution must satisfy the real part of

$$\frac{d}{dt} \begin{pmatrix} \delta I \\ \delta T \end{pmatrix} = - \begin{pmatrix} \frac{1}{\tau_{\text{el}}} & \frac{\mathcal{L}_I G}{I_0 L} \\ \frac{-I_0 R_0 (2 + \beta_I)}{C} & \frac{1}{\tau_I} \end{pmatrix} \begin{pmatrix} \delta I \\ \delta T \end{pmatrix} + \begin{pmatrix} 0 \\ \frac{\delta P_0}{C} \end{pmatrix} e^{i\omega t}. \quad (31)$$

We look for a particular solution of the form

$$\mathbf{f}(t) = A_+ e^{i\omega t} \mathbf{v}_+ + A_- e^{i\omega t} \mathbf{v}_-, \quad (32)$$

that, when substituted into (31), results in

$$\begin{pmatrix} 0 \\ \frac{\delta P_0}{C} \end{pmatrix} = A_+ \mathbf{v}_+ (i\omega + \lambda_+) + A_- \mathbf{v}_- (i\omega + \lambda_-) \quad (33)$$

Using the eigenvectors from (23), we solve for the prefactors

$$A_\pm = \mp \frac{\delta P_0}{C\tau} \frac{\lambda_\mp \tau + L_I - 1}{(\lambda_+ - \lambda_-)(\lambda_\pm + i\omega)}. \quad (34)$$

A general solution consists of this particular solution added to (21). However, the particular solution has sufficient information to calculate responsivity (the current and temperature fluctuation amplitudes due to a power fluctuation amplitude). Substituting (34) into (32) using (23), and substituting the inverse rise and fall times for the eigenvalues, yields an expression for the responsivity of the TES at angular frequency  $\omega$ :

$$s_I(\omega) = -\frac{1}{I_0 R_0} \frac{1}{(2 + \beta_I)} \frac{(1 - \tau_+/\tau_I)}{(1 + i\omega\tau_+)} \frac{(1 - \tau_-/\tau_I)}{(1 + i\omega\tau_-)}, \quad (35)$$

$$s_T(\omega) = \frac{1}{G} \frac{\tau_+ \tau_-}{\tau^2} \frac{(\tau/\tau_+ + \tau/\tau_- + \mathcal{L}_I - 1 + i\omega\tau)}{(1 + i\omega\tau_+)(1 + i\omega\tau_-)}. \quad (36)$$

Equations (35) and (36) are the power responsivity of a linear TES; the first is the power-to-current responsivity  $s_I(\omega)$ , and the second is the power-to-temperature responsivity  $s_T(\omega)$ . Here we use a lower-case  $s$  for responsivity to avoid confusion with noise power spectral density, which is an upper-case  $S$ .  $s_I(\omega)$  is one of the most important parameters for bolometric applications in which power levels are monitored rather than the energy impulses measured in calorimetry, since it allows measured currents to be referred back to input power signals. In this form, it rolls off at two poles associated with the rise and fall times of (22), including the pole-interaction effects. In the limit that the poles are widely separated and noninteracting,  $\tau_+$  and  $\tau_-$  reduce to the electric and effective zero-inductance thermal time constants of (28) and (29).

Equation (35) can be usefully expressed in terms of the inductance  $L$  instead of the time constants  $\tau_\pm$ :

$$\begin{aligned} s_I(\omega) = & -\frac{1}{I_0 R_0} \left[ \frac{L}{\tau_{el} R_0 \mathcal{L}_I} + \left( 1 - \frac{R_L}{R_0} \right) \right. \\ & \left. + i\omega \frac{L\tau}{R_0 \mathcal{L}_I} \left( \frac{1}{\tau_I} + \frac{1}{\tau_{el}} \right) - \frac{\omega^2 \tau}{\mathcal{L}_I} \frac{L}{R_0} \right]^{-1}. \end{aligned} \quad (37)$$

For a voltage bias case ( $R_L \ll R_0$ ) and strong feedback satisfying the condition

$$\mathcal{L}_I \gg \frac{R_l + R_0(1 + \beta_I)}{(R_0 - R_L)}, \quad (38)$$

the zero-frequency responsivity from (37) is simply

$$s_I(0) = -\frac{1}{I_0(R_0 - R_L)}, \quad (39)$$

and depends only on the bias circuit parameters. This result is discussed further in the next section.

The complex impedance, or the current response given a voltage excitation, can be computed in the same way as the responsivity was in (31) through (35). However, in this case it is more convenient to compute it by a harmonic expansion in a Fourier series [40, 50, 52, 53]. When a Thevenin-equivalent voltage signal with Fourier component  $V_\omega$  is applied to the bias, each component,  $I_\omega$ , of a Fourier-series expansion of the current in (19) satisfies

$$\begin{pmatrix} \frac{1}{\tau_{el}} + i\omega & \frac{\mathcal{L}_I G}{I_0 L} \\ \frac{-I_0 R_0 (2 + \beta_I)}{C} & \frac{1}{\tau_I} + i\omega \end{pmatrix} \begin{pmatrix} I_\omega \\ T_\omega \end{pmatrix} = \begin{pmatrix} \frac{V_\omega}{L} \\ 0 \end{pmatrix}. \quad (40)$$

This formalism is frequently used to analyze the differential equations of coupled mechanical systems, and it has been used to extract the complex impedance of a TES [52]. The inverse of the matrix in (40) has been referred to as a “generalized responsivity matrix,” because it contains both the current and temperature responses to a voltage or power input [53].

If we left-multiply both sides of the equation by the inverse of the matrix in (40), we arrive at a circuit complex impedance

$$Z_\omega = V_\omega / I_\omega = R_L + i\omega L + Z_{\text{TES}}, \quad (41)$$

where the complex impedance of the TES alone is

$$Z_{\text{TES}} = R_0(1 + \beta_I) + \frac{R_0 \mathcal{L}_I}{1 - \mathcal{L}_I} \frac{2 + \beta_I}{1 + i\omega \tau_I}. \quad (42)$$

It is also useful to derive the complex admittance of the full circuit,

$$Y(\omega) = s_I(\omega) I_0 \frac{\mathcal{L}_I - 1}{\mathcal{L}_I} (1 + i\omega \tau_I), \quad (43)$$

where we have used the power-to-current responsivity  $s_I(\omega)$  from (37).

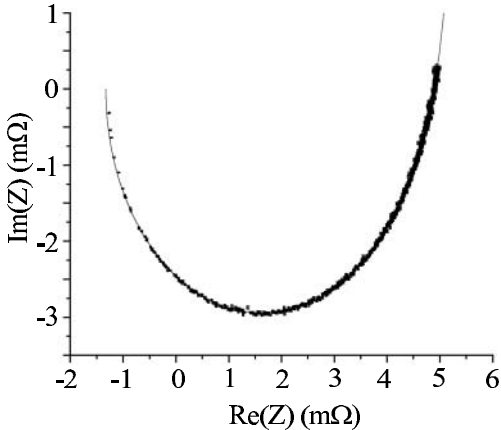


**Fig. 4.** The complex impedance of the bias circuit of a TES X-ray calorimeter measured at many different frequencies using a white noise source. The *line* is a fit of the data to  $Z(\omega) = R_L + i\omega L + Z_{\text{TES}}(\omega)$  using the expression for  $Z_{\text{TES}}(\omega)$  in (42). Figure courtesy of M. Lindeman, Univ. of Wisconsin

The complex impedance is useful as an experimental probe of the linear circuit parameters of a TES [52]. It can be difficult to accurately extract these parameters from the observed detector response to optical signals. By measuring the detector response to voltage signals applied to the bias line, the complex impedance can be measured as a function of frequency. These data can be fit to (41), making it possible to extract the parameters  $\beta_I$ ,  $\mathcal{L}_I$ ,  $\tau_I$ , and  $L$ . From these, using (18) and (14),  $C$  can also be extracted. An example of a fit to the measured complex impedance of a TES X-ray calorimeter is shown in Fig. 4.

## 2.4 TES Stability

The solution for the response of a TES can be either damped or oscillating, and it can be either stable or unstable [40, 48]. As will be seen in the next section, the desire for stable operation at high  $\mathcal{L}_I$  was a historical motivation for introducing voltage-biased operation [13]. We now determine the constraints that these equations place on the operating parameters for stable operation.

If the time constants  $\tau_{\pm}$  of (22) are real, the solution (26) is critically damped or overdamped (exponential, with no sinusoidal component). If they are complex, the response is underdamped (with a sinusoidal component), and if the real part is negative, the response is unstable, and signals grow over time.

From (22), the response of the calorimeter is overdamped if  $\tau_+ < \tau_-$ , and is critically damped if

$$\tau_+ = \tau_- . \quad (44)$$

Practically, this condition constrains the inductance in the bias circuit for damped response. Solving (22) and (44) for the inductance at critical damping, we arrive at

$$L_{\text{crit}\pm} = \left\{ \mathcal{L}_I \left( 3 + \beta_I - \frac{R_L}{R_0} \right) + \left( 1 + \beta_I + \frac{R_L}{R_0} \right) \right. \\ \left. \pm 2 \sqrt{\mathcal{L}_I (2 + \beta_I) \left[ \mathcal{L}_I \left( 1 - \frac{R_L}{R_0} \right) + \left( 1 + \beta_I + \frac{R_L}{R_0} \right) \right]} \right\} \frac{R_0 \tau}{(\mathcal{L}_I - 1)^2}. \quad (45)$$

For zero and very large  $L$ , the response of the calorimeter is overdamped. The response is underdamped when

$$L_{\text{crit}-} < L < L_{\text{crit}+}. \quad (46)$$

Operating at or below  $L_{\text{crit}-}$  is most interesting for voltage-biased calorimeters, as operation at or above  $L_{\text{crit}+}$  reduces the temperature-to-current responsivity of the TES at frequencies of interest, leading to a degradation due to amplifier noise.

In the case of voltage-bias, where  $R_L = 0$ , and strong feedback, where  $\mathcal{L}_I \gg 1, \beta_I$ , (45) reduces to

$$\frac{L_{\text{crit}\pm}}{R_0} = \left( 3 + \beta_I \pm 2\sqrt{2 + \beta_I} \right) \frac{\tau}{\mathcal{L}_I}. \quad (47)$$

This equation, in turn, reduces to the criterion for  $L_{\text{crit}\pm}$  in the limit  $\beta_I = 0$  [40]

$$\frac{L_{\text{crit}\pm}}{R_0} = \frac{\tau}{\mathcal{L}_I} \left( 3 \pm 2\sqrt{2} \right). \quad (48)$$

The response of the calorimeter is stable and tends to relax back to steady-state over time when the real part of both time constants  $\tau_{\pm}$  are positive. This is true when

$$\text{Re} \left[ \frac{1}{\tau_{\text{el}}} + \frac{1}{\tau_I} - \sqrt{\left( \frac{1}{\tau_{\text{el}}} - \frac{1}{\tau_I} \right)^2 - 4 \frac{R_0}{L} \frac{\mathcal{L}_I (2 + \beta_I)}{\tau}} \right] > 0. \quad (49)$$

Equation (49) can be simplified in both the overdamped and underdamped cases. If  $\tau_+ < \tau_-$ , the TES is overdamped, and (49) becomes

$$\frac{1}{\tau_{\text{el}}} + \frac{1}{\tau_I} > \sqrt{\left( \frac{1}{\tau_{\text{el}}} - \frac{1}{\tau_I} \right)^2 - 4 \frac{R_0}{L} \frac{\mathcal{L}_I (2 + \beta_I)}{\tau}}. \quad (50)$$

Substituting in (17) for the electrical time constant, this equation reduces to

$$R_0 > \frac{(\mathcal{L}_I - 1)}{(\mathcal{L}_I + 1 + \beta_I)} R_L . \quad (51)$$

Equation (51) is the criterion for stability of an overdamped TES. It places a constraint on the value of the Thevenin-equivalent load resistor  $R_L$  to prevent thermal runaway from positive feedback if  $\mathcal{L}_I$  is greater than one. It is automatically satisfied when  $R_0 > R_L$ , so a simple, linear, voltage-biased TES is always stable when it is over- or critically damped.

In the underdamped case, the real part of the square root in (49) vanishes, and the TES is stable when

$$\tau > (\mathcal{L}_I - 1) \tau_{el} , \quad (52)$$

or, equivalently, when

$$\mathcal{L}_I \leq 1, \quad \text{or} \quad \mathcal{L}_I > 1 \quad \text{and} \quad L < \frac{\tau}{\mathcal{L}_I - 1} [R_L + R_0 (1 + \beta_I)] . \quad (53)$$

Equation (52), and equivalently equation (53), represents the criterion for stability of an underdamped TES. It constrains how large the inductance can be (or how fast the detector response can be) before the onset of unstable electrothermal oscillations that grow over time. If a TES is critically damped, conditions (51), (52), and (53) are equivalent.

## 2.5 Negative Electrothermal Feedback

In the previous two sections, we developed the equations for the response and stability of a linear TES with arbitrary  $R_L$ . We now further discuss the effect of the value of  $R_L$  on the characteristics of the TES, considering in detail the important special case of strong negative electrothermal feedback: voltage bias ( $R_L \ll R_0$ ) and high low-frequency constant-current “loop gain” ( $\mathcal{L}_I \gg 1, \beta_I$ ). In this limit, there are significant simplifications and operational advantages, including stable operation with high  $\mathcal{L}_I$ , reduced sensitivity to TES parameter variation (making it possible to operate large arrays of TES devices), faster response time, self-biasing, and self-calibration.

The thermal and electrical circuits of a TES interact due to the cross-terms in the thermal-electrical differential equations (15) and (16). A temperature signal in a TES is transduced into an electrical current signal by the change in the resistance of the TES. In turn, the electrical current signal in the TES is fed back into a temperature signal by Joule power dissipation in the TES. This “electrothermal feedback” (ETF) process is analogous to electrical feedback in a transistor circuit. And, as in a transistor circuit, feedback can be either positive or negative.

In a TES,  $\alpha_I$  is positive, so the resistance of the TES increases as the temperature increases. Under current-bias conditions ( $R_L \gg R$ ), as the temperature and resistance increase, the Joule power,  $P_J = I^2 R$ , increases as

well, and the ETF is positive. Under voltage-bias conditions ( $R \gg R_L$ ), the Joule power,  $P_J = V^2/R$ , decreases with increasing temperature, and electrothermal feedback is negative. When the load is matched ( $R = R_L$ ) the Joule power is independent of temperature for small changes in  $R$ , and there is no electrothermal feedback.

There are significant advantages to using negative feedback in transistor circuits, and many of these advantages apply to TES circuits as well. When operated with positive feedback, an amplifier can easily become unstable. High-gain transistor amplifiers tend to have non-negligible variation in intrinsic parameters including the open-loop gain. When negative feedback is used, the (closed-loop) gain is determined by the extrinsic parameters of the bias circuit instead of the amplifier itself, making circuit performance more uniform and reproducible. Furthermore, negative feedback linearizes the detector response and increases the dynamic range.

When voltage biased, a TES is stable against thermal runaway even at high  $\mathcal{L}_I$ . As the temperature is increased, the reduction in Joule power acts as a restoring force. From (51), a damped (overdamped or critically damped) TES is stable when  $R_0 > R_L$ . In contrast, in a current-biased TES ( $R_L \ll R_0$ ), an increase in temperature results in increased Joule power. From (51), a damped, current-biased TES is stable from thermal runaway only when  $\mathcal{L}_I \leq 1$ , seriously restricting the range of available operational parameters. However, even a voltage-biased TES can sometimes be unstable due to growing electrothermal oscillations. Just as in an amplifier, unstable oscillations occur when the “loop gain” is above unity at a frequency where the phase shift in the feedback signal is larger than  $180^\circ$ . The condition to avoid unstable oscillations is (52).

Another attractive feature of a voltage-biased TES is that, over a certain range of signal power and bias voltage, it self-biases in temperature within its transition. This feature is important for array applications. If multiple pixels in an array have superconducting phase transition regions that do not overlap in temperature, it is impossible to bias them all at the same temperature. However, if they are voltage biased, and the bath temperature is much lower than the transition temperature, the Joule power dissipation in each pixel causes it to self-heat to within its respective phase transition. When the bath temperature is well below the transition temperature, the TES performance is also less sensitive to fluctuations in the bath temperature, easing the requirements for temperature stability.

Negative feedback also generally increases the bandwidth of an electrical system. This is also true for TES detectors. As is evident in (22) and more clearly in (29), if a TES is voltage biased, for high  $\mathcal{L}_I$  the thermal relaxation time  $\tau_- \propto \mathcal{L}_I^{-1}$ . In the strong feedback limit,  $\tau_- \ll \tau$ . Negative feedback has been experimentally shown to speed up the pulse fall time of a TES by more than two orders of magnitude. While the feedback speeds up the response time, when other parameters are held fixed, it does not increase the signal-

to-noise ratio at any frequency, so that it does not itself improve the energy resolution. However, it does increase the useful count rate. If multiple small pulses arrive within several effective time constants of each other, it can be difficult to deconvolve the two signals without a loss in energy resolution. More importantly, if multiple pulses drive the TES out of its linear range (or into saturation), degradation in energy resolution is unavoidable. As a result, pulse pileup is normally vetoed. Thus, negative feedback can lead to dramatic increases in useful bandwidth. Another advantage of a voltage bias is that it makes it possible to use a higher  $\mathcal{L}_I$  than a current biased TES without thermal runaway, so it provides more flexibility in the choice of design parameters. This flexibility may make it possible to design a sensor with better energy resolution.

The low-frequency power-to-current responsivity  $s_I(0)$  of a TES is, in general, dependent on the intrinsic TES parameters including  $\alpha_I$ ,  $\beta_I$ ,  $\mathcal{L}_I$  and  $R_0$ . There can be large pixel-to-pixel variation in intrinsic TES parameters across an array due to slightly different  $T_c$ , transition width, and magnetic field environment. However, as shown in equation (39), the low-frequency responsivity of a TES in the strong negative ETF limit is simply  $s_I = -1/(I_0(R_0 - R_L))$ , where the steady-state voltage across the TES is  $V_{\text{TES}} = I_0R_0$ . The low-frequency responsivity is a function solely of the steady-state bias voltage and the load resistance, and independent of the intrinsic TES parameters, making the response of many pixels across an array more uniform and reproducible than in the current-bias case. This simplification is a consequence of conservation of energy. For negative ETF with high  $\mathcal{L}_I$ , the temperature change approaches zero. Thus, the low-frequency power coming into a TES must approach the reduction in the Joule power due to ETF for small  $\delta I$ :

$$\Delta P_{\text{ETF}} = -I_0(R_0 - R_L)\delta I, \quad (54)$$

resulting in the responsivity of (39).

We have shown that the low-frequency current responsivity of a TES bolometer in the strong ETF limit is self-calibrating (i.e., it is a function only of the extrinsic bias circuit parameters). The energy pulses in a TES calorimeter are similarly self-calibrating. During a current pulse, the energy removed from a calorimeter by electrothermal feedback (i.e., by a reduction in the bias power from the steady-state value) is

$$E_{\text{ETF}} = - \int_0^\infty V_{\text{TES}}(t)\delta I(t) dt. \quad (55)$$

The voltage across the TES is

$$V_{\text{TES}}(t) = V - [I_0 + \delta I(t)]R_L - L \frac{d\delta I(t)}{dt}, \quad (56)$$

where  $\delta I(t)$  is negative and  $I_0$  is positive.

When (56) is substituted into (55), the inductive term goes to zero on integration since the energy stored in the inductor is the same before and after a pulse:

$$\int_0^\infty L\delta I(t)\frac{d}{dt}\delta I(t) dt = \frac{L}{2}\delta I^2(\infty) - \frac{L}{2}\delta I^2(0) = 0. \quad (57)$$

The pulse energy removed by electrothermal feedback is thus

$$E_{\text{ETF}} = (I_0 R_L - V) \int_0^\infty \delta I(t) dt + R_L \int_0^\infty \delta I^2(t) dt \quad (58)$$

which is independent of the inductance of the bias circuit. In the strong-feedback limit, the pulse fall time  $\tau_- \ll \tau$ , so the energy in the pulse must approach  $E_{\text{ETF}}$  by conservation of energy.

Equations (54) and (58) are frequently used to make initial estimates of power and energy in TES bolometers and calorimeters. However, detailed detector calibration is used for most real applications. This is necessary because  $\mathcal{L}_I$  is finite and errors of parts in a thousand are often important. However, the increased uniformity between pixels due to the voltage bias is important for array applications.

## 2.6 Thermodynamic Noise

Like all physical systems with dissipation, the response of a TES is affected by thermodynamic fluctuations of its state variables. In this section, we present an analysis of these thermodynamic noise sources. The thermodynamic fluctuations associated with an electrical resistance are referred to as Johnson or Nyquist noise, and the thermodynamic fluctuations associated with a thermal impedance are often referred to as phonon noise or thermal fluctuation noise (TFN). These noise sources set fundamental limits on the noise equivalent power and energy resolution of a TES. Additional noise sources degrade the performance of a TES from these fundamental limits. These extra noise sources include quantum fluctuations (which are usually negligible in a TES), fluctuations in the superconducting order parameter, flux motion, and thermodynamic fluctuations due to hidden state variables internal to the sensor, such as poorly-coupled heat capacity. In this section, we discuss the fundamental thermodynamic noise sources assuming no internal hidden variables (i.e., assuming Markovian noise processes). In Sect. 2.7, we discuss other noise sources.

When the power and voltage signals in the coupled differential equations (15) and (16) are stochastic forces determined by correlations in the state variables due to thermodynamic fluctuations, the differential equations are referred to as Langevin equations. The Langevin equations describe the

response of the state variables to these fictional random forces. The thermodynamic noise can be analyzed by applying the Fluctuation-Dissipation Theorem (FDT) to these Langevin equations. However, to properly apply the FDT, it is important to identify the conjugate forces associated with the state variables.

In the electrical differential equation, the current  $I$  is the state variable (the “velocity” term in the Lagrangian), and the voltage  $V$  is the associated conjugate force. It can be seen that  $V$  is the conjugate force by imagining a resistor in a simple circuit with an ideal linear inductor  $L$ . The circuit is connected to a heat bath at a fixed temperature, so fluctuations in the current follow the canonical, or “Gibbs” distribution. The free energy is the energy stored in the inductor,  $F = LI^2/2$ . The conjugate momentum is thus  $p = \partial F / \partial I = LI$  and the conjugate force is  $dp/dt = L dI/dt = V$ .

In the formalism of thermodynamics that we use here, the temperature  $T$  is allowed to fluctuate, and is considered to be the state variable [54, 55] (in other formalisms, temperature is defined as an equilibrium quantity that does not fluctuate [56]). The heat capacity of the TES is connected through a thermal conductance to a heat bath at a fixed temperature, so the canonical distribution also applies to the thermal circuit. Thus, when heat  $dQ$  flows between the heat bath and the bolometer, the free energy change is [54]  $dF = -S dT$ , where  $S$  is the entropy, and the conjugate momentum is  $p = \partial F / \partial T = -S$ . The heat flowing to the thermal circuit is  $dQ = T dS$ , so the conjugate force is  $dp/dt = -(1/T) dQ/dT = -P/T$ . The sign of the random power is arbitrary; here we use  $P/T$  as the conjugate force.

When analyzing coupled Langevin equations with the FDT, it is convenient to represent the Langevin equations as an “impedance” matrix  $Z$  connecting the vector of the state variables (the “velocity” vector) to the conjugate force vector. Then the Langevin equations are represented as

$$Z \begin{pmatrix} I_\omega \\ T_\omega \end{pmatrix} = \begin{pmatrix} V_\omega \\ P_\omega \\ T_0 \end{pmatrix}. \quad (59)$$

In (40), we presented a matrix for the coupled TES differential equations that is similar to the impedance matrix, but that does not use the conjugate forces. Converting (40) to the conjugate forces in (59), we arrive at an impedance matrix:

$$Z_{\text{ext}} = \begin{pmatrix} \left( \frac{1}{\tau_{\text{el}}} + i\omega \right) L & \frac{\mathcal{L}_I G}{I_0} \\ [-I_0 R_0 (2 + \beta_I)] \frac{1}{T_0} \left( \frac{1}{\tau_I} + i\omega \right) \frac{C}{T_0} \end{pmatrix}. \quad (60)$$

This equation was derived assuming that the Joule power dissipation in the TES is  $P_J = IV_{\text{TES}} = I^2 R$ , where  $V_{\text{TES}} = IR$  [see (12)]. In (60), any fluctuating voltage (such as Johnson noise) changes the current, and thus does

work on the TES. However, work done by the bias current on the fluctuating voltage is not included in this expression for  $P_J$ . Any power dissipated inside this voltage source is dissipated externally (the heat sink of the voltage source does not connect to the thermal circuit of the TES). Here we refer to this impedance matrix as the “external” impedance matrix  $Z_{\text{ext}}$ .

However, work done on a voltage source internal to the TES, such as work done on a Johnson noise voltage or a thermoelectric voltage, should cause power dissipation in the thermal circuit of the TES. The power dissipation is thus  $P_J = IV_{\text{TES}}$ , where  $V_{\text{TES}} = IR + V_{\text{noise}}$  includes the fluctuating noise voltage. Work that is done on a Johnson noise voltage source can be either positive or negative.

In previous work with the TES differential equations [47, 48, 50], power dissipation due to work done on internal voltage noise sources was accounted for by adding an extra power term in the random force vector on the right-hand side of (59). We instead include this power in the matrix on the left-hand side. The two approaches are mathematically equivalent, but the latter allows the straightforward derivation of the internal impedance matrix  $Z_{\text{int}}$  (which properly accounts for power dissipation in internal voltage sources). The derivation of  $Z_{\text{int}}$  allows a more direct consideration of the noise using the fluctuation-dissipation theorem.

To account for the work done on an internal voltage source, we replace equation (12) with the following expression for the Joule power dissipation in the TES:

$$P_J = IV_{\text{TES}} = I(IR + V_{\text{noise}}) = I \left( V_{\text{bias}} - IR_L - L \frac{dI}{dt} \right), \quad (61)$$

where, on the right-hand side of (61), we have used the fact that the total voltage around the loop in the bias circuit is zero. Unlike (12), (61) describes Joule power dissipation equal to the full dissipation in the circuit, except for the dissipation in the load resistor. In (61), work done by the bias current on a Johnson noise voltage source in the TES leads to Joule power dissipation in the sensor. Equation (61) can be Taylor expanded for small  $\delta I$  around  $I_0$ :

$$P_J = I_0^2 R_0 + I_0(R_0 - R_L)\delta I - I_0 L \frac{d\delta I}{dt}, \quad (62)$$

and harmonically expanded:

$$P_J(\omega) = [I_0(R_0 - R_L) - i\omega L I_0] I_\omega. \quad (63)$$

When inserted into (16) in the place of (12), we arrive at

$$Z_{\text{int}} = \begin{pmatrix} \left( \frac{1}{\tau_{\text{el}}} + i\omega \right) L & \frac{\mathcal{L}_I G}{I_0} \\ \left[ I_0(R_L - R_0) + i\omega L I_0 \right] \frac{1}{T_0} \left( \frac{1}{\tau} + i\omega \right) \frac{C}{T_0} & \end{pmatrix}, \quad (64)$$

where the coupled thermal-electrical differential equations become

$$Z_{\text{int,ext}} \begin{pmatrix} I_\omega \\ T_\omega \end{pmatrix} = \begin{pmatrix} V_{\text{int,ext},\omega} \\ \frac{P_\omega}{T_0} \end{pmatrix}. \quad (65)$$

The impedance matrix determines the correlations in the thermodynamic fluctuations of the state variables. In fact, any impedance  $Z$  that connects a state variable to a conjugate force in a physical system causes correlations in the state variable if  $Z$  has a non-zero real component. By the fluctuation-dissipation theorem, at equilibrium and when quantum fluctuations are small, the power spectral density of the fluctuations in the state variable  $u$  is [57]

$$S_u(\omega) = 4k_B T \operatorname{Re}[Y(\omega)] \quad (66)$$

where  $Y(\omega) \equiv Z^{-1}(\omega)$  is the admittance. These correlations can be considered to be caused by a fictional random force  $F$  with power spectral density [57]

$$S_F(\omega) = 4k_B T \operatorname{Re}[Z(\omega)]. \quad (67)$$

The corresponding matrix form of (66) is [58]

$$S_{u_i}(\omega) = 4k_B T \operatorname{Re}[Y_{ii}(\omega)], \quad (68)$$

where  $i$  is the vector index, and the power spectral density of the fluctuations in the velocity variable  $u_i$  is determined by the corresponding diagonal element of the admittance matrix  $Y_{ii}$ .

It is tempting to apply the matrix form of the fluctuation-dissipation theorem directly to the impedance matrix in (64). However, the predictions from this process are not consistent with experimental results. The problem arises from the fact that this simple FDT is rigorous only when applied to linear circuits at thermodynamic equilibrium. The Langevin equations may be at steady state, but as long as there is a non-zero bias current the temperature is not equal to the bath temperature, and the system is not at equilibrium. Then, the direct application of (68) gives misleading results.

It is conventional (but not rigorous) to use a simplifying ansatz that we refer to here as the linear equilibrium ansatz (LEA). This ansatz, introduced for the analysis of bolometers by *Mather* [50], asserts that the fictional random forces predicted by the fluctuation-dissipation theorem at equilibrium (when the current is zero) and with linear elements (i.e. ignoring both the current- and temperature- dependence of the resistance) is the same as the fictional random forces that determine the fluctuations in the state variables outside of equilibrium and with nonlinear resistors. Usually the LEA is implicitly assumed without discussion. The LEA is equivalent to the commonly used component-level resistor noise model that associates a random voltage with

power spectral density (PSD)  $S_V = 4k_B T R$  in series with each resistor  $R$ , or a Thevenin-equivalent random current PSD  $S_I = 4k_B T / R$  in parallel with each resistor, independent of the bias circuit. At equilibrium ( $I_0 = 0$ ) in the linear limit ( $\beta_I = 0$ ), the real parts of both (60) and (64) reduce to

$$\text{Re}[Z_{\text{int,ext}}] = \begin{pmatrix} R_0 + R_L & 0 \\ 0 & \frac{G}{T_0} \end{pmatrix}. \quad (69)$$

Then, by the fluctuation-dissipation theorem (67), the power spectral densities of the fictional random forces are determined by the diagonal elements of the equilibrium impedance matrix matrix (69):

$$\begin{pmatrix} S_V \\ \frac{S_{P_{\text{TFN}}}}{T_0^2} \end{pmatrix} = 4k_B T_0 \begin{pmatrix} R_0 + R_L \\ \frac{G}{T_0} \end{pmatrix}. \quad (70)$$

Here  $S_V = S_{V_{\text{TES}}} + S_{V_L}$ ,  $S_{V_{\text{TES}}} = 4k_B T_0 R_0$  is the Nyquist noise voltage of the TES,  $S_{V_L} = 4k_B T_0 R_L$  is the Nyquist noise voltage of the load resistor, and  $S_{P_{\text{TFN}}} = 4k_B T_0^2 G$  is the thermal fluctuation noise across the thermal conductance  $G$ . More generally, if the temperature of the load resistor  $T_L$  and the temperature of the heat bath  $T_{\text{bath}}$  are allowed to vary from  $T_0$ , the LEA predicts  $S_{V_{\text{TES}}} = 4k_B T_0 R_0$ ,  $S_{V_L} = 4k_B T_L R_L$ , and  $S_{P_{\text{TFN}}} = 4k_B T_0^2 G \times F(T_0, T_{\text{bath}})$ , where the form of the unitless function  $F(T_0, T_{\text{bath}})$  depends on the thermal conductance exponent and on whether phonon reflection from the boundaries is specular or diffuse.  $F(T_0, T_{\text{bath}})$  is defined as a function of the temperature of the TES, and typically lies between 0.5 and 1 [50, 59]. In the Chapter “Thermal Equilibrium Calorimeters – An Introduction” by *McCammon*, the function  $F_{\text{LINK}}(T_{\text{bath}}, n)$  was defined as a function of the bath temperature.  $F(T_0, T_{\text{bath}})$  can be derived from the results in the Chapter “Thermal Equilibrium Calorimeters – An Introduction” by *McCammon* by  $F(T_0, T_{\text{bath}}) = F_{\text{LINK}}(T_{\text{bath}}, n)(T_{\text{bath}}/T_0)^{n+1}$ . The random forces can be combined with (65) to determine the power spectral density of the fluctuations in the state variables.

The LEA assumes a linear resistor with no temperature dependence ( $\alpha_I = 0$ ) or current dependence ( $\beta_I = 0$ ) for the determination of the random voltage across the resistor. In reality, both current-dependent and temperature-dependent nonlinearity can change the random noise voltage across the resistor. Here we consider a modification to the LEA that approximately incorporates the affects of a current-dependent resistance but that still does not incorporate the effect of a temperature-dependent resistance. The analysis of noise in circuits with current-dependent nonlinearity ( $\beta_I \neq 0$ ) is complicated by several factors. The Thevenin theorem does not apply to circuits with current-dependent nonlinearity. Thus, component-level noise models with a series voltage noise source do not have a “Thevenin-equivalent”

parallel current noise source. Further, nonlinear resistors have non-Gaussian noise [60], so the Fokker–Planck equation, which has a Gaussian steady-state solution, cannot be used in the analysis.

Here we introduce a more general ansatz that we refer to as the nonlinear equilibrium ansatz (NLEA). The NLEA is equivalent to the LEA, except that it allows the resistor to have current-dependent nonlinearity, with  $\beta_I \neq 0$ . The noise is still determined assuming a system near equilibrium, except that the values of  $\beta_I$  and  $R_0$  are determined at the steady-state bias current,  $I_0$ . The dependence of the power spectral density of the voltage noise on nonlinearity can be written as

$$S_{V_{\text{TES}}} = 4k_{\text{B}}T_0R_0\xi(I_0), \quad (71)$$

where  $\xi(I)$  (unrelated to the superconducting coherence length) can be expressed as a Taylor expansion:

$$\xi(I) = 1 + \frac{d\xi}{dI}\Big|_{I=0} I + \mathcal{O}(I^2). \quad (72)$$

In the linear approximation or  $\xi(I_0) = 1$ , the NLEA reduces to the LEA.

The noise is Markovian if the real part of the load impedance in the bias circuit is frequency independent. Then, the nonlinear Markov fluctuation-dissipation relations can be used to analyze  $\xi(I)$ . The quadratic Markov fluctuation-dissipation relations have been used to consider a quadratic nonlinear resistor in a closed loop with an inductor  $L$  and a nonzero bias current  $I$  [55, 61]. We determine the value of  $d\xi/dI$  in the quadratic resistor approximation by fitting the TES resistance to a quadratic resistor with the same  $R_0 \equiv V/I$  and  $\beta_I$  at the steady-state bias point. The quadratic  $V$ – $I$  relationship is:

$$V = rI + \frac{1}{2}\gamma I^2, \quad (73)$$

where the resistance  $R_0$  approaches the value  $r$  for low current, and  $\gamma$  is a constant quantifying the nonlinearity. In this case, the nonlinear Markov fluctuation-dissipation relations [55, 61] give a voltage noise power spectral density (PSD):

$$S_V = 4k_{\text{B}}T \left[ r + \frac{3}{2}\gamma I + \mathcal{O}(I^2) \right]. \quad (74)$$

From (73), the resistance

$$R_0 \equiv \frac{V}{I} = r + \frac{1}{2}\gamma I, \quad (75)$$

and from (75),

$$\beta_I \equiv \frac{I}{R} \frac{dR}{dI} = \gamma \frac{I}{2R_0}. \quad (76)$$

Substituting (75) and (76) into (74), we have

$$S_V = 4k_B T R_0 [1 + 2\beta_I + \mathcal{O}(I^2)], \quad (77)$$

so we find that  $d\xi/dI = 2\beta_I/I$  in the quadratic resistor approximation.

It is also instructive to consider the case of a resistor with a quadratic conductance. The quadratic conductance is

$$I = gV + \frac{1}{2}\gamma V^2, \quad (78)$$

where the conductance  $G \equiv I/V = 1/R_0$  approaches the value  $g$  for low current, and  $\gamma$  is a constant quantifying the nonlinearity. If a quadratic conductor is biased in parallel with a capacitor, the nonlinear Markov fluctuation-dissipation relations [55, 61] give a parallel current noise PSD:

$$S_I = 4k_B T \left[ g + \frac{1}{2}\gamma V + \mathcal{O}(V^2) \right]. \quad (79)$$

From (78), the conductance

$$G \equiv \frac{I}{V} = g + \frac{1}{2}\gamma V. \quad (80)$$

Substituting (80) into (79), and using  $G = 1/R_0$ , we have

$$S_I = \frac{4k_B T}{R_0} + \mathcal{O}(V^2). \quad (81)$$

In the current-biased circuit, the parallel current source (81) is equivalent to a voltage source in series with the resistor with noise

$$S_V = \frac{4k_B T}{R_0} \left( \frac{dV}{dI} \right)^2 + \mathcal{O}(V^2) = \frac{4k_B T}{R_0} R_{\text{dyn}}^2 + \mathcal{O}(V^2). \quad (82)$$

Using (11) for  $R_{\text{dyn}}$ , we have

$$S_V = 4k_B T R_0 (1 + \beta_I)^2 + \mathcal{O}(V^2) = 4k_B T R_0 (1 + 2\beta_I + \beta_I^2) + \mathcal{O}(V^2). \quad (83)$$

Thus, the model of a quadratic resistor with a series voltage noise source (77) or that for a quadratic conductor with a parallel current noise source (81) are consistent with each other to order  $I$ , with  $d\xi/dI = 2\beta_I/I$ . An analysis of higher-order terms would require the use of the cubic Markov fluctuation-dissipation relations.

In this work, we use the NLEA, which reduces to the conventional LEA used by Mather in the linear approximation  $\xi(I) = 1$ . In the NLEA, the

use of  $\xi(I) > 1$ , such as the quadratic approximation of  $\xi(I) = 1 + 2\beta_I$ , may explain some of the excess noise observed in TES devices (Sect. 2.7). However, two caveats are in order. First, the noise of a nonlinear resistor is non-Gaussian, so the final uncertainty in the measurement of power or energy is also non-Gaussian. Due to the nonlinearity, the probability distribution is not subject to the usual Fokker–Planck stochastic diffusion equation. Instead, the fluctuation-relaxation process is described by a differential equation with a third derivative, leading to a non-Gaussian current distribution. In the balance of this chapter, we ignore the non-Gaussian nature of the noise in computing the energy resolution and noise-equivalent power (NEP). A more complete solution would require propagating the non-Gaussian distribution through the detector response functions. A second caveat is that, even if the resistor is linear, we are still using an ansatz, and a full nonlinear, nonequilibrium thermodynamic analysis of the problem is required for a rigorous solution.

The thermal conductance  $G(T)$  is dependent on the temperature, so it is nonlinear in the same way as a current-dependent  $R(I)$ . We thus expect a nonlinear contribution to the TFN. This noise term can also be analyzed using the nonlinear Markov fluctuation-dissipation relations. Here we assume that the correction to the power spectral density of the TFN due to nonlinear thermal conductance is properly included in  $F(T_0, T_{\text{bath}})$ . However, the TFN is non-Gaussian due to the nonlinear thermal conductance, so that a rigorous analysis would use a fluctuation-relaxation equation with higher-order terms than are included in the Fokker–Planck stochastic diffusion equation.

The power spectral density of the current noise due to both internal and external noise voltages can be found by using (65) to determine the internal and external admittance of the circuit. By using the internal form of the impedance matrix (64), we determine the internal admittance

$$Y_{\text{int}}(\omega) \equiv \frac{I(\omega)}{V_{\text{int}}(\omega)} = -s_I(\omega)I_0 \frac{1}{\mathcal{L}_I}(1 + i\omega\tau) . \quad (84)$$

By using the external form of the impedance matrix (60), we determine the external admittance,

$$Y_{\text{ext}}(\omega) \equiv \frac{I(\omega)}{V_{\text{ext}}(\omega)} = s_I(\omega)I_0 \frac{\mathcal{L}_I - 1}{\mathcal{L}_I}(1 + i\omega\tau_I) , \quad (85)$$

which is the same as the complex admittance of (43).

The noise sources that we consider in this section fall into the categories of external voltage noise with power-spectral density  $S_{V_{\text{ext}}}(\omega)$ , internal voltage noise  $S_{V_{\text{int}}}(\omega)$ , power noise due to thermal fluctuation noise  $S_{P_{\text{TFN}}}(\omega)$ , and amplifier current noise  $S_{I_{\text{amp}}}$ . If these four types of noise sources are uncorrelated, the overall current noise in a TES can be written

$$\begin{aligned} S_I(\omega) = & S_{V_{\text{ext}}}(\omega)|Y_{\text{ext}}(\omega)|^2 + S_{V_{\text{int}}}(\omega)|Y_{\text{int}}(\omega)|^2 \\ & + S_{P_{\text{TFN}}}(\omega)|s_I(\omega)|^2 + S_{I_{\text{amp}}}(\omega) , \end{aligned} \quad (86)$$

and the overall power-referred noise in the TES is:

$$S_P(\omega) = \frac{S_I(\omega)}{|s_I(\omega)|^2}. \quad (87)$$

These expressions are used in computing the limit on the energy resolution of the calorimeter in the next section.

We now compute both the current-referred and the power-referred noise from four important noise sources in the TES: the Johnson noise in the TES, the Johnson noise in the load resistor, the thermal fluctuation noise, and the amplifier noise. The power spectral density of the current noise due to Johnson noise voltages in the TES can be found by substituting (71) into (84):

$$S_{I_{\text{TES}}}(\omega) = 4k_B T_0 R_0 \xi(I) |Y_{\text{ext}}(\omega)|^2, \quad (88)$$

or

$$S_{I_{\text{TES}}}(\omega) = 4k_B T_0 I_0^2 R_0 \frac{\xi(I)}{\mathcal{L}_I^2} (1 + \omega^2 \tau_I^2) |s_I(\omega)|^2, \quad (89)$$

where  $s_I(\omega)$  is the power-to-current responsivity of (35). The TES Johnson noise referred to a power noise is then

$$S_{P_{\text{TES}}}(\omega) = \frac{S_{I_{\text{TES}}}(\omega)}{|s_I(\omega)|^2} = 4k_B T_0 I_0^2 R_0 \frac{\xi(I)}{\mathcal{L}_I^2} (1 + \omega^2 \tau_I^2). \quad (90)$$

Similarly, the power spectral density of the current noise due to Johnson noise voltages in the load resistor can be found from (85):

$$S_{I_L}(\omega) = 4k_B T_L I_0^2 R_L \frac{(\mathcal{L}_I - 1)^2}{\mathcal{L}_I^2} (1 + \omega^2 \tau_I^2) |s_I(\omega)|^2. \quad (91)$$

When referred to a power noise, (91) is

$$S_{P_L}(\omega) = 4k_B T_L I_0^2 R_L \frac{(\mathcal{L}_I - 1)^2}{\mathcal{L}_I^2} (1 + \omega^2 \tau_I^2). \quad (92)$$

We already determined that the thermal fluctuation noise is

$$S_{P_{\text{TFN}}} = 4k_B T_0^2 G \times F(T_0, T_{\text{bath}}), \quad (93)$$

which means that the current-noise fluctuations due to thermal fluctuation noise are

$$S_{I_{\text{TFN}}}(\omega) = 4k_B T_0^2 G \times F(T_0, T_{\text{bath}}) |s_I(\omega)|^2. \quad (94)$$

A final noise term that is routinely encountered in an ideal linear TES is the noise of the SQUID amplifier. SQUID amplifiers have both noise referred

to an input current and voltage noise due to the back action of the SQUID. Correlations in these two noise sources are important. Fortunately, for TES applications, the impedance of the TES is generally much higher than the noise impedance of the SQUID. Thus, we can neglect the correlated voltage noise terms. The current-referred amplifier noise is  $S_{I_{\text{amp}}}(\omega)$ , which makes the power-referred amplifier noise

$$S_{P_{\text{amp}}}(\omega) = \frac{S_{I_{\text{amp}}}(\omega)}{|s_I(\omega)|^2}. \quad (95)$$

A key figure of merit for a TES bolometer is the noise-equivalent power, which is the square root of the power spectral density of the power-referred noise,

$$\text{NEP}(\omega) = \sqrt{S_P(\omega)}. \quad (96)$$

The total noise of the TES,  $S_P(\omega)$ , is the sum of (90), (92), (93), and (95).

The most important figure of merit for a TES calorimeter is the energy resolution. From the Chapter “Thermal Equilibrium Calorimeters – An Introduction” by *McCammon*, the full width at half maximum (FWHM) energy resolution of a calorimeter is

$$\Delta E_{\text{FWHM}} = 2\sqrt{2 \ln 2} \left( \int_0^\infty \frac{4}{S_{P_{\text{tot}}}(f)} df \right)^{-1/2}, \quad (97)$$

where  $f = \omega/2\pi$  and  $2\sqrt{2 \ln 2} \approx 2.355$ . This equation assumes Gaussian noise sources. If there are nonlinear elements, such as nonlinear TES resistance or thermal conductance, the noise is non-Gaussian. Then (97) and the energy resolution calculations that follow are not rigorously applicable. These equations are a good first approximation, but a more detailed nonlinear analysis is needed. From (86) and (87),  $S_{P_{\text{tot}}}(f)$  in (97) is

$$\begin{aligned} S_{P_{\text{tot}}}(f) = & S_{P_{\text{TFN}}} + S_{V_{\text{TES}}} I_0^2 \frac{1}{\mathcal{L}_I^2} [1 + (2\pi f)^2 \tau^2] \\ & + S_{V_{\text{L}}} I_0^2 \frac{(\mathcal{L}_I - 1)^2}{\mathcal{L}_I^2} [1 + (2\pi f)^2 \tau_I^2] + \frac{S_{I_{\text{amp}}}(\omega)}{|s_I(\omega)|^2}, \end{aligned} \quad (98)$$

which includes the Johnson noise voltage of the TES  $S_{V_{\text{TES}}} = 4k_B T_0 R_0 \xi(I)$ , the Johnson noise voltage of the load resistor  $S_{V_{\text{L}}} = 4k_B T_{\text{L}} R_{\text{L}}$ , the thermal fluctuation noise  $S_{P_{\text{TFN}}} = 4k_B T_0^2 G \times F(T_0, T_{\text{bath}})$ , and current fluctuations in the amplifier  $S_{I_{\text{amp}}}$  (the SQUID noise).

The full form of (98) must be used for the general case including amplifier noise, but in the important limit that the amplifier noise  $S_{I_{\text{amp}}}$  is negligible, (97) and (98) integrate to the simple form:

$$\Delta E_{\text{FWHM}} = 2\sqrt{2 \ln 2} \sqrt{\frac{\tau}{\mathcal{L}_I^2} \sqrt{(\mathcal{L}_I^2 S_{P_{\text{TFN}}} + I_0^2 S_{V_{\text{TES}}} + (\mathcal{L}_I - 1)^2 I_0^2 S_{V_{\text{L}}}) (I_0^2 S_{V_{\text{TES}}} + I_0^2 S_{V_{\text{L}}})}}.$$

(99)

Equation (99) is often used in the limit of strong electrothermal feedback ( $\mathcal{L}_I \gg 1$ ), and zero load resistance  $R_L$ , in which case it simplifies to:

$$\Delta E_{\text{FWHM}} = 2\sqrt{2 \ln 2} \sqrt{\frac{\tau I_0}{\mathcal{L}_I} \sqrt{(S_{P_{\text{TFN}}})(S_{V_{\text{TES}}})}}, \quad (100)$$

and

$$\Delta E_{\text{FWHM}} = 2\sqrt{2 \ln 2} \sqrt{\frac{4k_B T_0^2 C}{\alpha_I} \sqrt{\frac{n\xi(I)F(T_0, T_{\text{bath}})}{1 - (T_{\text{bath}}/T_0)^n}}}, \quad (101)$$

where we have used (5) for the power flowing from the TES to the heat bath and  $\mathcal{L}_I \equiv P_0 \alpha_I / GT_0$ . The quadratic approximation of  $\xi(I) = 1 + 2\beta_I$ .

This equation is consistent with the expression in the literature [13]

$$\Delta E_{\text{FWHM}} = 2\sqrt{2 \ln 2} \sqrt{4k_B T_0^2 \frac{C}{\alpha_I} \sqrt{n/2}}, \quad (102)$$

for  $F(T_0, T_{\text{bath}}) = 1/2$ ,  $T_{\text{bath}} \ll T_0$ , and  $\xi(I) = 1$ .

## 2.7 Excess Noise

TES calorimeters and bolometers have achieved excellent noise performance. TES X-ray calorimeters have been demonstrated with energy resolution of  $\Delta E = 2.38 \pm 0.11$  eV FWHM at 5.9 keV, which at the time of this writing is the highest  $E/\Delta E$  achieved by any nondispersive (or energy-dispersive) photon detector. However, the performance of TES detectors still has not achieved the limits predicted by present theory. In addition to effects due to large pulses (Sect. 2.8), a key limitation on the noise performance of TES detectors is due to unexplained noise sources in excess of those calculated in Sect. 2.6. In this section, we describe these noise sources, including both a qualitative description of the different types of excess noise observed experimentally and their scaling with different device parameters, and a review of the status of theoretical explanations for these noise sources. A successful theoretical explanation of the noise will guide the design of TES detectors to achieve their full potential.

Many noise sources can degrade the noise performance of the TES due to imperfect experimental conditions. These include RF pickup, stray photon shot noise, microphonics in the leads, noise in the amplifier chain, contact resistance fluctuations, Johnson noise on the leads, fluctuations in the temperature bath, etc. In this section we ignore these noise sources and consider excess noise sources in the TES itself. The excess noise in the TES falls into four general categories according to its dependence on the thermal circuit

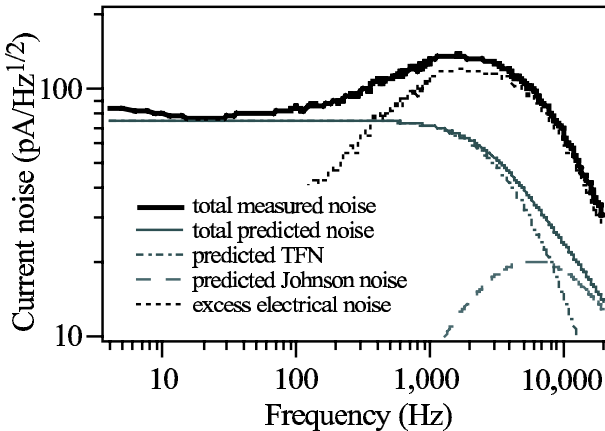


**Fig. 5.** Measured current noise in a Mo/Cu TES X-ray calorimeter at  $R_0 = 0.6 R_N$  and zero magnetic field. Predicted noise contributions and the difference between data and theory are shown. This difference is the excess electrical noise [66]

model of the detector, its frequency dependence, and its temporal structure. In some cases, the different types of excess noise are related.

The first type of excess noise is dependent on the thermal circuit model of the detector. This noise source has been well explained in terms of internal thermal fluctuations between distributed heat capacities inside the TES. It is referred to as internal thermal fluctuation noise (ITFN). It is often worse for high resistance TES detectors, which have low internal Wiedemann–Franz thermal conductance. The second type of excess noise has the same frequency dependence as Johnson noise voltage in the sensor, and tends to be worse for a lower resistance TES. We refer to this noise as “excess electrical noise.” The third type of noise is excess low-frequency noise in the TES, sometimes with  $1/f$  dependence, but often with a different exponent. Excess “low frequency” noise is often correlated with strong excess electrical noise. Finally, in some cases switching, or telegraph, noise is observed in the temporal response of a TES. Telegraph noise is also often correlated with excess electrical noise.

ITFN occurs when the simple lumped-element model used in previous sections is not sufficient [53, 62, 63]. Additional internal variables can lead to non-Markovian noise with non-white random forces. A realistic TES consists of distributed heat capacities connected by internal thermal impedances. In Sect. 2.6, we showed that thermal fluctuations were associated with the thermal conductance connecting a TES to the heat bath. Internal thermal fluctuations are similarly associated with internal thermal impedances. As in Sect. 2.6, an impedance matrix can be derived for a more complex thermal circuit model and used to compute excess noise due to ITFN. For a TES with high resistance, it may be necessary to use a more complex thermal circuit model for the TES itself, consisting of distributed heat capacities each in-

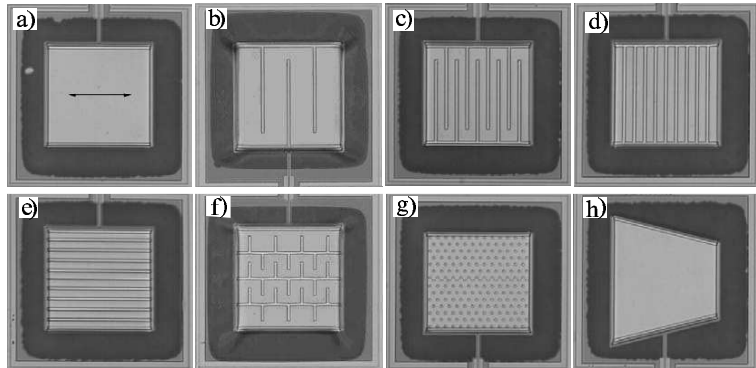


**Fig. 6.** Micrographs of TES sensors on  $\text{Si}_3\text{N}_4$  membranes. The *arrow* in (a) indicates the direction of bias current in all devices. Cu edge passivation is present on TES edges parallel to the bias current. Square sensors are 400  $\mu\text{m}$  on a side. (a) standard pixel with  $R_N = 14 \text{ m}\Omega$  (b) sparse normal bars partially span the device perpendicular to the bias current (c) dense partial perpendicular bars (d) dense full perpendicular bars (e) dense parallel bars (f) parallel and perpendicular bars (g) islands (h) wedge. Normal Cu bars are 10  $\mu\text{m}$  wide and 500 nm thick. Normal Cu islands are 5  $\mu\text{m}$  in diameter and 500 nm thick [66]

terconnected by a Wiedemann–Franz thermal conductance. A higher normal resistance can lead to higher ITFN excess noise.

For a low-resistance TES X-ray calorimeter with an attached absorber, a sufficient thermal circuit model often consists of an absorber heat capacity  $C_{\text{abs}}$  connected through an internal thermal conductance  $G_{\text{int}}$  (such as a bismuth film or an epoxy joint) to the TES heat capacity  $C$ . The TES is then connected through a thermal conductance  $G$  to a heat bath at temperature  $T$ . The two coupled differential equations of the previous section can then be extended to three [53], and solved in the matrix formalism for the full noise. The constraint that ITFN must not significantly degrade the energy resolution places further constraints on the internal thermal conductance and the heat capacity of the absorber.

Aside from ITFN, excess electrical noise with the same frequency dependence as Johnson noise has been observed by multiple research groups using many different TES geometries and materials [6, 7, 64, 65, 66, 67, 68] (Fig. 5). There is as yet no universally accepted theoretical explanation of this noise, although steps have been made to explain it using fluctuations in magnetic domains or phase-slip lines [25, 64, 65], fluctuations in the superconducting order parameter [69, 70], and fluctuations in normal and superconducting regions leading to complex percolation current paths [71].

Excess electrical noise exists in TES detectors where ITFN, which is well understood, does not contribute. This excess noise seems to be larger for lower detector normal resistance, and larger when biased lower in the transition.

The boundary conditions of the TES influence the excess electrical noise. If a normal-metal superconductor bilayer (3.1.2) is used as the TES, and the  $T_c$  is higher at the edges of the film than in the bulk, the excess electrical noise is often extremely high. This situation can be avoided by the fabrication of normal-metal banks on the boundaries parallel to the direction of current flow [72, 73] by the use of elemental superconductors, or by fabricating bilayers with the superconducting layer slightly narrower than the normal layer. It can be reduced much further by the use of normal-metal bars, or “weak links,” in the TES perpendicular to the direction of current flow. The use of perpendicular normal-metal bars to reduce excess noise is the subject of a patent [65], and numerous later publications [66, 67, 68, 74]. Excess electrical noise is also a strong function of the applied magnetic field [25, 66].

The most systematic study to date of the effect of magnetic field and TES geometry on excess electrical noise is that of *Ullom et al.* [66], in which a strong correlation was found between the logarithmic sensitivity  $\alpha$  of the TES and the excess noise. In this work, TES devices with many different geometries were tested (Fig. 6). In all cases, the materials were the same (Mo/Cu bilayers with Cu normal-metal features), the detector normal resistance was approximately the same, the bias point in the transition was held fixed, and in all cases normal-metal banks were used on the boundaries parallel to the direction of current flow. The excess noise is found to be a strong function of both magnetic field and geometry. Furthermore, the logarithmic sensitivity  $\alpha$  of the device was also a function of magnetic field and geometry. A strong correlation between  $\alpha$  and excess noise is observed as the geometry is varied (Fig 7). A very similar correlation is also observed in the case of magnetic field variation. This correlation, however, has been investigated for one only materials system, and for approximately fixed detector size, normal resistance, bias resistance, and thermal conductance. Nevertheless, any quantitative theory put forward to explain the excess electrical noise in TES detectors must be consistent with the strong observed correlations between  $\alpha$  and excess electrical noise.

Excess low-frequency noise is also sometimes observed in the TES. This excess low-frequency noise is problematic especially for bolometric applications, where  $1/f$  knees as low as 0.01 Hz are sometimes desired. Qualitatively, the excess low-frequency noise seems to be correlated with especially high values of the excess electrical noise discussed above. When excess electrical noise is low, the TES  $1/f$  knee appears to be lower than 0.1 Hz. The fundamental source of the  $1/f$  noise is not known.

Finally, telegraph noise is sometimes seen in the temporal response of the TES. The telegraph noise tends to be associated with particularly large excess electrical noise. It generally occurs at specific current and field bias points, and is suppressed by external magnetic fields [25] and normal-metal banks on the boundaries parallel to current flow. Suggested explanations for the telegraph noise include phase-slip line nucleation and denucleation [25, 65] and more

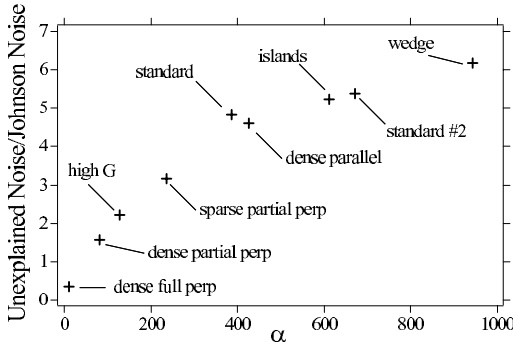


**Fig. 7.** Ratio of excess unexplained noise to Johnson noise versus  $\alpha$  for the TES geometries in Fig. 6. The geometries are measured with the same magnetic field and with resistance at the same fraction of the normal resistance (“perp” = perpendicular) [66]

general rearrangements of superconducting and normal-metal domains [71]. It is also observed that when the bias of the TES crosses one of the telegraph-noise regions, there is a step in the differential resistance of the TES, providing support for the interpretation of phase-slip line nucleation and denucleation or more general rearrangement of magnetic domains.

Before considering explanations for the excess electrical noise based on the details of superconductivity, it should be remembered that the small-signal TES thermodynamic noise theory put forward in previous sections is not rigorous, because TES devices are operated out of equilibrium and in the presence of nonlinear effects. Some of the “excess noise” may be due to nonlinearity or nonequilibrium effects, rather than the details of superconductivity. The NLEA in (71) suggests that some “excess” noise is due to nonzero  $\beta_I$ . The experimentally observed correlation between excess noise and  $\alpha_I$  may be at least partially explained by excess noise arising from nonzero  $\beta_I$ , accompanied by correlations between  $\beta_I$  and  $\alpha_I$ . More work needs to be done in determining correlations between nonlinear and non-equilibrium effects and observed excess noise. Furthermore, there is a need for a full theoretical analysis of the nonlinear, nonequilibrium thermodynamic system. However, while it is likely that nonlinear or nonequilibrium noise theory will provide an explanation for some of the excess noise, it is not likely that it will explain all excess noise, as the exceptionally large excess noise observed in some cases seems to be correlated with the details of superconductivity.

A number of possible mechanisms have been suggested for the excess electrical noise. The physics of the superconducting transition has already been described in Sect. 2.1. All of the mechanisms that have been proposed to explain the excess noise are related to these physical processes, so the mechanisms can be surveyed briefly here. These include either path instabilities or number fluctuations in normal channels or phase-slip lines [25, 40, 65, 75, 76],

fluctuations in the superconducting order parameter [69, 70], and fluctuations in vortex pairs in the Kosterlitz–Thouless transition [36, 64, 77]. To date, only one theory has provided quantitative predictions of noise that match experiment [70], but only in one specific and very noisy geometry. This work involved TES devices fabricated in an annular, or “Corbino” geometry, in which the radial dependence of the current density creates a clear superconducting-normal phase boundary. The Corbino geometry also radially constrains the current distribution, which makes it possible to find simple analytical solutions for the order parameter. In this work, thermodynamic fluctuations in the superconducting order parameter at the superconducting-normal phase interface provides an explanation for the observed noise.

Some sources of excess noise, including ITFN, can be eliminated by careful detector design. Other sources, such as excess electrical noise, can be characterized as an experimentally determined function of other detector parameters such as  $\alpha_I$  or  $\beta_I$ , allowing a computation of their effect on detector performance. If the measured excess electrical noise is written as a voltage-noise power spectral density  $S_{V_X}$ , the total voltage noise in the TES is  $S_{V_{\text{tot}}} = S_{V_{\text{TES}}} + S_{V_X} = (1 + \Gamma^2)S_{V_{\text{TES}}}$ . The ratio of excess noise to Johnson noise  $\Gamma(\alpha_I)$  is characterized in Fig. 7 for one material system, detector size, normal resistance, bias resistance, and thermal conductanc. Here  $S_{V_{\text{TES}}} = 4k_B T_0 R_0$  is the value from the LEA (Sect. 2.6), with  $\xi(I) = 1$ , and any noise from nonlinear resistance is considered part of the excess noise term  $S_{V_X}$ .

$S_{V_{\text{tot}}}$  can then be used to determine the energy resolution. In the common limit of negligible amplifier noise, the energy resolution including excess noise contributions can be written as (99):

$$\Delta E_{\text{FWHM}} = 2\sqrt{2 \ln 2} \times \left( \frac{\tau}{\mathcal{L}_I^2} \left\{ \left[ \mathcal{L}_I^2 S_{P_{\text{TFN}}} + I_0^2 S_{V_{\text{TES}}} (1 + \Gamma^2) + (\mathcal{L}_I - 1)^2 I_0^2 S_{V_L} \right] \right. \right. \\ \left. \left. \times \left( I_0^2 S_{V_{\text{TES}}} (1 + \Gamma^2) + I_0^2 S_{V_L} \right) \right\}^{1/2} \right)^{1/2}. \quad (103)$$

Using (100), in the limit of strong electrothermal feedback ( $\mathcal{L}_I \gg 1$ ), and  $R_L = 0$ , (103) reduces to:

$$\Delta E_{\text{FWHM}} = 2\sqrt{2 \ln 2} \sqrt{\frac{\tau I_0}{\mathcal{L}_I} \sqrt{(S_{P_{\text{TFN}}})(S_{V_{\text{TES}}})(1 + \Gamma^2)}}, \quad (104)$$

and, using (101),

$$\Delta E_{\text{FWHM}} = 2\sqrt{2 \ln 2} \sqrt{\frac{4k_B T_0^2 C}{\alpha_I} \sqrt{\frac{nF(T_0, T_{\text{bath}})(1 + \Gamma^2)}{1 - (T_{\text{bath}}/T_0)^n}}}, \quad (105)$$

which is consistent with the result in [66].

Significant progress is presently occurring in understanding and mitigating excess noise in TES devices. The use of weak-link noise-mitigation features has recently improved the energy resolution of X-ray calorimeters at 5.9 keV from  $\approx 4.0$  eV FWHM to  $2.38 \pm 0.11$  eV FWHM (Sect. 3.6.2). It is likely that over the next several years both the theoretical explanations and realized performance of TES devices will improve further.

## 2.8 Large Signals

In the development of the TES theory of Sects. 2.3–2.6, it is explicitly assumed that incident signals are small (e.g., a low-energy photon absorption in a calorimeter or a small power load in a bolometer). At many points in the derivations, parameters such as the TES resistance and Joule power dissipation are expanded in a Taylor series and the higher-order terms are dropped, leading to expressions depending only on first-order parameters such as  $\alpha_I$ ,  $\beta_I$ ,  $C$ , and  $G$ . In many important applications, however, the small-signal approximation is insufficient. Large energy photons and power loads can “saturate” the TES by driving it outside of its narrow transition region.

A full analysis of the performance of a TES in response to a large signal requires a numerical model with parameters determined by a detailed characterization of the resistance, heat capacity, thermal conductance, and noise as a function of the full range of temperature and electrical current. However, the small-signal theory can prove surprisingly accurate even in the presence of signals that nearly saturate the device. For instance, when (103) or (104) are used to compute the energy resolution of the calorimeter, the results can be within about 20% of experimentally determined values even for energies close to the saturation energy.

The saturation power of a TES bolometer can be written as

$$P_{\text{sat}} = P_{\text{bath}}(T) - \left( \frac{V}{R_L + R_N} \right)^2 R_N , \quad (106)$$

where  $P_{\text{bath}}(T) = K(T^n - T_{\text{bath}}^n)$  is the power flowing to the heat bath at temperature  $T$ , and  $R_N$  is the normal resistance. In the limit of a voltage bias ( $R_L = 0$ ), and a narrow transition, so that  $P_{\text{bath}}$  is approximately constant, (106) reduces to

$$P_{\text{sat}} = \left( 1 - \frac{R_0}{R_N} \right) P_{\text{bath}} . \quad (107)$$

A TES bolometer loses all sensitivity when the signal power exceeds  $P_{\text{sat}}$ . The thermal conductance must be chosen to be large enough that any important signal does not saturate the bolometer. Increasing the thermal conductance so that the highest signal power does not saturate, however, degrades

the NEP for even the lowest measured signal power. To alleviate this limitation, designs have been proposed that use two TES thermometers with different  $T_c$  connected in series [78]. If the saturation power of the lower  $T_c$  TES is exceeded, the TES automatically biases on the higher  $T_c$ , and the bolometer still has some (degraded) sensitivity. When the signal power allows operation on the lower  $T_c$  branch, lower NEP is achieved. A second scheme to improve this limitation is to use a variable thermal conductance [79], with a value changed by an applied magnetic field. When a lower signal power is being measured, the thermal conductance is set low, and lower NEP is achieved. At higher signal power, the thermal conductance is increased.

The “soft” saturation energy  $E_{\text{sat}}$  of a TES calorimeter is the pulse energy that drives the TES completely normal. When the soft saturation energy is exceeded, the top of the pulse becomes flat. The energy resolution is degraded when the pulse energy exceeds  $E_{\text{sat}}$ , but the energy of the pulse can still be estimated, as higher-energy photons lead to pulses that are saturated for longer periods of time. As long as the pulse recovery time is much smaller than  $\tau$ , the energy is still approximately equal to the energy removed by ETF (58). For even higher photon energies, the pulse recovery time becomes comparable to  $\tau$ , and the reponse becomes relatively insensitive to the pulse energy.

It can be shown that, in principle, the energy resolution of a TES calorimeter operated with strong negative feedback into saturation degrades approximately as  $\sqrt{E/E_{\text{sat}}}$  as long as the pulse recovery time is still much smaller than  $\tau$ . In the small-signal limit, the optimal analysis of the pulse energy uses the same filter function for each pulse. Optimal analysis for large pulses is more complicated, and different filter functions must be used for different energies due to pulse nonlinearity [80, 81]. The derivation of these filter function templates can be a laborious process.

In large pulses, the noise is, in general, non-stationary. At the top of the pulse, the TES has a higher resistance, and less noise than at the steady-state resistance value. Optimal analysis in the presence of non-stationary noise also leads to the use of different filter functions for different energies. The optimal analysis of data from a calorimeter with large pulses is derived by *Fixsen et al.* [80, 81]. As long as the pulses are smaller than  $E_{\text{sat}}$ , analysis is often done with small-signal theory, with a constant filter function, with only small degradation in energy resolution. Above  $E_{\text{sat}}$ , the use of varying filter functions is necessary to prevent much larger degradation in energy resolution.

### 3 Single-Pixel Implementation

TES-based calorimeters and bolometers consist of structures that perform three key functions: thermalization of the input energy, measurement of the

temperature change due to the input energy, and thermal isolation and mechanical support of the measurement structures. For the majority of detectors discussed here, an absorber thermalizes incident photon energy and delivers it to the TES to be measured. The energy raises the temperature of the electrons in the TES, causing an increase in the resistance. The TES and absorber must be sufficiently thermally isolated from the apparatus thermal ground, and the TES must be connected to the external readout circuit. In this section we will review the materials and geometries that have been used to implement single-pixel TES detectors and discuss the results obtained.

### 3.1 TES Thermometers

The key difference between TES detectors and other thermal detectors is the superconducting thermometer. The choice of the superconducting material used for this thermometer plays an important role in determining the detector characteristics. Of the superconductor properties, the superconducting transition temperature,  $T_c$ , of the thermometer has the largest effect on device performance. Because of the strong temperature dependence of physical parameters such as thermal conductance  $G$ , heat capacity  $C$ , and thermal noise, the choice of  $T_c$  has important implications in device design. Furthermore, considerations such as refrigeration often play an important role in constraining device design. As a result, most TESs have transition temperatures near either 400 mK ( $^3\text{He}$  cryostat operation), or 100 mK (operation with adiabatic-demagnetization and dilution refrigerators). Three methods are routinely employed to achieve transition temperatures in these ranges: the use of elemental superconductors, proximity multilayers, and magnetically doped superconductors. Proximity multilayers are the most commonly used of the three.

Both proximity multilayers and magnetically doped superconductors are attractive for use in TES detectors because of the tunability of the transition temperature in these systems. It is also possible in these systems to tune other materials properties such as the electrical resistivity  $\rho_{el}$ . In proximity multilayers, a composite superconductor is constructed by depositing one or more layers of both a superconductor and a normal metal. When the layers are thinner than the superconducting coherence length and the interface between the layers is sufficiently clean, the composite film exhibits a reduced  $T_c$  compared with the superconducting film. This effect, known as the proximity effect, has been widely studied, but was first applied as a technique to engineer a desired transition temperature in a TES by Nagel [82]. Nagel used Ir/Au bilayers to fabricate a TES with a transition temperature near 30 mK. Many additional proximity-effect bilayer and multilayer systems have been developed and will be described in more detail below. Another technique for modifying  $T_c$  is magnetic doping of superconductors. This effect has also been widely studied over the last four decades, but was first applied to a TES by

Young [83, 84], who demonstrated the suppression of  $T_c$  in W by implanted Fe ions.

The ability to controllably suppress  $T_c$  using the proximity effect or doping permits a much wider range of materials to be used in the fabrication of TES detectors. For example, there are 18 elements with bulk transition temperature less than 2 K. While many of these material have undesirable properties, five superconducting elements (Al, Ti, Mo, W, and Ir) have been widely reported in low-temperature TES detectors. Of these, all of the materials except Ir have frequent application in other areas of microelectronics. In addition to the elements listed, there are a wide variety of alloy and compound superconductors with transition temperatures in the range of interest. While these material may also have attractive properties for fabrication of TES detectors, they have not been widely used.

### 3.1.1 Elemental Superconductors

Elemental superconductors were among the first materials used in TES detectors. Early work on dark-matter detectors utilized both Ti and W thin films [8, 85, 86]. These researchers found that sputtered thin films of W can have  $T_c$  much higher than the bulk temperature of 15 mK by variation of the deposition conditions [85, 87, 88]. This type of behavior has been widely reported. In many cases, thin films do not have the same  $T_c$  as the bulk material, and the thin film  $T_c$  can be very sensitive to a variety of deposition and processing parameters.

Recent work [89] may shed light on the reasons for this difficulty controlling  $T_c$  in W. It has long been known that sputtered films of W can exist in two phases:  $\alpha$ , with a  $T_c$  near 15 mK. and  $\beta$ , with a  $T_c$  in the range of 1–4 K, and that a mixed phase is required to obtain transition temperatures in the desired range. Lita and coworkers [89] have used X-ray diffraction and resistivity measurements to show that mixed-phase samples can convert to  $\alpha$  phase at room temperature within a few hours of deposition. They have also shown that a thin underlayer of amorphous Si can prevent this change, allowing stable and reproducible fabrication of W films with transition temperatures that can be tuned through deposition conditions in the desired range, in their case near 100 mK.

Although W and Ti have been used in a variety of TES detectors, they have properties that limit their universal applicability. Both of these materials have fairly high electrical resistivities (and thus small Wiedemann–Franz thermal conductivities). For applications where the energy absorption is highly localized (such as a absorption of a single photon), the absorbed energy must spread throughout the entire TES in a time much less than the thermal time constant. The high resistivity places a limit on either the detector area or speed. Furthermore, the relatively high transition temperature of Ti (400 mK) limits the ultimate noise performance of titanium-based

detectors. Nevertheless, these materials have found wide application in dark-matter detectors [87], infrared and submillimeter bolometers [14, 90], and optical photon calorimeters [27].

### 3.1.2 Bilayers and Multilayers

The majority of low-temperature TES detectors have been constructed using proximity-coupled TES thermometers utilizing a superconductor normal-metal bilayer. The first bilayer TESs utilized Ir/Au to obtain transition temperatures in the range of 20–100 mK. Although excellent detector performance has been obtained using Ir/Au [91] this system can be difficult to fabricate. High quality Ir films have been obtained by electron-beam evaporation onto high-temperature (700 C) substrates under ultra-high vacuum conditions ( $< 1 \times 10^{-10}$  Torr). Later, suppression of  $T_c$  by over an order of magnitude by use of an Al normal-metal bilayer was demonstrated [92]. It was shown that very narrow superconducting transitions could be obtained even when the original starting material has an order of magnitude higher transition temperature than the desired  $T_c$ . Furthermore, very high performance X-ray calorimeters [93] were fabricated by a very simple method. Here the detectors were fabricated by simple electron-beam evaporation of Al and Ag through shadow-masks onto room-temperature substrates under high-vacuum conditions.

Although Al bilayers have been used to make sensitive TES detectors, there are several problems with this material. The combination of Al and any noble metal (Cu, Ag or Au) is not chemically stable and has many intermetallic phases that are formed at elevated temperatures. Furthermore, electrochemical effects in the Al/noble metal bilayer make wet processes such as photolithography challenging. Titanium interlayers have recently been used [94] in Al/Ti/Au multilayer as a means of alleviating these difficulties.

With the demonstration of high-quality proximity bilayers using hAl, a relatively high- $T_c$  superconductor, new elements (Mo,Ti) with higher  $T_c$  were quickly adopted. Molybdenum, which has a bulk  $T_c$  of 950 mK, was first used [95] in a Mo/Au bilayer system. Because the melting point of molybdenum is similar to that of Iridium, evaporated films of Mo require much the same care in deposition as Ir films. In order to obtain properties similar to the bulk, the films must be deposited onto substrates at very high temperature and under very clean vacuum. Fortunately high quality films of Mo with near-bulk properties can be obtained by magnetron sputtering, a technique that has been widely demonstrated in Mo/Cu bilayers [96] and multilayers [97]. Titanium, with a bulk  $T_c$  of 0.40 K, has also been used in Ti/Au bilayers for TES detectors [98].

There have been a variety of theoretical studies of the properties of proximity coupled bilayers. Two recent papers provide means for calculating the bilayer  $T_c$  [99, 100]. For example, in [99], the Usadel theory is used to show that the bilayer transition temperature is:

$$\begin{aligned}
T_c &= T_{c0} \left( \frac{d_s}{d_0} \frac{1}{1.13(1+1/\alpha)} \frac{1}{t} \right)^\alpha, \\
\frac{1}{d_0} &= \frac{\pi}{2} k_B T_{c0} \lambda_F^2 n_s, \\
\alpha &= d_n n_n / d_n n_s.
\end{aligned} \tag{108}$$

Here  $d_n$  and  $d_s$  are the normal and superconductor film thicknesses,  $n_n$  and  $n_s$  are the respective density of states,  $T_{c0}$  is the superconductor transition temperature,  $\lambda_F$  is the Fermi wavelength in the normal metal, and  $t$  is a unitless adjustable parameter of order 1 that describes the transmission through the bilayer interface. In practice, however, it is impossible to predict the transmission factor, which is strongly process-dependent. As a result, more empirical methods are generally employed where a recipe for a particular  $T_c$  and  $R_n$  is monitored over time so that small corrections to the thicknesses can be made.

### 3.1.3 Magnetically Doped Superconductors

A fairly comprehensive study of a variety of magnetic ions and superconductors has been carried out using ion implantation [101]. Here it was found that the  $T_c$  of both W and Mo films could be highly suppressed using small concentrations ( $\approx 100$  ppm) of implanted Fe. Furthermore, the suppression could be accurately described using an Abrikosov–Gor’kov pair breaking model. In contrast it was also found that the  $T_c$  of Al and Ti films were at best weakly dependent on Fe concentration, but strongly dependent on Mn concentration. In order to suppress  $T_c$  by a factor of 5, it has been found that a concentration of roughly 200 ppm of Mn is necessary for Ti, whereas concentrations nearer to 1000 ppm of Mn are necessary for Al. Further studies made on sputtered Al films deposited from doped targets [102, 103] indicate that the suppressed  $T_c$  in Al:Mn is due not to pair breaking, but to pair scattering from resonant magnetic impurity sites. Because the physical mechanism of  $T_c$  suppression is different, there may be very different effects on device performance for the different dopant systems.

Recently [104], a TES has been demonstrated using Al:Mn films with promising results. Although the resistivity of these doped films is higher at low temperatures than undoped films, a wide range of detector resistances is still attainable. The doped films (particularly those deposited in alloy form) can be made arbitrarily thick to reduce device resistance. This is not the case for multilayers, where the thickness of the superconducting film is limited to roughly the superconducting coherence length. An important concern is that the magnetic impurities may drastically increase the heat capacity of the films. While few measurements have been made, those to date indicate only small increases in heat capacity over undoped films.

### 3.2 Thermal Isolation

The design and fabrication of TES detectors requires a means to control the thermal conductance,  $G$ , of the TES to the thermal bath. At the low temperatures used for TESs, normal metals have a large thermal conductivity while superconductors and insulators have much lower thermal conductivity. This difference is due to the fact that in normal metals the heat is carried by the conduction electrons, while in superconductors and insulators it is carried by the phonons. By the Wiedemann–Franz law, the thermal conductivity for normal metals scales linearly with temperature, while the thermal conductivity for phonon-mediated materials scales as  $T^{n-1}$ , where  $n$  is material dependent, but usually ranges between 3 and 4. The strong temperature dependence of phonon thermal conductance is an important factor in choosing the operation temperature of a TES.

Controlling  $G$  has been accomplished in a variety of ways, depending on the application. In most cases this thermal isolation takes the form of micromachined supports to limit phonon transport between the substrate and the TES. In some cases however, the TES is placed directly on a substrate, and the phonon thermal conductance is controlled by acoustic mismatch between the film and the substrate, or by electron–phonon coupling in the TES.

#### 3.2.1 Micromachined Thermal Supports

Thin membranes of  $\text{Si}_3\text{N}_4$  and silicon-on-insulator (SOI) have been widely used as research tools in microelectronics for the last 25 years. In these techniques, a continuous film of the membrane material is made on the top surface of a Si wafer, and a small section of wafer is completely removed from the wafer back-side leaving a free standing membrane on the front surface. This type of structure has been used for such diverse applications as ultra-fine-feature electron beam lithography (backscatter from the substrate is eliminated) to radiation hardening (small device cross section), to capacitive pressure sensors. More recently, thin membranes of these and other materials are finding wide application in MEMS (microelectromechanical systems). The fabrication methods used to create MEMS are often referred to as micromachining. We will discuss bulk and surface micromachining methods for TES detectors in Sect. 4.1.

The use of thin membranes for thermal detectors was first pioneered by groups using semiconductor thermistors in IR bolometers [105, 106] and X-ray calorimeters [107]. In both cases, these groups applied a mix of micromachining and conventional microelectronic fabrication techniques to construct a hybrid electrical-thermal device. These ideas have been widely adapted for use with TES-based detectors.

In Fig. 8, we show an example of a simple micromachined thermal support, a solid insulating membrane. Here a TES calorimeter is placed in the

middle of a suspended  $\text{Si}_3\text{N}_4$  membrane. The thin insulating membrane limits the thermal conductance from the detector to the substrate. It is possible to further limit the thermal conductance by removing some fraction of the supporting membrane. Because of the high strength of  $\text{Si}_3\text{N}_4$ , it is possible to make structures with very limited support structures. A dramatic example of this is the “spider-web” geometry employed in a variety of IR bolometers [98, 106, 108]. Using this structure (Fig. 9) it is possible to create detectors with very small thermal conductances. Silicon nitride membranes are widely used in micromachining because it has very high strength, and the film stress can be widely varied by changing the film stoichiometry.

The thermal properties of  $\text{Si}_3\text{N}_4$  membranes have been studied experimentally [109, 110]. At the low temperatures of interest, the phonon mean free paths in  $\text{Si}_3\text{N}_4$  become long, and  $G$  is generally limited by scattering of the phonons from the membrane surface. These studies also show that the addition of scattering centers (small Ag particles) greatly reduces the film thermal conductivity. If phonon diffusion in the nitride film were responsible for the low thermal conductivity, additional metal particles on the surface would provide a parallel heat conduction path, increasing  $G$ . It was also found that removing membrane by micromachining reduces the thermal conductance by a factor much greater than the geometric loss of conduction path. This implies that the rough micromachined surfaces are also responsible for increased phonon surface scattering.

Micromachined silicon-on-insulator (SOI) has also been employed as a means to fabricate low- $G$  structures. Silicon-on-insulator wafers consist of two single-crystal regions of Si separated by an amorphous  $\text{SiO}_2$  insulating region. SOI wafers are typically fabricated using either wafer bonding and grinding techniques or ion-implantation. The group at NASA Goddard has employed SOI for TES detectors in their “pop-up” style infrared bolometers [111, 112]. An example of this detector type is shown in Fig. 10.

### 3.2.2 Phonon Decoupling

Some researchers have employed phonon scattering from interfaces as a means to achieve thermal isolation. Like the electron-phonon decoupling discussed below, this technique is particularly effective at very low temperatures due to the strong temperature dependence of the conduction. It is possible to theoretically estimate the thermal conduction between dissimilar solids based solely on acoustic considerations [113].

An additional means of controlling the thermal conductance of the TES is provided by the electron-phonon coupling in the TES itself. At sufficiently low temperatures, it is possible for the electrons and the phonons in a material to be at two different temperatures – a “hot electron” effect. A widely studied example of this is the heating of the electrons in a cooled resistor [114]. This effect is greatly enhanced in certain materials, with tungsten being one of the most notable. Because of the small electron-phonon coupling in W it is

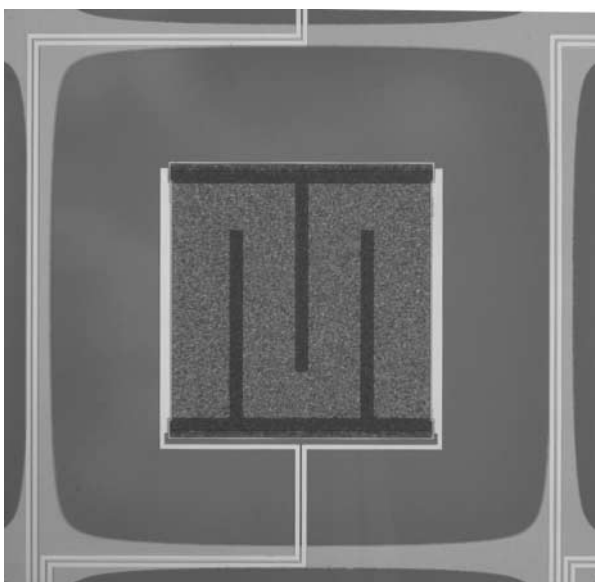


**Fig. 8.** TES X-ray calorimeter utilizing a  $\text{Si}_3\text{N}_4$  membrane for thermal isolation. Here the  $250 \mu\text{m}$  square TES detector sits on a  $450 \mu\text{m}$  membrane fabricated by deep reactive-ion etching to remove the back-side Si. The membrane thickness is  $350 \text{ nm}$ . The TES has additional normal-metal bars for noise suppression as well as a  $1.5 \mu\text{m}$  thick Bi absorber. The direction of current flow is parallel to the noise-suppression bars (*horizontal*)

possible to make TES detectors directly on a thick Si substrate, operating in a mode where the electron temperature is not in equilibrium with the phonons.

### 3.3 Absorbers

In order to be a useful detector, the TES must be efficiently coupled to the incoming radiation. The nature of this absorbing structure depends on the type of radiation being measured. In this section, we will briefly describe the methods employed for photons ranging from the millimeter through the gamma-ray wavelengths.

An ideal absorber should completely absorb the incoming radiation and quickly convert all of the incident energy to heat. This heat should be coupled into the TES with no additional paths for heat loss. The heat capacity of the absorber should be small compared to the TES, as extra heat capacity decreases sensitivity and increases noise.

In the far-infrared to millimeter wavelength regime, there are four principal schemes to couple the radiation to the TES: the use of absorbers with a broadband match to the impedance of free space, quarter-wave resonant

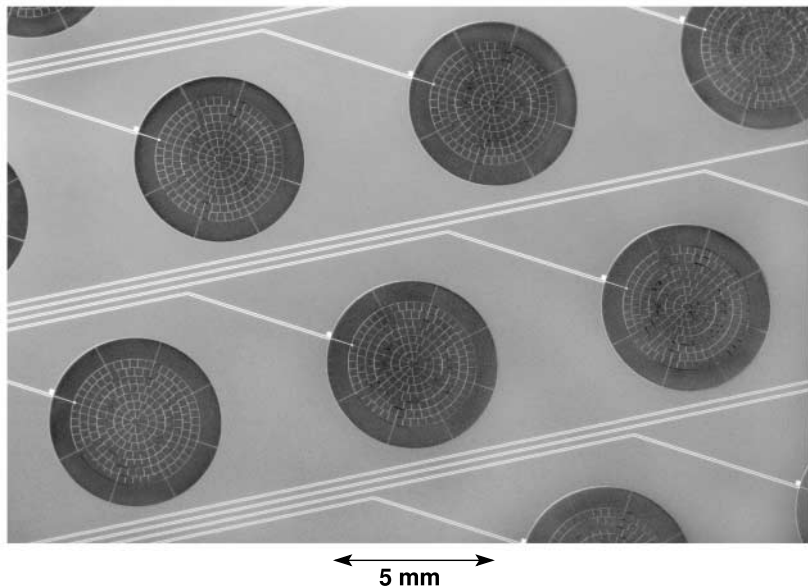


**Fig. 9.** Spider-web-style infrared bolometers. Here a  $\text{Si}_3\text{N}_4$  membrane is patterned into a structure resembling a spider-web. The outer legs of the web act as thermal isolation, while the inner legs are metallized to form the photon absorber. Photograph courtesy A.T. Lee, UC-Berkeley

cavities, feedhorns, and planar antennas. If an absorbing film is used that matches the impedance of free space ( $377 \Omega/\square$ ), an absorption efficiency of up to 50 % can be achieved over a wide bandwidth. A higher efficiency is possible with a narrower bandwidth using a quarter-wave resonant structure that employs a reflecting layer (backshort) and an absorbing layer separated by a spacing of  $\lambda/4$ . The absorbing layer must have a sheet resistance closely matched to the impedance of free space ( $377 \Omega/\square$ ). The absorbing layer must also be thermal contact with the TES. An example of this scheme is the FIBRE instrument [28], where an external reflector is placed behind each row of pop-up TES detectors. The detector has a  $377 \Omega/\square$  film (both Bi and PdAu alloy have been used) covering the majority of the detector surface. Heat absorbed is coupled through phonons to the small-area TES, which is in the same plane as the absorber, but which covers only a small fraction of the surface area. The detectors for SCUBA-2 [115] employ a different scheme. This absorber (a doped Si surface) and the reflector (the TES) are on opposite faces of an appropriately size silicon “brick”. Heat from the absorber is coupled to the TES through the brick. Feedhorns are typically employed with the spider-web bolometers described above [98, 108]. The bolometer is placed at the outlet of the feedhorn in an integrating cavity. For maximum efficiency, the absorbing film should have a sheet resistance that matches the feedhorn

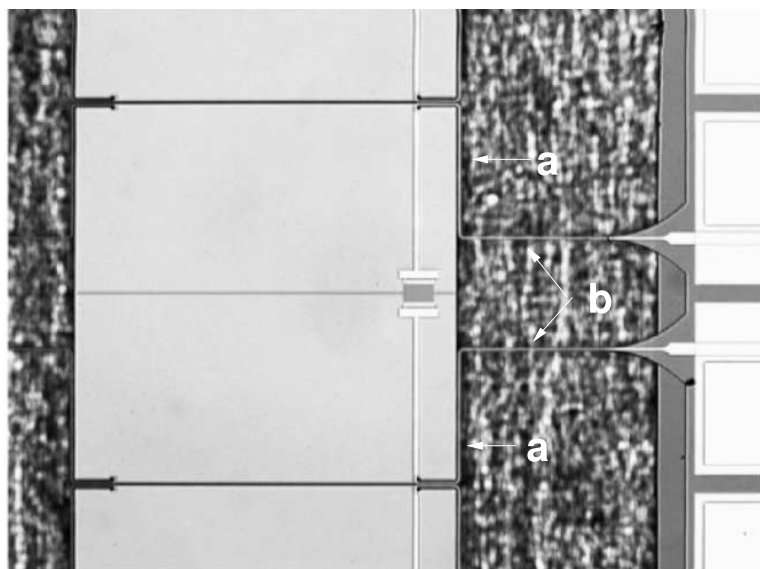


**Fig. 10.** Silicon micromachined “pop-up” detector. The thin support legs (*artificially highlighted white*) consist of thin (1–2  $\mu\text{m}$ ) Si. After fabrication the legs are folded, torsionally twisting the legs in the region labeled **a**. The *vertical* support sections (labeled **b**) now point into the page. Similar leg structures (not highlighted) support the left side of the pixel. Photograph courtesy of S.H. Moseley, NASA GSFC

output impedance. Typically, all but the outermost legs of the spider-web are coated with normal metal to make a low heat capacity absorber. Lastly, in antenna-coupled bolometers [94, 116], a superconducting planar antenna is fabricated that couples the free space radiation into a transmission line. This transmission-line is terminated with a resistor matched to the transmission-line impedance. The TES is then placed in thermal contact with the termination resistor.

Calorimeters in the near-IR, optical and UV have to-date used much simpler absorbers: they have utilized a tungsten TES itself as the absorber. Because tungsten has a sufficient absorption efficiency in these wavelengths ( $\sim 10$ –20%), detectors with good quantum efficiency have been made using only the TES as the absorber. For applications where higher quantum efficiency is required, techniques such as  $\lambda/4$  cavities or anti-reflection coatings can provide a large improvement. Rosenberg [117] has demonstrated a 97% absorption efficiency in tungsten TES using both anti-reflective coatings and a gold reflector placed underneath the TES.

Because of the extremely short wavelengths in the X-ray and gamma-ray bands, the use of the resonant structures described above is not possible. Instead, since the reflection coefficient at normal incidence is near zero at

these wavelengths, it is sufficient that the absorber have high photon stopping power to achieve good quantum efficiency. The requirements of high stopping power and low heat capacity place a constraint on the choice of materials for X-ray and gamma-ray absorbers. For applications in the important soft X-ray range of a few keV, the semi-metal Bi has been used as the absorber in all high-resolution results with high quantum efficiency. The high resistivity of Bi allows the absorber to be placed directly in contact with the TES without electrically shorting it out or causing a significant shift of  $T_c$ . In these devices, both electron and phonon excitations from the absorbed photon can easily couple to the TES. Evaporated films of Bi (with thicknesses of  $\sim 2\text{--}3 \mu\text{m}$  for 3 keV applications and  $\sim 10 \mu\text{m}$  for 10 keV applications) are patterned with conventional photolithography, making process integration simple. Many groups are beginning to apply “mushroom” absorbers [118] to this problem. Here a two-level photoresist stencil is used to make an absorber that is larger than the TES (Fig 11).

Work with low- $\alpha$  thermistor-based calorimeters, where heat capacity constraints rule out all absorbers except superconductors and insulators, has shown that high-purity Sn and HgTe absorbers provide good energy resolution [119, 120]. Recent work [97] on TES gamma-ray calorimeters also use glued tin absorbers.

### 3.4 Useful Formulas

In this section we will present some simple formulas useful in designing TES detectors, as well as values of material properties (Table 2) for a variety of elements used in TES construction.

#### 3.4.1 Electrical Conductivity of Normal-Metal Thin Films

It is useful to use a simple free-electron model to express the electrical conductivity,  $\sigma$  (and the resistivity  $\rho_{\text{el}}$ ) in terms of the electron mean free path  $\ell$ :

$$\frac{1}{\rho_{\text{el}}} = \sigma = \frac{ne^2\ell}{mv_F}, \quad (109)$$

where  $n$  is the density of free electrons,  $e$  is the electron charge,  $m$  is the effective electron mass, and  $v_F$  is the Fermi velocity. In this simplified model we ignore the temperature dependence of all terms but the mean free path. It is important to note that this approximation works well for alkali and noble metals, but is less useful for transition metals such as molybdenum. At room temperature the mean free path is controlled by inelastic electron–phonon scattering, which is strongly temperature dependent. At sufficiently low temperature, the mean free path is controlled by impurity scattering and thus becomes temperature independent. For this reason the RRR (room-temperature

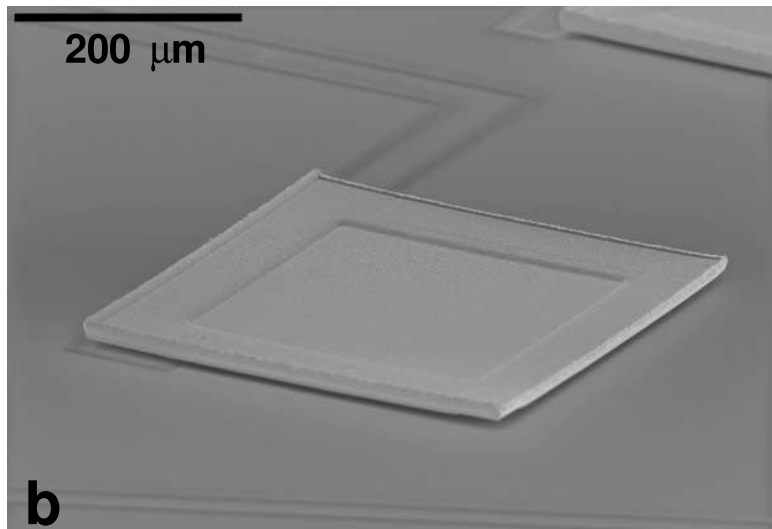
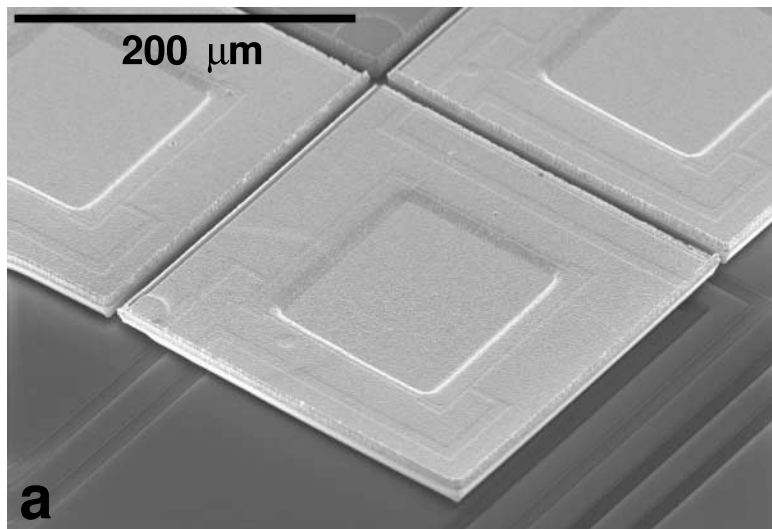


**Fig. 11.** Electron micrographs of Bi "mushroom" absorbers. The "cap" of the mushroom is show higher than the "stem", and is standing above the surface of the substrate. Photos courtesy J. A. Chervenak, NASA GSFC, SEM images by L. Wang

resistance ratio), which is the ratio of resistivity at room temperature to the temperature independent low-temperature resistivity, is a convenient measure of sample purity. As metals are cooled from room temperature, their electrical resistance decreases due to reduced scattering. At a sufficiently low temperature, phonon scattering becomes insignificant and the electrical re-

sistivity is dominated by impurity, isotope, or surface scattering, and the resistivity becomes independent of temperature.

For thin-film samples at low temperatures, it is important to consider the case where the mean free path exceeds the film thickness. Here we apply the Fuchs–Sondheimer model to determine the effective mean free path [121]:

$$\frac{1}{\ell(d)} = \frac{1}{\ell_0} + \frac{3(1-p)}{8d}, \quad (110)$$

where  $d$  is the film thickness and  $p$  is the probability of specular scattering at the surface. The probability  $p$  is often used as a fitting parameter, and can be zero for rough films. In more general theories,  $p$  is a function of the angle of incidence at the surface.

### 3.4.2 Heat Capacity

At low temperature the heat capacity of normal metals is almost entirely due to the electron heat capacity and thus is linear in temperature. A convenient form for the heat capacity is

$$C(T) = \frac{\rho}{A} \gamma V T, \quad (111)$$

where  $T$  is the temperature,  $V$  is the sample volume,  $\gamma$  is the molar specific heat,  $\rho$  is the mass density, and  $A$  is the atomic weight. The heat capacity for superconductors is more complicated because there are both phonon and electrical contributions with different temperature dependences. However, at  $T_c$ , BCS theory predicts that the heat capacity of a superconductor is 2.43 times the normal-metal value. Because the TES is operated within the superconducting transition, the heat capacity varies between  $C$  and 2.43  $C$  as the resistance changes. The actual value of  $C$  within the transition can be determined from the complex impedance measurement [52] shown in Fig 4.

## 3.5 Thermal Conductance

The thermal conductance  $G$  of normal metals at low temperature is dominated by Wiedemann–Franz thermal conductance of the normal electrons:

$$G = L_0 T / R. \quad (112)$$

Here  $L_0$  is the Lorenz number,  $T$  is the temperature and  $R$  is the electrical resistance. The Lorenz number can often be approximated using the value for a degenerate electron gas [122],  $L_0 \approx \pi^2 k_B^2 / (3e^2) = 24.4 \text{ nW} \cdot \Omega \cdot K^{-2}$ . Near  $T_c$ , the Lorenz number of a superconductor will be close to the normal value. However, well below  $T_c$ , the electron thermal conductance becomes

exponentially small, as the electrons are bound in Cooper pairs that do not scatter or conduct heat. This fact is often used as a means to make electrical contacts with low thermal conductance. By choosing a superconductor with  $T_c \geq 10 T_{\text{fridge}}$  the electron thermal conductance in the electrical leads can generally be assumed to be zero.

The thermal conductance  $G$  of  $\text{Si}_3\text{N}_4$  membranes at low temperatures [109] is often dominated by surface scattering effects, and it is possible to place only an upper limit on the conductance:

$$G = 4\sigma AT^3\xi . \quad (113)$$

Here  $\sigma$  has a value of  $15.7 \text{ mW/cm}^2\text{K}^4$ ,  $A$  is the cross-sectional area perpendicular to heat flow, and  $\xi$  is a numerical factor with a value of one in the case of specular surface scattering but with a value of less than one for systems with diffuse surface scattering.

In metals with small volume and high power densities, the thermal impedance between the electron and phonon systems can be important. The electrons will heat to a temperature well above the phonon temperature in the bath. In this case, the power flow from the electrons to the phonons will be  $P = \Sigma\Omega(T_{\text{el}}^5 - T_{\text{ph}}^5)$ , where  $\Omega$  is the material volume and  $\Sigma$  is a material-dependent constant ( $\sim 10^9 \text{ W}\cdot\text{m}^{-3}\cdot\text{K}^{-5}$ ). Hence, the thermal conductivity is

$$G = 5\Sigma\Omega T^4 . \quad (114)$$

It is interesting to note that for cases when  $G$  is dominated by electron-phonon conduction, since both  $C$  and  $G$  depend linearly on TES volume, the natural time constant  $\tau$  is independent of TES volume. Recent results [123] that for thin metal films disorder make increase the temperature exponent of the thermal conductance from 4 to 5.

### 3.6 Example Devices and Results

As previously stated, a large number of TES-based detectors have been developed with excellent performance for a variety of applications. In this section, we review the single-pixel performance results of two example TES calorimeters: an optical photon calorimeter and an X-ray calorimeter.

#### 3.6.1 Optical-Photon Calorimeters

An interesting new application of photon detectors is quantum cryptography [26]. Secure systems require detectors with single-photon sensitivity at telecommunication wavelengths ( $\sim 1.5 \mu\text{m}$ ) and very low dark counts. These characteristics can both be provided by calorimeters designed to operate at visible-photon wavelengths. Furthermore, such detectors provide photon

**Table 2.** Table of useful values for calculating TES properties

	$\rho_{\text{el}}^1$ $\mu\Omega \cdot \text{cm}$	$n^2$ $10^{28}/\text{m}^3$	$v_F^2$ $10^6 \text{ m/s}$	$\gamma^1$ $\text{mJ/mole} \cdot \text{K}^2$	$\rho/A$ $\text{mole/cm}^3$	$T_c^1$ K	$\lambda_L(0)$ nm
Al	2.74	18.1	2.03	1.35	0.100	1.140	$16^1$
Ti	43.1	10.5	0.041 <sup>4</sup>	3.35	0.094 4	0.39	$310^4$
Mo	5.3	38.6	0.60 <sup>4</sup>	2.0	0.107	0.92	
W	5.3	37.9	0.70 <sup>4</sup>	1.3	0.105	0.012	$82^5$
Ir	5.1	63.4	0.36 <sup>6</sup>	3.1	0.117	0.140	$29^6$
Nb	14.5	27.8	0.62 <sup>3</sup>	7.79	0.092 2	9.5	$39^1$
Cu	1.70	8.47	1.57	0.695	0.141		
Ag	1.61	5.86	1.39	0.646	0.097 4		
Au	2.20	5.90	1.40	0.729	0.098 3		
Bi	116.0	14.1	1.87	0.008	0.046 8		

Sources: <sup>1</sup>[124] <sup>2</sup>[125] <sup>3</sup>[126] <sup>4</sup>[127] <sup>5</sup>[128] <sup>6</sup>[129]

number-resolving capabilities not afforded by conventional detectors such as Si avalanche photodiodes. Tungsten TES calorimeters have been developed for quantum information applications in addition to optical astronomy [26, 27].

Using small-volume W films ( $25 \mu\text{m} \times 25 \mu\text{m} \times 35 \text{ nm}$ ) at temperatures below 100 mK, it is possible to obtain values of  $C$  and  $G$  necessary to fabricate a fast (10–50  $\mu\text{s}$  fall-time) calorimeter with saturation energies of roughly 10 eV. Because the dominant thermal impedance is provided by electron-phonon decoupling, fabrication of such a device is simpler than for calorimeters that rely on micromachined membranes. The W film is deposited and patterned into squares by wet etching in an alkaline ferricyanide solution. An aluminum wiring layer is then added using a lift-off process. A detector completed by this process is shown in Fig. 12. One difficulty with these detectors is the relatively low absorbance of the W film in the wavelengths of interest. Recent improvements include placing a mirror and dielectric underneath the W TES to make a quarter-wave absorbing cavity [117]. The improved structures show near-unity absorption.

In Fig. 13 we show a spectrum demonstrating both the number-resolving capability and the excellent energy resolution (0.2 eV FWHM) obtained with these detectors. These detectors show great promise for applications in the fields of quantum information, where they may be used for quantum cryptography, for experimental tests of Bell’s inequality, and in astronomy, where observations of pulsars require detectors with the ability to provide simultaneous measurements of photon energy and arrival time.

### 3.6.2 X-ray Calorimeters

The need for high-resolution detectors of soft X-rays is one of the primary drivers for developing cryogenic detectors. For this reason, X-ray calorime-

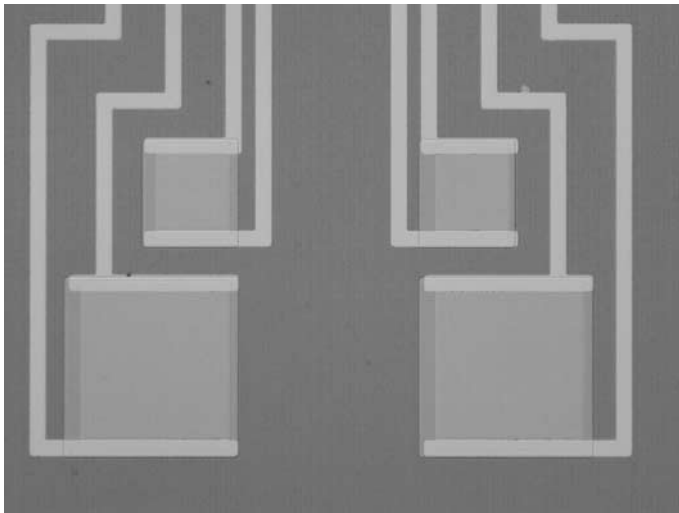


**Fig. 12.** Optical microphotograph of W optical-photon calorimeter showing four individual detectors and Al wiring. Photograph courtesy of A. E. Lita, NIST

ters have been one of the most active research areas in cryogenic detectors, with active developments in both semiconductor thermistor-based calorimeters (the Chapter “Semiconductor Thermistors” by *McCammon*) and TES calorimeters [74, 96, 130, 131, 132].

Recent studies [65, 67, 68, 133] have demonstrated that additional normal metal structures placed within a TES can greatly reduce excess noise. Furthermore [66] a relationship between excess noise and thermometer  $\alpha$  has been demonstrated (Fig. 7). Using this relationship and additional normal-metal structures to fabricate devices with a pre-determined value of  $\alpha_I$ , we have powerful tools to optimize TES energy resolution (Sect. 2.7).

A pixel designed using this procedure is shown in Fig. 8. The additional normal-metal bars are clearly visible underneath the  $1.5\text{ }\mu\text{m}$  thick Bi absorber. These detectors were fabricated using a standard TES process [73]. A Mo/Cu sputtered bilayer is fabricated on a  $\text{Si}_3\text{N}_4$  coated substrate; the TES and Mo wiring is defined by two wet-etch steps. The normal-metal Cu boundaries and additional transverse bars are deposited by a lift-off process, as is the Bi absorber. In the final step, the Si underneath the pixel membrane is removed with a deep reactive ion-etch process.

In Fig. 14 we show the  $^{55}\text{Fe}$  X-ray spectrum obtained by the pixel in shown Fig. 8. A fit to this spectrum of the Mn  $K\alpha$  lines indicates an instrument resolution of  $2.37 \pm 0.11\text{ eV FWHM}$ . This pixel has an area of  $250\text{ }\mu\text{m} \times 250\text{ }\mu\text{m}$  and a pulse fall-time of  $230\text{ }\mu\text{s}$ . A larger device ( $400\text{ }\mu\text{m} \times 400\text{ }\mu\text{m}$ ) has an energy resolution of  $2.9 \pm 0.1\text{ eV}$ , with a fall-time of  $90\text{ }\mu\text{s}$ .

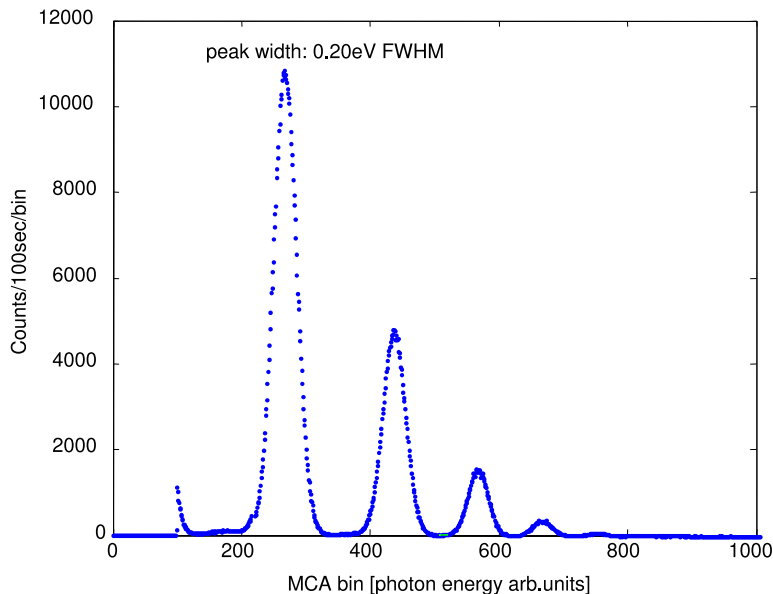


**Fig. 13.** Pulse-height spectrum obtained for highly attenuated pulses of  $1.55 \mu\text{m}$  laser photons (0.8 eV). Here, each pulse can contain 1 or more optical photons. The spectral peaks indicate differing photon numbers in each pulse. Figure courtesy of A. J. Miller, NIST

## 4 Arrays

Many applications require large arrays of TES detectors. TES arrays are being developed for astronomical imaging (including millimeter, submillimeter, optical, and X-ray cameras). They are also being developed as a means to increase the collecting area of detectors for terrestrial X-ray spectrometry.

In recent years, significant progress has been made in fabricating TES detector arrays. Lithographic techniques have made it possible to fabricate many pixels at one time. Advances in micromachining techniques have made it possible to separately thermally isolate the pixels.

Even though the fabrication of large arrays is now possible, new readout techniques are necessary before such arrays can be practically implemented. The difficulty of separately wiring a large number of low-temperature detectors from subkelvin temperatures to room temperature precludes all but very modest detector arrays (hundreds of pixels). For larger arrays, it is necessary to use cryogenic multiplexers to reduce the wiring count. One of the most compelling reasons for the widespread interest in TES detectors is the existence of viable multiplexing schemes. Numerous SQUID-base multiplexers are being developed to extend the single-pixel SQUID readout (Fig. 2) to a multiplexed readout where multiple detectors signals are carried on a single set of signal leads.

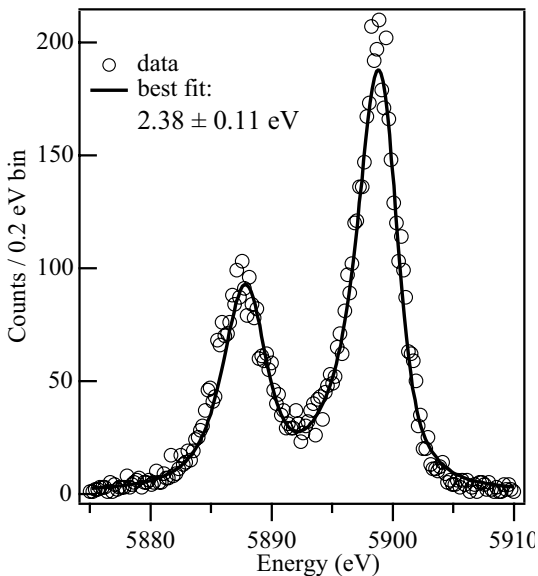


**Fig. 14.** X-ray spectrum of an  $^{55}\text{Fe}$  source measured with the TES calorimeter shown in Fig. 8. The data points are shown with statistical error bars, and the line is a fit to the Lorentzian natural linewidths of the Mn-K $\alpha$  complex [134] convolved with a Gaussian detector response

In this section we review recent developments in both TES detector array fabrication and cryogenic SQUID multiplexers.

#### 4.1 Array Fabrication and Micromachining

Arrays of TES microcalorimeters or bolometers must include absorbers, thermometers, and thermal isolation and support structures. Many applications require close-packed arrays with large active-detector filling fractions, which severely limits the area of the array that is available for functions such as support and wiring. Because of their compatibility with standard planar microelectronic processes, it is simple to replicate a large array of TES thermometers. The challenge is the development of thermal supports, wiring, and absorbers that are compatible with arrays.

In Sect. 4.1.1, we describe the anisotropic silicon wet etches that were used in most early single-pixel TES X-ray calorimeters as well as the plasma etch techniques that are presently most often used in array fabrication. In Sect. 4.1.2 we describe the recent development of surface-micromachined TES arrays.

### 4.1.1 Bulk Micromachining

Most TES detectors use the widely developed  $\text{Si}_3\text{N}_4$  membranes formed by bulk micromachining (BMM) for thermal isolation. A thin film of  $\text{Si}_3\text{N}_4$  is deposited on the wafer front side and the substrate underneath a region of the nitride film is etched from the backside to form a free-standing membrane. Various processes are used to form deep three-dimensional structures in the substrate [135]. For most BMM TES detectors, this implies that an etch step is performed on the back-side of the wafer to form a thermally isolated membrane on the top surface. While there are many different BMM methods, we describe only two: anisotropic wet etching of Si and deep reactive ion etching of Si.

The crystalline structure of the Si substrate can be used to significant advantage in bulk micromachining. The etch rates of Si in hot alkaline solutions such as KOH or tetramethylammonium hydroxide (TMAH) varies strongly with crystal direction. The etch rate for (110) planes is roughly 600 times higher than for (111) planes. Additionally, these etches have a high selectivity against etching silicon nitride, which forms an ideal etch stop. These “crystallographic etches” can be used to form a variety of features. For instance, if a  $\text{Si}_3\text{N}_4$ -coated  $\langle 100 \rangle$  Si wafer has a small square window opened in the  $\text{Si}_3\text{N}_4$ , a KOH etch results in an pyramidal etch pit in which each face is a (111) plane. If the window is large enough, the etch pit is a truncated pyramid with the front-surface membrane at the top, so that the  $\text{Si}_3\text{N}_4$  membrane is smaller than the etch pit on the backside of the wafer. This is a commonly used geometry for single pixels. The size of the window required on the backside of the wafer to produce a given membrane size on the front can be easily calculated using the thickness of the wafer and the angle between the (111) planes and the substrate face ( $54.7^\circ$ ). However, this angle prevents the fabrication of close-packed arrays by this process. In order to maintain support bars between pixels, there must be a space of  $2\sqrt{2}$  times the substrate thickness between membranes on the top surface.

Etch faces perpendicular to the wafer face can be obtained in  $\langle 110 \rangle$  wafers. In this geometry, it is possible to fabricate individual membranes separated by thin Si bars in one dimension, making close-packed arrays possible [136]. The crystallographic constraints, however, result in trapezoidal pits and membranes. Thus, in a close-packed square-pixel array, if adjacent pixels in a column are placed on different membranes, adjacent pixels in a row must be on the same membrane. In order to reduce thermal crosstalk between pixels within a row, normal-metal heat sinks are fabricated between pixels on the top surface of the membrane. Thermal isolation between pixels in a column is provided by the Si bars between each membrane. Such a device has been fabricated (Fig. 15) and measured [137] obtaining results similar to single pixels.

Anisotropic plasma etching can also be used for bulk micromachining. Commonly referred to as deep reactive ion etching (DRIE), this technique

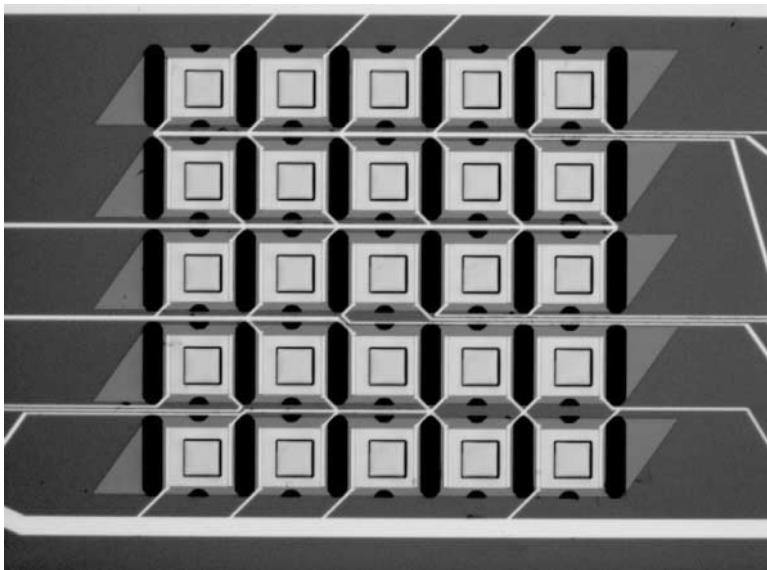


**Fig. 15.** Microphotograph of a  $5 \times 5$  pixel array of microcalorimeters fabricated by bulk micromachining on a Si  $\langle 110 \rangle$  wafer. The Si bars and  $\langle 111 \rangle$  planes run horizontally, with the trapezoidal etch terminations on the left and right side of the array. Each row of pixels is on a single membrane. Photograph courtesy of Marcel Bruijn, SRON-Sensor Research and Technology

utilizes ions directed at the wafer surface and edge passivation to etch arbitrarily shaped structures with nearly vertical sidewalls into Si. While several variations of this technique exist, the most common is the “Bosch process” [138, 139]. This process has two phases: an etching phase (using  $SF_6$  gas to etch the Si), and a passivation phase (using  $C_4F_8$  gas to grow protective polymer on exposed sidewalls). By rapidly switching between the etching and passivation phases it is possible to create very high aspect ratio structures with straight sidewalls. An example of structures created using this process is shown in Fig. 16. This process can also be used to fabricate membranes because of the high selectivity to  $SiO_2$  ( $> 100:1$ ) and  $Si_3N_4$  ( $> 30 : 1$ ). Because of the higher selectivity, silicon dioxide is generally used as the membrane etch stop. In a typical process, the membrane consists of a bilayer of  $SiO_2$  and  $Si_3N_4$ . The thickness of the oxide is determined by the selectivity, the wafer thickness, and the etching uniformity obtained in the tool, with layer thickness of  $\sim 100$  nm being typical.

The properties of DRIE make it a nearly ideal tool for fabricating close-packed TES arrays with bulk micromachining. Because of the good selectivity of this etch to  $SiO_2$ ,  $Si_3N_4$  and photoresist, and the large attainable aspect ratios ( $> 30 : 1$ ), close-packed arrays of thermally isolated TES detectors are now easily realized in a variety of geometries [140, 141, 142]. An example



**Fig. 16.** Electron micrograph of a test structure etched using DRIE, demonstrating the arbitrary geometries possible with this technique

array fabricated by DRIE is shown in Fig 17. Even with DRIE, portions of the array area must be dedicated to the supporting grid and pixel wiring.

Another consideration in BMM arrays is the thermal conduction within the support structure. Ideally, the interpixel supports would be perfect thermal grounds so that each pixel sees an identical thermal environment, and there is no thermal crosstalk between pixels. Realistically, a tradeoff must be made between the thermal considerations and the desired filling fraction. The thermal conductivity of the Si beams may be strongly dependent on processing. Beams etched by crystallographic etches typically are much smoother than structures etched by DRIE, which exhibit a typical roughness of 100 nm. This roughness can substantially reduce the thermal conductance [143]. The thermal conductance can be improved by coating the micromachined walls with normal metal. For many array geometries, this coating can be accomplished by back-side evaporation at oblique angles.

In order to obtain near-unity filling fractions, additional techniques are employed. In X-ray detectors, mushroom absorbers (Sect. 3.3) can be integrated with either DRIE or ⟨110⟩ wet-etched arrays, resulting in very high filling fractions. The overhanging region of the mushroom can be used to cover the supporting grid and wiring.

Because Si is transparent to infrared and submillimeter wavelengths, other means can be used to obtain high-filling-fraction TES arrays for these wavelengths. One method, first developed for semiconductor thermistor bolometers [144], uses this transparency to place the detector circuitry on the opposite side of the wafer from the incoming illumination. In this way, the electrical signals can be taken off-wafer to a separate readout circuit using wafer hybridization techniques such as indium bump-bonding.

This technique is currently being used for the TES detectors for SCUBA-2 [115]. A cross-sectional sketch of the SCUBA-2 detectors is shown in Fig. 18. DRIE is again used to create the thermal breaks between pixels and the support frame; however, here the pixels are composed of a thick region of silicon that is left behind the TES to form the quarter-wavelength absorbing cavity.

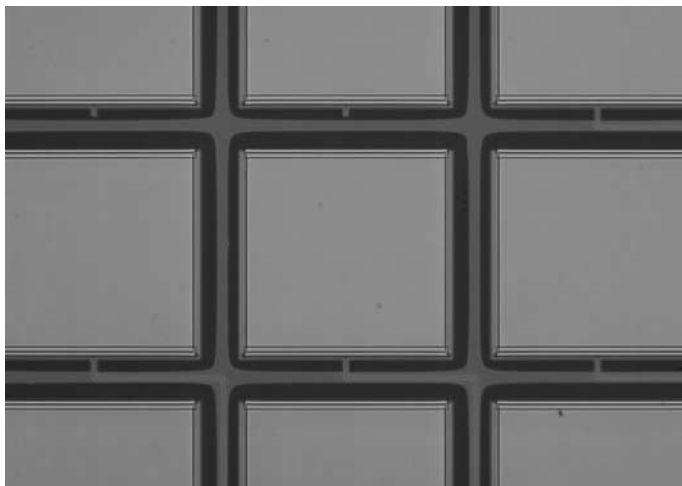


**Fig. 17.** Optical micrograph showing a portion of a TES X-ray microcalorimeter array fabricated using DRIE. The floating squares (*light gray*) are TES detectors located on  $\text{Si}_3\text{N}_4$  membranes (*black*), which are surrounded by the Si supporting grid (*dark gray*)

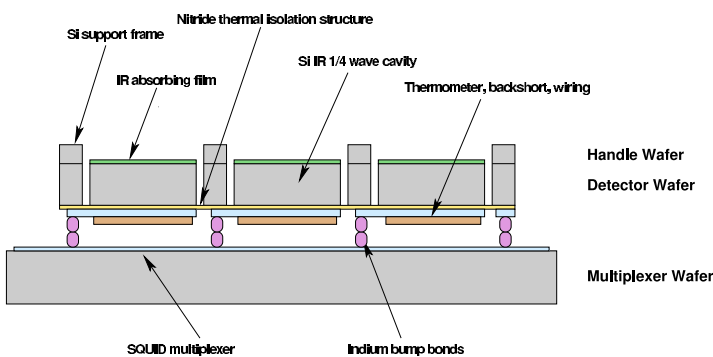


**Fig. 18.** Sketch showing the pixel architecture used for SCUBA-2. The detector wafer is fabricated by fusion-bonding two wafers (the “handle” and “detector” wafers) with the absorber and DRIE etch masks on the internal faces. The TES detectors are deposited on the fused wafer, and the detector wafer is indium bump-bonded to a multiplexer wafer to provide electrical readout. Finally, a DRIE etch is used to etch down to the absorber and thermally isolate the pixels

The TES forms the reflector, and doped Si is used to form the absorber. Indium bump-bonding is used to attach the side of the detector wafer containing the TES to a separate readout wafer, eliminating the need for pixel wiring on the detector wafer. The readout SQUID multiplexer wafer is discussed further in Sect. 4.2.3.

### 4.1.2 Surface Micromachining

Although bulk micromachining methods are in use, there are several drawbacks to this method, including the expense of the specialized DRIE tool and the delicate nature of the final array. Because of these drawbacks, several groups [145, 146, 147] are exploring the use of surface micromachining to fabricate arrays of TES detectors. In surface micromachining (SMM), all process steps take place on the front surface of the wafer. The thermal isolation is typically achieved by using a temporary mechanical support as a sacrificial layer that is removed near the end of the process. Because this is a planar process, which leaves the substrate under the platform intact, it is possible to fabricate the detectors on top of other structures such as wiring or readout electronics. SMM arrays thus have the potential of a higher level of integration than is achievable with BMM.

The basic ideas for TES surface-micromachined detectors derives from uncooled surface-micromachined bolometers [148, 149] that have been under development for many years and form the basis of several commercially available imaging products. In uncooled SMM bolometers, a platform of PECVD Si<sub>3</sub>N<sub>4</sub> is grown on a sacrificial mesa of polyimide. The silicon nitride membrane is patterned to have supporting legs that extend off the mesa, and the mesa is removed using an oxygen plasma. The resultant membrane is a three dimensional structure with a flat tabletop held above the surface of the wafer by curved supporting legs. While the specifics of this process are not applicable to TES detector arrays, many of the SMM TES approaches use similar techniques.

Because of the large thermal stresses incurred when cooling from room-temperature to the subkelvin operating temperatures, the membrane material must have very high strength. This has led researchers in SMM TES detectors to use Si<sub>3</sub>N<sub>4</sub> grown at high temperature ( $\sim 800$  C) by LPCVD as a membrane material. Silicon nitride membranes grown with lower temperature techniques (such as PECVD) are porous and have inferior mechanical properties. This high growth temperature has thus far limited the choice of sacrificial materials to Si. This sacrificial layer has come in the form of a plain Si wafer [145], a silicon-on-insulators wafer [150], and polysilicon [146, 147]. Recent measurements [151] indicate that polyimide may form a strong thermal isolation membrane that can be fabricated using much lower processing temperatures than LPCVD silicon nitride. This result may be very helpful in integrating under-pixel wiring or readout.

The removal of the sacrificial layer can be a difficult step. In many geometries, the lateral extent of the sacrificial layer under the membrane is much greater than the sacrificial layer thickness. This rules out the use of plasma etching, because the active plasma species experiences too many collisions and thus becomes inactive before reaching the sacrificial layer. For this reason, wet etches such as hydrazine [150] and TMAH are used [147] as is the dry plasma-less XeF<sub>2</sub> etch [145, 146]. The XeF<sub>2</sub> etch [152] is unique in that it

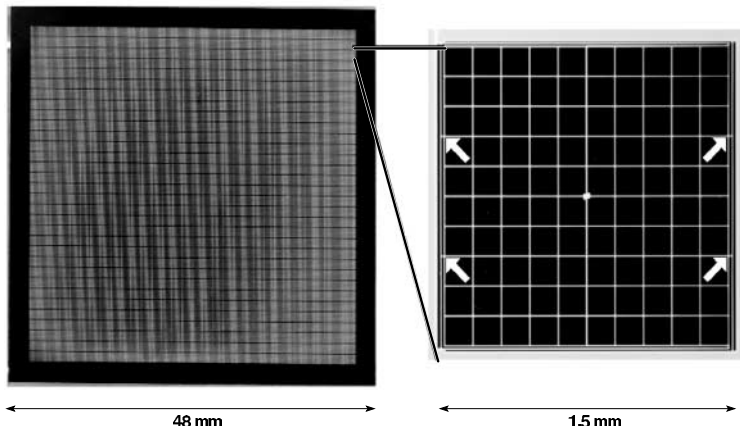


**Fig. 19.** Photographs showing close-packed spider-web far-infrared/millimeter detectors fabricated by  $\text{XeF}_2$  surface micromachining. *On the left* is an overview of the  $32 \times 32$  array, and *on the right* is a magnification of the pixel. The white lines are silicon nitride beams suspended above the wafer surface. The *four white arrows* indicate the web attachment points. Photograph courtesy A.T. Lee, UC-Berkeley

is a gas-phase chemical etch, and thus does not apply surface tension forces to the delicate etched structures. An example of a TES array etched using  $\text{XeF}_2$  is shown in Fig 19. Here a silicon nitride spider web is released from the substrate using the  $\text{XeF}_2$  etch.

Surface micromachined X-ray microcalorimeters are currently under development by two groups [146, 147]. Because of the relatively small pixels required (200 to 500  $\mu\text{m}$ ), and the high fill factors desired, X-ray arrays especially benefit from the potential extra substrate area that may be available for wiring with this technique. A portion of a SMM X-ray microcalorimeter array is shown in Fig 20.

## 4.2 Multiplexed Readout

Arrays of thousands of TES detectors are now being developed. As shown in Fig. 2, SQUID circuits to instrument a single TES require multiple wires to be run from cryogenic temperatures to room temperature. These can include the detector bias, first-stage SQUID bias, first-stage SQUID feedback, series-array SQUID bias/output, and series-array SQUID flux bias. If the same “brute force” techniques are used to read out each pixel in a large array, the complexity, cost, and power load due to many thousands of leads can become unmanageable. A cryogenic SQUID multiplexer can be used to reduce the number of leads.

A number of schemes have been developed to multiplex the outputs of many TES pixels into a small number of wires. These schemes can be divided into broad categories based on the frequency range (low frequency or

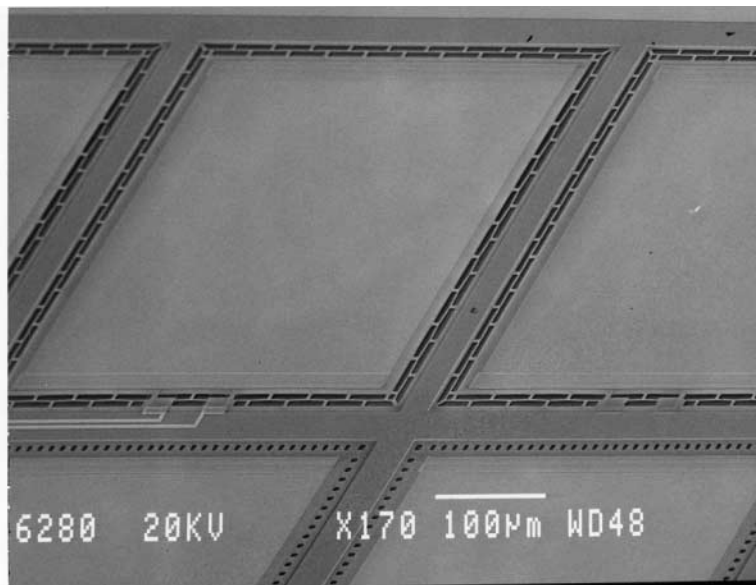


**Fig. 20.** Electron micrograph showing a portion of a TES X-ray microcalorimeter array fabricated BY XeF<sub>2</sub> surface micromachining. In this image, we show pixels with two different release/support geometries. The large membrane squares are 2  $\mu\text{m}$  above the wafer surface. The *dark area* are holes in the silicon nitride membrane. The underlying Si sacrificial layer was removed by XeF<sub>2</sub> etching through these holes

microwave) and the basis set used for encoding (principally boxcar functions for time division or sinewaves for frequency division).

At low frequencies, both time-division multiplexing (TDM) schemes with a SQUID switch at every pixel [153, 154] and frequency-division multiplexing (FDM) schemes with a large LC filter at every pixel [155, 156] are used to read out TES arrays. The advantage of low-frequency operation is that experimental techniques familiar in cryogenic detector work can be used, including low-power twisted-pair wiring and low-noise amplifiers with a few megahertz bandwidth. The disadvantage is that the filter elements required can be challenging (SQUID switches with relatively small inductive filters at every pixel for TDM, and large, but passive LC filters at every pixel for FDM), and the modest total bandwidth limits the number of signals that can be multiplexed in one wire.

At microwave frequencies, compact microwave filter elements can be used (either lumped or distributed elements), and the large total bandwidth makes it possible to multiplex more signals in each wire. However, microwave TES multiplexers are less mature, and the required room-temperature electronics are considerably more difficult. In a microwave SQUID multiplexer, a

SQUID is placed at every pixel in a high-Q resonant circuit [157]. In this approach, large arrays of SQUIDs could be frequency-division multiplexed into one coaxial cable with two additional coaxial cables to flux bias the SQUIDs. Hybrid schemes are also under development that use a low-frequency time-division multiplexer whose second-stage SQUIDs are frequency-division multiplexed in a microwave resonant circuit.

TES detectors have wideband noise, but only bandwidth-limited signals can be multiplexed without degradation. The development of a bandwidth-limiting filter is one of the most important considerations in implementing a multiplexing scheme. A variety of SQUID MUX schemes have been proposed that accept signal-to-noise ratio (SNR) degradation due to the absence of a bandwidth-limiting filter. For instance, the bias of multiple TES devices can be switched in a Hadamard code [158] and summed into a single SQUID. The signals can be demultiplexed using the Hadamard code, but the noise is increased by  $\sqrt{N}$  due to aliasing of noise at frequencies above the Nyquist frequency associated with the frame rate (the rate at which the entire sequence of Hadamard codes is implemented). While approaches that accept significant SNR degradation are useful in some cases (e.g., when photon noise dominates), we focus here on multiplexing approaches that do not degrade the signal-to-noise ratio.

#### 4.2.1 The Nyquist Theorem and Multiplexing

According to the Nyquist theorem, the information in a signal of bandwidth  $\delta f$  and duration  $\delta t$  can be exactly represented by  $2 \delta f \delta t$  real samples in time space. The same signal can be represented in frequency space as a Fourier series with  $2 \delta f \delta t$  real samples. The time and frequency samples form orthogonal basis sets to represent the bandwidth-limited function. Many other basis sets can also be used, such as Hadamard functions, wavelet-packet basis sets, or basis sets consisting of time samples within multiple frequency bands.

If an output SQUID channel has a bandwidth  $\delta F$  (larger than the signal bandwidth  $\delta f$ ) it is possible, in principle, for the output to carry signals without degradation in  $N \leq \delta F / \delta f$  different subsets of the output basis set. In order to multiplex, the bandwidth of the signal is limited by a filter, the information in each signal is moved to a different component of the output basis set (the signal is encoded), and the signals are summed in the output channel [156, 159]. The signals are encoded by multiplying them by a set of orthogonal modulation functions. The multiplication can be done either in the TES or the SQUID. In TDM, boxcar (low-duty-cycle square wave) modulation functions are used (Fig. 21). In FDM, sinusoids are used (Fig. 24). The signals are then added into one output channel. They can be separated and decoded using the same modulation functions. In the absence of SQUID noise, the fundamental limit on the number of signals that can be encoded

in one output channel with a given bandwidth is independent of the choice of orthogonal basis set.

#### 4.2.2 SQUID Noise and Multiplexing

Wideband SQUID noise is added to the signals after they are encoded. During decoding, all the noise outside of the noise bandwidth of the encoded signal is filtered out. The amount of noise that is added to the decoded signal depends on the noise bandwidth of the encoded signal. We assume here that the SQUID noise is white.

In TDM, the bandwidth of the encoded signal is set by the boxcar modulating function. In frequency space, the boxcar function is a sinc function,  $F_{\text{mod}}(f) = \sin(\pi f \delta t_s) / (\pi f \delta t_s)$ , where  $\delta t_s$  is the time that the multiplexer dwells on one pixel. The noise bandwidth of the sinc function is

$$\Delta B_{\text{noise}} = \int_0^\infty \left( \frac{\sin(\pi f \delta t_s)}{\pi f \delta t_s} \right)^2 df = \frac{1}{2\delta t_s}. \quad (115)$$

The noise above  $\Delta B_{\text{noise}}$  is filtered by the sinc function in the process of decoding, either in an analog circuit (a gated integrator), or digitally, by averaging an oversampled signal. The “frame rate,”  $1/(N\delta t_s)$ , is the rate at which all pixels are sampled. All the unfiltered noise above  $1/(2N\delta t_s)$ , the Nyquist frequency associated with the frame rate, is aliased into the signal band. The effective noise power of the SQUID is thus increased by a factor of  $2N\delta t_s/(2\delta t_s) = N$ . In order to maintain fixed SNR, the gain must be  $N$  times larger than it would be for a non-multiplexed TES: the number of turns on the SQUID input coil must be increased. SQUIDs are sufficiently quiet that, even with the required gain, it is possible to multiplex hundreds or thousands of signals into one output SQUID with TDM. Increasing the number of turns by  $\sqrt{N}$  to overcome the aliased SQUID noise also increases the required slew rate in the SQUID by  $\sqrt{N}$ . In applications with high dynamic range, such as fast X-ray calorimeter arrays, high-bandwidth feedback must be applied from room temperature to achieve sufficient slew rate.

In FDM, in contrast, the bandwidth of the encoded signal is the same as the bandwidth of the input signal. Multiplying by the modulating function, a sinusoid, moves the signal up to a high frequency but does not affect the bandwidth, and no aliasing of wideband SQUID noise occurs. However, in FDM, signals from all pixels are seen by the SQUID at all times. The slew rate requirements set by uncorrelated noise scales as  $\sqrt{N}$ , but the slew rate requirements due to the signal are typically more important. In a bolometer, if changes in the power seen by different pixels are uncorrelated, the slew rate requirements are modest. But if a common-mode power signal is seen in all detectors, the slew rate requirement on the SQUID increases as  $N$ , a more difficult slew-rate requirement than in TDM. This situation is expected, for instance, in a ground-based submillimeter camera when changes

in the weather cause a common-mode signal on all pixels. In a calorimeter, the slew-rate requirement is determined by the characteristics of the source. If coincident pulses are not expected in different pixels, the slew rate requirements are again modest. But if coincident signals are commonplace, the slew rate requirements increase approximately linearly with the maximum number of coincident signals allowed.

#### 4.2.3 Low-Frequency TDM

Time-division SQUID multiplexers have been developed for applications ranging from biomagnetism [160] and non-destructive evaluation [161] to the readout of TES arrays [153], using both dc SQUIDs and rf SQUIDs [162]. In TES readout applications, each TES is biased by a voltage  $V$  with some load resistance  $R_L$  and connected to a SQUID “switch.” The SQUIDs are turned on one at a time, and the outputs of many SQUIDs are added into one output channel.

The current noise of the TES is rolled off below the Nyquist frequency of the sampling in order to prevent degradation due to noise aliasing. From (94) and (35), the thermal-fluctuation noise in the TES,  $S_{I_{TFN}}(\omega)$ , is naturally rolled off by a one pole filter at the pulse fall frequency,  $1/(2\pi\tau_-)$  and a second pole at the pulse rise frequency  $1/(2\pi\tau_+)$ . However, from (89), (91) and (35), the TES Johnson noise  $S_{I_{TES}}(\omega)$  and load resistor Johnson noise  $S_{I_L}(\omega)$  are rolled off by only a single pole at  $1/(2\pi\tau_-)$ . Thus, the inductance in the loop (and consequently  $\tau_-$ ) must be large enough to avoid degradation due to aliasing of Johnson noise, yet still be small enough for stability. Often the critically damped condition is chosen to balance these constraints. Achieving critical damping sometimes requires adding an additional “Nyquist” inductor in the loop between the SQUID and the TES.

In first-generation “voltage summing” SQUID TDM, the modulation function is applied to the SQUID switches as a parallel address voltage to turn on a row of SQUIDs [153]. The SQUID output voltages in each column are summed into one output SQUID channel. Unfortunately, voltage-summing topologies are not practically scalable to two-dimensional arrays at temperatures well below 1 K. When wired in a two-dimensional array, parasitic currents in the two-dimensional network can lead to unacceptable crosstalk unless large address resistors are used to block the current flow. If large address resistors are used, there is unacceptably large Joule power dissipation. Second-generation SQUID TDM uses inductive summing of SQUID currents that prevents parasitic current flow without dissipation. This second-generation architecture is described here.

In “inductive summing” SQUID TDM [154, 163], boxcar address currents  $I_1(t), I_2(t) \dots I_N(t)$  are applied to turn on one row of  $M$  first-stage SQUIDs at a time (Fig. 21). An address resistor,  $R_A$ , shunts each first-stage SQUID. The value of the address resistor is typically chosen to be similar to the dynamic resistance of the SQUID to optimize a tradeoff between coupling,

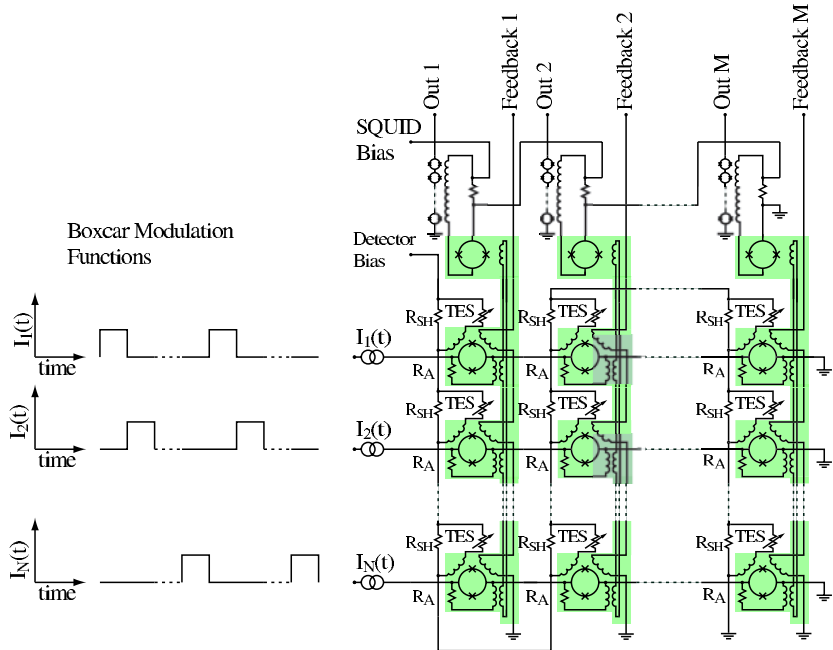


**Fig. 21.** Two-dimensional multiplexing of a TES array with a time-division SQUID MUX. A common detector bias current is applied to all of the TESs in series. Each TES is wired in parallel with its own shunt resistor,  $R_{SH}$ . Boxcar functions turn on one row of SQUID switches at a time. The outputs of all of the switches in a column are inductively summed into one output SQUID. A final series-array SQUID stage is used to amplify the signal before coupling to room-temperature electronics. A common feedback coil linearizes all SQUID switches in a column

bandwidth, and Johnson noise currents from the address resistors. The current through the address resistor is inductively coupled through a summing coil to a second-stage SQUID shared by all the first-stage SQUIDs in a column. A separate wire can be run to room temperature for every address line, or the address currents can be provided by a CMOS multiplexer circuit cooled to 4 K [160].

A feedback flux is used to linearize the SQUID switches. Only one SQUID in a column is on at a time, so one feedback coil can be common to all SQUIDS in the column (Fig. 21). The feedback is applied by room-temperature electronics that have an analog-digital converter (ADC), a field-programmable gate array (FPGA), and a digital-analog converter (DAC) for each multiplexed column [164]. When the SQUID associated with a pixel is on, its output is measured by the ADC. The appropriate feedback signal to null the flux of the “on” SQUID is applied by the DAC to the common feedback coil. When the SQUID is turned off, the value of the DAC voltage required to null

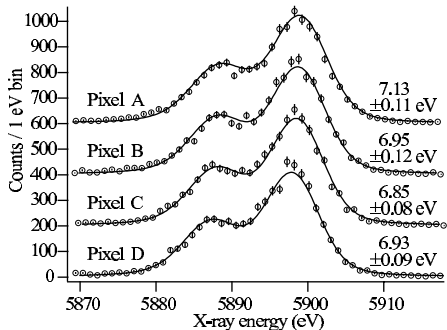


**Fig. 22.**  $^{55}\text{Fe}$  X-ray spectra measured simultaneously with an array of four TES X-ray calorimeters time-division multiplexed into one output channel. The spectra are offset vertically by 200 counts per eV. The data points are shown with statistical error bars, and the line is a fit to the Lorentzian natural linewidths of the Mn-K $\alpha$  complex [134] convolved with a Gaussian detector response

the SQUID flux is stored in the FPGA; the next time the pixel is turned on, the feedback algorithm is continued from the previous value of flux.

SQUID TDM has been used in FIBRE, an 8-pixel TES bolometer array in a submillimeter Fabry–Perot spectrometer. The SQUID multiplexer operated without significantly contributing to the noise of the bolometer [165]. FIBRE has been used in initial astronomical observations [28].

Doriese et al. have multiplexed four TES X-ray microcalorimeters in one output channel with good energy resolution [166]. The slight measured energy resolution degradation due to multiplexing (from  $\approx 6.5$  eV FWHM to  $\approx 6.9$  eV FWHM) is well understood, given the preliminary circuit parameters. Scaling to 32 pixels with less degradation is planned in a higher-bandwidth system.

A 1,280-pixel SQUID TDM chip has been developed for the SCUBA-2 instrument [29]. The SCUBA-2 MUX chip consists of 32 columns, each with 40 multiplexed SQUIDs (Fig. 23). The SCUBA-2 MUX chip is bump-bonded to a 1,280-pixel subarray of TES bolometers. The full SCUBA-2 instrument will combine 4 subarrays at 450  $\mu\text{m}$  and 4 subarrays at 850  $\mu\text{m}$ , for a total of 10,240 pixels.

SQUID TDM is being developed by groups at NIST, Jena [167], and Giessen [168]. It will be used in many instruments including a TES X-ray calorimeter array for NASA’s Constellation-X observatory [30], an X-ray microanalysis array at NIST, SAFIRE [169], a 288-pixel first-light instrument on SOFIA, the Penn Array on the Green Bank Telescope [170], the Millimeter Bolometer Array Camera for the Atacama Cosmology Telescope [15], and SCUBA-2 [29], a 10,240-pixel submillimeter bolometer camera to be deployed at the James Clerk Maxwell Telescope in 2006.

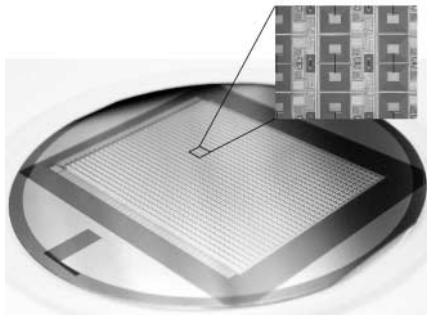


**Fig. 23.** A 1,280-pixel SQUID TDM multiplexer for the SCUBA-2 instrument. The multiplexer wafer is bump-bonded to a TES array. 8 of these “subarray” modules make up the full instrument. *Inset:* a close view of a few of the MUX elements

Finally, it may be possible to implement SQUID TDM using digital SQUIDs with rapid single flux quantum (RSFQ) logic [171]. However, significant reduction in the power dissipation would be required to make digital SQUIDs practical for operation well below 1 K.

#### 4.2.4 Low-Frequency FDM

The first frequency-division SQUID multiplexers were developed for biomagnetism applications [172]. In these circuits, different sinusoidal modulation functions are applied as flux signals to multiple SQUIDs before their output voltage is summed. However, in the SQUID FDM circuits presently used for the readout of TES arrays, the modulation is applied to the bias of the TESs [155], and the output of multiple TES detectors in a row is summed into one SQUID.  $N$  different sinusoidal modulation functions,  $I_1(t), I_2(t) \dots I_N(t)$ , are applied to bias a row of  $N$  different TESs. The TES signals are thus moved up to a frequency band around their respective modulation, or “carrier” frequency.

The bandwidth of the signal and noise from each TES is limited by an LCR tank filter formed by a tuned inductor and capacitor at each pixel and the resistance of the TES (Fig. 24). Since the resonant frequency  $\approx 1/(2\pi LC)$  is different for each pixel in the row, a single bias line can be used for an entire row. The bias line carries the sum of the modulation functions for all of the pixels (a “comb” in frequency space), but the LCR tank circuit for each pixel allows only the matched modulation frequency through to its respective TES.

In first-generation TES FDM, the outputs of the different TES channels is summed using a common transformer coil [155]. To improve the coupling efficiency, in present circuits (Fig. 24) the TES detectors are wired in parallel so that all of the signal currents are summed and flow through a common SQUID coil [173]. A feedback current is applied to each row SQUID to keep

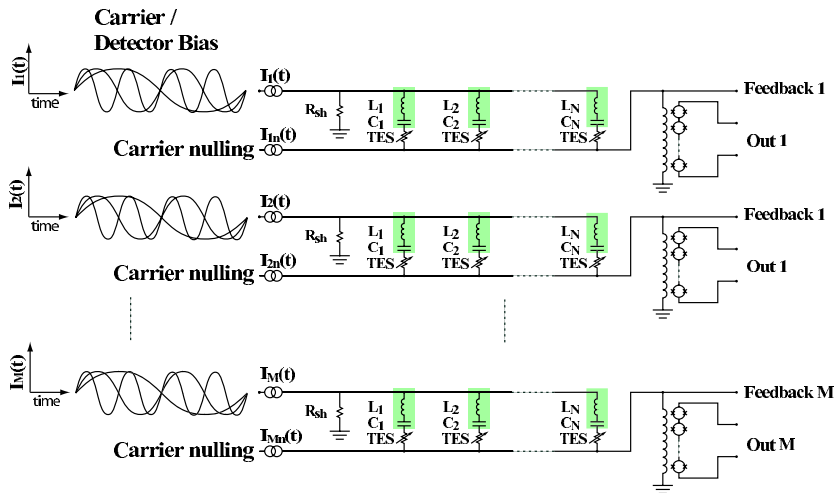


**Fig. 24.** Two-dimensional multiplexing of a  $N \times M$  TES array with a frequency-division SQUID MUX.  $N$  different sinusoidal carriers are applied on the bias line of a row of  $N$  TESs. Each TES in the row is part of an LCR tank circuit tuned to a different frequency. The current from all TESs is summed into the input coil of a series-array SQUID. A feedback signal is provided to make the input coil a virtual ground, and a carrier-nulling signal is provided to reduce the required SQUID flux slew rate

the total current through the SQUID coil fixed, providing a virtual ground that linearizes the SQUID and reduces crosstalk.

The amplitude of the carrier signals is generally larger than the low-frequency signals from the TESs. The combined carrier signals from all of the multiplexed TESs cause a significant flux slew rate in the SQUID and a large total flux swing. In order to reduce the required SQUID feedback slew rate, a carrier-nulling signal can be applied to the SQUID. All carrier-nulling signals for a row are applied to the row SQUID on one wire. The carrier-nulling signal is proportional to the carrier signal, but with phase and gain adjusted to minimize the load of the carrier on the SQUID (Fig. 24). Alternatively, the TES can be read out in a bridge configuration to null the carrier [174].

The resonant frequency of a series LRC resonator is  $f \approx 1/(2\pi LC)$ , and its bandwidth is  $\Delta B \approx R/(2\pi L)$ . Low-frequency FDM requires large inductive and capacitive filter elements. Example values are  $L = 40 \mu\text{H}$  and  $C = 0.64 \text{ nF}$  to  $4.4 \text{ nF}$  for operation at  $f = 380 \text{ kHz}$  to  $1 \text{ MHz}$  [173]. The inductors are typically large spiral lithographic superconducting coils. To achieve the high required capacitance values, it is necessary to use either component capacitors connected to every pixel or lithographic capacitors with large chip areas, very thin dielectrics, or insulators with high dielectric constant (such as  $\text{SrTiO}_3$  or  $\text{Nb}_2\text{O}_5$ ). The loss in the dielectric must be small enough that

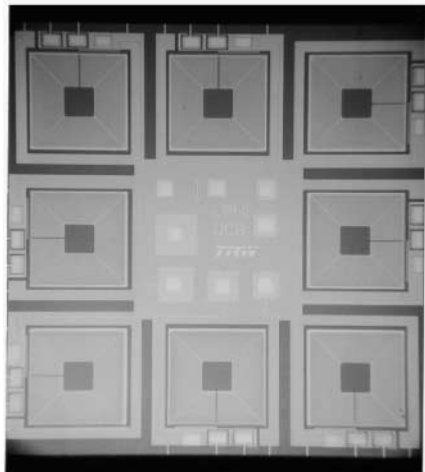


**Fig. 25.** Photograph of niobium LC filter chip fabricated by TRW (now Northrup-Grumman). The filters consist of eight spiral inductors and eight parallel-plate capacitors with  $\text{Nb}_2\text{O}_5$  dielectric. Photograph courtesy of Adrian Lee, UC Berkeley

the  $Q$  of the circuit is not degraded, which would widen the bandwidth of the filter. The Berkeley/LBNL group in collaboration with TRW has developed LC filter chips with 8 separate LC resonators (Fig. 25) on a  $10 \text{ mm} \times 10 \text{ mm}$  chip.

The UC Berkeley/LBNL group has demonstrated the multiplexing of an array of 8 TES bolometers in one output channel without significant degradation in NEP [175]. A collaboration of LLNL and Berkeley/LBNL [17, 176] has demonstrated the multiplexing of two TES gamma-ray calorimeters without significant degradation in energy resolution due to the multiplexing (Fig. 26). The gamma-ray calorimeters in this experiment have an energy resolution of 60 eV at 60 keV.

Low-frequency SQUID FDM is being developed by groups at Berkeley/LBNL [155], VTT/SRON [156], LLNL [17], and ISAS [174]. These groups are planning to use this approach in several instruments to study the cosmic microwave background at millimeter wavelengths, including APEX-SZ [16], the South Pole Telescope, and POLARBEAR [177]. Low-frequency SQUID FDM is also planned for the European Space Agency's XEUS X-ray observatory [156].

#### 4.2.5 Microwave SQUID Multiplexer

SQUID multiplexers operated at microwave frequencies are being developed due to the promise of compact passive filter elements and large total bandwidth. They have significant advantages for reading out large TES arrays, but they are less mature than low-frequency multiplexers. Large arrays of

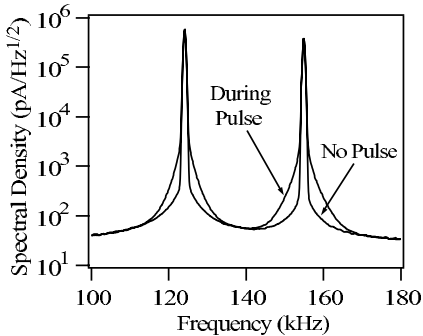


**Fig. 26.** Frequency-space representation of data from two multiplexed TES gamma-ray calorimeters [17]. The two TESs are in separate LRC resonant circuits at two different resonant frequencies, 124 kHz and 154 kHz. At steady state, the peaks are sharp, with high  $Q$ . When a gamma ray is absorbed, the TES resistance increases and the peak broadens. Figure courtesy of J.N. Ullom, NIST (formerly LLNL)

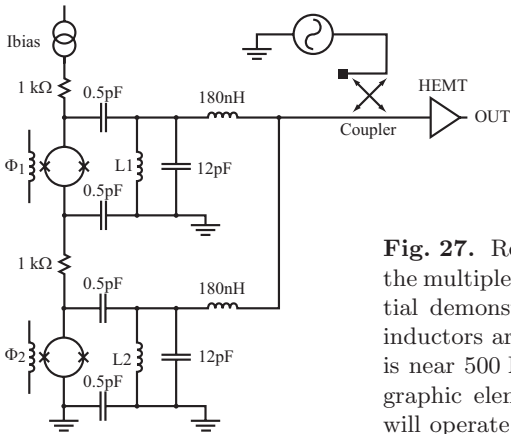


**Fig. 27.** Resonant circuit used to demonstrate the multiplexed readout of two pixels. In the initial demonstration, component capacitors and inductors are used, and the resonant frequency is near 500 MHz. Future circuits will use lithographic elements (lumped or distributed) and will operate near 5 GHz

SQUIDs operated at microwave frequencies could potentially be frequency-division multiplexed into one coaxial cable, with two additional coaxial cables used to flux bias the SQUIDs.

In a microwave reflectometer SQUID multiplexer [157], each SQUID is placed in a resonant circuit with a unique microwave resonant frequency. All of the resonant circuits are connected in parallel. A comb of microwave frequencies is used to simultaneously excite all resonant circuits. The amplitude and phase of the reflected microwave signal at each resonant frequency is a function of the magnetic flux in the associated SQUID, and thus of the current passing through the TES connected to its input coil. The reflected signal from all SQUIDs is summed into the input of one cryogenic high electron-

mobility transistor (HEMT). Similar techniques have previously been used to multiplex the readout of single electron transistors [178] and kinetic inductance detectors [179]. This microwave reflectometer readout can be used with either dc or rf SQUIDS.

Because SQUIDS have nonlinear periodic response functions, they are usually operated with flux feedback to linearize their response. In large arrays, however, it is impractical to provide a separate feedback line to every pixel. The SQUIDS in the microwave SQUID multiplexer are thus operated open-loop, without feedback. Open-loop operation is appropriate for applications with moderate dynamic range requirements, including the readout of most low-temperature detectors. Unlike low-frequency FDM schemes that couple many detectors and many carrier signals to one SQUID and thus require high dynamic range [155], the response of each SQUID in the microwave multiplexer can remain monotonic even with large signals in every detector. The signals are summed into a HEMT, which has large dynamic range. Operating open-loop leads to some nonlinearity in the SQUID response that must be corrected. In general, the response of a TES also has some nonlinearity that must be corrected. The software developed to correct the nonlinearity of the detectors can also be used to linearize the SQUIDS with no additional computational cost.

Microwave reflectometer readout of single SQUIDS has been demonstrated with good noise performance (flux noise  $\approx 0.5 \mu\Phi_0/\sqrt{\text{Hz}}$  at 4 K) and high bandwidth ( $\sim 100 \text{ MHz}$ ) [157]. Furthermore, multiplexed readout of two SQUIDS has been demonstrated in a microwave reflectometer circuit. In this multiplexed circuit (Fig. 27), two SQUIDS were placed in circuits with different resonant frequencies and a loaded  $Q$  of 60. The resonant circuits transform the impedance of the SQUIDS to  $\approx 50 \Omega$ . The reflected power at the two resonances is a function of the current through the input coil of the two SQUIDS (Fig. 28). Future circuits with lithographic filter elements are expected to have  $Q$ s of many thousands, allowing thousands of TES detectors to be multiplexed into one coaxial cable.

A microwave SQUID MUX is operated open-loop, but it is necessary to choose the flux bias of the SQUIDS to be on a sensitive, linear portion of the response curve. Time-division multiplexed circuits are being developed to flux bias each SQUID by trapping flux in a separate superconducting “flux-bias” coil coupled through an inductor,  $L_2$ , to the SQUID (Fig. 29). A flux-bias lead is inductively coupled to the flux-bias coil through inductor  $L_1$  only when a heat-actuated superconducting switch is opened. In order to flux bias the SQUID, the heat switch is actuated (driving a resistor normal), and the flux-bias lead injects flux into the flux-bias coil. The heat switch is then closed, trapping the appropriate flux in the flux-bias coil. An integral number of flux quanta are trapped in  $L_2$  when the switch is closed.  $L_2$  is only weakly coupled to the SQUID, so a large number of trapped flux quanta lead to only

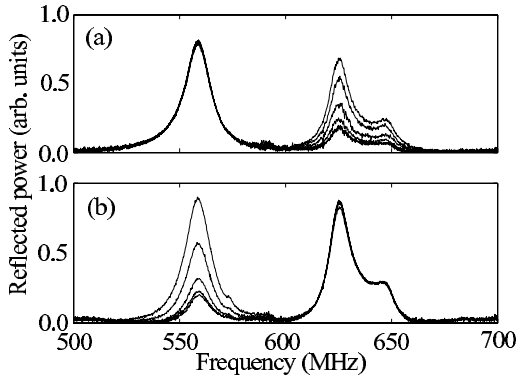


**Fig. 28.** Differential measurement of the scattering of a microwave signal off the circuit in Fig. 27, relative to the signal when the SQUIDs are off. (a) A family of curves for different flux in SQUID 1. (b) A family of curves for different flux in SQUID 2. The high-frequency shoulder is due to a reflection in the HEMT output, which is out of the specified band

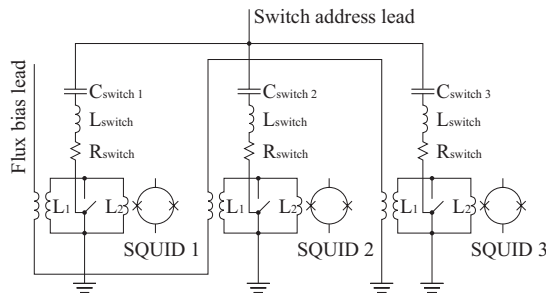


**Fig. 29.** Array of persistent current flux-bias circuits. Each circuit is addressed by applying a different excitation frequency to the switch address lead (driving it normal) and applying flux to the flux-bias lead

a fraction of a flux quantum in the SQUID. Thus, the flux bias can be set in fine steps.

The heat switches operate by using Joule power in a normal-metal film to heat the electrons in a superconducting film into the normal state. The structures are made small so that the thermal diffusion times are fast enough for high-bandwidth operation, and the films are thin so that they can be heated with low applied power.

In an array, the heat-switch resistors are placed in high- $Q$  LRC resonant circuits and driven normal using a microwave signal at the appropriate resonant frequency. All of the switch-address leads are tuned to different resonant frequencies and wired in parallel to a single coaxial cable (Fig. 29). The flux-bias lead passes in series through all of the flux-bias coils. When the array

is turned on, the switches are addressed one at a time until the flux bias for the full array is set.

Once fully developed, the microwave SQUID multiplexer will allow much larger TES arrays to be operated with only three coaxial cables to the base temperature: one to carry the reflectometer signal, one to address the multiplexed flux bias circuit, and one to apply flux to the multiplexed flux bias circuit.

Finally, hybrid schemes implementing both microwave SQUID FDM and low-frequency TDM are being developed at NIST. In this approach, the second-stage SQUIDs in the standard low-frequency TDM circuit of Fig. 21 are multiplexed at microwave frequencies into a single HEMT amplifier. This hybrid FDM/TDM basis set is similar to that used in time-division multiple access (TDMA) cell phones, in which different frequency bands are time-division multiplexed. While requiring more leads than the standard microwave SQUID MUX (including an address line for every row and a feedback line for every column), the “TDMA” approach would allow linearized, high dynamic range operation for fast pulses, and high bandwidth per column (potentially 32 hundred-megahertz columns in an octave of bandwidth at  $\sim 5\text{--}10\text{ GHz}$ , for a total of over 1,000 SQUID channels in one HEMT amplifier).

## 5 Future Outlook

The last decade has seen explosive growth in the development and use of superconducting transition-edge sensors in a variety of applications. Dramatic progress has been made in single-pixel performance. Micromachined arrays of cryogenically multiplexed TES calorimeters have been developed. In spite of the recent progress, there is still significant room for improvement in our understanding of the noise processes in these devices, in the single-pixel performance, and in the scale of the TES arrays.

The fundamental source of the excess “electrical” noise observed in TES detectors is still not understood. A full thermodynamic analysis of the nonlinear, non-equilibrium TES thermal–electrical circuit has yet to be completed. A number of sources have been suggested for additional noise, including fluctuations in the order parameter, vortex flow in the Kosterlitz–Thouless transition, and noise in phase-slip lines (both noise in stable lines and noise due to phase-slip-line nucleation/denucleation or path instability). Both theoretical and experimental work is required to understand these noise processes. An understanding of the noise sources should result in designs with improved single-pixel performance.

The first TES arrays with more than a thousand pixels are now being fabricated. This number of pixels is sufficient for many future millimeter-wave cameras, where constraints on the size of the focal plane limit the number of pixels that can be used. Improvements in longer-wavelength instruments

will likely result from improved absorbers, including antenna structures with polarization or frequency sensitivity. At shorter wavelengths, significantly larger pixel counts are desirable. The implementation of microwave readout techniques, such as the microwave SQUID multiplexer, may enable much larger arrays. For these larger arrays, it may be necessary to implement more intimate integration of the readout electronics and the TES pixels using techniques such as surface micromachining.

## Acknowledgement

We would like to thank D. McCammon, M. Lindeman, C. Kilbourne, K. Lehnert, J. Ullom, A. Luukanen, M. Niemack, T. Marriage and E. Feliciano-Figueroa for useful discussions in the preparation of this manuscript, and M. Lindeman, J. Ullom, W.B. Doriese, A. Lee, S.H. Moseley, J. Chervenak, L. Wang, J. Beall, S. Nam, A. Miller and M. Bruijn for contributing figures.

Contribution of an agency of the U.S. government; not subject to copyright.

## References

- [1] H. Kamerlingh Onnes: Leiden Comm. **120b** (1911) **63**
- [2] D. Andrews, W. Brucksch, W. Ziegler, E. Blanchard: Rev. Sci. Instrum. **13**, 281 (1942) **64**
- [3] D. Andrews, R. Fowler, M. Williams: Phys. Rev. **76**, 154 (1949) **64**
- [4] D. Andrews: American Philosophical Yearbook, 132 (1938) **64**
- [5] A. Goetz: Phys. Rev. **55**, 1270 (1939) **64**
- [6] M. Maul, M. Strandberg, R. Kyhl: Phys. Rev. **182**, 522 (1969) **64, 100**
- [7] J. Clarke, P. Richards, N. Yeh: Appl. Phys. Lett. **30**, 664 (1977) **64, 100**
- [8] B. Young, B. Cabrera, A. Lee, C. Martoff, B. Neuhauser, J. McVittie: IEEE Transactions on Magnetics **25**, 1347 (1989) **64, 107**
- [9] B. Neuhauser, B. Cabrera, C. Martoff, B. Young: Japanese Journal of Applied Physics, Supplement **26**, 1671 (1987) **64**
- [10] John Clarke, Alex I. Braginski: *The SQUID Handbook: Volume 1: Fundamentals and Technology of SQUIDs and SQUID Systems* (Wiley, 2004) **64, 71**
- [11] W. Seidel, G. Forster, W. Christen, F. von Feilitzsch, H. Gobel, F. Probst, R. Mossbauer: Phys. Lett. B **236**, 483 (1990) **64**
- [12] K. Irwin, S. Nam, B. Cabrera, B. Chugg, G. Park, R. Welty, J. Martinis: IEEE Trans. Appl. Supercond. **5**, 2690 (1995) **64**
- [13] K. Irwin: Appl. Phys. Lett. **66**, 1998 (1995) **65, 75, 83, 98**
- [14] A. Lee, P. Richards, Sae Woo Nam, B. Cabrera, K. Irwin: Appl. Phys. Lett. **69**, 1801 (1996) **65, 80, 108**
- [15] A. Kosowsky: New Astron. Rev. **47**, 939 (2003) **65, 134**
- [16] D. Schwan, F. Bertoldi, S. Cho, M. Dobbs, R. Guesten, N. Halverson, W. Holzapfel, E. Kreysa, T. Lanting, A. Lee, M. Lueker, J. Mehl, K. Menten,

- D. Muders, M. Myers, T. Plagge, A. Raccaelli, P. Schilke, P. Richards, H. Spieler, M. White: New Astron. Rev. **47**, 933 (2003) [65](#), [137](#)
- [17] M. Cunningham, J. Ullom, T. Miyazaki, S. Labov, J. Clarke, T. Lanting, A. Lee, P. Richards, Jongsoo Yoon, H. Spieler: Appl. Phys. Lett. **81**, 159 (2002) [65](#), [137](#), [138](#)
- [18] T. Miyazaki, J. Ullom, M. Cunningham, S. Labov: IEEE Trans. Appl. Supercond. **13**, 630 (2003) [65](#)
- [19] B. Cabrera, L. Krauss, F. Wilczek: Phys. Rev. Lett. **55**, 25 (1985) [65](#)
- [20] D. Bassi, A. Boschetti, M. Scontoni, M. Zen: Appl. Phys. B **26**, 99 (1981) [65](#)
- [21] D. Twerenbold, J. Vuilleumier, D. Gerber, A. Tadsen, B. van den Brandt, P. Gillevet: Appl. Phys. Lett. **68**, 3503 (1996) [65](#)
- [22] G. Hilton, J. Martinis, D. Wollman, K. Irwin, L. Dulcie, D. Gerber, P. Gillevet, D. Twerenbold: Nature **391**, 672 (1998) [65](#)
- [23] R. Abusaidi, D. Akerib, J. Barnes, P.D., D. Bauer, A. Bolozdynya, P. Brink, R. Bunker, B. Cabrera, D. Caldwell, J. Castle, R. Clarke, P. Colling, M. Crisler, A. Cummings, A. Da Silva, A. Davies, R. Dixon, B. Dougherty, D. Driscoll, S. Eichblatt, J. Emes, R. Gaitskell, S. Golwala, D. Hale, E. Haller, J. Hellmig, M. Huber, K. Irwin, J. Jochum, F. Lipschults, A. Lu, V. Mandic, J. Martinis, S. Nam, H. Nelson, B. Neuhauser, M. Penn, T. Perera, M. Perillo Isaac, B. Pritychenko, R. Ross, T. Saab, B. Sadoulet, R. Schnee, D. Seitz, P. Shestopole, T. Shutt, A. Smith, G. Smith, A. Sonnenschein, A. Spadafora, W. Stockwell, J. Taylor, S. White, S. Yellin, B. Young: Phys. Rev. Lett. **84**, 5699 (2000) [65](#)
- [24] G. Angloher, M. Bruckmayer, C. Bucci, M. Buhler, S. Cooper, C. Cozzini, P. DiStefano, F. von Feilitzsch, T. Frank, D. Hauff, T. Jagemann, J. Jochum, V. Jorgens, R. Keeling, H. Kraus, M. Loidl, J. Marchese, O. Meier, U. Nagel, F. Probst, Y. Ramachers, A. Rulofs, J. Schnagl, W. Seidel, I. Sergeyev, M. Sisti, M. Stark, S. Uchaikin, L. Stodolsky, H. Wulandari, L. Zerle: Astroparticle Physics **18**, 43 (2002) [65](#)
- [25] D. Wollman, K. Irwin, G. Hilton, L. Dulcie, D. Newbury, J. Martinis: J. Microsc. **188**, 196 (1997) [65](#), [100](#), [101](#), [102](#)
- [26] A. Miller, S. Nam, J. Martinis, A. Sergienko: Appl. Phys. Lett. **83**, 791 (2003) [65](#), [118](#), [119](#)
- [27] B. Cabrera, R. Clarke, P. Colling, A. Miller, S. Nam, R. Romani: Appl. Phys. Lett. **73**, 735 (1998) [65](#), [108](#), [119](#)
- [28] D. Benford, T. Ames, J. Chervenak, E. Grossman, K. Irwin, S. Khan, B. Maffei, S. Moseley, F. Pajot, T. Phillips, J.-C. Renault, C. Reintsema, C. Rioux, R. Shafer, J. Staguhn, C. Vastel, G. Voellmer: AIP Conf. Proc. **605**, 589 (2002) [65](#), [113](#), [134](#)
- [29] W. Holland, W. Duncan, B. Kelly, K. Irwin, A. Walton, P. Ade, E. Robson: Proc. SPIE **4855**, 1 (2003) [65](#), [134](#)
- [30] N. White, H. Tananbaum: Nucl. Instrum. Methods Phys. Res. A **436**, 201 (1999) [65](#), [134](#)
- [31] J. Bardeen, L. Cooper, J. Schrieffer: Phys. Rev. **108**, 1175 (1957) [66](#)
- [32] V. Ginzburg, L. Landau: Zh. Eksperim. i Teor. Fiz. **20**, 1064 (1950) [66](#)
- [33] L. Gor'kov: Zh. Eksperim. i Teor. Fiz. **36**, 1918 (1959) [66](#)
- [34] M. Tinkham: *Introduction to Superconductivity* (McGraw-Hill, 1995), 2nd edition [67](#)

- [35] M. Beasley, J. Mooij, T. Orlando: Phys. Rev. Lett. **42**, 1165 (1979) **67**
- [36] S. Doniach, B. Huberman: Phys. Rev. Lett. **42**, 1169 (1979) **67, 103**
- [37] W. Little: Phys. Rev. **156**, 396 (1967) **68**
- [38] J. Lukens, R. Warburton, W. Webb: Phys. Rev. Lett. **25**, 1180 (1970) **68**
- [39] R. Newbower, M. Beasley, M. Tinkham: Phys. Rev. B **5**, 864 (1972) **68**
- [40] K. Irwin, G. Hilton, D. Wollman, J. Martinis: J. Appl. Phys. **83**, 3978 (1998) **68, 69, 70, 77, 82, 83, 84, 102**
- [41] W. Skocpol, M. Beasley, M. Tinkham: J. Low Temp. Phys. **16**, 145 (1974) **69**
- [42] J. Clarke, J. Paterson: Appl. Phys. Lett. **19**, 469 (1971) **74**
- [43] M. Kiviranta, H. Seppa: IEEE Trans. Appl. Supercond. **5**, 2146 (1995) **74**
- [44] R. Welty, J. Martinis: IEEE Trans. Appl. Supercond. **3**, 2605 (1993) **74**
- [45] R. Welty, J. Martinis: IEEE Transactions on Magnetics **27**, 2924 (1991) **74**
- [46] M. Huber, P. Neil, R. Benson, D. Burns, A. Corey, C. Flynn, Y. Kitaygorodskaya, O. Massihzadeh, J. Martinis, G. Hilton: IEEE Trans. Appl. Supercond. **11**, 4048 (2001) **74**
- [47] K. Irwin: *Phonon-Mediated Particle Detection Using Superconducting Tungsten Transition-Edge Sensors*, Ph.D. thesis, Stanford University (1995) **75, 78, 80, 90**
- [48] M. Lindeman: *Microcalorimetry and the Transition-Edge Sensor*, Ph.D. thesis, University of California at Davis (2000) **75, 78, 83, 90**
- [49] J. Mather: Appl. Optics **23**, 584 (1984) **75, 78**
- [50] J. Mather: Appl. Optics **21**, 1125 (1982) **75, 78, 80, 82, 90, 91, 92**
- [51] S. Moseley, J. Mather, D. McCammon: J. Appl. Phys. **56**, 1257 (1984) **75, 78**
- [52] M. Lindeman, S. Bandler, R. Brekosky, J. Chervenak, E. Figueroa-Feliciano, F. Finkbeiner, M. Li, C. Kilbourne: Rev. Sci. Instrum. **75**, 1283 (2004) **82, 83, 117**
- [53] E. Figueroa-Feliciano: *Theory and development of position-sensitive quantum calorimeters*, Ph.D. thesis, Stanford University (2001) **82, 99, 100**
- [54] L. Landau, E. Lifshitz: *Statistical Physics* (Addison-Wesley Publishing Company, 1958), First edition **89**
- [55] R. Stratonovich: *Nonlinear Nonequilibrium Thermodynamics I: Linear and Nonlinear Fluctuation-Dissipation Theorems* (Springer-Verlag, Berlin 1992), first edition **89, 93, 94**
- [56] C. Kittel, H. Kroemer: *Thermal Physics* (W.H. Freeman and Company, 1980), Second edition **89**
- [57] H. Callen, R. Greene: Phys. Rev. **86**, 702 (1952) **91**
- [58] R. Greene, H. Callen: Phys. Rev. **88**, 1387 (1952) **91**
- [59] W. Boyle, K. Rodgers: J. Opt. Soc. Am. **49**, 66 (1959) **92**
- [60] Jr. Wyatt, J.L., G. Coram: IEEE Trans. Elect. Dev. **46**, 184 (1999) **93**
- [61] R. Stratonovich: Izv. VUZ Radiofizika **13**, 1512 (1970) **93, 94**
- [62] H. Hoevers, A. Bento, M. Bruijn, L. Gottardi, M. Korevaar, W. Mels, P. de Korte: Appl. Phys. Lett. **77**, 4422 (2000) **99**
- [63] J. Gildemeister, A. Lee, P. Richards: Appl. Opt. **40**, 6229 (2001) **99**
- [64] C. Knoedler: J. Appl. Phys. **54**, 2773 (1983) **100, 103**
- [65] G.C. Hilton, K.D. Irwin, J.M. Martinis, D.A. Wollman: Superconducting transition-edge sensor with weak links. U.S. Patent 6,239,431 (2001) **100, 101, 102, 120**

- [66] J. Ullom, W. Doriese, G. Hilton, J. Beall, S. Deiker, W. Duncan, L. Ferreira, K. Irwin, C. Reintsema, L. Vale: *Appl. Phys. Lett.* **84**, 4206 (2004) 99, 100, 101, 102, 104, 120
- [67] J. Staguhn, S. Moseley, B. Benford, C. Allen, J. Chervenak, T. Stevenson, W. Hsieh: *Nucl. Instrum. Methods Phys. Res. A* **520**, 336 (2004) 100, 101, 120
- [68] J. Ullom, W. Doriese, G. Hilton, J. Beall, S. Deiker, K. Irwin, C. Reintsema, L. Vale, Y. Xu: *Nucl. Instrum. Methods Phys. Res. A* **520**, 333 (2004) 100, 101, 120
- [69] G. Seidel, I. Beloborodov: *Nucl. Instrum. Methods Phys. Res. A* **520**, 325 (2004) 100, 103
- [70] A. Luukanen, K. Kinnunen, A. Nuottajarvi, H. Hoevers, W. Tiest, J. Pekola: *Phys. Rev. Lett.* **90**, 238306 (2003) 100, 103
- [71] M. Lindeman: A geometrical model of excess noise in transition edge sensors and related experiments (2004); Talk at the 2nd TES Workshop at the University of Miami 100, 102
- [72] G.C. Hilton, J.M. Martinis, K.D. Irwin, D.A. Wollman: Normal metal boundary conditions for multi-layer TES detectors; U.S. Patent 6,455,849 (2002) 101
- [73] G. Hilton, J. Martinis, K. Irwin, N. Bergren, D. Wollman, M. Huber, S. Deiker, S. Nam: *IEEE Trans. Appl. Supercond.* **11**, 739 (2001) 101, 120
- [74] W. Bergmann Tiest, H. Hoevers, W. Mels, M. Ridder, M. Bruijn, P. de Korte, M. Huber: *AIP Conf. Proc.* **605**, 199 (2002) 101, 120
- [75] M. Galeazzi, F. Zuo, C. Chen, E. Ursino: *Nucl. Instrum. Methods Phys. Res. A* **520**, 344 (2004) 102
- [76] R. Huebener, D. Gallus: *Phys. Rev. B* **7**, 4089 (1973) 102
- [77] G. Fraser: *Nucl. Instrum. Methods Phys. Res. A* **523**, 234 (2004) 103
- [78] J. Chervenak, D. Benford, S. Moseley, K. Irwin: Proceedings of the Second Workshop on New Concepts for Far-Infrared and Submillimeter Space Astronomy , 378 (2002) 105
- [79] C. Hunt, P. Mauskopf, A. Woodcraft: *Proc. SPIE* **5498**, 318 (2004) 105
- [80] D. Fixsen, S. Moseley, B. Cabrera, E. Figueroa-Feliciano: *AIP Conf. Proc.* **605**, 339 (2002) 105
- [81] D. Fixsen, S. Moseley, B. Cabrera, E. Figueroa-Feliciano: *Nucl. Instrum. Methods Phys. Res. A* **520**, 555 (2004) 105
- [82] U. Nagel, A. Nowak, H. Gebauer, P. Colling, S. Cooper, D. Dummer, P. Ferger, M. Frank, J. Igelson, A. Nucciotti, F. Probst, W. Seidel, E. Kellner, F. Feilitzsch, G. Forster: *J. Appl. Phys.* **76**, 4262 (1994) 106
- [83] B. Young, T. Saab, B. Cabrera, J. Cross, R. Clarke, R. Abusaidi: *J. Appl. Phys.* **86**, 6975 (1999) 107
- [84] B. Young, T. Saab, B. Cabrera, J. Cross, R. Abusaidi: *Nucl. Instrum. Methods Phys. Res. A* **444**, 296 (2000) 107
- [85] K. Irwin, B. Cabrera, B. Tigner, S. Sethuraman: Proceedings of the 4th International Workshop on Low Temperature Detectors for Neutrinos and Dark Matter (LTD 4), 290 (1992) 107
- [86] P. Ferger, P. Colling, C. Bucci, A. Nucciotti, M. Buhler, S. Cooper, F. von Feilitzsch, G. Forster, A. Gabutti, J. Hohne, J. Igelson, E. Kellner, M. Loidl, O. Meier, U. Nagel, F. Probst, A. Rulofs, U. Schanda, W. Seidel, M. Sisti, L.

- Stodolsky, A. Stolovich, L. Zerle: Nucl. Instrum. Methods Phys. Res. A **370**, 157 (1996) [107](#)
- [87] K. Irwin, S. Nam, B. Cabrera, B. Chugg, B. Young: Rev. Sci. Inst. **66**, 5322 (1995) [107, 108](#)
- [88] B. Young, S. Nam, P. Brink, B. Cabrera, B. Chugg, R. Clarke, A. Davies, K. Irwin: IEEE Trans. Appl. Supercond. **7**, 3367 (1997) [107](#)
- [89] A. Lita, Rosenberg D., Nam S., Miller A.J., Salminen A., Schwall R.E., Balzar D.: *Tuning Of Tungsten Thin Film Superconducting Transition Temperature For Fabrication Of Photon Number Resolving Detectors* (2004) [107](#)
- [90] S. Lee, J. Gildemeister, W. Holmes, A. Lee, P. Richards: Appl. Optics **37**, 3391 (1998) [108](#)
- [91] J. Hohne, M. Altmann, G. Angloher, P. Hettl, J. Jochum, T. Nussle, S. Pfnnur, J. Schnagl, M. Sarsa, S. Wanninger, F. van Feilitzsch: X-Ray Spectrom. **28**, 396 (1999) [108](#)
- [92] K. Irwin, G. Hilton, J. Martinis, B. Cabrera: Nucl. Instrum. Methods Phys. Res. A **370**, 177 (1996) [108](#)
- [93] K. Irwin, G. Hilton, D. Wollman, J. Martinis: Appl. Phys. Lett. **69**, 1945 (1996) [108](#)
- [94] C. Hunt, J. Bock, P. Day, A. Goldin, A. Lange, H. LeDuc, A. Vayonakis, J. Zmuidzinas: Proc. SPIE **4855**, 318 (2003) [108, 114](#)
- [95] F. Finkbeiner, T. Chen, S. Aslam, E. Figueroa-Feliciano, R. Kelley, M. Li, D. Mott, C. Stahle, C. Stahle: IEEE Trans. Appl. Supercond. **9**, 2940 (1999) [108](#)
- [96] K. Irwin, G. Hilton, J. Martinis, S. Deiker, N. Bergren, S. Nam, D. Rudman, D. Wollman: Nucl. Instrum. Methods Phys. Res. A **444**, 184 (2000) [108, 120](#)
- [97] D. Chow, M. Lindeman, M. Cunningham, M. Frank, Jr. Barbee, T.W., S. Labov: Nucl. Instrum. Methods Phys. Res. A **444**, 196 (2000) [108, 115](#)
- [98] F. Kiewiet, M. Bruijn, H. Hoevers, A. Bento, W. Mels, P. de Korte: IEEE Trans. Appl. Supercond. **9**, 3862 (1999) [108, 111, 113](#)
- [99] J. Martinis, G. Hilton, K. Irwin, D. Wollman: Nucl. Instrum. Methods Phys. Res. A **444**, 23 (2000) [108](#)
- [100] G. Brammertz, A. Golubov, P. Verhoeve, R. den Hartog, A. Peacock, H. Rogalla: Appl. Phys. Lett. **80**, 2955 (2002) [108](#)
- [101] B. Young, J. Williams, S. Deiker, S. Ruggiero, B. Cabrera: Nucl. Instrum. Methods Phys. Res. A **520**, 307 (2004) [109](#)
- [102] S. Ruggiero, A. Williams, W. Rippard, A. Clark, S. Deiker, L. Vale, J. Ullom: J. Low Temp. Phys. **134**, 973 (2004) [109](#)
- [103] S. Ruggiero, A. Williams, W. Rippard, A. Clark, S. Deiker, B. Young, L. Vale, J. Ullom: Nucl. Instrum. Methods Phys. Res. A **520**, 274 (2004) [109](#)
- [104] S. Deiker, W. Doriese, G. Hilton, K. Irwin, W. Rippard, J. Ullom, L. Vale, S. Ruggiero, A. Williams, B. Young: Appl. Phys. Lett. **85**, 2137 (2004) [109](#)
- [105] P. Downey, A. Jeffries, S. Meyer, R. Weiss, F. Bachner, J. Donnelly, W. Lindley, R. Mountain, D. Silversmith: Appl. Optics **23**, 910 (1984) [110](#)
- [106] J.J. Bock, D. Chen, P.D. Mauskopf, A.E. Lange: Space Science Reviews **1-2**, 229 (1995) [110, 111](#)
- [107] C. Stahle, R. Kelley, D. McCammon, S. Moseley, A. Szymkowiak: Nucl. Instrum. Methods Phys. Res. A **370**, 173 (1996) [110](#)

- [108] J. Gildemeister, A. Lee, P. Richards: *Appl. Phys. Lett.* **74**, 868 (1999) [111](#), [113](#)
- [109] W. Holmes, J. Gildemeister, P. Richards, V. Kotsubo: *Appl. Phys. Lett.* **72**, 2250 (1998) [111](#), [118](#)
- [110] M. Leivo, J. Pekola: *Appl. Phys. Lett.* **72**, 1305 (1998) [111](#)
- [111] M. Li, C. Allen, S. Gordon, J. Kuhn, D. Mott, C. Stahle, L. Wang: *Proc. SPIE* **3874**, 422 (1999) [111](#)
- [112] J. Staguhn, D. Benford, F. Pajot, T. Ames, J. Chervenak, E. Grossman, K. Irwin, B. Maffei, Jr. Moseley, S.H., T. Phillips, C. Reintsema, C. Rioux, R. Shafer, G. Voellmer: *Proc. SPIE* **4855**, 100 (2003) [111](#)
- [113] W. Little: *Can. J. Phys.* **37**, 334 (1959) [111](#)
- [114] F. Wellstood, C. Urbina, J. Clarke: *Phys. Rev. B* **49**, 5942 (1994) [111](#)
- [115] A. Walton, W. Parkes, J. Terry, C. Dunare, J. Stevenson, A. Gundlach, G. Hilton, K. Irwin, J. Ullom, W. Holland, W. Duncan, M. Audley, P. Ade, R. Sudiwala, E. Schulte: *IEE Proceedings-Science, Measurement and Technology* **151**, 110 (2004) [113](#), [125](#)
- [116] A. Lee, S. Cho, J. Gildemeister, N. Halverson, W. Holzapfel, J. Mehl, M. Myers, T. Lanting, P. Richards, E. Rittweger, D. Schwan, H. Spieler: Huan Tran, *Proc. SPIE* **4855**, 129 (2003) [114](#)
- [117] D. Rosenberg, S. Nam, A. Miller, A. Salminen, E. Grossman, R. Schwall, J. Martinis: *Nucl. Instrum. Methods Phys. Res. A* **520**, 537 (2004) [114](#), [119](#)
- [118] N. Tralshawala, S. Aslam, R. Brekosky, T. Chen, E. Feliciano, F. Finkbeiner, M. Li, D. Mott, C. Stahle, C. Stahle: *Nucl. Instrum. Methods Phys. Res. A* **444**, 188 (2000) [115](#)
- [119] C. Stahle, R. Kelley, S. Moseley, A. Szymkowiak, M. Juda, D. McCammon, J. Zhang: *J. Low Temp. Phys.* **93**, 257 (1993) [115](#)
- [120] C. Stahle, R. Brekosky, S. Dutta, K. Gendreau, R. Kelley, D. McCammon, R. McClanahan, S. Moseley, D. Mott, F. Porter, A. Szymkowiak: *Nucl. Instrum. Methods Phys. Res. A* **436**, 218 (1999) [115](#)
- [121] E. Sondheimer: *Adv. Phys.* **1**, 1 (1952) [117](#)
- [122] G. Chester, A. Thellung: *Proc. Phys. Soc. (London)* **77**, 1005 (1961) [117](#)
- [123] J. Karvonen, L. Taskinen, I. Maasilta: *Phys. Stat. Solidi* (in press) (2005) [118](#)
- [124] Charles Kittel: *Introduction to Solid State Physics* (John Wiley, 1996), seventh edition [119](#)
- [125] Neil W. Ashcroft, N. Mermin: *Solid State Physics* (Harcourt Brace, 1976) [119](#)
- [126] Liu Shumei, Zhang Dianlin, Jing Xiunian, Lu Li, Li Shanlin, Kang Ning, Wu Xiaosong, J. Lin: *Phys. Rev. B* **62**, 8695 (2000) [119](#)
- [127] V. Boiko, V. Gantranakherm, V. Gasparov: *Sov. Phys. JETP* **38**, 604 (1974) [119](#)
- [128] R. Johnson, O. Vilches, J. Wheatley: *Phys. Rev. Lett.* **16**, 101 (1966) [119](#)
- [129] D. Gubser, Jr. Soulen, R. J.: *J. Low Temp. Phys.* **13**, 211 (1973) [119](#)
- [130] M. Lindeman, R. Brekosky, E. Figueroa-Feliciano, F. Finkbeiner, M. Li, C. Stahle, C. Stahle, N. Tralshawala: *AIP Conf. Proc.* **605**, 203 (2002) [120](#)
- [131] P. de Korte, H. Hoevers, J. den Herder, J. Bleeker, W. Tiest, M. Bruijn, M. Ridder, R. Wiegerink, J. Kaastra, J. van der Kuur, W. Mels: *Proc. SPIE* **4851**, 779 (2003) [120](#)

- [132] Y. Ishisaki, U. Morita, T. Koga, K. Sato, T. Ohashi, K. Mitsuda, N. Yamasaki, R. Fujimoto, N. Iyomoto, T. Oshima, K. Futamoto, Y. Takei, T. Ichitsubo, T. Fujimori, S. Shoji, H. Kudo, T. Nakamura, T. Arakawa, T. Osaka, T. Homma, H. Sato, H. Kobayashi, K. Mori, K. Tanaka, T. Morooka, S. Nakayama, K. Chinone, Y. Kuroda, M. Onishi, K. Otake: Proc. SPIE **4851**, 831 (2003) [120](#)
- [133] W. Bergmann Tiest: *Energy Resolving Power of Transition-Edge X-ray Microcalorimeters*, Ph.D. thesis, University of Utrecht (2004) [120](#)
- [134] G. Holzer, M. Fritsch, M. Deutsch, J. Hartwig, E. Forster: Phys. Rev. A **56**, 4554 (1997) [122](#), [134](#)
- [135] G. Kovacs, N. Maluf, K. Petersen: Proc. IEEE **86**, 1536 (1998) [123](#)
- [136] M. Bruijn, H. Hoevers, W. Mels, J. Den Herder, P. De Korte: Nucl. Instrum. Methods Phys. Res. A **444**, 260 (2000) [123](#)
- [137] M. Bruijn, N. Baars, W. Tiest, A. Germeau, H. Hoevers, P. de Korte, W. Mels, M. Ridder, E. Krouwer, J. van Baar, R. Wiegerink: Nucl. Instrum. Methods Phys. Res. A **520**, 443 (2004) [123](#)
- [138] F. Lärmer, A. Schilp: Method for anisotropically etching silicon. German Patent DE4241045 (1992) [124](#)
- [139] S. McAuley, H. Ashraf, L. Atabo, A. Chambers, S. Hall, J. Hopkins, G. Nicholls: J. Phys D **34**, 2769 (2001) [124](#)
- [140] J. Chervenak, F. Finkbeiner, T. Stevenson, D. Talley, R. Brekosky, S. Bandler, E. Figueroa-Feliciano, M. Lindeman, R. Kelley, T. Saab, C. Stahle: Nucl. Instrum. Methods Phys. Res. A **520**, 460 (2004) [124](#)
- [141] M. Lindeman, S. Bandler, R. Brekosky, J. Chervenak, E. Figueroa-Feliciano, F. Finkbeiner, R. Kelley, T. Saab, C. Stahle, D. Talley: Nucl. Instrum. Methods Phys. Res. A **520**, 411 (2004) [124](#)
- [142] W. Doriese, J. Beall, J. Beyer, S. Deiker, L. Ferreira, G. Hilton, K. Irwin, J. Martinis, S. Nam, C. Reintsema, J. Ullom, L. Vale, Y. Xu: Nucl. Instrum. Methods Phys. Res. A **520**, 559 (2004) [124](#)
- [143] Z. Moktadir, M. Bruijn, R. Wiegerink, M. Elwenspoek, M. Ridder, W. Mels: Proc. IEEE Sensors 2002, 1024 (2002) [125](#)
- [144] P. Agnese, C. Buzzi, P. Rey, L. Rodriguez, J. Tissot: Proc. SPIE **3698** (1999) [125](#)
- [145] J. Gildemeister, A. Lee, P. Richards: Appl. Phys. Lett. **77**, 4040 (2000) [127](#)
- [146] G. Hilton, J. Beall, S. Deiker, J. Beyer, L. Vale, C. Reintsema, J. Ullom, K. Irwin: IEEE Trans. Appl. Supercond. **13**, 664 (2003) [127](#), [128](#)
- [147] M. Bruijn, W. Tiest, H. Hoevers, E. Krouwer, J. van der Kuur, M. Ridder, Z. Moktadir, R. Wiegerink, D. van Gelder, M. Elwenspoek: Nucl. Instrum. Methods Phys. Res. A **513**, 143 (2003) [127](#), [128](#)
- [148] P. Eriksson, J. Andersson, G. Stemme: Sens. Mater. **9**, 117 (1997) [127](#)
- [149] B. Cole, R. Higashi, R. Wood: Proc. IEEE **86**, 1679 (1998) [127](#)
- [150] K. Tanaka, T. Morooka, K. Chinone, M. Ukibe, F. Hirayama, M. Ohkubo, M. Koyanagi: Appl. Phys. Lett. **77**, 4196 (2000) [127](#)
- [151] R. Cantor (2004): private communication [127](#)
- [152] F. Chang, R. Yeh, G. Lin, P. Chu, E. Hoffman, E. Kruglick, K. Pister: Proc. SPIE **2611**, 117 (1995) [127](#)
- [153] J. Chervenak, K. Irwin, E. Grossman, J. Martinins, C. Reintsema, M. Huber: Appl. Phys. Lett. **74**, 4043 (1999) [129](#), [132](#)

- [154] P. de Korte, J. Beyer, S. Deiker, G. Hilton, K. Irwin, M. MacIntosh, Sae Woo Nam, C. Reintsema, L. Vale, M. Huber: Rev. Sci. Instrum. **74**, 3807 (2003) [129](#), [132](#)
- [155] Jongsoo Yoon, J. Clarke, J. Gildemeister, A. Lee, M. Myers, P. Richards, J. Skidmore: Appl. Phys. Lett. **78**, 371 (2001) [129](#), [135](#), [137](#), [139](#)
- [156] M. Kiviranta, H. Seppa, J. van der Kuur, P. de Korte: AIP Conf. Proc. **605**, 295 (2002) [129](#), [130](#), [137](#)
- [157] K. Irwin, K. Lehnert: Appl. Phys. Lett. **85**, 2107 (2004) [130](#), [138](#), [139](#)
- [158] B. Karasik, W. McGrath: Proceedings of the 12th International Symposium on Space Terahertz Technology, San Diego, February 13-16 (2001) [130](#)
- [159] K. Irwin: Physica C **368**, 203 (2002) [130](#)
- [160] K. Kazami, J. Kawai, G. Uehara: Jap. Journ. Appl. Phys. **35**, L1055 (1996) [132](#), [133](#)
- [161] H. Krause, S. Gartner, N. Wolters, R. Hohmann, W. Wolf, J. Schubert, W. Zander, Yi Zhang, M. v. Kreutzbruck, M. Muck: IEEE Trans Appl. Superconductivity **11**, 1168 (2001) [132](#)
- [162] M. Muck: IEEE Transactions on Magnetics **27**, 2986 (1992) [132](#)
- [163] K. Irwin, L. Vale, N. Bergren, S. Deiker, E. Grossman, G. Hilton, S. Nam, C. Reintsema, D. Rudman, M. Huber: AIP Conf. Proc. **605**, 301 (2002) [132](#)
- [164] C. Reintsema, J. Beyer, Sae Woo Nam, S. Deiker, G. Hilton, K. Irwin, J. Martinis, J. Ullom, L. Vale, M. MacIntosh: Rev. Sci. Instrum. **74**, 4500 (2003) [133](#)
- [165] D. Benford, C. Allen, J. Chervenak, M. Freund, A. Kutyrev, S. Moseley, R. Shafer, J. Staguhn, E. Grossman, G. Hilton, K. Irwin, J. Martinis, S. Nam, C. Reintsema: Int. J. Infrared Millim. Waves **21**, 1909 (2000) [134](#)
- [166] W. Doriese, J. Beall, S. Deiker, W. Duncan, L. Ferreira, G. Hilton, K. Irwin, C. Reintsema, J. Ullom, L. Vale, Y. Xu: Appl. Phys. Lett. **85**, 4762 (2004) [134](#)
- [167] T. May, V. Zakosarenko, E. Kreysa, W. Esch, S. Anders, L. Fritzsch, R. Boucher, R. Stolz, J. Kunert, H.-G. Meyer: (2004). Presented at the Applied Superconductivity Conference, Oct 4–8, 2004 [134](#)
- [168] M. Muck, C. Korn, A. Mugford, J. Kycia: Rev. Sci. Instrum. **75**, 2660 (2004) [134](#)
- [169] D. Benford, G. Voellmer, J. Chervenak, K. Irwin, S. Moseley, R. Shafer, J. Staguhn: Proc. SPIE **4857**, 125 (2003) [134](#)
- [170] D. Benford, M. Devlin, S. Dicker, K. Irwin, P. Jewell, J. Klein, B. Mason, H. Moseley, R. Norrod, M. Supanich: Nucl. Instrum. Methods Phys. Res. A **520**, 387 (2004) [134](#)
- [171] M. Radparvar: IEEE Trans. Appl. Supercond. **4**, 87 (1994) [135](#)
- [172] H. Furukawa, K. Shirae: Jap. Journ. Appl. Phys. **28**, pt.2, L456 (1989) [135](#)
- [173] T. Lanting, Hsiao-Mei Cho, J. Clarke, M. Dobbs, A. Lee, P. Richards, H. Spieler, A. Smith: Proc. SPIE **4855**, 172 (2003) [135](#), [136](#)
- [174] T. Miyazaki, M. Yamazaki, K. Futamoto, K. Mitsuda, R. Fujimoto, N. Iyomoto, T. Oshima, D. Audley, Y. Ishisaki, T. Kagei, T. Ohashi, N. Yamasaki, S. Shoji, H. Kudo, Y. Yokoyama: AIP Conf. Proc. **605**, 313 (2002) [136](#), [137](#)
- [175] A. Lee (2004): private communication [137](#)

- [176] J. Ullom, M. Cunningham, T. Miyazaki, S. Labov, J. Clarke, T. Lanting, A. Lee, P. Richards, Jongsoo Yoon, H. Spieler: IEEE Trans. Appl. Supercond. **13**, 643 (2003) [137](#)
- [177] M. Myers, W. Holzapfel, A. Lee, R. O'Brient, P. Richards, D. Schwan, A. Smith, H. Spieler, H. Tran: Nucl. Instrum. Methods Phys. Res. A **520**, 424 (2004) [137](#)
- [178] T. Stevenson, F. Pellerano, C. Stahle, K. Aidala, R. Schoelkopf: Appl. Phys. Lett. **80**, 3012 (2002) [139](#)
- [179] P. Day, H. LeDuc, B. Mazin, A. Vayonakis, J. Zmuidzinas: Nature **425**, 817 (2003) [139](#)

# Index

- Abrikosov–Gor’kov pair breaking, 109  
absorber, 112–117  
array, 121–141
- BCS theory, 66  
Bi absorber, 111  
bilayers  
    Mo/Cu, 101  
bolometer, 63  
bulk micromachining, 123
- closed-loop gain, 86  
coherence length, 66  
complex admittance, 95  
complex impedance, 71  
Cooper pairs, 66  
current-referred noise, 96
- deep reactive ion etching (DRIE), 123  
dirty limit, 67  
dynamic resistance, 77
- electron–phonon  
    coupling, 76, 110  
electron–phonon  
    decoupling, 69, 111  
excess noise  
    TES, 98
- fall time, 80  
frequency-division multiplexing, 129
- generalized responsivity matrix, 82  
Ginzburg–Landau Parameter, 67  
Ginzburg–Landau theory, 66
- high electron-mobility transistor  
    (HEMT), 138
- internal fluctuation noise, 99  
Johnson noise, 88, 90, 96
- Kammerlingh Onnes, 63  
Kosterlitz–Thouless transition, 67  
Kosterlitz-Thouless transition, 103
- Langevin equations, 88  
load resistor, 96  
London penetration depth, 66  
loop gain, 77  
Lorenz number, 69
- Markovian noise processes, 88  
membrane, 110  
microelectromechanical systems, 110  
micromachined thermal supports, 110  
microwave SQUID multiplexers, 137  
multiplexing  
    SQUID noise, 131
- negative electrothermal feedback, 85  
nonlinear Markov fluctuation-  
    dissipation relations, 94  
nonlinear thermal conductance, 95  
nonlinearity, 93  
Nyquist noise, 88  
Nyquist theorem, 130
- open-loop gain, 86
- phonon  
    noise, 88  
power responsivity, 70  
power-referred noise, 96  
power-to-current responsivity, 80, 96  
proximity bilayers, 108

- quasiparticles, 69
- rise time, 80
- saturation power, 104
- self-biasing, 85
- self-calibration, 85
- series-array-SQUID, 74
- $\text{Si}_3\text{N}_4$  membranes, 111
- silicon nitride, 76
- SQUID, 71
- SQUID noise, 131
- superconducting transition-edge sensor, 63–142
- small signal theory, 70–71
  - theory, 65–105
- surface micromachining, 127
- TES, 63–142
- array fabrication, 122
  - arrays, 121
  - bilayers, 108
  - current-biased, 86
  - electrical response, 71
  - elemental superconductors, 107
  - excess noise, 98
  - frequency-division multiplexing, 129
  - low-frequency FDM, 135
  - low-frequency TDM, 132
  - magnetically doped superconductors, 109
- microwave SQUID multiplexers, 137
- multiplexed readout, 128
- optical-photon calorimeters, 118
- proximity-coupled, 108
- saturation power, 104
- single-pixel implementation, 105
- small signal theory, 70–71
- stability, 83
- theory, 65–105
- thermal response, 71
- time-division multiplexing, 129
- voltage-biased, 86
- X-ray calorimeters, 119
- TFN, 88
- thermal conductance, 110
- $\text{Si}_3\text{N}_4$  membranes, 118
- thermal differential equation, 75
- thermodynamic fluctuation noise, 88
- Thevenin-equivalent circuit, 74
- Thevenin-equivalent load resistor, 85
- time-division multiplexing, 129
- type I superconductors, 67
- type II superconductors, 67
- vortex pairs, 103
- Wiedemann–Franz law, 110
- Wiedemann–Franz thermal conductance, 68
- zero-frequency responsivity, 82

# Metallic Magnetic Calorimeters

A. Fleischmann<sup>1</sup>, C. Enss<sup>1</sup>, and G.M. Seidel<sup>2</sup>

<sup>1</sup> Kirchhoff-Institut für Physik, Universität Heidelberg, Im Neuenheimer Feld 227, D 69120 Heidelberg, Germany

[andreas.fleischmann@kip.uni-heidelberg.de](mailto:andreas.fleischmann@kip.uni-heidelberg.de)

<sup>2</sup> Physics Department, Brown University, Providence, RI 02912, USA

**Abstract.** Magnetic calorimeters employ the magnetization of a paramagnetic sensor to detect temperature changes produced by the absorption of X-rays or other energetic particles. For typical applications, the detector consists of a metallic absorber and a paramagnetic sensor, which are in strong thermal contact with each other but have a rather weak coupling to a thermal reservoir. The absorption of energy in the calorimeter leads to a rise in temperature and a decrease in magnetization of the magnetic sensor, which can be measured accurately using a low noise, high bandwidth dc-SQUID magnetometer. Fast thermal response can be achieved by using a dilute concentration of paramagnetic ions in a metallic host as sensor material. The sensitivity of the calorimeter to the absorption of energy depends upon size, heat capacity, temperature, magnetic field, concentration of magnetic ions and the interactions among them. Theoretical models, which describe the thermodynamic properties of the calorimeter are discussed, and the conditions that optimize the performance of the detector are derived. Noise sources, especially magnetic Johnson noise and thermodynamic fluctuations of energy between the sub-systems of the calorimeter are analyzed. We discuss the demands placed on the SQUID magnetometer and present a theoretical analysis of the energy resolution. The performance of detector prototypes, including count rate, linearity and energy resolution are described. The measured resolution of devices which were designed for the detection of soft X-rays is  $E_{FWHM} = 3.4 \text{ eV}$  at an X-ray energy of 6 keV. Calculations indicate that fully optimized magnetic calorimeters will reach energy resolutions of the order of 1 eV under realistic experimental conditions.

## 1 Introduction

Thermometry based on the magnetic properties of solids has a long tradition in physics. The obvious reasons for this are that the magnetic properties of many materials are strongly dependent on temperature and that there exist very sensitive methods of measuring magnetization changes. In fact, the most sensitive thermometers in use today are magnetic in nature having a resolution of 1 part in  $10^{10}$  [1, 2, 3, 4]. Therefore, it is not surprising that magnetic sensors are also used in micro-calorimetry. To our knowledge the idea of low-temperature magnetic calorimetry for particle detection was first mentioned in the diploma thesis of W. Seidel of the Technical University in Munich in 1986 [5]. Subsequently, a development effort of applying paramagnetism to particle detection was started at the Walther-Meissner-Institute in Munich.

Within a few years, Umlauf and coworkers demonstrated the power of using the magnetization of  $4f$  ions in a dielectric host material to measure small energy inputs to an absorber with a large heat capacity [6, 7, 8, 9, 10, 11, 12, 13, 14]. Despite this success, magnetic calorimeters based on dielectric host materials were not attractive for many applications in particle detection, because of their inherently slow response. This principal problem arises from the weak coupling of the magnetic moments to phonons at low temperatures.

In 1993 it was suggested that this problem can be overcome by using magnetic ions in metallic host materials [15]. In a metal the interaction of the magnetic moments with the conduction electrons leads to relaxation times many orders of magnitude shorter than in insulating hosts. The penalty for the faster response is that the presence of the conduction electrons increases the heat capacity of the sensor and in addition leads to an enhanced interaction among the magnetic moments. Nonetheless, metallic magnetic calorimeters (MMC) have exhibited excellent resolving power, comparable to that of other leading micro-calorimeters [16]. In this chapter we will focus on the discussion of metallic magnetic calorimeters.

A MMC employs a paramagnet placed in a small magnetic field as a temperature sensor. An absorber suitable for stopping the particle being detected is in strong thermal contact with the sensor. These two components are weakly coupled to a thermal bath. An energy deposition in the absorber produces a temperature change in the absorber/sensor system, which can be monitored by measuring the change of magnetization of the paramagnetic sensor using a sensitive dc SQUID magnetometer.

MMCs are different in several ways from other micro-calorimeters. Unlike detectors with resistive sensors, the signal of an MMC is not based upon a transport property but is determined by the equilibrium thermodynamic properties of the sensor material. Hence, the performance of MMCs can be predicted with some confidence. Two other differences are significant in certain uses. MMCs are non-dissipative devices, and no contact leads to the micro-calorimeter itself are necessary to read out the sensor. As we shall discuss, these differences are important in designing MMCs for particular applications.

Currently, the application of MMCs lies mainly in high resolution X-ray spectroscopy. Examples of uses are X-ray fluorescence spectroscopy for material analysis and absolute activity measurements of X-ray sources. In addition, a development effort has been started to build large arrays of magnetic micro-calorimeters for space based X-ray telescopes. There are many conceivable applications of MMCs beyond X-ray detection ranging from rare event searches in nuclear physics such as the neutrinoless double beta decay to the mass spectroscopy of biological molecules.

## 2 Theoretical and Experimental Background

In this section the physics of MMCs will be discussed that is necessary to describe and optimize their performance. In addition, we outline different techniques for readout and data analysis.

### 2.1 Detection Scheme

Similar to other micro-calorimeters, MMCs consist of an absorber, whose temperature is monitored with a sensitive thermometer. In the case of MMCs the temperature information is obtained from the change of magnetization of a paramagnetic sensor, which is located in a small magnetic field. From equilibrium thermodynamics the change of magnetization caused by the absorption of energy  $\delta E$  is given by the simple relation

$$\delta M = \frac{\partial M}{\partial T} \delta T = \frac{\partial M}{\partial T} \frac{\delta E}{C_{\text{tot}}}, \quad (1)$$

where  $C_{\text{tot}}$  denotes the total heat capacity of thermometer and absorber. To measure the magnetization change the sensor is either placed in a pickup coil coupled to the input coil of a sensitive dc SQUID or is placed directly into the SQUID loop. The transfer function relating magnetization change to flux change in the SQUID depends, obviously, on the details of the geometry of the setup. This point will be discussed in Sect. 2.4.

### 2.2 Sensor Materials

The choice of sensor materials for a magnetic calorimeter is not trivial because the sensor needs to be optimized with respect to different and, in part, conflicting demands. For applications in particle detection the sensitivity and the thermalization time are of particular importance.

In terms of sensitivity cerium magnesium nitrate (CMN) is an obvious choice in the temperature range down to a few millikelvin. The magnetic dipole interaction between the Ce ions is particularly weak because of their location in a trigonal crystal structure and because of the highly anisotropic  $g$ -factor ( $g_{\parallel} = 0.25$  and  $g_{\perp} = 1.84$  [17]). As a consequence, magnetic ordering into a ferromagnetic state occurs for CMN only at very low temperatures ( $T_c \approx 1.9$  mK). This material has the advantage that the contribution to the heat capacity from interacting magnetic moments is very small despite the large spin concentration. However, the main drawback in using CMN, and other dielectric materials, as sensors in detectors arises from the extremely slow energy exchange between magnetic moments and phonons at very low temperatures. Spin-phonon relaxation times the order of seconds and longer are typical at millikelvin temperatures.

Notwithstanding the potential problem of long relaxation times, Umlauf and coworkers investigated the use of paramagnetic dielectrics for particle detection [6, 7, 8, 9, 10, 11, 12, 13, 14]. They used the compound Tm-Al-Garnet doped with 0.5%  $^{168}\text{Er}$  attached to a 120 g Si absorber operated in a field of 3 mT at 30 mK and achieved an energy sensitivity of 320 eV in experiments with 5 MeV  $\alpha$  particles [9]. Under optimal conditions the rise time of their signals was about 40 ms and the thermalization time with the bath was the order of 10 s. These values are unacceptably long for many applications in particle detection.

The principal problem of long relaxations times can be overcome by embedding the magnetic ions in metallic or semi-metallic host materials [15]. Here the strong coupling of the conduction electrons and the localized spins leads to rapid thermalization. Time constants for establishing thermal equilibrium within the sensor can be well below a microsecond.

The price one pays for this gain in detector speed is the additional heat capacity of the sensor and enhanced interaction between the localized magnetic moments via the Ruderman-Kittel-Kasuya-Yosida (RKKY) interaction because of the conduction electrons. This indirect exchange interaction has two undesirable consequences for the performance of magnetic calorimeters, namely an additional heat capacity associated with the exchange system and a reduction of the temperature dependence of the magnetization. Therefore, the system of choice is one with the smallest possible RKKY exchange interaction. Without exception, ions in the  $4f$  rare earth series are better in this regard than those in the  $3d$  and  $4d$  transition metal series because of their weaker interaction with conduction electrons. Among the rare earth ions, those with a small de Gennes factor [18],  $(g_J - 1)^2 J(J + 1)$ , are preferable for the same reason. Here  $g_J$  denotes the Landé  $g$ -factor of the free ion and  $J$  total angular momentum.

Another aspect that needs to be considered in selecting the best magnetic ion for magnetic calorimeters is related with its nuclear properties. A nuclear spin can lead to an unwanted hyperfine contribution to the heat capacity and to a reduction of the magnetization at the magnetic fields in which the sensor operates.

Based on the reasons given above, erbium appears to be a particularly good candidate for the magnetic ion, with the exception of the isotope  $^{167}\text{Er}$ , because of its nuclear spin (see Sect. 2.2.1).

In terms of metallic host system there are, in principle, a wide range of choices spanning from semi-metals, for example  $\text{Bi}_2\text{Te}_3$ , to noble metals such as gold. Semi-metals offer the advantage of having a much smaller conduction electron density and therefore a reduced exchange interaction. However, at this time very little is known about the properties of erbium in semi-metals, especially in terms of relaxation times, heat capacity, and magnetization. In addition, production and fabrication issues have to be studied before a judgment of their suitability as magnetic calorimeters can be determined.

For practical reasons most of the work to date has been done with gold as a host material and erbium as the magnetic ion. In addition to this alloy, LaB<sub>6</sub> doped with erbium [19], gold doped with ytterbium [20] and silver doped with erbium [21] have been investigated for use in metallic magnetic calorimeters. Since none of these materials have shown properties that are better than Au:Er we will concentrate in the following on this alloy.

### 2.2.1 Au:Er

Erbium in low concentrations forms a solid solution with gold. Erbium in the 3+ state substitutes for Au at regular fcc lattice sites giving three of its electrons to the conduction band. The Er<sup>3+</sup> ion has the electron configuration [Kr]4d<sup>10</sup>4f<sup>11</sup>5s<sup>2</sup>5p<sup>6</sup>. The paramagnetic behavior results from the partially filled 4f shell, having a radius of only about 0.3 Å and located deep inside the outer 5s and 5p shells. For comparison, the ionic radius of Er<sup>3+</sup> is about 1 Å. Because of this the influence of the crystal field is greatly reduced and the magnetic moment can be calculated from the orbital angular momentum  $\mathbf{L}$  the spin angular momentum  $\mathbf{S}$  and the total angular momentum  $\mathbf{J}$ , which are derived according to Hund's rules. To a good approximation the admixture of excited electronic states can be neglected and the magnetic moment  $\mu$  can be written as

$$\mu = g_J \mathbf{J} \quad (2)$$

with the Landé factor

$$g_J = 1 + \frac{J(J+1) + S(S+1) - L(L+1)}{2J(J+1)}. \quad (3)$$

For Er<sup>3+</sup>,  $L = 6$ ,  $S = 3/2$ ,  $J = 15/2$  and  $g_J = 6/5$ . In dilute Au:Er samples the magnetization can indeed be characterized by (2) at temperatures above about 100 K [22]. At lower temperatures it is necessary to include crystal field effects in the description. The crystal field with fcc symmetry lifts the sixteen-fold degeneracy of the Er<sup>3+</sup> ground state, splitting it into a series of multiplets (one  $\Gamma_6$  and one  $\Gamma_7$  doublet and three  $\Gamma_8$  quartets). The lowest lying multiplet is a  $\Gamma_7$  Kramers doublet. At sufficiently low temperatures and low magnetic fields the behavior of erbium in gold can be approximated as a two level system with effective spin  $\tilde{S} = 1/2$  with an isotropic  $g$  factor of  $\tilde{g} = 34/5$ . This theoretical value has been confirmed by several ESR experiments (see, for example [23]). The magnitude of energy splitting between the ground state doublet and the first excited multiplet ( $\Gamma_8$  quartet) has been reported in different experiments [22, 24, 25, 26] to be between 11 K and 19 K.

Figure 1 shows the magnetic susceptibility of Au doped with 600 ppm Er in the temperature range between 100 μK and 300 K. The data have been obtained in three different experiments [27, 28]. While the data at high temperatures ( $T > 100$  K) are in good agreement with the Curie law for  $J = 15/2$

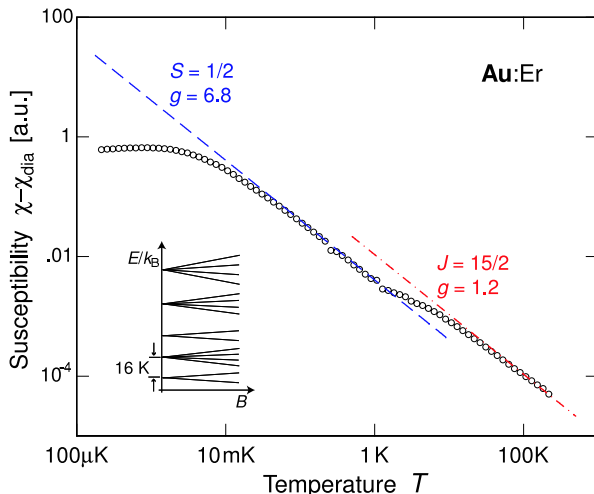


**Fig. 1.** Paramagnetic contribution to the magnetic susceptibility of Au containing 600 ppm Er as a function of temperature. The two straight lines represent the Curie susceptibility assuming  $\text{Er}^{+3}$  ions in the  $\Gamma_7$ -groundstate doublet and  $\text{Er}^{+3}$  ions without crystal field splitting. After [28]

and  $g_J = 6/5$  there is an increasing deviation from the high temperature approximation below 100 K. This is a result of the depopulation of the multiplets with higher energies. At temperatures below about 1.5 K the data follow a Curie law once again, but with a reduced Curie constant in agreement with the effective spin  $\tilde{S} = 1/2$  and  $g$  factor  $\tilde{g} = 6.8$  for the ground state doublet. At temperatures below 50 mK and in low magnetic fields such that saturation is unimportant ( $\tilde{g}\mu_B B < k_B T$ ), the susceptibility becomes much less temperature dependent. This is a result of the influence of the exchange interaction between the magnetic moments. Finally, at a temperature of about 0.9 mK a maximum in the magnetic susceptibility of the 600 ppm sample is observed, which is the result of a transition to a spin glass state.

### Heat Capacity and Magnetization

The performance of a magnetic calorimeter based on Au:Er is determined by the heat capacity and the magnetization. Since the calorimeter is operated at very low temperature (10–100 mK) we include in the calculations only the ground state crystal-field doublet.

The heat capacity of a system of non-interacting spins is given by the well-known Schottky expression

$$C_s = Nk_B \left( \frac{E}{k_B T} \right)^2 \frac{e^{E/k_B T}}{(e^{E/k_B T} + 1)^2}, \quad (4)$$

which exhibits a maximum when the thermal energy  $k_B T$  is about half the energy splitting  $E = \tilde{g}\mu_B B$ . Here  $\mu_B$  denotes the Bohr magneton. The magnetization of such a system is given by

$$M = \frac{N}{V} \tilde{g} \tilde{S} \mu_B \mathcal{B}_s(h) \quad (5)$$

with  $h = \tilde{g} \tilde{S} \mu_B / (k_B T)$  and the Brillouin function

$$\mathcal{B}_s(h) = \frac{2\tilde{S} + 1}{2\tilde{S}} \coth\left(\frac{(2\tilde{S} + 1)h}{2\tilde{S}}\right) - \frac{1}{2\tilde{S}} \coth\left(\frac{h}{2\tilde{S}}\right) \quad (6)$$

In the high temperature limit,  $h \ll 1$ , the magnetization varies as  $1/T$  as expected for the Curie law.

While the assumption of non-interacting spins is sufficient for a qualitative description of the response of MMCs, it is inadequate for a quantitative analysis. To calculate the signal of a MMC both the magnetic dipole-dipole interaction and the indirect exchange interacting between the spins must be taken into account.

Because of the isotropy of the  $\Gamma_7$  ground state doublet, the dipole-dipole interaction can be expressed in terms of the effective spins  $\tilde{\mathbf{S}}_i$  and  $\tilde{\mathbf{S}}_j$

$$H_{ij}^{\text{dipole}} = \Gamma_{\text{dipole}} \frac{1}{(2k_F r_{ij})^3} [\tilde{\mathbf{S}}_i \cdot \tilde{\mathbf{S}}_j - 3(\tilde{\mathbf{S}}_i \cdot \hat{\mathbf{r}}_{ij})(\tilde{\mathbf{S}}_j \cdot \hat{\mathbf{r}}_{ij})] \quad (7)$$

with prefactor  $\Gamma_{\text{dipole}} = (\mu_0/4\pi)(\tilde{g}\mu_B)^2(2k_F)^3$ . The quantity  $\hat{\mathbf{r}}_{ij}$  represents the unit vector in direction  $\mathbf{r}_i - \mathbf{r}_j$  and  $k_F$  the Fermi wave vector of the gold conduction electrons.<sup>1</sup>

The exchange interaction of the localized  $4f$  electrons of the erbium ions with the gold conduction electrons gives rise to an additional interaction between the erbium ions, the indirect exchange or Ruderman-Kittel-Kasuya-Yosida (RKKY) interaction. Expressed in terms of the effective spin, the RKKY interaction between two erbium spins can be written as

$$H_{ij}^{\text{RKKY}} = \Gamma_{\text{RKKY}} (\tilde{\mathbf{S}}_i \cdot \tilde{\mathbf{S}}_j) F(2k_F r_{ij}) \quad (8)$$

with the function  $F(2k_F r_{ij})$  being

$$F(2k_F r_{ij}) = \frac{1}{(2k_F r_{ij})^3} \left[ \cos(2k_F r_{ij}) - \frac{1}{2k_F r_{ij}} \sin(2k_F r_{ij}) \right] \quad (9)$$

and prefactor  $\Gamma_{\text{RKKY}}$  given by

$$\Gamma_{\text{RKKY}} = \mathcal{J}^2 \frac{4V_0^2 m_e^* k_F^4}{\hbar^2 (2\pi)^3} \frac{\tilde{g}^2 (g_J - 1)^2}{g_j^2}. \quad (10)$$

---

<sup>1</sup> The Fermi wave vector has been introduced artificially here to simplify the quantitative comparison with the indirect exchange interaction discussed later

Here  $\mathcal{J}$  denotes the coupling energy between the localized spins and the conduction electrons,  $V_0$  is the volume of the elementary cell and  $m_e^*$  is the effective mass of the conduction electrons. The expression for the RKKY interaction given above is derived under the assumption that the mean free path of the electrons is larger than the mean distance between the localized erbium ions. In principle, it is possible that the RKKY interaction is reduced due to a finite coherence length  $\lambda$  of the spin polarization of the conduction electrons. In this case an additional factor  $e^{-r/\lambda}$  would appear in (8). However, for Au:Er with suitable erbium concentrations for a MMC, the mean free path of the conduction electrons is always much larger than the mean separation of the erbium ions<sup>2</sup>.

The fact that both the dipole-dipole interaction and the RKKY interaction are proportional to  $1/r_{ij}^3$  allows us to compare their relative strength by a dimensionless parameter which is defined as the ratio of the two pre-factors

$$\alpha = \Gamma_{\text{RKKY}} / \Gamma_{\text{dipole}}. \quad (11)$$

Using this parameter  $\alpha$  the coupling energy  $\mathcal{J}$  can be expressed as<sup>3</sup>

$$\mathcal{J} \simeq \sqrt{\alpha} 0.145 \text{ eV}. \quad (12)$$

A determination of the heat capacity and magnetization of a system of randomly distributed, interacting erbium spins requires a numerical calculation. There is a number of ways to perform this kind of calculation in the framework of a mean-field approximation. The method that requires the least amount of CPU time assumes the specific form of the mean field distribution that has been derived by *Walker* and *Walstedt* [29,30] for magnetic moments randomly distributed in a continuous medium. These authors showed that this analytic representation of the mean field distribution agrees well with numerically calculated mean field distributions.

An alternative approach is to write down the Hamiltonian for a cluster of interacting, randomly distributed spins on the Au lattice and obtain the eigenvalues of the cluster. This process is repeated for a large number of configurations of randomly positioned spins with the heat capacity and magnetization obtained by averaging. The number of spins that should be included in a cluster and the number of different configurations of clusters that must be employed in the calculation depends upon the Er concentration. For concentrations the order of 1000 ppm at least  $10^4$  configurations of

---

<sup>2</sup> In measurements of the residual resistivity of dilute  $\text{Au}_{1-x}\text{Er}_x$  alloys  $\varrho = x 6.7 \times 10^{-6} \Omega \text{ m}$  was found [31], and one can conclude that the mean free path of the conduction electrons is about 4000 Å for an erbium concentration of 300 ppm

<sup>3</sup> The value of  $\mathcal{J}$  given by (12) refers to the definition of the exchange energy between a localized spin  $\mathbf{S}$  and a free electron  $\mathbf{s}$  being  $H = \mathcal{J} \mathbf{s} \cdot \mathbf{S}$ . The definition  $H = 2\mathcal{J} \mathbf{s} \cdot \mathbf{S}$  is often found in the literature, leading to values of the parameter  $\mathcal{J}$  being smaller by a factor of two

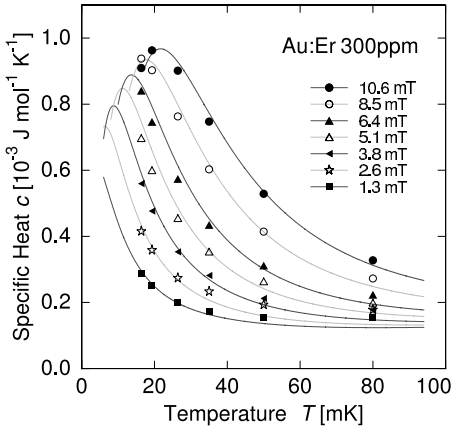


**Fig. 2.** Specific heat of Au:Er with 300 ppm enriched  $^{166}\text{Er}$  as a function of temperature at different applied magnetic fields. The *solid lines* are calculated numerically with a interaction parameter  $\alpha = 5$  [32]

clusters containing up to six spins are required to obtain a meaningful result. Clearly this procedure requires a large amount of CPU time, but the results are potentially more accurate than can be obtained from a mean field calculation. The interaction among spins in this method can employ the full Heisenberg Hamiltonian rather than the Ising approximation.

The appropriate averages over the results for different configurations have to be calculated. In case of Au:Er with moderate Er concentration this method provides a description the measured specific heat and magnetization rather well.

As an example we show in Fig. 2 the specific heat of an Au:Er sample having a concentration of 300 ppm of 97.8% enriched  $^{166}\text{Er}$ . The temperature of the maximum in the specific heat depends on the magnitude of the external magnetic field as expected for a Schottky anomaly. However, the maximum is about twice as wide as for a non-interacting spin system. Calculations based on averaging over spin clusters provides a quantitative agreement assuming a interaction parameter  $\alpha$  of 5. Although the calculated curves depend rather strongly on the choice of  $\alpha$ , the value of  $\alpha = 5$  should be viewed as a upper bound for the following two reasons. Firstly, the presence of  $^{167}\text{Er}$  in the enriched sample leads to a slight additional broadening of the curve because of the hyperfine contribution of this isotope. Secondly, additional broadening results from a variation of the applied magnetic field, of about 10 to 15%, over the sample due to the geometry of the field coil.

The magnetization is plotted as a function of  $1/T$  in Fig. 3 at several different magnetic fields for the 300 ppm sample. As in the case of the specific heat, the magnetization deviates for the behavior of isolated spins. The deviation is primarily due to the interaction between the magnetic moments, but

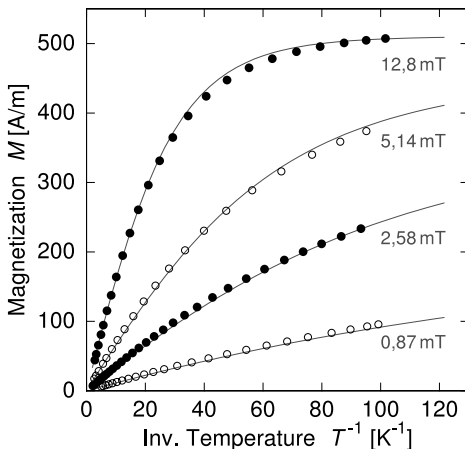


**Fig. 3.** Magnetization of Au:Er with 300 ppm enriched  $^{166}\text{Er}$  as a function of  $1/T$  at different applied magnetic fields. The *solid lines* are calculated numerically with a interaction parameter  $\alpha = 5$  [32]

a small contribution is also present due to the two reasons discussed above for the heat capacity. Again the data can be described satisfactorily by assuming an interaction parameter of  $\alpha = 5$ .

The magnetic properties of a weakly interacting spin system is perhaps most easily characterized in terms of the temperature dependence of the susceptibility given by the Curie-Weiss law,  $\chi = \lambda/(T + \theta)$ . The Curie constant  $\lambda$  is proportional to the concentration of the spins, as is the Weiss constant  $\theta$ , which is a measure of strength of the interactions. For the Au:Er system,  $\lambda = x 5.3\text{ K}$  and  $\theta = \alpha x 1.1\text{ K}$ .

## Response Time

A fast response time can be very important for calorimeters used as particle detectors. This is the main reason why metallic paramagnets such as Au:Er are chosen over dielectric compounds. The strong conduction electron-spin interaction in metallic paramagnets produces response times in the microsecond range even below 50 mK. Obviously, the response time of the calorimeter is not only determined by the properties of the sensor material, but by the choice of the absorber and the thermal connection between the two components. The only way to insure the fast response of the sensor is to employ a metal or semi-metal as absorber and to bond the absorber and sensor together in such a way that the conduction electrons carry the heat across the interface.

The absorption of an X-ray occurs primarily via the photoelectric effect resulting in the generation of an energetic electron. This electron loses its energy rather quickly by electron-electron scattering. After about  $10^{-13}\text{ s}$  the

mean energy of the athermal electrons is reduced to about 0.1 eV. At this energy the athermal electrons lose their energy predominately by the generation of high-frequency phonons. Subsequently, these high-frequency phonons thermalize via interaction with the conduction electrons. As the phonon and electron systems further thermalize most of the energy is returned into the electron system because of the larger heat capacity of conduction electrons at low temperature. By the time the local electron temperature has reached about 1 K the absorbed energy is distributed within a volume of a few cubic micrometers. The further thermalization within the absorber can be described by thermal diffusion. The time scale for this process is mainly determined by the geometry of the absorber and the presence of defects such as grain boundaries and dislocations. If we assume, for example, a pure gold absorber with dimensions  $250\text{ }\mu\text{m} \times 250\text{ }\mu\text{m} \times 5\text{ }\mu\text{m}$  having a resistance ratio of only  $R_{300\text{ K}}/R_{4\text{ K}} \approx 3$ , the thermalization time, using the Wiedemann–Franz law, can be estimated to be  $10^{-7}\text{ s}$ .

The time for the heat to flow from the absorber into the sensor is difficult to estimate since this depends very much on the nature of the thermal connection between the two components. By spot welding the gold absorber and Au:Er sensor together the contact can be made sufficiently strong that no degradation of the response time of the magnetic calorimeters due to the presence of the interface is observable.

Finally, the energy is shared with the magnetic moments in the sensor material giving rise of the signal. The response time of the spins is determined by the electron-spin relaxation time  $\tau$ , which is described by the Korringa relation  $\tau = \kappa/T$ , where  $\kappa$  denotes the Korringa constant. For Au:Er the Korringa constant has been determined in ESR measurements at 1 K to be  $\kappa = 7 \times 10^{-9}\text{ K s}$  [24]. This value of  $\kappa$  yields a spin-electron relaxation time of less than  $10^{-7}\text{ s}$  at 50 mK.

## Influence of Nuclear Spins

In the design of a magnetic calorimeter the possible influence of nuclear spins has to be considered. In the case of Au:Er there are two ways in which nuclei can affect the performance of the calorimeter. Firstly, the isotope  $^{167}\text{Er}$  with nuclear spin  $I = 7/2$  influences the magnetization and the heat capacity due to its hyperfine interaction with the  $4f$  electrons. Secondly, and more subtle, the 100% abundant  $^{198}\text{Au}$  nuclei with small magnetic moment but large quadrupole moment may contribute to the specific heat if the nuclei reside at positions where the electric field gradient is of non-cubic symmetry.

We consider first the hyperfine contribution of the erbium isotope  $^{167}\text{Er}$  having a natural abundance of 23%. This isotope, embedded in gold, has been investigated in ESR measurements [24]. From these measurements the hyperfine coupling constant is determined to be  $A/k_B = -0.0335\text{ K}$ , which results in zero magnetic field in a splitting of the energy levels into a doublet separated by 140 mK. In addition, the apparent nuclear  $g$  factor is found to

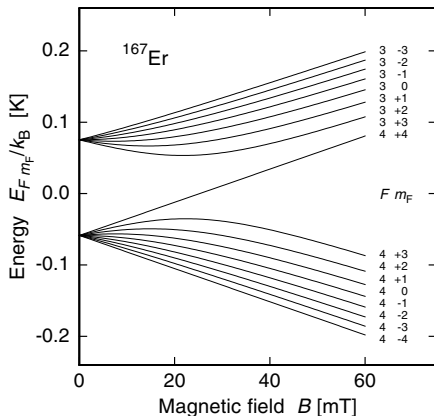


**Fig. 4.** Energy eigenvalues of the  $\Gamma_7$ -Kramers doublet of  $^{167}\text{Er}$  in Au as a function of the applied magnetic field

be strongly enhanced by internal fields to the value of  $g_N = -29$ . Using these results the level scheme of the  $\Gamma_7$  Kramers doublet can be calculated as a function of applied magnetic field. At low fields, as shown in Fig. 4, there are two groups of levels associated with the angular momentum quantum numbers  $F = 3$  and  $F = 4$ .

In the temperature and magnetic field range of interest for the operation of MMCs, the magnetization and heat capacity of  $^{167}\text{Er}$  ions is considerably different from that of Er isotopes with nuclear spin zero. The magnetization is reduced and the heat capacity enhanced. The specific heat of Au:Er sample with 480 ppm erbium with natural isotopic abundance at different applied magnetic fields is shown in Fig. 5. At low fields there are two distinct maxima visible. The one at low temperatures is caused by transitions within the  $F = 4$  multiplet and by the contributions of isotopes with zero nuclear spin. The temperature at which this maximum occurs depends strongly on the magnetic field. In contrast, the broad maximum at higher temperatures ( $T \approx 55\text{ mK}$ ) is nearly independent of magnetic field. It is caused by a redistribution in the population of spins between the two multiplets. At 10 mT and 50 mK this contribution makes up about 50% of the total specific heat. For maximum sensitivity it is necessary to eliminate this unwanted contribution by working with erbium deleted in the isotope  $^{167}\text{Er}$ .

Nuclei of the host metal can also influence the performance of an MMC. The  $^{198}\text{Au}$  nuclei have spin  $I = 3/2$ , a quadrupole moment of 0.547 barn and a magnetic moment sufficiently small to be neglected. In pure gold no contribution of the nuclear spins to the specific heat is expected at low fields, since the electric field of cubic symmetry does not lift the degeneracy of the nuclear levels. However, for Au nuclei in the vicinity of an  $\text{Er}^{3+}$  ion the electric field gradient can be substantial and can split the nuclear levels. This results

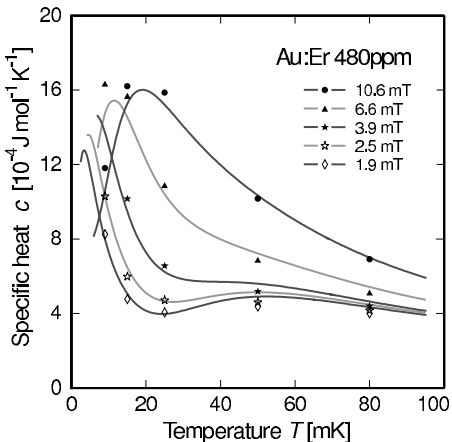


**Fig. 5.** Specific heat of Au:Er with 480 ppm of erbium with natural isotope abundance [33]

in an additional heat capacity. Fig. 6 shows the measured heat capacity of the Au nuclei as a function of temperatures for samples with different erbium concentrations. The data below 10 mK for the sample with 600 ppm is the total specific heat since at such low temperatures the contribution of the Au nuclei is substantially larger than that of all other degrees of freedom. The figure also shows a theoretical curve calculated assuming a quadrupole splitting of 70 MHz for Au nuclei in the immediate vicinity of erbium ions, the splitting decreasing for nuclei at larger distances in a manner similar to that measured in other dilute alloys such as Cu:Pt [34], Cu:Pd [35], and Gd:Au [36].

This unwanted contribution to the specific heat can only be eliminated by using a host material which has a nuclear spin  $I \leq 1/2$ . At first glance it would appear desirable to use silver as a host material rather than gold since the two isotopes of silver ( $^{107}\text{Ag}$  and  $^{109}\text{Ag}$ ) both have nuclear spin  $I = 1/2$ . However, the exchange energy  $J$  is 1.6 larger in silver than in gold as determined by ESR measurements[23]. Since the interaction parameter  $\alpha$  is quadratic in the exchange energy  $\alpha \propto J^2$ , silver is not an attractive choice as a host material for a magnetic sensor.

### 2.3 Scaling

The behavior of systems of dilute concentrations of magnetic ions in metals interacting via the RKKY mechanism have been studied for many years. One property possessed by such systems is that of scaling [37], of which we shall make use in discussing the optimization of the design of MMCs in Sect. 2.4. Scaling, in the context of magnetic ions in metals, is the property that the dependence of thermodynamic quantities on magnetic field and temperature

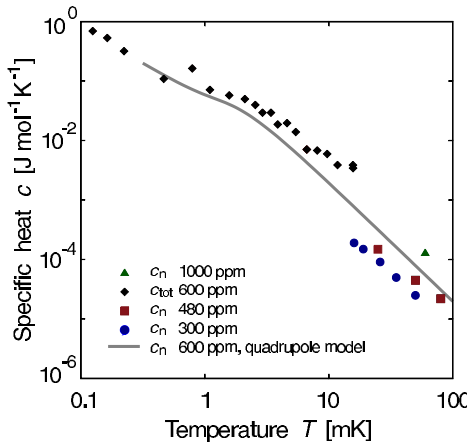


**Fig. 6.** Contribution of the Au nuclei to the specific heat of Au:Er samples with different concentrations. The *solid line* represents a theoretical curve assuming a quadrupole splitting of 70 MHz for Au nuclei, that are nearest neighbors of Er. Here  $c_{\text{tot}}$  denotes the total specific heat and  $c_n$  the contribution of just the Au nuclei to the specific heat. After [32]

at different concentrations are related to one another in a very simple way. The magnetization and heat capacity at a given  $B$  and  $T$ , for example, at one concentration are the same as that at another concentration at a field and temperature scaled by the ratio of the different concentrations. We outline the well known argument briefly below.

The effective field on a magnetic ion resulting from interactions with all surrounding ions through the RKKY coupling, given by (8), can be expressed as

$$B_i = \mathcal{A} \sum_{j > i} \frac{\cos(2k_F r_{ij}) - \sin(2k_F r_{ij})/(2k_F r_{ij})}{(2k_F r_{ij})^3}. \quad (13)$$

The prefactor  $\mathcal{A}$  depends on  $\Gamma_{\text{RKKY}}$  as it is defined in (8) to (10). The probability distribution of fields, obtained by calculating  $B_i$  for all possible random arrangements of magnetic ions, is the quantity of interest in computing the thermodynamic properties of the system.

For dilute concentrations the separation between ions is much larger than the inverse of the Fermi wavevector, the factor  $2k_F r_{ij}$  is large, and the term containing the sine function in (13) can be neglected. Also for dilute concentrations, the cosine function oscillates in space with a wavelength that is very short compared to the spacing of the magnetic ions. As a consequence, the probability distribution of fields does not depend on the wavelength of oscillation, or, to invert the argument, the concentration dependence of the field distribution is independent of the cosine function. In considering the dependence of  $B_i$  on concentration, therefore, the oscillatory terms in the

numerator of (13) are irrelevant. But since the product,  $xr^3$ , of concentration and cube of inter-ion spacing, which appears in the denominator of (13), is independent of concentration, then,  $B_i/x \propto \sum 1/(xr_{ij}^3)$  is independent of  $x$  as well. The fields  $B'_i$  at one concentration can be obtained from the fields  $B_i$  at another concentration by the relation  $B'_i = nB_i$  where  $n = x'/x$ . The probability distribution of fields at a concentration  $x'$  and applied field  $B$  is, then,  $P(B + nB_i) = nP(B/n + B_i)$ . The distribution is a function of  $B/n$ .

In the mean field approximation, with the energy of an ion given by  $\mathcal{E} = g\mu_B(B + nB_i)m_S$ , the partition function is

$$\begin{aligned} Z(B, T, n) &= \prod_i P(B + nB_i) \sum_{m_S} \exp\left(\frac{-g\mu_B(B + nB_i)m_S}{k_B T}\right) \\ &= \prod_i n P(B/n + B_i) \sum_{m_S} \exp\left(\frac{-g\mu_B(B/n + B_i)m_S}{k_B T/n}\right). \end{aligned} \quad (14)$$

Hence,

$$Z(B, T, n) = nZ\left(\frac{B}{n}, \frac{T}{n}\right). \quad (15)$$

The dependence of thermodynamic functions on  $B$  and  $T$  all scale with concentration as  $B/n$  and  $T/n$ .

## 2.4 Optimization of Signal-to-SQUID-Noise Ratio

The magnitude of the output signal of a SQUID circuit measuring the response of a magnetic calorimeter depends on a number of parameters that are related to the calorimeter itself, to the measuring circuit, and to the coupling of the calorimeter to the circuit. In general, one wants to optimize the performance of a calorimeter, having a particular set of operating constraints, by maximizing the signal-to-noise ratio. We discuss the considerations associated with the process of optimization below.

The discussion in Sect. 2.2.1 of the thermodynamic properties of Au:Er suggests that the magnetic response of an MMC can be calculated either by computer simulations or analytically using mean field approximations. This ability to calculate the response provides a means of designing calorimeters that have the largest output signal per unit of energy input. Since the noise performance of SQUIDs is often characterized in terms of magnetic flux noise, we start our discussion of signal size in terms of flux that is generated in the sensing inductance of the magnetometer for a given energy deposition. Later we include the noise of the SQUID to optimize the overall performance by maximizing the signal-to-noise ratio.

### 2.4.1 Basic Ideas

Up to now we have described the response of the calorimeter by (1),  $\delta m = V(\partial M/\partial T)(\delta E/C_{\text{tot}})$ . This expression suggests that the temperature sensor

should be made out of a magnetic material having a small heat capacity and large dependence of magnetization on temperature. Let us, for the moment, neglect any other contribution to the heat capacity of the calorimeter except for that of the spins. For non-interacting spins the quantities  $\partial M/\partial T$  and  $c$ , the specific heat per unit volume of the spins, are related by the thermodynamic expression  $\partial M/\partial T = c/B$ . In this simple case

$$\delta m = \frac{\delta E}{B}. \quad (16)$$

A picture of the physics described by this relation can be obtained by noting the occupation numbers of the energy levels of the spins. For an ensemble of non-interacting spins with  $S = 1/2$ , the Zeeman energy splitting of the levels is  $E_Z = g\mu_B B$ . A deposition of energy  $\delta E$  induces a change in the number of spins  $\delta N = \delta E/E_Z$  from the lower to the upper energy level. The resulting change in the magnetic moment of the ensemble is, then,  $\delta m = \delta N g\mu_B = \delta E/B$ , which is (16). For a typical magnetic field of  $B = 10\text{ mT}$  and  $g = 6.8$ , the Zeeman splitting is  $E_Z \simeq 4\text{ }\mu\text{eV}$ . In the energy regime MMCs are expected to be used the large number of excitations precludes statistical fluctuations in their number being a factor limiting the energy resolution.

If a sample of non-interacting spins were placed inside a circular loop of wire of radius  $r$ , the flux change resulting from a change of magnetization within it is given by

$$\delta\Phi = \mu_0 \frac{G}{r} \delta m, \quad (17)$$

where  $\mu_0$  is the magnetic permeability of free space and  $G$  is a dimensionless factor that depends on the geometry of the spins within the loop. For spins restricted to a small volume at the center of the loop  $G = 1/2$ . The combination of (16) and (17) lead to strategies for maximizing the signal size, which, in principle, are applicable to the discussion in the remainder of this article. 1. Since the coupling of a magnetic moment to a wire decreases with distance between them, the spins should be placed as close to the wire of the magnetometer as possible. And 2. the external field should be as small as possible so as to increase  $\delta m$ . However, as we now discuss, using a simple model, there are other factors that limit how low the field can profitably be made. The heat capacity of the calorimeter must include that of the absorber as well as that of the spins. If  $C_a$  describes the heat capacity of the absorber and non-spin degrees of freedom of the sensor (e.g. electrons, lattice), then only the fraction  $\beta = C_s/(C_s + C_a)$  of the deposited energy reaches the spin system,  $C_s$ . The flux change in a circular loop, again for non-interacting spins, is

$$\delta\Phi = \mu_0 \frac{G}{r} \frac{C_s}{C_s + C_a} \frac{\delta E}{B}. \quad (18)$$

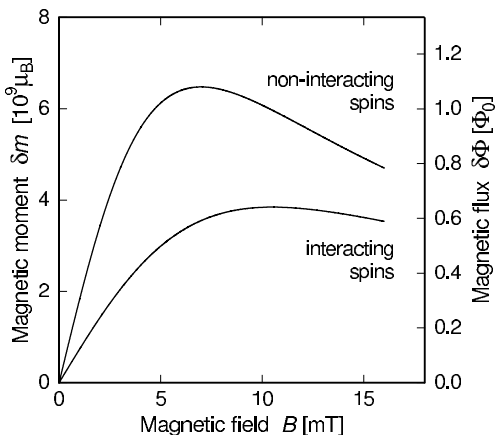


**Fig. 7.** Signal size of a magnetic calorimeter with an absorber heat capacity of  $C_a = 1.1 \text{ pJ/K}$  as a function of magnetic field in the case of interacting and non-interacting spins. The detector parameters assumed for calculating these curves are described in the text

At small fields such that  $E_Z \ll k_B T$ ,  $C_s \propto B^2$  for non-interacting spins, and the signal size,  $\delta\Phi$ , increases linearly with magnetic field in the low-field limit. Provided there are a large enough number of spins<sup>4</sup>, the signal size has a maximum where  $C_s(B) = C_a$  and decreases at higher field proportional to  $B^{-1}$ .

The calculated dependence of change in magnetic moment on magnetic field assuming non-interacting spins is illustrated by the *upper curve* on the *left vertical axis* in Fig. 7. The parameters for the calculated curve are  $\delta E = 5.9 \text{ keV}$ ,  $T = 50 \text{ mK}$ , and  $C_a = 1.1 \text{ pJ/K}$ , which corresponds to the heat capacity of a gold absorber  $250 \times 250 \times 5 \mu\text{m}^3$  at this temperature. The sensor is assumed to be a cylindrical disc having a diameter  $52 \mu\text{m}$  and height of  $6.5 \mu\text{m}$ , made of 900 ppm Au:Er. The calculated change in magnetization has a maximum at a field of about 7 mT, which corresponds to the heat capacity of the spins being approximately equal to that of the absorber, as expected from the discussion above.

The *right vertical axis* shows the corresponding change in flux in a circular loop where the loop is taken to be made of a thin film of superconducting niobium having an inner radius equal to the radius  $r$  of the sensor and a width  $w$  of the niobium  $w = 0.1r$ . The coupling factor,  $G$ , depends on both the geometry of the sensor and that of the loop. In Fig. 10a the coupling factor is plotted as a function of the ratio  $\xi = h/2r$  for both an infinitely thin loop and for the value  $w = 0.1r$  used in calculating the flux plotted in Fig. 7.

<sup>4</sup> In order to stay within the small field approximation, the heat capacity of the spins at the maximum of the Schottky anomaly must be larger than the additional heat capacity  $C_a$

What has been left out of the discussion to this point are the interactions among the spins, which can have a significant influence not only on the magnitude of the response but also on the dependence of the response on parameters such as temperature and field. The *lower curve* in Fig. 7 is the calculated dependence of the change in magnetic moment including dipole-dipole and RKKY interactions with  $\alpha = 5$ . All other parameters are the same as used for the non-interacting case. The effect of the interactions is to reduce the response and to shift the maximum to somewhat higher fields. The reduction can be understood in that the interactions increase the heat capacity and decrease the temperature dependence of the magnetization.

We are now at a point where we need to consider the optimization of the performance of a magnetic calorimeter, including the noise of the magnetometer used to read out the paramagnetic sensor. That discussion is outlined in the following sections for the case of a cylindrical sensor in a circular loop, being followed by an extension of the arguments to the case of planar sensors with pickup coils of meander shape.

#### 2.4.2 SQUID-based sensor readout

In this section we review several properties of dc-SQUIDs that will later be used in discussing the signal-to-SQUID-noise ratio of magnetic calorimeters. For a detailed discussion of the properties and the fabrication of SQUIDs we refer to [38] and the references therein.

Dc-SQUIDs are the most sensitive devices for monitoring the magnetization of the paramagnetic sensors of MMCs. For an MMC to have the highest possible energy resolution it should be read out with a SQUID having low noise and high dynamic range. A dc-SQUID can be operated with reasonably small power dissipation ( $P < 1 \text{ nW}$ ) at very low temperatures ( $T \leq 4.2 \text{ K}$ ), thereby permitting the fabrication of integrated detectors working at temperatures of a few tens of millikelvin.

A dc-SQUID can be used as a sensitive flux-to-voltage converter. Figure 8a shows a schematic drawing of a dc-SQUID, consisting of a superconducting loop of wire, which is interrupted by two Josephson contacts marked by crosses. Each Josephson contact acts as a weak link between the adjacent superconductors. This region of suppressed superconductivity is small enough that Cooper pairs can tunnel through it. The small distance between the electrodes of each contact results in a parasitic capacitance denoted as  $C$ . Each junction is shunted by a resistor  $R$  in order to suppress hysteretic behavior of the device.

If small currents are driven through the device, the current can be carried by tunneling Cooper pairs without dissipation. However, if the device is biased at a current close to two times the critical current of *one* junction, a voltage drop develops across the device. Due to the Josephson effect, the dc-voltage across the device depends periodically on the magnetic flux through the inductance  $L_s$  of the SQUID, where the periodic flux range is given by

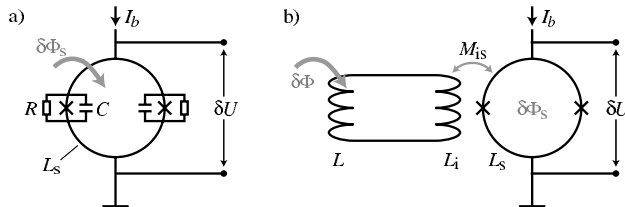


**Fig. 8.** Schematic of a dc-SQUID, where the flux to be measured is (a) directly coupled to the sensing inductance of the SQUID, (b) coupled to the SQUID via a superconducting flux transformer

one flux quantum  $\Phi_0 = h/2e = 2.07 \times 10^{-15}$  Vs. Operated at a steep point of this flux-voltage characteristic, the device can be used as a sensitive flux-to-voltage converter. A flux-locked-loop electronics, which applies negative feedback to compensate the flux change resulting from a signal, is often used in order to linearize the flux-voltage characteristic of the SQUID.

The shunt resistors  $R$ , which are needed for damping, cause current and voltage noise, and limit the apparent flux sensitivity of the SQUID. The spectral power density of flux noise  $S_{\Phi s}$  as well as the energy sensitivity  $\epsilon_s$  are frequently used parameters to characterize the noise of a dc-SQUID, the relation between the two being

$$\epsilon_s = \frac{S_{\Phi s}}{2L_s}. \quad (19)$$

The knowledge of the dependence of these quantities,  $\epsilon_s$  and  $S_{\Phi s}$ , on the inductance of the SQUID is important for optimizing the energy resolution of MMCs, as we shall discuss in the next section.

As discussed in [38], it is difficult in practice to give a simple relation of the dependence of SQUID noise on inductance. Many parameters, such as the parasitic capacitance and the critical current, may be constrained by the requirements of the fabrication process so as to provide for high yield and reproducibility. Taking the junction capacity of the fabrication process to be the limiting parameter, and assuming an optimal value for the resistive shunt  $R$ , one can express the optimum energy sensitivity of a dc-SQUID as

$$\epsilon_s \simeq 16k_B T \sqrt{L_s C}. \quad (20)$$

The relation suggests that the flux noise  $\sqrt{S_{\Phi s}}$  increases with increasing SQUID inductance as  $\sqrt{S_{\Phi s}} \propto L_s^{3/4}$ . However, in the low-temperature limit the energy resolution of a SQUID should ultimately reach the quantum limit,  $\epsilon_s \geq \hbar$ , leading to  $\sqrt{S_{\Phi s}} \propto \sqrt{L_s}$ . When optimizing the signal-to-SQUID-noise ratio in the following sections, we shall use this dependence of the flux noise in the pickup loop on its inductance, although we are not aware of any work on magnetic sensors where the quantum limited operation of SQUIDs has been encountered.

The use of  $\sqrt{S_{\Phi_s}} \propto \sqrt{L_s}$  is also consistent with the following argument. Assume the change in flux in a sensor is read out by a superconducting coil with inductance  $L$ , which forms a completely superconducting circuit with a second coil  $L_i$  coupled by mutual inductance to a SQUID, as illustrated in Fig. 8b. For clarity, capacitance and shunt resistor have been omitted in Fig. 8b. The combination of a SQUID and a strongly coupled input coil  $L_i$  is usually called a current-sensor SQUID. The circuit formed by  $L$  and  $L_i$  is often called a flux transformer, because a change of magnetic flux  $\delta\Phi$  in the pickup coil  $L$  causes the flux in the SQUID to change by

$$\delta\Phi_s = \frac{k\sqrt{L_s L_i}}{L + L_i} \delta\Phi \leq \frac{1}{2} \sqrt{\frac{L_s}{L}} \delta\Phi. \quad (21)$$

Here  $k\sqrt{L_s L_i} = M_{is}$  denotes the mutual inductance between the input coil and the SQUID. The dimensionless coupling constant  $k$  can have a value close to unity for SQUIDs fabricated by a multi-layer niobium thin-film process. Best coupling is achieved, corresponding to the equal sign in the relation on the right, if the inductance  $L_i$  of the input coil equals the inductance  $L$  of the pickup coil.

Assuming best coupling, we can describe the flux noise referred to the pickup coil by

$$\sqrt{S_\Phi} = \sqrt{2L\epsilon} \geq 2\sqrt{2L\epsilon_s}, \quad (22)$$

where  $\epsilon$  and  $\epsilon_s$  represent the energy sensitivity referred to the pickup coil and to the SQUID<sup>5</sup>, respectively. The equal sign in the last relation is achieved if  $k = 1$ . Two points are worthy of note. 1. If a SQUID has a fixed energy sensitivity with a well coupled input coil, whose inductance  $L_i$  can be varied over a reasonably large range, then the flux noise referred to a transformer-coupled pickup coil is proportional to the square root of its inductance,  $\sqrt{S_\Phi} \propto \sqrt{L}$ . Therefore, when optimizing the signal-to-SQUID-noise ratio of MMCs in the next section we shall maximize the change of flux in a pickup up coil per energy input in the detector and per square root of pickup coil inductance. 2. The energy sensitivity of a transformer-coupled pickup coil is about 4 times worse than the energy sensitivity of the SQUID. However, there are situations where this loss in sensitivity may be compensated by other benefits of transformer-coupled sensor readout. Firstly, the fabrication of SQUIDs with good energy sensitivity becomes increasingly difficult with increasing SQUID inductance. In cases where the inductance of the preferred pickup

---

<sup>5</sup> In this configuration the energy sensitivity  $\epsilon_s$  of the SQUID might be reduced due to a reduction of self inductance of the SQUID, which is caused by the screening current in the flux transformer. In the case of best coupling,  $L = L_i$ , this effect should in first order be independent of the input inductance  $L_i$  and therefore does not change the qualitative dependence of flux noise on inductance discussed here

coil is rather large, *i.e.*,  $L \gg 100$  pH, transformer coupling may even lead to the smaller effective flux noise. Secondly, transformer coupling allows for a spatial and thermal separation of sensor and SQUID. This may be very helpful in the context of large detector arrays consisting of several thousand pixels. Low noise readout of a dc-SQUID requires a power of 10 pW to 1 nW to be dissipated in the SQUID. This power is in part transformed into heat in the shunt resistors, and in part radiated at the Josephson frequency and higher harmonics, leading to eddy-current heating in the sensor. The use of unshunted SQUIDs [39] may help to reduce the heat from dissipation in the shunt resistors, but handling the residual heat load on a silicon chip at millikelvin temperatures becomes increasingly hard with an increasing number of detectors. Having SQUIDs and sensors on separate chips with appropriate filters in the interconnects appears to be a means of handling this problem, as the power dissipation on the sensor chip can be made almost arbitrarily small in this configuration.

In the remainder of this section we discuss a few of the possible sensor/SQUID coupling schemes in more detail. Fig. 9a shows a cylindrical paramagnetic sensor surrounded by a circular loop of wire, which forms the inductance of a SQUID. An additional, non-magnetic absorber for particle detection is assumed to be connected to the top surface of the sensor. The sensor as well as the SQUID are exposed to a homogeneous magnetic field oriented perpendicular to the surface of the substrate. The optimization of signal size and signal-to-SQUID-noise of this configuration will be discussed in detail in the next section.

Fig. 9b illustrates a configuration in which the SQUID-inductance is split into two counterwound circular loops connected in series, forming a planar gradiometer of first order. Each of the loops is filled with a cylindrical sensor. Again, sensor and SQUID are exposed to a homogeneous external field. Depositions of energy in the left and in the right sensor produce changes of flux in the SQUID of opposite sign and can therefore be distinguished. The advantages of this setup are a reduced sensitivity to fluctuations of external fields and a reduced sensitivity to fluctuations of the temperature of the substrate, which may be caused by energetic particles being stopped in adjacent sensors of an array or by a fluctuating power dissipation in the SQUID readout. Moreover, in an array of detectors, the number of wires can be reduced by a factor of two. One disadvantage of this configuration is that the intrinsic noise of two detectors is summed in one electronic channel. Also, the inductance of the pickup loop, which is the SQUID in this case, is increased by a factor of two, leading to a  $\sqrt{2}$  times larger flux noise. Both penalties together result in the ultimate energy resolution of this detector being larger by a factor of  $\sqrt{2}$  compared to the energy resolution of a single pixel detector.

Fig. 9c is a schematic diagram of a cylindrical sensor with wire-wound pickup coil, which is transformer coupled to a dc-SQUID. As discussed above, in this configuration one pays the penalty of increased energy noise referred to

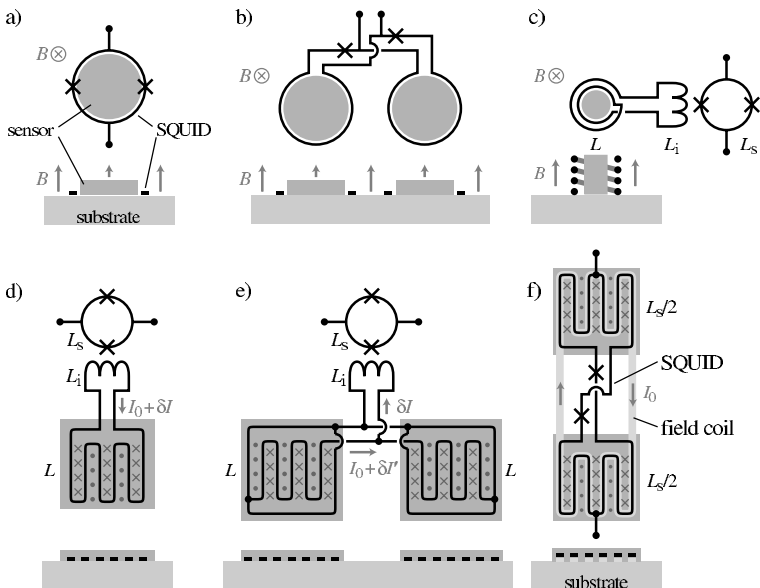


**Fig. 9.** Several examples of possible coupling schemes to measure the magnetization of paramagnetic sensors with a dc-SQUID. (a)–(c) assume a homogeneous external magnetic field  $B$ . In (d) and (e) a persistent current  $I_0$  in the meandering superconducting wire of the pickup loop produces an inhomogeneous field in the volume of the sensor. In (f) a persistent current  $I_0$  flowing in a closed superconducting loop (light grey) underneath the SQUID loop generates an inhomogeneous magnetic field in the volume of the sensor

the pickup coil. On the other hand, the setup permits the spatial and thermal separation of SQUID and sensor. This kind of setup can also be extended to a pickup coil which is split into two counterwound coils connected in series to readout two separate sensors. Benefits and costs of this configuration are similar to those discussed in relation to that of Fig. 9b.

The setup depicted in Fig. 9d differs from the ones discussed so far, as it does not make use of a homogeneous external magnetic field. Instead, a large persistent current  $I_0$  is injected into the superconducting circuit of the flux transformer, *e.g.*, by using a superconducting persistent current switch. The current  $I_0$  produces a strongly inhomogeneous field around the meandering wire of the pickup loop within the volume of the sensor. Upon the deposition of energy  $\delta E$  in the sensor, its magnetic susceptibility decreases by  $\delta\chi$ , resulting in a change of inductance  $\delta L \propto \delta\chi$  of the pickup coil and a change of flux  $\delta\Phi_s = M_{is}\delta I \propto \delta\chi \propto \delta E$  in the SQUID. The setup shares all the properties due to transformer coupling that configuration c) possesses. The expected signal-to-noise-ratio of this configuration will be discussed in detail in a subsequent section. It has several advantages. 1. As the bias field for the sensor is produced by the pickup coil itself, even sensor material outside the

area enclosed by the pickup loop can contribute positively to the flux signal in the coil. This sensor/coil configuration has a large filling factor. 2. If very thin sensor films and a very fine pitch of the meander structure are used, one can fabricate sensors of rather large area without a reduction in signal-to-noise ratio. This may be helpful in some applications. 3. The magnetic response of the sensor can no longer be described by a dipolar field, as is the case for in the first three examples. Rather, the field is a multipole of high order, and the magnetic crosstalk in an array of detectors can be reduced significantly. Meander coils are likely to find application in large detectors with thin sensors formed by vapor deposition. In such a geometry it is possible to contemplate placing sensor material on both sides of the plane of the meandering pickup coil, thereby doubling the filling factor. This improves the signal-to-SQUID-noise ratio by  $\sqrt{2}$ .

Fig. 9e illustrates a setup based on meander-shaped pickup coils to read out two sensors simultaneously. The two meanders together with the input coil of a current-sensor SQUID are connected in parallel to form a flux transformer, where best coupling,

$$\left. \frac{\delta\Phi_s}{\delta\Phi} \right|_{\max} = \left. \frac{k\sqrt{L_i L_s}}{L + 2L_i} \right|_{\max} = \frac{1}{2\sqrt{2}} \sqrt{\frac{L_s}{L}}, \quad (23)$$

is achieved if the inductance  $L_i$  of the input coil equals half of the inductance  $L$  of one meander. An advantage of this configuration is that the rather large current  $I_0$ , which is needed to produce the bias field for the sensor, needs not to flow through the input coil of the SQUID. It can be injected into the superconducting loop formed by the two meanders. The input coil and the interconnects between the current-sensor SQUID and the pickup coils only have to carry the small current change  $\delta I$ , which is caused by the deposition of energy in one of the sensors. This configuration has several advantages. 1. The fields are small in the vicinity of the SQUID. 2. There are no special requirements for the critical current of the wires of the input coil. 3. There should be reduced sensitivity to fluctuations of the inductance of the interconnects resulting from vibrations of those wires.

Again, the sign of the flux change in the SQUID can be used to determine which of the two sensors was hit, and the setup is insensitive to temperature fluctuations of the substrate. In addition, note that each of the meanders in configuration e) is enclosed in a square superconducting loop. This gradiometer structure helps to suppress the pickup of alternating external fields and fields caused by Johnson-noise currents within the metallic sensors and absorbers. The idea to use meander-shaped pickup coils being enclosed by a superconducting loop has first been suggested by Zink et al. [40] and we shall show some of their results in a later section of this chapter.

Figure 9f is a sketch of a two-pixel detector in which the wires of the meander are the inductive loop of the SQUID. As it is non-trivial problem to have persistent currents flowing in the SQUID inductance, a second superconducting circuit is added to provide the field, whose wiring (light grey) lies

directly underneath the wiring of the SQUID (black). Note that the wires of the SQUID are crossed in the center, in order to form a gradiometer with respect to the field coil. Otherwise flux conservation within the field coil in persistent mode would prohibit flux changes in the SQUID. For the sake of clarity we have omitted enclosing the meanders within a superconducting loop, as illustrated in Fig. 9e. Setup 9f in principle shares all advantages with that of setup 9e. However, due to the absence of a flux transformer one has to expect a stronger thermal coupling between SQUID and sensor, a condition which might be disadvantageous in the context of large detector arrays, as mentioned above. In the case of small detector arrays and meander inductances below 100 pH, the elimination of the factor of 4 loss due to transformer coupling may make this a desirable configuration.

#### 2.4.3 Cylindrical Sensors

The first question to ask is: what best characterizes the performance of an MMC and therefore should be optimized? In an earlier discussion[32], the flux change per unit energy input  $\delta\Phi/\delta E$  in the SQUID loop was the parameter that was maximized. This quantity can be written as

$$\frac{\delta\Phi}{\delta E} = \mu_0 \frac{G}{r} \frac{1}{C_s + C_a} V \frac{\partial M}{\partial T}. \quad (24)$$

However, what is ultimately of importance is not the size of the signal but the ratio of the size of the signal to that of the noise. In the event that the flux noise were independent of the input coil, then optimizing  $\delta\Phi$  would be appropriate. But if the flux noise,  $\sqrt{S_\Phi}$ , referred to the input coil depends upon the input inductance, as is typically the case, it is the ratio of  $\delta\Phi/\delta E$  to  $\sqrt{S_\Phi}$ , which should be optimized.

To take a specific example, we assume a SQUID whose noise is quantum limited, that is, the noise energy  $\epsilon_s$  per Hz is some multiple of Planck's constant. Then the flux noise per  $\sqrt{\text{Hz}}$  is  $\sqrt{S_\Phi} = \sqrt{2\epsilon_s L}$ ,  $L$  being the inductance of the loop. For a circular loop the inductance is proportional to the radius,  $L = \mu_0 \lambda r$ , where the constant  $\lambda$  depends on the geometry of the loop. (For  $w = 0.1r$ ,  $\lambda = 3.72$ , where, as before,  $w$  is the width of the thin loop.)

A comparison of signal to noise involves the question of the time dependence of the signal. Rather than enter into the details of that discussion here, we leave such considerations to the next section and focus on the physical properties of the sensor that lead to the best signal to noise, irrespective of temporal response. Then, the quantity we wish to optimize is

$$S = \frac{\delta\Phi/\delta E}{\sqrt{L}} = \mu_0 \frac{G}{r} \frac{1}{C_s + C_a} V \frac{\partial M}{\partial T} \frac{1}{\sqrt{\mu_0 \lambda r}}, \quad (25)$$

or

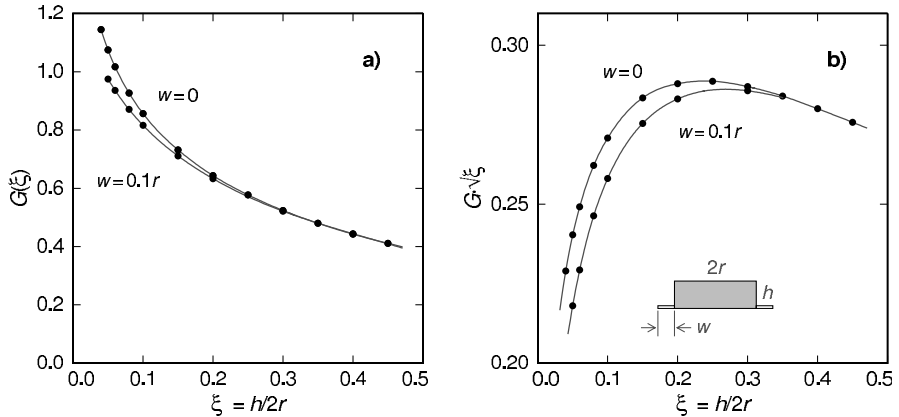


**Fig. 10.** (a) Coupling factor  $G$  as a function of reduced sensor height  $\xi = h/2r$ .  
(b) Product  $G\sqrt{\xi}$  to be maximized for optimal signal-to-SQUID-noise ratio

$$\mathcal{S} = \frac{\delta\Phi/\delta E}{\sqrt{L}} = \sqrt{\frac{\mu_0}{\lambda}} \frac{G}{r^{3/2}} \frac{V}{Vc + C_a} \frac{\partial M}{\partial T}. \quad (26)$$

with  $c$  being the heat capacity of the spins per unit volume. The quantity  $\mathcal{S}$  is of little physical significance except insofar as its optimization is relevant for maximizing the signal to noise when the noise is dependent on inductance. It depends upon a number of parameters.

$$\mathcal{S} = \mathcal{S}(C_a, g, \alpha, T, x, r, h, B). \quad (27)$$

Four parameters – the heat capacity of the absorber  $C_a$ , the  $g$ -factor of the paramagnetic ions, the strength of the RKKY interaction  $\alpha$ , and the operating temperature  $T$  – are generally fixed by the experimental conditions and choice of materials. However, the other four – the concentration of ions  $x$ , the radius  $r$  and height  $h$  of the cylindrically shaped sensor, and the applied magnetic field  $B$  – are adjustable. The values of these latter four parameters can be varied so as to maximize  $\mathcal{S}$ .

First consider  $r$  and  $h$ , and replace  $h$  using  $\xi = h/2r$  and write  $G/r^{3/2} = \sqrt{2\pi\xi/V} G$ . Then

$$\mathcal{S} = \sqrt{\frac{\mu_0}{\lambda}} \sqrt{2\pi\xi} G \frac{\sqrt{V}}{Vc + C_a} \frac{\partial M}{\partial T}. \quad (28)$$

The coupling factor,  $G$ , is independent of volume and is a function of  $\xi$  only. Figure 10 shows the coupling factor  $G$  as well as the product  $G\sqrt{\xi}$  as a function of  $\xi$  for two different widths of the pickup loop. For  $w = 0.1r$ , the product  $G\sqrt{\xi}$  has a maximum at  $\xi = 0.268$  or  $h \approx 0.54r$ ,  $[G\sqrt{\xi}]_{\max} = 0.286$ .

The volume dependence of  $\mathcal{S}$  is contained in the factor  $\sqrt{V}/(Vc + C_a)$ , which leads to the condition  $Vc = C_a$ , namely, the heat capacity of the sensor

should equal the heat capacity of the absorber for maximum signal-to-noise. When  $V$  is replaced by  $C_a/c$ , the optimized  $\mathcal{S}$  becomes

$$\mathcal{S}_{\text{opt}} = \sqrt{\frac{\mu_0}{\lambda}} G \sqrt{\frac{\pi \xi}{2}} \frac{1}{\sqrt{C_a}} \frac{1}{\sqrt{c}} \frac{\partial M}{\partial T} \Big|_{\text{opt}} . \quad (29)$$

The last factor,  $(1/\sqrt{c})(\partial M/\partial T)$ , contains the information on how the concentration and magnetic field should be adjusted to maximize  $\mathcal{S}_{\text{opt}}$  given the values of the fixed parameters,  $T$ ,  $g$ , and  $\alpha$ . Because of the spin interactions, a calculation of the optimal conditions can only be performed numerically. However, given the scaling laws obeyed by spins interacting through the RKKY mechanism, as discussed earlier, the functional dependence of  $x$  and  $B$  on  $T$ ,  $g$ , and  $\alpha$  for optimization can be deduced without numerical evaluation. Since all thermodynamic parameters scale as  $T/x$  and  $B/x$ , the concentration that optimizes  $S$  must be proportional to the operating temperature,  $x \propto T$ . For fixed  $g$ , and  $\alpha$ ,  $B_{\text{opt}}/x_{\text{opt}} = \text{constant}$  so that  $B_{\text{opt}} \propto T$ . And since  $B$  is always multiplied by  $g$ , it follows that  $B_{\text{opt}} \propto 1/g$ .

Within the mean field approximation the energy splitting of a spin with  $S = 1/2$  is

$$\mathcal{E} = -g\mu_B(B + xB_i) = g\mu_B B(1 + xB_i/B), \quad (30)$$

where the dependence on the magnitude of the interactions arises through  $B_i$ . Again, because of scaling  $xB_i/B$  must be a constant under optimal conditions. Since  $B_i \propto g\alpha$  it follows that

$$x_{\text{opt}} \propto T g^{-2} \alpha^{-1}. \quad (31)$$

The heat capacity of the spins is  $c_{\text{opt}} \propto x_{\text{opt}}(\mathcal{E}/k_B T)^2$ . Since  $\mathcal{E}/(k_B T)$  is independent of the variables,  $c_{\text{opt}}$  has the same dependence on the variables as  $x_{\text{opt}}$ .

There is one caveat that one has to append to this discussion. The heat capacity  $c$  of the sensor is not simply that of the spins, as has been implicitly assumed to this point, but contains the heat capacity of the conduction electrons<sup>6</sup>. But since the electronic heat capacity,  $c_e$ , is proportional to temperature, the dependence of  $c_{\text{opt}}$  on  $T$  is unchanged by the inclusion of  $c_e$ . The same holds true for the temperature dependence of  $x_{\text{opt}}$  and  $\mathcal{S}_{\text{opt}}$ , discussed below. However, because  $c_e$  is unrelated to the spins, the functional dependencies of the optimized parameters on  $g$  and  $\alpha$  are not strictly valid. Under typical conditions the electronic heat capacity is only a few percent of the spin heat capacity, and there is little error in maintaining the functional form obtained from scaling. In deriving the numerical results below for Au:Er, we have included the electronic heat capacity.

The temperature derivative of the magnetization has the form  $\partial M/\partial T \propto x g^2 B T^{-2}$ . Hence  $(\partial M/\partial T)_{\text{opt}} \propto g^{-1} \alpha^{-1}$ , and therefore  $\mathcal{S}_{\text{opt}}$  has the form

---

<sup>6</sup> The heat capacity of the lattice is very small and not considered

$$\mathcal{S}_{\text{opt}} \propto (C_a \alpha T)^{-1/2}. \quad (32)$$

The quantities  $\sqrt{c}$  and  $(\partial M/\partial T)$  have the same dependence on  $g$ -value. Hence  $\mathcal{S}_{\text{opt}}$  is independent of  $g$ .

**Table 1.** The dependence of the variable parameters  $B$ ,  $x$ ,  $r$ ,  $h$ , upon the operational parameters  $C_a$ ,  $T$ ,  $g$ , and  $\alpha$  such that the sensitivity  $\mathcal{S} = (\delta\Phi/\delta E)/\sqrt{L}$  is optimized. The *last column* contains explicit values for an Au:Er sensor ( $g = 6.8, \alpha = 5$ ) at 50 mK connected to an absorber that has a heat capacity of  $C_a = 1 \times 10^{-12} \text{ J/K}$

Parameters, that maximize $\mathcal{S} = (\delta\Phi/\delta E)/\sqrt{L}$ for cylindrical sensors	Example: Au:Er, $T = 0.05 \text{ K}$
$B_{\text{opt}} = 2.1 \text{ T K}^{-1} \times T g^{-1}$	15 mT
$x_{\text{opt}} = 10.3 \text{ K}^{-1} \times T g^{-2} \alpha^{-1}$	2200 ppm
$r_{\text{opt}} = 0.64 \text{ cm} \frac{\text{K}^{2/3}}{\text{J}^{1/3}} \times (C_a g^2 \alpha T^{-1})^{1/3}$	10.7 $\mu\text{m}$
$h_{\text{opt}} = 0.53 \times r_{\text{opt}}$	5.7 $\mu\text{m}$
$\mathcal{S}_{\text{opt}} = 0.093 \times (C_a \alpha T)^{-1/2}$	

The results of a numerical calculation of  $(1/\sqrt{c})(\partial M/\partial T)$  to obtain the numerical coefficients in the expressions for  $x_{\text{opt}}$  and  $B_{\text{opt}}$  are given in Table 1. The dependence on the fixed parameters of  $r_{\text{opt}}$  and  $h_{\text{opt}}$ , which follow from equating heat capacities, are also given in the table. And finally the optimum signal-to-noise is obtained when

$$\mathcal{S}_{\text{opt}} = 0.093 (C_a \alpha T)^{-1/2}. \quad (33)$$

The *right column* of Table 1 contains explicit values for  $B_{\text{opt}}$ ,  $x_{\text{opt}}$ ,  $r_{\text{opt}}$  and  $h_{\text{opt}}$  for a specific example. At first glance, the value for the optimal concentration of 2200 ppm may seem somewhat high considering that the calculation assumes the small concentration limit. However, the spin glass transition temperature at this concentrations is still about one order of magnitude lower than the operational temperature  $T = 0.05 \text{ K}$  assumed in this example.

In [28] and [32] the quantity that was maximized was the change in flux through a circular loop. In the event that the noise limiting the resolution of the calorimeter is independent of the inductance of the input coil, this is the appropriate quantity to consider. The expression for flux change per unit energy input to the calorimeter is given by (24). The condition that  $\delta\Phi$  is a maximum leads to the condition  $C_s = Vc = 2C_a$ . Again using  $\xi = h/2r$ ,  $\delta\Phi_{\text{max}}/\delta E$  can be expressed as<sup>7</sup>

$$\left( \frac{\delta\Phi}{\delta E} \right)_{\text{max}} = \mu_0 G (2\pi\xi)^{1/3} \frac{2^{2/3}}{3} \frac{1}{C_a^{1/3}} \left( \frac{1}{c^{2/3}} \frac{\partial M}{\partial T} \right)_{\text{max}}. \quad (34)$$

<sup>7</sup> In this case we use the subscript *max* rather than *opt* for ease in distinguishing the two different optimizations

The results of analyzing the factor containing  $c$  and  $\partial M/\partial T$  numerically are given in Table 2. The dependences of the optimal values of  $B$ ,  $x$ , and  $r$  on the fixed parameters  $C_a$ ,  $g$ ,  $\alpha$ , and  $T$  are the same for  $S_{\text{opt}}$  and  $[\delta\Phi/\delta E]_{\text{max}}$  but the numerical coefficients are different. The coefficients for  $r_{\text{max}}$  and  $h_{\text{max}}$  in Table 2 are somewhat different than given in [32] so as to correspond to the configuration of the pickup loop used here of  $w = 0.1r$ . Also, the numerical factor in  $(\delta\Phi/\delta E)_{\text{max}}$  differs slightly because of a more detailed analysis. We find

$$\left(\frac{\delta\Phi}{\delta E}\right)_{\text{max}} = 1.3 \times 10^{-9} \left(\frac{g}{C_a \alpha T^2}\right)^{1/3} \Phi_0 / \text{eV}, \quad (35)$$

where  $\Phi_0 = 2.07 \times 10^{-15}$  Vs is the flux quantum.

**Table 2.** The dependence of the variable parameters  $B$ ,  $x$ ,  $r$ ,  $h$ , upon the operational parameters  $C_a$ ,  $T$ ,  $g$ , and  $\alpha$  such that the sensitivity  $[\delta\Phi/\delta E]_{\text{max}}$  is maximized. The last column contains explicit values for an Au:Er sensor ( $g = 6.8$ ,  $\alpha = 5$ ) at 50 mK connected to an absorber that has a heat capacity of  $C_a = 1 \times 10^{-12}$  J/K

Parameters, that maximize $\delta\Phi/\delta E$ for cylindrical sensors	Example: Au:Er, $T = 0.05$ K $C_a = 1 \times 10^{-12}$ J/K
$B_{\text{max}} =$	$1.5 \text{ T K}^{-1} \times T g^{-1}$
$x_{\text{max}} =$	$4.2 \text{ K}^{-1} \times T g^{-2} \alpha^{-1}$
$r_{\text{max}} =$	$1.6 \text{ cm}^{\frac{2}{3}} \text{ K}^{\frac{1}{3}} \times (C_a g^2 \alpha T^{-1})^{1/3}$
$h_{\text{max}} =$	$0.25 \times r_{\text{max}}$
$[\delta\Phi/\delta E]_{\text{max}} =$	$1.3 \times 10^{-9} \frac{\Phi_0}{\text{eV}} \frac{\text{J}^{1/3}}{\text{K}} \times (g C_a^{-1} \alpha^{-1} T^{-2})^{1/3}$
	$1.0 \times 10^{-4} \frac{\Phi_0}{\text{eV}}$

Note that  $(\delta\Phi/\delta E)_{\text{max}}$  in (35) has a different dependence on  $C_a$ ,  $g$ ,  $\alpha$ , and  $T$  than does  $S_{\text{opt}} = [(\delta\Phi/\delta E)/\sqrt{L}]_{\text{opt}}$  in (33). In particular,  $(\delta\Phi/\delta E)_{\text{max}}$  depends on the  $g$ -value of the spins, whereas  $S_{\text{opt}}$  does not. The difference in functional dependence of these two optimized quantities on the fixed parameters does not carry over to magnetic field, concentration and radius. In both cases the optimal value of field is proportional to  $T/g$ , but the constant of proportionality is somewhat larger for the case of  $S_{\text{opt}}$  than it is for  $(\delta\Phi/\delta E)_{\text{max}}$ . The situation is similar for the concentration. This is related to the fact that  $S$  is less sensitive to the heat capacity of the spins than is  $\delta\Phi/\delta E$ .

The fact that  $S_{\text{opt}}$  does not depend upon the  $g$ -value of the spins does not mean that  $g$  is an irrelevant parameter when  $(\delta\Phi/\delta E)/\sqrt{L}$  is a measure of the signal to noise<sup>8</sup>. For technical reasons it may be desirable to work

<sup>8</sup> The fact that  $S_{\text{opt}}$  is independent of  $g$ , while  $\delta\Phi/\delta E$  is not, is a consequence of the manner in which we chose to describe the exchange interaction in terms of the parameter  $\alpha$  so that  $B \propto x g \alpha$

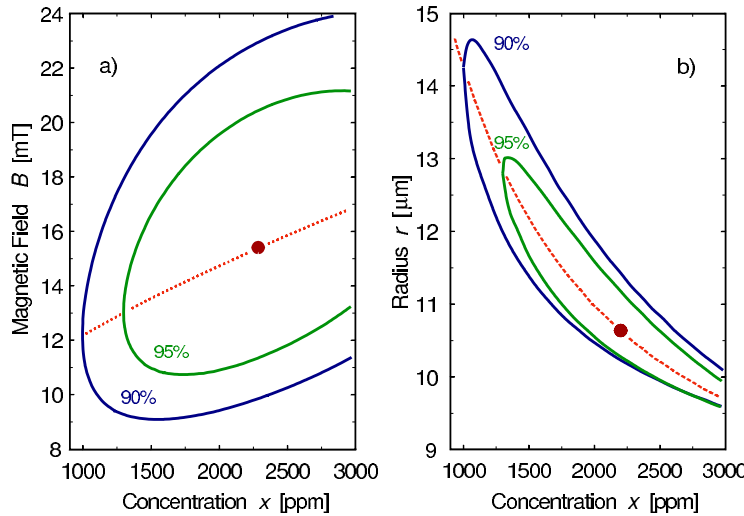


**Fig. 11.** (a) Contours of constant  $\mathcal{S} = (\delta\Phi/\delta E)/\sqrt{L}$  in the field/concentration plane for values of  $S$  that are 5% and 10% less than  $S_{\text{opt}}$  at  $T = 0.05$  K,  $g = 6.8$  and  $\alpha = 5$ . The dotted line indicates the fields for which  $\mathcal{S}$  is a maximum at a given concentration. (b) Contours in the radius/concentration plane for the same conditions and  $C_a = 10^{-12}$  J/K. The dotted line indicates the radius of the cylindrical sensor for which  $\mathcal{S}$  is a maximum at a given concentration

with as low an applied magnetic field and concentration of spins as possible, conditions which favor a system with high  $g$ -value. In this regard, note that  $\mathcal{S}$  is not a particularly strong function of the values of the magnetic field and concentration in the vicinity of its maximum. In Fig. 11a we have plotted contours of constant  $\mathcal{S}$  at 90% and 95% of  $S_{\text{opt}}$  in the field/concentration plane for the conditions  $T = 0.05$  K,  $g = 6.8$  and  $\alpha = 5$ . The magnetic field can be decreased by a third and concentration by more than a factor of 2 without decreasing the signal to noise by more than 10%. If one adopts a strategy of reducing  $B$  and  $x$ , then the dimensions of the sensor must be increased to maintain the equality of the heat capacity of the sensor to that of the absorber, as shown in Fig. 11b. In order to achieve a signal to noise of 90% of  $S_{\text{opt}}$  with the field and concentration reduced to their lowest levels, the radius of the sensor must be increased by about 40%.

#### 2.4.4 Meander Geometry

For many applications, a magnetic calorimeter with a sensor in the form of a small circular cylinder may have technical disadvantages. A large-area pickup loop of meander geometry with a thin sensor and an absorber vapor-deposited on top of it may provide significant improvements in both sensitivity and ease of fabrication. The reason why a meander loop can be made, in principle,

more sensitive than a circular loop is that the spins of the magnetic sensor are on average closer to the pickup loop with the meander geometry. The coupling between spins and pickup loop is larger. Given the fact that the meander-shaped pickup coil is likely to be transformer coupled to a SQUID, the quantity  $(\delta\Phi/\delta E)/\sqrt{L}$  is in most cases probably the relevant quantity to optimize. This issue is the topic of the present section.

The discussion here is restricted to a design in which the magnetic field is produced not by an external coil but rather by passing a current through the same meander pattern that is used to measure the change in magnetization of the sensor. Using the same loop for field generation and pickup is a much more important option to consider for a meander with the sensor uniformly distributed above it than for a circular loop enclosing a cylindrical sample within it. The field generated by a current in the meander is highly non-uniform both in magnitude and direction. Directly between two stripes the field is perpendicular to the plane of the meander varying in sign between successive gaps between stripes. Directly above a stripe the field is parallel to the meander plane. But because of reciprocity, a change in magnetization of the spins, aligned locally with the magnetic field, produces a flux change in the meander in proportion to the magnitude of the local field with sign independent of position.

If finite size effects can be neglected, the inductance of a meander-shaped pickup loop can be written as

$$L = \ell \mu_0 \frac{A}{p}, \quad (36)$$

where  $p$  is the pitch of the meander structure (center-to-center distance of two neighboring conductors) and  $A$  is the area covered by the meander. The constant  $\ell$  depends on the relative width of the stripes,  $w/p$ , which are assumed to be made of niobium. A plot of  $\ell$  versus the ratio  $w/p$  is given in Fig. 12a. These results are obtained from a finite element calculation where the niobium is assumed to be a perfect diamagnet. With  $w/p = 0.425$ , the value of  $\ell$  is 0.246.

In all following calculations we assume the thickness of the niobium structures to be 0.05 times the pitch (e.g. 500 nm thick for a pitch of  $p = 10 \mu\text{m}$ ). Also, the meander is covered with an insulating layer having a thickness of  $0.025 p$ . This is of relevance in the calculation of field distributions. A schematic cross section of the meander with sensor is illustrated in Fig. 12b.

The magnetic field produced by a current passing through the meander depends strongly on position. The average of the magnitude of the field in a plane parallel to that of the meander drops exponentially with increasing distance between the two planes as illustrated in Fig. 13a. The distribution of fields over a sensor of reduced thickness  $\xi$  defined in reference to the pitch by the expression  $\xi = h/p$  can be calculated by standard finite-element techniques. With superconducting stripes, the distribution  $P(B, \xi, w/p)$  of the magnitude of the field for the particular case  $\xi = 0.36$ ,  $w/p = 0.425$  and an

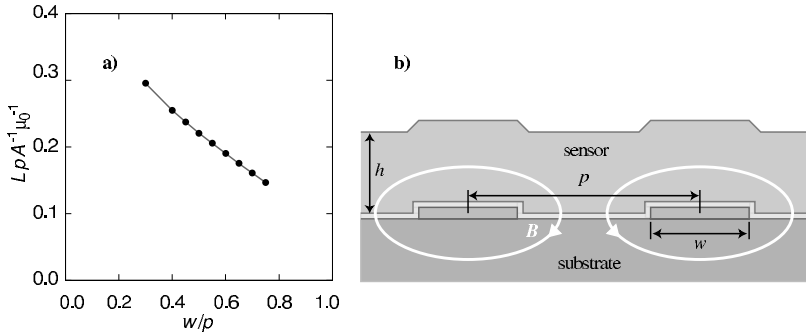


**Fig. 12.** (a) Normalized inductance of a meander shaped coil as a function of the ratio of the width of the superconducting niobium structures  $w$  and the pitch  $p$  (center-to-center distance of two neighboring niobium stripes). (b) Schematic of the cross section of the sensor and the meandering pickup coil wires perpendicular to the current flow. The pitch  $p$ , width of the stripes  $w$  and height of the sensor  $h$  are indicated

average field of  $\overline{B} = 12.8$  mT is shown in Fig. 13b. We shall see later that this is the optimal configuration for  $g = 6.8$  and  $T = 50$  mK. The optimal thickness of the sensor,  $\xi_{\text{opt}} = 0.36$ , turns out to be independent of all other parameters, at least to within 1% of the numerical results.

The quantity  $G$ , which is displayed on the top axis of Fig. 13b, has the same meaning as the dimensionless geometrical coupling factor of Sect. 2.4.1. However as used previously,  $G$  was an average over the volume of the magnetic sensor whereas here  $G$  is a local coupling factor and is a function of the position within the sensor. The equivalent of (17) is, then,

$$d(\delta\Phi) = \mu_0 \frac{G(\mathbf{r}/p)}{p} \delta M(\mathbf{r}) dV, \quad (37)$$

where  $d(\delta\Phi)$  is the change of flux in the pickup coil caused by a change of magnetic moment  $\delta M(\mathbf{r}) dV$  in the volume element  $dV$  at position  $\mathbf{r}$ .

As indicated by the use of  $G$  in Fig. 13b, this parameter by reciprocity also characterizes the relationship between the magnetic field at a position  $\mathbf{r}$  and the current  $I_0$  in the meander. The relationship is

$$B(\mathbf{r}) = \mu_0 G(\mathbf{r}/p) \frac{I_0}{p}. \quad (38)$$

Because  $G$  depends on the reduced position vector  $\mathbf{r}/p$ , it is independent of the overall dimensions of the meander, but it does depend on the width to pitch ratio  $w/p$  of the stripes.

The change of flux  $\delta\Phi$  in a meander-shaped pickup coil caused by the deposition of energy  $\delta E$  in the calorimeter can be obtained by placing  $d(\delta\Phi)$  of (37) into (24) and integrating. Since the calorimeter is measured on time

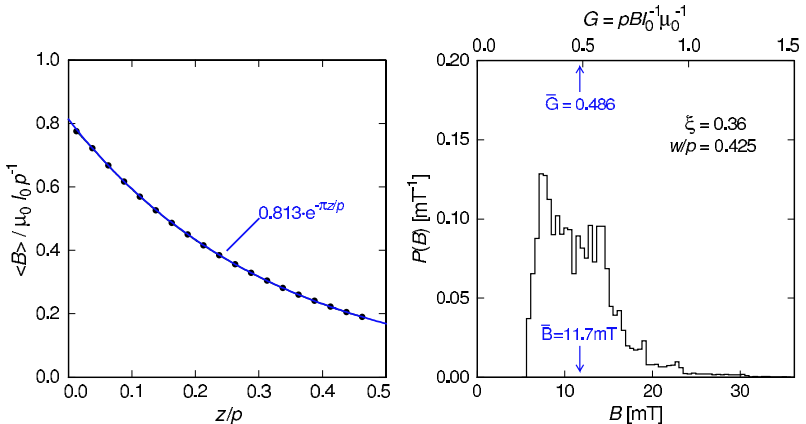


**Fig. 13.** (a) Average magnetic field in a thin layer of sensor material as a function of the distance  $z$  between this layer and the surface of the insulating layer, which covers the pickup coil and the meander. The meander has a pitch  $p$  and carries a current  $I_0$ . (b) Distribution of the magnitude of the magnetic field in the volume of a sensor with  $\xi = 0.36$ . The average field of  $\bar{B} = 12.8$  mT corresponds to the optimum field for the operation of a sensor with  $g = 6.8$  at a temperature of  $T = 50$  mK

scales such that it is in thermal equilibrium internally, the temperature rise due to the energy input  $\delta T = \delta E/C_{\text{tot}}$  is a constant and can be taken out of the integral. The resulting expression is

$$\delta\Phi = \frac{\delta E}{C_{\text{abs}} + \int_V c(\mathbf{r}) d^3r} \int_V \mu_0 \frac{G(\mathbf{r}/p)}{p} \frac{\partial M[B(\mathbf{r}), T]}{\partial T} d^3r, \quad (39)$$

where  $c$  is the specific heat per unit volume of the sensor material. The integration of the position-dependent heat capacity of the spins and of  $\partial M/\partial T$  can be performed separately.

Since the thermodynamic parameters are functions of field and the distribution  $P(B, \xi, w/p)^9$  of magnetic fields within the sensor has already been determined, it is more convenient to integrate over magnetic fields, or rather  $G$ , instead of volume. Defining the average value of  $\mathcal{X}$  as

$$\langle \mathcal{X} \rangle = \int P(G, \xi, w/p) \mathcal{X} dG, \quad (40)$$

the expression for  $\delta\Phi/\delta E$  becomes

$$\frac{\delta\Phi}{\delta E} = \frac{V}{C_a + V\langle c \rangle} \left\langle \mu_0 \frac{G}{p} \frac{\partial M}{\partial T} \right\rangle. \quad (41)$$

<sup>9</sup> We explicitly note the dependence on  $w$  as well as  $\xi$

As with the cylindrical sensor, the quantity we wish to maximize is  $\mathcal{S} = (\delta\Phi/\delta E)/\sqrt{L}$ . With  $L$  given by (36) and the volume of the sensor expressed as  $V = Ah$ ,  $\mathcal{S}$  is

$$\mathcal{S} = \sqrt{\frac{\mu_0}{\ell}} \frac{h\sqrt{A/p}}{C_a + Ah\langle c \rangle} \left\langle G \frac{\partial M}{\partial T} \right\rangle. \quad (42)$$

The quantity  $\mathcal{S}$  for a calorimeter employing a meander geometry is a function, with some modifications, of the same parameters as for the case of a cylindrical calorimeter. The parameters  $C_a$ ,  $g$ ,  $\alpha$ ,  $T$ , and  $x$  are obviously the same in the two cases. The field is changed from  $B$  to  $\bar{B}$ , which is replaced in the equations by the experimentally measurable  $I_0$ . In place of  $r$  we now have the area  $A$  of the meander, and  $h$ , characterized by the reduced height  $\xi$  is now  $h/p$ . What is different in the present discussion is the addition of the parameter  $w/p$ . The response of a meander is more sensitive to the width of the niobium stripes than is the response in the case of a circular loop, in the optimizing the response of which  $w$  was taken as a constant. Altogether  $\mathcal{S}$  depends on nine parameters

$$\mathcal{S} = \mathcal{S}(C_a, g, \alpha, T, x, \bar{B}, A, \xi, w/p). \quad (43)$$

As before, we consider the first four of these parameters fixed by the material and operating conditions and discuss the values of the remaining parameters that produce the maximum value of  $\mathcal{S}$ .

Equation (42) has a form similar to that of (28). The condition on the volume (or heat capacity) of the spins, which maximizes  $\mathcal{S}$ , is that  $V\langle c \rangle = C_a$ . As a condition on  $A$  this is

$$A_{\text{opt}} = \frac{C_a}{h\langle c \rangle}. \quad (44)$$

With this result, the optimized value of  $\mathcal{S}$  can be written as

$$\mathcal{S}_{\text{opt}} = \frac{1}{2} \sqrt{\frac{\mu_0}{\ell}} \frac{1}{\sqrt{C_a}} \sqrt{\frac{\xi}{\langle c \rangle}} \left\langle G \frac{\partial M}{\partial T} \right\rangle. \quad (45)$$

The optimal values of the geometrical factors – the ratio  $w/p$  and the thickness of the sensor, characterized by  $\xi = h/p$  – are independent of the materials parameters and operating temperature. We find that the maximum value of  $\mathcal{S}$  is obtained for  $\xi_{\text{opt}} = 0.36$  and  $(w/p)_{\text{opt}} = 0.425$ . These quantities are principally defined by the current distribution around the meander stripes. It is interesting to note that the filling factor defined as the ratio of the integral of  $B^2$  over the volume of the sensor to the integral of  $B^2$  over all space,

$$F(\xi, w/p) = \frac{\int_V B^2 d^3r}{\int B^2 d^3r}, \quad (46)$$

**Table 3.** The dependence of the variable parameters  $\overline{B}$ ,  $x$ ,  $A$ ,  $h$  for a meander geometry upon the operational parameters  $C_a$ ,  $T$ ,  $g$ , and  $\alpha$  such that the sensitivity  $S$  is optimized. Values for  $I_{\text{opt}}$ ,  $\langle c \rangle_{\text{opt}}$  and  $\langle G(\partial M/\partial T) \rangle_{\text{opt}}$  are also included to facilitate computations. The *last column* contains explicit values for an Au:Er sensor ( $g = 6.8$ ,  $\alpha = 5$ ) at 50 mK and  $p = 10 \mu\text{m}$  connected to an absorber that has a heat capacity of  $C_a = 1 \times 10^{-12} \text{ J/K}$

Parameters that maximize $S = (\delta\Phi/\delta E)/\sqrt{L}$ for planar sensors with meander shaped pickup coil		Example: Au:Er, $T = 0.05 \text{ K}$ $p = 10 \mu\text{m}$ , $C_a = 1 \text{ pJ/K}$
$\overline{B}_{\text{opt}} =$	$1.8 \text{ T K}^{-1} \times T g^{-1}$	$13 \text{ mT}$
$I_{\text{opt}} =$	$2.9 \times 10^6 \text{ A m}^{-1} \text{ K}^{-1} \times T g^{-1} p$	$0.21 \text{ A}$
$x_{\text{opt}} =$	$9.2 \text{ K}^{-1} \times T g^{-2} \alpha^{-1}$	$2000 \text{ ppm}$
$\langle c \rangle_{\text{opt}} =$	$1.8 \times 10^6 \text{ J m}^{-3} \text{ K}^{-2} \times T g^{-2} \alpha^{-1}$	$390 \text{ J m}^{-3} \text{ K}^{-1}$
$\langle G \rangle_{\text{opt}} =$	$2.8 \times 10^5 \text{ Am}^{-1} \text{ K}^{-1} \times g^{-1} \alpha^{-1}$	$8.1 \times 10^3 \text{ A m}^{-1} \text{ K}^{-1}$
$A_{\text{opt}} =$	$1.5 \times 10^{-6} \text{ m}^3 \text{ K}^2 \text{ J}^{-1} \times C_a g^2 \alpha T^{-1} p^{-1}$	$700 \mu\text{m}^2$
$h_{\text{opt}} =$	$0.36 \times p$	$3.6 \mu\text{m}$
$L_{\text{opt}} =$	$4.7 \times 10^{-13} \text{ H m}^2 \text{ K}^2 \text{ J}^{-1} \times C_a g^2 \alpha T^{-1} p^{-2}$	$22 \text{ pH}$
$S_{\text{opt}} =$	$0.14 \times (C_a \alpha T)^{-1/2}$	$0.1 \Phi_0 \text{ keV}^{-1} L_{\text{opt}}^{-1/2}$

has the value of  $F \simeq 0.39$ . This is close to the maximum achievable value of 0.50 for a sensor on only one side of the meander.

Because of scaling, the functional dependence of  $x_{\text{opt}}$ ,  $\overline{B}_{\text{opt}}$ , and  $S_{\text{opt}}$  on  $C_a$ ,  $g$ ,  $\alpha$ , and  $T$  must be the same for the meander geometry as for the cylindrically shaped sensor, i.e.,  $x_{\text{opt}} \propto T g^{-2} \alpha^{-1}$  etc. The results of numerical calculations using the mean field approximation as well as using the diagonalization of the Hamiltonian for clusters of interacting spins, as discussed in Sect. 2.2.1, confirm this result. The coefficients expressing the dependence of the independent parameters that maximize  $S$  on those that are considered fixed are shown in Table 3. The numerical results for the different methods of accounting for the exchange interaction among spins – mean field approximation and the diagonalization of the Hamiltonian of spin clusters – differ for most parameters by less than 5% except in the case of  $\overline{B}_{\text{opt}}$  where the spread is close to 20%. The relations in Table 3 represent a reasonable average of the results of the different numerical methods. In addition, we list in the table several other quantities that are of interest for calculations.

As was the case for a cylindrical sensor, the dependence of  $S$  near its maximum is not a strong function of concentration and field. We have plotted in Fig. 14a contours of constant  $S$  at 95% and 90% of  $S_{\text{opt}}$  in the field/concentration plane for the conditions indicated in the caption. Also plotted is the field for which the  $S$  is a maximum as a function of concentration. Even at a concentration of 550 ppm, approximately one fourth of the optimal concentration of 2000 ppm, it is possible to achieve a signal that is 80% of the maximum. The penalty of employing a concentration of less than the optimal value is small provided, of course, the field and area of the

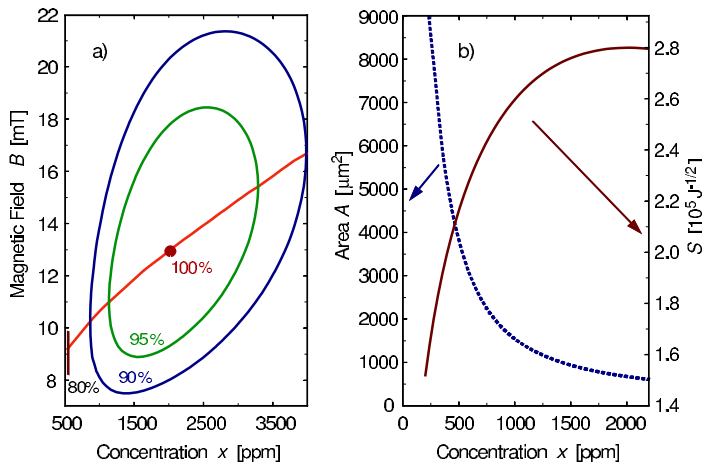


**Fig. 14.** (a) Contours of constant  $S$  at 95% and 90% of  $S_{\text{opt}}$  in the field/concentration plane. The line indicates the fields for which  $S$  is a maximum at a given concentration. Also indicated is the concentration at which  $S = 0.80 S_{\text{opt}}$ . The parameters associated with the graph are  $C_a = 1 \text{ pJ K}^{-1}$ ,  $g = 6.8$ ,  $\alpha = 5$ ,  $T = 0.05 \text{ mK}$  and  $p = 10 \mu\text{m}$ . (b) A plot of the maximum value of  $S$  achievable and the area of the meander required to obtain that value as a function a concentration for the conditions in (a). The height of the sensor is  $3.6 \mu\text{m}$

meander can be adjusted accordingly. The maximum value of  $S$  that can be obtained for a particular value of concentration less than the  $x_{\text{opt}}$  is plotted in Fig. 14b. An empirical equation that fits this curve is

$$S = S_{\text{opt}}[1 - (240\delta x)^2 - (430\delta x)^6], \quad (47)$$

where  $\delta x = (x_{\text{opt}} - x)$ . This equation fits the calculated values of  $S$  to a few percent for the range  $0.2 > \delta x/x_{\text{opt}} > 0$ . The plot for  $S$  in Fig. 14b and (47) is for the specific values of the parameters  $C_a$ ,  $g$ ,  $\alpha$ , and  $T$  listed in the caption. The plot and empirical fit is valid for different sets of parameters  $C_a$  and  $T$ , with the replacement of  $S_{\text{opt}}$  and  $x_{\text{opt}}$  by the appropriate scaled values. However, because of the inclusion of the heat capacity of the conduction electrons, the plot and empirical expression are not valid except in the immediate vicinity of  $S_{\text{opt}}$ , ( $S > 0.95 S_{\text{opt}}$ ). As the concentration decreases and the area of the meander increases, as indicated in Fig. 14b, the contribution of the electronic heat capacity becomes an ever larger factor.

The area of the meander required to maximize the signal for a given concentration increases substantially as the concentration decreases, as illustrated by the plot in Fig. 14b. This curve for the area is fit well by the empirical expression

$$A = A_{\text{opt}}[1 - (400\delta x) + (800\delta x)^2 - (640\delta x)^8]. \quad (48)$$

Again, this equation obeys scaling in  $T$  but not in  $g$  and  $\alpha$  except in the immediate vicinity of the optimal conditions. Also, it should be remembered that all these expressions are derived assuming that finite-size effects are unimportant in computing the fields and inductance. This is certainly not a good approximation, for example, for the optimal conditions in the case illustrated in Fig. 14, where  $p = 10\text{ }\mu\text{m}$  and the area covered by the meander-shaped coil is only  $A_{\text{opt}} = 700\text{ }\mu\text{m}^2$ . But the numbers given in Table 3 and Fig. 14 still provide a useful starting point to derive optimal parameters for meander-shaped pickup coils with smaller pitch or sensors with larger heat capacity and area, where finite size corrections are less important.

The optimization performed above includes many assumptions, such as the volume of the sensor is a variable. There may be situations where this is not the case, for example, the area and thickness of the sensor along the heat capacity of the absorber may be dictated by conditions of the experiment. In such cases the optimal concentration and field could be very different from what is calculated above.

Detectors using a meander pickup may be transformer coupled to a SQUID for best performance. In order to match the meander to the transformer it is essential to have a reasonable estimate of its inductance. In this regard we note that the susceptibility of the sensor under the conditions of optimal signal to noise may be sufficient to warrant its inclusion in the calculation of inductance. For Au:Er at  $T = 0.05\text{ K}$  the optimal concentration is  $x_{\text{opt}} = 0.002$ , and the susceptibility, using the expressions given in Sect. 2.2.1, is  $\chi = 0.18$ .

The calculated signal-to-SQUID-noise ratio of MMCs with meander-shaped pickup coil is about 1.5 times better than the result for MMCs with cylindrical sensors in an homogeneous external field. This difference is essentially due to the different filling factors of the two geometries. The fact that we used the meandering wire of the pickup coil to generate the bias field for the sensor allowed for placing sensor material inside as well as outside the area enclosed by the wire of the pickup loop. There might be numerous other sensor/pickup coil geometries with slightly better filling factor and possibly other advantages for certain applications that make use of the same idea.

## 2.5 Magnetic Johnson Noise

A source of noise, inherent to metallic magnetic calorimeters because of their very nature, is magnetic Johnson noise – noise in the magnetic field or flux, which is generated by thermally induced currents in a conductor. An MMC, consisting of a metallic sensor in close proximity to a pickup loop designed to measure flux changes produced by the sensor, is a system particularly susceptible to the effects of this noise source. Noise can be generated, as well, by a metallic absorber, and other materials in the vicinity of the pickup loop. And while it is noise that must be considered in developing high resolution

MMCs, there are standard means of ameliorating its influence to a degree that it is unlikely to be an important factor in setting limits on performance.

Magnetic Johnson noise has been observed and studied since the development of sensitive SQUIDS. A number of authors [41, 42] have calculated the fluctuations in the magnetic field arising from the thermal currents in a conductor starting from the random motion of the charges. Alternatively, as pointed out by Harding and Zimmerman [43], the flux noise generated in a coil or loop as a consequence of fluctuating currents in a conductor can be calculated using the reciprocity theorem. A time-varying current at frequency  $\omega$  in a coil produces eddy currents in nearby conductors, and the resulting losses can be described by an apparent resistive impedance  $R(\omega)$  of the coil. The impedance can then be used to deduce the flux noise in the coil or loop. This approach was followed in [32] to compute the flux noise in a circular SQUID loop of internal radius  $r$  enclosing a cylindrical metallic sensor of the same radius and height  $h$ . For this geometry the *rms* flux noise per  $\sqrt{\text{Hz}}$  is

$$\sqrt{S_\phi} = \mu_0 \sqrt{\frac{\pi}{8} C_c \sigma k_B T h r^2}, \quad (49)$$

where  $\sigma$  is the conductivity of the sensor and  $C_c$  is a numerical constant that depends on the pickup loop. For the case considered in Sect. 2.4.3 where the width of the loop is  $w = 0.1r$ , the constant is  $C_c \approx 2$ .

Equation 49 is valid for frequencies such that the dimensions of the sensor are small compared to the skin depth,  $\delta = \sqrt{2/(\mu_0 \sigma \omega)}$ . It is not possible to write simple analytic expressions for the noise when this condition is not satisfied [41]. The noise drops off rapidly with increasing frequency when the finite skin depth limits the fluctuations from coupling to the loop. In any event, one is unlikely to be concerned about noise in this frequency range, since any change in magnetization of the sensor at these frequencies would be attenuated as well.

The conductivity of  $\text{Au}_{1-x}\text{Er}_x$  can be obtained from the work of Arajs and Dunmyre [31], who found the residual resistivity of this alloy to vary linearly with concentration as  $\varrho = x 6.7 \times 10^{-6} \Omega \cdot \text{m}$ . For a cylindrical Au:Er sensor optimized for the conditions discussed in Sect. 2.4.3, namely,  $T = 0.05 \text{ K}$ ,  $C_a = 1 \times 10^{-12} \text{ JK}^{-1}$  for which  $r_{\text{opt}} = 10.7 \mu\text{m}$ ,  $h_{\text{opt}} = 0.53r$  and  $x_{\text{opt}} = 2200 \text{ ppm}$ , the magnitude of the magnetic Johnson noise is  $\sqrt{S_\phi} \approx 1 \times 10^{-7} \Phi_0/\sqrt{\text{Hz}}$ .

A metallic absorber attached to the sensor is also a potential source of magnetic Johnson noise. A large conducting sheet of thickness  $t$ , parallel to the plane of a circular loop of wire and separated from it by a distance  $z$ , produces a spectral flux noise density in the loop of

$$\sqrt{S_\phi} = \mu_0 \pi r^2 \sqrt{\frac{\sigma k_B T t}{8 \pi z (z + t)}}. \quad (50)$$

A  $5\text{ }\mu\text{m}$  thick absorber with a conductivity of  $2 \times 10^8 \Omega^{-1}\text{m}^{-1}$  (roughly that of vapor-deposited Au) placed  $5.7\text{ }\mu\text{m}$  above a  $10.7\text{ }\mu\text{m}$  radius loop generates a flux noise of  $\sqrt{S_\phi} \approx 2 \times 10^{-7} \Phi_0/\sqrt{\text{Hz}}$ .

The magnetic Johnson noise can always be reduced by decreasing the conductivity of the metal with non magnetic impurities.

The magnetic Johnson noise for a meander has not been worked out in detail. One can, using numerical methods, calculate the eddy currents losses in the sensor induced by an ac current flowing in the meander strips. This, in turn, can be used to compute the flux noise in the meander generated by fluctuating currents in the sensor. The fluctuating currents principally responsible for producing noise are those that flow parallel to the stripes of the meander. A rough estimate of the contribution of these fluctuations is given by the expression

$$\sqrt{S_\phi} = \mu_0 \sqrt{\mathcal{C}_m \sigma k_B T V}, \quad (51)$$

where  $V$  is the volume of the sensor and  $\mathcal{C}_m$  is a parameter that depends on details of the geometry of the meander. This equation, by itself, is helpful only in showing the obvious dependence on conductivity and temperature. The parameter  $\mathcal{C}_m$  depends on thickness of the sensor. An optimally designed sensor, for which the ratio of thickness to pitch is  $\xi = h/p = 0.36$ , has a volume which is  $V \propto Ap$ , where  $A$  is the area of the total meander. A rough calculation of  $\mathcal{C}_m$  for an optimal sensor yields  $\mathcal{C}_m \approx 0.02$ . Hence, for a meander with a pitch of  $10\text{ }\mu\text{m}$  and  $A = 1\text{ mm}^2$  used at  $50\text{ mK}$  with a Au:Er sensor having a conductivity of  $1.3 \times 10^{-8} \text{ mho m}^{-1}$  (corresponding to an Er concentration of  $1000\text{ ppm}$ ), the rms flux noise is  $\sqrt{S_\phi} \approx 3 \times 10^{-6} \Phi_0/\sqrt{\text{Hz}}$ . This is an order of magnitude larger than the noise estimated above for a cylindrical sensor and loop, but this is not surprising. The Johnson noise from the sensor in both the cylindrical and meander geometry is proportional to the volume, albeit with a proportionality constant that is different for the two geometries. The volume of the meander sensor chosen in this example is  $10^3$  times larger than that taken above for the cylinder.

While the fluctuating currents in the sensor flowing parallel to the stripes of the meander are a significant source of magnetic Johnson noise, they are not the only source or even the largest noise source, depending on how the circuit containing the meander is constructed. Consider the three circuits diagrammed in Fig. 15 with the same meander but different configurations of the leads<sup>10</sup>. In the first configuration fluctuating currents in the sensor covering the meander do not couple to the leads. In the latter two configurations where the leads lie very near the sensor there is obvious coupling, but with very different results in the two cases.

---

<sup>10</sup> Configuration a) is not one that is likely to be used in practice because of the inductance associated with the large area enclosed in bringing the leads together away from the metallic sensor

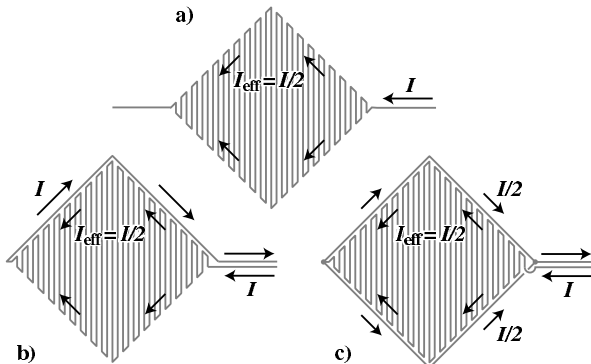


**Fig. 15.** A meander with three different configurations of the leads connecting it to the remainder of the measuring circuit

In calculating the eddy currents flowing in the sensor to estimate Johnson noise by reciprocity, we need to consider the net current at the boundaries of the meander and not just the current in the stripes. In configuration a) one can approximate the effective current on each side of the meander as  $I/2$ ,  $I$  being the total current flowing in the meander. The currents in the upper and lower boundaries flow in the same direction with the result that eddy currents induced in the sensor tend to cancel except in the vicinity of the edges. There is, nonetheless, a contribution to the Johnson noise from fluctuating currents near the edges, but it is not large. The leads play no role in determining the Johnson noise in configuration a).

The same is not true in configuration b), where the return current of  $I$  in the lead running along the upper boundary flows in the opposite direction to the effective current of  $I/2$  in the meander edge. As a result there is an apparent circumferential current flowing around the meander. A current of  $I/2$  flows along the upper and lower boundaries in circular fashion. Time-varying currents in the meander produce large circular eddy currents in the sensor, similar to those in a cylindrical sensor enclosed by a circular loop. The Johnson noise from fluctuating thermal currents is therefore much larger in configuration b) than in a). The noise from fluctuating currents running parallel to the boundaries is estimated to be comparable in magnitude to that produced by currents flowing parallel to the stripes.

The large enhancement of Johnson noise resulting from dressing the lead to lie along the one-half of the meander boundary as in configuration b) can be eliminated by doubling the lead, running one part along the boundary of the upper half of the meander and the other part along the lower half. This is illustrated in configuration c) of Fig. 15. Provided the two halves are symmetric and the current flow is the same in the two parts of the split lead, there is no net current flow around the boundary of the meander. Time-varying currents in the meander produce no circulating eddy currents, or,

to turn the argument around, circular fluctuating thermal currents do not induce voltage or flux noise in the circuit.

As this discussion illustrates, the magnetic Johnson noise in a meander depends on the details of the layout of the circuit and its coupling to the sensor. If necessary, the noise in a meander can be reduced by introducing discontinuities (laminations) in the metallic sensor so as to inhibit thermal currents from flowing in directions that couple either to the stripes or to the edges. This can presumably be accomplished without appreciably changing the area of the sensor and hence the signal response.

The flux noise of MMCs with both, cylindrical sensors with circular pickup loop and planar sensors with meander shaped pickup loop, scale as the volume of the sensor. However, as the change of flux in a meander-shaped pickup coil per unit of deposited energy increases with decreasing pitch of the meander (and decreasing thickness of the planar sensor), the signal-to-Johnson-noise ratio can be made significantly larger in this geometry.

## 2.6 Energy Resolution

Generally speaking, the energy resolution of metallic magnetic calorimeters and other near-equilibrium calorimetric low-temperature particle detectors depends on two properties: the time-dependent signal-to-noise ratio and the time-structure of the signal. If we assume the total noise of the detector signal to be stationary, the discussion of energy resolution is most conveniently carried out in the frequency domain, as discussed in detail by D. McCammon in the introductory chapter of this book.

The energy resolution of MMCs can generally be degraded by numerous effects, such as fluctuations of the detector temperature, electromagnetic interference caused by nearby instruments, magnetic cross-talk between the detectors of a detector-array, infra-red photons due to insufficient screening, and so on. When discussing the ultimate energy resolution of MMCs in the remainder of this section we assume that all these external contributions to noise can be suppressed sufficiently by a proper design of the detector and the refrigerator. In this case we are left with the more intrinsic sources of noise of magnetic calorimeters, being the magnetic Johnson noise caused by the thermal motion of electrons in the metallic sensor, the flux noise (or energy sensitivity) of the SQUID-magnetometer and thermal fluctuations of the magnetic moment of the sensor.

In anticipating the results of the following discussion, we make the following points: 1. magnetic Johnson noise is one of potentially limiting sources of noise. Assuming the sensor to be made of Au:Er, we shall see that its contribution is noticeable in the case of cylindrical sensors. In the case of sensors with meander-shaped pickup coils or materials with smaller conductivity the contribution is marginal. 2. In the preceding section we optimized the signal of MMCs with respect to the flux noise referred to the pickup coil. We shall

see later that the flux-noise of the SQUID magnetometer is a small contribution to the energy resolution of a fully optimized MMC. It is worth keeping in mind that the signal-to-SQUID-noise ratio was found to be best if the heat capacity of the absorber equals the heat capacity of the sensor. We shall see that the optimization of energy resolution, limited by thermodynamic fluctuations of energy, will essentially lead to the same optimal relation between heat capacities, justifying the separation of the two optimizations. 3. The following discussion will show that the most fundamental limitation to the energy resolution of MMCs is set by thermodynamic fluctuations of energy between the thermal subsystems of the calorimeter and fluctuations between the calorimeter and the thermal reservoir.

We discuss the influence of thermodynamic energy fluctuations on the energy resolution in two steps, using two simplified thermodynamic models of the detector. The contribution of the other sources of noise to energy resolution will be discussed in a later section of this chapter.

### 2.6.1 First Approach – A Canonical Ensemble

In our first approach the calorimeter is described by a simple canonical ensemble. We assume that the detector has a heat capacity  $C$ , which is coupled to a thermal reservoir of temperature  $T_0$  by a thermal link with conductance  $G$ . In addition, we assume that absorbed energy from energetic particles thermalizes instantly and that we are able to measure the energy content of the calorimeter infinitely fast and with infinite precision.

In the absence of incident particles, the energy content of the calorimeter fluctuates around its mean value with a standard deviation of

$$\delta e_{\text{rms}} = \sqrt{k_B C T^2}. \quad (52)$$

Due to the finite values of heat capacity and thermal conductance, the spectral power density of energy fluctuations is restricted to frequencies below  $f_0 = (2\pi\tau)^{-1}$ ,

$$S_e = k_B C T^2 \frac{4\tau}{1 + (2\pi f\tau)^2}, \quad (53)$$

where  $\tau = C/G$  is the characteristic relaxation time of this configuration.

The deposition of an energy  $E$  in the calorimeter causes the energy content to increase instantly and relax back to its mean value following

$$\delta e(t > 0) = E e^{-t/\tau}. \quad (54)$$

The Fourier spectrum of the signal is described by

$$|\tilde{e}|(f) = E \frac{\tau}{\sqrt{1 + (2\pi f\tau)^2}}, \quad (55)$$

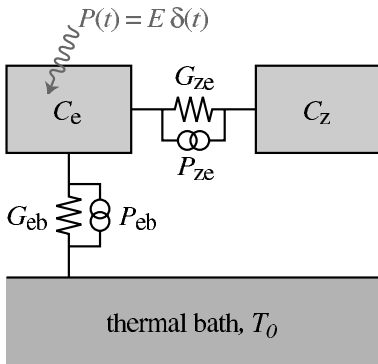


**Fig. 16.** Thermal model of a magnetic calorimeter consisting of two subsystems, the spins with heat capacity  $C_z$  and the conduction electrons of the absorber and the sensor having heat capacity  $C_e$

where  $f \in [-\infty, \infty]$ . Note that the spectrum of noise and signal have the same dependence on frequency, thus the signal-to-noise ratio is independent of frequency.

When analyzing the data, the information contained in any frequency bin  $\delta f$  can be used to obtain a value for the deposited energy. The uncertainty of the signal in any bin is independent of the center frequency of the frequency interval  $\delta f$ , as long as the width  $\delta f$  is fixed. If the results of  $N$  frequency intervals are averaged, the total uncertainty decreases proportionally to  $N^{-1/2}$ . As the signal-to-noise ratio is independent of frequency, the result of averaging over an infinite number of frequency bins leads to a vanishing uncertainty of the estimated energy.

Of course this result does not reflect the behavior of a real detector. Nonetheless, we learn from this result that the instrumental line width of the detector decreases both by increasing the signal-to-noise ratio in frequency domain and by increasing the usable bandwidth. In a real detector the usable bandwidth can be limited by any of the noise contributions mentioned above. In the following section we show that the thermal fluctuations of energy between the subsystems of the detector already lead to a significant limitation of achievable energy resolution.

## 2.6.2 Canonical Ensemble Consisting of Two Subsystems

Figure 16 shows a model of a metallic magnetic calorimeter, which consists of two thermal systems, the conduction electrons of the absorber (and the sensor) and the magnetic moments, having heat capacities  $C_e$  and  $C_z$ , respectively. In order to keep the model as simple as possible, the small contribution of phonons to the total heat capacity is neglected. Moreover, we assume that any deposition of energy  $E$  in the detector thermalizes instantly within the system of the conduction electrons. The two systems are connected by a thermal link of conductance  $G_{ze}$ . The conduction electrons are connected to a thermal bath of temperature  $T_0$  by a conductance  $G_{eb}$ .

In addition, the magnetic moments are assumed to be non-interacting, in the sense that the interaction energy between moments is much smaller than the Zeeman-splitting in the external field. In this case, the total magnetic moment  $m$  of the paramagnetic sensor is a measure of the energy content  $e_z$  of the spins, being related by  $e_z = -mB$ . The magnetic moment, in turn, is proportional to the magnetic flux in the pickup loop,  $\delta\Phi \propto \delta m$ . Therefore, the flux in the SQUID represents a direct measure of the energy content of the spin system, provided the intrinsic flux noise of the SQUID is neglected.

The time evolution of the energy content of the two systems can be described by the following two differential equations:

$$\dot{e}_z = C_z \dot{T}_z = -(T_z - T_e) G_{ze} + P_{ze}, \quad (56)$$

$$\dot{e}_e = C_e \dot{T}_e = -(T_e - T_z) G_{ze} - (T_e - T_0) G_{eb} - P_{ze} + P_{eb} + P(t), \quad (57)$$

where the quantities  $P_{ze}$  and  $P_{zb}$  represent randomly fluctuating fluxes of heat through the thermal links with a white power spectrum of  $S_{P_{ze}/P_{eb}} = 4k_B T^2 G_{ze/eb}$ . The deposition of an energy  $E$  at time  $t_0$  in the detector appears in this set of equation as an external power input  $P(t) = E\delta(t - t_0)$  in (57).

### *Energy Fluctuations.*

To derive the power spectrum  $S_{e_z}$  of the energy fluctuations of the spins (Zeeman-system), we set  $P(t) = 0$  in (57) and transform both equations into the frequency domain. Since both noise sources,  $P_{ze}$  and  $P_{eb}$ , contribute incoherently, the power spectrum is

$$S_{e_z}(f) = k_B C_z T^2 \left( \alpha_0 \frac{4\tau_0}{1 + (2\pi f \tau_0)^2} + \alpha_1 \frac{4\tau_1}{1 + (2\pi f \tau_1)^2} \right), \quad (58)$$

where  $\tau_{0/1}$  represent the characteristic time constants of the system,

$$\tau_{0/1} = \frac{C_e G_{ze} + C_z (G_{ze} + G_{eb})}{2 G_{ze} G_{eb}} \mp \sqrt{\frac{[C_e G_{ze} + C_z (G_{ze} + G_{eb})]^2}{4 G_{ze}^2 G_{eb}^2} - \frac{C_z C_e}{G_{ze} G_{eb}}}. \quad (59)$$

The dimensionless factors  $\alpha_{0/1}$  are similarly cumbersome functions of  $C_e$ ,  $C_z$ ,  $G_{ze}$  and  $G_{eb}$ , which fulfill the simple relation  $\alpha_0 + \alpha_1 = 1$ . In situations relevant for the following discussion, we take  $0.1 < C_z/C_e < 10$ ,  $\tau_0 \ll \tau_1$  and approximate  $\alpha_{0/1}$  by

$$\alpha_0 = 1 - \beta, \quad (60)$$

$$\alpha_1 = \beta, \quad (61)$$

where

$$\beta = \frac{C_z}{C_e + C_z} \quad (62)$$

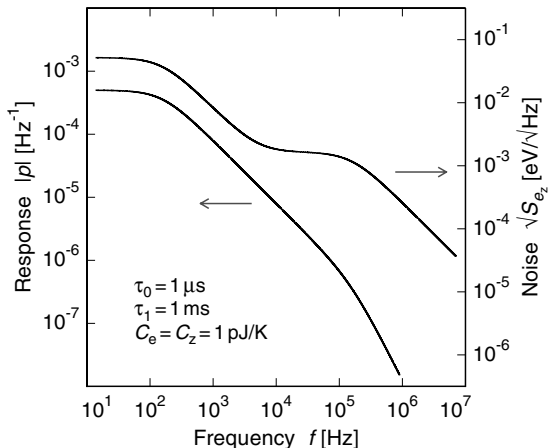


**Fig. 17.** Frequency spectrum of the response of a MMC (*left axis*) and spectral power density of the energy fluctuations of a MMC. The values correspond to a detector with  $C_e = C_z = 1 \text{ pJ/K}$ ,  $\tau_0 = 1 \mu\text{s}$ ,  $\tau_1 = 1 \text{ ms}$  at a temperature of  $T = 50 \text{ mK}$

is the relative contribution of the heat capacity of the spins to the total heat capacity of the calorimeter.

Figure 17 shows the frequency spectrum of energy fluctuations of the spin system for a detector having heat capacities  $C_e = C_z = 1 \text{ pJ/K}$  and time constants  $\tau_0 = 1 \mu\text{s}$ ,  $\tau_1 = 1 \text{ ms}$  at a temperature of  $T = 50 \text{ mK}$ .

The spectrum is the incoherent sum of two step-like contributions. Fluctuations between the spins and the absorber cause a plateau of amplitude  $\sqrt{S_{e_z}} = \sqrt{4k_B C_z T^2 \tau_0 (1 - \beta)}$  at high frequencies. Energy fluctuations between the spins and the thermal bath contribute  $\sqrt{S_{e_z}} = \sqrt{4k_B C_z T^2 \tau_1 \beta}$  to the spectrum at frequencies below  $(2\pi\tau_1)^{-1}$ . As expected, the integral of  $S_{e_z}$  gives

$$\int_0^\infty S_{e_z} df = k_B C_z T^2, \quad (63)$$

which corresponds to the energy fluctuations of a canonical ensemble of heat capacity  $C_z$  at temperature  $T$ .

*Response.*

In order to calculate the response  $e_z(t)$  of the detector upon the deposition of energy  $E$ , we neglect the random noise sources  $P_{ze}$  and  $P_{eb}$  in (56) and (57) and obtain

$$\frac{e_z(t > 0)}{E} = p(t > 0) \simeq \beta(e^{-t/\tau_1} - e^{-t/\tau_0}). \quad (64)$$

The energy content of the spins rises, approaches a maximum value with a time constant  $\tau_0$  and relaxes back to its equilibrium value with a time constant  $\tau_1$ . The responsivity  $p$  of the detector is best described in frequency domain by

$$|\tilde{p}|(f) \simeq \frac{\beta\tau_1}{\sqrt{1 + (2\pi f\tau_0)^2}\sqrt{1 + (2\pi f\tau_1)^2}}, \quad (65)$$

where  $f \in [-\infty, \infty]$ . Again, we assumed  $\tau_0 \ll \tau_1$ . Figure 17 shows the frequency spectrum of the detector response (*left axis*). The response is a maximum at low frequencies, decreases proportional to  $f^{-1}$  at frequencies above  $f_1 = (2\pi\tau_1)^{-1}$  and twice as fast,  $\tilde{p} \propto f^{-2}$ , at frequencies beyond  $f_0 = (2\pi\tau_0)^{-1}$ . From Fig. 17 it is apparent that the signal-to-noise ratio cannot be improved by summing over an ever increasing frequency range. Hence, the energy resolution is limited to finite values within this model.

The responsivity  $\tilde{p}$  as defined in (65) can also be interpreted as the ratio between the amplitude of oscillations of energy content  $e_z$  of the spin system and the amplitude of a harmonic power input  $P$  into the electron system of the detector. It is therefore straight forward to define the noise-equivalent power NEP by  $\text{NEP}^2 = S_{e_z}/(\tilde{p}^* \tilde{p})$ . Using the results from above

$$\text{NEP}^2(f) = \text{NEP}_0^2 [1 + (f/f_{\text{eff}})^2] \quad (66)$$

with a constant minimum value of

$$\text{NEP}_0^2 = 4k_B T^2 G_{\text{eb}} \left(1 + \frac{G_{\text{eb}}}{G_{\text{ze}}}\right) \simeq \frac{4k_B C_z T^2}{\beta\tau_1} \quad (67)$$

up to a frequency of

$$f_{\text{eff}} = \frac{1}{2\pi C_e} \sqrt{G_{\text{ze}} G_{\text{eb}} \left(1 + \frac{G_{\text{eb}}}{G_{\text{ze}}}\right)} \simeq \sqrt{f_0 f_1} \sqrt{\frac{\beta}{1 - \beta}}. \quad (68)$$

Again, the approximations are applicable in the case of  $\tau_0 \ll \tau_1$ . The effectively usable bandwidth of the detector signal is limited to frequencies below  $f_{\text{eff}}$ , because the noise-equivalent-power increases as  $\text{NEP} \propto f$  at frequencies beyond this.

### *Energy Resolution.*

The energy resolution of thermal detectors with frequency-dependent noise-equivalent power was discussed in detail by D. McCammon in the introductory chapter of this book. Within the framework of optimal filtering it was shown that the energy resolution of a detector is related to  $\text{NEP}(f)$  by

$$\Delta E_{\text{rms}} = \left( \int_0^\infty \frac{4df}{\text{NEP}^2} \right)^{-1/2}. \quad (69)$$

When applied to the present model of thermal fluctuations between the subsystems of the detector and to the thermal bath the result is

$$\Delta E_{\text{rms}} = \sqrt{4k_B C_e T^2} \left[ \frac{G_{\text{eb}}}{G_{\text{ze}}} + \left( \frac{G_{\text{eb}}}{G_{\text{ze}}} \right)^2 \right]^{1/4}. \quad (70)$$

Note that  $\Delta E$  increases linearly with temperature and square root of absorber heat capacity. However, this expression implies that the energy resolution can be improved without limit if there is a perfect thermal conductance  $G_{\text{ze}}$  between the absorber (electrons) and the thermometer (spins). But for a given sensor material, e.g. Au:Er, the thermal conductance between electrons and spins is not a freely adjustable parameter. The limiting material parameter is the electron-spin relaxation time, which obeys the Korringa relation  $\tau_K T = \kappa$  in the limit of small spin concentrations. For this reason we rewrite (70) in terms of relaxation times and obtain

$$\Delta E_{\text{rms}} = \sqrt{4k_B C_e T^2} \left( \frac{1}{\beta(1-\beta)} \frac{\tau_0}{\tau_1} \right)^{1/4}. \quad (71)$$

Given that the signal rise time  $\tau_0$  is fixed by the sensor material and the recovery time  $\tau_1$ ,  $C_e$  and  $T$  are determined by the requirements of a given application, there is only one free parameter,  $\beta$ , that can be used to optimize the energy resolution of the detector. The energy resolution  $\Delta E_{\text{rms}}$  is a minimum for  $\beta = 1/2$ , meaning that the heat capacity of the spins should match the heat capacity of the absorber. This is consistent with the result of the optimized signal-to-SQUID-noise. Within these assumptions, the intrinsic energy resolution of a magnetic calorimeter can be expressed as [44]

$$\Delta E_{\text{rms}} = \sqrt{4k_B C_e T^2} \sqrt{2} \left( \frac{\tau_0}{\tau_1} \right)^{1/4}. \quad (72)$$

There are a number of comments that may help putting this result into perspective.

1. Due to its very nature, an MMC, being a thermal detector with finite relaxation time for internal equilibration, has an energy resolution that is intrinsically limited. This is true even though, in the model discussed here, the amplifier is assumed to be infinitely fast and noiseless.

2. As the power dissipation to read out the sensors can be made almost arbitrarily small – at least in comparison to resistive temperature sensors – in some applications it may be possible to improve the energy resolution in the limit of long recovery times  $\tau_1$ , albeit at the expense of a significant limitation to count rate. If an MMC could be used together with a fast heat switch it might be possible to combine the benefits of a long thermal relaxation time  $\tau_1$  with high count rates. The transient signal upon the deposition of energy could be analyzed at high signal-to-noise and then afterwards the detector

could be returned rapidly to thermal equilibrium. A similar reduction of the effective thermal recovery time could be achieved by electro-thermal feedback, where the temperature of the calorimeter is elevated above bath temperature by a heater current through the sensor, which is reduced upon the deposition of energy in the detector.

3. The simplified model discussed here does not include the RKKY interaction between the localized magnetic moments. An accurate treatment of the influence of this interaction on energy resolution appears rather complex. A simple argument, which can be used to estimate the order of magnitude of the degradation of resolution, is the following. As discussed above, the magnetic susceptibility of the sensor material can be described by a Curie-Weiss relation  $\chi = \lambda/(T + \theta)$ . For the material Au:Er  $\lambda = x 5.35\text{ K}$  and the interaction between the spins is described by  $\theta = x\alpha 1.1\text{ K}$ . Sensors with the best signal-to-SQUID-noise have an erbium concentration of  $x_{\text{opt}} \simeq 0.040\text{ T/K}$ . From the Curie-Weiss relation we see that the interaction between the spins reduces the susceptibility of free magnetic ions by about  $\theta/T$ , which has a value of  $\theta_{\text{opt}}/T = 0.22$ . Only about 3/4 of the magnetic moments appear to act as non-interacting spins, as assumed in the simplified model. The other 1/4 contribute to the heat capacity of the spin system without contributing to the signal. If we further assume that the relaxation time of this latter system is the order of  $\tau_0$ , we can conclude that the high frequency plateau of the noise spectrum raised, resulting in a reduction of the effectively usable bandwidth. Within this picture, the effect on energy resolution can be estimated via (71), with the increase of  $\Delta E_{\text{rms}}$  being less than 15%. However, this simple argument does not hold in the limit of high concentrations and low temperatures, where paramagnetic alloys enter the spin glass state and strong spin-spin correlations lead to an increased amplitude of the fluctuations of the magnetic moment. The frequency dependence of the spectral density,  $S_m \propto f^{-1}$ , is due to a broad distribution of relaxation times. In the examples given above, the sensors are operated at a temperature which is about one order of magnitude higher than the spin-glass temperature of the sensor material, and spin-spin correlations are expected to have a minor effect in this regime.

4. It seems attractive to improve the intrinsic energy resolution of the detectors by choosing a sensor material with a short electron-spin relaxation time. However, due to the underlying physics it is likely that this strategy will also lead to a stronger indirect exchange interaction between the localized magnetic moments, leading to a degradation of energy resolution as discussed above in comment (3.).

5. In our discussion above, we assumed that the signal rise time is determined by the Korringa time  $\tau_K$ . A more detailed discussion should include the fact that electron-spin relaxation time also depends on the ratio of Zeeman splitting  $g\mu_B B$  to thermal energy  $k_B T$ . This leads to an increase of  $\tau_K$  in large magnetic fields. In addition, if the heat capacities of the elec-

tron system and the spins are of similar size, the effective relaxation time is reduced to  $\tau_0 = (1 - \beta)\tau_K$ . If this relation is inserted into (71) the factor  $[\beta^{-1}(1 - \beta)^{-1}\tau_0\tau_1^{-1}]^{1/4}$  is replaced by  $(\beta^{-1}\tau_K\tau_1^{-1})^{1/4}$ . Now  $\Delta E$  has a minimum at  $\beta = 1$ , which is smaller by a factor of  $2^{1/4}$  than the value at  $\beta = 1/2$ . However, this limit is unlikely to be reached in experiments. For fixed  $C_e$  the limit  $\beta \rightarrow 1$  is equivalent to  $C_z \rightarrow \infty$ , and there is a corresponding increase of energy fluctuations at low frequencies. Theoretically, this increase in noise is compensated by a larger usable bandwidth, since the height of the high frequency plateau of the noise decreases. In practice, there are other effects such as the thermal diffusion time within the absorber that will limit the relaxation time between the absorber and the spins and make considerations of corrections to  $\tau_K$  mute.

6. The intrinsic limitation of energy resolution, which is discussed in this section, is caused by thermal fluctuations of energy between the absorber and the spins, resulting in a second plateau in the noise spectrum at high frequencies, having an amplitude of  $\sqrt{S_{e_z}} = \sqrt{4k_B C_z T^2 \tau_0 (1 - \beta)}$ . The spectral power density of flux noise  $S_\Phi$  in the pickup coil caused by these fluctuations of energy can be estimated from this value by the factors  $\delta\Phi/\delta E$  and  $(\delta\Phi/\delta E)/\sqrt{L}$ , which were derived in the previous sections, resulting in  $\sqrt{S_\Phi} \simeq \beta^{-1} \sqrt{S_{e_z}} \delta\Phi/\delta E$ . We shall use this relation to discuss the contribution of magnetic Johnson noise and SQUID noise to the energy resolution of the detector in the following example.

### *Example.*

A microcalorimeter working at a temperature of 50 mK, having an X-ray absorber made of gold with an active area of  $240 \mu\text{m} \times 240 \mu\text{m}$  and a thickness of  $5 \mu\text{m}$  might be regarded as a useful detector for high resolution X-ray spectroscopy. The heat capacity of the absorber at this temperature  $C_a = 1.0 \text{ pJ/K}$ . In order to obtain an estimate of the intrinsic energy resolution of the calorimeter, we assume relaxation times of  $\tau_0 = 1 \mu\text{s}$  and  $\tau_1 = 1 \text{ ms}$ . From (72) the energy resolution is  $\Delta E_{\text{FWHM}} = 1.4 \text{ eV}$ .

In this example we take the sensor to have cylindrical geometry and to be made of Au:Er with parameters listed in Table 1, which on the one hand correspond to optimum signal-to-SQUID-noise and on the other hand fulfill  $C_{\text{sensor}} = C_a$ , in agreement with the condition  $\beta = 1/2$  for optimal intrinsic energy resolution. The sensor has a radius of  $10.7 \mu\text{m}$ , a thickness of  $5.7 \mu\text{m}$  and an erbium concentration of 2200 ppm. It is placed in a field of 15 mT and the circular pickup loop, which is used to read out the sensor, has an inductance of  $L = 50 \text{ pH}$ . As discussed above, the interaction between the magnetic moments at this concentration will cause the energy resolution of the detector to be degraded by about 15%, leading to  $\Delta E_{\text{FWHM}} \simeq 1.6 \text{ eV}$ .

From the values listed in Table 1 and  $L = 50 \text{ pH}$  we can derive  $\delta\Phi/\delta E = 1.0 \times 10^{-4} \Phi_0/\text{eV}$ . Hence, the high frequency plateau of energy fluctuations,

$\sqrt{S_{e_z}} = 1.65 \times 10^{-3} \text{ eV}/\sqrt{\text{Hz}}$ , corresponds to a flux noise in the pickup coil of  $\sqrt{S_\Phi} = 0.33 \mu\Phi_0/\sqrt{\text{Hz}}$ .

This value can now be compared to the flux noise of the SQUID and to flux noise generated by magnetic Johnson noise. Assuming the energy sensitivity of the SQUID to be  $\epsilon_s = 25\hbar$ , its contribution to flux noise is  $\sqrt{S_\Phi} = 0.25 \mu\Phi_0/\sqrt{\text{Hz}}$ . This reduces the usable bandwidth of the detector signal by 25 % and causes a degradation of energy resolution of 12%, resulting in  $\Delta E_{\text{FWHM}} \simeq 1.8 \text{ eV}$ .

The contribution of magnetic Johnson noise of the sensor to the total flux noise was calculated in the preceding section to be  $\sqrt{S_\Phi} \simeq 0.1 \mu\Phi_0/\sqrt{\text{Hz}}$ . It also adds incoherently to the magnitude of the high frequency plateau, but its effect on the energy resolution is only the level of 2% and can be neglected.

Since the intrinsic energy resolution for an optimized detector is independent of geometry, a planar sensor with a meander shaped pickup coil would have an almost identical intrinsic energy resolution as a sensor with cylindrical geometry. However, the degradation of the energy resolution by both SQUID noise and magnetic Johnson noise would be somewhat less.

At a given temperature the relative contributions of the three sources of noise to the energy resolution should also hold for detectors that have an absorber heat capacity differing from the example discussed here, because all these contributions scale as  $\sqrt{C_a}$ . However, if the detector is operated at lower temperatures, the flux noise of the SQUID becomes increasingly important.

### 3 Status of Development

Based on the results of a theoretical analysis of signal optimization and of fundamental noise contributions, several prototype detectors have been constructed and tested. Since optimized SQUIDs for MMCs have not yet been fabricated, these prototypes are not fully optimized detectors. They are primarily devices for demonstrating the potential of MMCs for particle detection. In this section we present selected results that have been achieved with these prototype detectors. We focus our discussion mostly on X-ray spectroscopy, one of the main applications for this type of device. In addition, we discuss applications in metrology and gamma-ray detection. At the beginning of this section we briefly mention a few details of the experimental setup for operating magnetic calorimeters.

#### 3.1 Experimental Setup

In the first part of this section we shall describe a cryogenic system that has been used to operate magnetic calorimeters. This should be seen just as an example for a typical cryogenic environment for MMC detectors and serves to illustrate some noteworthy details. In the second part of this section a few important aspects of a suitable SQUID magnetometer setup are discussed.

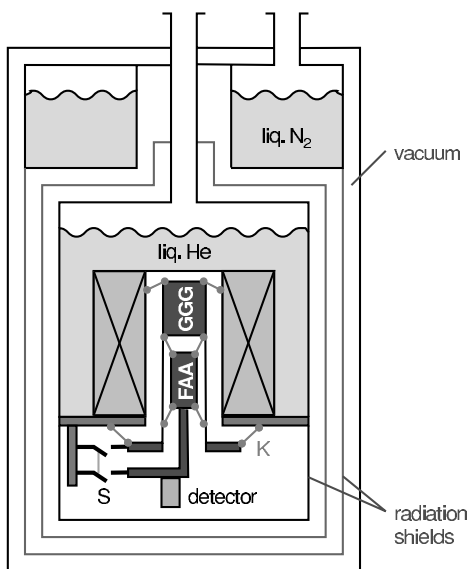


**Fig. 18.** Schematic of an adiabatic demagnetization refrigerator (ADR)

### 3.1.1 Cryogenics

The prototypes discussed in the remainder of this chapter were operated in a variety of different cryostats, <sup>3</sup>He/<sup>4</sup>He-dilution refrigerators as well as adiabatic demagnetization refrigerators (ADR). In order provide an idea of the typical cryogenic environment of magnetic calorimeters, we provide a brief description of the cryostat that was used in the experiments on high resolution X-ray spectroscopy discussed in Sect. 3.2.

A sketch of the cryostat is shown in Fig. 18. The commercial 2-stage ADR<sup>11</sup> has a common isolation vacuum, a liquid nitrogen bath and a liquid helium bath. The helium bath provides a platform at a temperature of 4.2 K, which can be lowered to  $T = 1.5$  K by pumping. A paramagnetic salt pill (GGG<sup>12</sup>) is suspended from this platform by kevlar strings (K). A second paramagnetic pill (FAA<sup>13</sup>) with lower spin concentration is suspended from the GGG pill also by kevlar strings. Each salt pill has good thermal contact to a separate experimental platform. Both platforms can be thermally connected to the cold platform of the helium bath via mechanical heat switches (S). The salt pills are located in the common vacuum space of the cryostat and surrounded by a superconducting magnet, which is located in the helium bath. Starting the adiabatic demagnetization process of the paramagnetic salt pills at a temperature of  $T \simeq 1.5$  K and a field of  $B = 6$  T results in base temperatures of  $T_{\text{GGG}} \simeq 200$  mK and  $T_{\text{FAA}} \simeq 21$  mK. After full

<sup>11</sup> VeriCold Technologies GmbH, Ismaning, Germany, [www.vericold.com](http://www.vericold.com)

<sup>12</sup> GGG: Gadolinium-Gallium-Garnet

<sup>13</sup> FAA: Ferric-Ammonium-Alum

demagnetization, the time for the FAA pill to warm up to temperatures above 30 mK is approximately 3 days, providing enough time for long continuous measurements.

The magnetic calorimeters are mounted on the cold platform of the FAA salt pill. All wires running from He-temperature to the detectors are made of material with low thermal conductivity (e.g. NbTi, CuNi) and heat sunk at the GGG-platform. The temperature of the FAA platform is measured using a RuO<sub>2</sub> resistance thermometer with  $d \log R/d \log T \simeq 1.5$  at  $T \simeq 35$  mK and a AVS-47 resistance bridge<sup>14</sup>. A fully analog as well as a digital PID controller were used for regulating the current through the magnetizing coil of the ADR, in order to stabilize the temperature of the FAA platform to within  $\delta T_{\text{rms}} \simeq 2$   $\mu\text{K}$  in the temperature range between 30 mK and 35 mK.

For MMCs to be used as high resolution X-ray detectors a temperature stability on this level or better is indeed required. The dependence of the detector sensitivity  $\delta\Phi/\delta E$  on the operating temperature can be characterized by  $d \log(\delta\Phi/\delta E)/d \log T \simeq -1$  for MMCs with sensor parameters close to optimum. Therefore, the variations of operating temperature quoted above already contribute  $\Delta E_{\text{FWHM}}/E \simeq 1.5 \times 10^{-4}$  to the energy resolution of the detector.

### 3.1.2 SQUID Magnetometer

Low noise, high bandwidth readout of the SQUID magnetometer of an MMC can be achieved by 2-stage SQUID electronics, as illustrated in Fig. 19. The signal of the primary SQUID (detector SQUID) is amplified by a secondary SQUID (amplifier SQUID) before it is read out by an amplifier operating at room temperature. In order to achieve a high transfer coefficient  $\delta U_2/\delta\Phi_1$  of flux  $\Phi_1$  in the primary SQUID to voltage  $U_2$  across the secondary SQUID, a dc flux is applied to the secondary SQUID to make the steepest points of the  $U$ - $\Phi$ -characteristics of the two single SQUIDs fall on top of each other.

Figure 20 shows the  $U_2$ - $\Phi_1$ -characteristics of the 2-stage SQUID configuration, which was used for the high resolution X-ray detector discussed in Sect. 3.2. The steepest point of the common characteristics is marked with a dot. Linearization of the flux-voltage characteristics is achieved by applying negative feedback to the flux in the primary SQUID and stabilizing the system at the steepest point (working point) of the common characteristics.

The flux-to-flux gain  $G_\Phi$  between the two SQUIDs at the working point can be adjusted by the resistor  $R_g$ . To allow for stable operation and to avoid multiple working points, the maximum flux swing in the secondary SQUID caused by the voltage swing of the primary SQUID should not exceed one flux quantum  $\Phi_0$ . This limits the flux gain to values of about  $G_\Phi < 3$ .

One major benefit of the 2-stage configuration is the fact that a SQUID with a high critical current and large voltage swing (or even a series-SQUID-

---

<sup>14</sup> Pico-Watt Electronica, Finland

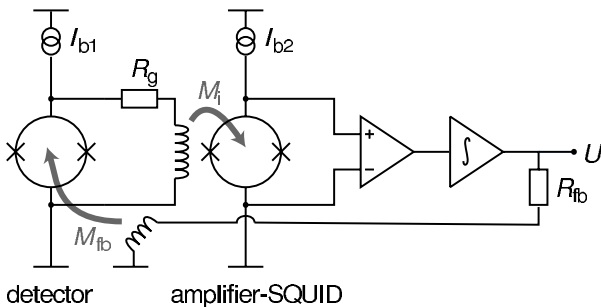


**Fig. 19.** Schematic circuit diagram of a two-stage SQUID-magnetometer

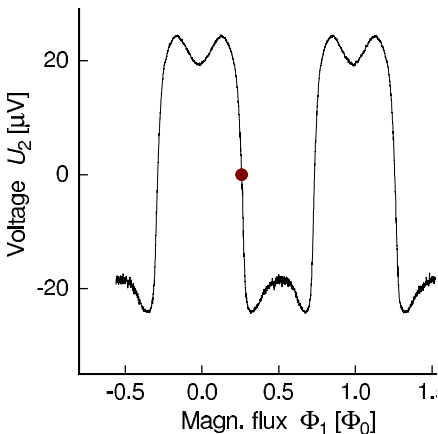


**Fig. 20.** Flux–voltage characteristics of a 2-stage SQUID configuration. The flux gain at the working point is  $G \simeq 2.7$

array impedance matched to the room temperature electronics) can be used as the amplifier. On the other hand, the critical current and voltage swing of the detector SQUID can be small without degradation of the noise performance. A dissipated power in the detector SQUID in the range of (10 pW to 100 pW) is desirable in many setups since the thermal bath of the calorimeter is often provided by the SQUID chip itself.

### 3.2 High Resolution X-ray Spectroscopy

The prototype X-ray detectors discussed in this section are based on commercially available SQUID chips [45], which are designed as first-order gradiometers having two planar loops of 50 μm diameter wound in opposition. To turn these SQUID susceptometers into magnetic calorimeters small discs of Au:Er (diameter 50 μm, thickness 25 μm, containing 300 ppm of isotopically enriched <sup>166</sup>Er) are placed by hand into each loop of the gradiometer. The

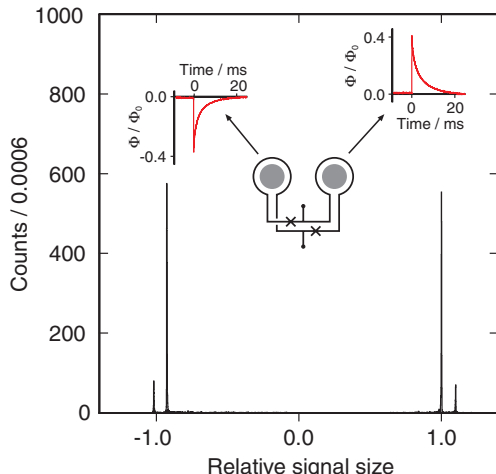


**Fig. 21.** Response of a two-pixel magnetic calorimeter with single stage SQUID readout. The *insert* is a schematic of the setup of the SQUID gradiometer with an Au:Er sensor in both loops. In addition, a single pulse from each detector pixel is shown. Also, a pulse height distribution is shown that was obtained with the two-pixel detector using a  $^{55}\text{Fe}$  source [46]

Au:Er discs are attached with a thin layer of vacuum grease to the substrate and serve in the following experiment as both paramagnetic sensor and X-ray absorber, having a quantum efficiency of effectively 100% at 6 keV.

In this gradiometer configuration fluctuations in the magnetization due to variations of the temperature of the SQUID chip are canceled. In addition, the sensor, or in other experiments the sensor/absorber combination, in each loop is a separate pixel that is read out by the same SQUID. Depending on which pixel is hit by a X-ray, a negative or a positive flux change is registered. Fig. 21 shows the resulting flux change of single 5.9 keV events into each of the two pixels along with a sketch of the gradiometer. The signal size and the thermalization time were the same for both pixels to within 10%. The detector was operated at 25 mK in a field of 2 mT. The thermalization time was roughly 10 ms due to the very weak thermal link between the sensor and the substrate via the vacuum grease. The pulse height spectrum obtained with this device using a  $^{55}\text{Fe}$  source is shown in the lower part of Fig. 21. The  $K_{\alpha}$  and  $K_{\beta}$  lines of  $^{55}\text{Mn}$  are clearly seen by both pixels. The pulse heights are plotted on a relative scale normalized to the  $K_{\alpha}$  line measured with positive flux change. The count rates of the two pixels were slightly different, because of a small difference in the collimator masks. The energy resolution at 6 keV is almost identical for the two pixels, being about 9 eV. The slight difference in resolution observed in this experiment originated from the small difference in the signal size of the two pixels.

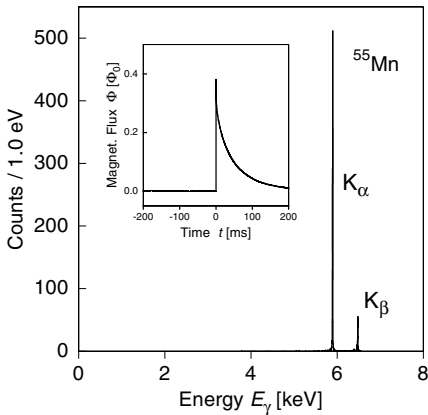


**Fig. 22.** X-ray spectrum of  $^{55}\text{Mn}$ . The *insert* shows the flux change caused by a single 5.9 keV X-ray [16]

In this experiment the magnetic field for the sensor was produced by a superconducting wire wound coil, which was surrounding the SQUID chip. Therefore the entire SQUID chip, with Josephson junctions, was located in a field of about 2 mT. In such a field the critical current of the detector SQUID is reduced from  $8\text{ }\mu\text{A}$  to about  $2\text{ }\mu\text{A}$ , which results in a voltage swing  $\Delta V$  of only  $7\text{ }\mu\text{V}$ . This, in turn, translates into a slope of the characteristic curve of  $20\text{ }\mu\text{V}/\Phi_0$ . This low value results in a high noise level of the flux modulated SQUID used in this experiment, which in part explains the instrumental resolution of only 9 eV obtained with this detector.

The situation can be considerably improved by using a 2-stage SQUID with direct readout. In such a configuration the white-noise level of the readout can be reduced while maintaining the lower bias current of the detector SQUID by employing a second SQUID in a current-sensor configuration as a low noise amplifier, as discussed in Sect. 3.1.2. Using an amplifier SQUID from the IPHT in Jena [47], the effective white-noise level of the two-stage SQUID system was lowered to  $1.1\text{ }\mu\Phi_0/\sqrt{\text{Hz}}$ . As mentioned previously, this level still effects the resolution, but it is sufficiently low that the potential of MMCs for high resolution measurements can be demonstrated. The  $^{55}\text{Mn}$  spectrum shown in Fig. 22 has been obtained with a two-stage SQUID configuration. In this experiment the X-rays were not absorbed by the magnetic sensor itself but in separate absorbers made of gold foils (each  $150\text{ }\mu\text{m} \times 150\text{ }\mu\text{m} \times 5\text{ }\mu\text{m}$ ). The quantum efficiency for 6 keV X-rays of this thickness of Au is higher than 98%. These absorber foils were joined with the Au:Er sensors using a wedge bonder. The detector was cooled to a temperature of about 35 mK and its performance tested using a  $^{55}\text{Fe}$  source. The spectrum shown in Fig. 22 contains the  $K_\alpha$  and  $K_\beta$  lines of  $^{55}\text{Mn}$ . Due to the high quantum efficiency of the gold absorber the spectrum is very clean indicating that very few events are not associated with the expected lines. The trigger level was set at about 100 eV in this experiment.

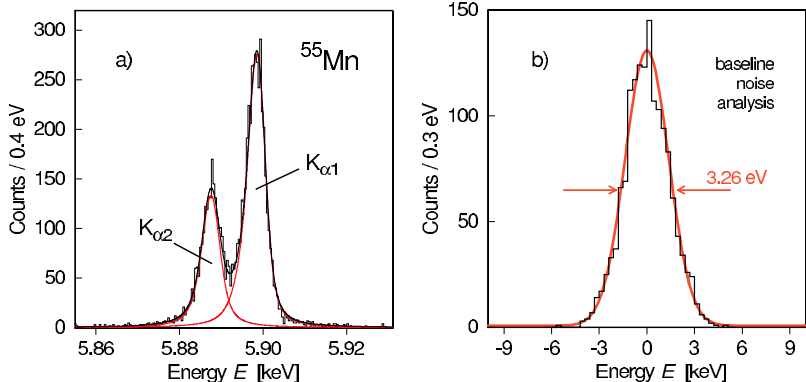


**Fig. 23.** (a)  $K_{\alpha}$  line of  $^{55}\text{Mn}$  [16]. The *solid line* represents a fit of the data taking into account the natural linewidth as determined with a crystal spectrometer [48]. (b) Baseline distribution determined from random noise traces without pulses, acquired simultaneously with the spectrum [16]

The *insert* of Fig. 22 shows an unfiltered single pulse. In the actual experiment a 10 Hz high pass and a 3 kHz low pass were used. The rise time of the signal is about 2  $\mu\text{s}$  and, as stated before, is determined by the slew rate of the SQUID system. The thermalization time is about 60 ms due to the weak coupling to the thermal bath via vacuum grease.

To determine the instrumental resolution of the detector the  $K_{\alpha}$  line was fitted with the natural line-shape as determined with a crystal spectrometer [48]. The experimental spectrum is best described with an instrumental resolution of 3.4 eV. Fig. 23a shows a blow-up of the data for the  $K_{\alpha}$  line together with the theoretical spectrum taking into account the natural and instrumental linewidths. The baseline noise in this experiment was determined to be 3.26 eV by constructing a histogram from baselines (Fig. 23b) recorded at the same time as the actual spectrum. Hence, random noise dominated the instrumental resolution of the detector.

Surprisingly, the expected noise from thermodynamic fluctuations, magnetic Johnson noise and SQUID noise can only explain this baseline width in part. About half of this width is caused by the presence of an additional noise component. The spectral function of this excess noise is proportional to  $1/f$ . Figure 24 shows the noise spectra taken at different temperatures. It is only observed with the Au:Er sensor placed in the SQUID loop. At first glance a thermally driven  $1/f$  component in a system of interacting spins might not be surprising. However, as depicted in Fig. 24, the experimentally observed  $1/f$  noise is independent of temperature over almost two orders of magnitude. This puzzling feature seems to rule out most of the straight forward explanations and further experimental studies are necessary to gain more insight into the physical origin of this phenomenon. At this point it remains

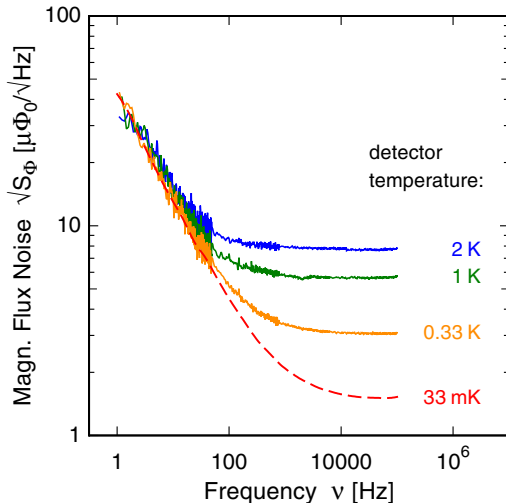


**Fig. 24.** Noise spectra of the high resolution detector taken at different temperatures. The *dashed line* shows the noise spectrum calculated from the baselines recorded while obtaining the X-ray spectrum shown in Fig. 23a

unclear, whether the excess  $1/f$  is a fundamental property of paramagnetic alloys, or just a characteristic of Au:Er, or whether it is not caused by the material itself, but a result of the complex interplay of the electronic and thermal properties of the specific readout circuit of this experiment.

The shape of the  $K_\beta$  line of  $^{55}\text{Mn}$  has been shown to depend strongly on the chemical environment in which the manganese is located [49, 50]. Using the instrumental resolution of 3.4 eV, the measured  $K_\beta$  line can be described satisfactorily. Fig. 25 shows the  $K_\beta$  line together with the theoretical spectrum of metallic manganese (red line) and of manganese oxide (blue line). The shape of the  $K_\beta$  line measured in this experiment is consistent with the fact that the source was metallic  $^{55}\text{Fe}$ .

The spectrum shown in Fig. 22 can be used to determine the non-linearity of the detector. A second order polynomial fit of the peak energies reveals that the non-linearity at 6.5 keV is  $\Delta E/E \approx 0.016$ . The non-linearity results from the temperature dependence of the heat capacity and magnetization. The observed non-linearity agrees with calculations based on the theoretical description in Sect. 2.1.

As discussed above, the thermalization time for this prototype detector was rather slow due to the weak thermal coupling via vacuum grease between the Au:Er sensor and the SQUID chip. This thermal link can be improved dramatically by attaching the sensor to a gold pad on the SQUID chip by ultrasonic bonding or by gluing it with a small amount epoxy. In this manner thermalization times as fast as 70  $\mu\text{s}$  at 50 mK have been achieved [51]. Fig. 26 shows the flux change resulting from the absorption of a 5.9 keV X-ray in a

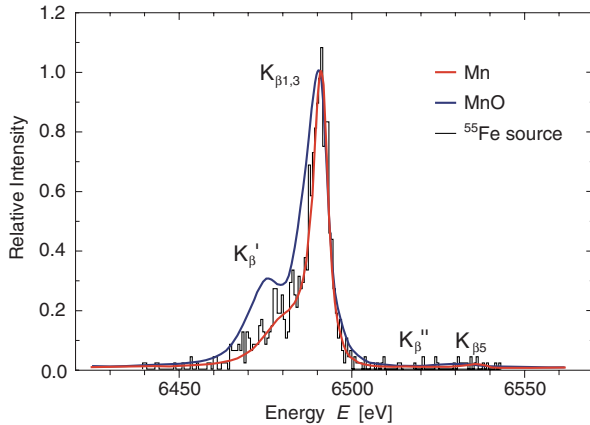


**Fig. 25.**  $K$  line of  $^{55}\text{Mn}$  [16]. The red line represents a fit of the data taking into account the natural linewidth as determined with a crystal spectrometer for metallic manganese [50]. The blue line is the corresponding fit for MnO

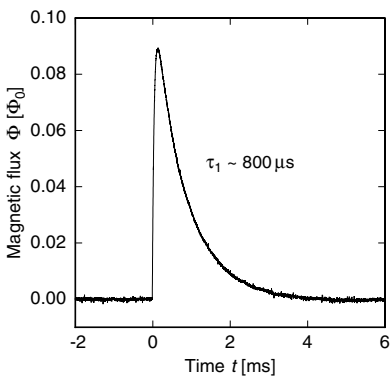


**Fig. 26.** Flux change caused by the absorption of a 5.9 keV X-ray photon at 50 mK in the absorber of a prototype detector in which the Au:Er sensor was glued with epoxy to the SQUID chip [51]

prototype detector in which the Au:Er sensor was glued with epoxy to the SQUID chip. In this case the thermalization time at 50 mK is approximately 1 ms. This is sufficiently fast for many applications.

### 3.3 Self-Inductance Magnetic Calorimeter

Recently, a MMC with planar sensor and meander-shaped pickup coil has been developed by Zink *et al.* [40]. Rather than measuring a flux change within a superconducting loop, the change in inductance of a superconducting circuit resulting from the variation of the magnetic susceptibility  $\chi$  within it is used to determine the absorption of energy, as it is discussed in Sect. 2.4.4. A paramagnetic film (Au:Er) is deposited on top of a Nb meander strip which carries a moderately large current. When a particle is absorbed, the change in permeability of the paramagnetic material modifies the self-inductance of

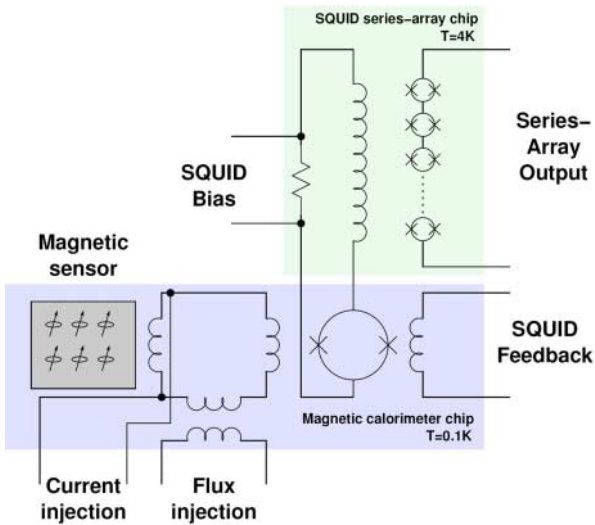


**Fig. 27.** Schematic of the circuit of a self-inductance MMC. After [40]

the meander line, leading to a change of the current through the SQUID that is inductively coupled to the pick-up circuit. A schematic of the circuit is shown in Fig. 27.

The dc current through the SQUID can be nulled by a flux applied through a separate coil (flux injector). Large magnetic fields at the SQUID can be avoided by ensuring that most of the injected current flows through the pick-up meander. The signal from the detector SQUID is fed to a series array SQUID for amplification.

An optical micrograph of a prototype self-inductance MMC pick-up meander is shown in Fig. 28a. A picture of the meander with a  $2\mu\text{m}$  Au:Er film deposited on top by sputtering is displayed in Fig. 28b.

Two different techniques for producing the Au:Er films have been explored, co-evaporation and sputtering. Surprisingly, the heat capacity of both types of films has turned out to be considerably larger than that measured for bulk samples having similar Er concentrations [40]. Also, the specific heat of the vapor-deposited films under the condition that  $g\mu_BB/k_B T \ll 1$  was observed to increase with increasing temperature, which is contrary to what is expected and found for bulk samples. It should be pointed out that in the case of the self-inductance devices the magnetic field in the paramagnetic material has a rather large distribution, and a comparison using just a mean value for the field may not be very accurate. However, the qualitative and quantitative discrepancies between the heat capacity observed for films and bulk samples are so large that the field distribution cannot explain the differences. It seems likely at this point that the properties of the films themselves are responsible for the observations. A detailed understanding, however, is lacking.

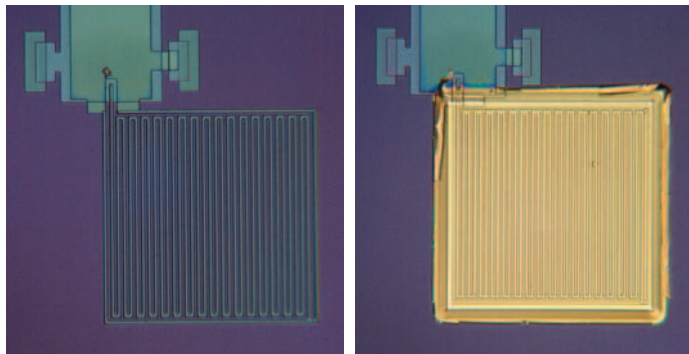


**Fig. 28.** Optical micrograph of a prototype MMC pick-up meander before (a) and after (b) deposition of a  $2\text{ }\mu\text{m}$  Au:Er film. The detector area is about  $100\text{ }\mu\text{m} \times 100\text{ }\mu\text{m}$ . Courtesy B. Zink

The performance of the prototype self-inductance MMCs were tested using a  $^{55}\text{Fe}$  source. As expected, the thermal coupling of the Au:Er to the SQUID was much stronger than that of sensors attached by vacuum grease, which were discussed in the previous section. The thermalization times range from  $200\text{ }\mu\text{s}$  to  $1\text{ ms}$  at  $50\text{ mK}$ . The energy resolution obtained with a sputtered Au:Er film containing 720 ppm of natural Er was  $115\text{ eV}$  at  $6\text{ keV}$ . Two factors are mainly responsible for the rather poor energy resolution of these early self-inductance devices, the unexplained high heat capacity of the Au:Er film and a strong  $1/f$  noise component from the electronics.

### 3.4 Activity Measurements in Metrology

Various fields of research such as environmental studies, nuclear waste management and geochronology require a better knowledge of the properties of radioisotopes having long half-lives or emission at low-energy. The difficulty in obtaining such information is mainly due to source self-absorption and to the dramatic decrease of detection efficiency of conventional detectors for low-energy photons and electrons. Cryogenic detectors have the potential to overcome such problems in that a detection efficiency of close to 100% is possible in the range from a few eV up to  $10\text{ keV}$  for both X-rays and electrons.

Magnetic calorimeters have been used to demonstrate the potential of cryogenic detectors for absolute activity measurements [52, 53]. The goal of these investigations was to measure the relative activity of  $^{55}\text{Fe}$ , decaying by electron capture from the  $K$ ,  $L$  and  $M$  shells. Theoretical calculations predict that the probabilities for capture occurring from the  $K$ ,  $L$  and  $M$  shells of  $^{55}\text{Fe}$  should be 88.5%, 9.8% and 1.7%, respectively. The  $L$  captures arise almost exclusively the  $L1$  sub-shell. The probability of capture from the  $L2$  and  $L3$  sub-shells is negligible for practical measurements. The relative probabilities

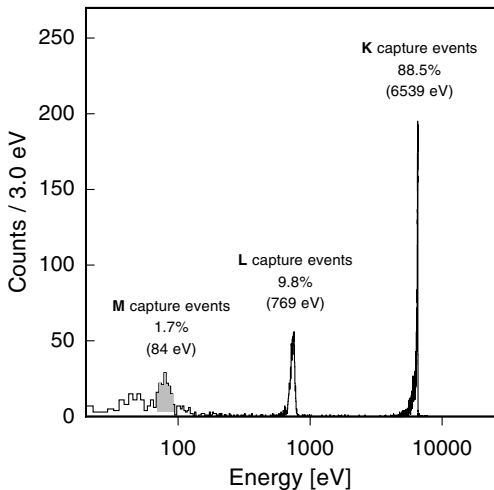


**Fig. 29.** Spectrum of a  $^{55}\text{Fe}$  source fully encapsulated in a gold absorber [53]. The insert shows a schematic of the absorber/sensor arrangement

for capture from the five  $M$  sub-shells cannot be calculated reliably and are unknown experimentally. The rearrangement of the shells after the capture process is accompanied by the emission of a cascade of Auger electrons and X-rays. The total energy released in each cascade equals the binding energy of the captured electron. Therefore, if all emitted electrons and X-rays of a cascade are detected within the detector, one line is to be expected at 6.539 keV for  $K$  capture events, one line at 769 eV for  $L$  capture, and at least one line at 84 eV for  $M$  capture.

The main difficulty in performing an experiment to measure the relative probabilities is to detect the several lines at very different energies and activities with close to 100% quantum efficiency. This was achieved by enclosing the  $^{55}\text{Fe}$  source in a gold absorber so as to record all events emitted in a  $4\pi$  solid angle. A drop of  $^{55}\text{Fe}$  in solution was deposited onto a 30  $\mu\text{m}$  thick gold foil. During the drying of the drop, small crystals formed on the surface of the gold. The foil was then folded and re-laminated to a final thickness of about 20  $\mu\text{m}$ . A rectangular piece of foil,  $\sim 75 \mu\text{m} \times 150 \mu\text{m}$ , fully containing the source, was cut out as the detector absorber. The effective absorber thickness was about 10  $\mu\text{m}$  resulting in a quantum efficiency of over 99.9% for 6.5 keV X-rays. The absorber was then attached by ultrasonic welding to a Au:Er sensor disc (60  $\mu\text{m}$  diameter, 20  $\mu\text{m}$  thick) containing about 900 ppm of enriched Er. The absorber/sensor combination was placed in a SQUID loop and fixed using a small amount of vacuum grease. Because the 60  $\mu\text{m}$  diameter of the sensor exceeded the 50  $\mu\text{m}$  diameter of the SQUID loop, the signal size was somewhat reduced.

The detector was operated at a temperature of 25 mK in a magnetic field of about 3 mT. Figure 29 shows a spectrum on a logarithmic energy scale that was obtained by counting for about 6 hours at a count rate of

about 0.5/s. Three distinct peaks are observed, as expected. This is the first time all three capture lines have been seen in a single spectrum. To analyze the spectrum quantitatively, the  $K$ -line was used to adjust the energy scale, assuming that the detector is approximately linear up to this energy.<sup>15</sup> The measured energies for the  $M$  and  $L$  lines are in very good agreement with the theoretical values. The experimentally determined relative activities of the  $K$ ,  $L$  and  $M$  lines are 88.2%, 10.3% and 1.5%, respectively. Within the accuracy of the experiment these values are in agreement with the theoretical calculations.

The small tails observed on the low-energy side of the  $K$  and  $L$  lines most likely originate from the absorption of Auger electrons within the source crystals, the energy not being fully transferred to the gold during the duration of a typical pulse signal. It should be possible to avoid this effect by electrolytic deposition of the source material. The energy resolution of  $\Delta E \approx 16$  eV (determined from baseline noise) and the counting statistics at low energies were not sufficient to resolve a possible  $M$  shell substructure. The energy resolution was poorer than the best detector discussed in Sect. 3.2 for several reasons. The sensor/absorber heat capacity was large, the size of the sensor was not appropriate for the SQUID loop, and temperature fluctuations introduced noise because the calorimeter was not operated in a gradiometer configuration. The background at low energies is mainly the result of radioactivity in the materials surrounding the detector. We expect, that the precision of this experiment can be increased significantly by raising the activity of the source, lowering the radioactive background and improving the energy resolution of the calorimeter.

### 3.5 Gamma-Ray Spectroscopy

Because of the weak dependence of the sensitivity of a magnetic calorimeter on the absorber heat capacity, this type of device can be considered for applications requiring a large absorber mass, such as needed in high-resolution gamma-ray spectroscopy. Indeed, a prototype of a MMC detector for gamma rays has already been studied [54, 55, 56].

The spectrum of a  $^{57}\text{Co}$  source as measured with a MMC detector is shown in Fig. 30a. In addition to the lines at 122 keV and 136 keV, several lines at lower energies are observed, which are due to the escape of X-ray fluorescence photons of Au. The additional broad low-count background is mostly due to electron escape processes and to gamma rays that deposit only part of their energy by Compton scattering. Note that the 14 keV line also expected for  $^{57}\text{Co}$  was not observed in this experiment because of absorption in the material encapsulating the source.

---

<sup>15</sup> Given the large heat capacity of the absorber/sensor package this should be a good approximation

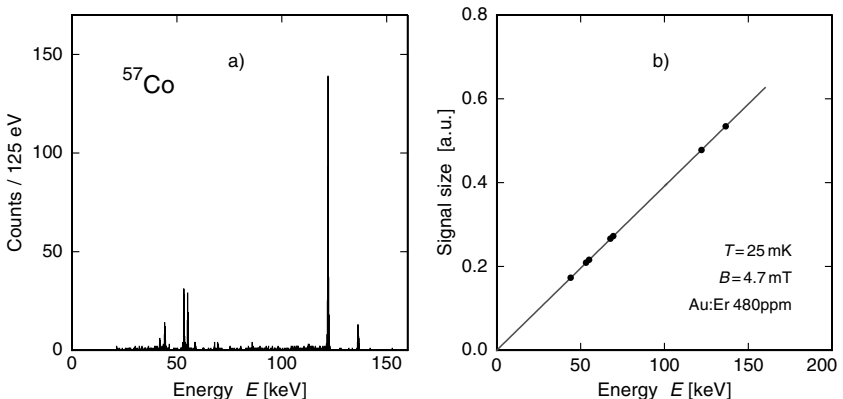


**Fig. 30.** (a) Spectrum of a  $^{57}\text{Co}$  source measured with a prototype MMC detector operated at  $T = 25\text{ mK}$  and in a magnetic field of  $B = 4.7\text{ mT}$  [56]. (b) Measured signal size versus the energy of the expected lines in the  $^{57}\text{Co}$  spectrum shown in (a) [56]

In this experiment a gold cylinder ( $360\text{ }\mu\text{m}$  diameter,  $500\text{ }\mu\text{m}$  long) containing  $480\text{ ppm}$  of natural erbium was used both as absorber and sensor. The quantum efficiency for detecting  $122\text{ keV}$  gamma rays hitting directly the  $500\text{ }\mu\text{m}$  thick gold is approximately  $80\%$ . At the operating conditions of  $T = 25\text{ mK}$  and  $B = 4.7\text{ mT}$  the heat capacity of the Au:Er cylinder is approximately  $4 \times 10^{-9}\text{ J/K}$ . This is more than three orders of magnitude higher than the heat capacity of the high resolution X-ray detectors discussed in Sect. 3.2.

Given the large heat capacity of the detector the absorption of a single  $122\text{ keV}$  photon causes a temperature change in the sensor of about  $5\text{ }\mu\text{K}$ , which corresponds to a relative change of  $\delta T/T = 2 \times 10^{-4}$  at  $25\text{ mK}$ . This implies that the detector exhibits a high degree of linearity up to the maximum energy recorded in this experiment. This is demonstrated in a plot of the measured pulse heights of the  $^{57}\text{Co}$  gamma ray lines and the known escape peaks of Au as a function of their energies, as shown in Fig. 31b. No deviation from linearity outside of the experimental error of  $5 \times 10^{-4}$  was found. The calculated non-linearity is an order of magnitude smaller than this.

The Au:Er cylinder was located inside a 32-turn coil of superconducting wire, which was connected to the input coil of a commercial, flux-modulated SQUID to form a superconducting flux transformer. Since the Au sensor was spot-welded to a large block of copper, which served as the thermal reservoir, the thermalization time was approximately  $200\text{ }\mu\text{m}$ . A signal produced by a single  $122\text{ keV}$  gamma ray is shown in Fig. 30a.

The energy resolution determined by the FWHM of the line at  $122\text{ keV}$  is  $340\text{ eV}$ . The two main broadening mechanisms of approximately equal im-

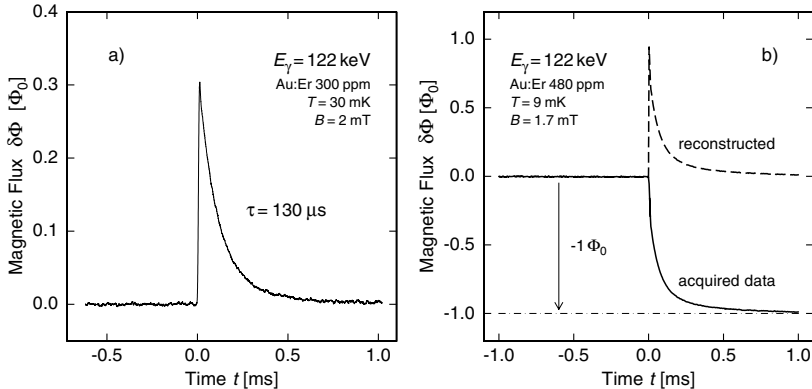


**Fig. 31.** (a) Signal resulting from the absorption of a single 122 keV gamma ray. (b) The *solid line* shows a single 122 keV event with  $\Phi < 0.5 \Phi_0$  as recorded with a SQUID electronics with a slew rate of  $20 \Phi_0/\text{ms}$ . The *dashed line* shows the reconstructed pulse after recalculation of the working point [57]

portance are random noise at low frequencies, as determined from baseline traces, and insufficient temperature stability of the cryostat. The incoherent sum of the noise from these two sources accounts almost entirely for the observed energy resolution.

Due to the use of a flux transformer the sensitivity of the detector was somewhat reduced. However, this was not an important limitation in this experiment because the slew rate ( $20 \Phi_0/\text{ms}$ ) of the SQUID electronics restricted the size of the flux changes to about  $0.5 \Phi_0$ . With larger signals, flux jumps occurred, which prohibited an accurate determination of the total flux change. Under optimal conditions the signal size from the 122 keV gamma ray was considerably larger than  $\Phi_0$ . A typical event with flux jump is shown in Fig. 31b.

The prototype gamma ray detector discussed in this section was not optimized for a specific application, but was used to demonstrate the potential of MMCs in gamma ray detection. An optimized detector would include an absorber. To give a specific example of the capabilities of an optimized detector we assume an absorber with a heat capacity of  $C_a = 1 \text{ nJ/K}$ , a value which is similar to that of the prototype detector and corresponds roughly to a gold absorber of  $(650 \mu\text{m})^3$ . In addition, we assume an operational temperature of  $T = 50 \text{ mK}$  and relaxation times of  $\tau_0 = 1 \mu\text{s}$  and  $\tau_1 = 1 \text{ ms}$  as in the example discussed in Sect. 3.2. Such a detector is expected to have an intrinsic energy resolution of about  $\Delta E_{\text{FWHM}} = 60 \text{ eV}$ .

## 4 Summary and Outlook

We have discussed the basic thermodynamic properties of metallic magnetic calorimeters and the paramagnetic sensor material. Furthermore, a model has been presented which allows for the optimization of the signal to SQUID noise ratio for different detector geometries. Based on these findings, the principle limitations of the energy resolution of metallic magnetic calorimeters have been discussed and guidelines for the design of MMCs with optimized energy resolution have been derived. Results obtained with several prototype detectors have been presented.

Magnetic calorimeters have reached a level of development at which many interesting applications are conceivable. However, several important issues will need to be addressed in the further development of MMC detectors: 1. Suitable techniques are required for the micro-fabrication of fully integrated MMC detectors. In this context it will be necessary to study the magnetic properties of thin paramagnetic films produced by sputtering or vapor deposition techniques. 2. The origin of the unexplained  $1/f$  excess noise needs to be investigated. If this noise contribution cannot be sufficiently reduced, it will likely be a limiting factor in the energy resolution of MMCs. To investigate the origin of  $1/f$  noise, the properties of temperature sensors based on other paramagnetic materials need to be studied. 3. Advanced readout schemes including multiplexing techniques have to be developed to allow for large MMC arrays. Although the underlying physics of MMC and TES detectors is quite different it seems conceivable that the development of SQUID based multiplexing schemes for MMCs can benefit to a large extent from the enormous progress that has been made in multiplexing TES detectors.

These and many other aspects of magnetic calorimeters have to be investigated to make use of the full potential of this kind of cryogenic detector.

## Acknowledgements

We would like to thank S.R. Bandler, J. Beyer, H.F. Braun, A. Burck, T. Daniyarov, D. Drung, H. Eguchi, S. Hunklinger, K.D. Irwin, Y.-H. Kim, E. Leblanc, M. Linck, M. Loidl, H.-G. Meyer, H. Rotzinger, J. Schönenfeld, M.v. Schickfus, R. Stoltz, V. Zakosarenko, and B.L. Zink for many useful and stimulating discussions.

## References

- [1] T.C.P. Chui, D.R. Swanson, M.J. Adriaans, J.A. Nissen, J.A. Lipa: Phys. Rev. Lett. **69**, 3005 (1992). [151](#)
- [2] P. Day, I. Hahn, T.C.P. Chui, A.W. Harter, D. Rowe, J.A. Lipa: J. Low Temp. Phys. **107**, 1 (1997). [151](#)
- [3] P.B. Welander, I. Hahn: Rev. Sci. Instrum. **72**, 3600 (2001). [151](#)

- [4] B.J. Klemme, M.J. Adriaans, P.K. Day, D.A. Sergatskov, T. L. Aselage, R.V. Duncan: *J. Low Temp. Phys.* **116**, 133 (1999). [151](#)
- [5] W. Seidel: Diploma Thesis, Technische Universität München 1986, unpublished. [151](#)
- [6] M. Bühler, E. Umlauf: *Europhys. Lett.* **5**, 297 (1988) [152](#), [154](#)
- [7] E. Umlauf, M. Bühler: *Proc. Symp. Supercon. and Low-Temp. Detectors*, eds. G. Waysand and G. Chardin, 309 (North-Holland, Amsterdam 1989). [152](#), [154](#)
- [8] E. Umlauf, M. Bühler: *Proc. Int. Workshop on Low Temperature Detectors for Neutrino and Dark Matter (LTD4)*, eds. N.E. Booth and G.L. Salmon, 229 (Editors Frontieres, Gir-sur-Yvette 1991). [152](#), [154](#)
- [9] M. Bühler, E. Umlauf: *Proc. Int. Workshop on Low Temperature Detectors for Neutrino and Dark Matter (LTD4)*, eds. N.E. Booth and G.L. Salmon, 237 (Editors Frontieres, Gir-sur-Yvette 1991). [152](#), [154](#)
- [10] E. Umlauf, M. Bühler: *Proc. SPIE Conference* **1743**, 391 (San Diego 1992). [152](#), [154](#)
- [11] M. Bühler, E. Umlauf, D. Drung, H. Koch: *Proc. 5th Int. Conf. on Supercon. Quantum Devices and their Application*, eds. H. Koch and H. Lübbig (Springer, Heidelberg 1992) [152](#), [154](#)
- [12] M. Bühler, T. Fausch, E. Umlauf: *Europhys. Lett.* **23**, 529 (1993) [152](#), [154](#)
- [13] E. Umlauf, M. Bühler, T. Fausch: *Proc. Phonon Scattering in Condensed Matter VII*, eds. M. Meissner and R.O. Pohl, (Springer, Berlin 1993). [152](#), [154](#)
- [14] T. Fausch, M. Bühler, E. Umlauf: *J. Low Temp. Phys.* **93**, 703 (1993). [152](#), [154](#)
- [15] S.R. Bandler, C. Enss, R.E. Lanou, H.J. Maris, T. More, F.S. Porter, and G.M. Seidel: *J. Low Temp. Phys.* **93**, 709 (1993). [152](#), [154](#)
- [16] A. Fleischmann, M. Linck, T. Daniyarov, H. Rotzinger, C. Enss, G.M. Seidel: *Nucl. Instr. Meth.* **A520**, 27 (2004). [152](#), [204](#), [205](#), [207](#)
- [17] A.H. Cooke, H.J. Duffus, W.P. Wolf: *Phil. Mag.* **44**, 623 (1953). [153](#)
- [18] P.G. de Gennes: *Comp. Rend. Acad. Sci.* **247**, 1836 (1966). [154](#)
- [19] M. Bühler, E. Umlauf, K. Winzer: *Nucl. Inst. Meth. Phys. A* **370**, 621 (1996). [155](#)
- [20] M. Böe: Diploma thesis, Universität Heidelberg 1998, unpublished. [155](#)
- [21] C. Enss, A. Fleischmann, T. Görlich, Y.H. Kim, G.M. Seidel, H.F. Braun: *AIP Conference Proceedings* **605**, 71 (2002). [155](#)
- [22] G. Williams and L.L. Hirst: *Phys. Rev.* **185**, 407 (1969). [155](#)
- [23] L.J. Tao, D. Davidov, R. Orbach, and E.P. Chock: *Phys. Rev. B* **4**, 5 (1971). [155](#), [163](#)
- [24] M.E. Sjöstrand and G. Seidel: *Phys. Rev. B* **11**, 3292 (1975). [155](#), [161](#)
- [25] D. Davidov, C. Rettori, A. Dixon, K. Baberschke, E.P. Chock, and R. Orbach: *Phys. Rev. B* **8**, 3563 (1973). [155](#)
- [26] W. Hahn, M. Loewenhaupt and B. Frick: *Physica B* **180&181**, 1698 (2000). [155](#)
- [27] T. Herrmannsdörfer, R. König and C. Enss: *Physica B* **284-288**, 1698 (2000). [155](#)
- [28] A. Fleischmann: PhD Thesis, Universität Heidelberg, (2003). [155](#), [156](#), [177](#)
- [29] L.R. Walker and R.E. Walsted: *Phys. Rev. Lett.* **38**, 514 (1977). [158](#)

- [30] L.R. Walker and R.E. Walsted: Phys. Rev. B**22**, 3816 (1980). **158**
- [31] S. Arajs and G.R. Dunmyre: J. Less-Common Metals **10**, 220 (1966); see also L. R. Edwards and S. Levgold, J. Appl. Phys. **39**, 3250 (1968). **158, 187**
- [32] C. Enss, A. Fleischmann, K. Horst, J. Schönenfeld, J. Sollner, J.S. Adams, Y.H. Huang, Y.H. Kim, G.M. Seidel: J. Low Temp. Phys. **121**, 137 (2000). **159, 160, 164, 174, 177, 178, 187**
- [33] A. Fleischmann, C. Enss, J. Schönenfeld, J. Sollner, K. Horst, J.S. Adams, Y.H. Kim, G.M. Seidel, S.R. Bandler: Nucl. Instr. Meth. A**444**, 100 (2000) **163**
- [34] K. Konzelmann, G. Majer, and A. Seeger: Z. Naturforsch. A**51**, 506 (1996). **163**
- [35] M. Minier and C. Minier: Phys. Rev. B**22**, 21 (1980). **163**
- [36] B. Perscheid, H. Büchsler, M. Forker: Phys. Rev. B**14**, 4803 (1976). **163**
- [37] J. Souletie, R. Tournier: J. Low Temp. Phys. **1**, 95 (1969). **163**
- [38] *The SQUID Handbook* edited by J. Clarke and A.I. Braginski, ISBN 3-527-40229-2, Wiley-VCH (2004). **168, 169**
- [39] H. Seppä, M. Kiviranta and L. Grönberg: IEEE Tran. Appl. Supercond. **5**, 3248, (1995). **171**
- [40] B.L. Zink, K.D. Irwin, G.C. Hilton, D.P. Pappas, J.N. Ullom, M.E. Huber: Nucl. Instr. Meth. B **520**, 52 (2003). **173, 207, 208**
- [41] T. Varpula and T. Poutanen: J. Appl. Phys. **55**, 4015 (1984), see also B.J. Roth, J. Appl. Phys. **83**, 635 (1998). **187**
- [42] D.T. Gillespie: J. Appl. Phys. **83**, 3118 (1998). **187**
- [43] J.T. Harding and J.E. Zimmerman: Phys. Lett. A **27**, 670 (1968). **187**
- [44] A. Fleischmann: Adv. Solid State Phys. **41**, 577 (2001) **196**
- [45] M.B. Ketchen, D.D. Awschalom, W.J. Gallagher, A.W. Kleinsasser, R.L. Sandstrom, J.B. Rosen, B. Bumble: IEEE Trans. Mag. **25**, 1212 (1989). **202**
- [46] A. Fleischmann, T. Daniyarov, H. Rotzinger, C. Enss, G.M. Seidel: Physica B **329-333**, 1594 (2003). **203**
- [47] M.A. Espy, A.N. Matlachov, R.H. Kraus, and J.B. Betts: IEEE Tran. Appl. Supercond. **13**, 731, (2003). **204**
- [48] G. Hölzer, M. Fritsch, M. Deutsch, J. Hartwig, and E. Förster: Phys. Rev. A **56**, 4554 (1997). **205**
- [49] K. Tsutsumi, H. Nakamoi, K. Ichikawa: Phys. Rev. B **13**, 929 (1976). **206**
- [50] K. Sakurai, H. Eba: Nucl. Instr. Meth. B **199**, 391 (2003). **206, 207**
- [51] T. Daniyarov, C. Enss, A. Fleischmann, M. Linck, H. Rotzinger, G.M. Seidel: to be published. **206, 207**
- [52] M. Loidl, E. Leblanc, J. Bouchard, T. Branger, N. Coron, J. Leblanc, P. de Marcillac, H. Rotzinger, T. Daniyarov, M. Linck, A. Fleischmann, C. Enss: Appl. Rad. Isotopes **60**, 363 (2004). **209**
- [53] M. Loidl, E. Leblanc, T. Branger, H. Rotzinger, T. Daniyarov, M. Linck, A. Fleischmann, C. Enss: Nucl. Instr. Meth. B **520**, 73 (2004). **209, 210**
- [54] S.R. Bandler, C. Enss, J. Schönenfeld, L. Siebert, G.M. Seidel, R. Weis: *Proceedings of the 7th International Workshop on Low Temperature Detectors LTD-7*, (S. Cooper ed.), 145 (1997). **211**
- [55] J.S. Adams, S.R. Bandler, C. Enss, A. Fleischmann, Y.H. Huang, H.Y. Kim, J. Schönenfeld, G.M. Seidel, R. Weis: *Proceedings of the International Symposium on Optical Science and Technology (SPIE)* **4140**, 445 (2001). **211**

- [56] A. Fleischmann, C. Enss, J. Schönefeld, J. Sollner, K. Horst, J.S. Adams, Y.H. Kim, G.M. Seidel, S.R. Bandler: Nucl. Instr. and Meth. A **444**, 211 (2000).  
[211](#), [212](#)
- [57] C. Enss: AIP Conference Proceedings **605**, 5 (2002). [213](#)

# Quantum Giaever Detectors: STJ's

P. Lerch and A. Zehnder

Paul Scherrer Institute, 5232 Villingen, Switzerland

[alex.zehnder@psi.ch](mailto:alex.zehnder@psi.ch)

**Abstract.** Solid state detectors rely on the interaction of energy with matter. The absorbed energy from for example, a charged particle, a photon or a phonon is degraded and shared among a number of electronic, thermal and/or magnetic excitations. Quantum Giaever detectors are usually called super-conducting tunneling junction devices, in short STJ's by the community. In these devices, energy is absorbed in a metallic electrode in its super-conducting state. The energy breaks Cooper pairs and an "excess" number of electronic excitations, called quasi-particles is created. The number of these quasi-particles is a measure of the energy absorbed in the electrode which can be determined in a tunneling experiment. The sensitivity is sufficient to perform 1 eV photon counting.

In this review we describe the physical processes governing the *creation, loss* and *collection* of quasi-particles in an STJ used as photon sensor. We shall first emphasize the importance of device parameters on the quasi-particle *creation* efficiency. In the second part we focus on the physical processes and device parameters affecting the quasi-particle *collection* efficiency. Intrinsic and experimental noise sources are discussed in separate sections. Finally, we attempt to browse a portrait of the line of development followed in different laboratories during the last decade or so.

## 1 Introduction

In 1968 *Wood* and *White* [1] used  $\alpha$ -particles irradiate super-conducting tunneling junctions (STJ) fabricated with Sn. The junctions were operated in the Giaever mode [2]. They observed current pulses and argued the signal to be the consequence of Cooper pair break-up in the films. It was soon realized that this device concept could not be easily scaled-up to produce sensors with large absorber volumes. Spectral response was measured by *Kurakado* and *Mazaki* in 1980 [3] who also irradiated a Sn-device with  $\alpha$ -particles and began to develop a more accurate picture of the physics within the device. The  $\alpha$ -particle transfers its energy to hot electrons and phonons, scattering processes degrade the energy further until a significant fraction is carried by non-thermal quasi-particles which are created upon Cooper pair breaking.

The breaking of a Cooper pair is a process that requires a minimum of energy  $2\epsilon$  and creates 2 excited electronic states called quasi-particles. The number  $N_0$  of quasi-particles is proportional to the amount of absorbed energy so that  $N_0 = E_0/\epsilon$ . Ideally,  $\epsilon = \Delta$ , the energy gap of the superconducting

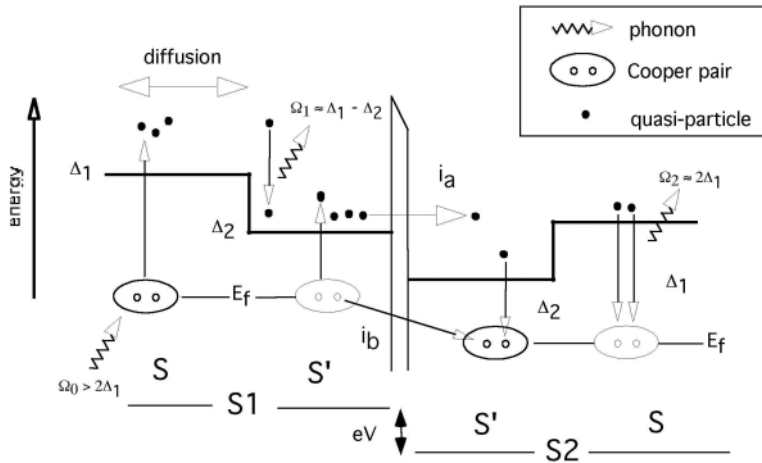


**Fig. 1.** Main processes taking place in a S1–I–S2 superconducting tunneling junction. Each electrode S is a bi-layer made with two superconductors S( $\Delta_1$ ), S'( $\Delta_2$ ) with  $\Delta_1 > \Delta_2$ . A phonon of energy  $\Omega_0$  breaks a Cooper pair in S. A fraction of excess quasi-particles diffuse to S' where they relax to a lower energy state by releasing phonons with energies  $\Omega_1$ . The inverse process is the excitation of quasi-particles by phonon absorption. Direct tunneling  $I_a$  and Cooper pair mediated back-tunneling  $I_b$  are the dominant charge transfer processes. A quasi-particle that has tunneled once has gained energy eV. Quasi-particle recombination into a Cooper pair release a phonon of energy  $\Omega_2$ , sketched here in S2. Phonons can transfer through the barrier from one electrode to the other or be lost in the substrate. The gap profile is a sketch only

absorber. It is important to realize that these quasi-particles come in *excess* of a thermal background  $N_{\text{th}} \propto \exp(-1.76T_c/T)$ . To observe a signal  $N_0$  must be larger than  $N_{\text{th}}$ , thus the temperature must be smaller than  $T/T_c \approx 0.1$ . To measure the energy  $E_0$ , one needs to measure the number of electronic excitations  $N_0$ . Several detection schemes allow to measure changes in the quasi-particle distribution. In the following we will focus on those devices that use quasi-particle tunneling in order to measure the charge  $Q_0 = N_0e$  which is proportional to  $E_0$ .

Tunneling devices are microfabricated with two superconducting electrodes separated by a thin (nm) electrical insulating barrier to form a superconducting tunneling junction (STJ).

A STJ offers two possibilities for electrical transport across the barrier. First, Cooper pairs can proceed through the barrier without dissipation. This current has a maximum value,  $I_J(T)$ , and is the manifestation of the well known *dc* Josephson effect [4]. The second way, uses the so-called quasi-particle branch of the current-voltage curve. A temperature dependent tunneling current flows and conditions must be established in order for this current to be smaller than  $I_J$  and the current excursions we are interested

in. In order to be able to measure the quasi-particle current, the supercurrent needs to be suppressed. This can be done with a well defined external magnetic field [5] applied parallel to the plane of the tunnel barrier. Excess quasi-particles in the superconductor can tunnel from either electrode to the other. The application of a potential difference  $V$  across the barrier favors tunneling in one direction because excited states in S1 face empty states across the barrier in S2. At constant bias voltage, thermal background and *excess* quasi-particle currents are superposed. After the absorption of energy, quasi-particles are generated within a nsec. This population recombines into Cooper pairs exponentially on a much longer time scale because the thermal background is low,  $T \approx 0.1T_c$ . The *excess* tunneling current can thus be integrated  $Q_m = \int I(t) dt \propto N_0$ .

In order to enhance the measured electrical signal  $Q_m$  quasi-particles need to be confined [6]. This can be achieved with a device configuration as shown in Fig. 1. Each electrode of this device is a bi-layer fabricated with superconductors of different gaps,  $\Delta_2 < \Delta_1$ , in good electrical contact. The proximity effect between the two layers [7] modifies their superconducting properties. Quasi-particles diffusing into a region influenced by proximity effect face a large number of available low energy states into which they can relax by the emission of a phonon. This process is illustrated as a  $\Omega_1$  phonon in Fig. 1. Hence a region like S' acts as a quasi-particle trap. The “geometrical confinement” on both sides of the tunneling barrier enhances the tunneling probability and another mechanism called back-tunneling can be exploited to further enhance the collected signal. Back-tunneling is a Cooper pair mediated process [8] in which a quasi-particle (which is a quantum superposition of electron and hole [9]) is transferred against the potential drop, whereas electron transport proceeds along the potential difference. Back-tunneling results in true signal gain and allows the electrical signal to be larger than electronics noise. This unique feature among cryogenic sensors allows for single photon spectrometry in the energy range of visible light.

It is important to realize that the gap profile as sketched in Fig. 1 is widely used in the literature and has not the same signification than the order parameter. This is often a source of confusion. We will discuss this in more detail in Sect. 2.

Early assumptions for Sn and Pb as absorber materials predicted  $\epsilon = 1.74\Delta$  [10, 11]. This value is about 3 decades smaller than the energy required to generate a Frenkel (electron–hole) pair in a semi-conductor. For Ta,  $\epsilon = 1.2$  meV (Table 1) so that the intrinsic responsivity [12] to the deposition of energy  $E_0$  is of the order of 850 “electrons”/eV (in Si, the intrinsic responsivity is 0.3 “electrons”/eV only). The precision of this measurement is limited by the statistical fluctuations, the variance, of the number of charge carriers,  $\sigma_{N_0} = \delta N_0 = \sqrt{FE_0/\epsilon}$ . Thus, the intrinsic energy resolution FWHM is given by

$$\delta E_0 = 2.35 \sqrt{\epsilon F E_0} \quad (1)$$

where  $F \approx 0.1 - 0.2$  is the Fano factor [13] accounting for independent processes. Using (1) we obtain  $\delta E_0 \approx 80\text{ meV}$  and  $1\text{ eV}$  at  $E_0 \approx 1\text{ eV}$  and  $1\text{ keV}$ , respectively. The fact that in practice  $\epsilon$  is larger than  $\Delta$  indicates that only a fraction of the absorbed energy is transferred into electronic excitations and collected.

Following early experiments advances were made in 1986 when single X-ray photons were detected by *Twerenbold et al.* [14] and *Kraus et al.* [15] independently. They measured an energy resolution of  $\approx 100\text{ eV}$  from the pulse height spectrum of a thin film  $\text{Sn}/\text{SnO}_x/\text{Sn}$  device irradiated with the  $5.9$  and  $6.4\text{ keV}$  lines emitted by a radioactive  $^{55}\text{Fe}$  source.

**Table 1.** Properties of some elemental superconductors.  $\xi_0 = \sqrt{\xi l}$  where  $\xi = 0.18\hbar v_F/k_B T_c$  is the Pippard coherence length and  $l$  a typical value for the electronic mean free path. The quantity  $\lambda$  is the London penetration depth

	$T_c$ (K)	$\Delta(0)$ (meV)	$B_0$ (G)	$\xi_0$ (nm)	$\lambda$ (nm)	
Al	1.14	0.17	105	1 600	$\pm 584$	68 $\pm 35$
Ti	0.39	0.06	100			
V	5.38	0.79	1 420			$44.5 \pm 7$
Zn	0.875	0.12	53			
Ga	1.09	0.16	51	120	$\pm 10$	
Nb	9.5	1.47	1 980	44		40 $\pm 1.9$
Mo	0.92	0.14	95			
In	3.4	0.53	293	60	$\pm 11$	268 $\pm 25$
Sn	3.72	0.58	309	58	$\pm 12$	190 $\pm 72$
Ta	4.48	0.7	830	92.5		34.5
Pb	7.19	1.36	803	47.4	$\pm 6.8$	89 $\pm 32$
La	6.0	0.83	1 100			
Re	1.4	0.21	198			
Hg	4.15	0.82	412	73		
NbN	14	2.13	67		3.09 $\pm 1.5$	
Ir	0.11	0.02				
Hf	0.13	0.02				

Lithography permitted definition of narrower contact leads which helped to confine the quasi-particles near the tunneling region, the signal amplitude increased, and the spectroscopic performance improved ( $48\text{ eV}$  at  $6\text{ keV}$ ) [16]. A weak nonlinear response in energy was observed [17] in Sn and the importance of quasi-particle diffusion was recognized [16, 18]. Sn devices did not cycle well between operation and room temperature. In the field of SQUID instrumentation for instance, the Nb-based thin film technology was already established and, with the fabrication of low leakage  $\text{Nb}/\text{AlO}_x/\text{Nb}$  devices the results obtained with Sn junctions were reproduced and improved [19, 20, 21]. The charge amplification concept [8] proved to be applicable [22] as well. Interestingly, the first generation of Nb-based devices demonstrated potential

as X-ray spectrometers and at the same time their use in the visible part of the electromagnetic spectrum was envisaged [23]. The potential for single photon spectroscopy in the visible was first demonstrated by *Rando et al.* [24]. Since then, progress has been significant. Small arrays of some tens of pixels are used as technology demonstrators in optical astronomy [25], STJ-sensors are used in mass spectrometers [26, 27, 28, 29], fluorescence X-ray absorption spectroscopy work is carried out with small arrays of STJs at synchrotron beam-lines [30].

The theoretical limit given by (1) has, despite extensive work, never been reached. Devices exhibit non-homogeneous response to the deposition of energy and additional noise sources were identified. Best results are 22 eV at 6 keV for a Ta-based device irradiated through a pin-hole [31], 21 eV for a  $280 \times 280 \mu\text{m}^2$  large Nb-based device fully irradiated with 2.6 keV photons [32], 12 eV at 6 keV for a  $100 \times 100 \mu\text{m}^2$  large Al junction [33], and 13 eV at 6 keV for the same type of device microfabricated on a membrane and acoustically coupled to a lead absorber [34]. A resolution of 13 eV at 6 keV was measured over a  $20 \times 100 \mu\text{m}^2$  large Ta absorber read out by 2 Al devices [35]. At energy below  $\approx 1$  keV the resolution in energy is close to the limit placed by creation and tunneling noise statistics [36, 37].

In the following we shall describe the main processes leading to charge *creation, loss* and *collection* in thin film devices. Useful review work is available to the reader in references [38, 39, 40]. Most of the results are spread through the numerous contributions published during the series of workshops dedicated to the development of low temperature detectors [41]. Throughout this work we first discuss the “established picture” and follow with a presentation of new ideas when this applies. We limit the discussion to devices using the quasi-particle tunneling detection mechanism and present briefly some alternatives in the outlook.

## 2 Theoretical Background

### 2.1 Charge Creation

It is generally accepted that the cascade that converts the energy of the original photo-electron into a population of non-equilibrium phonons and quasi-particles occurs in three distinct stages. In the first phase the down-conversion of the energy  $E_0$  carried by the photo-electron is dominated by the strong electron–electron interactions with characteristic time scale  $\tau_{ee}$  in the order of femtoseconds. The energy level  $E_1$  describing the end of this phase is subject to some controversy [42, 43] and ranges between 1 eV and  $\Omega_D$ , where  $\Omega_D$  is the Debye energy of the material. During the second stage,  $E_1$  to  $E_2$ , the electron–phonon scattering [44] with typical time  $\tau_s$  replaces the electron–electron interaction and the energy is stored in a distribution of high energy phonons (phonon bubble). Again there is no consensus about the precise value

of  $E_2$ . The first and second stages are not easily accessible by experiments because the processes are very fast.

During the third stage phonon and quasi-particle distributions further relax, and can be involved in additional processes like diffusion, (de)trapping, tunneling, heating, cooling, etc. The electron–phonon scattering  $\tau_s$ , the quasi-particle recombination into Cooper pair  $\tau_r$  and the pair-breaking processes  $\tau_B$  play, together, the dominant roles. For a homogeneous superconductor the energy and temperature dependences of the rate of these processes were calculated in detail [44]. The pair breaking rate  $1/\tau_B$  is much faster than the phonon escape rate. This leads to the so-called phonon trapping mechanism, in which recombination phonons continuously break Cooper pairs and therefore *enhances* the effective quasi-particle lifetime. The time scale of these processes is often expressed in units of a characteristic material dependent time  $\tau_0$  [44] (Table 2). It should be emphasized that quasi-particle generation at this stage is only possible in a superconductor since  $\Delta < \Omega_D$ . In silicon, for instance, the energy threshold for electron-hole production is in the eV range, a value larger than the Debye energy.

Calculations of the quasi-particle production take into account a Debye phonon spectrum. Early Monte Carlo simulations made for superconducting Sn and Nb predict  $\epsilon = 1.74\Delta$  [11, 20], a value that assumes a relaxation of the quasi-particles down to the energy gap  $\Delta$ . This approach is only reasonable provided the relaxation proceeds faster than other processes involving quasi-particles. There are many low energy states available at the beginning of the cascade, and the situation may change as the relaxation proceeds towards the gap edge because the availability of lower energy states rarefies and only low energy phonons can be emitted.

*Chang and Scalapino* [45] studied a superconductor under steady state energy injection within the kinetic equation framework. They solved numerically the linearized kinetic equations coupling quasi-particles and phonons and obtained solutions for quasi-particle and phonon distributions. This work was extended by one of us [46] for the case of local deposition of energy in which the quasi-particle and phonon distributions were obtained as numerical solutions of the full coupled kinetic equations presented in [45]. The explicit phonon and quasi-particle diffusion as well as the full energy dependence [44] of the relaxation processes were included. It was shown that the fraction of initial energy converted into the electronic system and available for the detection process increases a) with increasing  $\Omega_D/\Delta$  ratio, as shown in Fig 2 and b) with the electronic mean free path in the absorber.

A description of the quasi-particle production in a non-equilibrium situation along the  $E_1 \longrightarrow E_2$  stage has been provided by *Ovchinnikov* et al. [43], who also adopted the kinetic equation approach assuming an instantaneous response of the phonon distribution to changes in the electronic distribution. More recently, *Kozorezov* et al. [47] proposed clear definitions for the values of  $E_1$  and  $E_2$  and provide an analytical solution of the coupled kinetic equa-

**Table 2.** The electronic contribution to the specific heat  $\gamma_{\text{exp}}$  is taken from *CRC-Hand Book of Chemistry and Physics* 1976, D-169. The energy density  $E_{\text{crit}}$  threshold necessary to convert a given material from the superconducting to the normal state is estimated with known values of the the specific heat. The Fermi velocity  $v_F$  has been calculated assuming the free electron model to be valid. \*see K.H. Huang: PhD. thesis, Univ. Cambridge (1991). K: The density of state  $N(0)$  was taken from Phys. Rev. B **14**, 4854 (1976); Z:  $N(0)$  was taken from Phys. Rev. B **59**, 8875 (1999);  $\gamma_{\text{exp}}$ :  $N_0$  was calculated using  $N(0) = 3\gamma_{\text{exp}}/\pi^2 k_B^2$  expressed in states/(J mol), and giving  $N(0) = 3\gamma_{\text{exp}}e\rho/M_a\pi^2 k_B^2$ , where  $\rho$  is the density in g/cm<sup>3</sup> and  $M_a$  the molar mass in g, if expressed in states/(eV cm<sup>3</sup>)

	$\gamma_{\text{exp}}$ mJ/mol K <sup>2</sup>	$E_{\text{crit}}$ keV/ $\mu\text{m}^3$	$\tau_0$ ns	$\tau_{\text{th}}$ ps	$v_F$ 10 <sup>8</sup> cm/s	$\uparrow\downarrow N(0)$ 10 <sup>22</sup> 1/eV cm <sup>3</sup>	$\Theta_D$ meV
Al	1.35	0.82	438	242	2.03	3.44 <sup>γ</sup> 1.22 <sup>K</sup> 3.48 <sup>Z</sup>	34
Ti	3.35	0.40				8.04 <sup>γ</sup>	
V	9.26	150	1.7	56	0.37	26.95 <sup>γ</sup>	
Zn	0.64	0.24	780	2310	1.83	1.78 <sup>γ</sup>	20.1
Ga	0.6	0.25			1.92	0.65 <sup>γ</sup>	20.1
Nb	7.79	300	0.149	4.2	1.37	18.32 <sup>γ</sup> 3.17 <sup>K</sup> 18 <sup>Z</sup>	23.7
Mo	2.0	0.79			0.47	5.44 <sup>γ</sup>	32.7
In	1.69	6.01	0.8	170	1.74	2.75 <sup>γ</sup>	11.1
Sn	1.78	7.1	2.3	110	1.90	2.7 – 2.8 <sup>γ</sup>	22.4
Ta	5.9	51	1.78	23	1.6*–1.86	13.84 <sup>γ</sup> 4.08 <sup>K</sup>	20.7
Pb	2.98	42	0.196	34	1.83	4.19 <sup>γ</sup>	9.05
La	10	80	0.074	130		12.33 <sup>γ</sup>	11.4
Re	2.3	2.56				6.63 <sup>γ</sup>	
Hg	1.79	10.7	0.075	135	1.58	3.08 <sup>γ</sup>	8.6
NbN	3.3	50	0.03	0.57			
Ir	3.14					9.40	36.2
Hf		(1 000)	(20 000)				21.7

tions for interacting quasi-particles and phonons.  $E_1$  is determined by the cross-over condition  $\tau_{ee}^{-1}(E_1) = \tau_s^{-1}(E_1)$ , which leads to the result that  $E_1$  is larger than  $\Omega_D$ . In their framework,  $E_2 = 3\Delta$  corresponds to the threshold below which recombination phonons cannot break Cooper pairs anymore. Thus, processes below  $E_2$  do not increase the quasi-particle population. Their analytical calculation suggests the existence of two distinct phases along the  $E_1 \rightarrow E_2$  cascade, and allows for a classification of materials [47].

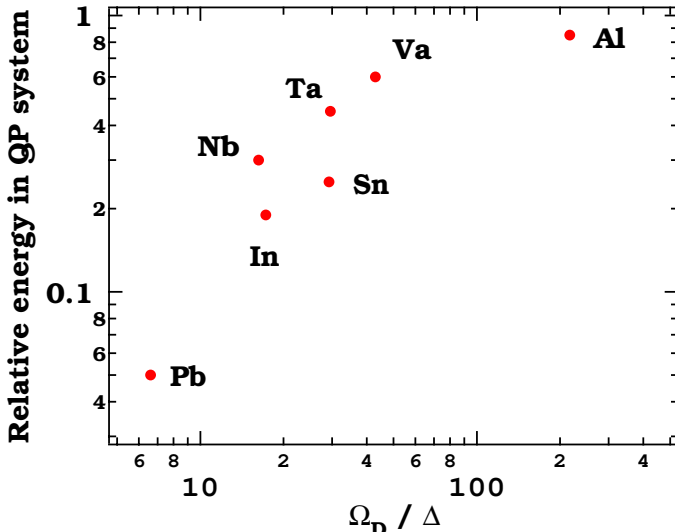


**Fig. 2.** Fraction of the deposited energy stored in the electronic system for a 20 nm electronic mean free path. Data from [46]

## 2.2 Quasi-Particles and Phonons in the *Operational Stage*

The results of the cascade of the first and second phases can be used as the input parameters for the description of the third phase. As already mentioned, at energy level  $E_2$  and below, quasi-particles and phonons form tightly coupled systems. Two quasi-particles recombining into a Cooper pair release a phonon whose energy can, if  $E_\Omega > 2\Delta$ , break another Cooper pair. Because the probability for a phonon to be transferred from one film to another is about,  $10^{-1}$  and larger than the chance for a quasi-particle to be transferred by tunneling,  $10^{-4}$ , phonons need to be taken into account explicitly.

Assume for this discussion a system formed by two homogeneous electrodes S1 and S2 as in Fig. 1 (in which the S' material is absent) in weak electrical contact through a tunneling barrier and coupled acoustically through the substrate. The Rothwarf-Taylor (RT) equations [48] describe phenomenologically the rate of change of the quasi-particle  $N_i(t)$  and phonon  $N_i^*(t)$  populations in each electrode  $i$ ,

$$\frac{dN_1(t)}{dt} = 2\Gamma_B N_1^*(t) + \Gamma_{t,21} N_2(t) - \left( 2\Gamma_{\text{rec}} + 2R \frac{N_1(t)}{V_1(t)} + \Gamma_{t,12} + \Gamma_l \right) N_1(t), \quad (2)$$

$$\frac{dN_1^*(t)}{dt} = \left( \Gamma_{\text{rec}} + R \frac{N_1(t)}{V_1(t)} \right) N_1(t) + \Gamma_{\text{esc},21} N_2^*(t) + \frac{1}{2} \Gamma_l N_1(t) - (\Gamma_B + \Gamma_{\text{esc},1} + \Gamma_{\text{esc},12}) N_1^*(t), \quad (3)$$

$$\frac{dN_2(t)}{dt} = 2\Gamma_B N_2^*(t) + \Gamma_{t,12} N_1(t) - \left( 2\Gamma_{\text{rec}} + 2R \frac{N_2(t)}{V_2(t)} + \Gamma_{t,12} + \Gamma_l \right) N_2(t), \quad (4)$$

$$\frac{dN_2^*(t)}{dt} = \left( \Gamma_{\text{rec}} + R \frac{N_2(t)}{V_2(t)} \right) N_2(t) + \Gamma_{\text{esc},12} N_1^*(t) + \frac{1}{2} \Gamma_l N_2(t) - (\Gamma_B + \Gamma_{\text{esc},2} + \Gamma_{\text{esc},21}) N_2^*(t) \quad (5)$$

and take into account quasi-particle and phonon exchange processes. In their present form, these equations do not describe spatial variations of the phonon and quasi-particles populations. The first two positive terms in (2) account for quasi-particle creation, whereas the sum of all negative terms describe quasi-particle reduction. The quasi-particle enhancement is due to Cooper pair breaking ( $\Gamma_B = 1/\tau_B$ , [44]) and to back-tunneling ( $\Gamma_{t,21} \propto I_b$ ) out of the adjacent electrode. The term  $R$  describes self-recombination and is discussed further below see (10). The quasi-particle number decreases with thermal recombination ( $2\Gamma_{\text{rec}}$ ), self-recombination ( $2R \frac{N_1(t)}{V_1(t)}$ ), and tunneling out ( $\Gamma_{t,12} \propto I_a$ ) of the electrode. The factor  $N_1(t)/V_1(t)$  describes the self-recombination of excess quasi-particles, which is time dependent due to diffusion processes. The last term ( $\Gamma_l$ ) describes additional not well defined processes and is often considered as a free parameter.

The three positive contributions to the phonon number in (3) are due to the recombination of quasi-particles ( $\Gamma_{\text{rec}} + R \frac{N_1(t)}{V_1(t)}$ ), to phonons that have been generated in the other electrode ( $\Gamma_{\text{esc},21}$ ) and couple into the system, and to recombination phonons ( $\frac{1}{2}\Gamma_l$ ) associated with quasi-particle relaxation into traps, respectively. The next three terms reduce the population of phonons.  $\Gamma_B$  describes pair-breaking,  $\Gamma_{\text{esc},1}$  and  $\Gamma_{\text{esc},12}$  take into account  $2\Delta$  phonon losses through the substrate and coupling into the other electrode, respectively. The anharmonic phonon decay has been neglected. Equations (4) and (5) are the equivalent relations for the other electrode.

The two electrodes are coupled through quasi-particles and phonons exchange by tunneling and diffusion, respectively. The above system of equations can be simplified if, following [49] one realizes that the phonon pair-breaking  $\Gamma_B \approx 10^{10}/\text{s}$  is much faster than other processes like phonon escape

and phonon absorption by a quasi-particle near the gap. In this situation, the equilibrium between phonons and quasi-particle densities remains unaffected and the system of equations reduces to

$$\frac{dN_1(t)}{dt} = (\Gamma_{t,21} + \Gamma_{pc})N_2(t) - (\Gamma_r + \Gamma_{pc} + \Gamma_{t,12} + \Gamma_{loss})N_1(t), \quad (6)$$

$$\frac{dN_2(t)}{dt} = (\Gamma_{t,12} + \Gamma_{pc})N_1(t) - (\Gamma_r + \Gamma_{pc} + \Gamma_{t,21} + \Gamma_{loss})N_2(t) \quad (7)$$

in which the phonon coupling  $\Gamma_{esc,ij}$  and phonon loss  $\Gamma_{esc,i}$  processes are translated into equivalent quasi-particle rates  $\Gamma_{pc}$  and  $\Gamma_r$ . The term  $\Gamma_{loss}$  is a free parameter describing quasi-particle losses,  $\Gamma_{t,ij}$  are the quasi-particle tunneling rates,  $\Gamma_r$  is the recombination rate for quasi-particles, which includes recombination with a thermal partner as well as self-recombination [51].

### 2.3 Quasi-Particle Losses

Beyond diffusion out of the system, the only way to lose quasi-particles is the escape of the recombination phonon. The quasi-particle recombination rate is given by

$$\Gamma_r = (n_x + 2n_{th})R^*. \quad (8)$$

The quantity  $n_x$  is the time dependent density of excess quasi-particles,  $n_{th}$  corresponds to the low temperature limit of the quasi-particle density [50],

$$n_{th} = 2N(0) \left( \frac{2\pi\Delta(T)}{k_B T} \right)^{1/2} \exp[-\Delta(T)/k_B T], \quad (9)$$

where  $N(0)$  is the single spin density of states, and  $R^*$  is the effective recombination coefficient reduced by the phonon trapping effect. For Al kept at 250 mK, the density of thermal quasi-particle is in the order of  $2000/\mu\text{m}^3$ . The recombination coefficient  $R$  for quasi-particle is obtained from [44, 51], under the assumption that at low temperature quasi-particles obey a Boltzmann energy distribution

$$R = \frac{\Delta^2(0)}{(k_B T_c)^3} \frac{4}{N(0)} \frac{1}{\tau_0}, \quad (10)$$

where  $\tau_0$  is a material dependent quasi-particle time constant taken from [44] and shown in Table 2 together with the density of states  $N(0)$ . For Al,  $R \approx 8 \mu\text{m}^3/\text{s}$ .

The phonon trapping factor actually *reduces* the quasi-particle recombination rate and is defined:

$$\frac{R^*}{R} = \left( \frac{\Gamma_{pl}}{\Gamma_B + \Gamma_{pl}} \right), \quad (11)$$

where  $\Gamma_B$  is the phonon pair-breaking rate [44]. If the quasi-particles involved in a recombination process have an energy  $\epsilon > \Delta$ , the emitted phonon can break another Cooper pair, unless it is lost. The phonon loss rate is given by [52]

$$\Gamma_{\text{pl}} = \frac{\eta v_{\text{ph}}}{4d}, \quad (12)$$

where  $\eta \approx 0.29$  is the Nb phonon transmission coefficient [53],  $v_{\text{ph}} \approx 3700$  m/s is the average phonon velocity [53], and  $d$  the film thickness leading to  $\Gamma_{\text{pl}} \approx 10^9/\text{s}$  for Nb. The phonon coupling term  $\Gamma_{\text{pc}}$  in (6) and (7) is defined in a similar way.

In order to illustrate the situation, we can further simplify the problem and assume identical electrodes,  $\Gamma_{t,12} = \Gamma_{t,21} = \Gamma_t$ , neglect  $\Gamma_{\text{pc}}$  for a while, and write  $\Gamma_{\text{eff}} = \Gamma_{\text{rec}} + \Gamma_{\text{loss}}$ . Equations (6) and (7) can then be solved and the solutions reads

$$N_i = N_0 \exp(-\Gamma_{\text{eff}} t) [1 + \exp(-t\Gamma_t/2)]/2. \quad (13)$$

The tunneling current can be calculated with

$$I(t) = e(N_1 \Gamma_{t,12} + N_2 \Gamma_{t,21}) \approx N_0 e \Gamma_t \exp(-t\Gamma_{\text{eff}}), \quad (14)$$

which illustrates the competition between tunneling,  $\Gamma_t$ , and quasi-particle losses,  $\Gamma_{\text{eff}}$ . The case for different tunnel rates has been calculated in [54].

Several authors compared the energy dependence of the measured integrated tunneling current  $Q_m = \int I(t) dt$  generated in an STJ to the prediction made by the RT equations. Early symmetric Sn devices [14, 17] as well a Nb-based [55] and Al [33] devices present a weak nonlinear response in the soft X-ray energy range which could be reasonably described within the framework presented above. The RT equations predict that the measured charge per unit of energy (the responsivity) of an STJ decreases with increasing energy. Since at higher photon energy the density of excess quasi-particles  $n_x$  increase and the opportunities to recombine with partners increases as  $n_x^2$ , self-recombination dominates and limits the charge output. The charge output is dominated by  $\Gamma_{\text{eff}}$  whereas the deviation from linearity is governed by the phonon parameters  $\Gamma_{\text{pc}}$  and  $\Gamma_{\text{pl}}$ . See Sect. 4.3.5 for more details.

## 2.4 Tunneling

A nice introduction to quasi-particle tunneling can be found in [4], a more detailed treatment is presented in [56]. The quasi-particle transfer from one electrode to the other can be determined with the help of Fermi's Golden Rule. The tunneling Hamiltonian of two superconductors  $S(\Delta_1)$  and  $S(\Delta_2)$  exchanging quasi-particles across a resistive barrier  $R_n$ , biased at  $eV$  kept

below ( $\Delta_1 + \Delta_2$ ) and neglecting branch-imbalance [57] reduces to 4 contributions [56, 58, 59]:

$$I_{a1} = \frac{1}{eR_n} \int_{\Delta_1}^{\infty} \rho_1(\epsilon) \rho_2(\epsilon + eV) f_1(\epsilon, T_1) [1 - f_2(\epsilon + eV, T_2)] d\epsilon, \quad (15)$$

$$I_{a2} = \frac{-1}{eR_n} \int_{\Delta_1}^{\infty} \rho_1(\epsilon) \rho_2(\epsilon + eV) [1 - f_1(\epsilon, T_1)] f_2(\epsilon + eV, T_2) d\epsilon, \quad (16)$$

$$I_{b1} = \frac{1}{eR_n} \int_{\Delta_2+eV}^{\infty} \rho_1(\epsilon) \rho_2(\epsilon - eV) [1 - f_1(\epsilon, T_1)] f_2(\epsilon - eV, T_2) d\epsilon, \quad (17)$$

$$I_{b2} = \frac{-1}{eR_n} \int_{\Delta_2+eV}^{\infty} \rho_1(\epsilon) \rho_2(\epsilon - eV) f_1(\epsilon, T_1) [1 - f_2(\epsilon - eV, T_2)] d\epsilon, \quad (18)$$

where  $\rho_i$  are the energy dependent density of states and  $f_i$  the Fermi distribution in the film  $i, j$ , respectively. The sum  $I_a = I_{a1} + I_{a2}$  is the net transfer of mainly quasi-electrons from film 1 to 2.  $I_b = I_{b1} + I_{b2}$  is the net transfer of mainly quasi-holes. The total electrical current is  $I = I_a + I_b$ , whereas the net flow of quasi-particles from film 1 to 2 is given by  $I_{\text{flow}} = (I_{a1} - I_{b2}) - (I_{b1} - I_{a2})$ . The general relations (15)–(18) can be used to calculate in detail the current voltage curve of a STJ. Equation (15) can be identified with the main tunneling processes shown in Fig. 1 and describes the probability to leave an occupied state of energy  $\epsilon$  and to fill an empty state of energy  $\epsilon + eV$ . Equation (17) describes back-tunneling [8] responsible for charge gain. In the process labeled  $I_b$  in Fig. 1 a quasi-particle existing in the right-hand side (r.h.s) electrode can form a Cooper pair with a partner quasi-particle that results from the break-up of a Cooper pair in the left hand side (l.h.s) electrode. The partner quasi-particle in the l.h.s electrode is again available for tunneling, and this cycle can be repeated many times. Thus, tunneling cannot be considered as a loss process, the number of back-tunneling cycles being limited by the effective life time of the quasi-particles. Note that (15) to (18) allow for a temperature difference between the electrodes. It is therefore possible to estimate the actual tunnel current as a deviation from the thermal background. Equations (16) and (18) describe secondary processes which could reduce the signal amplitude [60] in non-symmetric STJ's biased below and near  $(\Delta_1 - \Delta_2)/e$ . The above relations were used to estimate the voltage dependent *electrical* tunneling rate [8, 59, 61].

Assuming a BCS density of states and that the normal conducting density of states  $N(0)$  near the Fermi energy remains constant, the thermal tunneling rate for a symmetric STJ is given by [5, 51]

$$\Gamma_t = \frac{1}{4e^2 N(0)} \frac{1}{R_n A d_i} \frac{\Delta + eV_b}{\sqrt{(\Delta + eV_b)^2 - \Delta^2}}, \quad (19)$$

where  $R_n$  is the resistance of the tunneling barrier,  $A$  its area,  $d_i$  the thickness of the electrode out of which tunneling is considered and  $V_b$  the voltage drop at the tunneling barrier. If the voltage is larger than  $\Delta/e$  relation (19) reduces to the well known result of *Ginsberg* [62]. For a 250 nm thick Nb film, a device size of  $50 \times 50$  microns and a barrier resistance of  $R_n = 0.1 \Omega$   $I_t \approx (0.13 - 0.64) \times 10^5 / s$  depending on the value of  $N(0)$  taken from Table 1.

## 2.5 Diffusion

The typical distance a quasi-particle can diffuse is estimated as  $x_D = \sqrt{D\tau_{qp}}$ , where  $\tau_{qp}$  is the inverse of the effective quasi-particle loss rate  $\Gamma_{\text{eff}}$ . Using an experimental value for the normal state resistivity of Ta,  $\rho = 0.5 \mu\Omega \cdot \text{cm}$  together with the (single spin) density of states value given in Table 2 we estimate the normal state diffusion constant for electrons by  $D_n = 1/(\rho e^2 N(0)) \approx 180 \text{ cm}^2 \cdot \text{s}^{-1}$ . In the superconducting state D depends on the energy of the quasi-particles, and is reduced compared to the normal state because the quasi-particle dispersion relation, which governs the group velocity, has a minimum at the gap edge. When electron-impurity scattering dominates, the low temperature value for the diffusion constant of quasi-particles is given by [63, 64]  $D_{qp}/D_n = \sqrt{2k_B T/\pi\Delta}$ . Assuming quasi-particles in a device at  $T/T_c = 0.1$  we expect  $D_{qp}/D_n \approx 0.1$ . However, there is accumulating experimental evidence that the quasi-particle diffusion rates measured in Ta [65, 66, 67] and in Nb [68] are lower than predicted by the above considerations. Aluminum, seems less affected by a low diffusivity [65]. It is speculated that the low quasi-particle diffusion rate, which correlates with a short effective lifetime, is due to the presence of traps.

## 2.6 Quasi-Particle Trapping

The quasi-particle trapping mechanism proposed by *Booth* [6] takes place when a quasi-particle in a superconductor with  $\Delta_1$  diffuses out into another region where states of lower energy near  $\Delta_2$  are available and encounter a potential well. The trapping rate is given by

$$\Gamma_{\text{trap}} = \Gamma_s \frac{V_2}{V_1}, \quad (20)$$

where  $\Gamma_s$  is the energy ( $\omega$ ) dependent quasi-particle scattering rate [44] which varies with  $\approx (\omega/\Delta_1)^3$  for  $\omega \gg \Delta_1$  and  $V_2/V_1$  represents the fraction of time the quasi-particles spend in volume  $V_2$  if  $V_1 \gg V_2$ . The concept has been demonstrated [69, 70, 71] and is now widely used. If the energy difference  $\Delta_1 - \Delta_2$  is larger than  $2\Delta_2$ , the relaxation phonons can, unless they are lost, break Cooper pairs. This process leads to quasi-particle multiplication [72, 73, 74].

Trapping can be used in device design as illustrated in Fig. 1. The tunneling current is enhanced provided the tunneling rate is faster than the

effective recombination rate in the trap. However, quasi-particles can be lost if they diffuse into traps away from the tunneling barrier. Such regions are likely to be found near the edges and surfaces of a device, on oxidized/dirty Nb surfaces, near magnetic impurities, or within an Abrikosov vortex in the electrode [75, 76]. Quasi-particles in such traps are likely to get lost because their relaxation phonons have too little energy to break another Cooper pair. The parameter  $\Gamma_{\text{loss}}$  takes into account such processes. De-trapping, on the other hand needs to be considered because a trapped quasi-particle has a chance to be excited out of the trap by the absorption of a phonon [77, 78] or can recombine with a thermal quasi-particle. If the energy of the partner quasi-particle is sufficient, the recombination phonon breaks a Cooper pair, releasing quasi-particles. This mechanism, not accounted for in the RT equations presented above, has received more attention recently [79]. The competition between trapping and de-trapping was invoked to explain recent experimental results and will be discussed further below.

## 2.7 Proximity Effects and Band-Gap Engineering

All the characteristic times discussed above assumed homogeneous superconducting properties and neglected the consequences of the proximity effect which causes spatial variations of the superconducting properties. The abrupt gap profile sketched in Fig. 1 does not describe the situation precisely and merely illustrates the fact that quasi-particles can relax to different energy levels distributed within the device. Moreover, modeling a hetero-junction with only two electrodes (and therefore two RT equations) is questionable if trapping dynamics has to be included. A more accurate description requires to take into account all the consequences related to proximity effect(s) between the superconducting layers and the inclusion of (de)trapping effects [78].

The proximity between the S and S' layers in a SS' system modifies the properties of both layers and introduces a spatial dependence of the order parameter and of the density of states. Assuming only a 1D dependence in a direction  $x$  perpendicular to the films, microscopic calculations, valid in the case of arbitrary transparency at the S/S' interface, of thin ( $d_{S'} < \xi_{S'}$ ) S' layer in the dirty limit ( $l < \xi$ ) were performed [80, 81, 82]. The model requires several input parameters; the critical temperature ratio of the unperturbed films, their respective effective coherence length  $\xi_i^* = \sqrt{\hbar D_i / 2\pi k_b T}$ , thicknesses  $d_i$ , single spin density of states  $N(0)_i$  and Fermi velocity  $v_{F,i}$ . Two additional quantities,  $\gamma_B$  and  $\gamma$  enter into the model [80]. The output of the model are the critical temperature of the bi-layer, the gap parameter  $\Delta_g$ , the order parameter  $\Delta(x)$  and the density of density of states  $N(x)$  both of which are calculated at several  $x$  coordinates in the SS' system. The relation for  $\gamma_B$  and  $\gamma$  read

$$\gamma_B = \frac{R_B}{\rho_{S'} \xi_{S'}}, \quad \gamma = \frac{\rho_S \xi_S}{\rho_{S'} \xi_{S'}}, \quad (21)$$

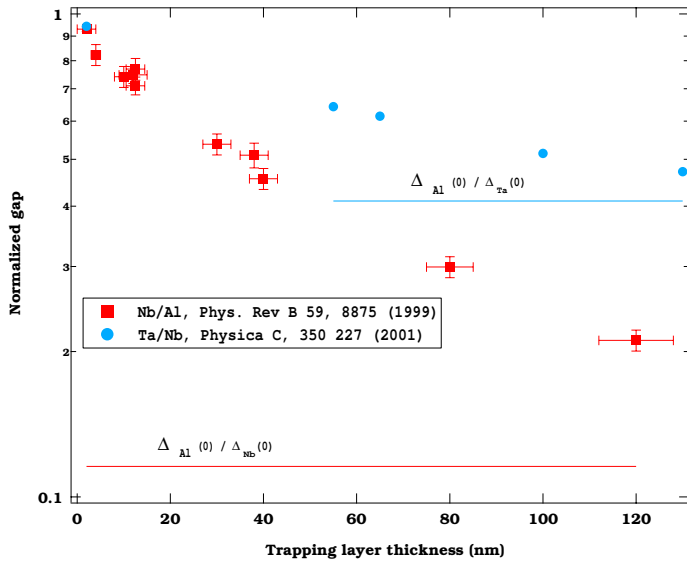


**Fig. 3.** Experimental values of the normalized gap parameter  $\Delta_g(d_{Al})/\Delta(0)$  measured on Nb/Al/AlO<sub>x</sub>/Al/Nb device as a function of the Al film thickness [82]. The behavior for Ta/Al devices is similar see [83]

where  $R_B$  is the interface resistance · area product,  $\rho_{S,S'}$  are the normal state resistivities, and  $\xi_{S,S'}$  the coherence length. Note that the coherence length  $\xi_{S'}$  is normalized  $\xi_{S'} = \xi_{S'}^* \sqrt{T_{c,S'}/T_{c,S}}$ . Since  $D_i = 1/[\rho_i e^2 N_i(0)]$  one has  $\gamma \propto \sqrt{D_{S'}/D_S}$ . The coherence lengths of materials like Nb, Ta and Al are very different,  $\xi_{Nb,Ta} \ll \xi_{Al}$ .

It turns out that the model calculations are strongly influenced by the couple of  $\gamma - \gamma_B$  values and several experimental approaches were used to test the numerical predictions. The value of  $\gamma$  can be estimated from measured values of  $\xi$ , and  $\rho$ . Further  $\gamma_B$  can be calculated assuming [80] known values of the electronic transmission coefficient at interfaces, or can be left as an adjustable parameter [82]. The model is then compared to the measured temperature dependence of the gap parameter  $\Delta_g(T)$ , the critical current  $I_J(T)$ , and the shape of current-voltage curves recorded at different film thicknesses  $d_{S'}$  [80, 82]. Recently a generalized model valid for any film thickness and any values of  $\gamma_B$  was proposed. The temperature dependences of the measured gap energy  $\Delta_g(T)$  and critical current  $I_J(T)$  could well be reproduced for several values of  $d_{S'}$ , by using one couple of  $(\gamma_B - \gamma)$  values determined separately [83, 84, 85].

The most salient feature predicted by all flavors of the proximity effect models and well supported by experiments is the reduction of the gap parameter  $\Delta_g$  with increasing thickness  $d_{S'}$  of the trapping films. In Fig. 3, we show  $\Delta_g$  measured from the quasi-particle current-voltage curves [82] of sev-

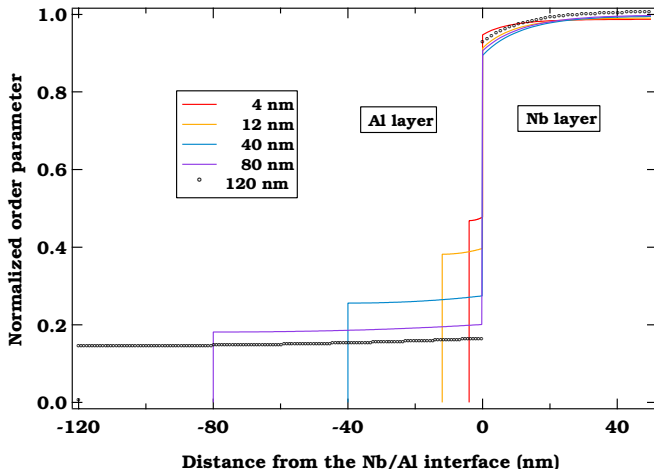


**Fig. 4.** Calculated profile of the normalized order parameter  $\Delta(x)/\Delta(\text{Nb}_{\text{bulk}})$  in a Nb/Al/AlO<sub>x</sub>/Al/Nb device for several values of the Al film thickness. Data from [82]

eral symmetric devices. The interpretation of  $\Delta_g$  needs to be distinguished from the one of the order parameter  $\Delta(x)$ . The gap parameter is measured from the current-voltage curves as the energy at which the current rise near the sum-gap  $\Delta_1 + \Delta_2$  takes place. This value represents the energy threshold required to generate quasi-particles upon Cooper pair breaking. Since Cooper pairs extend on a scale of the coherence length this quantity cannot be localized and is thought to remain constant through the thickness of the device.

On the other hand, the profile of the order parameter  $\Delta(x)$  within the SS' system and shown in Fig. 4 illustrates the variation of the strength of the superconducting coupling within the bi-layer. This quantity can be calculated using measured values of  $\Delta_g$  together with other input parameters required by the model [80, 82]. The order parameter has almost a constant value in S', with  $\Delta_{\text{S}}(x) > \Delta_g > \Delta_{\text{S}}(x)$ . Thus,  $\Delta_g$  is indeed determined by the thickness  $d_{\text{Al}}$ .

The microscopic model allows to calculate the density of states functions required to model current-voltage curves which in turn are compared to measured curves. The output of such a calculation is presented in Fig. 5. Below  $\Delta_g$  there are not states available for quasi-particles. However, the energy at which the density of states has a maximum is clearly position dependent.

The density of states calculated far from the Nb/Al interface at  $x = \infty$  in the Nb electrode of the device made with 12 nm thick traps shows almost a BCS dependence. Close to the interface at  $x = +0$  the deviation from the canonical behavior is already significant. On the other side of the interface, the density of states shows little position dependence, and the gap reduction

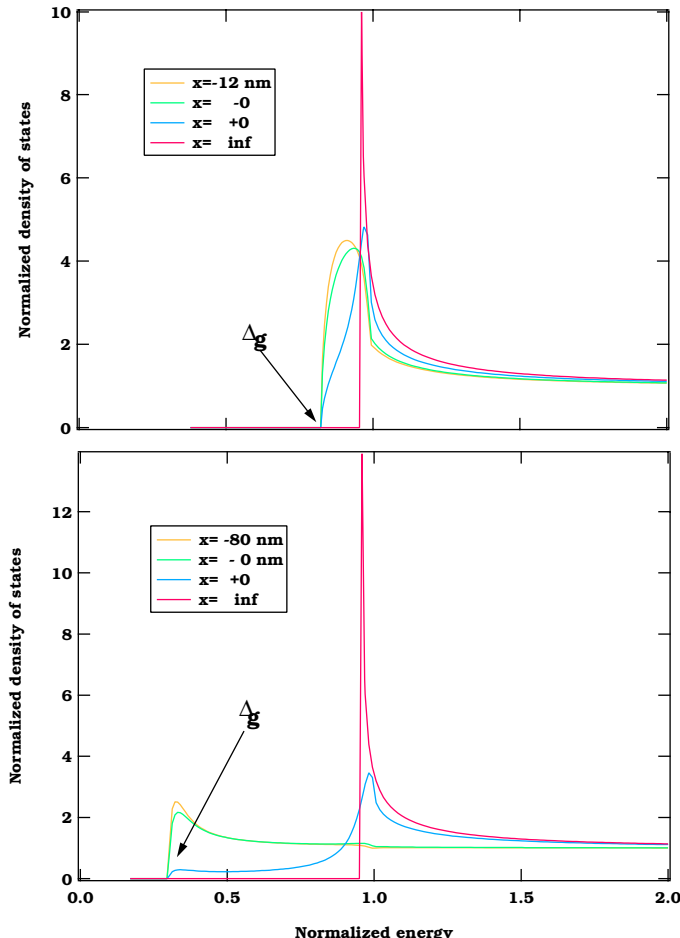


**Fig. 5.** Normalized density of states  $N(\epsilon)/N_{Nb}(0)$  as a function of normalized quasi-particle energy  $\epsilon/\Delta(Nb)$  used to fit the current-voltage curves of two devices made with 12 and 80 nm thick trapping layers, respectively [82]. The density of states varies within the thickness of the device, but the value of the gap energy remains constant

at 12 nm is moderate. Quasi-particles in such a device will not be confined efficiently in the Al trap. For the sample calculated with 80 nm thick traps, the gap reduction is much more important, and the energy range over which quasi-particles can find available states extends from  $\Delta_g(80 \text{ nm})$  to  $\Delta(Nb)$ . In that case the availability of low energy states in the Al is at the origin of the quasi-particle confinement effect called *trapping*.

The order parameter and density of states outputs of the generalized model [84, 85, 86] are shown in Fig. 6 for comparison. The situation in Ta is

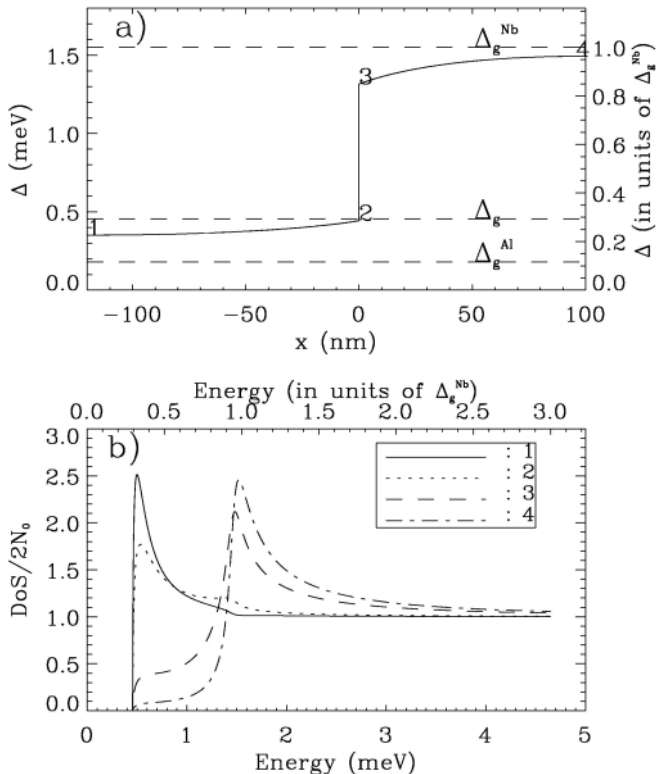


**Fig. 6.** (a) Order parameter profile calculated for a Nb/Al system using the generalized proximity effect model. Nb is 100 nm thick, Al is 120 nm thick. The intermediate dashed line is the energy gap of the bilayer as determined from Fig. 6b. The boundary parameters  $\gamma_b \approx 4$  and  $\gamma \approx 1$ . (b) Density of states vs. energy at several locations (indicated 1, 2, 3, 4 in Fig. 6(a)) within the bi-layer. Reproduced with permission from [86]

qualitatively very similar. The generalized model has been successfully tested against experimental data.

The variation of the density of states across the bi-layer has a profound impact on the quasi-particle dynamics. The scattering rate  $\Gamma_s$ , the trapping rate  $\Gamma_{\text{trap}}$ , the recombination rate  $\Gamma_{\text{rec}}$  as well as the tunneling rate  $\Gamma_t$  all depend on the density of states in the system. Thus, in order to take into account proximity effect, all these quantities were re-calculated [77, 78, 80]. This extends the work of Kaplan to the non-homogeneous case.

### 3 Statistical Fluctuations

The energy resolution limit predicted by (1) can only be reached if each and every quasi-particle tunnels only once. Strictly speaking, all the processes taking place after the creation of  $N_0$  primeval charges have their own gain or loss factors. Thus, they are all subject to fluctuations. Assume  $N_0$  quasi-particles are created, and they all have a probability  $\beta$  to get lost from the absorber either by out-diffusion or by recombination into (unwanted) traps away from the tunneling barrier [87]. The remaining average number of quasi-particles is  $(1 - \beta)N_0$ . Further, quasi-particles can diffuse into (wanted) deep trapping regions and relax to a lower energy state by phonon emission. If we have  $N_{\text{relax}}$  quasiparticles that generate relaxation phonons with sufficient energy to break Cooper pairs in the trap, the available number of quasi-particles will raise by an amount  $2N_{\text{relax}}$ . This corresponds to a gain factor  $\alpha_t = (1 + 2N_{\text{relax}}/N_0)$  [87]. The gain due to back-tunneling is measured by the average number  $\bar{n}$  a quasi-particle cycles before it is lost. Cancelation currents are taken into account with a reverse tunneling probability  $\gamma_c$  leading to a loss factor of  $(1 - 2\gamma_c)$  [87]. With all these processes the measured charge number is given by

$$N_m = N_0 (1 - \beta) \alpha_t \bar{n} (1 - 2\gamma_c). \quad (22)$$

The variance of the primeval charges is  $\sigma_{N_0}^2 = FE_0/\epsilon$  is called creation noise. The variance of the absorber loss process is estimated by assuming that the number of lost quasi-particles  $N_{\text{loss}} = \beta N_0$  follows a binomial distribution. The probability for a quasi-particle to be lost is  $\beta$ , and the probability not to be lost is  $1 - \beta$ , thus  $\sigma_\beta^2 = \beta(1 - \beta)/N_0$  [87].

The variance of the trapping process also assumes a binomial distribution of the  $N_{\text{relax}}$  quasi-particles. The probability that a quasi-particle multiplies is  $p = (1 - \alpha_t)/2$ , and the probability that it does not multiply is  $(3 - \alpha_t)/2$  where  $\alpha_t$  is the gain factor. The variance due to trapping is estimated to be  $\sigma_{\alpha_t}^2 = (\alpha_t - 1)(3 - \alpha_t)/N_0$  [87].

Back-tunneling due to the Gray effect enhances the collected charge, but its contribution to the noise [22, 88] is significant and takes the form

$$\sigma_{\bar{n}}^2 = \bar{n}^2 G/N_0, \quad G = \frac{P_1 - P_1^2 + 3P_1P_2 + P_1^2P_2}{(P_1 + P_1P_2)^2}, \quad (23)$$

where the tunneling probabilities  $P_i$  are expressed in terms of already known quantities

$$P_i = \frac{\Gamma_{t,i}}{\Gamma_{t,i} + 2\Gamma_{\text{rec},i}^* + \Gamma_{\text{qp},i}}. \quad (24)$$

In order to avoid back-tunneling induced fluctuations,  $P_2$  should be zero, a condition difficult to realize in practice. In a SIN device, there is no back-tunneling, however. For a device with equal tunneling probabilities,  $P_1 =$

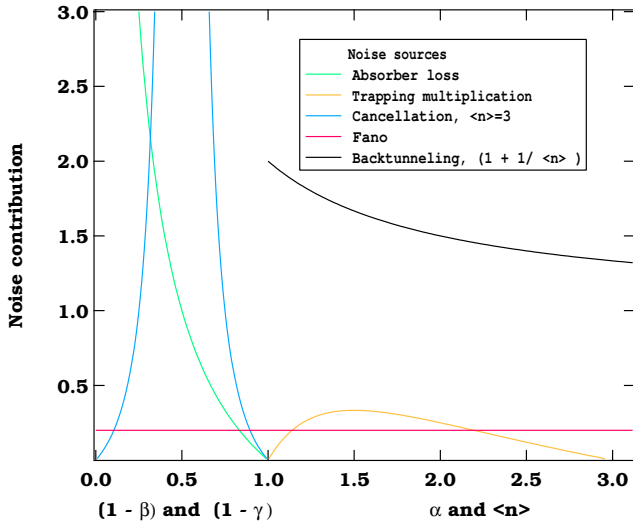


**Fig. 7.** Equivalent Fano factor contributions of several noise sources present in a superconducting tunneling device. The *horizontal scale* between 0 and 1 displays  $(1 - \beta)$  and  $(1 - \gamma_c)$ , whereas the scale between 1 and 3 represents  $\alpha_t$  and  $\bar{n} = \langle n \rangle$

$P_2 = P$  the noise factor reduces to  $G = (1 + 1/\bar{n})$  [22], where  $\bar{n} = Q/Q_0 = P/(1 - P)$  is the charge gain. Thus,  $\bar{n} = \Gamma_t/(2\Gamma_{\text{rec}}^* + \Gamma_{\text{loss}})$  illustrates the role of a large tunneling rate.

The last source of fluctuations considered here is related to variations in the cancellation tunneling of quasi-particles. This process leads to incomplete charge collection was discussed recently [89, 90]. The reverse tunneling probability  $\gamma_c$  is important at low bias voltage and leads to a reduction  $(1 - 2\gamma_c)$  of the actual transferred charge. The fluctuations associated with the reverse current are given by  $\sigma_{\gamma_c}^2 = \gamma_c(1 - \gamma_c)/\bar{n}N_0$ . The total noise can now be estimated by computing the error propagation on (22) and the result can be cast in the following form

$$\delta E = 2.35 \sqrt{\epsilon(F + \frac{\beta}{1 - \beta} + \frac{(\alpha_t - 1)(3 - \alpha_t)}{\alpha_t^2} + G + \frac{4\gamma_c(1 - \gamma_c)}{\bar{n}(1 - 2\gamma_c)^2})E_0}. \quad (25)$$

In practice it appears rather difficult to estimate with precision all the gain and loss parameters discussed above. However, the results of (25) and displayed in Fig. 7 clearly illustrate the relative importance of each noise channel. Although useful in order to bring a signal above the level of electronics noise, back-tunneling generates a significant amount of noise. Cancellation and absorber losses should clearly be minimized, and the charge multiplication due to trapping should be kept to a minimum or made clearly large.

Devices using a lateral trapping geometry [87] allow to some extend to disentangle the one or the other of the above mentioned noise sources. See the discussion on the charge division approach in the experimental section. Moreover, one has to bear in mind that fluctuations generated by the readout electronics and related to variations of the impedance of the device during operation play an important role and may further contribute to entangle the situation [89]. The noise due to stray IR radiation may be of concern as well, see the next section.

## 4 Experimental

In this section we discuss issues related to device fabrication and readout electronics. We present results obtained with *single pixels* separately from knowledge gathered with the so-called *charge division* approach involving the coherent readout of more than one pixel. Work on arrays is presented in the outlook.

### 4.1 Devices

Several fabrication routes have been explored. In order to define the geometry of thin film devices, mechanical masks are useful provided the materials can be deposited with a thermal evaporation technique. If the materials require the use of sputtering techniques, the very short mean free path associated with the high ( $\approx 0.01\text{--}0.1\text{ mBar}$ ) gas pressure in the vacuum chamber precludes the use of mechanical masks, unless not too small structures are required [91]. Full wafer deposition or sputtering through a micro-fabricated stencil followed by one or more lift-off steps are then the options. In order to enhance the electronic mean free path of the absorber layer, this one is often grown on substrates maintained at elevated temperature. In this case lift-off through a stencil is not possible and the desired geometry is obtained after several lithography and selective etching steps. The choice of the absorber layer is determined by the energy of the photons to be absorbed. Applications in the X-rax energy range need a high- $Z$  material absorber of 1–2 microns thickness, whereas the detection of visible photons requires an absorber with a low reflection coefficient.

The growth of the tunnel barrier is of extreme importance and cannot be done at high temperature. Fabrication procedures often include the cooling of the sample before the growth of the barrier starts. Aluminum has proven to be an excellent material for the growth of a homogeneous layer of  $\text{AlO}_x$ . A high quality device has a typical ( $R_n \cdot \text{area}$ ) product of  $1\text{--}2\,\mu\Omega \cdot \text{cm}^2$ . Alternative tunnel barrier materials have been investigated, with moderate success, however. The trapping layers are usually made with Al as well because it is technically convenient to perform an Al deposition on top of its oxide, and because of its long quasi-particle lifetime.

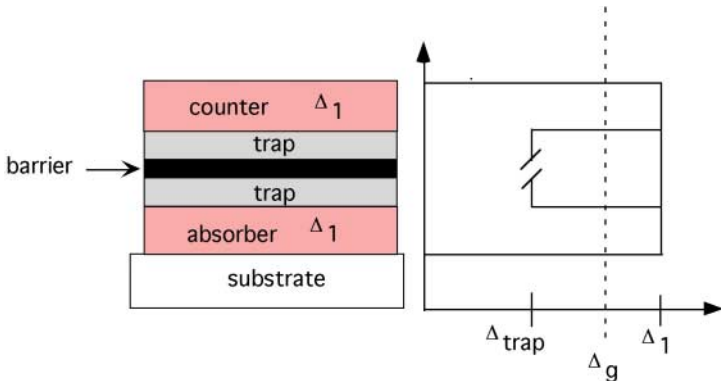


**Fig. 8.** Vertical trapping device. The value of the gap parameter  $\Delta_g$  is determined by proximity effect. The superconducting order parameter  $\Delta(x)$  on the other hand shows a strong variation at the interfaces. Vertical dimensions are not to scale

The counter electrode required to wire the device to the readout electronics cannot be grown at elevated temperature and is usually of polycrystalline nature. The interface between absorber and lower trapping layer as well as between upper trapping layer and counter electrode affects the strength of the proximity effect ( $\gamma_B$  parameter). The contact electrode is often deposited through a lift-off mask or as a film which is subsequently patterned, and which contacts the device through vias etched in passivation layers. The width of the leads plays a role in quasi-particle out-diffusion. The size of STJ devices made in the vertical trapping scheme as shown in Fig. 8 ranges between 10 and 300 microns squared. It appears difficult to grow uniform pin-hole free tunnel barriers of much larger area. In addition, the large dielectric constant of the oxide layer will increase the capacitance of the larger device to an unacceptable level. The growth of the desired stack of layers in the same vacuum run is of advantage since the conditions at the various interfaces can be controlled in a reproducible manner.

In order to operate an STJ in the Giaever mode the *dc* Josephson current as well as the Fiske resonances [92, 93] need to be attenuated with a precisely tuned constant external magnetic field of a few tens of Gauss applied parallel to the plane of the tunnel barrier. In this respect, the shape of the STJ is of importance and in practice devices have often a square geometry and the field is applied along one of the diagonals. Diamond, quartic as well as annular geometries have been studied [94, 95].

In Fig. 9 we show the cross section of a device using the lateral trapping scheme. The main feature is that the bottom trapping layer in contact with the absorber is almost not affected by proximity effect. This enhances the quasi-particle confinement strength. Moreover, if the energy difference between the gap of the absorber and the trap is larger than twice the value in the trap, relaxation phonons are likely to cause additional signal gain

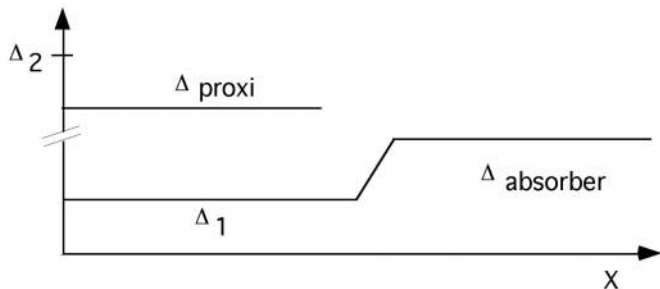
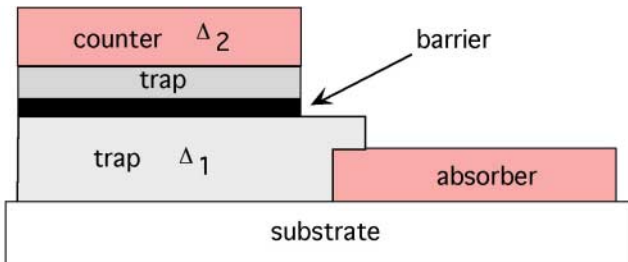


**Fig. 9.** Example of a device using the lateral trapping scheme. The gap parameter in the absorber, in the bottom trapping layer and in the counter electrode layers has bulk value. In that case, order and gap parameters are the same. In the top trapping layer the gap is determined by proximity effect. The potential well created by the bottom trap in the lateral geometry is deeper than the well that results from the vertical trapping scheme. Dimensions are not to scale

[ $\alpha_t$  parameter in (25)]. The fabrication of these devices requires an additional vacuum run since bottom trap and absorber are at the same level on the substrate [96]. Measures to guarantee a high electrical transparency at the interface after breaking the vacuum are thus required.

## 4.2 Readout Schemes

The principle of operation is simple; a device is placed on a stable point of its current-voltage curve at a given temperature and deviations due to energy absorption events are recorded with a dedicated electronics. Devices need to be operated below  $0.1T_c$  in order to reduce the population of thermal quasi-particles  $i_{\text{th}}(T) \propto n_{\text{th}}(T)$ , see (9). The quantities that are readily accessible from a full current-voltage curve are the superconducting gap parameter  $\Delta_g$ , the resistance of the tunnel barrier  $R_n$ , and the magnitude of the thermal current  $i_{\text{th}}(T)$  describing the quiescent state at the equilibrium bath temperature  $T$ . The circuit required to record such a curve uses a current or better, a voltage bias configuration.

A sudden deviation from equilibrium following a photon absorption event results, in the voltage bias mode, in a current pulse  $I(t)$ , whose decay time is directly related to the quasi-particle life-time. This signal can be measured with a current amplifier (CA). A time integration allows to measure the charge  $Q_m$ . For devices with highly transparent barriers (large tunneling barrier area) it is possible to place the STJ in series with the superconducting input coil of a low noise SQUID current amplifier [32, 97, 98, 99]. A passive voltage bias is obtained with a shunt resistor kept at low temperature and wired in parallel to the STJ and the coil connected in series. The SQUID amplifier needs to be shielded from the *dc* field required to operate the STJ, so that the two devices cannot be mounted close together.

In most cases the impedance of the STJ is large and does not match well to the input coil of a SQUID system, however. It is then adequate to use a transimpedance amplifier circuit [100, 101] that converts the current excursions into voltage pulses. By increasing the impedance of the feed-back network it is possible to convert a CA into charge sensitive amplifier (CSA). Figure 17 in the appendix presents such a circuit together with the main noise sources. The use of a passive current bias network is straightforward, but imposes restrictions in range of accessible voltage  $V_b$ . It is of great advantage to use an active voltage bias for biasing a device near a negative differential resistance region of the current-voltage curve. Such regions are invariably present along the quasi-particle branch of STJs, due to Fiske resonances [92, 93, 102], to the asymmetry in the S1 – I – S2 configuration [60] or to other intricacies [103, 104]. An example of a circuit using an active voltage bias and a current amplifier can be found in [105]. A stiff  $V_b$  reduces the variations of  $Q_m$  due to the bias dependence of the tunneling rate [see (19)]. Often, the bandwidth of these fluctuations can be made narrower than the full signal band. Adequate pulse shaping can reduce the noise induced by the back-tunneling process [106, 107]. We shall emphasize again that back-tunneling results in true signal gain of order 10 to 50 and allows counting of single low energy photons. In order to reduce the amount of electronics noise as well as the capacitance of the wiring between the device and the front-end elements, the latter are often mounted on a intermediate cryogenic stage as close as possible to the sample. Careful grounding [108] as well as shielding against *emi* and stray IR radiation [109, 110] need to be taken into account. The concern with stray IR radiation needs to be taken seriously, in particular if low gap materials like Al are used in the fabrication of the devices and if low energy photons need to be detected; photons emitted near the peak of the black body spectrum of a 10 K surface have an energy of  $\approx 4.3$  meV. In bolometer language, the detectivity  $D^* = \text{area}/\text{NEP}$  of an STJ biased with 100 pA current and which has a responsivity of 20 000 e/eV is expected to range between  $10^{12}$  and  $10^{13} \text{ cm Hz}^{1/2}/\text{W}$ . In the UV and soft X-ray energy range, the use of a cascade of cold and thin Al filters is the adequate measure.

We would like to emphasize at this point that the traditional noise treatments of a CA or CSA circuit [100, 111] include shot and thermal noise sources of device and components in the circuit but neglect variations of the actual impedance of the STJ *during an event*. This noise source is often underestimated. Variations of the dynamical resistance of a device during an event may affect the linearity of the circuit as well as the noise behavior [112]. This effect depends on the actual shape of  $I(t)$  and is discussed in [87, 89].

Some aspects of array readout will be discussed in the outlook.

### 4.3 Single Pixel

#### 4.3.1 Nb-Based Devices

The gap parameter of a symmetric Nb/Al/AlO<sub>x</sub>/Al/Nb device using the vertical trapping scheme as shown in Fig. 8 and fabricated with Al traps of only a few nm thickness is not much affected by proximity effect and almost bulk values of  $\Delta$  in the absorber and the counter electrodes are observed. The charge collected upon irradiation with X-rays depends on the bias voltage and increases with device area [55, 113]. The latter effect could be due to a reduction of quasi-particle loss at the edges of the device since the area to perimeter ratio increases with device size. Low temperature scanning electron microscopy [114, 115, 116] demonstrated quite convincingly that the response to the deposition of energy near device edges, and along the perimeter of the contact leads, is different from the response in the rest of the device. The deposition of a passivation layer on top of the counter electrode reduces the quasi-particle loss rate [117]. If the passivation layer is a superconductor with a larger gap parameter than the electrode, the effect could be explained in terms of enhanced quasi-particle confinement and back-tunneling only.

However, a positive effect was also observed for a (thin) passivation layer with  $\Delta_{\text{pass}} < \Delta$  [118]. Thus edges and boundaries are suspect, in particular since Nb has a natural tendency to form oxides [119] which can form traps for quasi-particles. The measured quasi-particle loss rate  $\Gamma_{\text{eff}}$  is dominated by  $\Gamma_{\text{loss}}$ .

Energy spectra of devices studied at X-ray energy most often show a double response due to photons stopped in the base and counter electrode, respectively. Data can be discriminated with a pulse rise-time selection scheme [111, 120]. Polycrystalline electrodes have a higher quasi-particle loss rate than epitaxially grown absorbers [55]. Therefore, the measured energy resolution is best with high quality absorbers. In addition, the broadening of the spectral response in polycrystalline material is influenced by the width of the contact leads [121]. This is again, together with the observation that collected charge reduces with increasing leads width [122], a strong indication that quasi-particles are lost by diffusion. The spectral line shapes invariably show a low energy tail which is attributed to spatial variation of the energy response and diffusion losses [123]. The energy dependence of the resolution

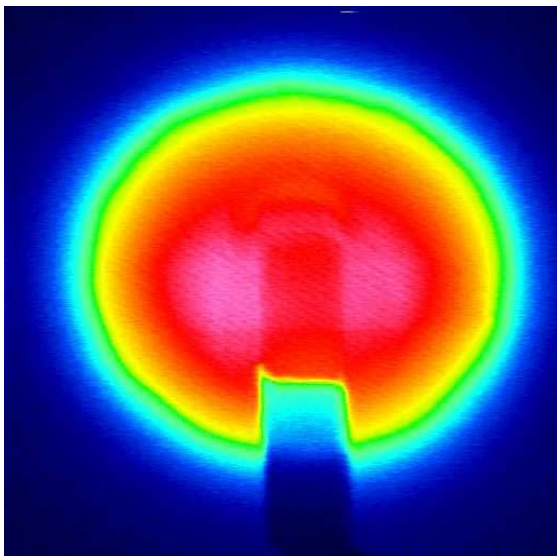


**Fig. 10.** Low temperature scanning electron micrograph of the top electrode of a Nb/Al/AlO<sub>x</sub>/Al/Nb device. Edges and contact electrode area show a different response

given by (25) requires the introduction of a phenomenological factor  $\alpha_s E_0^2$  taking into account spatial non-uniformities. The response shows, as for early Sn devices, a weak nonlinearity in energy attributed to self-recombination of quasi-particles [55] via the phonon coupling mechanism. More recently, the RT equations were modified in order to include diffusion losses and spatial inhomogeneities [124, 125].

#### 4.3.2 Nb-Based Devices and Trapping

Increasing the thickness  $d_{\text{Al}}$  of the Al trapping layers in Nb-based devices, results in a decrease of the gap parameter due to the proximity effect [80, 82], and an increase in the collected charge [22, 126]. This important effect is due to quasi-particle trapping and enhanced back-tunneling, as well as to a *reduction* of the quasi-particle loss rate in thicker Al [127]. For a constant value  $d_{\text{Al}}$ , the measured gap parameter decreases with increasing device size [128]. This variation correlates with the presence of an undercut at the perimeter of the device. Such undercut are likely created if a wet etching process is used during device fabrication.

The significant charge gain, combined with the benefit of narrow contact leads, allows signal generated by an optical photon  $\approx 1 \text{ eV}$  to be amplified above the noise level of room temperature electronics ( $\approx 2000 \text{ e}^- \text{ FWHM}$ ). Counting visible photons is now possible [24, 130]. However, the responsivity

in the visible-UV energy range, defined as the measured charge normalized by the photon energy  $S = Q_m/E \approx 2000 - 4000 \text{ e}^-/\text{eV}$ , is, for some samples, much lower than for X-rays [79, 131]. This observation cannot be explained within the framework of the RT equations where self-recombination ( $\propto N_{\text{exc}}^2$ ) limits the charge output.

#### 4.3.3 Improvement with Ta-Based Devices

Ta has a lower gap parameter than Nb (Table 1) and forms a single oxide, whereas Nb forms two substances, one being a very low temperature superconductor. These two differences make Ta a very good candidate to replace Nb at least as an absorber electrode [31]. Ta- and Nb-based devices behave in a similar way. The gap reduction observed with increasing Al film thickness, the increases of the charge output with increasing device size and thickness of the Al trap layers are well confirmed [36, 132]. In addition, Ta has a lower quasi-particle loss rate than Nb, favouring the rapid development of imaging arrays [133, 134].

#### 4.3.4 Al-Based Devices

For Al/AlO<sub>x</sub>/Al devices designed without intentional trapping layers, spectroscopic performances in the X-ray energy range are better than with single pixel Nb-based or Ta-based devices. The absorption efficiency in the soft X-ray range Al remains rather weak, however. The nonlinear energy response gets even weaker with increasing device size [135]. This could be explained with a smaller quasi-particle density followed by reduced self-recombination or by weaker impact of quasi-particle losses at the edges.

In order to compensate for the low absorption coefficient in Al, a composite device has been fabricated. A lead absorber was coupled acoustically through a natural AlO<sub>x</sub> layer to a Al/AlO<sub>x</sub>/Al device [34]. Further acoustical decoupling between sensor and substrate was achieved by coating the latter with a normal metal prior the STJ fabrication, and by thinning the substrate underneath the STJ using a silicon nitride membrane technology. The normal metal reduces phonon noise due to substrate events, whereas the membrane reduces phonon loss out of the Al electrode. This device [34] has the best measured spectral response obtained with a single pixel STJ in the X-ray energy range, 12 eV FWHM at 6 keV, and the largest reported absorption efficiency of  $\approx 50\%$  for a Pb volume of  $90 \times 90 \times 1.3 \mu\text{m}^3$ .

#### 4.3.5 Charge Gain and Linearity

In Fig. 11 we present the variation of  $Q_m/V_0$  with photon energy for data obtained with single pixel devices. The published data  $Q_m$  has been divided by the active volume  $V_0$  (absorber and trapping layers) of each STJs. Most

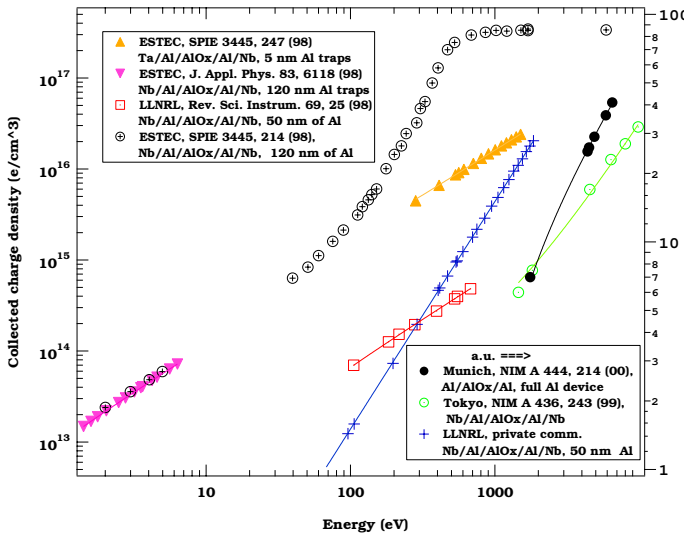


**Fig. 11.** Charge vs. photon energy for single pixel devices using the vertical trapping geometry. In most devices, back-tunneling is present. The Al device from Munich has no intentional traps. A weak nonlinearity is present at high energy for almost all devices. The strong nonlinear behavior above 100 eV is reported for the ESTEC devices made with thick Al traps only

of the data show a linear response, with only moderate nonlinearities at high energy. Strong nonlinear behavior has been observed by the ESTEC collaboration only [79] for 20 microns side length Nb devices fabricated with 120 nm thick Al traps. This behavior seems to be important at high quasi-particle density. Nb-based devices designed with 50 nm thick Al traps from Livermore show a responsivity of  $\approx 7300 \text{ e}^-/\text{eV}$  between 100 and 1000 eV. This corresponds to a effective charge gain of about 20 if (neglecting losses and gain)  $\epsilon \approx 1.76\Delta(\text{Nb})$  and a gain of 35 if Fig. 2 is used to estimate  $\epsilon \approx 3.33\Delta(\text{Nb})$ . This responsivity is almost a factor two larger than the number measured by ESTEC, had their device not deviated from the linear regime. Clearly, the various gain and loss processes are very sample dependent and their precise origin is difficult to isolate.

The strong nonlinear behavior observed above 100 eV and 500 eV with the Nb device cannot be explained within the framework of the RT-equations (2–5). In order to explain their data, Poelaert and co-workers [79] have introduced the dynamics of (de)trapping and formulated a set of modified RT-equations. The novelty [79, 136] is the inclusion of competition between quasi-particle trapping and de-trapping processes into the model. As already mentioned, de-trapping is due to the absorption of a phonon or results from the recombination of a trapped quasi-particle with a energetic (unconfined) partner. The number of this variety of partners could well be enhanced by

multiple tunneling and slow relaxation. If the energy of the partner quasi-particle is larger than the sum of the gap energy and the energy depth of the well, the recombination phonon will be able to break a Cooper pair. The resulting quasi-particles are, to begin with, not confined. If de-trapping is very effective, it can compensate for trapping induced losses and the total number of quasi-particle increases as the energy increases. This balance  $c_t(N_t - n_t/V)$  introduces a trapping rate  $\Gamma = c_t N_t$ , where  $c_t$  is a trapping coefficient,  $N_t$  the density of traps in the electrode of volume  $V$ , and  $n_t$  the number occupied of traps. On the other hand, the saturation of the responsivity observed at  $\approx 700$  eV and above can be explained by self-recombination. These ideas have been used to model the nonlinear energy response of symmetric back-tunneling device [79, 136].

The main assumption of the RT equations is that quasi-particle relaxation is extremely fast. Further, all the processes like recombination, losses, tunneling etc assume a narrow quasi-particle distribution in energy. A rather involved model which includes the full energy dependence of the quasi-particles that tunnel, relax and get lost was developed [86, 138]. In this approach, the energy-, position- and time-dependent kinetic equation [45] for quasi-particles was solved. In addition to well known and measurable quantities, five fitting parameters enter the model: the effective quasi-particle loss time  $\tau_{\text{eff}}$ , the phonon escape rate  $\Gamma_{\text{pl}}$ , the trapping probability  $c_t$ , the number of traps in the electrodes  $N_t V$ , and the energy depth of the traps. The temperature dependence of the responsivity was measured and a trapping depth of  $200 \mu\text{eV}$  was extracted for Nb, Ta and Al. The responsivity of Ta and Al devices was also studied and a weak nonlinearity seems to be present at low energy already [86]. We should again emphasize that only one group reports such a strong nonlinear energy response.

Data obtained at low energy is interesting because nonlinear effects are expected to be weak and self-recombination losses can safely be neglected in devices of a few tens of microns side size. Figure 12 shows that an increase of the Al traps thickness results in a larger responsivity. Several parameters affect  $Q_m$ . The proximity effect reduces  $\Delta_g \propto \epsilon$  and the value of  $Q_0 = E/\epsilon$  increases. This effect is unsufficient to explain the data since the responsivity increases approximately with the gap variation  $\Delta_0 - \Delta(d_{\text{Al}})$ . Multiplication by trapping cannot take place in such devices because the trapping well is not deep enough. At this quasi-particle density, the de-trapping mechanisms are unlikely to play a dominant role. Therefore, the observed charge gain is most likely the consequence of the competition between multiple tunneling processes and losses. An increase of the Al film thickness changes the absorber-trap volume ratio (20) and the trapping rate increases. These ideas were tested by modeling the device with four [78] quasi-particle populations coupled by the *classical* RT equations [139]. Back-tunneling is included but not cancellation, however. This approach yields an effective quasi-particle loss time in Al  $\tau_{\text{eff}} \approx 35 \mu\text{s}$ , much longer than in Ta. This result assumes a very

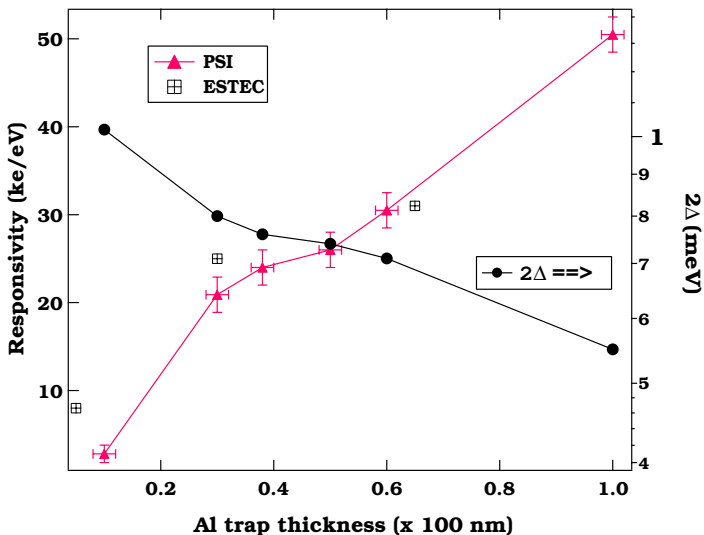


**Fig. 12.** Left scale: responsivity as a function of Al trap thickness measured with 2 eV photons. Right scale: measured variation of  $\Delta_g$

fast quasi-particle trapping process. The energy and temperature dependence of this model should now be tested and compared to the approach advocated by the ESTEC collaboration.

#### 4.3.6 Energy Resolution

Figure 13 shows a selection of energy resolution data (IR and electronic noise subtracted). The intrinsic energy resolution measured as a function of energy at a synchrotron beam-line [140] on Nb-based device with 50 nm Al traps follows reasonably the prediction of (25) between 300 and 1000 eV if we assume an effective Fano factor (statistics + back-tunneling) of 1.5 and  $\epsilon = 3.3\Delta_{\text{Nb}}$ . The factor 3.3 has been obtained from Fig. 2 and is twice the value predicted by the Monte Carlo simulation valid for a homogeneous superconductor. The agreement appears satisfactory if one bears in mind that there are most certainly additional noise sources that are difficult to quantify separately. Moreover, we believe that the value of  $\epsilon$  is overestimated because of the proximity effect. Above 1 keV, the data for  $\delta E$  deviates from the expected  $\sqrt{E}$  dependence. Only a fraction of this deviation can be explained by the line broadening of the monochromator used in the experiment. A significant fraction is most likely due to the unknown non-homogeneous response of the device. At lower energy, line broadening could be due to the fact that photons are stopped in Al rather than in Nb [141]. The best results at high energy were obtained with Ta [35] and Al [34] devices respectively. Back-tunneling

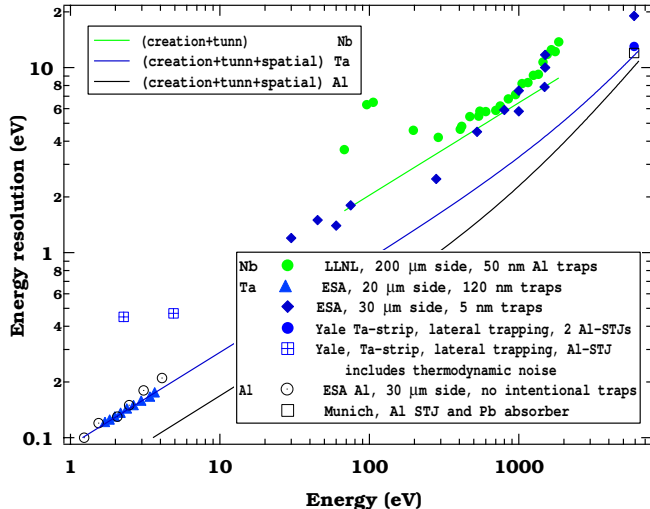


**Fig. 13.** Intrinsic energy resolution (electronic noise subtracted) of Nb-, Ta-, and Al devices. The Nb- and Ta-based devices use vertical trapping and Al as quasi-particle traps. The Al devices have no intentional trapping layers. The Yale data are from a Al device (Ta absorber and lateral trapping) that includes additional noise source [145]. All devices have a certain back-tunneling contribution

as well as a quadratic ad-hoc contribution  $\alpha_s E^2$  with  $\alpha_s = 4.5 \times 10^{-7}$  has been included in the solid lines drawn in Fig. 13 for Ta and Al.

The low energy data measured at ESTEC on Ta devices with thick Al traps [134] shows a resolution close to predictions, back-tunneling being included. The result in the soft X-ray range with thin traps suffer from additional noise [142, 143]. The results for the Al device at low energy [86, 144] are similar to those for Ta. The expected improvement due to the reduced gap is obviously compensated by additional noise sources. The two points with  $\approx 0.4$  eV resolution between 2 and 4 eV were measured at Yale with a device using lateral trapping and which includes additional thermodynamical noise [145] (see below).

Mo-Al devices as well as V-Al devices were investigated as well [86]. Mo-Al device showed large leakage current, and VAl devices suffer from a large quasi-particle loss rate and a low responsivity presumably due to the presence of traps [146]. The reactivity of V with oxygen forms metallic oxide inclusions which in turn can lead to regions of reduced gap parameter capable to increase quasi-particle trapping.

#### 4.4 Charge Division Approach

Charge division, also called distributed readout, occurs in the situation where the photon absorption site and the charge collection processes are spatially

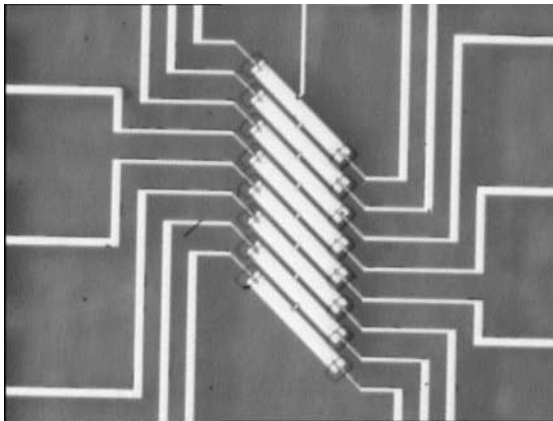


**Fig. 14.** Prototype distributed readout array. Each strip is a Ta absorber read out by two Al/AlO<sub>x</sub>/Al/Nb devices deposited on top of the Ta absorber at each end of the strips (vertical trapping). The strips are interconnected with Nb plugs to form a common ground. This device has the equivalent of  $\approx 8 \times 10$  pixels and would require 16 readout channels only

separated. If an absorber is larger than the STJ, quasi-particle diffusion takes place on such a scale that more than one charge readout channel may be needed to record a maximum of signal. For instance, a crystal absorber *acoustically* connected to an array of STJ devices could form an efficient sensor. The energy deposited in the absorber generates phonons which transfer into the STJs where they break Cooper pairs. The charge  $Q_m$  is the sum of the signals  $Q_{xy}$  recorded by each STJs and is proportional to the absorbed energy. The distribution of  $Q_{xy}$  within the array contains positional information. This approach enhances the absorption efficiency at the expense of degraded spectral resolution because the phonons that reach the STJs after many scattering processes have energies that are no longer related to the energy of the original photon [147]. Such systems were envisaged as phonon sensors in the field of dark matter search [148, 149]. More recently, series-junction arrays deposited on  $5 \times 5 \text{ mm}^2$  large absorber have been investigated and correction methods for the positional dependence of the response were proposed [150, 151, 152].

Another approach is to use a superconducting absorber *electrically* connected to a matrix of STJs through quasi-particle traps. By separating the absorber function from the charge collection function the competing requirements of good energy resolution, high efficiency, large collection area and imaging may be easier to achieve. The performance degradation observed above 1 keV in single pixel device could be less severe if photons are stopped in a dedicated well defined absorber separated from the STJ device itself. This arrangement would at least localize some of the potential problems that arise at the edges, interfaces, contact leads and due to proximity effects. For

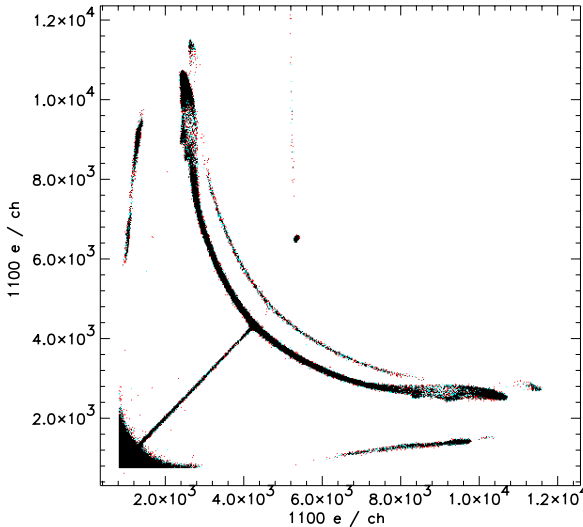


**Fig. 15.** Scatter plot of  $Q_1$  vs.  $Q_2$  measured on a  $200\text{ }\mu\text{m}$  long Ta absorber illuminated with 5.9 and 6.4 keV photons. The two parallel banana-shaped curves are due to 5.9 keV and 6.4 keV photons, respectively. The events along the diagonal leaving the origin are photons absorbed in a common electrode.  $\alpha_{\text{abs}} = 1$

optimal operation the excess quasi-particles generated in the absorber need to be transported efficiently and fast from the position of impact to the STJ.

Following the early demonstration experiments [19, 70] it has been shown that high quality STJs can be fabricated on highly polished Nb and Ta single crystals [153]. However, subsequent work showed that the quasi-particle diffusion rate in high purity annealed crystals as well as the effective quasi-particle life time were much shorter than expected [68, 154], making the high efficient  $1\text{ cm}^2$  detector dream rather difficult to realize. Present work using charge division rather concentrates on devices made with thin film absorbers.

Charge division is straightforward in the 1D-strip geometry; the absorber is of length  $L$  and width  $w \ll L$  with STJs connected at each end [69, 155]. Devices using the vertical trapping scheme [67, 128, 156] are relatively easy to fabricate since all the critical layers can be deposited in one vacuum run. Two devices like the one sketched in Fig. 8 are connected through a thin film absorber. Excess quasi-particles generated in the strip diffuse and are collected by the devices, which are read out “simultaneously” by two channels. Neglecting quasi-particle losses, the sum of the charge  $Q_1$  and  $Q_2$  collected at each STJ is proportional to the deposited energy,  $Q_m \propto E = Q_1 + Q_2$ , whereas their ratio  $Q_1/Q_2$  measures the position of the event. This method allows, in principle, to conceive  $N \times N$  equivalent energy resolving imaging devices with  $2N$  readout channels. (The rooted readout scheme requires one readout channel for each pixel). In Fig. 14 we show a Ta-absorber prototype currently

under study. This device has an equivalent absorber area of  $8 \times 10$  pixels of  $30 \times 30 \mu\text{m}^2$  each and requires  $2 \times 8$  readout channels only. The price for imaging with charge division is a reduction of the count rate. If one uses a current sensing method, the count rate is limited by the signal decay time which is the quasi-particle life time  $\tau_{\text{eff}}$  near the junction. If the time required to diffuse the distance  $L$  from the absorption site to the STJs  $\tau_d^2 = L^2/D$  exceeds  $\tau_{\text{eff}}$ , the maximum count rate is limited by  $\approx 1/\tau_d$ . In the charge sensing configuration, the signal risetime is  $\propto \tau_{\text{eff}}$  and the discharge time of the feedback network is usually longer.

The 1D-strip configuration [66, 67, 69, 87, 158] allows to measure absorber losses separately from other factors by analyzing the curvature of the  $Q_1$  vs.  $Q_2$  curves. The main assumption is that relaxation processes in the absorber are fast so that quasi-particle transport can be treated within the framework of a 1D diffusion model. An example of such a curve is given in Fig. 15. One has to bear in mind that the determination of the absorber loss factor  $\alpha_{\text{abs}}^2 = L/D\tau_{\text{eff}}$  is delicate and depends on the trapping efficiency near the STJs [69], on the possible diffusion losses in a common electrode, as well as on a signal loss due to variations of the impedance of the STJ during a pulse [87, 159]. Once absorber losses are known, it is possible to convert the data into an energy vs. position plot, opening a route for imaging spectrometers. The best energy resolution measured at 6 keV with a 1D-strip using a Ta absorber is about 13 eV [35]. It was shown that increasing the impurity content of the absorber has a negative impact on the energy resolution [159]. This result confirms observations made with single pixel devices. Two dimensional imaging capability with a square absorber and several STJs distributed around its perimeter has been modeled [160] and tested on a  $200 \times 200 \mu\text{m}^2$  device [156, 161]. All the experiments made with 1D and 2D geometries confirm a low diffusion rate in Ta between  $8 \text{ cm}^2/\text{s}$  and  $18 \text{ cm}^2/\text{s}$ . The true reasons for that remain unknown.

Quasi-particle losses in Ta appear uniform, as shown in Fig 16. The quality of the thin Ta films grown epitaxially at  $700^\circ\text{C}$  on single crystal sapphire substrates in our laboratory is most likely different from the polycrystalline material grown on silicon substrates at Yale [162]. The resistance ratio of the epitaxial material is always 40 and more. However, the loss factor in the polycrystalline material appears *smaller*. It is likely that the acoustic match between absorber and substrate is better for epitaxial material than it is for polycrystalline films. A better acoustic match could enhance phonon losses. If this assumption is correct, it implies that phonons play a role in the absorber relaxation processes on a longer time scale than traditionally assumed.

Devices using the lateral trapping geometry (Fig. 9) were connected to 1D strip-absorbers [87, 89, 96, 162]. In this configuration it is possible to achieve deeper traps since the absorber is not directly (from the proximity effect point of view) part of the electrode of the junction. A certain amount of multiplication by trapping can thus be achieved [ $\alpha_t$  in (25)]. The price to pay is a lower

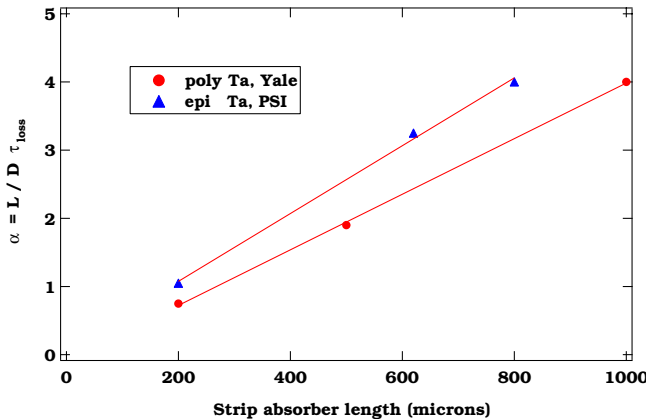


**Fig. 16.** Absorber loss parameter  $\alpha_{\text{abs}} = L/\sqrt{D\tau_{\text{eff}}}$  as a function of strip-absorber length  $L$  tested with quasi-particle injection due to 6 keV photons absorption.  $D$  and  $\tau_{\text{eff}}$ ,  $D$  are the quasi-particle diffusion and loss rate, respectively

temperature of operation because the STJ behaves more like an Al-device whose thermal current  $\propto \exp[-\Delta(\text{Al})/k_B T]$  with  $\Delta(\text{Al}) < \Delta(\text{Ta} - \text{Al})$ . The benefit is that the relaxation processes in the absorber and the dynamics in the traps followed by tunneling can be studied separately, without the complication introduced by proximity effect. In addition, the material of the counter electrode can be varied in order to modify the amount of quasi-particle confinement [ $\bar{n}$  in (25)]. Remember that an ideal STJ detector should avoid back-tunneling completely. It is therefore essential to attempt to suppress quasi-particle confinement after tunneling. The results obtained at Yale indicate that a device *with* back-tunneling and probed with low energy photons exhibits excess noise [145, 163]. The quasi-particle distribution appears to be at a higher temperature than the lattice temperature.

## 5 Outlook

A STJ with performances limited solely by *creation* statistics remains to be demonstrated. Below 1 keV, the results are close to the limit given by *creation* and *back-tunneling* statistics. Below 5 eV, Ta devices with 120 nm thick Al traps reach the expected limit [134]. Improved performances are expected with devices without any back-tunneling and multiplication gain ( $G$  and  $\alpha_t$ ), however. A device with no charge gain at all envisaged to detect low energy 1 eV photons will require very low noise readout electronics. The charge generated in say, pure Ta is in the order of 800 electrons/eV. Assuming a charge sensitive configuration including a 1 pF feedback capacitor, the fluctuations due to 800 electrons generate at the output a *rms* voltage noise of

$4.5\,\mu\text{V}$ . A front-end amplifier with a total equivalent voltage noise density of  $4\,\text{nV}/\sqrt{\text{Hz}}$  and a bandwidth of  $500\,\text{kHz}$  has almost the same noise level.

Above  $1\,\text{keV}$ , an Al-device *acoustically* coupled to a Pb-absorber has demonstrated the best energy resolution,  $12\,\text{eV}$  at  $6\,\text{keV}$  [34]. This result confirms that Al is an ideal material for the fabrication of an STJ in which the uniformity of the tunnel barrier and a long quasi-particle lifetime are essential. Photons are absorbed in a dedicated layer and a significant amount of the energy carried by the phonons produced at the beginning of the cascade is transferred into the Al where Cooper pair break-up is taking place. Phonon loss was minimized with the use of micro-fabricated membranes. This scheme presents several advantages. First, the absorber can be designed for high efficiency (50% at  $6\,\text{keV}$  in [34]) and its size could in future design be made larger than the one of the underlying STJ. This appears possible with a fabrication process producing “mushroom-shaped” structures. Second, an efficient absorber layer strongly reduces the peak doublets. These doublets are due to absorption events in both electrodes revealed by back tunneling.

Moreover, the electrical decoupling between the absorber and the actual recording device removes most of the intricacies introduced by the proximity effects between the metals. The price to pay for this level of performance is a temperature of operation below  $100\,\text{mK}$ . A weak nonlinear response in energy was observed [171]. Along the same vein, neutrons have been detected via the energy released in the capture reaction in crystals of  $\text{Li}_2\text{B}_4\text{O}_7$  [172].

In devices with *electrical* coupling between the absorber and the STJ, additional noise sources possibly due to absorber losses, quasi-particle trapping, current cancellation, fluctuations related to incomplete cooling as well as additional preamplifier noise due to dynamical impedance variations of the STJ conspire to form a rather complex situation. Clearly, more work is required to fully disentangle the various processes. Noise studies varying the photon energy together with the temperature of operation appear necessary. The energy and temperature variations of  $Q_m$  reported by the ESTEC collaboration deserves a critical and independent confirmation. The lateral trapping approach favored by Yale presents the advantage that relaxation processes in the absorber followed by trapping, cooling and (back)tunneling in the devices can be studied sequentially. Proximity effects can be avoided as well.

Current energy resolution performances can nevertheless be improved provided the quasi-particle current is further reduced. This requires a lower temperature of operation as well as devices with smaller area. The area reduction will reduce the capacitance  $C_d$ , so that it may become necessary to reduce the stray capacitance due to the wiring between the device and the amplifier; cooling the front-end electronics seems unavoidable. Improvement may also be achieved by choosing absorber materials with lower energy gap. However, because the characteristic time  $\tau_0$  scales approximately with  $\Delta_g^{-3}$ , the quasi-particle cooling rate reduces whereas the tunneling rate remains temperature independent. This may, in turn, favor back-tunneling of un-

laxed quasi-particle. Thus, the energy gained by repeated tunneling affects even more the quasi-particle distribution [164]. A decrease of the tunneling rate by increasing the tunnel barrier thickness as well as an increase of the bias voltage  $V_b$  are possible measures to solve this issue. For back-tunnelling devices with low gap materials the well known RT-equations were claimed inadequate to describe the evolution of the phonon and quasi-particle distributions and alternatives have been suggested [138, 173].

Array work has started and is successful. A  $6 \times 6$  array built by the ESTEC collaboration allows to image and measure the energy and time or absorption (3 dimensional detector) of single photon events in the visible. The instrument [174] has been placed in the focus of an optical telescope, and astronomical observations were performed. Each STJ on the array requires its individual bias and readout electronics. Work is in progress on a  $10 \times 12$  pixels system [175]. A  $3 \times 3$  array of Nb/Al devices has been built by the Livermore collaboration and is operated as a multichannel soft X-ray spectrometer for fluorescence absorption spectroscopy [176]. This class of experiments generates fortunately a moderate count rate because of the low fluorescence yield combined with the reduced solid angle. The count rate delivered by a usual transmission experiment with synchrotron light could not be handled by an STJ detector. Small arrays of 16 devices are used as time and energy sensors in time-of-flight mass spectrometers that are currently reaching the market [177].

All these applications require efficient IR flux reduction measures. In the visible as well as in the soft X-ray range a cascade of cold filters appear adequate. In the VUV dedicated high-pass filters are more difficult to design. In mass spectrometry, 300 K radiation is present as well and IR blocking windows are not allowed. Thus, rejection must be obtained with a design that reduces the solid angle between the sensor and the 300 K source. Our experience shows that the IR load tolerable with 30 microns side length STJs should not exceed a few 1/100 pW.

The best energy resolution obtained with a device using charge division is 13 eV at 6 keV [35]. This approach has demonstrated intrinsic multiplexing capabilities in the range of energy UV to X-ray. The real advantage of a imaging device like the prototype shown in Fig. 14 is the reduction of the number of leads. The count-rate reduction associated with charge division is important, however. A detector using 500  $\mu\text{m}$  long 1D strip of width 30  $\mu\text{m}$  has the same collecting area that 15 square devices having 30  $\mu\text{m}$  side length. The total count rate that can be accommodated with 15 isolated pixels is in the order of 150 000 counts/s. The rate that can be measured with the 1D strip is reduced by almost two orders of magnitude.

A matrix readout scheme has been proposed and tested in a  $2 \times 2$  device [178], a 12 by 8 device using only 20 readout lines connected to dedicated readout electronics is under test [179]. Predictions [180] are that the overall energy resolution degrades with the associated increase of the input

capacitance (parallel connection). However, an increase in signal to noise ratio results from the correlated readout of rows and columns. This benefit can recover a fraction of the above mentioned degradation.

Despite the involvement of cryogenic operation, the further development of cryogenic detectors is of importance because they offer the unique opportunity to perform spectroscopy at the single photon level. Large format arrays are very desirable in the fields of astronomy or as instruments at synchrotron beamlines, for example. However, it will be difficult to significantly scale-up the present arrays using the direct readout approach. Several practical problems need to find a solution. The STJ operated in the Giaever mode does not store the information like the wells in a CCD allows it. Thus, the readout electronics needs to be “on-line” all the time. The multiplexing schemes currently under study for the readout of low impedance micro-calorimeters may prove unpractical for arrays of high impedance STJs.

Engineering large format array will be a major technological challenge. Obviously, the number of leads must be minimized in order to reduce thermal load. An immediate measure is that the bottom (or top) electrode of each STJ share a common potential. The junction area cannot be increased at will (shot noise + capacitance). A  $100 \times 100$  microns device has already substantial  $100\text{ pF}$  capacitance. The packing density should be optimized, quasi-particle losses (and cross talk) through leads minimized, and each STJ must be biased properly in the high impedance region of its current-voltage curve. The suppression of the *dc*-Josephson current and the Fiske resonances require a magnetic field parallel to the tunnel barrier of all devices. Thus, a high degree of fabrication uniformity will be required in order to allow a large number of devices be biased with the *same* value of magnetic field. Devices with square shape and reading out along one diagonal allows a high packing density and efficient background currents suppression. Alternatives using a annular configuration [181, 182] are currently under study. The connection between the base electrodes is advantageously made with bridges of higher gap material like Nb. The Nb will act as a quasi-particle reflector. The current lithography resolution limit of say  $2\mu\text{m}$  constrains the smallest lead width as well as the number of devices in a row. Efforts to contact the devices from the top (bump bonding) need to be considered as well, because the packing density of the contact leads and the lithography resolution will limit the number of devices. Several of the above mentioned considerations assume a transparent substrate through which illumination in the near IR-V energy range of the array takes place. If the device is to be used at higher energy, illumination through the substrate is no longer possible and any high packing density of leads will, at some level, cover most of the pixel area so that new architectures must be considered [165].

A linear array would in principle be easier to design because contacting leads could occupy space on each side of the linear device. Such devices could find application as order sorting detectors in echelle spectrographs [166].

The overall benefit would be a reduction of the time required to perform an astronomical observation.

Cryogenic amplifiers with high input impedance based on the RF-single electron transistors (RF-SET) [167,168] are presently investigated as building blocks for multiplexers using a wavelength division scheme [169, 170]. However, reading out an STJ of current size with an RF-SET may prove difficult because of the requirement of a very small capacitance of the input gate.

As concluding remarks, a few speculative points. The hot-electron microcalorimeter [183] (NIS device) has not been discussed in this review. The absorption of energy takes place in the normal metal (N electrode). No excess charge is made free, rather electrons in N are heated up, and the temperature change  $\delta T$  is proportional to amount of absorbed energy. Thus,  $\delta T = E/C$  where  $C$  is the electronic heat capacity. The change in electron temperature is recorded as a change in the quasi-particle density in the opposite superconducting layer (S electrode). This change in turn corresponds to a change in tunneling current. This device has no intrinsic charge gain. Therefore we expect its use as visible photon counter be possible with a small heat capacity only. In the UV to soft X-ray energy range the NIS detector [183] may present two advantages. First, its use does not require the application an external magnetic field. Second, the NIS can in principle be operated with a low impedance readout electronics (SQUID) in the voltage biased mode, or with a conventional high impedance readout circuit in the current biased mode. Moreover, if recent work done on the quasi-particle trapping transistor (QTT) [184] is successful, the NIS device could possibly be engineered as part of a 3-terminal device that has current gain. This may open a yet unexplored route of development.

The kinetic inductance thermometer [185] responds to quasiparticle density variations by a change in the surface impedance. A asymmetric SIS tunneling device [186] biased in the region of negative differential resistance exhibits relaxation oscillations. Such a device, connected in series with an inductance and biased with a stiff voltage source would respond to a perturbation by a variation of the relaxation oscillation frequency. If the expected high sensitivity can be demonstrated, this class of device may allow frequency domain multiplexing.

## Acknowledgements

The authors would like to thank Guy Brammertz, Fred Finkbeiner, Stephan Friedrich, Iwan Jerjen, Alexander Kozorezov, Hans Rudolf Ott, Dan Prober, Nicola Rando, Kenneth Segall, Peter Verhoeve and Christopher Wilson for providing useful comments and/or data used in this review. We would like to thank Eugenie Kirk for device fabrication in our own laboratory.

## 6 Appendix

### 6.1 Readout Circuit and Electronics Noise

In Fig. 17 the passive current bias approach is shown together with the voltage bias approach for illustration purposes only. The STJ is modeled as a current source  $I_x$  in parallel, with a capacitor  $C_d$  and a (valiable) resistor  $R_d$ , forming the impedance of the device  $Z_d$ . The coupling capacitor  $C_c$  is used to separate the *dc* part of the circuit from its *ac* part. Current deviations  $I_x(t)$  produce a voltage change  $\delta V = Z_d(I_x - I_f)$  sensed at the input. The first stage is a low noise FET transistor followed by a transimpedance. The feed-back element  $Z_f$  formed by  $C_f$  in parallel with  $R_f$ . The current biased mode is technically less involved but intrinsically unstable close to negative differential resistance regions of the device. The current amplifier configuration allows to study more precisely the quasi-particle dynamics in the STJ because the shape of  $I_x(t)$  can be recorded whereas the maximum output of the charge amplifier is proportional to the  $Q_m$ . The falling edge of the current pulse contains the quasi-particle dynamics information. For a charge pulse, this information is partly recovered by studying the risetime of the signal.

The analysis of the above circuit [100, 108, 112] yields an expression for the output signal as a function of the STJ current  $I_x$

$$V_{\text{out}} = -I_x \frac{1}{Z_f^{-1} + \frac{1}{Z_d A}} = -I_x \frac{AZ_d Z_f}{Z_f + AZ_d} . \quad (26)$$

Here  $C_d$  entering  $Z_d$  includes the stray and input capacitances of the front-end FET  $C_i$ . In the ideal case the stray capacitance is negligible,  $C_i \approx C_d$ , and  $1/Z_d = 1/R_d + i\omega(C_d + C_i)$ . The quantity  $A$  is the frequency dependent open loop gain.

We refer all the noise sources to the input. The thermal voltage fluctuations of the feed-back resistor generate a current noise  $\langle i_f^2 \rangle = 4k_B T / R_f$ . The current noise  $\langle i_p \rangle$  is the quadratic sum of the shot noise due to the bias current  $I_{\text{th}}$ , the thermal noise of  $R_d$ , the shot noise due to the leakage current  $I_g$  through the gate of the FET, and the device current noise so that  $\langle i_p^2 \rangle = 2eI_{\text{th}} + 4k_B T / R_d + 2eI_g + I_{\text{STJ}}^2$ . The voltage noise  $\langle V_n \rangle$  term of the input FET is due to the shot noise of the drain current and to the  $1/f$  noise,  $\langle V_n^2 \rangle = 4k_B T_g / g_m + C/f$ . Here  $g_m$  is the transconductance of the FET,  $T_g$  the temperature of operation of the junction. Self-heating can be used to keep  $T_g$  at the optimum value of 120–90 K for Si-based J-FET.  $\langle V_n^2 \rangle$  is converted into an equivalent current noise through the impedance  $Z_d$  (again taking the total input capacitance  $C_i + C_d$ ) so that

$$\langle I_n^2 \rangle = \langle I_p^2 \rangle + \langle I_f^2 \rangle + \langle V_n^2 \rangle \left( \frac{1}{R_d} + \omega C_i \right)^{-2} . \quad (27)$$

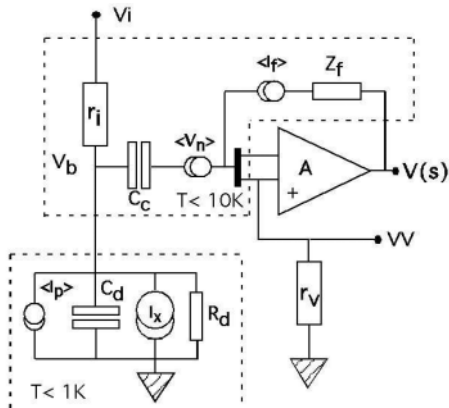


**Fig. 17.** Two possible STJ bias schemes using a transimpedance amplifier. In the current bias mode (no applied  $VV$  and no  $r_V$  resistor),  $V_i$  applies the bias  $V_b$ , the resistor  $r_i$  limits the current through the device and the capacitor  $C_c$  is required as a blocking capacitor. In the voltage bias mode ( $V_i = 0$ , no  $r_i$  resistor and no  $C_c$  capacitor), a voltage  $VV$  is applied at the virtual ground of the op-amp (an additional feed-back loop between  $V_b$  and the inverted input is not shown). The elements  $C_f$  and  $R_f$  in parallel form the feed-back impedance  $Z_f$ . If  $C_f$  is and kept to a minimum and  $R_f$  not significantly larger than  $R_d$ , the circuit behaves as a current amplifier. If  $R_f$  is several tens of  $M\Omega$  the circuit behaves more like a charge sensitive amplifier. In order to reduce the capacitance of the wiring between the device and the FET and to reduce the noise contributions due to  $r_i$  and  $Z_f$  it is of advantage to mount these elements on an intermediate cryogenic stage.  $\langle I_f \rangle$  is the thermal noise of the feed-back resistor.  $\langle V_n \rangle$  is the voltage noise of the input field effect transistor.  $I_x = I_f + I_d$  is the signal source of the STJ,  $R_d$  its dynamical resistance,  $C_d$  its capacitance, and  $\langle I_p \rangle$  all the noise sources related to the STJ. The quantity  $V(s)$  is the output signal

The total noise over the full bandwidth is

$$V_{no}^2 = \frac{1}{2\pi} \int_{-\infty}^{\infty} \langle I_n^2(\omega) \rangle \left( \frac{AZ_d(\omega)Z_f(\omega)}{Z_f(\omega) + AZ_d(\omega)} \right)^2 \delta\omega \quad (28)$$

can be estimated provided the shape of  $I_x(\omega)$  is known.

## References

- [1] G.H. Wood, B.L. White: Appl. Phys Lett. **15**, 237 (1969) 217
- [2] I. Giaever: Phys. Rev. Lett. **5**, 147 (1960), I. Giaever, H. R. Hart, K. Megerle: Phys. Rev. **126**, 941 (1962) 217
- [3] M. Kurakado, H. Mazaki: Phys. Rev. **B 22**, 168 (1980) 217
- [4] T. Van Duzer and C.W. Turner: *Principles of Superconducting Device and Circuits* (Elsevier, Amsterdam 1981) ISBN 0-444-0041-4, chapter 4 218, 227

- [5] I. Giaever and K. Megerle: Phys. Rev **122**, 1101 (1961) [219](#), [228](#)
- [6] N. E. Booth: Appl. Phys. Lett. **50**, 293 (1987) [219](#), [229](#)
- [7] P. G. de Gennes: *Superconductivity of Metals and Alloys* Ed. W. A. Benjamin, (New York, 1966) and P. G. de Gennes, Rev. Mod. Phys 36, 225 (1964) [219](#)
- [8] K. E. Gray: Appl. Phys. Lett. **32**, 392 (1978) [219](#), [220](#), [228](#)
- [9] M. Tinkham: *Introduction to Superconductivity* 2nd edition, (Mc Graw Hill, New-York 1996) [219](#)
- [10] M. Kurakado and H. Mazaki: Nucl. Instr. & Meth. in Phys. Res. A **185**, 141 (1980) and Nucl. Instr. & Meth. in Phys. Res. A **185**, 149 (1980) [219](#)
- [11] M. Kurakado: Nucl. Instr. & Meth. in Phys. Res. A **196**, 275 (1982) [219](#), [222](#)
- [12] The responsivity is defined as "generated charge/absorbed energy" and has units e/eV. This is equivalent to the usual "signal current / absorbed power" unit used in bolometer work. [219](#)
- [13] U. Fano: Phys. Rev. **B72**, 26 (1942) [220](#)
- [14] D. Twerenbold: Euro. Phys. Lett. **1**, 209 (1986) [220](#), [227](#)
- [15] H. Kraus, Th. Peterreins, F.v. Feilitzsch, R.L. Mössbauer, V. Zacek and E. Umlauf: Euro. Phys. Lett. **1**, 161 (1986) [220](#)
- [16] W. Rothmund and A. Zehnder: *Superconductive Particle Detectors* p. 52, Ed. A. Barone (Singapore, World Scientific 1988) [220](#)
- [17] W. Rothmund: ETH Thesis Nr. 9445, PSI, Villigen, Switzerland (1991) [220](#), [227](#)
- [18] compare Figs. 3 and 4 in F. Probst, H. Kraus, Th. Peterreins and F. Von Feilitzsch, Nucl. Instr. & Meth. in Phys. Res. A **280**, 251 (1989) [220](#)
- [19] M. Kurakado, T. Takahashi and A. Matsumura: Appl. Phys. Lett. **57**, 1933 (1990) [220](#), [249](#)
- [20] N. Rando, A. Peacock, A. van Dordrecht, C. L. Foden, R. Engelhardt, B. G. Taylor, P. Gare, J. Lumley, C. Pereira: Nucl. Instr. & Meth. in Phys. Res. A **313**, 173 (1992) [220](#), [222](#)
- [21] N. Rando, A. Peacock, C. Foden, A. van Dordrecht, J. Lumley, and C. Pereira: J. Appl. Phys. **73**, 5098 (1993) [220](#)
- [22] C. A. Mears, S. E. Labov, A. T. Barfknecht: Appl. Phys. Lett. **63**, 2961 (1993) [220](#), [235](#), [236](#), [242](#)
- [23] M. A. C. Perryman, C. L. Foden, and A. Peacock: Nucl. Instr. & Meth. in Phys. Res. A **325**, 319 (1993) [221](#)
- [24] N. Rando, P. Verhoeve, A. van Dordrecht, A. Peacock, M. Perryman, S. Andersson, J. Verveer, B. Collaudin, D. J. Goldie, R. Venn: Nucl. Instr. & Meth. in Phys. Res. A **370**, 85 (1996) [221](#), [242](#)
- [25] N. Rando, S. Andersson, B. Collaudin, F. Favata, P. Gondoin, A. Peacock, M. Perryman, J. Verveer, P. Verhoeve, and D. J. Goldie: Nucl. Instr. & Meth. in Phys. Res. A **444** 441, (2000) and refs. therein [221](#)
- [26] D. Twerenbold, J. L. Vuilleumier, D. Gerber, A. Tadsen, B. van den Brandt, and P.M. Gillevet: Appl. Phys.Lett **68**, 3503 (1996) [221](#)
- [27] M. Frank, C. A. Mears, S. E. Labov, W. H. Benner, D. Horn and A. F. Barfknecht: Rapid Comm. in Mass Spectrom. **10**, 1946 (1996) [221](#)
- [28] D. Twerenbold, D. Gerber, D. Gritti, Y. Gonin, A. Netuschill, F. Rossel, D. Schenker and J.L. Vuilleumier: Proteomics **1** 66, (2001) [221](#)

- [29] D. Twerenbold, A. Netuschill, N. F. de Rooij, Ph. Luginbuhl, D. Gerber, D. Gritti, Y. Gonin and J. L. Vuilleumier: Proteomics **2**, 436 (2002) [221](#)
- [30] V. Lordi, V. Gambin, S. Friedrich, T. Funk, T. Takizawa, K. Uno, and J. S. Harris: Phys. Rev. Lett. **90**, 145505 (2003) [221](#)
- [31] P. Verhoeve, N. Rando, A. Peacock, A. van Dordrecht, and D. J. Goldie: Appl. Phys. Lett. **72**, 3359 (1998) [221](#), [243](#)
- [32] C. A. Mears, S. E. Labov, M. Frank, H. Netel, L. J. Hiller, M. A. Lindeman and D. Chow: IEEE Trans. Appl. Supercond. **7**, 3415 (1997) [221](#), [240](#)
- [33] G. Angloher, B. Beckhoff, M. Bühler, F. v. Feilitzsch, T. Hertrish, P. Hettl, J. Höhne, M. Huber, J. Jochum, R. L. Mössbauer, J. Schnagl, F. Scholze and G. Ulm: Nucl. Instr. & Meth. in Phys. Res. A **444** 214, (2000) [221](#), [227](#)
- [34] G. Angloher, P. Hettl, M. Huber, J. Jochum, F. v. Feilitzsch, R. L. Mössbauer: J. Appl. Phys. **89** 1425, (2001) [221](#), [243](#), [246](#), [252](#)
- [35] L. Li, F. Frunzio, C. M. Wilson, D. E. Prober, A. E. Szymowiak, and S. H. Moseley: J. Appl. Phys. **90**, 3645 (2001) [221](#), [246](#), [250](#), [253](#)
- [36] P. Verhoeve, N. Rando, A. Peacock, A. van Dordrecht, A. Poelaert, and D. J. Goldie: IEEE Trans. Appl. Supercond. **7**, 3359 (1997) [221](#), [243](#)
- [37] J. B. le Grand, C. A. Mears, L. J. Hiller, M. Frank, S. E. Labov, H. Netel, D. Chow, and A. T. Barfknecht: Appl. Phys. Lett. **73**, 1295 (1998) [221](#)
- [38] A. Barone: Nucl. Phys. B **44**, 645 (1995) [221](#)
- [39] N. E. Booth and D. J. Goldie: Supercond. Sci. Technol. **9**, 493 (1996) [221](#)
- [40] D. Twerenbold: Rep. Progr. Phys. **59**, 394 (1996) [221](#)
- [41] Proceedings of the last 5 International Workshops on Low Temperature Detectors: LTD5, J. Low Temp. Phys. **93**, 185-858 (1993). LTD6, editors H. R. Ott and A. Zehnder, Nucl. Instr. & Meth. in Phys. Res. A **370** xvii - xxii (1996). LDT7, editor S. Cooper, Proceedings of the Seventh Intern. Workshop on Low Temperature Detectors, published by the Max Planck Institute of Physics, ISBN 3-00-002266-x (1997). LDT8, editors P. De Korte and T. Peacock, Nucl. Instr. & Meth. in Phys. Res. A **444** xvii - xxiv (2000). LTD9, editors F. S. Porter, D. Mc Cammon, M. Galeazzi, C. K. Stahle, AIP Conf. Proc. **605**, (2002). LTD10, editor F. Gatti, Nucl. Instr. & Meth. in Phys. Res. A **520** xvii - xxix (2004). [221](#)
- [42] D. van Vechten and K. S. Wood: Phys. Rev. B **43**, 12852 (1991) [221](#)
- [43] Y. N. Ovchinnikov and V. Z. Kresin: Phys. Rev. B **58**, 12421 (1998) [221](#), [222](#)
- [44] S. B. Kaplan, C. C. Chi, D. N. Langenberg, J. J. Chang, S. Jafarey and D. J. Scalapino: Phys. Rev. B **14**, 4854 (1976) [221](#), [222](#), [225](#), [226](#), [227](#), [229](#)
- [45] J. J. Chang and D.J. Scalapino: Phys. Rev. B **15**, 2651 (1977) [222](#), [245](#)
- [46] A. Zehnder: Phys. Rev. B **52**, 12858 (1995) [222](#), [224](#)
- [47] A. G. Kozorezov, A. F. Volkov, J. K. Wigmore, A. Peacock, A. Poelart and R. den Hartog: Phys. Rev. B **61**, 11807 (2000) [222](#), [223](#)
- [48] A. Rothwarf and B. N. Taylor: Phys. Rev. Lett. **19**, 27 (1967) [224](#)
- [49] J. B. le Grand: Ph.D. thesis, University of Utrecht (1994) [225](#)
- [50] P. W. Epperlein, K. Lassmann and W. Eisenmenger: Z. Phys. B **31**, 377 (1978) [226](#)
- [51] P. A. J. de Korte, M. L. van den Berg, M. J. Bruijn, M. Frericks, J. B. le Grand, J. G. Gijsbertsen, E. P. Houwman, and J. Flokstra: Proc. SPIE **1743**, 24 (1992) [226](#), [228](#)

- [52] D. N. Langenberger: Procs. LT14, Ed. M. Krusius and M. Vuorio, (North Holland, **5**, 223 (1975) [227](#)
- [53] S. B. Kaplan: J. Low Temp. Phys. **37**, 343 (1979) [227](#)
- [54] O. J. Luiten, H. L. van Lieshout, F. A. Michels, P. Valko, M. P. Bruijn, F. Kiewiet, P. A. J. de Korte, D. J. Adlerhof, A. W. Hamster, C. G. S. Brons, and J. Flokstra: Nucl. Instr. & Meth. in Phys. Res. A **370** 72, (1996) [227](#)
- [55] P. Verhoeve, N. Rando, J. Verveer, A. van Dordrecht, A. Peacock, P. Videler, M. Bavdaz, D. J. Goldie, T. Lederer, F. Scholze, G. Ulm and R. Venn: Phys. Rev B **53**, 809 (1996) [227](#), [241](#), [242](#)
- [56] E. L. Wolf: *Principles of Electron Tunneling Spectroscopy*, (Oxford Science Publications 1985) [227](#), [228](#)
- [57] Branch imbalance relaxation time is about 2 orders of magnitude shorter than the tunnel time in *Al*, see J. Clarke in *Non-equilibrium Superconductivity*, ed. by D. N. Langenberger and A. I. Larkin (Elsevier, Amsterdam, 1986) [228](#)
- [58] J. L. Paterson: J. Low Temp. Physics, **33**, 285 (1978) [228](#)
- [59] P. L. Brink: PhD. thesis, Oxford University, (1995) [228](#)
- [60] H. Kraus, M. Gutsche, P. Hettl, J. Jochum, B. Kemmather: J. Supercond. **9**, 245 (1996) [228](#), [240](#)
- [61] A. F. Cattell, A. R. Long, A. C. Hanna, and A. M. Mac Leod: J. Phys. F Met. Phys. **13**, 855 (1983) [228](#)
- [62] D. M. Ginsberg: Phys. Rev. Lett. **8**, 204 (1962) [229](#)
- [63] V. Narayanamurti, R. C. Dynes, P. Hu, H. Smith, and W. F. Brinkman: Phys. Rev. B **16**, 6041 (1978) [229](#)
- [64] J. N. Ullom, P.A. Fischer, and M. Nahum: Phys. Rev. B **58**, 8225 (1998) [229](#)
- [65] P. Hettl, G. Angloher, M. Bruckmayer, F. v. Feilitzsch, J. Jochum, R.L. Mössbauer: Proceedings of LTD 7, 21, Ed. S. Cooper, published by the Max Planck Institute of Physics, ISBN 3-00-002266-X. [229](#)
- [66] S. Friedrich, K. Segall, M. C. Gaidis, C. M. Wilson, D. E. Prober, A. E. Szymkowiak, S. H. Moseley: Appl. Phys. Lett. **71**, 3901 (1997) [229](#), [250](#)
- [67] Th. Nussbaumer, Ph. Lerch, E. Kirk, A. Zehnder R. Füchslin, P. F. Meier, H.R. Ott: Phys. Rev. B. **61**, 9719, (2000) [229](#), [249](#), [250](#)
- [68] M.L van den Berg, F.B. Kiewiet, M.P. Bruijn, O.J. Luiten, and P.A. de Korte: IEEE Trans. Appl. Supercond., **9**, 2951 (1999) [229](#), [249](#)
- [69] H. Kraus, F. v. Feilitzsch, J. Jochum, R.L. Mössbauer, Th. Peterreins, F. Pröbst: Phys. Lett. B **231**, 195 (1989) [229](#), [249](#), [250](#)
- [70] D.J. Goldie, N.E. Booth, C. Patel, G.L. Salmon: Phys. Rev. Lett., **64**, 954 (1990) [229](#), [249](#)
- [71] S. E. Labov, C. A. Mears, G. W. Morris, C. E. Cunningham, M. A. Le Gros, E. H. Silver, A. T. Barfknecht, N. W. Madden, D.A. Landis, and F. S. Goulding: Proc. SPIE **1743** 328 (1992) [229](#)
- [72] D. J. Goldie, N. E. Booth, C. Patel, and G. L. Salmon: Physica B **169**, 443 (1991) [229](#)
- [73] D. J. Goldie, C. Patel, N. E. Booth, and G. L. Salmon: Superconduc. Science Technol. **6**, 203 (1993) [229](#)
- [74] G. Burnell, P. A. Warburton and M. G. Blamire: J. Appl. Phys. **76**, 1105 (1994) and refs. therein [229](#)

- [75] M. Ohkubo, K. Tanabe, K. Suzuki, H. Pressler, M. Ukibe, N. Kobayashi, T. Nakamura, M. Kishimoto, M. Katagiri, D. Fukuda, H. Takahashi and M. Nakazawa: Nucl. Instr. & Meth. in Phys. Res. A **444** 237, (2000) [230](#)
- [76] M. Ohkubo, K. Suzuki, K. Tanabe, H. Pressler, and M. Ukibe: AIP *Low Temperature Detectors* CP **605** 55, (2002) [230](#)
- [77] A. A. Golubov and E. P. Houwmann: Physica C **205**, 147 (1993) [230, 234](#)
- [78] A. A. Golubov, E. P. Houwman, J. G. Gijsbertsen, J. Flokstra, H. Rogalla, J. B. le Grand, and P. A. J. de Korte: Phys. Rev. B **49**, 12953 (1994) [230, 234, 245](#)
- [79] A. Poelaert, A. Kozorezov, A. Peacock, and J. K. Wigmore: Phys. Rev. Lett. **82**, 1257 (1999) [230, 243, 244, 245](#)
- [80] A. A. Golubov, E. P. Houwman, J. G. Gijsbertsen, V. M. Krasnov, J. Flokstra, H. Rogalla, and M. Y. Kupriyanov: Phys. Rev. B **51**, 1073 (1995) [230, 231, 232, 234, 242](#)
- [81] W. Belzig, C. Bruder, and G. Schön: Phys. Rev. B **54**, 9443 (1996) [230](#)
- [82] A. Zehnder, Ph. Lerch, S.P. Zhao, Th. Nussbaumer, E. Kirk and H.R. Ott: Phys. Rev. B **59**, 8875, (1999) [230, 231, 232, 233, 242](#)
- [83] G. Brammertz, A. Golubov, A. Peacock, P. Verhoeve, D. J. Goldie, and R. Venn: Physica C **350**, 227 (2001) [231](#)
- [84] G. Brammertz, A. Poelaert, A. A. Golubov, P. Verhoeve, A. Peacock, H. Rogalla: J. Appl. Phys. **90**, 355 (2001) [231, 233](#)
- [85] G. Brammertz, A. A. Golubov, P. Verhoeve, R. den Hartog, A. Peacock, H. Rogalla: Appl. Phys.Lett. **80**, 2955 (2002) [231, 233](#)
- [86] G. Brammertz: PhD, University of Twente, 2003 [233, 234, 245, 247](#)
- [87] K. J. Segall: PhD Thesis, Yale University, (2000) [235, 237, 241, 250](#)
- [88] D. J. Goldie, P. L. Brink, C. Patel, N. E. Booth, and G. L. Salmon: Appl. Phys. Lett. **64**, 3169 (1994) [235](#)
- [89] K. E. Segall, C. Wilson, L. Frunzio, L. Li, S. Friedrich, M. C. Gaidis, D. E. Prober, A. E. Szymkowiak and S. H. Moseley: Appl. Phys. Lett. **76**, 3998 (2000) [236, 237, 241, 250](#)
- [90] V. V. Samedov and V. A. Andrianov: *Ninth International Workshop on Low Temperature Detectors* Eds. F. S. Porter et al, AIP *Low Temperature Detectors* CP **605** 47, (2002) [236](#)
- [91] S.P. Zhou, F. Finkbeiner, Ph. Lerch, A. Jaggi, A. Zehnder, and H.R. Ott: Physica C **214**, 354 (1993) [237](#)
- [92] R. E. Eck, D. J. Scalapino, B. N. Taylor: Proceedings of 9th Low Temperature Physics Conference, Ed. J. G. Daunt, Plenum, New York 1964 [238, 240](#)
- [93] M. D. Fiske: Rev. Mod. Physics **36**, 221 (1964) [238, 240](#)
- [94] J. G. Gijsbertsen, E. P. Houwman, J. Flokstra, H. Rogalla: Physica C **194-196**, 1705 (1994) and J. G. Gijsbertsen, E. P. Houwman, B. B. G. Klopman, J. Flokstra, H. Rogalla, D. Quenter and S. Lemke: Physica C **249**, 12 (1995) [238](#)
- [95] R. Cristiano, M. P. Lissitskii and C. Nappi: Supercond. Sci. Technol. **13**, 542 (2000) [238](#)
- [96] M. C. Gaidis: Ph. D. thesis, Yale University, (1994) [239, 250](#)
- [97] M. Frank et al: Nucl. Instr. & Meth. in Phys. Res. A **370** 41, (1996) [240](#)

- [98] T. Ikeda, H. Kato, K. Kawai, H. Miyasaka, T. Oku, W. Ootani, C. Otani, H. Sato, H. M. Shimizu, and H. Watanabe: IEEE Trans. Appl. Supercond. **9**, 3858 (1999) 240
- [99] T. Oku, T. Ikeda, H. Kato, K. Kawai, H. Miyasaka, W. Ootani, C. Otani, H. Sato, H.M. Shimizu, Y. Takizawa, H. Watanabe, H. Nakagawa, H. Akho, M. Aoyagi and T. Taino: Nucl. Instr. & Meth. in Phys. Res. A **444** 136, (2000) 240
- [100] E. Kowalski: *Nuclear electronics*, Springer Verlag, Berlin, 1970 240, 241, 256
- [101] E. Gatti and P. F. Manfredi: Rivista del Nuovo Cimento, **9**, 1 (1986) 240
- [102] S. Friedrich, M. F. Cunningham, M. Frank, S. E. Labov, A. T. Barfknecht and S. P. Cramer: Nucl. Instr. & Meth. in Phys. Res. A **444** 151, (2000) 240
- [103] M. Octavio, M. Tinkham, G. E. Blonder, and T. M. Klapwijk: Phys. Rev. B **27**, 6739 (1983) 240
- [104] R. Cristiano, L. Frunzio, R. Monaco, C. Nappi, and S. Pagano: Phys. Rev. B **49**, 429 (1994) 240
- [105] S. Friedrich, K. Segall, M. C. Gaidis, C. M. Wilson, D. E. Prober, P. J. Kindlmann, A. E. Symkowiak and S. H. Moseley: IEEE Trans. Appl. Supercond. **7**, 3383 (1997) 240
- [106] L. J. Hiller, M. L. van den Berg, and S. E. Labov: Appl. Phys. Lett. **79**, 4441 (2001) 240
- [107] P. Verhoeve, R. den Hartog, A. Kozorezov, D. Martin, A. van Dordrecht, J. K. Wigmore and A. Peacock: Appl. Phys. Lett. **92**, 6072 (2002) 240
- [108] P. Horowitz and W. Hill: *The art of electronics*, ( Cambridge University Press, Cambridge 1986) 240, 256
- [109] J. B. le Grand, C. A. Mears, S. E. Labov, P. Jakobsen, P. Verhoeve, M. Bavdaz, and A. Peacock: Proc. LTD7, 106 , Ed. S. Cooper, Max Plank Institute, Münich (1997) 240
- [110] N. Rando, P. Verhoeve, P. Gondoin, B. Collaudin, J. Verveer, M. Bavdaz and A. Peacock: Nucl. Instr. & Meth. in Phys. Res. A **444** 457, (2000) 240
- [111] D. Twerenbold and A. Zehnder: J. Appl. Phys. **61**, 1 (1987) 241
- [112] J. Jochum, H. Kraus, M. Gutsche, B. Kemmather, F. v. Feilitzsch and R. L. Mössbauer: Nucl. Instr. & Meth. in Phys. Res. A **338** 458, (1994) 241, 256
- [113] S. E. Labov, M. Frank, J. B. le Grand, M. A. Lindeman, H. Netel, L. J. Hiller, D. Chow, S. Friedrich, C. A. Mears, G. Caldara, and A. T. Barfknecht: Proc. LTD7, 82, Ed. S. Cooper, Max Plank Institute, Münich (1997) 241
- [114] P. A. J. de Korte, M. L. van den Berg, M. P Bruijn, J. Gomez, F. Kiewiet, H. L. van Lieshout, O. J. Luiten, C.G.S. Brond, J. Flokstra and A. W. Hamster: Proc. SPIE **2808**, 506 (1996) 241
- [115] J. Martin, S. Lemke, R. Gross, R. P .Hubener, P. videler, N. Rando, T. Peacock, P. Verhoeve, F. A. Jansen: Nucl. Instr. & Meth. in Phys. Res. A **379** 88, (1996) 241
- [116] J. B. le Grand, M. P. Bruijn,C. Patel, P. A. J. de Korte, S. Lemke, R. Gross and R. P Hubener: Physica C **279**, 85 (1997) 241
- [117] N. Rando, P. Verhoeve, A. Poelaert, A. Peacock, and D. J. Goldie: J. Appl. Phys. **83**, 5536 (1998) 241
- [118] F. Pantaleit, T. Schroeder, J. Martin, R. P. Hubener, F. B. Kiewiet, M. L. van den Berg, and P. A. J. de Korte: J. Appl. Phys. **85**, 565 (1999) 241
- [119] M. Grundner and J. Halbritter: Surf. Sci **136**, 144 (1984) 241

- [120] M. Ohkubo, D. Fukuda, I. Sakamoto, N. Hayashi, J. Martin, F. Panteleit, and R. Hubener: *J. Appl. Phys.* **85**, 595 (1999) [241](#)
- [121] D. H. Lumb, A. van Dordrecht, A. Peacock, N. Rando, P. Verhoeve, J. Verveer, D. J. Goldie, and J. Lumley: *Proc. SPIE*, **2518**, 278 (1995) [241](#)
- [122] P. Verhoeve, N. Rando, A. Peacock, A. van Dordrecht, D. Lumb, D. J. Goldie and R. Venn: *Nucl. Instr. & Meth. in Phys. Res. A* **370** 136, (1996) [241](#)
- [123] L. Parlato, G. Ammendola, R. Christiano, E. Esposito, L. Frunzio, H. Kraus, M. Lisitskii, C. Nappi, S. Pagano, G. Peluso, G. Pepe, and A. Barone: *Nucl. Instr. & Meth. in Phys. Res. A* **444** 15, (2000) [241](#)
- [124] A. G. Kozorezov, J. K. Wigmore, R. den Hartog, D. Martin, P. Verhoeve and A. Peacock: *Phys. Rev. B* **66**, 094510 (2002) [242](#)
- [125] R. den Hartog, A. G. Kozorezov, J. K. Wigmore, D. Martin, P. Verhoeve, A. Peacock, A. Poelaert, and G. Brammertz: *Phys. Rev. B* **66**, 094511 (2002) [242](#)
- [126] P. Verhoeve, N. Rando, A. Poelaert, A. van Dordrecht, A. Peacock, D. H. Lumb, D.J. Goldie, and R. Venn: *Proc. SPIE*, **2518**, 278 (1995) [242](#)
- [127] A. Poelaert, P. Verhoeve, N. Rando, A. Peacock, D. J. Goldie, and R. Venn: *Proc. SPIE*, **2808**, 523 (1996) [242](#)
- [128] R. den Hartog, A. Golubov, D. Martin, P. Verhoeve, A. Poelaert, A. Peacock and M. Krumrey: *Nucl. Instr. & Meth. in Phys. Res. A* **444** 28, (2000) [242](#), [249](#)
- [129] R. den Hartog, A. Golubov, P. Verhoeve, A. Poelaert, D. Martin, A. Peacock, A. van Dordrecht, and D. J. Goldie: *Phys. Rev B* **63**, 21407 (2001)
- [130] P. Verhoeve, N. Rando, A. Peacock, A. van Dordrecht, A. Poelaert, D. J. Goldie and R. Venn: *J. Appl. Phys.* **83**, 6118 (1998) [242](#)
- [131] A. Poelaert, A. Peacock, P. Verhoeve, A. van Dordrecht, A. Owens, N. Rando, A. Kozorezov and K. Wigmore: *Proc. SPIE*, **3445**, 214 (1998) [243](#)
- [132] P. Verhoeve, N. Rando, A. Peacock, A. van Dordrecht, M. Bavadz, J. Verveer, D. J. Goldie M. Richter, and G. Ulm: *Proc. LTD7*, 97, Ed. S. Cooper, Max Plank Institute, Münich (1997) [243](#)
- [133] N. Rando, S. Andersson, P. Gondoin, J. Verveer, P. Verhoeve, R. den Hartog, A. Peacock, B. Collaudin, R. Venn, and J. Salmi: *Proc. LTD7*, 101 , Ed. S. Cooper, Max Plank Institute, Münich (1997) [243](#)
- [134] N. Rando, J. Verveer, S. Anderson, P. Verhoeve, A. Peacock, A. Reynolds, M. A. C. Perymann, and F. Favata: *Rev. Sci. Instrum.*, **71**, 4582 (2000) [243](#), [247](#), [251](#)
- [135] G. Angloher, M. Huber, J. Jochuim, F. von Feilitzsch, R. L. Mössbauer and G. Sáfrán: *J. Low Temp. Phys.* **123**, 165 (2001) [243](#)
- [136] A. Poelaert: PhD. Thesis, University of Twente (1999) [244](#), [245](#)
- [137] A. G. Kozorezov, J. K. Wigmore, A. Peacock, A. Poelaert, P. Verhoeve, R. den Hartog, and G. Brammertz: *Appl. Phys. Lett.* **78**, 3654 (2001)
- [138] G. Brammertz, A. G. Kozorezov, J. K. Wigmore, R. den Hartog, P. Verhoeve, D. Martin, A. Peacock A. A. Golubov and H. Rogalla: *J. Appl. Phys.* **94**, 5854 (2003) [245](#), [253](#)
- [139] I. Jerjen, E. C. Kirk, Ph. Lerch, A. Mchedlischvili, M. Furlan, D. Twerenbold, A. Zehnder, H. R. Ott: *Nucl. Instr. & Meth. in Phys. Res. A* **520** 519, (2004) [245](#)
- [140] S. Friedrich: LLNRL, private communication [246](#)

- [141] S. Friedrich, A. Vailionis, O. Drury, Th. Niedermayr, T. Funk, W. N. Kang, E.M. Choi, H.J. Kim, S.I. Lee, S. P. Cramer, C. Kim, and S. E. Labov: IEEE Trans. Appl. Supercond. **13** 1114 (2003) **246**
- [142] P. Verhoeve, S. Kraft, N. Rando, A. Peacock, A. van Dordrecht, R. den Hartog, D. J. Goldie, R. Hart, and D. Glowacka: IEEE Trans. Appl. Supercond. **9**, 3342 (1999) **247**
- [143] S. Kraft, P. Verhoeve, A. Peacock, N. Rando, D. J. Goldie, R. Hart, and D. Glowacka, F. Scholze, and G. Ulm: J. Appl. Phys. **86**, 7189 (1999) **247**
- [144] G. Brammertz, A. Peacock, P. Verhoeve, D. Martin, and R. Venn: Instr. and Meth. in Phys. Res. A **520** 508, (2004) **247**
- [145] C. M. Wilson, L. Frunzio and D. E. Prober: Phys. Rev. Lett. **87**, 067004 (2001) **247, 251**
- [146] G. Brammertz, A. Peacock, P. Verhoeve, A. Kozorezov, R. den Hartog, N. Rando and R. Venn: AIP *Low Temperature Detectors* CP **605** 59, (2002) **247**
- [147] C. Erd, A. Poelaert, P. Verhoeve, N. Rando, A. Peacock: SPIE Proceedings, **2518**, 268 (1995) and A. Poelaert, C. Erd, A. Peacock, N. Rando, P. Verhoeve, A. G. Kozorezov, and J. K. Wigmore: J. Appl. Phys. **79**, 7362 (1996) **248**
- [148] A. D. Hahn, R. J. Gaitskell, N. E. Booth and G. L. Salmon: J. Low Temp. Phys. **93**, 611 (1993) **248**
- [149] R. J. Gaitskell, A. D. Hahn, N. E. Booth, G. L. Salmon and D. L. Kazakovtsev: J. Low Temp. Phys. **93**, 683 (1993) **248**
- [150] S. Kamihirata, M. Kurakado, A. Kagamihata, K. Hirota, H. Hashimoto, R. Katano, K. Taniguchi, H. Sato, Y. Takizawa, C. Otani, and H. M. Shimizu: AIP *Low Temperature Detectors* CP **605** 149, (2002) **248**
- [151] M. Kurakado, S. Kamihirata, A. Kagamihata, K. Hirota, H. Hashimoto, H. Sato, H. Hotchi, H. M. Shimizu and K. Taniguchi: Nucl. Instr. & Meth. in Phys. Res. A **506** 134, (2003) **248**
- [152] H. Sato, Y. Takizawa, S. Shiki, C. Otani, M. Kurakado, H. M. Shimizu: Nucl. Instr. & Meth. in Phys. Res. A **520** 613, (2004) **248**
- [153] M. P. Bruijn, F. B Kiewiet, M. L. van den Berg, O. J. Luiten, P. A. J. de Korte, A. W. Hamster, C. G. S. Brons, and J. Flokstra: Appl. Phys. Lett. **71**, 1252 (1997) **249**
- [154] M. van den Berg: Ph. D. Thesis, University of Utrecht, (1999) **249**
- [155] J. Jochum, H. Kraus, M. Gutsche, B. Kemmather, F. v. Feilitzsch, R.L. Mössbauer: Ann. Physik **2**, 611 (1993) **249**
- [156] R. den Hartog, D. Martin, A. Kozorezov, P. Verhoeve, N. Rando, A. Peacock, G. Brammertz, M. Krumrey, D. J. Goldie, and R. Venn: SPIE Proceedings, **4012**, 237 (2000) **249, 250**
- [157] P. Verhoeve, R. den Hartog, D. Martin, N. Rando, A. Peacock, and D. Goldie: SPIE Proceedings, **4008**, 683 (2000)
- [158] L. Li, L. Frunzio, C. M. Wilson, and D. E. Prober: J. Appl. Phys. **93**, 1137 (2003) **250**
- [159] E.C. Kirk, Ph. Lerch, J. Olsen, A. Zehnder, H.R. Ott: Nucl. Instr. & Meth. in Phys. Res. A **444** 201, (2000) **250**
- [160] L. Li, L. Frunzio, K. Segall, C. M. Wilson, D. E. Prober, A. E. Szymkowiak and S. H. Moseley: Nucl. Instr. & Meth. in Phys. Res. A **444** 228, (2000) **250**
- [161] R. den Hartog, P. Verhoeve, D. Martin, N. Rando, A. Peacock, M. Krumrey, and D. J. Goldie: Nucl. Instr. & Meth. in Phys. Res. A **444** 278, (2000) **250**

- [162] L. Li: Ph. D. thesis, Yale University, (2003) [250](#)
- [163] C. Wilson, L. Frunzio, K. Segall, L. Li, D. E. Prober, D. Schiminovich, B. Mazin, C. Martin and R. Vasquez: IEEE Trans. Appl. Supercond. **11**, 645 (2001) [251](#)
- [164] A. G. Kozorezov, J. K. Wigmore, A. Peacock, R. den Hartog, G. Brammertz, P. Verhoeve, and N. Rando: AIP *Low Temperature Detectors* CP **605** 51, (2002) [253](#)
- [165] F. M. Finkbeiner, C. Adams, E. Apodaca, J. A. Chervenak, J. Fischer, N. Doan, M. J. Li, C. K. Stahle, R. P. Brekosky, S. R. Bandler, E. Figueorora-Feliciano, M. A. Lindeman, R. L. Kelley, T Saab and D. J. Talley: Nucl. Instr. & Meth. in Phys. Res. A **520** 463, (2004) [254](#)
- [166] M. Cropper, M. Barlow, M. A. C. Perryman, K. Horne, R. Bingham, M. Page, P. Guttridge, A. Smith, A. Peacock, D. Walker and P. Charles: Mon. Not. R. Astron. Soc. **344**, 33 (2003) [254](#)
- [167] R. J. Schoelkopf, P. Wahlgren, A. A. Kozhevnikov, P. Delsing and D. E. Prober: Science **280**, 1238 (1998) [255](#)
- [168] K. Segall, K. W. Lehnert, T. R. Stevenson, and R. J. Schoelkopf, P. Wahlgren, A. Aassime, and P. Delsing: Applied Physics Letters, **81**, 4859 (2002) [255](#)
- [169] T. R. Stevenson, A. Aassime, P. Delsing, R. Schoelkopf, K. Segall, C. M. Stahle: IEEE Trans. Appl. Supercond. **11**, 692 (2001) [255](#)
- [170] T. R. Stevenson, F. A. Pellerano, C. M. Stahle, K. Aidala, R. J. Schoelkopf: Appl. Phys. Lett. **80**, 3012 (2002) [255](#)
- [171] M. Huber, S. Bechstein, B. Beckhoff, F. v. Feilitzsch, J. Jochum, M. Krumrey, A. Rüdig and G. Ulm: Nucl. Instr. & Meth. in Phys. Res. A **520** 234, (2004) [252](#)
- [172] T. Nakamura, M. Katagiri, M. Ubike, T. Ikeuchi and M. Ohkubo: Nucl. Instr. & Meth. in Phys. Res. A **520** 67, (2004) [252](#)
- [173] A. G. Kozorezov, J. K. Wigmore, A. Peacock, R. den Hartog, D. Martin, G. Brammertz, P. Verhoeve and N. Rando: Phys. Rev. B **69**, 184506-1 (2004) [253](#)
- [174] P. Verhoeve: AIP *Low Temperature Detectors* CP **605** 559, (2002) and refs. therein [253](#)
- [175] D. D. E. Martin, P. Verhoeve, A. Peacock, A. van Dordrecht, J. Verveer and R. Hijmering: Nucl. Instr. & Meth. in Phys. Res. A **520** 512, (2004) [253](#)
- [176] S. Friedrich, T. Funk, O. Drury, S. E. Labov, and S. P. Cramer: Rev. Sci. Instrum. **73**, 1629 (2002) [253](#)
- [177] see <http://www.comet.ch/index.php?id=270> [253](#)
- [178] D. D. E. Martin, A. Peacock, P. Verhoeve, A . Poelaert, and R. Venn: Nucl. Instr. & Meth. in Phys. Res. A **444** 115, (2000) [253](#)
- [179] D.D. Martin, P. Verhoeve, A. Peacock, A. van Dordrecht, J. Verveer and R. Hijmering: Nucl. Instr. & Meth. in Phys. Res. A **520** 512, (2004) [253](#)
- [180] D. D. E. Martin, A. Peacock, P. Verhoeve, and A. Poelaert: Rev. Sci. Instrum. **71**, 3543 (2000) [253](#)
- [181] R. Cristiano, E. Esposito, L. Frunzio, M. P. Lisitskii, C. Nappi, G. Ammendola, A. Barone, L. Parlato, D. V. Balashov, and V. N. Gubankov: Appl. Phys. Lett. **74**, 3389 (1999) [254](#)

- [182] M. P. Lissitski, M. Ejrnaes, C. Nappi, R. Cristiano, M. Huber, K. Rottler, J. Jochum, F. von Feilitzsch: Nucl. Instr. & Meth. in Phys. Res. A **520** 240, (2004) [254](#)
- [183] M. Nahum and J. Martinis: Appl. Phys. Lett. **63**, 3075 (1993) and Appl. Phys. Lett. **66**, 3203 (1995) [255](#)
- [184] N. E. Booth, P. A. Fisher, M. Nahum and J. N. Ullom: Supercond. Sci. Technol. **12**, 203 (1999) and G. P. Pepe, G. Ammendola, G. Peluso, A. Barone, L. Parlato, E. Esposito, R. Monaco, and N. E. Booth: Appl. Phys. Lett. **77**, 447 (2000) and G. P. Pepe, R. Scaldaferrri, L. Parlato, G. Peluso, C. Granata, M. Russo, G. Rotoli, and N. E. Booth, Supercond. Sci. Technol. **14**, 987 (2001) [255](#)
- [185] P. K. Day, H. G. LeDuc, B. A. Mazin, A. Vayonakis and J. Zmudzinas: Nature **425**, 817 (2003) [255](#)
- [186] I. P. Nevirkovets: Supercond. Sci. Technol. **11**, 711 (1998)  
[255](#)

# Index

- absorber loss, 235, 250
- array, 253, 254
- back-tunneling, 218, 219, 235, 240, 252, 253
- bolometer, 240
- cancellation, 236
- charge division, 247
- charge sensitive amplifier, 240
- Cooper pairs, 217
- diffusion, 229
- distributed readout, 247
- excess quasiparticles, 219
- fabrication, 237, 239
- FET, 256
- Fiske, 238, 240, 254
- fluctuations, 235
- interface, 231
- IR radiation, 240
- Josephson, 218
- kinetic equation, 222
- pair breaking, 226
- phonon, 217, 219, 224, 225
- losses, 226
- trapping, 222, 226
- proximity effect, 219, 230, 242, 250, 252
- quasiparticles, 217, 218, 224
- losses, 226, 241
- readout, 239, 251, 253, 256
- recombination, 226
- relaxation, 222
- responsivity, 219, 227, 240, 243–245
- Rothwarf-Taylor, 224, 227, 253
- SQUID, 240
- supercurrent, 219
- trapping, 233
- trapping rate, 229
- tunnel barrier, 237
- tunneling, 218, 227, 228

# Electron Probe Microanalysis with Cryogenic Detectors

D. E. Newbury<sup>1</sup>, K. D. Irwin<sup>2</sup>, G. C. Hilton<sup>2</sup>, D. A. Wollman<sup>1</sup>,  
J. A. Small<sup>1</sup>, and J. M. Martinis<sup>2</sup>

<sup>1</sup> National Institute of Standards and Technology, Gaithersburg,  
MD 20899-8371 USA  
[dale.newbury@nist.gov](mailto:dale.newbury@nist.gov)

<sup>2</sup> National Institute of Standards and Technology, Boulder, CO 80305-3328 USA  
[irwin@boulder.nist.gov](mailto:irwin@boulder.nist.gov)

**Abstract.** Electron probe X-ray microanalysis (EPMA) is based upon the use of a focused, high current density electron beam, 5 to 30 keV in energy, to excite characteristic X-rays from a picogram mass of a solid target. X-ray spectral measurements are currently performed with the broad bandpass semiconductor energy dispersive X-ray spectrometry (Si-EDS) and/or the high resolution crystal diffraction wavelength dispersive spectrometry (WDS). The strengths and weaknesses of WDS and EDS are mutually complementary. Nevertheless, existing EPMA/WDS/EDS technology has limitations which become extreme when applied to the newly emerging field of low voltage microanalysis, where the beam energy is less than 5 keV. The microcalorimeter EDS provides both high spectral resolution and energy dispersive operational character, two key features of the ideal spectrometer for EPMA. The NIST prototype microcalorimeter EDS achieves impressive performance for EPMA in terms of resolving key elemental interferences, detecting chemical state induced peak shifts, high sensitivity, and applicability to low voltage microanalysis. Further technical developments should extend these capabilities, and commercialization will bring the advantages of the microcalorimeter EDS to critical applications.

## 1 Introduction

### 1.1 Low Temperature X-ray Detectors for Analytical Applications

The emergence of low-temperature X-ray detectors capable of spectral resolution on the order of 10 eV or better has attracted great interest in the X-ray analysis community [1]. Such detectors have the potential to provide revolutionary new capabilities for a variety of X-ray analysis applications, including methods based upon primary excitation with photons, ions, and electrons. For instance, *Friedrich* et al. have demonstrated synchrotron-based fluorescence-detected absorption spectroscopy using superconducting tunnel junctions, and *Niedermayr* et al. have also used superconducting tunnel junctions to probe the X-ray spectroscopy of ion-surface interactions [2, 3]. However, by far the most advanced application of low-temperature detectors in X-ray analysis is in electron beam excitation systems for electron-probe X-ray microanalysis (EPMA). The application of low-temperature detectors to EPMA

was first proposed by *Lesyna* et al. [4]. Early demonstrations of electron-probe microanalysis were made using both transition-edge sensor (TES) microcalorimeters for EPMA of titanium films, and neutron-transmutation doped (NTD) thermistor microcalorimeters for EPMA of tungsten films [5,6]. TES microcalorimeters have now been developed into sophisticated systems for EPMA and used in a large number of measurements [1,7,8]. In this chapter, we focus on a detailed description of the TES-microcalorimeter-based EPMA systems developed at NIST, including a comparison to conventional energy-dispersive and wavelength-dispersive technology, an analysis of practical issues associated with the implementation, and a discussion of the future of this technology.

## 1.2 Electron Probe X-ray Microanalysis

EPMA is a critical technique for characterizing the chemical (elemental) composition of matter on micrometer to nanometer lateral and depth scales [9]. EPMA is widely applied in those scientific and engineering disciplines where knowledge of the chemical microstructure is critical to understanding the relationship of fine structure to macroscopic physical and chemical properties and behavior. Fields that regularly employ EPMA include materials science (e.g., metallurgy, ceramics, composites, semiconductors, etc.), semiconductor device manufacturing, geology, mineralogy, environmental science, biology, and failure analysis in many branches of engineering.

The physical basis of EPMA is the production of characteristic X-rays through inner shell ionization by inelastic scattering of the energetic primary beam electrons [9]. Depending upon the particular analytical strategy being applied, the incident beam energy is conventionally selected within the range 5 keV–30 keV, with special cases below and above this energy range. The X-ray spectrum that results from this type of excitation is illustrated in Fig. 1a, which shows a simulated ideal X-ray spectrum from copper-yttrium-barium oxide ( $\text{YBa}_2\text{Cu}_3\text{O}_{7-x}$ , the “123” high  $T_c$  superconductor) as it emerges from the surface of a bulk specimen before any artifact associated with any X-ray detection process has occurred. (This spectrum was simulated using NIST-NIH Desktop Spectrum Analyzer, a software engine for X-ray spectrometry available *gratis* from the National Institute of Standards and Technology [10].) The spectrum consists of narrow peaks, the characteristic X-rays, on a background, the X-ray continuum. On the energy scale being presented in the figure, the characteristic peaks are shown as lines, since their natural width is approximately the order of 1 eV (Fig. 2) while the bins of the spectrum histogram are 10 eV wide. The complexity of the multiple X-ray peaks of the L-shell family for copper, yttrium, and barium can be seen in Fig. 1b, along with the relatively simple oxygen K-shell peak. The peaks are found to be riding on a continuous X-ray background that (ideally) consists of the X-ray bremsstrahlung, or “braking radiation”, created as a result of inelastic scattering of the beam electrons in the Coulombic field

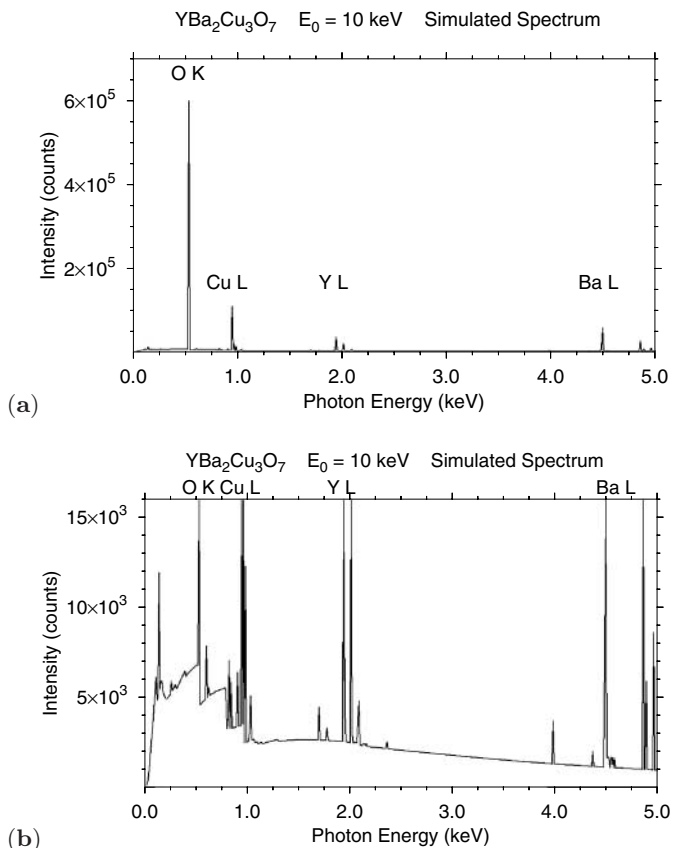


**Fig. 1.** (a) Simulated “ideal” spectrum of  $\text{YBa}_2\text{Cu}_3\text{O}_7$  as it leaves the specimen following specimen absorption. Incident beam energy = 10 keV. Simulation performed with NIST-NIH Desktop Spectrum Analyzer. (b) Expansion of (a) showing discontinuities in the X-ray continuum due to changes in the mass absorption coefficient at absorption edges (critical excitation energies)

of the atoms of the target. The continuum photons range in energy from the practical measurement threshold of 100 eV to the maximum energy of the incident beam,  $E_0$ . This “ideal” spectrum has actually already undergone modification from the spectrum generated within the specimen because of the action of X-ray absorption during propagation of the X-rays to the surface. The effect of self-absorption of X-rays within the specimen is evidenced by the discontinuities in the continuum background caused by sharp changes in the mass absorption coefficient associated with ionization energies.

Modern EPMA instrumentation is based upon a scanning electron microscope (SEM) platform [9]. The SEM’s high resolution electron imaging yields morphological information about the specimen with a spatial resolution as

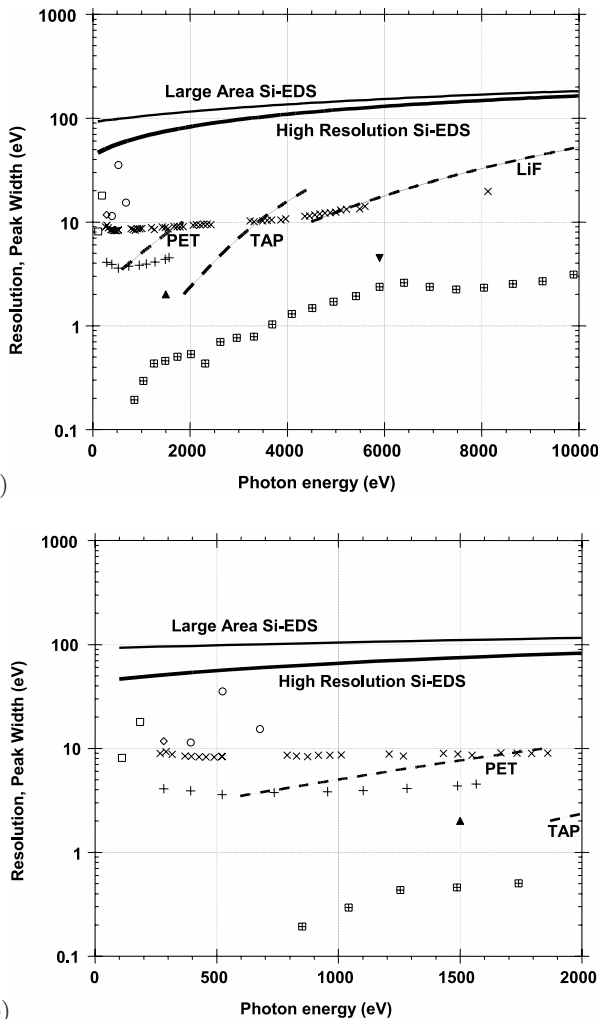


**Fig. 2.** Resolution (FWHM) versus photon energy for various types of X-ray spectrometers. (a) 0–10 keV; (b) 0–2 keV. Key: Solid lines: Si-EDS large area (150 eV at MnK $\alpha$ ) and “high” resolution (129 eV at MnK $\alpha$ ); dashed lines: WDS for various diffractors, LiF, TAP (thallium acid phthalate), PET (pentaerythritol); open squares, diamonds, circles: WDS with synthetic multilayer diffractors;  $\times$ : first generation NIST microcalorimeter EDS, with analog processing;  $+$ : second generation NIST microcalorimeter EDS, optimized for low photon energy, with analog processing;  $\blacksquare$ : second generation NIST microcalorimeter EDS, broad range version (at Mn K $\alpha$ ) and low photon energy version (at Al K $\alpha$ ) with optimized digital processing; point-centered squares: K $\alpha$ 1 width (FWHM) for various elements

fine as a few nanometers in optimum cases. For X-ray microanalysis, the SEM provides a finely focused probe ranging in diameter from nanometers to micrometers, depending on the total beam current required, that can be addressed to a user-selected location, usually under computer control. The beam is stable in its incident energy and current to 0.1% or better for time periods of hours or more, and depending on the details of the electron source, the beam current in the focused probe can range from picoamperes to microamperes.

In this Chapter, the following arbitrary (customary within the EPMA field) naming convention will be used to describe levels of concentration,  $C$ :

Major:  $C > 0.1$  mass (weight) fraction,

Minor:  $0.01 \leq C \leq 0.1$ ,

Trace:  $C < 0.01$ .

## 2 EPMA with Si-EDS

The simplest, and by far most common, form of EPMA is the SEM equipped with an energy dispersive X-ray spectrometer that utilizes a semiconductor detector, usually based on silicon (Si-EDS), although germanium detectors (Ge-EDS) are also available [9]. The combination of high resolution SEM imaging and Si-EDS qualitative/quantitative X-ray microanalysis is so powerful that SEM/Si-EDS is found in virtually all advanced industrial, government, and academic laboratories throughout the world. The SEM/Si-EDS combination is so effective that it is unusual to find an SEM that is not equipped with an Si-EDS.

The popularity of the Si-EDS for SEM/EPMA applications arises principally because of the energy dispersive aspect of its operation [9]. The photon detection mechanism of the Si-EDS is based upon photoelectric absorption within the Si crystal, followed by inelastic scattering of the photoelectron, creating charge carriers proportional in number to the original photon energy. While this detection process is serial in time for single photons, it is effectively parallel in photon energy. That is, the entire energy range of photon production can be continuously monitored with the Si-EDS, from a threshold of about 100 eV to the photon energy equal the incident electron beam energy  $E_0$ , which may be 20 keV or more. Within the photon energy range from 100 eV to approximately 12 keV, a useful characteristic X-ray peak from the K-, L-, and/or M-shells can be detected for every element in the Periodic Table with atomic number,  $Z \geq 4$  (Be). Since a typical analysis strategy in SEM/Si-EDS involves investigating many individual locations within a specimen, so that local variations in composition can be studied, the capability of measuring a complete spectrum at every location is extraordinarily powerful. The information embedded in the energy dispersive spectrum is potentially so complete that the analyst should be able to perform a complete qualitative

analysis (i.e., identification) of the elements present at every location sampled, at least for all major and minor constituents. Detection, identification, and measurement of trace constituents demands an adequate electron dose to obtain the necessary counting statistics above the continuum background. Even then, trace peaks are inevitably more susceptible to interference from nearby peaks of major and minor constituents.

Si-EDS does suffer from several drawbacks in its capacity to measure the X-ray spectrum. The principal limitation of Si-EDS is relatively poor energy resolution when compared to the natural peak width. Measured at a photon energy of 5890 eV (MnK $\alpha$ ), the optimum resolution is approximately 125–130 eV (depending on detector size), where resolution is defined as the full peak width at half the maximum peak intensity, FWHM, which can be compared with a “natural” peak width of approximately 1.5 eV for Mn K $\alpha$  [11]. This substantial peak broadening is a consequence of the limited number of charge carriers (electron-hole pairs) generated by inelastic scattering of the photoelectron that is ejected from a silicon atom following the absorption of an X-ray photon. The number of charge carriers (electrons or holes) liberated is approximately:

$$n_{e,h} = E_p / 3.6 \text{ eV} , \quad (1)$$

where  $E_p$  is the photon energy. For Mn K $\alpha$  at 5890 eV, this gives an average of 1636 charges. One sigma ( $\sigma$  for counting or Poisson statistics is equal to  $\sqrt{n}$ , where  $n$  is the number of counts) of this number is 40.4, or about 2.47%. The FWHM of a Gaussian peak is  $2.355\sigma$ , which thus predicts a value of  $\Delta E/E$  of 5.8% based upon the simple counting statistics, while the observed optimum FWHM of the Si-EDS is  $129 \text{ eV} / 5890 \text{ eV} = 2.2\%$ . This substantially better resolution performance arises from solid state effects upon event correlation. The resolution depends on the photon energy, as plotted in Fig. 2 for a small cross sectional area detector ( $10 \text{ mm}^2$ , referred to as “high resolution”) and a large cross sectional area ( $60 \text{ mm}^2$ , “large solid angle”) detector. The impact of the Si-EDS detection process upon the ideal spectrum of Fig. 1 is shown in Fig. 3, where the L-family members of copper and yttrium are no longer distinguishable and even for the more energetic barium L-family, the family members are not completely resolved, even though a “high resolution” Si-EDS was used (129 eV at Mn K $\alpha$ ).

There are several consequences of the significant broadening that the characteristic X-ray peak undergoes due to the poor resolution of the Si-EDS measurement process:

1. Peak Interference: There are numerous practical examples of peak interference that are encountered in Si-EDS spectrometry beyond the intrafamily interference situations that occur for Cu, Y, and Ba shown in Fig. 3: e.g., BaL and TiK in BaTiO<sub>3</sub>; SiK and WM in tungsten silicide (WSi<sub>2</sub>); SiK and TaM in tantalum silicide; SK, MoL, and PbM in

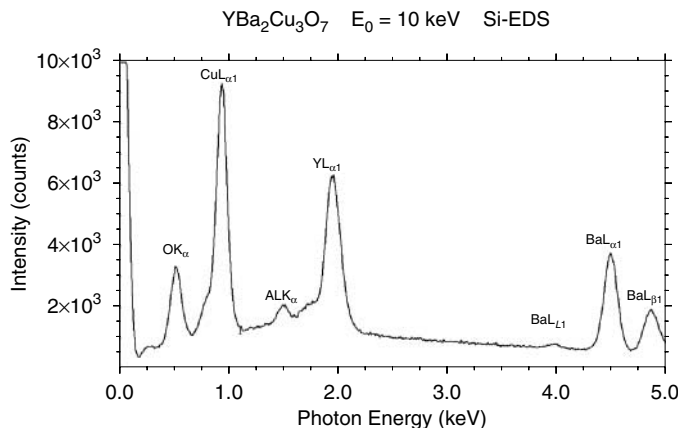


**Fig. 3.** X-ray spectrum of  $\text{YBa}_2\text{Cu}_3\text{O}_7$  (Al-doped) as measured with a semiconductor energy dispersive X-ray spectrometer (Si-EDS, resolution, 129 eV, FWHM, at Mn  $\text{K}\alpha$ , 5895 eV). Incident beam energy = 10 keV

$\text{MoS}_2$  and  $\text{PbS}$ ; and the interferences throughout the first transition series where the  $\text{K}\beta$  peak of element  $Z$  interferes with the  $\text{K}\alpha$  peak of the next higher atomic number element,  $Z+1$  [9]. These first transition series elements include iron and many of the major alloying elements of steel. Peak interference influences both qualitative and quantitative analysis procedures, particularly impacting on the determination of minor and trace level constituents.

2. Deteriorated Limits of Detection: The mere spreading out of the characteristic photons over a wider energy range due to the Si-EDS measurement process would have no particular consequences upon detection sensitivity except for the fact that the characteristic peak spreads out over the X-ray continuum of all photon energies. The characteristic X-ray peaks are situated upon this continuum background, and any attempt at a quantitative measurement must proceed from a separation of the two spectral components so that the characteristic X-ray intensity is accurately measured. An estimate of the background under the peak must be subtracted from the total intensity. The natural statistical variance in this continuum background forms the eventual limit to the recognition of the characteristic peak, and thus defines the limit of detection. The poorer the resolution, the more background radiation incorporated in any measurement of a characteristic peak, and therefore more variance, which gives a poorer limit of detection. For practical measurement conditions, e.g., 100 s accumulation at a count rate that produces 30% detector dead-time and best Si-EDS resolution (129 eV at  $\text{MnK}\alpha$ ), the limit of detection is typically about 0.002–0.005 mass fraction for a peak located in a region of the spectrum that has no significant interference [9].

### 3 EPMA with Wavelength Dispersive X-ray Spectrometry

Wavelength dispersive X-ray spectrometry (WDS) historically preceeded Si-EDS as the X-ray measurement technology for EPMA [9, 11]. WDS is based upon Bragg diffraction of the X-rays produced as a virtual point source (micrometer dimensions compared to centimeter diffractometer dimensions) at the electron beam impact on the specimen. By establishing the proper geometric arrangement for the specimen X-ray source, the diffraction crystal, and the detector, X-ray diffraction will produce a scattering maximum for a crystal with atomic plane spacing,  $d$ , and for a particular X-ray wavelength,  $\lambda$ , at the the Bragg angle,  $\theta_B$ ,

$$n\lambda = 2d \sin \theta_B , \quad (2)$$

where  $n$  is an integer giving the order of the reflection. For a given wavelength, the intensity generally decreases as  $n$  increases. The WDS is much sharper in energy resolution than the Si-EDS because the diffraction process changes efficiency rapidly with a small angular change in crystal orientation relative to the X-ray source (the beam impact on the specimen). The resolution depends upon the crystal chosen and the photon energy, but it is generally about 2 to 15 eV FWHM for the commonly used diffractors needed to span the photon energy range of interest, as illustrated in Fig. 2. The construction of a WDS involves a high precision mechanical platform that can move the diffractor and detector along a focusing circle relative to a fixed X-ray source (beam striking the specimen) with tolerances of milliradians in angular position and micrometers in spatial position. In fact, in order to present the specimen at a location that is reproducible within micrometers, a fixed optical microscope with shallow depth of focus is used to define the position of optimum WDS transmission. The specimen is moved mechanically along the  $z$ -axis (i.e., parallel to the optic axis of the SEM) to bring it into focus in the fixed optical microscope, thus consistently establishing a position with a reproducibility of a few micrometers [9].

The diffraction process acts to limit the instantaneous transmission of X-rays through the spectrometer to a narrow band that is essentially a fraction of the resolution, or typically a few eV at most. Thus, the WDS is a serial spectrometer in photon wavelength (or equivalently, photon energy) in which the vast majority of the spectrum emitted from the specimen is wasted at any instant. To view the peak shape, or an extended portion of the spectrum, the WDS must be mechanically scanned by moving the diffractor and the detector on an ideal focusing circle so that (2) is continuously satisfied for a succession of wavelengths. The geometry of the spectrometer constrains the wavelength range that can be diffracted from a crystal with a specific d-spacing. To cover the wavelength range that corresponds to X-rays

$\text{YBa}_2\text{Cu}_3\text{O}_7$   $E_0 = 10 \text{ keV}$  WDS LDE1 TAP and LiF scans

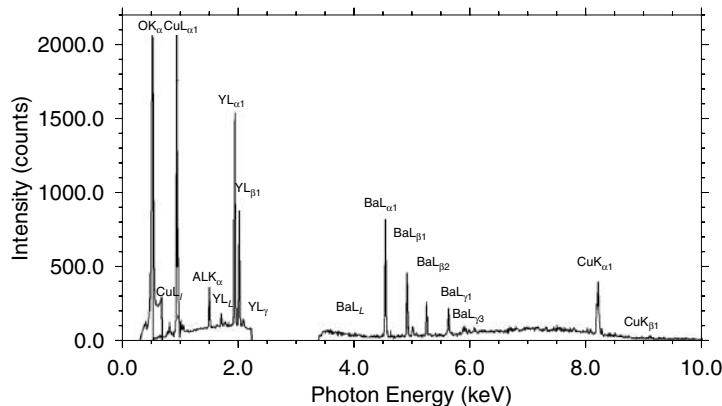


**Fig. 4.** X-ray spectrum of  $\text{YBa}_2\text{Cu}_3\text{O}_7$  (Al-doped) as measured with wavelength dispersive X-ray spectrometry and various diffractors (LDE1 (W-C layered synthetic material), TAP, and LiF). Incident beam energy = 10 keV; 200 nA; 1000 s per diffractor. Wavelength scans converted to the energy axis with DTSA [10]

with energies from 100 eV to 12 keV requires at least four different diffractors. WDS spectrometers are typically constructed to accommodate two or four diffractors on a turret. Thus, to obtain a spectrum by WDS that covers the complete energy range, each crystal must be scanned in succession and changed, a process which is invariably automated. However, the absolute efficiency of a WDS is low because of the small solid angle (compared to Si-EDS) and the losses in the diffraction process, which leads to requirements for high beam currents ( $> 100 \text{ nA}$ ) and long dwell times per spectrometer step. Thus, a scan of the complete photon energy range of a diffractor might require 100 s to 1000 s at beam currents as high as 100 nA. An example of a multi-diffractor WDS scan of copper-yttrium-barium oxide (“123” high  $T_c$  superconductor) is shown in Fig. 4. To record this spectrum required a total of 1000 s scanning time per diffractor at a beam current of 200 nA.

#### 4 EPMA with Si-EDS and WDS: The Complementarity of WDS and Si-EDS

Because of the large time penalty required to record a full WDS spectrum, it is not common practice to perform a full qualitative analysis with WDS at every specimen location analyzed. The Si-EDS, however, is extremely well suited for qualitative analysis, since it inevitably measures the entire excited X-ray spectrum at every location. This is just one aspect that illustrates the complementary nature of the Si-EDS and WDS spectrometries. As shown in Table 1, on many points critical to efficient and successful analysis, the

strengths and weaknesses of the Si-EDS and the WDS actually complement each other. This complementarity has led to the development of an EPMA equipment configuration that combines Si-EDS and WDS capabilities, often with multiple WDS spectrometers. Such an EDS/WDS system is supported by computer-aided analysis software to optimize the data collection and processing and to combine EDS and WDS measurements [9, 12]. Extensive analytical procedures can be executed under completely automatic control. For example, good analytical strategy for an EPMA with both Si-EDS and WDS uses the Si-EDS spectrum for qualitative analysis at every location being analyzed, at least for major and minor constituents. The WDS can then be addressed to measure the elemental peaks that present special problems such as interference from a nearby major constituent peak, or if an element of special interest is anticipated to be near the Si-EDS limit of detection. Finally, to perform a quantitative analysis, the peak intensities measured with Si-EDS for major constituents can be combined with those measured by WDS, typically assigned to minor and trace elements. Alternatively, for maximum data quality, the WDS can be used to measure peak intensities for all constituents identified during the EDS qualitative analysis phase.

## 5 EPMA with Low-temperature X-ray Detectors

Considering the level of performance that can be achieved with the EPMA when equipped with combined Si-EDS and WDS, why is there interest in adapting low temperature X-ray spectrometers to the EPMA, given the added complexity of the low temperature operation? Consider the potential performance for EPMA applications of the most highly developed of the low temperature spectrometry options, the NIST Transition Edge Sensor Microcalorimeter-EDS, whose construction and operation are described elsewhere in this volume [7]. First, as listed in Table 1, the microcalorimeter-EDS combines in one device some of the key performance characteristics of both the WDS and the Si-EDS. With these capabilities, the microcalorimeter-EDS approaches the performance of the “ideal” spectrometer for EPMA, as described below. Second, the EPMA/microcalorimeter-EDS will greatly advance analytical operations in the so-called “low voltage” microanalysis regime, where the incident beam energy is 5 keV or less, giving remarkable improvements in lateral and depth spatial resolution that are currently difficult or impossible to achieve with Si-EDS because of resolution or WDS because of efficiency [9].

**Table 1.** Comparison of WDS, semiconductor-EDS, and microcalorimeter EDS

	WDS	Semiconductor-EDS	Microcalorimeter-EDS
Energy range	0.1–14 keV with 5 diffractors	0.1–25 keV (Si) 0.1–100 keV (Ge)	0.15–10 keV (Bi)
Resolution	2–30 eV, depending on $\lambda$ and diffractor	129 eV at 5.89 keV $MnK\alpha$	4.5 eV at 5.89 keV 2.0 eV at 1.49 keV <sup>1</sup>
“Constant” energy coverage	1–15 eV, fraction of the resolution	full spectrum	full spectrum 0.2–2.5 keV <sup>1</sup>
Deadtime	1 $\mu$ s	50 $\mu$ s	250 $\mu$ s
Detector size	crystal area $A =$ 5 cm <sup>2</sup> $r = 20$ cm	10 mm <sup>2</sup> at 20 mm	0.4 $\times$ 0.4 mm at 59 mm
Solid angle	$csc \theta (A/4r^2)$ 0.012 sr at 15° 0.0034 sr at 65°	0.025 sr	0.000046 sr 0.0138 sr with optic
Overall efficiency	< 30%, variable	3 mm Si 100% $(4\text{--}15\text{ keV})^2$ 87% 2 keV <sup>3</sup> 69% 1 keV <sup>3</sup> 25% 0.5 keV <sup>3</sup> 13% 0.25 keV <sup>3</sup>	2 $\mu$ m Bi 80% $(4\text{--}15\text{ keV})^2$ 87% 2 keV <sup>3</sup> 69% 1 keV <sup>3</sup> 25% 0.5 keV <sup>3</sup> 13% 0.25 keV <sup>3</sup>
Maximum count rate	100 kHz ( $\sim$ 10 eV window selected by diffractor)	< 3 kHz (best resolution) 25 kHz (max rate)	1 kHz
Spectrum collec- tion time for minor element sensitivity	tens of minutes per diffractor	10–100 s	10–100 s
Special strengths	interference reso- lution, high speed compositional mapping	qualitative analysis	qualitative analysis, inter- ference resolution, low voltage microanalysis

<sup>1</sup> Two separate devices different photon energy optimization<sup>2</sup> Detector thickness defines efficiency<sup>3</sup> Window defines efficiency

## 5.1 Prototype Microcalorimeter EDS in an SEM/EPMA Environment

As described in detail in a separate chapter in this book, microcalorimeter-EDS determines the energy of an X-ray by measuring the temperature rise of a metal target when the X-ray is absorbed, as illustrated schematically in Fig. 5a (see Chapter by *Irwin and Hilton*). The amplitude of the temperature–time response and the time constant of its decay both depend upon the heat capacity of the absorber. The heat capacity must be minimized for optimum measurement conditions: pulse amplitude maximized and time constant minimized. A suitably low heat capacity can be realized for a metallic conductor with an operating temperature selected near 100 mK. The thermometry circuit for measuring individual X-ray events is illustrated schematically in Fig. 5b, and the detector components are shown in cross section in Fig. 6. This electrothermal circuit consists of a constant voltage/current source, an inductor, the metal absorber, and the transition edge sensor (TES), which consists of an Al–Ag or Cu–Mo bilayer whose individual layer thicknesses can be tailored to place the superconducting transition temperature at approximately 90 mK. With a current flowing in this circuit, the entire system is cooled down by an external refrigerator. As the components cool, the resistance of the whole system begins to decrease, and the current flowing in the circuit increases, resulting in increased Joule heating. When the system reaches the superconducting transition temperature of the TES, the circuit establishes a dynamic equilibrium. This equilibrium is disrupted when an X-ray is absorbed because the photon’s energy is converted into heat in the absorber, raising the temperature and increasing the circuit resistance, which therefore causes a decrease in the current flowing in the circuit, including the inductor. The changing current in the inductor creates a changing magnetic field, which is detected by the superconducting quantum interference device (SQUID) cryogenic amplifier. Thus, the time integral of the changing magnetic field as the electrothermal circuit deviates from and then returns to equilibrium is the measure of the energy of the X-ray photon.

The operating temperature of approximately 100 mK is reached in three stages with the cryostat shown in cross section in Fig. 7 [7]. The first stage uses liquid nitrogen for cooling to 77 K, while liquid helium in the second stage establishes 4 K. An adiabatic demagnetization refrigerator (ADR) provides cooling down to the operating temperature and establishes a reservoir at 50 mK to which heat accumulated by the operating detector is exhausted. The mounting of the microcalorimeter EDS cryostat on a conventional scanning electron microscope is shown in Fig. 8, where a commercial Si-EDS with its liquid nitrogen cryostat can also be seen. The axis of the detector is oriented at 90° to the electron beam axis. This arrangement requires that the specimen must be tilted from the horizontal toward the detector to gain a positive X-ray take-off angle. A tilt angle of 45° was used for all measurements reported in this Chapter. While this detector arrangement can be used satisfactorily for

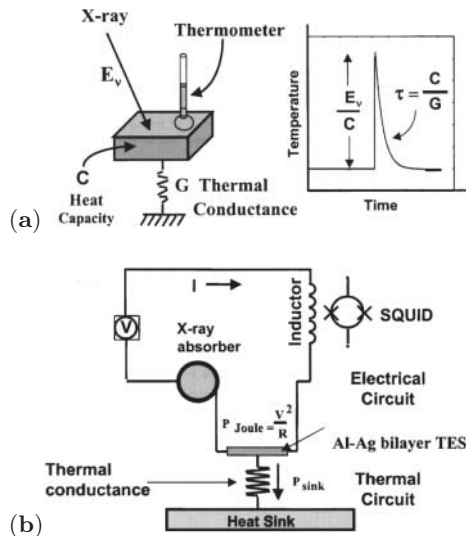


**Fig. 5.** (a) Principle of X-ray measurement with the microcalorimeter-EDS. An X-ray is absorbed in a metal target (normal conducting state), and the deposited energy causes a rise in temperature. The size of the pulse and the time constant of decay depend on the heat capacity of the target. (b) Diagram of electrical and thermal circuits used to implement the measurement principle:  $V$  = voltage/current source; inductor, metal target absorber, and transition edge sensor (a metal bilayer, with Al-Ag or Mo/Cu). A change in the current flowing in the circuit creates a changing magnetic field, which is detected by the superconducting quantum interference device (SQUID) amplifier

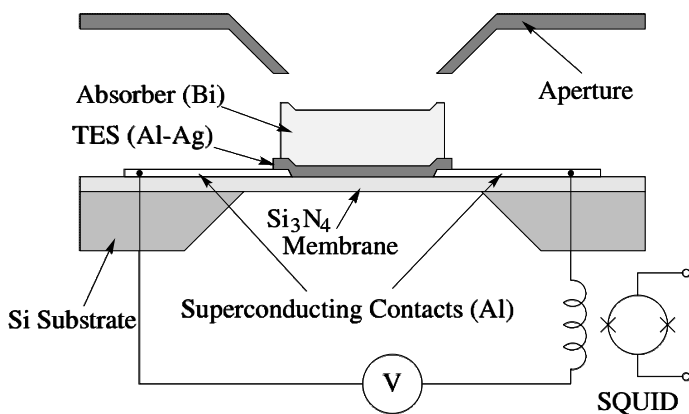


**Fig. 6.** Cross section schematic showing arrangement of the various components of the electrothermal circuit shown in Fig. 5

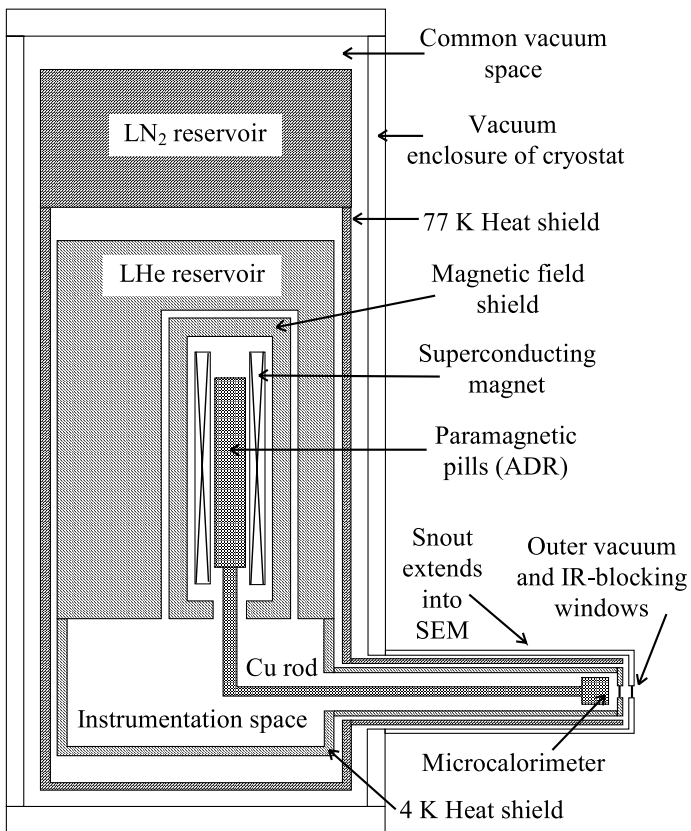


**Fig. 7.** Cross section of the cryostat used to achieve and maintain the low temperatures of the detector system described in Figs. 5 and 6. Note the liquid nitrogen and liquid helium reservoirs, as well as the adiabatic demagnetization refrigerator

flat, polished specimens, irregularly-shaped specimens such as particles and rough surfaces present a more difficult measurement situation. Because of the local surface curvature of a particle or rough bulk surface, the absorption path is poorly defined to a X-ray spectrometer that views the specimen along a direction perpendicular to the incident electron beam [9]. This absorption path ambiguity can be reduced by first determining the effective position of the X-ray detector in the SEM image. The beam should then be consistently placed on that side of the particle facing the detector while avoiding the backside of the particle, where the X-rays must pass through the thickness of the particle to escape to the detector.

The results presented in this Chapter were derived from three generations of the microcalorimeter EDS [7, 13, 14]:

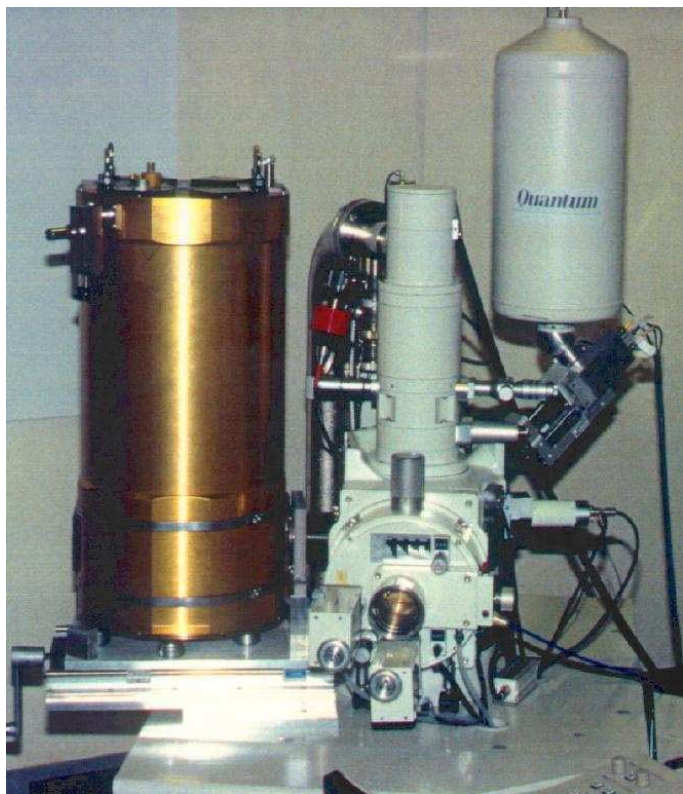


**Fig. 8.** Cryostat mounted on an SEM platform. Also shown is a conventional semiconductor EDS

1. broad photon energy band (250 eV–10 keV), Al (55 nm) Ag (105 nm) bilayer TES and a 2  $\mu\text{m}$  Ag absorber, giving a resolution of 8 eV at Mn K $\alpha$  (5895 eV);
2. broad photon energy band (250 eV–10 keV), Cu (200 nm) Mo (60 nm) bilayer TES and a 2  $\mu\text{m}$  Bi absorber, giving a resolution of 4.5 eV at Mn K $\alpha$  (5895 eV);
3. low photon energy range (250 eV–2.25 keV), Al (150 nm) Ag (150 nm) bilayer TES and a 1.5  $\mu\text{m}$  Ag absorber.

## 5.2 Characteristics of an Ideal X-ray Spectrometer for EPMA Compared with the Microcalorimeter-EDS

The “ideal” X-ray spectrometer would faithfully record the “ideal” spectrum as emitted from the specimen, i.e., following specimen absorption but with no further degradation introduced by the measurement process, as illustrated in Fig. 1. How well does the performance of the microcalorimeter EDS match

these characteristics? “Ideal” performance would include the following characteristics:

### 5.2.1 Energy Dispersive Character

The photon energy range of practical analytical interest for X-ray spectrometry of bulk specimens extends from approximately 100 eV to 14 keV and provides one or more K, L, or M-family lines for elements with  $Z \geq 4$  (Be) [9]. (For the high voltage analytical electron microscope, the full X-ray energy range to 100 keV may be of interest [15].) Continuous spectral coverage across this range without any adjustment of the spectrometer operational characteristics, termed “energy dispersive” operation, is highly desirable. One of the key reasons the Si-EDS has so broadly replaced the diffraction-based wavelength dispersive spectrometer (WDS) in the SEM/EPMA community is the Si-EDS capability of constantly monitoring the entire X-ray spectrum, which is an extraordinarily powerful attribute for qualitative analysis. Natural and synthetic materials tend to have complex chemical microstructures so that the capability of recognizing unexpected variations in the local composition at each location measured is often critical to achieving a meaningful result. WDS scanning invokes such a serious time penalty that it is impractical to fully scan at each analytical location.

The energy dispersive character of the microcalorimeter EDS is the first of two parameters with which it most closely approaches the performance of the “ideal” spectrometer. EDS operation is demonstrated by the spectrum in Fig. 9, which shows the K-shell peak oxygen (OK 523 eV), and the L-shell families for copper (Cu L $\alpha$  928 eV), yttrium (Y L $\alpha$  1922 eV), and barium (Ba L $\alpha$  4467 eV). The low energy limit of the accessible photon energy range is approximately 250 eV, as demonstrated by the spectrum for pure carbon in Fig. 10. This lower limit is determined by absorption in the vacuum-protection and infrared-isolation windows. The high energy limit of the measurable photon energy range is determined by photon penetration through the absorber as well as the limit imposed by the extent of TES sensor transition. For the broad energy range microcalorimeter EDS configuration, the practical upper limit imposed by the TES is approximately 10 keV, where the absorption of the 2  $\mu\text{m}$  thick Bi target is still greater than 20%.

### 5.2.2 Resolution

As shown in Fig. 1, X-ray spectra are complicated, with many lines occurring in the L- and M-families of the intermediate and heavy elements. For atomic numbers  $Z > 10$ , peak overlaps frequently occur within individual families when the spectrum is measured with modest resolution. For specimens of complex composition with many elements present, peak overlaps often occur between peaks from different elements, frequently resulting in severe limitations for the analyst. Spectrometer resolution approaching or even better

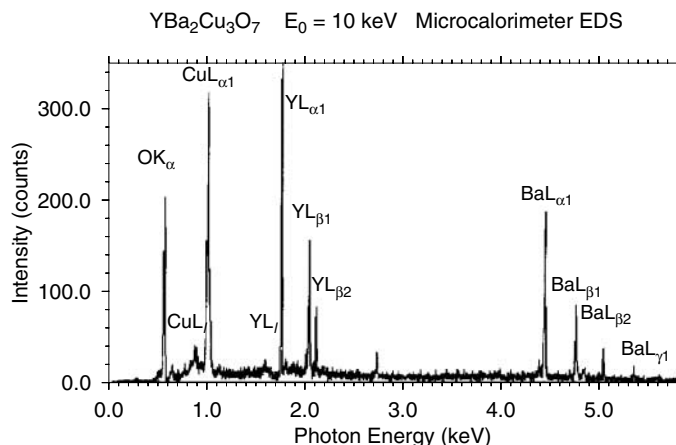


**Fig. 9.** Electron-excited X-ray spectrum of YBa<sub>2</sub>Cu<sub>3</sub>O<sub>7</sub> as measured with the NIST microcalorimeter-EDS on an SEM;  $E_0 = 10$  keV

than the 1 eV natural linewidth (an approximate value, with the exact value depending upon  $Z$ , as shown in Fig. 2) would be advantageous for minimizing peak interferences. High resolution also improves the limit of detection, since the peak intensity is distributed over fewer background channels, thus reducing the significance of variance in the background to the peak intensity measurement.

The resolution of the microcalorimeter-EDS is the second of two parameters with which it most closely approaches the performance of an “ideal” spectrometer. The spectrum of YBa<sub>2</sub>Cu<sub>3</sub>O<sub>7</sub> shown in Fig. 9 reveals the major and minor peaks that make up the L-families for Cu, Y, and Ba with resolution performance similar to the WDS multiple crystal scan. Figure 2 includes the measured resolution performance as a function of the photon energy for the microcalorimeter-EDS as compared with the Si-EDS and the WDS with various diffractors, as well as the natural peak width of the K $\alpha$ 1 peaks for various elements. The second generation microcalorimeter-EDS (with a Cu-Mo TES) shows better resolution than the LiF diffractor over much of the photon energy range above 5 keV. The microcalorimeter-EDS designed for low photon energy ( $E_p < 2$  keV) measurements is much better in resolution performance than the layered synthetic material (LSM) diffractors for the elements with  $Z \leq 9$  (fluorine).

### 5.2.3 Energy Efficiency

To record the spectrum without introducing a bias in the relative peak intensities as a function of photon energy, uniform efficiency (response per photon) across the full photon energy range would be desirable. The efficiency of a practical detector deviates from unity due to absorption losses in the vari-

ous windows as well as photon penetration through the detector at higher energies.

Figure 11a plots the absorption efficiency as a function of photon energy for a second generation microcalorimeter-EDS with a 2-micrometer thick bismuth absorber, as calculated with NIST Desktop Spectrum Analyzer [10]. The absorption efficiency of  $2\text{ }\mu\text{m}$  thick bismuth decreases below unity for low energy photons above approximately 1.5 keV and shows a complex response with discontinuities at the M- and L-edges. The absorption efficiency of the  $2\text{ }\mu\text{m}$  Bi target is still 25% at 10 keV and 20% at 15 keV.

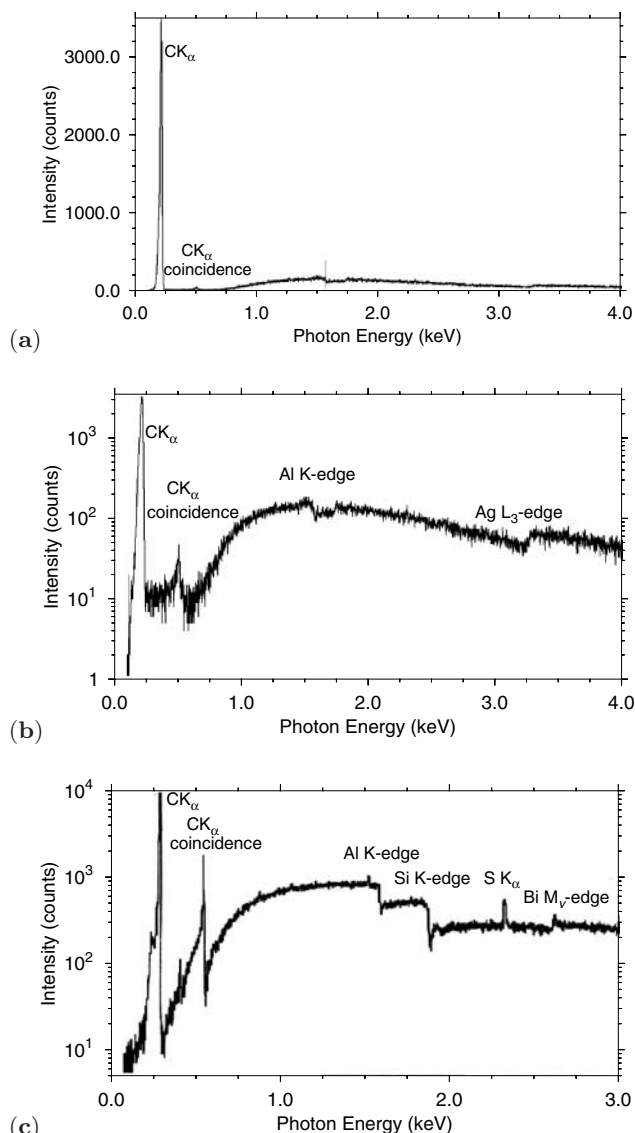
The vacuum isolation window and the infrared isolation window(s) also inevitably act to cause losses in the photons incident on the detector, affecting primarily the low energy photons. The response of the window system for the microcalorimeter EDS with a 400 nm thick aluminum infrared shield (total thickness, actually placed in three separate layers) is shown in Fig. 11b.

Figure 11c shows the overall efficiency with photon energy when both window absorption and detector absorption are convolved. The impact of the detector response function on an actual measurement can be seen in the spectrum of carbon shown with a logarithmic intensity scale in Fig. 9b, where discontinuities in the continuum X-ray intensity are noted at the Al K-absorption edge from the 400 nm Al infrared shield and at the Ag L<sub>III</sub>-absorption edge associated with the Ag metal detector.

#### 5.2.4 Geometric Efficiency

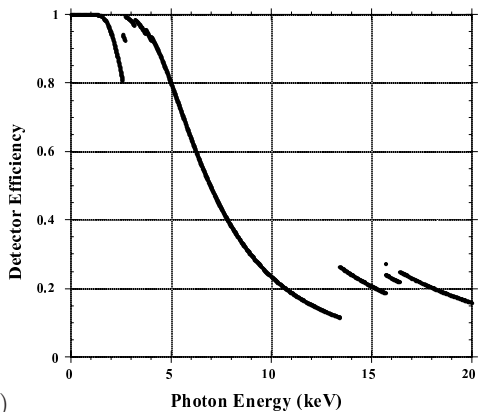
All aspects of X-ray spectrometry measurements are limited by the number of photons that can be accumulated within the available measurement time, or alternatively, for a specified dose of primary radiation. We therefore wish to have the maximum count rate possible for the beam current supplied to the specimen. Characteristic X-rays are generated and emitted isotropically into a spherical solid angle of  $4\pi$  steradians. For a thick specimen, only a hemisphere of  $2\pi$  steradians is effectively accessible. After specimen self-absorption, the isotropic generation pattern is modified toward a cosine distribution, with much greater attenuation along paths that make a large angle to the specimen normal. Ideally, the detector should occupy as much of the accessible solid angle as physically possible to intercept the largest possible number of X-rays. A conventional Si-EDS with optimum resolution performance ( $10\text{ mm}^2$  area) placed at 20 mm from the electron-excited source subtends a solid angle of 0.025 sr, or 0.4% of the possible unit hemisphere. Large area Si-EDS detectors (area  $60\text{ mm}^2$  placed at 20 mm from the source) subtend 0.15 sr, or approximately 2.4% of the unit hemisphere.

The prototype NIST microcalorimeter EDS has a very small area detector, typically only  $400\text{ }\mu\text{m} \times 400\text{ }\mu\text{m}$ . Moreover, the cryostat necessary to reach the operating temperature of 100 mK places constraints on the nearest distance that the detector can approach the electron-excited X-ray source



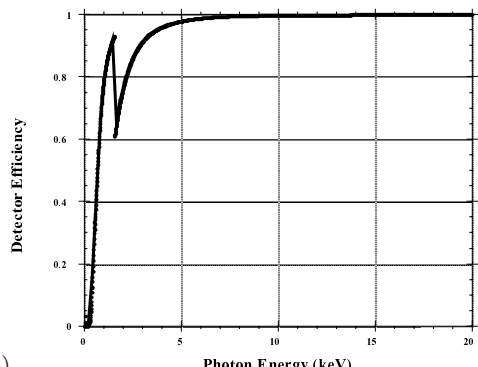
**Fig. 10.** (a) Electron-excited X-ray spectrum of carbon as measured with the microcalorimeter-EDS on an SEM;  $E_0 = 10$  keV; (b) as (a) but with logarithmic intensity axis showing coincidence peak and discontinuities in the X-ray continuum at the Al K-edge due to absorption in the Al infrared shielding windows and at the Ag L-edge, due to increased absorption above the edge in the Ag metal target; (c) Another spectrum of carbon with logarithmic intensity scale obtained with polycapillary optic in place, showing additional absorption at Si K-edge due to glass

Bismuth Detector (2 micrometers thick)



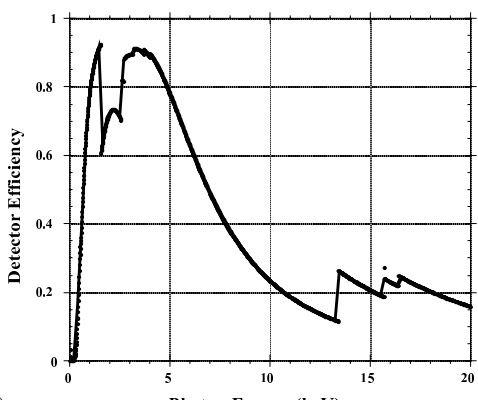
(a)

Microcalorimeter Window and Shield



(b)

Overall Detector Efficiency



(c)

**Fig. 11.** (a) Absorption efficiency for a bismuth target 2  $\mu\text{m}$  in thickness, as a function of photon energy; (b) transmission efficiency of the vacuum-isolation window and Al infrared shield; (c) convolution of (a) and (b) to give overall efficiency of the microcalorimeter-EDS

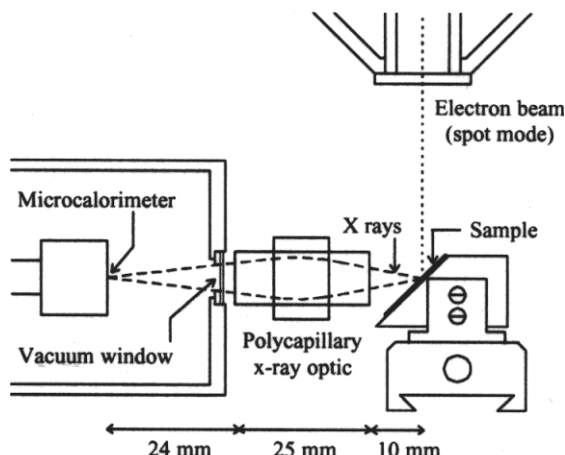


**Fig. 12.** Schematic showing double-focusing polycapillary X-ray optic used to couple the electron-excited X-ray source to the metal absorber of the microcalorimeter-EDS

on the specimen. This distance is on the order of 59 mm, so that the detector solid angle is  $4.6 \times 10^{-5}$  sr, or approximately 0.00073% of the available unit hemisphere. To increase the solid angle, a capillary X-ray optic (X-ray Optical Systems, Inc.) with a double taper was placed between the X-ray source generated where the beam strikes the specimen and the absorber of the microcalorimeter-EDS, as shown schematically in Fig. 12 [16]. Because the capillary X-ray optic has sharply defined focusing properties, a multi-axis positioner was needed to optimize the transmission. When properly aligned, the capillary X-ray optic increased the effective solid angle of collection by a factor of approximately 340 for Ti L $\alpha$  (0.452 keV), as shown in Fig. 13. This is a sufficient increase in useful solid angle to make it possible to operate the microcalorimeter EDS with incident electron beam currents of 1 nA or less. Because of the dependence upon photon energy of the critical scattering angle in the capillary optic, the efficiency is dependent upon photon energy. As shown in Fig. 13, the efficiency of the capillary optic for Ti K $\alpha$  X-rays at 4.510 keV is reduced by approximately 20% relative to Ti L $\alpha$ . The lateral spatial filtering action of the X-ray optic is also demonstrated in Fig. 13, where a movement of the source by 65 micrometers off the optic axis decreases the transmission by approximately 50% for both Ti L $\alpha$  and Ti K $\alpha$ .

### 5.2.5 High Count Rate

Given that an X-ray detector intercepts a sufficiently large solid angle, or alternatively, that the electron beam current can be increased to increase the X-ray production into the available detector solid angle, it is highly desirable

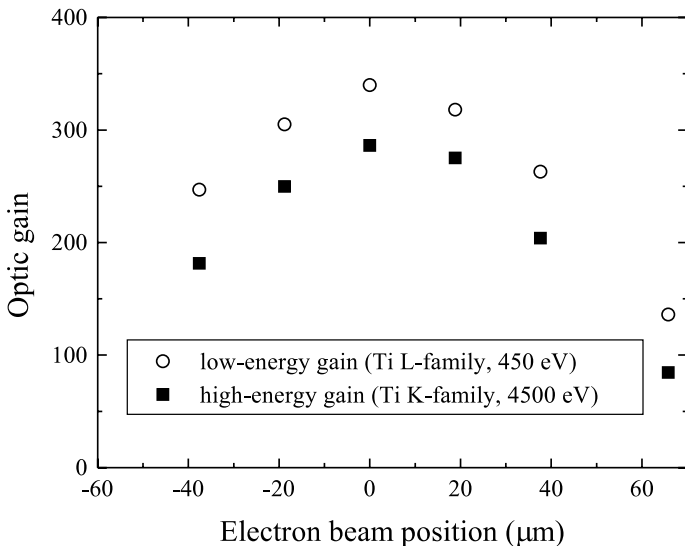


**Fig. 13.** Increased gain in X-ray collection with the polycapillary X-ray optic [16]. Lateral spatial transmission characteristics of X-ray optic for the TiL X-ray at 0.452 keV compared to the TiK X-ray at 4.508 keV

that the detector be capable of processing X-rays at the highest possible rate without losing X-rays or introducing artifacts into the recorded spectrum.

In its maximum resolution mode of operation (i.e., use of the longest time constant), a Si-EDS detector is limited to an output count rate of approximately 3000 counts per second at 50% deadtime [9]. If resolution can be sacrificed by operating with a shorter amplifier time constant, output count rates as high as 25 000 counts per second are possible at 50% deadtime. For WDS, the flow proportional gas detectors used for X-ray detection are capable of count rates as high as 100 000 counts per second, which is confined to the narrow energy bandpass of the diffraction process [9].

Both the Si-EDS and the WDS are subject to deadtime artifacts, in which the finite time that the detector requires to measure an X-ray event becomes a significant overhead burden at high count rates. Pathological events occur such as pulse coincidence, which produces spurious peaks (characteristic X-ray peak coincidence) and continuum features such as a pileup shelf (continuum X-ray coincidence), as well as loss of X-rays due to the detector busy state. In Si-EDS spectrometric practice, loss of possible photons while the detector is “busy” is compensated by the use of “deadtime correction” circuitry, which notes the amount of detector busy time and adds on a correction time period at the end of the specified clock time. For WDS, this time-addition method can be used, or for modest deadtimes, 10% or less, the relationship between input and output is sufficiently linear that a simple arithmetic calculation of a correction factor [true count rate = measured

count rate/(1-measured count rate $\cdot\tau$ ), where  $\tau$  is the deadtime] can suffice to correct for deadtime.

The limiting count rate of the prototype microcalorimeter EDS is in the range 500–1000 counts per second, and it is subject to deadtime and pulse pileup artifacts. A sum peak for C K can be seen in Fig. 10a–c, as well as a low energy shoulder on the parent and sum peaks

### 5.2.6 Linearity

As an operational convenience, it is desirable for the output of the spectrometer to be linear in energy. This permits straightforward application of database tools that generate peak positions and relative peak heights for “KLM” X-ray peak markers [9]. The Si-EDS is highly linear when calibrated over the range from 1 keV to 10 keV. However, low photon energy peaks with  $E < 1$  keV show systematic deviations from the calibration due to the effects of incomplete charge collection that act to change the peak shape and to shift the peak position lower in energy.

WDS spectral scans can be converted into EDS spectra using the relation between wavelength and energy:

$$\lambda = hc/eE = 1.2398/E \quad (\lambda \text{ in nm and } E \text{ in keV}), \quad (3)$$

where  $h$  is Planck’s constant,  $c$  is the speed of light, and  $e$  is the electron charge [9]. Over narrow wavelength ranges the resulting spectrum shows good linearity, but because of the reciprocal relation in (3), conversion of long wavelength ranges results in non-linear distortions due to forced constant bin width.

The basis of the measurement of the X-ray energy in the prototype microcalorimeter EDS is effectively an exploration of the superconducting transition response of the TES (i.e., resistivity vs. temperature). Higher energy photons deposit more energy, which creates a greater temperature rise, eventually moving out of the linear region into the non-linear portion of TES resistivity vs. temperature curve, and producing a non-linear energy scale. As the photon energy is increased further, the response eventually saturates.

To provide a practical solution to extend the effective linear response, a pulse inspection scheme has been developed to calculate the appropriate shift to compensate for the non-linear response of the TES before the pulse is binned in the digital spectral display. A fourth-order polynomial fit to the non-linear response of the TES was developed from direct calibration with a series of known X-ray peaks. A special NIST glass composition (K3670) was synthesized to provide characteristic X-ray peaks spaced about 100 eV to 200 eV from C K (provided by the carbon coating needed to stabilize the charging situation of the insulating glass) to 2.5 keV, with additional characteristic X-rays at intervals of 250 to 500 eV at high photon energies, as shown in Fig. 14. By determining the fitting coefficients from this array of X-ray

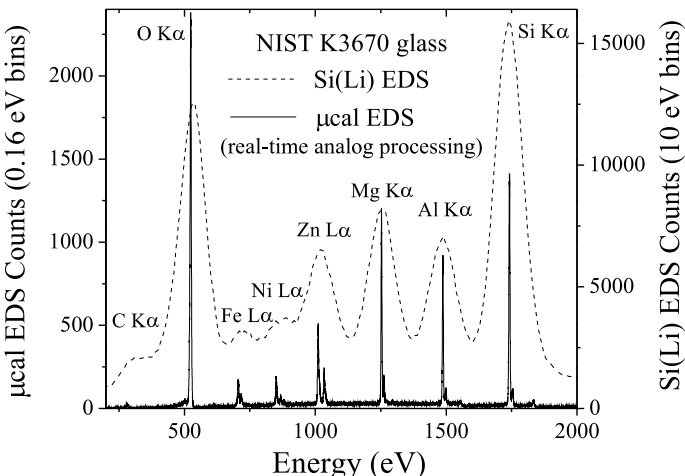


**Fig. 14.** Microcalorimeter-EDS spectrum of NIST glass K3670, compared with the spectrum obtained with a Si-EDS (resolution 129 eV FWHM at Mn K $\alpha$ ). K3670 is a special calibration glass devised to place a characteristic X-ray peak at frequent locations throughout the spectral range of interest

lines, the linearization of the spectrum could be extended to span a range from 250 eV to 6 keV or more. For the low photon energy, high resolution microcalorimeter-EDS, linear response within a few electron volts could be obtained from 250 eV to 2.5 keV.

### 5.2.7 Lack of Spectral Artifacts

The ideal X-ray spectrometer should not introduce any artifacts into the measured X-ray spectrum. Artifacts are familiar to users of Si-EDS, where coincidence peaks and silicon-escape peaks are routinely observed, and to users of WDS, where the principal artifact is the multiple order reflection, due to the integer term  $n$  in (2).

The spectra of carbon in Fig. 10 illustrate the main artifacts observed in X-ray spectra measured with the microcalorimeter EDS. Although it is energy dispersive in operation, the microcalorimeter EDS can only process one event at a time, so it is subject to paralyzable deadtime and pulse pile-up, resulting in coincidence peaks, as shown in Figs. 10b and c. The action of absorption effects in certain detector components can also be directly observed in the spectrum, as shown in Fig. 10b. The Al infrared shield is the source of the discontinuity in the continuum at 1.55 keV in Fig. 10b, where the continuum intensity above the Al K-edge decreases relative to the pre-edge intensity due to increased mass absorption. The increase in the intensity above the Ag L3-edge occurs because the Ag metal absorber becomes more efficient for photons above the edge. In Fig. 10c, the C spectrum was recorded with

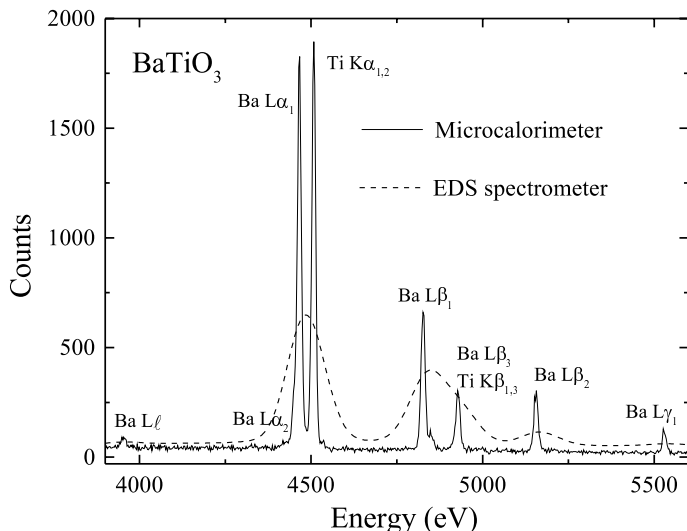


**Fig. 15.** Microcalorimeter-EDS spectrum of BaTiO<sub>3</sub> excited with an electron beam energy of 10 keV

the polycapillary X-ray optic, which contributes the SiK-edge due to silicon fluorescence induced in the glass walls of the capillaries, and the detector was made of bismuth, so that the Bi M-edge is the source of a discontinuity.

### 5.3 Performance of the Microcalorimeter EDS in Classic EPMA Applications

#### 5.3.1 Resolving Peaks in an EDS Mode

From the point-of-view of practical analysis problem solving, the key contribution of the microcalorimeter EDS is the combination in a single detector of the energy dispersive measurement character of the Si-EDS with the spectral resolution of WDS. Figure 15 (BaTiO<sub>3</sub>) and Fig. 16 (WSi<sub>2</sub>) show two examples of classic spectral interferences that are completely resolved with the WDS and microcalorimeter EDS, but which are so severe as to be effectively inaccessible with Si-EDS. Because of the energy dispersive character of the microcalorimeter, the analyst will always have the necessary spectral information to fully identify the constituents of the specimen at every location sampled by the beam. The time penalty required for WDS scanning means that measurement of the full spectrum at every analysis location is simply too time intensive for practical analysis. Thus, the microcalorimeter EDS can gain a critical advantage in qualitative analysis of complex and heterogeneous specimens which vary at every beam location.

In the examples presented in Fig. 15 and Fig. 16, all elements of the compounds were present as major constituents ( $C > 0.1$  mass fraction). When

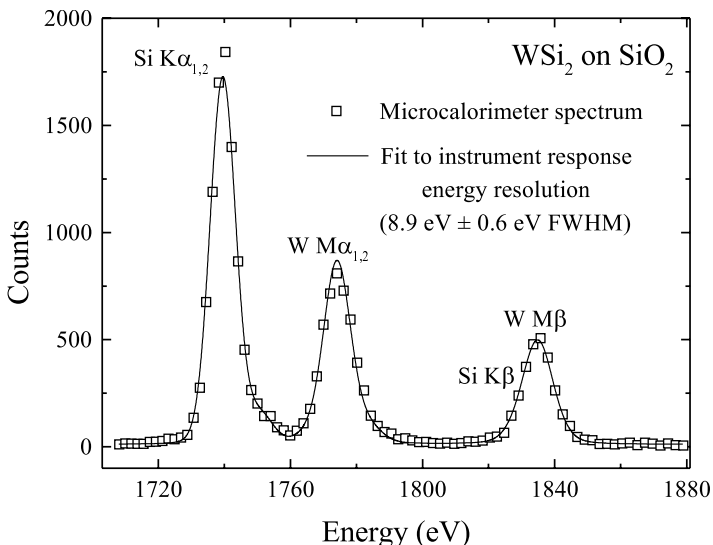


**Fig. 16.** Microcalorimeter-EDS spectrum of  $\text{WSi}_2$  on  $\text{SiO}_2$  excited with an electron beam energy of 10 keV

one of the constituents of interest is present at a minor or trace level, the analytical problem involves accurately measuring a low intensity peak by separating the contribution of the continuum background, and often the contribution from the tail of a nearby interfering major peak(s). An example of this type of situation is illustrated in Fig. 17a for AlGaAs, where the AlK peak suffers severe interference from the GaL family in the Si-EDS spectrum, while these peaks are completely resolved with the microcalorimeter EDS.

As an example of an even more complex material with the possibility of multiple interferences, Fig. 18 shows a spectrum in which all of the transition elements from Mn to Cu are present at major and minor levels. All of the elements are detectable through at least their  $L\alpha$  and  $L\beta$  peaks, and for the higher concentration components, the  $L\gamma$  peak is also detectable.

### 5.3.2 Limits of Detection

One key measure of analytical performance is the concentration minimum mass fraction,  $C_{\text{MMF}}$ , that can be detected under specified measurement conditions when a particular mixture of elements is present. For a spectral situation in which peak interference is not an issue and only the variance in the background sets a limit on the extraction of the peak intensity, the  $C_{\text{MMF}}$  can be estimated from measurements made on pure element targets with the equation described by Ziebold [17]:

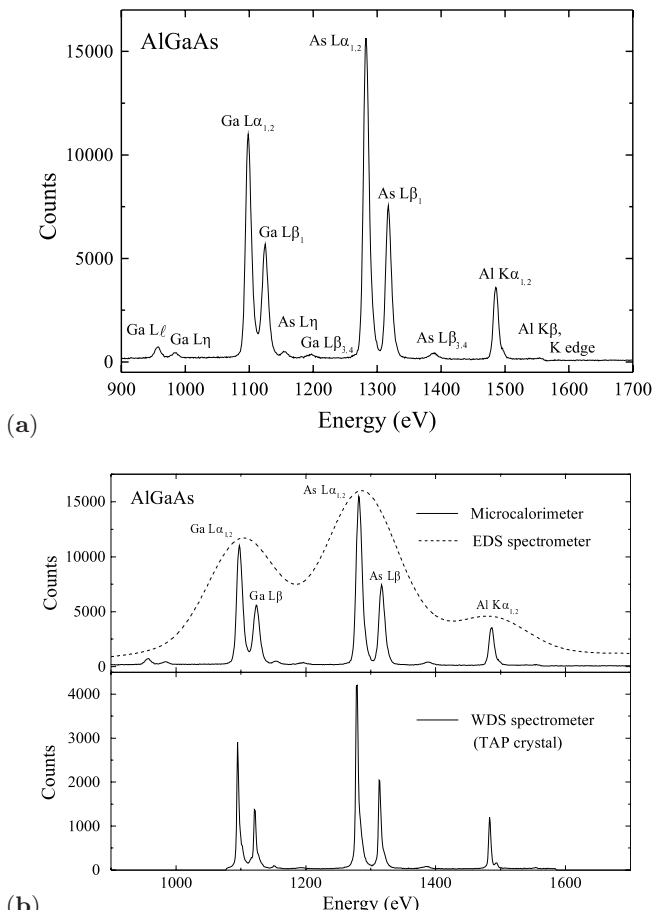


**Fig. 17.** (a) Microcalorimeter-EDS spectrum of AlGaAs excited with an electron beam energy of 10 keV. (b) Comparison of Si-EDS, microcalorimeter-EDS, and scanned WDS spectra of AlGaAs

$$C_{\text{MMF}} = 3.29a/[n\tau P(P/B)]^{0.5} . \quad (4)$$

In (4),  $n$  is the number of measurements,  $\tau$  is the integration time in seconds,  $P$  is the peak counting rate (counts per second), and  $(P/B)$  is the spectral peak-to-background. The term  $a$  is the factor in the Ziebold-Ogilvie hyperbolic relation between the concentration ( $C$  can take on any value from 0-1) and the experimentally-measured  $k$ -value ( $k = I_{\text{UNK}}/I_{\text{STD}}$ , where “UNK” is the unknown, “STD” is the standard, and  $I$  is the peak intensity for the same X-ray peak measured under the same beam and spectrometer conditions) [18]:

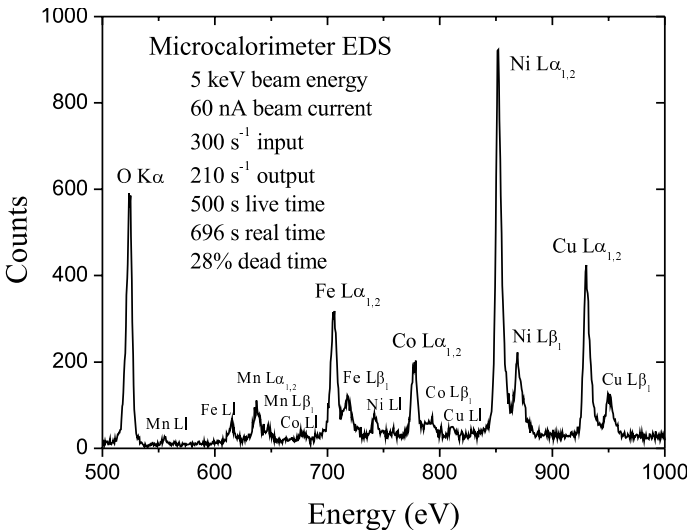


**Fig. 18.** Microcalorimeter-EDS spectrum of mixed oxides of transition elements Mn, Fe, Co, Ni, and Cu excited with an electron beam energy of 5 keV

$$(1 - C)/C = a(1 - k)/k . \quad (5)$$

It should be recognized that (4) gives an estimate of the limit of detection for the special case in which the peak of interest is isolated on the background. Only the background intensity determines the eventual irreducible variance in the signal that sets the limit against which the peak of interest must be detected. There is no contribution from other interfering peaks to this limiting variance.

Using (4) for the calculation of  $C_{\text{MMF}}$ , consider the problem of measuring low levels of aluminum in a matrix of  $\text{SiO}_2$ . This is a case in which the characteristic X-ray peaks are sufficiently well resolved with conventional Si-EDS to permit easy separation with multiple linear least squares fitting. Moreover, for elements like Al and Si with similar atomic numbers, critical ionization energies and X-ray energies, the  $a$  factor in (4) is close to unity. Take the following choice of measurement conditions:  $E_0 = 5 \text{ keV}$ ;  $I_B = 1 \text{ nA}$ ;  $\tau = 100 \text{ s}$ ;  $n = 1$ . Table 2 compares the performance characteristics as implemented on an SEM platform of the first generation NIST microcalorimeter EDS augmented with polycapillary optics compared with WDS and Si-EDS. Typical values of detector solid angle, efficiency, and other performance characteristics have been used in preparing this table. Table 2 also gives the  $C_{\text{MMF}}$  calculated for Al in  $\text{SiO}_2$  for the WDS (TAP crystal), Si-EDS, and the microcalorimeter EDS with polycapillary X-ray optics.

Surprisingly, for this case the values of  $C_{\text{MMF}}$  only span a range of 1.5 for the three very different types of spectrometers [19]. This unexpected behavior can be understood by considering the contribution of the key factors,

**Table 2.** Comparison of sensitivity

	WDS	Semiconductor-EDS	Microcalorimeter-EDS
Resolution (at AlK)	3.8 eV (TAP)	78 eV	8.5 eV
Al peak count rate at 5 keV	260 c/s/nA	5200 c/s/nA	540 c/s/nA
Limiting count rate	$10^5$ c/s (peak channel)	3000 c/s (whole spectrum)	800 c/s (whole spectrum)
$P/B$ on Al (5 keV)	272/1 (TAP)	14.5/1	79.2/1
$C_{MMF}$ (5 keV, 1 nA, 100 s)	0.0012	0.0018	0.0016

$P$  and  $(P/B)$ , in (4). Note that both the peak counting rate,  $P$ , and the spectral peak-to-background,  $P/B$ , enter (4) with equal weight. The WDS is a high resolution spectrometer so that the  $P/B$  is very high but the absolute efficiency is poor, so that with the beam current limited to 1 nA, the resulting peak counting rate,  $P$ , is low. For the Si-EDS, the  $P/B$  is low compared to WDS, but the geometric efficiency is very high, so that the peak count rate for a 1 nA beam current is high compared to WDS, resulting in a similar  $C_{MMF}$ . Finally, the microcalorimeter EDS with polycapillary optic has a P/B approaching the WDS while having a better geometric efficiency than the WDS, giving a higher  $P$  for a 1 nA beam current than that of WDS, so that again the  $C_{MMF}$  is comparable.

When peak interference occurs, the calculation for  $C_{MMF}$  inevitably deteriorates relative to the background-only case because of the additional error associated with the extraction of the second peak, particularly if the second peak is larger than the peak of interest. A simple formula like (4) for the  $C_{MMF}$  is no longer possible. Statham [20] has analyzed the separate roles of the peak counting rate,  $P$ , and the full width at half maximum, a measure of the resolution which directly affects the peak-to-background,  $P/B$ . When the peak of interest approaches the spectral background, the impact of the resolution, as expressed by the FWHM of the spectrometer, becomes more important than the count rate. The limit of detection follows a series of broad rules depending on the  $\text{FWHM}^w$ , where the exponent depends on the severity of the interference of other peaks and the number of peaks. For multiple peaks with severe interference, Statham has proposed a general rule that the exponent  $w = m - 0.5$ , where  $m$  is the number of peaks involved [20].

The impact of peak interference upon measuring low intensity peaks in the vicinity of high intensity peaks is shown in Fig. 19 for an NIST glass with low peaks of SiK and TaM originating from trace concentration levels of these elements in the vicinity of high intensity peaks from high concentrations of Al and P. For the Si-EDS (129 eV at MnK $\alpha$ ) spectrum shown in Fig. 19a,

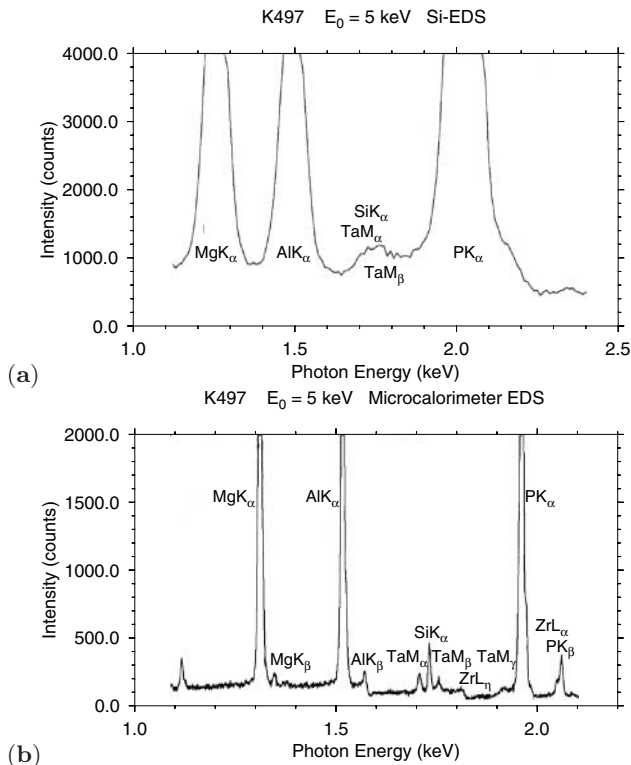


**Fig. 19.** (a) X-ray spectrum of NIST Glass K497 as measured with a semiconductor energy dispersive X-ray spectrometer (Si-EDS, resolution, 129 eV, FWHM, at Mn K $\alpha$ , 5895 eV); (b) X-ray spectrum of NIST Glass K497 as measured with microcalorimeter-EDS. Incident beam energy = 5 keV

the SiK and TaM peaks are unresolved and not really even recognizable during qualitative analysis. Calculating a limit of detection in this case is really meaningless because the peaks themselves cannot be recognized. The resolution of the microcalorimeter EDS is sufficient, as seen in Fig. 19b, to fully separate these peaks, so that in determining a limit of detection, the non-interference equation (4) is still appropriate.

When choosing an optimum strategy for trace level measurements, the microcalorimeter EDS and the WDS have distinctly different capabilities that profoundly affect the strategy. The WDS has the capability of extremely high counting rates (100 000 cps), which moreover is isolated to the narrow range of the spectrum that corresponds to the resolution of the particular diffractor, since the diffraction process is so sharply peaked. This feature is important for trace analysis because it means that intense peaks generated from the major constituents of a specimen are usually completely excluded from the WDS X-ray detector. Thus, as long as the specimen can withstand

the possible radiation and heating damage from high beam currents, the analyst can increase the beam current to achieve an acceptable counting rate from the spectral region where the trace element peak is expected while avoiding detector saturation from the major constituent peaks. A WDS trace measurement involves measuring the intensity at the peak position and at two background positions located above and below the peak location to enable an estimate of the background under the peak.

The microcalorimeter EDS like all EDS systems has a paralyzable dead-time and, lacking any filter before the detector except for the vacuum and infrared isolation windows, is sensitive to the entire excited X-ray spectrum above a threshold of approximately 200 eV. The system deadtime is thus dominated by the contributions of the highly excited peaks of the major constituents, which means that proportionally little counting time remains for the trace element peak. Thus, for a single trace element determination, a WDS system will always have an advantage over the microcalorimeter EDS. However, the microcalorimeter EDS becomes more competitive for trace element determination when several trace elements are determined at the same time, as illustrated for two trace elements in Fig. 19b [20]. For multiple trace elements, the energy dispersive capability of the microcalorimeter EDS means that the full peak for each trace element can be recognized, and all peak and background information is readily accessible for accurate peak extraction and for rigorous, spectrum-specific limits of detection calculations. WDS rapidly loses its advantage when scanning must be used to examine the peak and background regions for trace measurements. Finally, when the beam current is limited to low values, e.g., 1 nA, the time advantage greatly shifts to the microcalorimeter EDS because of the inefficiency of the WDS [1].

### 5.3.3 Detecting “Chemical Shifts” with the Microcalorimeter EDS

The high spectral resolution of the microcalorimeter EDS enables another type of measurement to be performed that was previously restricted to WDS operations, namely detection of “chemical shifts”. It has long been observed by WDS that characteristic peaks with energies below 1 keV are subject to changes in position (absolute energy), peak shape, and relative intensity according to the chemical bonding. Some of these effects (peak energy, peak width) arise because the outer electron energy levels of the atom are modified by chemical bonding effects [9]. Other spectral features, such as changes in the relative ratio of peaks within the L-family of transition metals, e.g.,  $\text{La}/\text{L}\beta$ , in compounds with different metal valence and therefore different cation-to-anion ratios, are actually a result of the effects of X-ray absorption that arises because of the location of the  $\text{L}_3$  absorption edge among the peaks [21]. Figure 20 shows an example of chemical effects observed in iron metal and hydrated iron oxide as recorded with WDS (TAP diffractor)

scanning and with the microcalorimeter EDS augmented with a polycapillary X-ray optic. Approximately equal times were spent in accumulating the data, but the beam current was a factor of 200 lower for the microcalorimeter EDS. In Fig. 20a and Fig. 20b, similar results are found with WDS (TAP diffractor) scanning and the microcalorimeter EDS: the Fe L $\alpha$  peak shifts position (a chemical bonding effect) and the Fe L $\beta$ /Fe L $\alpha$  ratio decreases between the oxide and the metal because of increased absorption of the Fe L $\beta$  in the metal simply because of the higher concentration of iron. The particular advantage of the microcalorimeter EDS is illustrated in Fig. 20c, where the advantage of energy dispersive collection is clearly evident with the simultaneous recording of the OK peak and the Fe Ll and Fe L $\eta$  peaks, unambiguously identifying the oxide phase. For WDS scanning, detecting oxygen would require an additional diffractor to be scanned.

### 5.3.4 Application of the Microcalorimeter-EDS to Low Voltage Microanalysis

Low voltage scanning electron microscopy (LV-SEM) and microanalysis is an emerging technique of critical importance to technology, especially the examination of semiconductor and optical materials during research and manufacturing. Arbitrarily defined as spanning the beam energy range of 5 keV and lower, LV-SEM holds great interest due to the very high spatial resolution that becomes possible as a consequence of the limited range of the beam electrons. There are various equations to describe the electron range, of which one convenient form is the Kanaya–Okayama range [9]:

$$R_{KO}(\text{nm}) = \left[ 27.6A / (\rho Z^{0.89}) \right] (E_0^{1.67} - E_c^{1.67}). \quad (6)$$

Where  $A$  is the atomic weight (g/mole),  $\rho$  is the density (g/cm<sup>3</sup>),  $Z$  is the atomic number,  $E_0$  (keV) is the incident beam energy, and  $E_c$  (keV) is the critical excitation energy for the X-ray of interest.

This range can be thought of as the radius of a hemisphere centered on the beam impact point on a flat surface set normal to the beam, where the hemisphere contains approximately 95% of the electron trajectories in the solid. Values of the Kanaya-Okayama range are listed in Table 3, which spans the conventional beam energy range as well as the LV-SEM range. The collapse of the electron range as the incident beam energy is reduced is evident from the table. An example of the spatial resolution that can be achieved is illustrated in Fig. 21, which shows a Monte Carlo electron trajectory simulation of the region excited by a 2.5 keV beam incident on BaTiO<sub>3</sub> [22].

Interest in LV-SEM has been driven by the evolution of SEM platforms based on field-emission gun (FEG-SEM) technology that achieves very high electron beam performance: a 1-nm diameter beam with 100 pA to 1 nA of

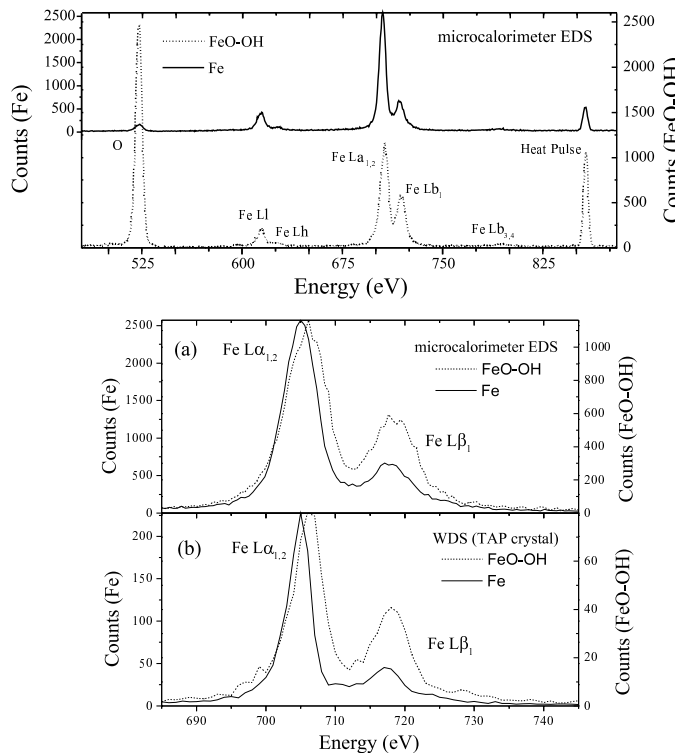


**Fig. 20.** “Chemical effects” on X-ray spectra, as measured with the (a) microcalorimeter EDS and (b) WDS (TAP crystal) for the Fe-L family on iron metal and hydrated iron oxide (FeO-OH, goethite). 3rd generation, high resolution low energy photon microcalorimeter. Peak shifts and changes in the relative heights of the L $\alpha$  and L $\beta$  peaks are observed with both types of spectrometer. (c) Expanded energy display for the microcalorimeter EDS. The energy dispersive nature of the microcalorimeter EDS also provides access to the OK peak, as well as the rest of the excited spectrum

**Table 3.** (a) Range of generation of detection of copper X-rays in various matrices conventional microanalysis strategy (Cu K-shell;  $E_c = 8.98$  keV) (b) Low voltage microanalysis strategy (Cu L-shell;  $E_c = 0.933$  keV)

(a)					(b)		
Matrix	$E_0 = 25$ keV	20 keV	15 keV	10 keV	Matrix	$E_0 = 5$ keV	2.5 keV
C	6.3 $\mu$ m	3.9 $\mu$ m	1.9 $\mu$ m	270 nm	C	490 nm	130 nm
Si	5.7 $\mu$ m	3.5 $\mu$ m	1.7 $\mu$ m	250 nm	Si	440 nm	120 nm
Fe	1.9 $\mu$ m	1.2 $\mu$ m	570 nm	83 nm	Fe	150 nm	40 nm
Au	1.0 $\mu$ m	630 nm	310 nm	44 nm	Au	80 nm	21 nm

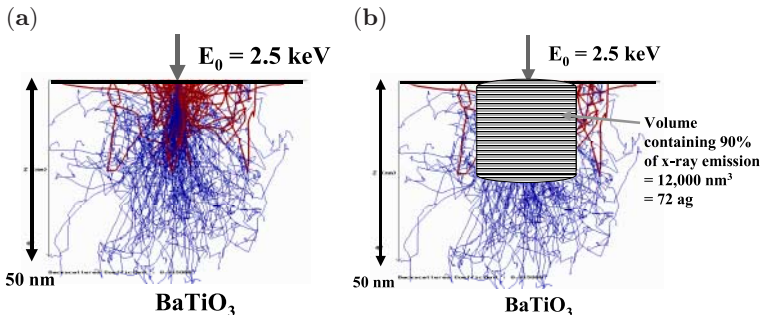


**Fig. 21.** (a) Monte Carlo simulation of electron trajectories in BaTiO<sub>3</sub> for a  $E_0 = 2.5$  keV beam. (b) Volume that contains 90% of the X-ray production. Monte Carlo simulation of Hovington et al. [22]. Thick traces = electrons that eventually backscatter; thin traces = electrons that lose all their initial energy and remain in the target

beam current. At conventional beam energies (10 keV and above), such a fine scale probe is not a significant advantage because the spatial resolution of analysis is controlled by the primary electron range, which is orders of magnitude larger than a 1 nm beam. In the LV-SEM regime, the range collapses to values of tens of nanometers, so that it becomes a great advantage to have the 1 nm probe of a FEG-SEM rather than the 10–200 nm diameter probe that is produced by conventional low brightness thermal emission guns in the low voltage range.

This LV-SEM beam performance of the FEG-SEM can be readily exploited for imaging, and the beam current in the nanoprobe is suitable for Si-EDS X-ray spectrometry, making the combination of LV microscopy and microanalysis possible. Indeed, there are key problems that this technology can solve, specifically those cases where the X-ray peaks are well separated and which have a high specific yield, such as K-shell peaks. Unfortunately, the low energy of the beam in the LV range inevitably restricts the shell ionization energy that can be probed. The critical parameter is the overvoltage,  $U$ , which is the ratio of the incident beam energy,  $E_0$ , to the ionization energy,  $E_c$ :

$$U = E_0/E_c . \quad (7)$$

Ionization is possible for  $U > 1$ , but  $U = 2$  is desirable to produce strong excitation. A value of  $U = 1.1$  is the practical minimum to detect major elements ( $C > 0.1$  mass fraction) with K-shell X-rays. With  $E_0 = 5$  keV, the highest atomic number accessible with the K-shell is Sc (practical K-shell range  $4 \leq Z \leq 23$ ). Elements with higher atomic numbers must be measured with L-shell or M-shell X-rays, which have a much lower fluorescence yield,  $\omega$ , which is the fraction of ionization events that lead to photon emission rather

than Auger electron emission, compared to K-shell X-rays of similar photon energy. As  $E_0$  is reduced below 5 keV, the practical K-shell range is reduced, and more elements must be measured with the L- or M-shells. With the poor resolution of the Si-EDS, this constraint on the X-ray shells can lead to some severe restrictions. The third generation microcalorimeter EDS, which is designed to work at low photon energy ( $E < 2.5$  keV) is ideal for this application [14].

### *Low Voltage Microanalysis of Barium Titanate*

The optoelectronic material barium titanate ( $\text{BaTiO}_3$ ) is an excellent example of the difficulty of performing low voltage microanalysis. As shown in Fig. 21b, by reducing the incident beam energy to 2.5 keV, the analytical volume is reduced to  $12\,000 \text{ nm}^3$  with linear dimensions of approximately 25 nm and with a mass of 72 ag that contains 90% of the emission from OK, TiL, and BaM [19]. The practical difficulty in simultaneously measuring OK, TiL, and BaM with Si-EDS (FWHM 129 eV at  $\text{MnK}\alpha$ ) is shown in Fig. 22a (excitation  $E_0 = 3$  keV), where the OK peak dominates the spectrum. Although O ( $C = 0.206$  mass fraction), Ti ( $C = 0.205$ ), and Ba ( $C = 0.589$ ) are all present as major constituents, the low fluorescence yield reduces the BaM peaks to nearly unrecognizable bumps on the background which do not match well with the published relative yields of BaM-family peaks. For the TiL peaks, the situation is further complicated by severe interference from the OK peak, where the Ti L-family peaks are located on the low energy shoulder of the OK peak, in the same region as the incomplete charge distortion of the OK peak. It is really not possible to recognize this material as  $\text{BaTiO}_3$  from the Si-EDS results under LV-SEM conditions. The microcalorimeter EDS spectrum under the same conditions, Fig. 22b, reveals the multiplicity of BaM peaks as well as the Ti  $L\alpha$  and Ti  $L\ell$  peaks well resolved from the OK, permitting a complete and unambiguous identification and analysis of  $\text{BaTiO}_3$ . The low fluorescence yields of TiL and BaM relative to OK are manifest in the low relative peak heights. The relative abundances of the BaM-family peaks are indeed seen to be substantially different from the published values.

### *Low Voltage Microanalysis of Titanium Nitride*

Low voltage microanalysis of titanium nitride (TiN) demonstrates the need for resolution and energy dispersive operation. This example also points out the complication of interferences, which can still occur even with high spectral resolution, when chemical effects are also present. Figure 23a shows the TiL and NK region of the spectrum of TiN, excited with a beam energy of 2 keV to limit the penetration and reduce the specimen self-absorption of these low energy X-rays. The peaks of interest show interferences even with the resolution of the microcalorimeter EDS: Ti  $L\ell$  and Ti  $L\eta$  interfere with NK, and the Ti  $L\beta_{3,4}$  interferes with OK. With Si-EDS, a spectrum from which is also shown in Fig. 23a, the interference situation is hopeless.

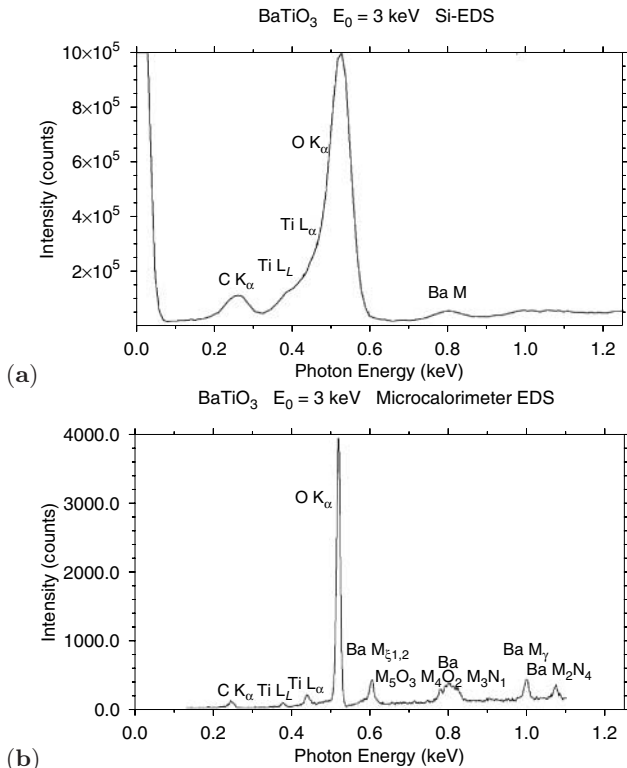


**Fig. 22.** BaTiO<sub>3</sub> excited at  $E_0 = 3.0$  keV. (a) Si-EDS spectrum (129 eV at Mn K $\alpha$ ) (b) microcalorimeter EDS spectrum showing separation of the Ti L-family from the OK peak and the detection of the Ba M-family members, although with much different weights than those in the published database

Figure 23b demonstrates that interference problems can remain in the microcalorimeter EDS spectrum, despite the high resolution. The spectrum of bare Ti metal (obtained by scraping the surface under flowing helium to remove the native oxide followed by rapid insertion into the vacuum system) contains significant intensity in the Ti L $\ell$  and Ti L $\eta$  peaks that interferes with the NK peak. In principle, this peak could be deconvolved by multiple linear least squares fitting against a measured peak reference, except that the Ti L $\alpha$  and Ti L $\beta$  peaks show a dramatic change in shape and relative height, with the Ti L $\alpha$  essentially flat-topped in TiN, apparently due to chemical effects between the bonding of Ti atoms in metallic Ti and in TiN. Interestingly, this dramatic effect is not seen in Ti metal compared with oxidized TiO<sub>2</sub>, shown in Fig. 23c, where the Ti L $\alpha$  and Ti L $\beta$  peaks are nearly identical in these materials so that multiple linear least squares fitting would be justified. Accurate measurement of the contribution of the Ti L $\ell$  and Ti L $\eta$  peaks to the NK peak thus will require very careful consideration, and obviously, even

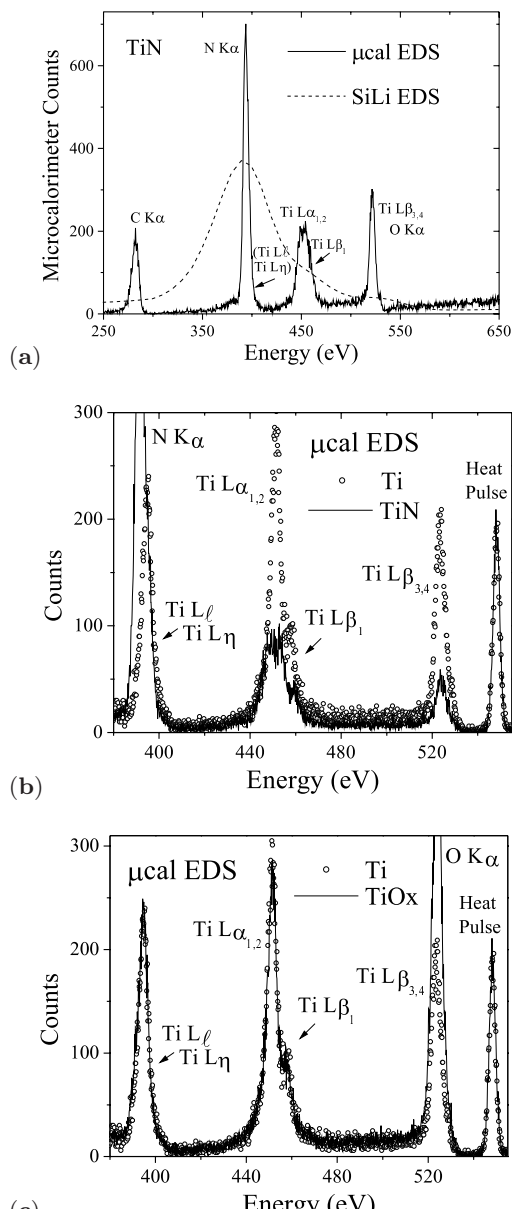


**Fig. 23.** TiN, excited with a beam energy of 2 keV to limit the penetration and reduce the specimen self-absorption of these low energy X-rays. **(a)** Comparison of microcalorimeter EDS (3rd generation, low photon energy) and Si-EDS. **(b)** Interference problems in Ti spectra with the microcalorimeter EDS. The spectrum of bare Ti metal (obtained by scraping the surface to remove the native oxide followed by rapid insertion into the vacuum system) contains significant intensity in the Ti L $\ell$  and Ti L $\eta$  peaks that interferes with the NK peak. Ti L $\alpha$  and Ti L $\beta$  peaks show a dramatic change in shape and relative height, with the Ti L $\alpha$  essentially flat-topped, due to chemical effects between the bonding of Ti atoms in metallic Ti and in TiN. **(c)** Comparison of Ti metal compared with oxidized TiO<sub>x</sub>, where the Ti L $\alpha$  and Ti L $\beta$  peaks are nearly identical in these materials.

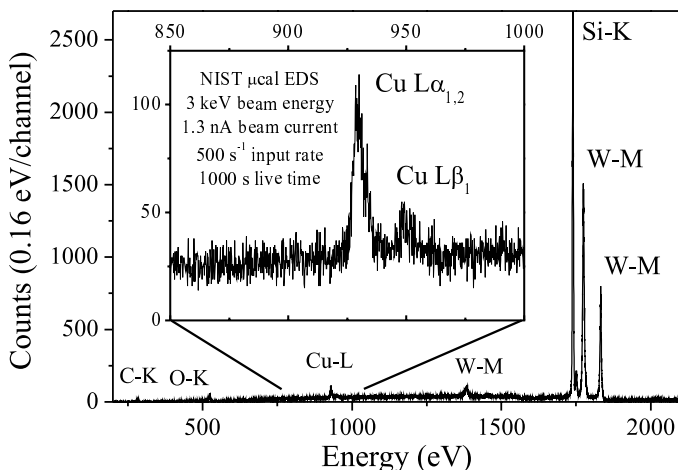


**Fig. 24.** Microcalorimeter EDS spectrum of  $\text{WSi}_2$ , with a trace addition of 0.007 mass fraction of copper ( $E_0 = 3 \text{ keV}$ ;  $i_B = 1.3 \text{ nA}$ )

better spectral resolution would be a great help. The critical need to visualize the entire spectral region, and not just the peak positions employed with simple WDS measurements, is clearly demonstrated by this example.

#### *Trace Element Measurement in Low Voltage Microanalysis*

As an example of trace element measurement in low voltage microanalysis, Fig. 24 shows the microcalorimeter EDS spectrum of  $\text{WSi}_2$ , a metal silicide of importance in semiconductor device manufacturing, with a trace addition of 0.007 mass fraction of copper. As shown in the inset, this low level of copper is readily detectable under low voltage conditions ( $E_0 = 3 \text{ keV}$ ;  $i_B = 1.3 \text{nA}$ ). Both the Cu L $\alpha$  and Cu L $\beta$  peaks are detectable, which greatly increases the confidence in the qualitative identification of copper. The peak-to-background is sufficiently high to suggest that a concentration limit-of-detection of 0.0007 mass fraction should be achievable under these conditions.

#### *Detection of a Thin Surface Layer on a Substrate*

An important aspect of low voltage microanalysis is the improved sensitivity to shallow surface layers that occurs because of the reduced range of the beam electrons, and the consequent reduction in the self-absorption of X-rays. An example is shown in Fig. 25 of TaSiN films on an Si substrate. Spectra from several thicknesses are superimposed. A film as thin as 3.5 nm is readily detectable, with a peak-to-background that suggests that a film of 1 nm thickness should represent the threshold of detection.

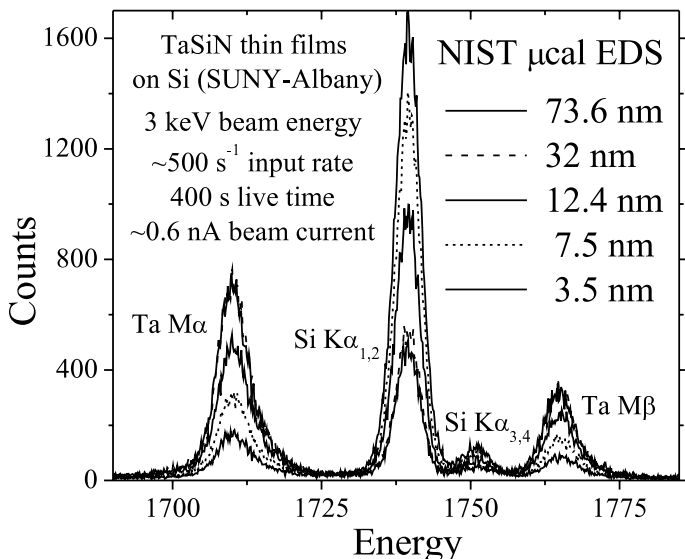


**Fig. 25.** TaSiN films of various thicknesses on an Si substrate;  $E_0 = 3$  keV

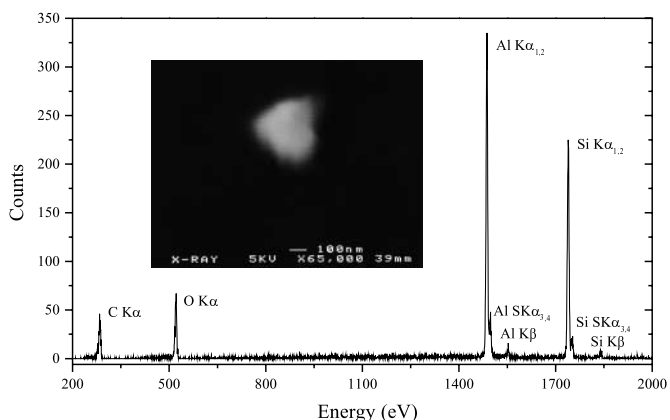


**Fig. 26.** Microcalorimeter EDS spectrum of an  $0.3\text{ }\mu\text{m}$  diameter  $\text{Al}_2\text{O}_3$  particle on a silicon substrate, excited with a 5 keV electron beam

#### Particle Analysis with Low Voltage SEM

An important application of low voltage SEM and microanalysis to semiconductor manufacturing is the problem of particle analysis (“defect review”) [23, 24]. When particle contamination is discovered during in-process monitoring of partially fabricated semiconductor wafers, it is critical to preserve yield by quickly determining the nature of the particles without in-

troducing damage to the nearby useful portions of the partially completed electronic structure. To avoid electron beam-induced damage, the SEM is operated in low voltage mode, with the beam energy chosen to be as low as possible consistent with analyzing the elements of interest. A typical contaminant might be an alumina particle on a silicon substrate. Figure 26 shows an example of an  $\text{Al}_2\text{O}_3$  particle with a maximum dimension of 300 nm detected on a silicon substrate. While  $\text{Al}_2\text{O}_3$  particles could be measured in the presence of silicon with a conventional Si-EDS, the superior resolution of the microcalorimeter EDS permits the analyst to detect smaller alumina particles, by an order of magnitude or more, than would be possible with a Si-EDS for similar beam conditions. Figure 27 illustrates two problems that can only be solved with the superior resolution of the microcalorimeter EDS. In Fig. 27a, an 0.3  $\mu\text{m}$  particle of tungsten on a silicon substrate is easily detected from both the W  $\text{M}\alpha$  and W  $\text{M}\beta$  peaks despite the interference of the SiK peak. In Fig. 27b, an 0.3  $\mu\text{m}$  particle of  $\text{TiO}_2$  on a silicon substrate is detected with the Ti L-family peaks. In low voltage operation ( $E \leq 5 \text{ keV}$ ), the Ti K-shell X-rays are not excited, so that the Ti L-shell must be used instead. However, TiL suffers severe interference with OK, as shown in the  $\text{BaTiO}_3$  example in Fig. 22a. There is enough of an oxygen signal from the native oxide on silicon to provide a significant OK peak that overwhelms the Ti L-peaks from a small particle with conventional Si-EDS. These Ti L-peaks are easily detected with the microcalorimeter EDS, as seen in Fig. 27b.

## 5.4 Future Prospects, Further Developments, and Commercialization

The testing of the prototype microcalorimeter EDS in an SEM environment has demonstrated the extraordinary potential of this technology to advance electron beam X-ray microanalysis. Future possibilities depend on two parallel lines of development: commercialization based upon the first generation technology and research to advance the size and speed of the detector.

### 5.4.1 Commercialization

NIST licensed the microcalorimeter EDS technology to two commercial firms, EDAX of Mahwah, NJ and Thermo NORAN of Middleton, WI. As evidenced by reports presented at conferences, commercial prototypes based upon the NIST design have been developed [25, 26]. While the NORAN effort uses a liquefied gas/adiabatic demagnetization refrigerator (ADR) cryostat similar to the NIST prototype to maintain the operating temperature, the EDAX effort (in collaboration with VeriCold Technologies GmbH) has been directed toward developing a closed cycle cryogenic refrigerator that does not have to be filled with cryogenic fluids on a daily basis. Such a refrigeration system is more desirable in an industrial setting, especially for semiconductor fabrication where operation within the low contamination environment is vital. The

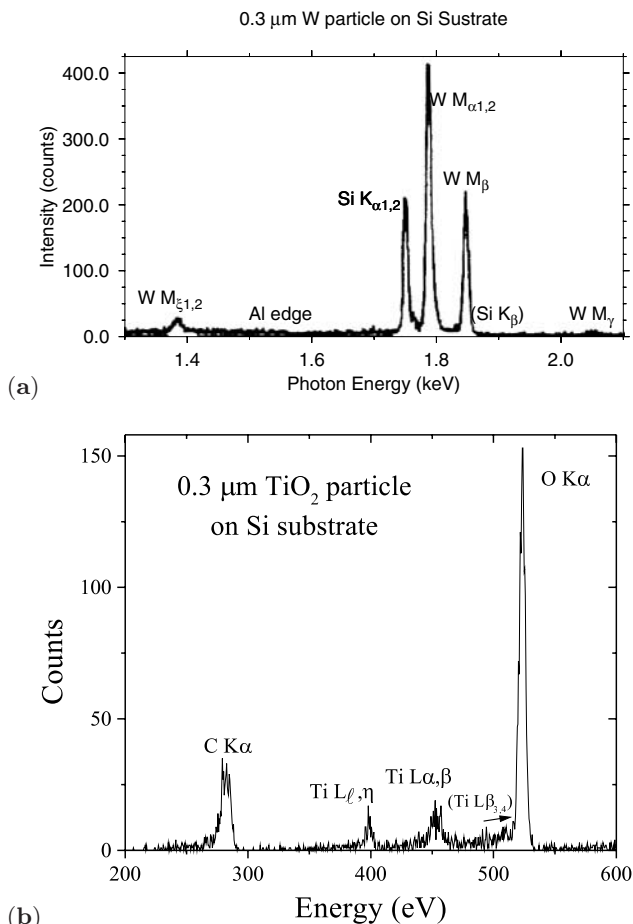


**Fig. 27.** (a) Microcalorimeter EDS spectrum of an  $0.3\text{ }\mu\text{m}$  diameter  $\text{WSi}_2$  particle on a silicon substrate, excited with a 5 keV electron beam. (b)  $0.3\text{ }\mu\text{m}$   $\text{TiO}_2$  particle on Si

EDAX system uses a mechanical cryocooler based upon a pulse-tube refrigerator to reach 4 K and an adiabatic demagnetization refrigerator to reach the 100 mK operating temperature. Figure 28 shows a schematic of the cryocooler with two pulse-tube stages and the mechanical design of spectrometer mount for an SEM. The vibration associated with the expansion chamber of the cryocooler has been sufficiently damped to permit operation of the SEM at  $100\,000\times$  magnification without serious image degradation.

Examples of spectra recorded with this pulse-tube cryocooler microcalorimeter EDS mounted on an SEM are shown in Fig. 29 [27]. Figure 29a shows the performance at low photon energy, where the spectrum of BN shows the boron K-peak at 185 eV and the nitrogen K-peak at 392 eV, as well as

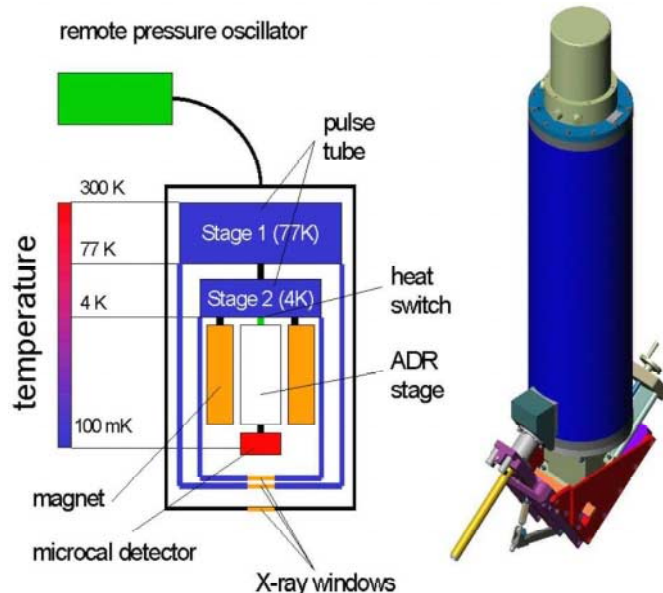


**Fig. 28.** Schematic diagram of the cryogenic refrigeration system of the EDAX microcalorimeter EDS showing the two pulse-tube stages of the cooling system. (Figure courtesy of Del Redfern, EDAX, Inc., Mahwah, NJ)

CK (282 eV) from a conductive coating and OK (523 eV) from an unknown source, perhaps oxidation of the BN. Figure 29b shows an example of the spectrum of a complex material ( $\text{SrBi}_2\text{Ta}_2\text{O}_9$ ) in thin film form where the microcalorimeter resolution is sufficient to separate the major spectral components of the Sr L-family and the Ta M-family.

#### 5.4.2 Anticipated Future Developments

The prototype NIST microcalorimeter EDS has two major shortcomings that impact upon its application to EPMA, specifically the small area ( $0.4 \text{ mm} \times 0.4 \text{ mm}$ ) of the high resolution detector and the limited counting speed ( $< 1 \text{ kHz}$ ). On-going research into arrays of microcalorimeter detectors may lead to critical improvements that will overcome these limitations.

The double focusing polycapillary X-ray optic provides a useful solution to increase the solid angle of a small area detector. The improvement is limited to a factor of approximately 300, dependent on the photon energy, which is sufficient to raise the effective solid angle within a factor of two of a Si-EDS “high resolution” detector ( $10 \text{ mm}^2$  detector at 20 mm source-to-detector distance). However, the geometric efficiency of the optics-augmented microcalorimeter is still less than 1% of the available  $2\pi$  steradian solid angle of X-ray emission. Moreover, the polycapillary optic introduces an energy dependent bias to the

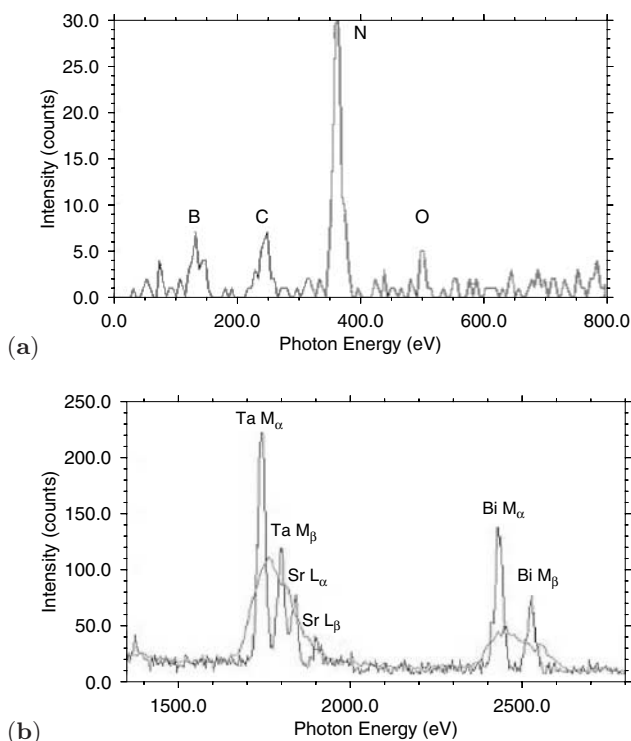


**Fig. 29.** (a) EDAX/VeriCold microcalorimeter EDS (pulse-tube cryocooler) spectra: (a) BN showing K-family peaks of B, C, N, and O as measured on an SEM. (b)  $\text{SrBi}_2\text{Ta}_2\text{O}_9$  thin film showing separation of the major spectral components of the Sr L-family and the Ta M-family

spectrum (decreasing transmission with increasing photon energy), and because of its focusing properties, it also acts as a spatial filter. To obtain the maximum transmission, the X-ray source must be located within a volume of space that has linear dimensions of tens of micrometers relative to the input face of the polycapillary X-ray optic. The microcalorimeter detector must be placed with similar accuracy relative to the exit face of the polycapillary, but this positioning can be rigidly maintained once it has been established by attaching the output end of the optic directly to the microcalorimeter. The input source position depends upon where the beam strikes the specimen, which can vary significantly for an irregularly-shaped specimen. Careful optimization of the measured X-ray signal is necessary to locate the “sweet spot” for each new specimen.

Progress has been reported toward fabricating an array of microcalorimeter detectors, as illustrated in Fig. 30 [28, 29]. An array of discrete detectors would have several obvious advantages. First, the area of the effective integrated detector would be enlarged by a multiplicative factor of  $n \times m$ , where  $n$

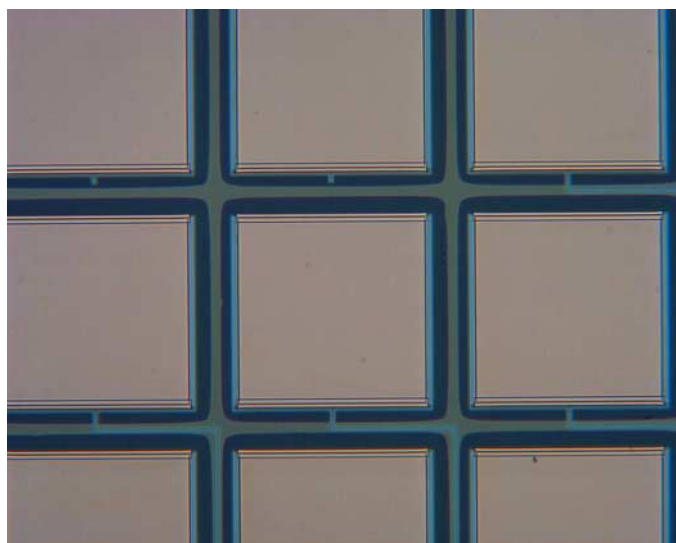


**Fig. 30.** Photograph of the interior portion of an  $8 \times 8$  array of microcalorimeters. In this device 24 of the 64 detectors in this array are wired to external pads

is the number of rows of detectors and  $m$  is the number of columns. A detector array with a large number of elements could be used directly without the polycapillary, thus avoiding the energy dependent transmission artifact, and the array detector could still equal or exceed the area of a conventional Si-EDS ( $10\text{ mm}^2$ ). If it was still desirable to employ a polycapillary to further increase the solid angle, or to make use of the spatial filtering of the X-ray source to eliminate remotely generated artifactual X-rays, it would only be necessary to use a single tapered polycapillary (taper facing the X-ray source). The large physical size of the array would mean that the collected X-rays would be “parallelized” in a large area of parallel capillaries for presentation to the array. With only one taper, the transmission efficiency of the optic would increase.

The microcalorimeter detector array would also solve the problem of a low limiting count rate, since the  $1\text{ kHz}$  maximum count rate of each detector would be multiplexed into an aggregate signal a factor of  $m \times n$  faster. Because of the variability of the individual detectors, it is expected that there will be a resolution penalty when combining the individual detector contributions of the microcalorimeter detector array. Nevertheless, the possibility of an energy dispersive X-ray spectrometer with a limiting count rate of  $100\text{ kHz}$  or higher count rate combined with  $10\text{ eV}$  resolution would be an extraordinary asset in EPMA, X-ray fluorescence, synchrotron X-ray excitation, etc. Such a system would permit “flash” X-ray spectrum measurements that could be of important use in high speed process control in industry.

## 6 Summary

The microcalorimeter EDS offers extraordinary capabilities for advancing the technique of electron probe X-ray microanalysis. The microcalorimeter EDS provides the critical combination of the high spectral resolution of the wavelength dispersive (crystal diffraction) spectrometer with the energy dispersive character of the semiconductor energy dispersive X-ray spectrometer. The resolution and energy dispersive character are the attributes that correspond most closely to the performance of an “ideal” X-ray spectrometer. This combination of capabilities is particularly effective for application in the emerging field of low voltage scanning electron microscopy and microanalysis, where the low excitation efficiency of X-ray peaks demands maximum spectral performance to achieve adequate detection and to separate the peak interferences that can render semiconductor EDS ineffective. Future improvements to make larger detectors with greater total counting speed through the use of detector arrays will further advance the applicability of the microcalorimeter EDS and bring it closer to the performance of the ideal X-ray spectrometer.

## Acknowledgements

The figures showing the EDAX microcalorimeter detector and examples of its application are courtesy of Del Redfern. Support for the research that lead to the development and advancement of the NIST microcalorimeter EDS was contributed by the NIST Office of Microelectronic Programs. Any mention of commercial products within this Chapter is for information only; it does not imply recommendation or endorsement by NIST.

## References

- [1] D.E. Newbury, D.A. Wollman, G.C. Hilton, K.D. Irwin, N.F. Bergren, D.A. Rudman, J.M. Martinis: *J. Radioanal. Nucl. Chem.* **244**, 627 (2000) 267, 268, 297
- [2] S. Friedrich, T. Funk, O. Drury, S.E. Labov, S.P. Cramer: *Rev. Sci. Instrum.* **73**, 1629 (2002) 267
- [3] T. Niedermayr, S. Friedrich, M.F. Cunningham, M. Frank, J.P. Brand, S.E. Labov: *AIP Conf. Proc.* **605**, 363 (2002). 267
- [4] L. Lesyna, D. DiMarzio, S. Gottesmann, M. Kesselman: *J. Low Temp. Phys.* **93**, 779 (1993) 268
- [5] K.D. Irwin, G.C. Hilton, D.A. Wollman, J.M. Martinis: *Appl. Phys. Lett.* **69**, 1945 (1996) 268
- [6] E. Silver, M. LeGros, G. Austin, N. Madden, J. Beeman, E. Haller: *X-Ray Spectrom.* **26**, 265 (1997) 268
- [7] D.A. Wollman, K.D. Irwin, G.C. Hilton, L.L. Dulcie, D.E. Newbury, J.M. Martinis: *J. Microsc.* **188**, 196 (1997) 268, 276, 278, 280

- [8] J. Hohne, U. Hess, M. Buhler, F.V. Feilitzsch, J. Jochum, R.V. Hentig, T. Hertrich, C. Hollerith, M. Huber, J. Nicolosi, K. Phelan, D. Redfern, B. Simmnacher, R. Weiland, D. Wernicke: AIP Conf. Proc. **605**, 353 (2002) **268**
- [9] J. Goldstein, D. Newbury, D. Joy, C. Lyman, P. Echlin, E. Lifshin, L. Sawyer, J. Michael: *Scanning Electron Microscopy and X-ray Microanalysis*, (Kluwer Academic Plenum, New York 2003) **268, 269, 271, 273, 274, 276, 280, 282, 288, 289, 297, 298**
- [10] C. Fiori, C. Swyt, R. Myklebust: *Desktop Spectrum Analyzer (DTSA), a Comprehensive Software Engine for Electron-excited X-ray Spectrometry*, National Institute of Standards and Technology, Standard Reference Data Program (Gaithersburg, MD, 1991); available from the following WorldWideWeb site: <http://www.cstl.nist.gov/div837/Division/outputs/software.htm> **268, 275, 284**
- [11] K. Heinrich: *Electron Beam X-ray Microanalysis*, (Van Nostrand Reinhold, New York 1981) **272, 274**
- [12] V.D. Scott, G. Love, S.J.B. Reed: *Quantitative Electron-Probe Microanalysis*, (Ellis Horwood, New York 1995) **276**
- [13] K.D. Irwin, G.C. Hilton, J.M. Martinis, S. Deiker, N. Bergren, S.W. Nam, D.A. Redman, D.A. Wollman: Nucl. Instrum. Methods Phys. Res. A**444**, 184 (2000) **280**
- [14] D.A. Wollman, S.W. Nam, D.E. Newbury, G.C. Hilton, K.D. Irwin, N.F. Bergren, S. Deiker, D. A. Rudman, J.M. Martinis: Nucl. Instrum. Methods Phys. Res. A**444**, 145 (2000) **280, 301**
- [15] D.C. Joy, A.D. Romig Jr., J.I. Goldstein: *Principles of Analytical Electron Microscopy*, (Plenum Press, New York 1986) **282**
- [16] D.A. Wollman, C. Jezewski, G.C. Hilton, Q.-F. Xiao, L.L. Dulcie, J.M. Martinis: Microscopy and Microanalysis **3**, 1075 (1997) **287, 288**
- [17] T.O. Ziebold: Anal. Chem **39**, 858 (1967) **292**
- [18] T.O. Ziebold, R.E. Ogilvie: Anal. Chem. **36**, 322 (1964) **293**
- [19] D. Newbury, D. Wollman, K. Irwin, G. Hilton, J. Martinis: Ultramicroscopy **78**, 73 (1999) **294, 301**
- [20] P.J. Statham: in *X-ray Spectrometry in Electron Beam Instruments* (D.B. Williams and J.I. Goldstein, D.E. Newbury, eds), 101, (Plenum, New York 1995) **295, 297**
- [21] J.T. Armstrong: Anal. Chem. **71**, 2714 (1999) **297**
- [22] P. Hovington, D. Drouin, R. Gauvin: **19**, 1 (1997) **298, 300**
- [23] D.A. Wollman, G.C. Hilton, K.D. Irwin, L.L. Dulcie, N.F. Bergren, D.E. Newbury, K. Woo, B.Y.H. Liu, A.C. Diebold, J.M. Martinis: AIP Conf. Proc. **449**, 799 (1998) **305**
- [24] A.C. Diebold, D.A. Wollman, G.C. Hilton, K.D. Irwin, J.M. Martinis, B.Y.H. Liu: Diffus. Defect Data **B65-66**, 199 (1999) **305**
- [25] J. Howard, D. Hammermeister, J. McCarthy: Micros. Microanal. **7**, 1048 (2001) **306**
- [26] D. Redfern, J. Nicolosi, U. Hess, J. Hohne: Micros. Microanal **7**, 1056 (2001) **306**
- [27] D. Redfern, J. Nicolosi, J. Hohne, R. Weiland, B. Schimmnacher, C. Hollerith: Micros. Microanal. **8**, 80, (2002) **307**

- [28] S.W. Nam, D.A. Wollman, D.E. Newbury, G.C. Hilton, K.D. Irwin, D.A. Rudman, S. Deiker, N.F. Bergren, J.M. Martinis: *Micros. Microanal.* **7**, 1050 (2001)
- [29] K.D. Irwin, J.A. Beall, S. Deiker, G.C. Hilton, L. King, S.W. Nam, D.E. Newbury, C.D. Reintsema, J.A. Small, L.R. Vale: *Micros. Microanal.* **8** 78 (2002)  
**309 309**

# Index

- adiabatic demagnetization refrigerator, 278
- ADR, 278
- AlGaAs, 293
- BaTiO<sub>3</sub>, 291, 300–302
- BN, 309
- carbon, 285
- chemical shift, 297
- count rate, 287
  - microcalorimeter, 289
  - Si-EDS, 288
  - WDS, 288
- defect review, 305
- diffraction, 274
- EDS, 271, 275
- efficiency
  - geometric, 284
  - electron probe microanalysis, 267
  - electron range, 298
  - energy dispersive X-ray spectrometer, 271
  - energy linearity, 289
  - EPMA, 267
    - applications, 291
  - ideal X-ray spectrometer, 281
  - layered sample, 304
  - limits of detection, 273, 292
  - linearity correction
    - microcalorimeter, 289
    - low voltage microanalysis, 298
    - LVSEM, 298
  - microcalorimeter
    - efficiency, 286
    - microcalorimeter array, 310
    - microcalorimeter EDS, 278
    - minimum mass fraction, 293
    - natural linewidth, 283
    - overvoltage, 300
    - particle analysis, 305
    - peak interference, 272, 295
    - peak-to-background, 295
    - pulse-tube cryocooler, 307
    - qualitative analysis, 291
    - resolution, 282
    - scanning electron microscope, 269
    - SEM, 269
      - low voltage, 298
      - Si-EDS, 271
        - limitations, 272
        - resolution, 272
        - WDS, TES comparison, 277
      - spectral artifacts, 290
      - spectrometer efficiency, 283
      - SrBi<sub>2</sub>Ta<sub>2</sub>O<sub>9</sub>, 309
    - TES, 278
      - WDS, Si-EDS comparison, 277
      - TiN, 301, 303
      - trace detection, 296
      - trace element, 304
    - wavelength dispersive X-ray spectrometry, 274
    - WDS, 274, 275
      - diffractors, 275

- resolution, 274  
scanning, 274  
Si-EDS, TES comparison, 277  
WSi<sub>2</sub>, 292, 304      X-ray optic, 287  
YBa<sub>2</sub>Cu<sub>3</sub>O<sub>7</sub>, 273, 275, 283

# Dark Matter Direct Detection

G. Chardin

DSM/DAPNIA/SPP, Bâtiment 141, CEA/Saclay,  
F-91191 Gif-sur-Yvette Cedex, France  
[Chardin@hep.saclay.cea.fr](mailto:Chardin@hep.saclay.cea.fr)

**Abstract.** Solving the Dark Matter enigma represents one of the key objectives of contemporary physics. Recent astrophysical and cosmological measurements have unambiguously demonstrated that ordinary matter contributes to less than 5% of the energy budget of our Universe, and that the nature of the remaining 95% is unknown. Weakly Interacting Massive Particles (WIMPs) represent the best motivated candidate to fill the Dark Matter gap, and direct detection Dark Matter experiments have recently reached sensitivities allowing them to sample a first part of supersymmetric models compatible with accelerator constraints.

Three cryogenic experiments currently provide the best sensitivity, by nearly one order of magnitude, to WIMP interactions. With systematic uncertainties far less severe than other present techniques, the next generation of cryogenic experiments promises two orders of magnitude increase in sensitivity over the next few years. The present results, perspectives and experimental strategies of the main direct detection experiments are presented. Challenges met by future ton-scale cryogenic experiments in deep underground sites, aiming at testing most of the SUSY parameter space, are critically discussed.

The Dark Matter enigma was first formulated by Zwicky [1] in the early thirties. From observations of the velocity dispersion of eight galaxies in the Coma cluster, Zwicky found that the velocities of these galaxies were far too large to allow them to remain trapped in the cluster's gravitational well. Converting the observed velocity dispersion in terms of mass deficit, Zwicky concluded that visible stars only contribute 0.5% of the total mass present in the Coma cluster. Today, although the reevaluations of the distance scale and the Hubble parameter lead to a revised estimate of the missing mass factor, Zwicky's observations appear as one of the most astonishing and profound insights of modern physics.

## 1 Motivations for Non-Baryonic Dark Matter

Determining the precise nature of Dark Matter is one of the main open questions of contemporary physics. Its resolution will probably entail a major Copernican revolution since baryonic matter, which is constituting our environment, represents only a small fraction of the total energy content in the Universe. But despite impressive experimental progress and effort over the

last ten years [2, 3, 4], the precise nature of this Dark Matter has not yet been uncovered.

### 1.1 Searching for Baryonic Dark Matter

Over the last few years, several candidates have been proposed to solve the Dark Matter enigma. These include anomalous gravity [5], Massive Compact Halo Objects (MACHOs) [6, 7], massive neutrinos [8], axions [9] and atomic hydrogen [10]. The observation in 1998 of an accelerating universe [11, 12] has created a considerable surprise, leading to a new incarnation of the concept of ether, called quintessence [13]. With this variety of candidates, it would seem presumptuous to believe that the solution is close at hand.

Still, the precision in the determination of the cosmological parameters has recently dramatically increased. In particular, the value of the Hubble expansion parameter appears now fixed at a value of  $H_0 \sim 71 \pm 4 \text{ km/s Mpc}$  [14]. Also, the non-zero cosmological constant term has considerably reduced the age problem of the universe, now estimated to be  $\approx 13.7 \pm 0.2 \text{ Gyr}$  [14].

An impressive amount of data has been collected by studying the rotation curves of galaxies which, apart from a few exotic galaxies, always seem to require halos extending much beyond the extent of luminous matter. Already at this galactic scale, typically more than 80% of the matter is dark and,

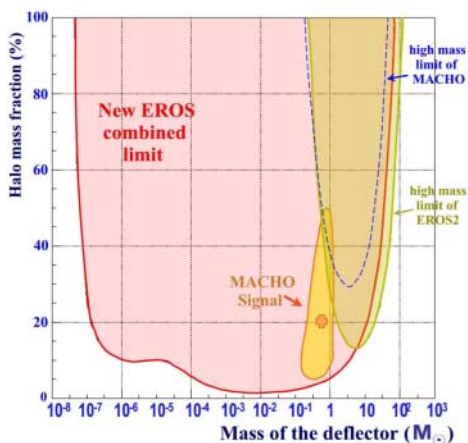


**Fig. 1.** Exclusion diagram (95% C.L.) on the halo mass fraction in the form of compact objects of mass  $M$ , for the standard halo model ( $4 \times 10^{11}$  solar masses inside 50 kpc), from all LMC and SMC EROS data. The *thick line* is the combined limit from all EROS sub-experiments. The *dotted line* indicates the high mass limit of the MACHO experiment, while the enclosed region, marked by an *arrow*, represents the signal reported by the MACHO experiment, and excluded by EROS. For MACHOs with mass between  $10^{-6}$  and 3 solar masses, the EROS result shows that the MACHO contribution to the galactic halo is less than 10% (after [16]).

despite extensive efforts, no conventional counterpart has yet been found. For example, after the initial excitement created by the observation of a small set of compact halo objects, detected by their micro-lensing effects on very large samples of stars [6, 7], more precise measurements [15, 16, 17] over a period of nearly ten years have revealed that these MACHOs represented less than  $\sim 15\%$  of a standard halo composed of objects with a mass between  $2 \times 10^{-7} M_{\text{sol}}$  and  $1 M_{\text{sol}}$  at the 95% C.L.

The present experimental situation of the MACHO searches is summarized in Fig. 1 where the limits reached by the EROS microlensing search [16, 17], monitoring  $\sim 55$  million stars in the Small and Large Magellanic clouds, are now excluding most of the mass range of MACHOs. Similarly, observations of the Hubble Deep Field Space Telescope were initially interpreted to demonstrate that white dwarf stars, of low luminosity and intermediate mass, could represent as much as 50% of the galactic Dark Matter [18]. More recent data, on the other hand, indicated that this proportion is in fact  $\leq 5\%$  [19]. Therefore, at present, no conventional candidate has been found that could explain the Galactic Dark Matter rotation curves.

## 1.2 Cosmological Constraints

The Dark Matter problem is even more glaring at large scales where the proper motions of galaxies in clusters, the study of velocity fields, the X-ray emission temperature in clusters, the lensing methods and the Cosmic Microwave Background (CMB) measurements all converge to indicate that the matter content at the supercluster scale:

$$\Omega_m = \varrho_m / \varrho_c \quad (1)$$

is of the order of 0.3 when expressed in terms of the critical density  $\varrho_c$ :

$$\varrho_c = (3H_0^2 / 8\pi G) \approx 1.88 \times 10^{-26} h^2 \text{ kg m}^{-3}, \quad (2)$$

where  $H_0$  is the Hubble parameter,  $G$  is the gravitational constant and  $h = H_0/100 \text{ km/Mpc/s}$  is the reduced Hubble parameter.

The considerable Dark Matter densities observed at very large scales appear to imply that a large part of this hidden matter must be non-baryonic. This statement is based on the success of homogeneous nucleosynthesis [20] and its ability to predict the light element abundances, and notably that of helium and deuterium.

Today, the baryonic content density, expressed in terms of a fraction of the critical density, has narrowed to [21, 22]:

$$\Omega_b h^2 = 0.023 \pm 0.001 \quad (3)$$

with an uncertainty on the Hubble parameter  $H_0 \approx 71 \text{ km/s} \cdot \text{Mpc}$  is now of the order of 5%.

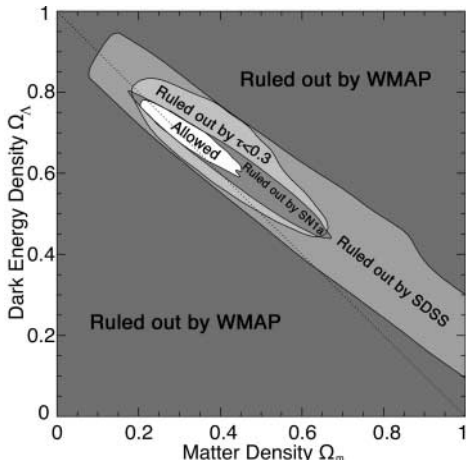


**Fig. 2.** Observational constraints on the matter density  $\Omega_{\text{matter}}$  and on the cosmological constant density  $\Omega_\Lambda$  (95% C.L.). *Shaded dark grey* region is ruled out by the Cosmological Microwave Background (CMB) WMAP satellite experiment alone. *Shaded light grey* region is ruled out when adding the structure constraints imposed by the Sloane Digital Sky Survey (SDSS) information. The next two regions are ruled out when adding the constraints from the reionization optical depth  $\tau < 0.3$  and when including the constraints from SN-Ia supernovae, respectively. The allowed (*white*) region is centered on  $\Omega_{\text{matter}} \sim 0.3$  and  $\Omega_\Lambda \sim 0.7$ . Models on the *diagonal dotted line* are flat, those below are open and those above are closed (adapted after Tegmark et al. [14])

Therefore, we are led to accept that, on the one hand, a significant part of the baryons are hidden and, secondly, that as much as 85% of the matter content of the Universe is made of non-baryonic matter. The requirement of a large non-baryonic dark matter component appears also substantiated by the CMB data analysis. After initial measurements at large angular scale by the COBE satellite [23], the BOOMERANG [24], MAXIMA [25], DASI [26], ARCHEOPS [27] and CBI [28] balloon and ground-based experiments have constrained the total cosmological density to be within  $\sim 3\%$  of the critical density. More recently, the WMAP satellite experiment [29] together with the SDSS and 2dF surveys [14] have further reduced the uncertainty on these cosmological parameters.

The combined analysis of the WMAP, SDSS and 2dF data (Fig. 2) strongly favors a flat universe with a non-zero value of cosmological constant, with preferred values  $\Omega_m \approx 0.28$ ,  $\Omega_\Lambda \approx 0.72$

On the other hand, the recent apparition in the cosmological landscape of a non-zero cosmological constant or some other “quintessential” component has brought some uneasiness to the emerging  $\Lambda$ -CDM Standard Model: our Universe appears to be a strange mixture of 2/3 of some cosmological repul-

sive component, 1/3 of matter, with only a few percent of ordinary (baryonic) matter: 95% of the universe content is unknown, while the minority matter component is composed at nearly 85% of a weakly interacting component.

It seemed initially [30, 31] that massive neutrinos could fill the Dark Matter gap. But although we have now good evidence that neutrinos are indeed massive, the sensitivity reached by present searches excludes that neutrinos can play this role: experimental constraints impose that they contribute at most a few percent to the missing mass. Generically predicted by supersymmetric (SUSY) theories, Weakly Interacting Massive Particles (WIMPs) are therefore presently considered as the best motivated candidate to solve the missing matter enigma.

Overall, the so-called  $\Lambda$ -CDM “concordance” model, with a small admixture of neutrinos, reproduces nicely the available data, with a few important points on galactic central density profiles and satellite galaxies still being discussed. In addition, for the first time, direct and indirect detection experiments are beginning to test regions of supersymmetric model parameter space compatible with cosmological and accelerator constraints.

## 2 Weakly Interacting Massive Particles (WIMPs)

### 2.1 Phenomenology

In particle physics, heavy neutrinos and supersymmetric relic particles represent two rather natural candidates for non-baryonic Cold Dark Matter. In fact, as noted previously and as shown by initial semiconductor experiments [30, 31], most, if not all, of the mass range of Dirac neutrinos is already excluded experimentally. Today, the most popular candidates are given by supersymmetric particles for two main reasons.

First, for models incorporating the conservation of a R-parity quantum number, it is natural to expect that the lightest supersymmetric particle will be stable. This supersymmetric particle, or sparticle, is often supposed to be the neutralino, which is its own antiparticle and a linear combination of the photino (supersymmetric partner of the photon), the zino (partner of the  $Z^0$  weak boson), the Higgsinos, and of axinos (partners of the axion, if it exists).

Secondly, it is a fascinating coincidence that, for a relatively large mass range, the cross-sections requested to produce a dark matter density of  $\sim 0.3$  are characteristic of electroweak interactions. In this sense, particle physics provides a natural explanation for the Cold Dark Matter problem. On the other hand, the constraints on the mass of supersymmetric particles are only phenomenological, and the LEP accelerator data only impose a lower bound on SUSY particle masses of  $\approx 35$  GeV under the MSSM hypothesis.

The phenomenology of WIMPs and in particular of the Minimal Supersymmetric Standard Model (MSSM) models has been described by a number of authors [32], with a rather considerable uncertainty in the predicted event

rates since more than 100 parameters remain to be fixed to determine a specific SUSY model. Scalar and axial terms can be a priori considered for WIMP coupling to ordinary matter. Scalar terms lead typically to an approximate  $A^2$  dependence of the cross-section with the number of nucleons  $A$ , and are therefore usually predominant compared to axial couplings, which depend on the spin of the target nucleus.

Interactions rates range from a few events/kg day for the most optimistic models, down to about  $10^{-7}$  event/kg day. Models favored by particle theorists typically provide event rates of a few  $10^{-3}$  event/kg day or below. Exploring a significant part of SUSY models will therefore require an increase in sensitivity by at least four orders of magnitude. Direct and copious production of SUSY particles, on the other hand, is expected to be observed at the Large Hadron Collider (LHC) around the year 2008, but dark matter direct detection experiments are complementary since they can test the existence of stable weakly interacting supersymmetric particles, a priori undetectable in an accelerator experiment.

It might seem that the existence of a cosmological constant term contributing typically  $2/3$  of the total energy content of the universe would further increase the difficulty for experimentalists to detect dark matter particles. Surprisingly, the  $\Omega_A$  term usually results in an increase in the number of interactions with ordinary matter. This is due to the fact that a cosmological term will have no significant contribution to the local Dark Matter density inferred from local measurements to be  $\sim 0.3\text{--}0.5\,\text{GeV}/\text{cm}^3$ . On the other hand, a lower dark matter density at decoupling requires a higher annihilation cross-section and, rather generally, a higher interaction cross-section.

We also expect that these remnant particles will be trapped in the Galactic gravitational potential well. Since these particles, unlike ordinary matter, can hardly dissipate their kinetic energy, their halo is usually considered to be grossly spherical and non rotating (although Sikivie has argued that infalling Dark Matter might result in strong inhomogeneities or even caustics [33]). This halo would then extend to much larger distances than the dissipating ordinary matter and explain the rotation curves observed in galaxies. The standard parameters used to describe the WIMP halo include its local density in the  $0.3\text{--}0.5\,\text{GeV}/\text{cm}^3$  range, an assumption of a Maxwellian velocity distribution with r.m.s. velocity  $v_{\text{rms}} \approx 270\,\text{km/s}$  and a WIMP escape velocity from the halo  $v_{\text{esc}} \approx 650\,\text{km/s}$ . Using this picture of a WIMP halo, and following the seminal paper by *Drukier* and *Stodolsky* [34] on coherent neutrino interactions, *Goodman* and *Witten* [35] proposed the method of WIMP direct detection involving elastic collisions of a WIMP on a nucleus, schematically represented on Fig. 3.

Except at high WIMP masses, where the momentum transfer requires to take into account more precisely the form factor of the nucleus, the interaction

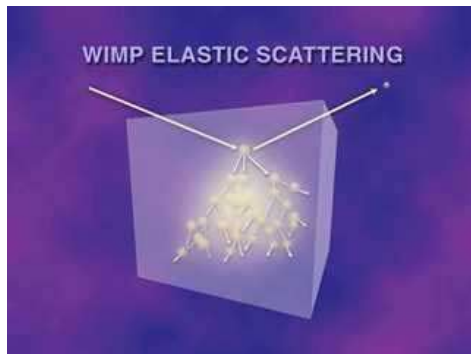


**Fig. 3.** Schematic principle of a WIMP direct detection experiment. A WIMP scattering induces a low energy (a few keV to a few tens of keV) nuclear recoil, which can be subsequently detected by the phonon, charge or light signals produced in the target material

is coherent over the whole nucleus and the average energy in the collision can be approximated by the expression [36]

$$\langle E \rangle = m_A \frac{\langle v^3 \rangle}{\langle v \rangle} \left( \frac{m_X}{m_X + m_A} \right)^2 \approx 1.6 A \text{ keV} \left( \frac{m_X}{m_X + m_A} \right)^2 \quad (4)$$

where  $A$  is the atomic number of the target nucleus. It can readily be seen that for a target mass  $m_A = m_X$ , this energy is approximately  $0.4 \times A \text{ keV}$ , giving typical energy transfers in the few keV to a few tens of keV range for SUSY particles with mass compatible with the constraints issued from the LEP experiments.

## 2.2 Experimental Signatures

With the previous characteristics of the WIMP halo particles, the exponentially decreasing shape of the WIMP recoil energy spectrum is anything but distinctive from the radioactive background, whose energy distribution is usually also raising at low energies. For obvious kinematical arguments, however, WIMPs give detectable recoils almost exclusively on nuclear recoils, as opposed to the radioactivity, which involves mostly electron recoils at low energies. Therefore, several methods have been devised to distinguish as efficiently as possible nuclear from electron recoils. When this discrimination is achieved, the main remaining backgrounds are due to neutrons and heavy nuclear recoils associated with radon surface contamination.

In addition, two other signatures may be used. Firstly, in the hypothesis of a non-rotating spherical halo, the interaction rate is expected to be modulated by the variation in relative velocity between the galactic halo and the Earth

in its trajectory around the Sun [37]. The velocity of the Earth through the Galaxy can be represented by the following expression:

$$v_{\text{Earth}} = v_{\text{Sun}} + v_{\text{orb}} \cos \gamma \cos [\omega(t - t_0)], \quad (5)$$

where  $v_{\text{orb}} \approx 30 \text{ km/s}$  is the Earth's orbital velocity around the Sun, the angle  $\gamma \approx 60^\circ$  is the inclination of the Earth orbital plane with respect to the galactic plane,  $\omega \approx 2\pi/365 \text{ radian/day}$ , and the phase is given by  $t_0 = \text{June 2nd}$ .

Secondly, a detector sensitive to the recoil direction would be able to measure its diurnal modulation due to the Earth rotation on its axis [38]. However, at the very low energies involved in the WIMP interactions, this represents an ambitious objective, which has yet to be realized. Once a WIMP signal will have been observed in a first detector type, the interaction rates on different target materials (e.g. Ge, Si, Xe, W, Bi, ...) should be compared to test the consistency of the WIMP hypothesis, and establish the scalar, vector or axial coupling of their interactions with ordinary matter.

A different experimental identification is provided by the indirect detection techniques, which use the fact that WIMPs are expected to accumulate at the center of the Earth, of the Sun or at the galactic center [39, 40, 41]. The WIMPs may then annihilate in sufficient quantities for the high energy neutrino component produced in the disintegrations to be detectable at the surface of the Earth and identified through their directional signature.

In the following, we will review the direct detection experiments according to their radioactive background identification capabilities (nuclear versus electron recoils) and discuss the specific features of cryogenic Dark Matter experiments.

### 3 WIMP Direct Detection: Initial Results and the DAMA Candidate

For WIMPs virialized in our galaxy, typical recoil energies range from a few keV to a few tens of keV, and interaction cross-sections range from a few  $10^{-6}$  to less than  $10^{-11} \text{ pb}$ . Initial direct detection experiments were unable to reach such small cross-sections and used detectors mainly dedicated to other purposes, e.g. double-beta decay search, using conventional germanium detectors [30, 31, 42].

The main significant achievement of these experiments, using a set of ultrapure isotopically enriched  $^{76}\text{Ge}$  crystals, was the experimental demonstration that massive Dirac neutrinos could not be the solution to Dark Matter over essentially all the cosmologically relevant mass interval [30, 31, 42]. Further improvements in the sensitivity of these experiments were mostly due to the passive reduction of internal  $^{68}\text{Ge}$  cosmogenic activation by deep-underground storage [43]. Attempts to use an anti-Compton strategy resulted

in the dedicated Heidelberg Dark Matter Search (HDMS), using a well-type germanium detector protecting a smaller 200 g germanium inner detector [44]. Although efficient at MeV energy, this technique resulted in only a factor two gain at the lowest energies (a few keV) relevant for WIMP searches and is not yet competitive at larger WIMP mass with the previous result of the Heidelberg–Moscow experiment. The International Germanium Experiment (IGEX) [45] is reaching a better sensitivity over most of the WIMP mass range but remains above the sensitivity level required to test the first SUSY models.

Sodium iodide NaI scintillating crystals [46, 47, 48], with larger target mass but much lesser energy resolutions, have also been used, notably by the DAMA, the UKDMC and the Saclay groups, to reach sensitivities of the order of  $10^{-5}$  pb. Despite the NaI inefficient discrimination at low energies, where the number of collected photons is small ( $\lesssim 6$  per keV of electron recoil) and the scintillation time constants for electron and nuclear recoils are less separated, the DAMA experiment, using a total mass of  $\sim 100$  kg of high purity NaI crystals, reported in 1998 a first indication of an annual modulation [49] using a data set of  $\sim 12.5$  kg  $\times$  yr, recorded over a fraction of a year. Apart from the ELEGANT–V experiment [50], which is using NaI scintillators of total mass 730 kg as a veto for a double-beta decay experiment, the DAMA group has recently started operating the largest mass NaI detector for WIMP search using a new 250 kg NaI setup, LIBRA. Compared to ELEGANT–V, DAMA is using NaI crystals with a lower radioactive background, with differential rates at low energies of  $\sim 1\text{--}2$  events/kg/keV d down to an energy of 2 keV electron equivalent (e.e.), corresponding to  $\sim 25$  keV recoil energy on iodine.

### 3.1 The DAMA Annual Modulation Candidate

In 2000, the DAMA group published an analysis involving a 160 kg  $\times$  year data sample recorded over three full annual cycles [51]. Recently, the group has published the analysis of three additional annual cycles [52] and the DAMA observation now presents a  $6.2\sigma$  statistical significance, with both phase and amplitude consistent over a period of more than six years with a WIMP signature, using a 107 800 kg  $\times$  d total data sample (Fig. 4). Assuming standard halo parameters [53] and interpreted in terms of a WIMP candidate, the annual modulation would correspond to a WIMP mass  $\sim (52 \pm 10)$  GeV and WIMP-nucleon cross-section  $\sim (7 \pm 1)10^{-6}$  pb.

EDELWEISS [54, 55, 56], in three data takings with a total exposure of 30 kg  $\times$  day was the first experiment testing and excluding a first sample of supersymmetric models. Under the assumption of spin-independent interactions, this experiment also excluded the whole DAMA region compatible with accelerator constraints without background subtraction. The DAMA group has contested this contradiction, invoking the uncertainty in the WIMP halo parameters. But *Copi* and *Krauss* [57] have shown that, for spin-independent

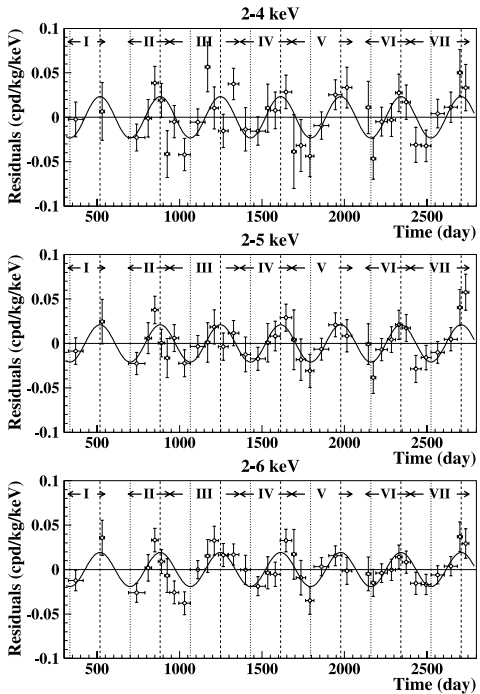


**Fig. 4.** Annual modulation amplitude reported by the DAMA experiment using a  $\sim 10^5 \text{ kg} \times d$  data sample, recorded over a period of seven years. The statistical significance of the detected modulation is  $\sim 6.2$  standard deviations (from Bernabei et al. [52])

couplings, the contradiction remains model-independent when the relative sensitivity of both experiments is considered, unless unconventional couplings are used.

There remained the possibility that a mixture of spin-dependent and spin-independent couplings could be used to reconcile the conflicting experimental results. But Kurylov and Kamionkowski [58] and Savage et al. [59] have shown that it appears impossible to reconcile the DAMA result with other negative results for all WIMP mass  $> 18 \text{ GeV}$ .

The ZEPLIN experiment [60] has used a background discrimination based on the different scintillation time constants for nuclear and electron recoils. In a  $290 \text{ kg} \times d$  data sample using a 4.5 kg liquid cell, ZEPLIN announces a maximum sensitivity of  $1.1 \times 10^{-6} \text{ pb}$ . However, the electronic background rate at low energies is 50 times higher than the CDMS or EDELWEISS  $\gamma$ -ray background rate and the claimed sensitivity requires a background subtraction at low energies by a factor  $> 1000$ , in a region where the nuclear/electron recoil discrimination is only statistical. Also, the energy resolution is much poorer than that of the cryogenic detectors: at 40 keV nuclear recoil energy

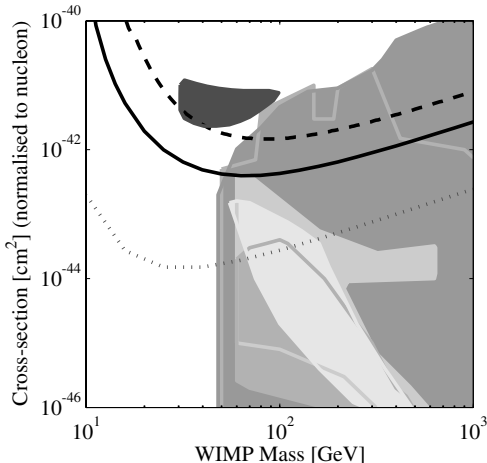


**Fig. 5.** Experimental sensitivities of the present most sensitive WIMP direct detection experiments (after [61]). The CDMS-II result (*full black line*), excludes the full  $3\sigma$  zone of the DAMA signal (*dark grey, upper left corner*) compatible with accelerator constraints, independently of the WIMP halo model parameters. The EDELWEISS and CRESST experiments have rather similar sensitivities approximated by the *black dashed line*. The expected sensitivity of the next generation of cryogenic direct detection experiments is represented by the *dotted line*. Regions allowed by various SUSY models are represented by the *light-grey regions*, with WIMP-nucleon cross-sections extending down to  $\sim 10^{-12}$  pb

( $\sim 6.5$  keV electron equivalent), the energy resolution is  $> 100\%$ , which makes it impossible to deconvolve the electron and nuclear recoil contributions. Additionally, no reliable calibrations of quenching factor and scintillation time constants exist for nuclear recoils below  $\sim 40$  keV recoil energy, and there is a considerable discrepancy (a factor  $\sim 3$ ) between the quenching factor measurements realized by the DAMA and by the ZEPLIN groups. These two parameters must be determined with precision before the present ZEPLIN sensitivity can be considered as established. Figure 5 shows the constraints of the present most sensitive experiments, assuming standard halo parameters, together with the three sigma contour reported by the DAMA experiment.

## 4 Cryogenic Detectors: Motivations

Over the last ten years, cryogenic detectors for dark matter detection have been developed by several groups [62, 63, 64, 65, 66]. Their development was motivated by the fact that, at very low temperatures, the heat capacity approximately follows a Debye law with a  $T^3$  dependence and it becomes possible to consider real calorimetric measurements down to very small energy deposition. Energy thresholds below 1 keV of recoil energy have already been



**Fig. 6.** Detector assembly in the CRESST low-radioactivity setup, in the Gran Sasso underground laboratory (Italy). Most of the elements close to the detectors are made of ultrapure copper, while no soldering is used. The 240 g sapphire detectors, using tungsten TES sensors, are operated at a temperature of  $\sim 10$  mK and benefit from an energy threshold of 580 eV (99% efficiency)

achieved [64, 67]. Indeed, at a temperature of 10 mK, a 1 keV energy deposited in a 100 g detector results in a typical temperature increase of about 1  $\mu$ K, which can be measured using conventional electronics.

In addition, the energy cost of an elementary phonon excitation is much lower ( $< 1$  meV) than that of classical detectors such as semiconductors or scintillators. Therefore, cryogenic detectors offer the possibility of unprecedented sensitivities and energy resolutions. The fundamental resolution of these detectors can be approximated by the thermodynamic fluctuations in the energy of the detector:

$$\Delta E_{\text{FWHM}} \approx 2.35 \sqrt{k_B C T^2}, \quad (6)$$

where  $k_B$  is the Boltzmann constant,  $C$  is the heat capacity of the detector, and  $T$  is the temperature. This resolution lies in the tens of electron-volt range for a 100 g detector at a temperature of 20 mK. As an explicit example, the 240 g sapphire detectors of the CRESST-I experiment, using tungsten transition edge sensors sensors, have been operated at a temperature of  $\sim 10$  mK and displayed an energy threshold of 580 eV (99% efficiency) (Fig.4).

Calorimetric measurements are realized in two rather different phonon collection modes. Although the high energy phonons produced in a particle interaction are rapidly degraded, they benefit from relatively long lifetimes for individual phonon energies of the order of  $10^{-4}$  eV (about 1 K). These

phonons can be detected in the nearly thermal mode [62, 63, 67, 68, 70, 71, 72, 73], or when they are still out of equilibrium [64, 74, 75, 76], with sub-keV energy resolutions at low energies in both cases.

But the most important impact of cryogenic detectors for Dark Matter search has been related to the background discrimination performances and the information redundancy obtained by these detectors, with real event-by-event identification capabilities between electron recoils, associated with the gamma, beta and alpha radioactive background, and nuclear recoils, observed in neutron and WIMP interactions. Table 1 summarizes the main characteristics of some of the main cryogenic WIMP direct detection experiments.

**Table 1.** Main cryogenic WIMP direct detection experiments together with their main characteristics. The first group of experiments use background discrimination, either through simultaneous measurement of phonon and light, or of phonon and charge

Name	Location	Discrim	Target	Mass	Start
EDELWEISS-I	Modane (France)	Ch/Ph	Ge	1 kg	1996
EDELWEISS-II	Modane (France)	Ch/Ph	Ge	10–35 kg	2005
CDMS-I	Stanford (USA)	Ch/Ph	Ge/Si	1 kg Ge, 250 g Si	1996
CDMS-II	Soudan (USA)	Ch/Ph	Ge/Si	7 kg Ge, 1.4 kg Si	2003
CRESST-II	Gran Sasso (Italy)	L/Ph	CaWO <sub>4</sub>	10 kg	2003
ROSEBUD	Canfranc (Spain)	L/Ph	BGO, Al <sub>2</sub> O <sub>3</sub>	0.5 kg	2001
CRESST-I	Gran Sasso (Italy)		Al <sub>2</sub> O <sub>3</sub>	1 kg	1999
CUORICINO	Gran Sasso (Italy)		TeO <sub>2</sub>	40 kg	2003
CUORE	Gran Sasso (Italy)		TeO <sub>2</sub>	760 kg	~ 2007
Tokyo-DM	Kamioka (Japan)		LiF	168 g	2001
ORPHEUS	Bern (Switzerland)		Sn	450 g	1995
MACHe3	Grenoble (France)		<sup>3</sup> He	0.02 g	1998

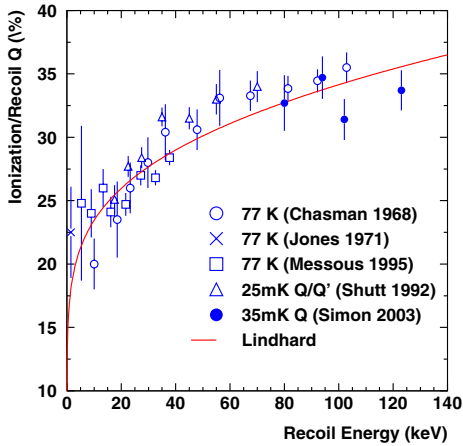


**Fig. 7.** Variation of the ionization quenching factor in germanium as a function of recoil energy. The measurements by several groups have been realized using tagged neutron beams where the nuclear recoil energy is determined in an absolute way, by the kinematics of the reaction. The *solid line* is the Lindhard prediction (after [84])

## 5 Charge-Phonon Detectors

Charge-phonon detectors provide a first discrimination method between electron recoils and nuclear recoils based on their different ionization efficiency, or quenching factor. This quenching factor is measured experimentally using neutron sources and tagged neutron beams. The energy dependence of this parameter is predicted theoretically by phenomenological models, such as the Lindhard model [77]. Germanium detectors, with a gap energy at low temperatures of  $\sim 0.7$  eV, require in average  $\sim 2.9$  eV of deposited electron energy to produce an electron–hole pair. For nuclear recoils, the ionization efficiency is typically a factor 3 lower than for electron recoils and depends on the deposited energy (Fig. 7). Using cooled Field-Effect Transistors (FETs) and SQUID (the acronym of Superconducting Quantum Interference Device) electronics, these detectors present efficient discrimination performances down to recoil energies of  $\sim 10$  keV.

Following initial developments on small Si detectors [78], which demonstrated the charge-phonon discrimination, two experiments, CDMS [62, 79] and EDELWEISS [63, 80] have implemented this technique in Dark Matter experiments. They provide presently the best sensitivity to WIMP interactions [55, 82]. Two important classes of detectors can be defined: detectors with low-impedance transition edge phonon sensors (TES), sensitive to energetic out-of-equilibrium phonons, and detectors measuring the phonon signal in the thermal regime, with high-impedance sensors, either Neutron Trans-

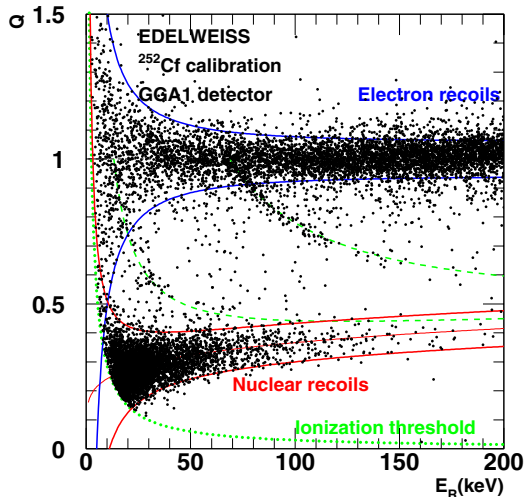


**Fig. 8.** Projection in the ( $E_R$ ,  $Q$ ) plane of the events recorded in a 320 g Ge detector of the EDELWEISS experiment during a  $^{252}\text{Cf}$  calibration. The *thick lines* represent the 90% nuclear and electronic recoils zone ( $\pm 1.645\sigma$  around the neutron and gamma ionization efficiencies  $\langle Q_n \rangle$  and  $\langle Q_\gamma \rangle$  respectively). The *dot-dashed line* is a 3 keV  $ee$  cut on ionisation energy. The *dashed lines* show where events associated with the inelastic scattering of neutrons on  $^{73}\text{Ge}$  are expected (and observed)

muted Doped (NTD) or thin films sensors in the Metal-Insulator Transition (MIT).

### 5.1 Charge-Phonon Detectors with MIT Sensors

Germanium charge-phonon detectors using NTDs as thermal sensors have been developed by the Berkeley group [62] in the CDMS experiment, and in the EDELWEISS experiment [63, 80, 83]. With respective mass of 60 and 70 grams, these prototype detectors presented excellent energy resolutions ( $\sim 1$  keV FWHM on both charge and phonon channels) and  $> 99\%$  discrimination capabilities between gamma-ray background and nuclear recoils when using neutron calibration sources (usually Am/Be or  $^{252}\text{Cf}$ ).

However, the first low-background data takings in the shallow SUF site and in the Frejus underground laboratory, under the Alps, revealed within a few days what appeared then as the major limitation of this technique: surface interactions.

#### 5.1.1 Solving the Problem of Surface Events

The problem raised by surface interactions can be understood with the help of a simple model. A particle interaction generates hot electron-hole pairs,

which degrade rapidly their energy, forming a plasma of limited extension (a small fraction of 1 mm). The plasma screens the external electric field, used to collect electrons towards one electrode while holes drift towards the opposite electrode. Ramo's theorem [85] shows that, to a first and usually excellent approximation, the charge signal is proportional to the integral of charge drift lengths for all carriers. If the charge carriers are trapped by the wrong electrode, their contribution to the charge signal is then lost.

More precisely, the plasma screening the external collecting field is rapidly evaporated by removal of the charge carriers on the plasma outskirts, where the external field can still be partially felt. However, during this evaporation time, electron and holes suffer a random diffusion walk in the crystal. For interactions occurring within a few tens of microns from the surface, this diffusion process may bring them within reach of the metallic electrode, which will then trap charge carriers that should otherwise have drifted towards the opposite electrode.

At the low electric fields used to collect charges in a cryogenic detector (a few volts), the charge signal for a surface event is then typically 50% of the full collection signal since  $\sim 50\%$  of the carriers will drift and be captured by the wrong electrode. Although at energies of a few tens of keV these surface events can be efficiently separated from nuclear recoils, they become dangerously close to the signal region below  $\sim 10$  keV electron-equivalent, where a large fraction of WIMP interactions are expected.

Surface events also represent at low energies a well-known problem for classical germanium detectors [86], operated at liquid nitrogen temperatures. A technique to alleviate the problem of incomplete collection was proposed by the LBL group [87, 88, 89, 90]. Thin amorphous silicon or germanium films are sputtered on the detector surface before the deposition of metal electrodes. These amorphous films are partially conducting ( $\sim 1$  G $\Omega$  per square) and lead to a more efficient charge collection, possibly due to the modified bandgap of the amorphous layer, which can then act as a repulsive barrier for the charge carriers [89].

Attempts have also been made to increase the collecting electric field, to reduce the initial diffusion time of charge carriers when shielded by the plasma. However, it seems difficult to use collection voltages much beyond  $\sim 10$  V since the *Neganov-Luke* [91, 92] effect will then hide the initial phonon signal in the extra Joule heating generated by the dissipation induced by the charge drift. For high collection voltages, the phonon signal will only duplicate the charge signal information and the charge-phonon discrimination method can no longer be used.

## 5.2 Charge-Phonon Detectors with TES Sensors

The Stanford group [74, 75, 76] has developed in the CDMS experiment a particularly elegant and integrated method using superconducting aluminum



**Fig. 9.** Photograph of a  $Z$ -sensitive ionisation-phonon (ZIP) detector of the CDMS experiment in its mount. The photolithographically-fabricated thin film on the surface is the phonon sensor, trapping non-equilibrium phonons in Al fins. The aluminum film is coupled to tungsten sensors in the superconductor-normal transition. Silicon and germanium ZIPs, weighing 100 g and 250 g respectively, have been operated in the Stanford shallow underground laboratory and are presently operated in the Soudan (Minnesota) underground laboratory

traps [93], which collect phonons with individual energies exceeding the aluminum 1 K gap ( $\sim 10^{-4}$  eV) (Fig. 9). The quasiparticles created in the aluminum films are then partially transferred to thin ( $1\mu\text{m}$ ) tungsten sensor lines maintained by electrothermal feedback [94] in the normal-superconductor transition at a relatively comfortable temperature of  $\sim 70\text{ mK}$ , adjusted by  $^{56}\text{Fe}$  implantation. The aluminum 1 K gap allows these detectors to be fairly insensitive to thermal phonons, and therefore to base temperature fluctuations and microphonics. In addition, the fast response of transition edge sensors, associated with a SQUID-array readout [95], provides a timing of the phonon signal at the few microsecond level.

Using TES sensors imposes a severe constraint on the total mass of the TES tungsten sensors due to their large heat capacity in the normal state or close to the transition. Superconducting Al fins are then used to increase the phonon collection area, thereby reducing the phonon collection time, using the phonon down-conversion and trapping technique proposed and developed by *Booth* [93]. Propagation properties of trapped phonons require to use small size Al fins ( $380\mu\text{m} \times 50\mu\text{m}$ ) coupled to a large number of  $1\mu\text{m}$  wide TES elements, implying a hierarchical structure. The design at a  $1\mu\text{m}$  precision allows a reduction of the tungsten heat capacity but requires a challenging degree of the crystal flatness after etching.

This design can be compared to that used in the CRESST experiment, where a single TES sensor, representing a small window to capture the phonon signal, induces a larger collection time. While the design of the CRESST detectors appears to lead to a better energy resolution of the phonon channel

at high energies than the ZIP detectors, it does not allow position reconstruction.

These ZIP ( $Z$ -sensitive ionization-phonon) detectors benefit in their present design from four quadrant phonon sensors (Fig. 9). The signal amplitude repartition in these sensors is then used to obtain a millimeter position resolution of the interaction, making these detectors also interesting for real-time solar neutrino detection. The four sensors help reducing the position dependence of the phonon signal amplitude and significantly improve the energy resolution at low energies. In the 5–20 keV recoil energy interval, sub-keV resolutions are obtained on both charge and phonon channels.

In addition, these fast phonon detectors allow the identification of surface events by the relative timing between the phonon and the ionization measurements [79, 82, 96]. The reason for this behavior is as yet unexplained but could be possibly attributed to an anisotropic emission of ballistic phonons in the Luke process, or to the non-linear response of a phonon sensor when one of its elements becomes saturated by the energy deposited locally by a surface event. Pragmatically, phonon sensor risetime cuts of  $> 12 \mu\text{s}$  for Ge and  $> 6 \mu\text{s}$  for Si provide an almost pure recoil population, at the expense of an energy-dependent fiducial cut efficiency for nuclear recoil events varying from 10–15% at 10 keV to 40–45% at 20 keV, and saturating at 50% above 80 keV recoil energy.

The CDMS-I experiment, at the Stanford Underground Facility (SUF), has demonstrated the discriminating properties of these ZIP detectors in a data taking of several months [81]. A tower comprising four 250 gram Ge and two 100 gram ZIPs was used in this experiment. Although limited in the shallow Stanford site by the fast neutron background induced by deep-inelastic scattering of muons in the surrounding rock, these detectors benefited from their very low energy threshold (down to  $\sim 5$  keV recoil energy) and therefore provided an excellent sensitivity to low mass WIMPs ( $\lesssim 40$  GeV).

These detectors have then been installed in the deep site Soudan facility (Minnesota), along with a second tower comprising 4 Si and 2 Ge ZIPs. In this deep-underground site, the muon flux is attenuated by a factor  $\sim 10000$  compared to that of SUF. The analysis of a first data sample of  $\sim 20 \text{ kg} \times \text{d}$  has led, using a blind analysis based on high statistics control data samples, to the best present sensitivity for all WIMP mass compatible with accelerator constraints [82].

Additional data takings by the CDMS-II experiment in Soudan using 5 towers of ZIP detectors, totalling  $\sim 3.5$  kg Ge and  $\sim 1.5$  kg Si, are expected to further improve the sensitivity to WIMP interactions by one order of magnitude.

### 5.3 Thin Film Sensors in the Metal-Insulator Transition

Neutron Transmuted Doped (NTD) sensors represent an aberration for an ultra-low background experiment since these sensors are made from germanium

nium exposed in a nuclear reactor to fast neutrons, which generate radioactive contaminants (such as  $^{68}\text{Ge}$ , or the relatively long-lived  $^{60}\text{Co}$ , and the ubiquitous tritium, with its low-energy beta spectrum). The tritium can be removed from the NTD sensors by heating while the other radioactive contaminants can be identified with high precision, since they lead to electron recoils. Nevertheless, it can be expected that a small fraction of these low energy interactions will leak into the signal nuclear recoil band where the WIMP signal is expected.

Thin film sensors, with a lower mass per sensor, and using ultrapure elements, present a more controllable radioactivity. High impedance thin film sensors in the metal-insulator transition (MIT) constitute an alternative to NTD sensors, and already present excellent ( $\sim 1\text{ keV FWHM}$ ) energy resolution in the thermal regime [83]. Comparable to NTD sensors in terms of sensitivity, these film sensors may benefit in the future from large-scale production, with a manufacturing process allowing them to be deposited on a detector surface by co-evaporation under electron beam heating, without radioactive contaminants, and without the delicate manual intervention required by NTD sensors.

Thin film sensors in the MIT can be used in large surface sensors, trapping efficiently energetic phonons. Their heat capacity, for a film thickness in the 100 nm range, remains comparable to that of massive dielectric crystals in the 10 mK range. But obviously, the total volume must remain small, below typically  $1\text{ mm}^3$  to a few  $\text{mm}^3$ .

Another important feature of the thin MIT film sensors is, similarly to ZIP sensors, their ability to distinguish surface from volume interactions [83]. The different pulse shape for surface events in thin film sensors, with an additional fast component, appears to be due to an efficient trapping of out-of-equilibrium phonons, and correspondingly to a large fast athermal signal for interactions close to the thin film sensor. Although allowing a rejection of surface interactions, this effect does not lead to a real 3-D position determination.

Using this technique, EDELWEISS has studied thin  $\text{Nb}_x\text{Si}_{1-x}$  films which show large differences in pulseshape depending on interaction depth, with a sensitivity to surface interactions down to a depth of 0.5–0.1 mm [83]. However, like in ZIP detectors, a real determination of the  $z$ -coordinate in the detector is not yet available. The use of at least four thin film sensors covering a large fraction of the crystal surface might allow such a real 3-D position reconstruction by analysis of the relative fast vs. thermal amplitudes on each sensor.

## 5.4 Charge Regeneration

For all types of charge-phonon detectors, it was found extremely important to avoid the formation of space charge in semiconductor detectors, which could reduce, or even cancel completely, the electric field inside the detector.

In the non-equilibrium state of semiconductor detectors under a bias voltage at very low temperatures, a fraction of charge carriers produced in particle interactions may be trapped on acceptor and donor impurities present in the crystal. If a net charge density is created in this process, there exists a critical charge density above which the electric field inside the detector is cancelled on a particular separating surface, creating a virtual electrode inside the detector. If further charge trapping occurs, the region of zero (or strongly reduced) electric field will grow, separated from the active volume of the detector by this (moving) virtual electrode.

For this reason, it was found necessary to periodically regenerate the detectors either by illumination by LEDs, and/or by irradiation by radioactive sources (usually  $^{137}\text{Cs}$  or  $^{60}\text{Co}$   $\gamma$ -ray sources). The presence of virtual electrodes inside the detectors, delimiting a region of zero internal field, where charges created during an interaction will not drift and therefore not produce any ionization signal, can be controlled by periodic calibration runs.

Free germanium and silicon surfaces (without metal electrodes) also represent sites where charge carriers can be trapped efficiently and lead to the construction of regions with degraded fields and charge collection properties in the detector. The controlled degradation of the charge state of the CDMS and EDELWEISS detectors has been studied by the Stanford and Orsay groups, respectively [97, 98, 99].

The use of amorphous Ge and Si underlayers, associated with periodic charge regeneration procedures, has reduced to a large extent the problem of surface events in charge-phonon detectors. Rejection factors of the  $\gamma$ -ray background at a  $> 99.99\%$  level have for example been obtained in the CDMS and EDELWEISS experiments in germanium detectors with both types of amorphous underlayers (Fig. 10). Similarly, the ZIP detectors developed in the CDMS experiment benefit from amorphous silicon underlayers.

## 5.5 Developments and Perspectives

Although not strictly necessary, a real 3-D determination of the interaction position in the detector would allow both a rejection of surface events and a much more precise control of the radioactive contaminants in the vicinity of the (a priori extremely pure) semiconductor detectors. But the strongest motivation for a precise determination of the interaction position is the identification of heavy nuclear recoils from radon disintegration products at the surface of the detectors, or from materials facing them (see section “Event categories”).

In future developments, the CDMS experiment intends to develop detectors with phonon sensors on both surfaces, in order to achieve this full 3-D position determination. For germanium detectors, where the speed of sound is lower than in silicon, massive detectors in the few hundred gram range may provide time arrival differences between the two sets of phonon sensors allowing a measurement of the interaction depth in the detector. Combined

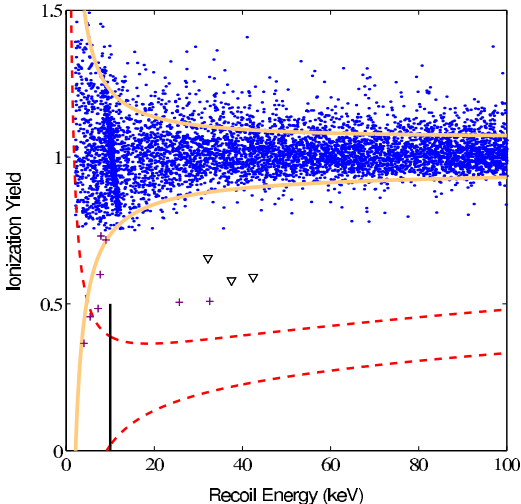


**Fig. 10.** Scatter diagram of the ionization efficiency, normalized to electron recoils, as a function of recoil energy for all events with energy  $< 100$  keV recorded by the CDMS-II experiment in the fiducial volume of  $4 \times 250$  gram Ge detectors (after [82]). The gamma-ray background is mostly contained within the region delimited by *full lines*. Nuclear recoils are expected in the region (90% efficiency) delimited by *dashed lines*. No nuclear recoils are observed in a  $\sim 20$  kg  $\times$  d exposure. With an effective mass 200 smaller than the DAMA NaI crystals, and an exposure 5000 times shorter, the CDMS-II exceeds by a factor  $> 10$  the sensitivity of the DAMA experiment

with the surface position determination already achieved in ZIPs, this would allow, at least at energies larger than a few tens of keV, a complete 3-D determination of the interaction profile. However, the time difference required to reconstruct the axial coordinate in the detector –a few microseconds– appears difficult to be obtained at low energies, where most of the WIMP interactions are expected.

The determination of the interaction depth using the charge signal has been realized by the Orsay group [100] for charge signal amplitudes  $\gtrsim 50$  keV electron equivalent (e.e.). But the signal/noise ratio is not sufficient to allow a precise position determination below  $\sim 30$  keV e.e. On the other hand, since a real 3-D position determination of the interaction is possible at higher energies, this feature could be used to discriminate signal from background events in future double-beta decay experiments [101]. Additionally, the position reconstruction of interactions would lead to a better understanding of the radioactive contaminants present in key components of the next generation of WIMP detectors: sensors, cables, etc. Figure 11 illustrates the present 2-D position reconstruction of the ZIP detectors developed in CDMS-II.

Due to the difficulty to develop Si detectors with purity levels as high as in germanium, the EDELWEISS experiment has chosen to use only ger-

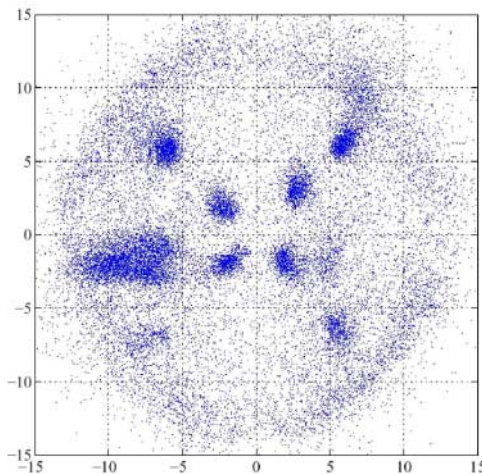


**Fig. 11.** Two-dimensional position reconstruction capability of a ZIP detector of the CDMS experiment. The relative amplitudes detected by four phonons sensors are used to recover the  $x$ - $y$  coordinates of an interaction in the detector. A series of radioactive point sources have been used to illuminate the detector and their contributions can be easily separated

manium detectors. The contamination of nuclear recoil events by neutron interactions is then estimated by the coincidence rate between different detectors. Proportions of multiple interactions are still difficult to predict with precision, due to the systematic uncertainties in neutron simulations, but the quality of predictions gradually improves with high statistics neutron calibrations realized by the CDMS and EDELWEISS experiments. Future extended data takings in deep underground sites will allow to test and compare both neutron identification strategies.

In conclusion, despite the problem of incomplete charge collection for surface events, charge-phonon detectors are still far from being limited by systematic uncertainties. They benefit from excellent crystal purities and energy resolution, allowing a precise comprehension of the background structure down to an energy of a few keV relevant for WIMP interactions. With present technology, it seems reasonable to assume that a  $10^{-8}$  pb sensitivity can be reached with cryogenic detector mass in the 50 kg range and a few years of exposure.

In the near future, both the CDMS-II and EDELWEISS-II experiments will greatly increase their low background exposures using detectors sets of total mass in the  $\sim 10\text{--}30$  kg range. These extended data takings will help define the improvements required to go beyond the sensitivity goal of this second generation of discriminating experiments.

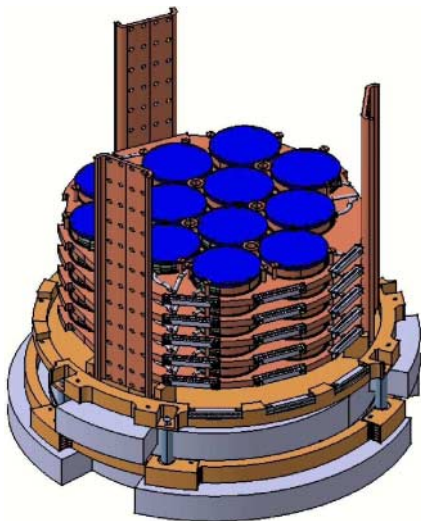
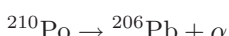


**Fig. 12.** Drawing of the EDELWEISS-II detector set-up. Up to 120 Ge detectors of mass 320 g can be accommodated in a compact hexagonal arrangement at 10 mK. The lower plate, made of ultra-pure archeological lead, shields the detectors from the radioactivity of the dilution cryostat (not shown)

## 6 Event Categories

It is tempting, but incorrect, to consider that the problem of discriminating the alpha, gamma-ray and beta-induced radioactivity from WIMP- and neutron-induced nuclear recoil interactions is reduced to the problem of fitting two distributions, the distribution of nuclear recoils and the distribution of electron recoils. When the overlap between the distributions is limited, as in cryogenic detectors, or when no background subtraction is realized, the danger is limited, but when the discrimination capabilities are insufficient to clearly separate the nuclear and electron populations, at low energies or for intrinsic reasons, the sensitivity derived from a two-parameter adjustment of the spectrum observed in low-background data might be at considerable variance from the real populations.

Even for single element targets, such as germanium or xenon, the experimentalist is confronted not only to the separation of electron recoils and germanium or xenon recoils but to several other populations. In particular, as noted previously, it is necessary to consider the heavy nuclear recoils from implantation of radon daughter nuclei, or from the U/Th disintegration chains originating from either the crystals or the surrounding materials. For instance, the  $\alpha$ -disintegration of  $^{210}\text{Po}$  into the reaction:



will obviously induce polonium recoils. Conservation of energy-momentum in the  $\alpha$ -disintegration shows that these heavy nuclear recoils have an energy equal to  $\sim 103\text{ keV}$  for this particular reaction, and ranging from  $\sim 70\text{ keV}$  to  $\sim 110\text{ keV}$  for most other alpha disintegrations. These recoils can only be distinguished from WIMP interactions by detectors with excellent energy resolution and discrimination capabilities.

Yet another population must be taken into account with alpha tracks escaping the detector in the direction opposite to heavy nuclei. These alpha tracks have a quenching factor usually intermediate between electron recoils and heavy nuclear recoils for the same deposited energy. The energy released in the detector by the alpha particle depends on the implantation depth and the angle of emission with respect to the normal of the detector surface. It ranges from zero to the full alpha energy, leading to a continuous spectrum. Alpha tails, associated with alpha particles escaping from materials surrounding the detectors, such as copper supporting structures, provide yet another population since these stopping alpha particles have a much lower velocity and ionization power than the alpha particles leaving the detector after a few keV of energy loss. This is presently the most important background experienced by the CUORICINO experiment in its search for double-beta decay interactions.

Until now, we discussed the simple case of targets with a single nucleus (e.g. Ge, Xe, Ar). For targets containing several nuclei, the different responses of each participating nucleus must be taken into account. For example, in NaI targets, sodium and iodine recoils lead to rather different quenching factors,  $\sim 1/3$  for Na recoils and  $\sim 1/12$  for iodine recoils, complicating the interpretation of the observed energy spectrum. The situation is similar for bismuth germanate (BGO) and calcium tungstate ( $\text{CaWO}_4$ ) targets, where the detector response must be calibrated for each individual nucleus.

It results from this discussion that important systematic errors will result from the usual assumption of the existence of only two populations of electron and nuclear recoils. This is particularly true for experiments, using e.g. NaI and liquid xenon detectors, deriving their sensitivity limits after important background subtraction and with energy resolutions  $\gtrsim 100\%$  at the low energies relevant to WIMP interactions. The fact that the DAMA experiment has never reported the observation of the additional populations observed in the UKDMC [102] and the Saclay NaI experiments [48] with a subset of the crystals used by the DAMA group, illustrates the systematic uncertainties of this experiment.

## 7 Light-Phonon Detectors

### 7.1 Introduction

Detectors able to detect simultaneously light and phonon signals provide another powerful technique to distinguish a WIMP signal from the various components of the radioactive background. After initial developments at MeV energies [103, 104], two experiments, CRESST [64, 65] and ROSEBUD [105], are presently testing the phonon-scintillation discrimination scheme. Similarly to the charge-phonon detectors, the light output per unit energy is significantly different for nuclear and electron recoils. The ratio between the total energy, measured by the phonon signal, and the energy of the photons emitted in the interaction is then used to discriminate the nuclear and electron recoil interactions.

Various dielectric crystals have been tested by the CRESST and ROSEBUD experiments and have been shown to be luminescent at low temperatures with scintillation time constants less than a few millisecond. The fraction of energy effectively detected in the form of light is  $\sim 1\%$  for the best scintillators, which should be compared to the  $\sim 10\text{--}20\%$  fraction of energy converted into ionization in Ge and Si monocrystals. The existence of a variety of materials scintillating at very low temperatures has the important consequence that nuclear elements other than germanium and silicon can be considered as targets for WIMP interactions, which might prove essential to ascertain the existence of potential WIMP candidates.

Another important characteristic of the light-phonon detectors is the absence, at the present level of study, of any significant surface effects for electron recoil interactions, such as observed in charge-phonon surface interactions, where charge is badly collected. On the other hand, heavy nuclear recoils from radon disintegration products may represent an important background for these detectors since they are nearly indistinguishable from recoils of the heavier nuclei in the crystal itself (e.g. tungsten in  $\text{CaWO}_4$  crystals, or bismuth in BGO crystals).

### 7.2 Schematics of a Light-Phonon Detector

At the millikelvin temperatures required by the operation of massive phonon detectors, the use of conventional photodetectors is prohibited by their dissipation. The photon detector is therefore realized by a calorimeter with very small heat capacity, usually a very thin crystal wafer covered with a film absorber. The heat capacity of the light detector is minimized to allow the detection of the small number of photons emitted during the particle interaction and finally absorbed in the photon calorimeter. It should be noted that for a 1 keV electron recoil, only a few tens of photons are emitted, and that this number is further reduced by the quenching factor for a nuclear recoil and by the light collection efficiency.



**Fig. 13.** Photograph of a light-phonon detector of the ROSEBUD experiment. The phonon signal is determined by the temperature variation of a transparent 91 gram BGO crystal, while the light detector is constituted by a 25 mm diameter germanium wafer. Both detectors use NTD thermometers and are surrounded by a silvered copper reflector. This detector has been operated in the Canfranc underground laboratory (Spain)

This quenching factor was measured to be  $Q \approx 1/7.4$  for oxygen recoils, and room-temperature measurements have established that tungsten nuclear recoils lead to quenching factors of  $\approx 40$ . Therefore, while oxygen recoils give rise to observable light signals down to  $\approx 10\text{ keV}$ , tungsten recoils usually lead to very small light signals, compatible with noise over most of the WIMP recoil energy interval.

Figure 13 shows the principle of operation of a light-phonon detector developed in the ROSEBUD experiment [105]. This detector is constituted by a massive BGO (bismuth germanate) absorber facing a thin germanium wafer, 50–100 micron thick. To optimize light collection, both light and phonon detectors are placed inside a reflecting enclosure made of silvered copper. The temperature increase of the BGO crystal and the light detector are both measured by the impedance variation of a NTD (Neutron Transmuted Doped) sensor.

The detectors developed by the CRESST experiment are based on a similar principle, using a  $\text{CaWO}_4$  massive detector facing the light detector constituted by a  $30 \times 30 \times 0.4\text{ mm}^3$  silicon wafer. The main difference lies in the sensor technology: instead of NTD sensors, TES (Transition Edge Sensors) made of tungsten are used to measure the temperature increase of both the phonon and light channels of the detector. The detectors are operated at a temperature of  $\approx 10\text{ mK}$ , in the middle of the superconducting to normal con-

ducting state of the tungsten sensor. Sensors constituted by Ir/Au bilayers have also been realized and present similar but somewhat lesser sensitivities. TES sensors benefit presently from a better sensitivity than NTD sensors.

### 7.3 Discussion

For dielectric materials with reasonable Debye temperatures, the measurement of the phonon signal, i.e. of the major part of the total energy deposited in a particle interaction, has already been realized on massive detectors in the several hundred gram range such as CaWO<sub>4</sub>, BGO or TeO<sub>2</sub>. Energy thresholds of a few keV are now routinely achieved on such massive detectors by several groups.

Detection of the light signal appears more challenging as it requires several constraints on the target crystal. The scintillation efficiency must be sufficiently large for the light signal to emerge from the thermal noise. Moreover, the high energy cost of a single photon has for consequence that only a small fraction of the energy of a particle interaction is converted into photons for low-energy nuclear recoils. The crystal must then have a good transparency at the fluoresced wavelength to ensure a homogeneous signal response within the detector. Also, crystals must be selected that present relatively fast scintillation time constants at very low temperatures, although this constraint is partially attenuated by the relative sluggishness of the thermal detectors, with thermal relaxation times usually in the millisecond range. In addition, the quenching factor –here the scintillation efficiency for a nuclear recoil compared to electron recoils of the same energy– must be sufficiently different from unity to provide a clear identification of nuclear recoils down to low energies, but sufficient for light and phonon signals to be detectable for nuclear recoil events.

Only a few tens of photons are emitted in a 1 keV electron recoil in a CaWO<sub>4</sub> or a BGO crystal. This number is further reduced by the quenching factor when the interaction is due to a nuclear recoil. For CaWO<sub>4</sub>, the quenching factor is  $\sim 1/7.4$  for oxygen recoils, and the number of photons per keV of recoil energy is limited to a few units per keV. The scintillation quenching factor is presently not measured for germanium and bismuth recoils in BGO, but phenomenological models lead to expect quenching factors for these nuclei significantly smaller than for oxygen recoils. A neutron beam test facility to measure quenching factors using tagged mono-energetic neutron beams has been developed by the CRESST and EDELWEISS experiments [106]. This facility is a fundamental tool to calibrate detector responses to electron and nuclear recoils.

### 7.4 First Results

Initial data takings by the CRESST-II experiment, using two CaWO<sub>4</sub> 300 g detectors, exhibited a population of phonon-only events, for which the am-

plitude of the light signal was compatible with zero. The event rate, a few events per kg and per day, was a priori too high to be attributed to WIMP interactions, as it would contradict both the CDMS and EDELWEISS results, or to neutron interactions, predicted to be a factor  $\approx 10$  smaller. These events were therefore attributed to dissipative events related to stress on the detector crystals and were suppressed by replacing the teflon supports holding the crystal with copper-beryllium springs. Another improvement on the detectors was achieved by polishing the surface of the detectors to reduce the effect of total internal reflection and provide a better homogeneity of the light response and resolution. The phonon channel resolution at the 46.5 keV  $^{210}\text{Pb}$   $\gamma$ -ray peak is improved to  $\approx 1$  keV FWHM. Finally, a polymeric foil with very high reflectivity [107] ( $\approx 99\%$  at 420 nm) was used to optimize the scintillation light collection.

Further data takings using the modified detectors showed a residual population of events compatible with oxygen nuclear recoils, with a small but non-zero light signal. The absence, for the  $\text{CaWO}_4$  detector with the best resolution, of any phonon-only event between 20 keV and 40 keV shows that light-phonon detectors can be used to discriminate oxygen recoils from calcium and tungsten nuclear recoils, the latter recoil population providing negligible light emission. Presently limited by the neutron background, expected to induce a nuclear recoil event rate compatible with the observed rate, CRESST presents in its latest result [108] a sensitivity comparable to that of EDELWEISS. In its upgraded phase with a polyethylen neutron shield and a plastic scintillator muon veto, starting at the beginning of 2005, the CRESST-II experiment, using a total of 10 kg of  $\text{CaWO}_4$  crystals, is expected to improve its sensitivity down to the level of a few  $10^{-8}$  pb.

Figure 14 shows the quenching factor distribution obtained by the simultaneous measurement of light and phonon signals for a  $\text{CaWO}_4$  crystal irradiated by  $\gamma$ -ray and neutron sources. It can be seen that the separation of the two populations of electron recoils and oxygen recoils is excellent down to  $\sim 15$  keV recoil energy, sufficient in principle to detect a significant fraction of WIMP interactions with mass compatible with accelerator constraints. However, it should be noted that only oxygen recoils are observed in Fig. 14, while most of the WIMP-nucleon interaction cross-section will be, at least for a scalar coupling, associated with the heavier tungsten and calcium nuclei (respectively germanium and bismuth for BGO). With the sensitivities currently reached by the present CRESST detectors, interactions on these heavier nuclei would lead to a light signal hardly emerging from thermal noise.

For this reason, the number of phonon-only events, associated with spurious heating of the detector due, for example, to micro-fractures in the crystals, dissipation associated with vibrations in its supporting structure, or electromagnetic spurious heating, must be reduced to a negligible level in order to compete with the cryogenic charge-phonon experiments. Phonon-only events

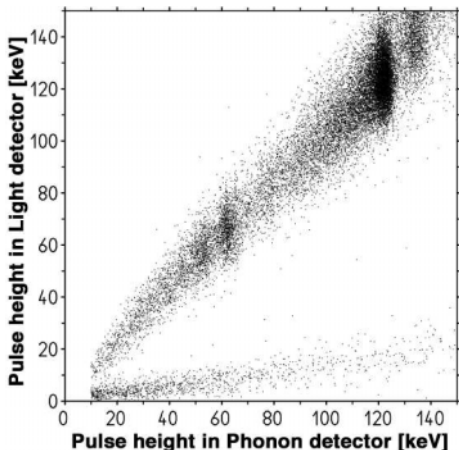


**Fig. 14.** Projection in the ( $E_{\text{Recoil}}, Q$ ) plane of the events recorded in a 15 g CaWO<sub>4</sub> light-phonon prototype detector of the CRESST experiment during a <sup>252</sup>Cf neutron calibration. A clear separation of the electron recoil and nuclear recoil populations can be observed down to an energy of  $\sim 15$  keV recoil energy. No intermediate population, due e.g. to surface interactions, is apparent in this light-phonon discrimination scheme

have been observed by the CDMS-I and EDELWEISS-I experiments, using germanium detectors, and in a first version of the CRESST experiment, using sapphire detectors. These phonon-only events are not expected to represent a problem for charge-phonon detectors down to sensitivities  $< 10^{-8}$  pb since it is possible for these experiments to reject events lacking a simultaneous ionization signal. In addition, for the new generation of ZIP [79] detectors used in the CDMS-II experiment, these phonon-only events will a priori not be detected since only phonons with an individual energy sufficient to break Cooper pairs of the Al fins, well above the detector temperature of  $\sim 20$  mK, are detected.

Clearly, the light-phonon technique is still in development and further improvements on light collection and sensitivity to WIMP interactions are expected over the next few years.

## 7.5 Conclusions

The present performances of light-phonon detectors offer an excellent discrimination between electron and nuclear recoils, a key feature for WIMP detection. On the other hand, for all scintillators at low temperatures presently tested, the small quenching factor for light emission by heavy nuclear recoils (such as bismuth in BGO, or tungsten in CaWO<sub>4</sub>) leads to a challenging light detection for these nuclei, which represent a very large fraction of the cross-section for spin-independent WIMP interactions. At present, the fact that the

signal amplitude of the light channel is still compatible for these nuclei with thermal noise imposes to accept dissipative (“phonon only”) events as WIMP interaction candidates. The number of these events must obviously be kept negligible. Also, heavy nuclear recoils from radon disintegration products will be indistinguishable from WIMP-induced heavy nuclear recoils in the target crystal. To fight this dangerous background, CRESST has used scintillating coatings of the light reflectors to detect the associated alpha particle escaping the detector. Using this veto scheme, CRESST-II is able to reject a large fraction ( $\sim 80\%$ ) of these radon-induced nuclear recoils.

Despite these constraints, the present sensitivity of the CRESST-II experiment is already at the level of the CDMS and EDELWEISS sensitivities, while still mostly limited by its neutron background. Therefore, it appears extremely important to pursue this line of development since further improvements in the light collection efficiency might lead to the possibility to detect the light signal of higher mass nuclei. Also, some presently untested scintillators may be found to present a more favorable light yield for nuclear recoils. Solving the present difficulties of this detection scheme will allow using additional target materials, an essential feature to ascertain the WIMP origin of a signal.

## 8 Other Cryogenic Detectors

### 8.1 MACHe3: $^3\text{He}$ , the Purest of All Materials

Germanium and silicon monocrystals benefit from extremely low levels of impurities. In detector quality crystals, the difference in acceptor and donor impurities can be as low as a few  $10^9$  per  $\text{cm}^3$ , and the concentration of radioactive impurities is much lower than this already impressively small number, assuming the cosmogenic production of radioactive isotopes has been limited. But superfluid  $^3\text{He}$  and  $^4\text{He}$  surpass these semiconductor materials, with an impurity concentration practically reduced to zero. At subkelvin temperatures for superfluid  $^4\text{He}$ , and below 1 mK for  $^3\text{He}$ , essentially no impurities can remain in a stable way within these liquids: they just sink at the bottom of the helium container (or float for electrons and hydrogen). At a temperature of  $100\mu\text{K}$ , not even a single atom of the chemical twin  $^4\text{He}$  is able to remain diluted at equilibrium in a kilogram of superfluid  $^3\text{He}$ !

This extreme purity has been a motivation for proposing a dark matter detector where the temporary intrusion of an external particle creates quasiparticles which are detected by the attenuation of a vibrating wire inside the liquid. Energy thresholds of a few keV have already been achieved with small  $^3\text{He}$  samples, and a multicell detector has been proposed [109, 110]. Two drawbacks, however, are reducing the attractiveness of this elegant detector: the cost of  $^3\text{He}$  is of the order of 1000 Euro per gram, and there is no discrimination proposed against the very low energy X-ray background which

may mimic WIMP interactions. Present event rates per unit mass and time are several orders of magnitude higher than the rates reached by the CDMS, CRESST and EDELWEISS experiments.

## 8.2 ORPHEUS: Superconducting Superheated Granules

The ORPHEUS experiment, located in a shallow underground laboratory in Bern (Switzerland), has developed a digital cryogenic detector, using superconducting tin granules in a metastable state [111, 112]. At very low temperatures, deposition of a few keV of energy is able to trigger a transition from the superconducting to the normal state for individual tin granules with diameters of  $28\text{ }\mu\text{m}$  and  $36\text{ }\mu\text{m}$ . The detection of the transition of a single grain is made possible by measuring the magnetic flux change induced by the disappearance of the Meissner effect, expelling magnetic field lines from a superconductor. The digital character of this detector is then related to the fact that the magnetic field change in a single granule transition is only related to the transition itself and largely independent of the deposited energy.

A total mass of  $450\text{ g}$  of tin granules set in  $56 \times 8\text{ g}$  modules at a temperature of  $\sim 115\text{ mK}$  has been used in the ORPHEUS experiment. It should be noted that diamagnetic interactions between the individual granules impose a reduced filling factor for this detector: tin granules are mixed with teflon powder to reduce these interactions and  $\sim 10\%$  of the total mass of a module is active in the present stage of the experiment. This parameter is particularly important as it directly relates to the possibility of rejecting an important fraction of the Compton gamma-ray background, expected to produce a large fraction of multiple site energy depositions.

Preliminary results have been presented by ORPHEUS [113], showing background event rates in the  $2 \times 10^3$  events/kg/day range, with only a limited fraction of background events rejected by the multiplicity of grain transitions. Although in principle the background energy spectrum of this detector can be determined by varying the temperature and magnetic field, inhomogeneities in individual grain response and diamagnetic interactions make a precise determination of the background spectrum unlikely. The present sensitivity of the ORPHEUS experiment to scalar WIMP interactions is  $\sim 5 \times 10^{-1}\text{ pb}$ , and therefore  $\sim 4$  orders of magnitude above that of the discriminating cryogenic experiments.

## 8.3 The Tokyo LiF Bolometer Experiment

The Tokyo group [72, 114] has used lithium fluoride bolometers at a temperature of  $\sim 10\text{ mK}$  to take advantage of the excellent axial WIMP-nucleon cross-sections of the fluoride nucleus [115] and, to a lesser extent, of the lithium nucleus. After an initial experiment in a shallow laboratory, close

to surface, which used a set of  $8 \times 21\text{ g}$  LiF detectors [72], a second experiment was performed in the Kamiokande underground laboratory to benefit from the reduced cosmic-ray induced background [114]. Surprisingly enough, the Kamiokande measurements have not led until now to improvements in background performances and the sensitivity reached by the Tokyo LiF detectors still falls short by nearly three orders of magnitude of the sensitivity required to sample the most optimistic SUSY models. While this experiment provides an illustration of the fact that a large variety of target materials can be used in bolometers, it also confirms that most of these detectors, lacking background discrimination capabilities, are unable to provide sensitivities comparable to indirect detection experiments such as Superkamiokande [116] and Amanda [117]. These experiments, searching for high-energy neutrinos from the core of the Sun, provide much more stringent constraints for spin-dependent WIMP-nucleon couplings than those obtained by these non-discriminating experiments [118].

Recently, the ROSEBUD experiment has shown that LiF crystals emit light under particle interactions, and offer the possibility to distinguish electron recoils from alpha particle and nuclear recoil interactions by their different light/phonon ratio [119]. However, the light yield in these interactions appears until now too limited to be used to efficiently discriminate low energy nuclear recoils from the gamma-ray background. Still, this development could lead to use LiF bolometers as sensitive neutron detectors.

## 8.4 Detecting the recoil direction

Assuming a non-rotating halo relative to the galaxy, WIMPs will exhibit a strong anisotropy with respect to the laboratory frame, rotating with a daily period and reflected in nuclear recoil directions induced within a detector [38]. Therefore, several groups [120, 121, 122, 123, 124, 125, 126, 127, 128] have addressed the challenging experimental question of determining the recoil direction under a WIMP interaction in order to use this strong directional signature. Compared to the annual modulation signature, which presents at best a modulated amplitude of 7%, the recoil direction, at least for nuclei with a mass comparable to that of the incident WIMP, might present much larger anisotropies, of the order of 50%. In addition, the directional signature will increase with the recoil energy and is therefore much less sensitive to threshold effects than the annual modulation technique. The difficulty lies of course in the possibility to reconstruct the recoil direction in an interaction of a few tens of keV at most.

For such small deposited energies, the nucleus typically recoils by sub-micron sized distances in usual solid state detectors. To keep track of the anisotropy information of these low energy interactions, an original method has been proposed in the context of the HERON project [122] for real-time solar neutrino detection. In the remarkably homogeneous medium of superfluid helium, a local deposition of energy with a high density will create an

opaque roton cylinder around the track. Due to Lambert's law, the resulting roton emission is then anisotropic and can be correlated to the incident particle direction [123]. However, this beautiful experiment has only been demonstrated with alpha, gamma and electron sources with energies larger than 300 keV, and appears to be inoperative at the much smaller recoil energies characteristic of WIMP interactions.

Therefore, at present, the most promising technique to identify the recoil direction under a WIMP interaction is under development in the context of the DRIFT (Directional Recoil Identification From Tracks) project [127, 128], at room temperature, using low density gas targets such as  $\text{CS}_2$ .

## 9 Towards Ton-Scale Dark Matter Experiments

The best sensitivity to WIMP interactions mis presently obtained by the CDMS experiment [82], using four Ge detectors of total mass 1 kg and fiducial mass  $\sim 0.5$  kg. It corresponds to a maximum sensitivity of  $\sim 4 \times 10^{-7}$  pb, assuming standard halo parameters. The CRESST [129] and EDELWEISS [55, 130] experiments provide similar, although somewhat lesser sensitivities. Although some of the most optimistic SUSY models are tested by these experiments, models favored by SUSY theorists correspond to cross-sections  $\lesssim 6 \times 10^{-8}$  pb, requiring one order of magnitude increase in sensitivity to be tested. A first part of these models is expected to be sampled by the next generation of cryogenic experiments, such as CDMS-II, CRESST-II and EDELWEISS-II, using target masses in the 10 to 35 kg range.

Reaching a sensitivity to WIMP cross-sections in the  $10^{-10}$  pb range, allowing to test a much larger fraction of SUSY models, requires ton-scale targets: a cross-section of  $10^{-10}$  pb would provide  $\sim 10$  events per ton and per year for germanium and xenon targets, assuming full detection efficiency above 15 keV recoil energy. Naively, a larger number of events would be expected for heavier nuclear targets such as xenon, iodine or tungsten than for germanium, but the loss of coherence at energy transfers larger than a few tens of keV saturates the number of events as a function of the atomic number  $A$  of the target. Therefore, the above nuclear targets all provide similar WIMP event rates per unit of target mass. Reaching the  $10^{-10}$  pb grail will obviously be extremely difficult even for ton-scale experiments.

### 9.1 Ton-Scale Experiments without Background Discrimination

Three groups have proposed ton-scale Dark Matter experiments involving detectors with limited or no background discrimination. The DAMA/LIBRA and GENIUS-TF/GENIUS experiments use detectors at room temperature and liquid nitrogen temperatures respectively, while the CUORI-CINO/CUORE experiment is using cryogenic detectors at a temperature of  $\sim 10$  mK.



**Fig. 15.** Photograph of a detector subset of the GENIUS-TF (Test Facility) experiment, comprising 14 Ge detectors, with a total active mass of  $\sim 40\text{ kg}$ . These naked detectors, with minimal material other than germanium, are operated in liquid nitrogen, which can be continuously recirculated and purified. This experiment, dedicated in its first stage to Dark Matter search, is presently in operation in the Gran Sasso underground laboratory

### 9.1.1 The DAMA/LIBRA Experiment

The DAMA group, presently operating the LIBRA NaI detector with a total detector mass of 250 kg, has proposed to increase its sodium iodide detector mass to one ton [131], with the objective to confirm its evidence for an annual modulation. However, the present systematic limitations of this experiment, which already accumulated an exposure of  $\sim 100\text{ ton} \times \text{d}$ , make it improbable that significant improvements in sensitivity will be reached using this technique.

### 9.1.2 The GENIUS-TF/GENIUS Experiment

The GENIUS project [132], mainly devoted to the study of double-beta decay, is proposing two stages with 1 ton and 10 tons of enriched  $^{76}\text{Ge}$  detectors. This project has based its approach on the excellent purity of germanium crystals. The analysis of data accumulated over several years by the Heidelberg–Moscow experiment indicated that the most prominent contributions to the background originated from the copper structure surrounding the

detectors. Therefore, GENIUS intends to reduce all detector materials other than germanium to a minimum, with a proposed shielding consisting of a 13 m diameter tank of liquid nitrogen, constantly recirculated. Prototype detectors have been operated successfully in liquid nitrogen with FETs deported at distances of up to several meters, with energy resolutions comparable or even exceeding those obtained with conventional detectors. According to the GENIUS proponents, the main limiting factors are therefore the radioactivity of all other materials than the germanium target. The internal radioactivity of germanium itself, resulting from cosmogenic activation, and most notably  $^{68}\text{Ge}$ , is then the second most prominent background. The success of GENIUS requires that all materials other than liquid nitrogen and germanium (wiring, charge collection electrodes, etc.) are of limited mass and maintained radioactively ultrapure.

However, to reach the GENIUS target sensitivity of  $2 \times 10^{-9} \text{ pb}$ , the radioactive background at low energies must be reduced by more than three orders of magnitude compared to the best present background levels, reached by the IGEX and the Heidelberg-Moscow experiments after several years of development. This level of extrapolation requires an intermediate test, which is presently attempted with the GENIUS-TF facility [133], using a total of 14 HPGe-detectors with a total active mass of  $\sim 40 \text{ kg}$ . The cosmogenic activation of  $^{68}\text{Ge}$  and  $^{71}\text{Ge}$ , and the ubiquitous presence of tritium also represent two particularly dangerous low energy backgrounds for the GENIUS project. Underground crystal fabrication is explored, as this would reduce the  $^{68}\text{Ge}$  activation by one to two orders of magnitude (depending on the fabrication site and transport duration to the deep-underground experimental site). Also mainly aimed at the detection of double-beta decay, the MAJORANA project [134] will involve 500 kg of enriched  $^{76}\text{Ge}$  and intends to test the existence of WIMPs down to cross-sections  $\sim 10^{-8} \text{ pb}$  through the annual modulation signature.

### 9.1.3 The CUORICINO/CUORE Experiment

The CUORICINO experiment [135], test stage of the CUORE experiment [136], is using a compact structure of  $44 \times 760 \text{ g}$  and  $18 \times 340 \text{ g}$   $\text{TeO}_2$  bolometric detectors, operated at  $T \sim 10 \text{ mK}$ , with a total target mass of  $\sim 40 \text{ kg}$  (Fig. 16). The main scientific aim of the CUORICINO/CUORE experiment is, similarly to GENIUS, the observation of  $0\nu$ -double-beta decay. This experiment also aims at the observation of a WIMP signal through the challenging annual modulation signature [136, 137, 138]. The cosmogenic activation is not a problem here since radioactive isotopes of oxygen and tellurium are short-lived. The main problem encountered by the CUORICINO experiment appears to be related to U/Th contamination in the copper supporting structure, and to the surface implantation of heavy nuclear elements in crystals resulting from radon disintegration products. While an important

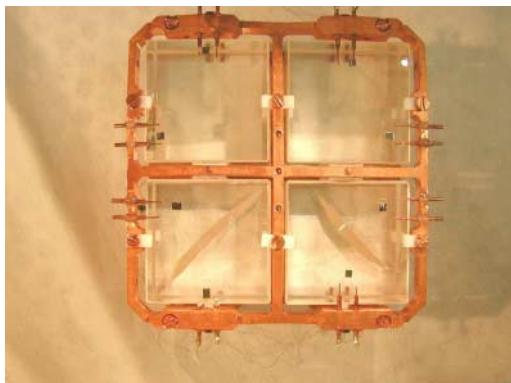


**Fig. 16.** Top view of the detector tower of the CUORICINO experiment. Each plane of the tower comprises four detectors, weighing 760 g each, except for two of the lower planes, each comprising  $9 \times 340$  g. The energy of an interaction is measured by the impedance variation of a Neutron Transmuted Doped (NTD) Ge sensor. These detectors are operated at a temperature of  $\sim 10$  mK in the Gran Sasso underground laboratory (Italy)

part of this background is observed at MeV energies, these surface implantations lead in all experiments to a continuous background extending down to energies characteristic of WIMP interactions, through the escape of alpha tracks and by the low energy surface beta contaminations (from, e.g.,  $^{210}\text{Bi}$  and  $^{210}\text{Pb}$   $\beta$ -decays).

Therefore, the techniques presently developed in the main non discriminating WIMP direct detection experiments require an extrapolation by more than three orders of magnitude in their background performances to reach their target sensitivities of a few  $10^{-9}$  pb.

## 9.2 Large-Scale Cryogenic Discriminating Experiments

A different strategy is proposed by the cryogenic experiments. The emphasis here is not so much on the radioactive purity, obviously still necessary, but on the quality of the discrimination between electron and nuclear recoils to identify a possible WIMP signal. During the next few years, the CDMS-II, CRESST-II and EDELWEISS-II second-generation experiments will each use a mass of detectors in the 10 kg range to test the various discrimination strategies (simultaneous measurement of fast phonons and charge, thermal phonons and light, or thermal phonons and charge) while already testing a significant part of the SUSY allowed models.

To reach the goal of a one-ton cryogenic experiment, cryogenics does not appear per se as the main challenge. In this respect, cooling down a 2.3 ton Al antenna at a temperature of 100 mK has already been achieved by the NAUTILUS cryogenic search for gravitational waves [139], while in future

years, the GRAIL project intends to develop a 150-ton gravitational antenna at a temperature of  $\sim 10\text{ mK}$  [140].

On the other hand, cryogenic experiments still have to demonstrate that they can reliably operate very large numbers of detectors. As mentioned previously, the CUORICINO experiment [135] is presently successfully operating a total of  $\sim 40\text{ kg}$  of crystals, representing the present largest cryogenic experiment for dark matter and double beta decay search. In a few years, the recently approved CUORE project [136] intends to use a thousand  $760\text{ g}$   $\text{TeO}_2$  crystal detectors at a temperature of  $10\text{ mK}$ , almost reaching the one ton objective. Although the CUORE project, principally aimed at the neutrino mass measurement, will hardly be competitive with future dark matter searches due to its present lack of discrimination capabilities, this experiment shows that large numbers of detectors at very low temperatures can be considered and realized.

For such large-scale experiments, ease of fabrication and reliability represent two essential factors. In this respect, thin film and magnetic sensors might offer an elegant solution to the problems of reproducibility and channel multiplicity. Several groups [64, 94, 141, 142] have developed such MIT, TES and magnetic sensors with sensitivities comparable or even exceeding that of conventional thermal sensors such as Neutron Transmutation Doped sensors (NTDs), used in the CUORE and EDELWEISS experiments.

### 9.3 Strategy For Ton-Scale Dark Matter Cryogenic Experiments

Aside from the difficulty of integrating a thousand cryogenic detectors at temperatures in the  $10\text{ mK}$  range, ton-scale discriminating cryogenic experiments must address the identification of neutron background, which will mimic WIMP-induced nuclear recoils. In addition, an increase of the individual detector mass appears desirable, while maintaining an excellent energy resolution required by a particle identification on an event-by-event basis.

#### 9.3.1 The Neutron Background

Three main neutron components are present in a deep underground laboratory, required to operate a Dark Matter direct detection experiment below the present sensitivity to WIMP interactions of  $\sim 10^{-6}\text{ pb}$  reached by the CDMS, CRESST and EDELWEISS experiments.

The first component comes from the spontaneous fission of uranium and from spallation reactions in the rock and concrete walls of the underground laboratory shielding the experiment from the muon-induced background. For both fission and  $\alpha$ -n reactions, neutrons are emitted at typical energies of a few MeV. For the best sites, neutron fluxes are of the order of  $10^{-6}\text{ neutrons/cm}^2 \cdot \text{s}$ . This neutron flux component can be efficiently reduced by several orders of magnitude, at levels corresponding to WIMP cross-sections less than  $10^{-9}\text{ pb}$ , by using typically  $60\text{ cm}$  of low-Z shielding, such



**Fig. 17.** Setup of the CDMS-II experiment in the Soudan underground laboratory (Minnesota). The cold box, made of ultrapure copper, is surrounded by a passive polyethylene shielding against neutrons from the rock and concrete. An external lead shield is used as a further protection against the gamma-ray background. In the Soudan laboratory, the muon flux is reduced by a factor  $\sim 10^5$  compared to ground level, but a muon veto (not shown on the photograph) is used to identify the remaining muons or showers crossing the detector setup

as polyethylene. The protection setup used by the CDMS-II experiment in the Soudan underground laboratory is shown in Fig. 17. Without this protection, this neutron flux component has already been detected by discrimination experiments like EDELWEISS and CRESST, operating in deep-underground sites. It is presently the main background limiting the sensitivity of the first stage of the CRESST-II experiment, without neutron protection.

A second neutron component is associated with the neutron production by muons crossing the copper and lead shieldings, used as gamma-ray protections but acting here as neutron multipliers. This neutron background can be effectively reduced to a negligible level by identifying and vetoing the muons crossing the protective setup around the detectors. The CDMS-II, CRESST-II and EDELWEISS-II cryogenic experiments are using plastic scintillator veto to identify muons and reject this fast neutron background. Different strategies are followed by EDELWEISS and CDMS in their control of muon-induced neutron background: in EDELWEISS, the polyethylene shielding is external to the low-radioactivity lead shielding, favoring the neutron production associated with muons close to the detectors, while the reverse solution has been chosen by CDMS. The higher muon flux in the Soudan underground laboratory, by a factor  $\sim 40$  compared to the Frejus underground laboratory, strongly constrains the solution chosen by the CDMS experiment, unless an extremely efficient muon veto is used.

Finally, even under the protection of thousands meters of water equivalent, high-energy muons with energies in the TeV range may lose in a catastrophic way a large fraction of their energy in a single deep-inelastic

scattering interaction on a nucleus. Typically 10% of the long range hadronic component is then carried away by several thousand neutrons, at very low shower densities, making this fast neutron background extremely difficult to detect. A large active scintillator shield, as used, for example, in the Borexino or the KARMEN neutrino experiment [143, 144] can strongly reduce this small but dangerous background.

Beyond these three neutron backgrounds, it is probably illusory to believe that it will be possible to reduce at a level below a few neutrons per year the internal neutron emission, by U/Th and alpha-n reactions, by a Dark Matter setup of total mass  $> 100$  tons, and particularly of the  $\sim 10$  tons of various materials (cryostat, shielding, cabling, electronics) in the immediate vicinity of the detectors.

The residual neutron background can be efficiently monitored by studying the multiple scatter interactions in an array of densely packed detectors, since fission and spallation neutrons will suffer tens of scatterings before reaching energies of a  $\sim 0.1$  MeV, where their scatterings become undetectable. For example, the compact detector arrangement presently studied in the CUORI-CINO experiment (Fig. 16) involves a series of 760 g detectors in direct close view of each other. Similarly, EDELWEISS-II will be using up to ten planes with hexagonal paving of 12 Ge detectors. In the CUORE detector setup, the rejection factor by identification of multiple scatter neutron events for the 512 inner detectors will reach two orders of magnitude. Such a compact arrangement of detectors will be necessary to clearly identify the residual internal neutron background. Using such a multiple scattering strategy, the neutron background can probably be kept below the level of a few  $10^{-5}$  evt/kg · keV · d, corresponding to WIMP interaction cross-sections of  $\sim 10^{-10}$  pb.

A different strategy has been used by the CDMS experiment, with interspersed germanium and silicon detectors to measure the neutron flux on two different target materials. For WIMPs with mass compatible with accelerator constraints and predominant scalar couplings, Ge is  $\sim 10$  times more sensitive per unit of mass than Si to WIMP interactions, and it is therefore expected that Si detectors will mainly detect the remaining fast neutron flux, at the expense of a reduction of the fiducial mass for WIMP detection.

### 9.3.2 Detector Mass and Resolution

Similarly to CUORE, which is using 760 g detectors, it appears important to increase the individual detector mass of discriminating experiments, presently in the 250–320 g range, to  $\sim 1$  kg. Going much beyond this mass will degrade the energy resolution, while the cost of individual crystals will increase rapidly. For example, it seems difficult at present to obtain high purity Ge crystals with diameter significantly larger than 100 mm. For a 1 kg detector, this corresponds to a thickness of  $\sim 30$  mm. Further increasing the thickness is possible, but will reduce the electric field used to collect charges in the crystal since the collecting voltage must not exceed a few volts due to

the Neganov–Luke effect. With such 1 kg detectors, the energy resolution at WIMP interaction energies (a few keV) can be kept below 1 keV : EDELWEISS 320 g and CDMS 250 g Ge detectors have shown energy resolutions  $\sim 300$  eV. With the optimization of sensor parameters, energy resolutions better than 500 eV are expected for these 1 kg detectors. These performances should be compared to the energy resolution of present liquid xenon detectors, where a 100% energy resolution is only obtained at  $> 50$  keV recoil energy ( $\sim 8$  keV e.e.) Similarly, the CRESST and ROSEBUD experiments are developing detectors with individual mass in the 1 kg range with resolutions in the keV range, and the comprehension of the background structure at low energies appears as a key feature in favor of cryogenic experiments.

## 10 Conclusions

Three cryogenic experiments, CDMS, CRESST and EDELWEISS, presently provide the best sensitivity to WIMP interactions, one order of magnitude better than their present competitors and still far from being limited by systematic uncertainties. Despite the complexity of their operation, they provide a much better background control than other competing experiments, presently limited by much poorer energy resolutions and background discrimination performances. Obtained with small prototype detectors, in the few hundred gram range, these performances are susceptible to a further sensitivity increase of nearly two orders of magnitude during the next few years. Starting from the present sensitivity to cross-sections of  $\sim 10^{-6}$  pb, which probes a first region of optimistic SUSY models, the present techniques of charge-phonon and light-phonon detectors should allow to test SUSY models down to cross-sections of  $\sim 10^{-8}$  pb, a region of SUSY parameter space considered as more realistic by particle theorists [145].

Cryogenic experiments at the 10 kg scale will start being operated early in 2005, but exploration of most of SUSY models will require reaching the fantastic sensitivity of  $\sim 10^{-10}$  pb. At this level, the integrated number of events in the relevant energy range is only a handful per ton of detector and per year. Therefore, based on existing technology, experiments in the 100 kg to 1 ton range are already designed in the EURECA (European Underground Rare Event search with Calorimeter Array) and SDMS projects, although new developments in background rejection will probably be required to reach the limit sensitivity of ton-scale experiments.

Particularly important, among the developments that might mark a further progress in discrimination performances, are the identification with high efficiency of surface events, and most notably heavy nuclear recoils associated with surface radon decay products. Light-phonon detectors, provided they are able to keep to a negligible level their dissipative (“phonon-only”) events, which might otherwise be confused with heavy nuclear recoils, will provide an alternative set of nuclear targets, essential to finally identify a

potential WIMP signal. For these three techniques, in order to reach the one-ton scale at a reasonable cost, it will be important to increase the individual detector size to  $\sim 1$  kg. A full 3-D position determination of the interaction down to low energies would also allow to check the homogeneity of the WIMP candidates events together with the location of the remaining radioactivity, but this capability appears as a daunting technical development below  $\sim 10$ –20 keV recoil energy.

Finally, developments realized for dark matter direct detection with cryogenic detectors may also be beneficial to other physics applications. In particular, charge-phonon detectors might allow to identify and reject the two main radioactive backgrounds of present double beta decay experiments: surface alpha interactions and Compton  $\gamma$ -ray interactions. Other applications are the observation of coherent neutrino scattering, which can be easily achieved in future neutrino factory beams with present charge-phonon and light-phonon detectors, a high sensitivity search for the neutrino magnetic moment, and possibly real-time solar neutrino detection using the ZIP position resolution in the several hundred keV range.

In the same way that CMB measurements are now almost impossible to imagine without the help of cryogenic detectors, direct detection WIMP searches, now led by three cryogenic experiments, together with low-energy particle detection will strongly benefit from the development of these detectors, with their outstanding energy resolution and background identification properties.

## References

- [1] F. Zwicky: Helv. Phys. Acta **6**, 110 (1933). 313
- [2] Y. Ramachers: in *Proc. XXth Int. Conf. Neutrino Physics and Astrophysics*, May 25-30, 2002, Munich, Germany; astro-ph/0211500. 314
- [3] L. Bergstrom: Rept. Prog. Phys. **63**, 793 (2000); hep-ph/0002126. 314
- [4] A. Morales: Nucl. Phys. Proc. Suppl. **114**, 39 (2003). 314
- [5] M. Milgrom: Ap. J. **270**, 371 (1983) and astro-ph/0211446. 314
- [6] C. Alcock *et al.*: (MACHO Collaboration), Nature **365**, 621 (1993). 314, 315
- [7] E. Aubourg *et al.*: (EROS Collaboration), Nature **365**, 623 (1993). 314, 315
- [8] Y. Fukuda *et al.*: Phys. Rev. Lett. **81**, 1562 (1998). 314
- [9] P. Sikivie: Phys. Rev. Lett. **51**, 1415 (1983); Phys. Rev. Lett. **52**, 695 (1984) (Erratum) 314
- [10] D. Pfenniger and F. Combes: Astron. Astroph. **285**, 79 (1994); ibid. 94 314
- [11] S. Perlmutter *et al.*: Nature **391**, 51 (1998). 314
- [12] A.G. Riess *et al.*: Astrophys. J. **116**, 1009 (1998). 314
- [13] I. Zlatev, L. Wang and P.J. Steinhardt: Phys. Rev. Lett. **82**, 896 (1999). 314
- [14] M. Tegmark *et al.*: Phys. Rev. D**69**, 103501 (2004); astro-ph/0310723 314, 316
- [15] C. Alcock *et al.*: (MACHO Collaboration), Ap. J. **542**, 281 (2000). 315

- [16] P. Tisserand: PhD Thesis, Orsay University (2004), unpublished ; P. Tisserand *et al.*, EROS Collaboration, in preparation [314](#), [315](#)
- [17] EROS Collaboration, Astron. Astrophys. **400**, 951 (2003); astro-ph/0212176. [315](#)
- [18] R. Ibata *et al.*: Ap. J. **524**, L1 (1998). [315](#)
- [19] B. Goldman, *et al.*: (EROS collaboration), Astron. Astroph. **389**, L69 (2002). [315](#)
- [20] D.N. Schramm, and M.S. Turner: Rev. Mod. Phys. **70**, 303 (1998). [315](#)
- [21] R.H. Cyburt, B.D. Fields, K.A. Olive: Phys. Lett. B **567**, 227 (2003); astro-ph/0302431. [315](#)
- [22] A. Cuoco, F. Iocco, G. Mangano, G. Miele, O. Pisanti, P.D. Serpico: astro-ph/0307213. [315](#)
- [23] G. Hinshaw *et al.*: Ap. J. **464**, L17 (1996). [316](#)
- [24] P. de Bernardis *et al.*: Nature **404**, 955 (2000). [316](#)
- [25] A. T. Lee *et al.*: Ap. J. **561**, L1 (2001); astro-ph/0104459. [316](#)
- [26] J. Kovac, E.M. Leitch, C. Pryke, J.E. Carlstrom, N.W. Halverson, W.L. Holzapfel: Nature **420**, 772 (2002); astro-ph/0209478. [316](#)
- [27] A. Benoit, *et al.*: Astron. Astrophys. **399**, L25 (2003); astro-ph/0210306. [316](#)
- [28] S. Padin, *et al.*: Ap. J. **549**, L1 (2001). [316](#)
- [29] D.N. Spergel *et al.*: Astrophys. J. Suppl. **148**, 97 (2003); astro-ph/0302209/. [316](#)
- [30] S.P. Ahlen, *et al.*: Phys. Lett. B **195**, 603 (1987); D.O. Caldwell, *et al.*, Phys. Rev. Lett. **61**, 510 (1988). [317](#), [320](#)
- [31] D.O. Caldwell, *et al.*: Phys. Rev. Lett. **65**, 1305 (1990). [317](#), [320](#)
- [32] B. W. Lee, S. Weinberg: Phys. Rev. Lett. **39**, 165 (1977); E. Witten: Phys. Rev. D **30**, 272 (1984); K. Griest: Phys. Rev. D **38**, 2357 (1988); G. Jungman: M. Kamionkowski, K. Griest: Phys. Rep. **267**, 195 (1996); J. Ellis, T. Falk, K.A. Olive, and M. Schmitt: Phys. Lett. B **413**, 355 (1997); J. Edsjo and P. Gondolo: Phys. Rev. D **56**, 1879 (1997); R. Arnowitt and P. Nath: hep-ph/9902237 and Phys. Rev. D **60**, 044002 (1999), and references therein [317](#)
- [33] P. Sikivie: Phys. Rev. D **60**, 063501 (1999); Phys. Lett. B **432**, 139 (1998). [318](#)
- [34] A.K. Drukier and L. Stodolsky: Phys. Rev. D **30**, 2295 (1984). [318](#)
- [35] M. W. Goodman and E. Witten: Phys. Rev. D **31**, 3059 (1985). [318](#)
- [36] J. Rich: Astropart. Phys. **4**, 387 (1996). [319](#)
- [37] A.K. Drukier, K. Freese and D.N. Spergel: Phys. Rev. D **33**, 3495 (1986); K. Freese, J. Friedman and A. Gould: Phys. Rev. D **37**, 3388 (1988). [320](#)
- [38] D. Spergel: Phys. Rev. D **37**, 1353 (1988); C.J. Copi, J. Heo and L.M. Krauss: Phys. Lett. B **461**, 43 (1999). [320](#), [344](#)
- [39] J. Silk, K. Olive and M. Srednicki: Phys. Rev. Lett. **55**, 257 (1985); L.M. Krauss, M. Srednicki and F. Wilczek: Phys. Rev. D **33**, 2079 (1986). [320](#)
- [40] J. Silk, K. Olive and M. Srednicki: Phys. Rev. Lett. **55**, 257 (1985); L.M. Krauss, M. Srednicki and F. Wilczek: Phys. Rev. D **33**, 2079 (1986). [320](#)
- [41] P. Gondolo, J. Silk: Phys. Rev. Lett. **83**, 1719 (1999) [320](#)
- [42] M. Beck, *et al.*: Heidelberg-Moscow Collaboration, Phys. Lett. B **336**, 141 (1994). [320](#)
- [43] L. Baudis, *et al.*: Phys. Rev. D**59**, 022001 (1999). [320](#)
- [44] L. Baudis, *et al.*: Phys. Rev. D**63**, 022001 (2001). [321](#)

- [45] A. Morales, *et al.*: Phys. Lett. **B532**, 8 (2002), hep-ex/0110061. [321](#)
- [46] R. Bernabei, *et al.*: Phys. Lett. **B389**, 757 (1996). [321](#)
- [47] P.F. Smith, *et al.*: Phys. Lett. **B379**, 299 (1996). [321](#)
- [48] G. Gerbier, *et al.*: Astropart. Physics **11**, 287 (1999). [321](#), [336](#)
- [49] R. Bernabei, *et al.*: Phys. Lett. **B424**, 195 (1998); Phys. Lett. **B450**, 448 (1999). [321](#)
- [50] H. Ejiri, *et al.*: in *Proceedings of the Second International Workshop on the Identification of Dark Matter*, eds. N.J.C. Spooner and V. Kudryavtsev (World Scientific, Singapore, 1999), p. 323. [321](#)
- [51] R. Bernabei, *et al.*: Phys. Lett. **B480**, 23 (2000). [321](#)
- [52] R. Bernabei, *et al.*: Riv. Nuovo Cim. **26**, 1 (2003); astro-ph/0307403. [321](#), [322](#)
- [53] J.D. Lewin and P.F. Smith: Astropart. Phys. **6**, 87 (1996). [321](#)
- [54] A. Benoit, *et al.*: Phys. Lett. B **513**, 15 (2001) and astro-ph/0106094/. [321](#)
- [55] A. Benoit *et al.*: Phys. Lett. B **545**, 43 (2002). [321](#), [326](#), [345](#)
- [56] V. Sanglard: the EDELWEISS collaboration, astro-ph/0406537, to appear in Phys. Rev. D [321](#)
- [57] C.J. Copi, L.M. Krauss: Phys. Rev. **D67** 103507 (2003); astro-ph/0208010/. [321](#)
- [58] A. Kurylov and M. Kamionkowski: Phys. Rev. **D69**, 063503 (2004); hep-ph/0307185. [322](#)
- [59] C. Savage, P. Gondolo, K. Freese, astro-ph/0408346, submitted to Phys. Rev. D [322](#)
- [60] N.J.T. Smith *et al.*: in *Proceedings of the 4th International Workshop on Identification of Dark Matter (idm2002)*, eds. N.J. Spooner and V. Kudryavtsev, (World Scientific, Singapore, 2003) [322](#)
- [61] R. Gaitskell and V. Mandic: Interactive WIMP Limits Plotter, <http://dmtools.berkeley.edu/limitplots/> [323](#)
- [62] T. Shutt, *et al.*: Phys. Rev. Lett. **69**, 3452 (1992) ; Phys. Rev. Lett. **69**, 3531 (1992). [323](#), [325](#), [326](#), [327](#)
- [63] D. L'Hôte, X-F. Navick, R. Tourbot, J. Mangin and F. Pesty: J. Appl. Phys. **87**, 1507 (2000). [323](#), [325](#), [326](#), [327](#)
- [64] M. Bravin, *et al.*: Astropart. Phys. **12**, 107 (1999). [323](#), [324](#), [325](#), [337](#), [349](#)
- [65] P. Meunier, *et al.*: Appl. Phys. Lett. **75**, 1335 (1999). [323](#), [337](#)
- [66] N. Coron, *et al.*: Astron. Astrophys. **278**, L31 (1993). [323](#)
- [67] S.Cebrian, *et al.*: Astropart.Phys. **15**, 79 (2001); astro-ph/0004292. [324](#), [325](#)
- [68] R. Abusaidi *et al.*: Phys. Rev. Lett. **84**, 5699 (2000). [325](#)
- [69] D. Abrams *et al.*: CDMS collaboration, Phys. Rev. **D66**, 122003 (2002); astro-ph/0203500.
- [70] A. Alessandrello, *et al.*: Nucl. Instrum. Meth. A **370**, 241 (1996). [325](#)
- [71] A. Alessandrello, *et al.*: Phys. Lett. B **408**, 465 (1997). [325](#)
- [72] W. Ootani, *et al.*: Phys. Lett. B **461**, 371 (1999); Nucl. Instr. Meth., A **436**, 233 (1999). [325](#), [343](#), [344](#)
- [73] P. Di Stefano, *et al.*: Astropart. Phys. **14**, 329 (2001); astro-ph/0004308/ [325](#)
- [74] B. Young, *et al.*: Nucl. Instrum. and Meth. A **311**, 195 (1992). [325](#), [328](#)
- [75] K.D. Irwin, *et al.*: Rev. Sci. Instr. **66**, 5322 (1995). [325](#), [328](#)
- [76] B. Cabrera, *et al.*: Appl. Phys. Lett. **73**, 735 (1998). [325](#), [328](#)
- [77] J. Lindhard, *et al.*: Mat. Fys. Medd. Dan. Vid. Selsk **10**, 1 (1963). [326](#)

- [78] N.J.C Spooner, *et al.*: Phys. Lett. B **273**, 333 (1991). [326](#)
- [79] R.M. Clarke, *et al.*: Appl. Phys. Lett. **76**, 2958 (2000). [326, 330, 341](#)
- [80] X.F. Navick, *et al.*: Nucl. Instrum. Meth. A **444**, 361 (2000). [326, 327](#)
- [81] CDMS Collaboration, hep-ex/0306001, Phys. Rev. D**68**, 082002 (2003). [330](#)
- [82] D. Akerib, *et al.*: the CDMS Collaboration, astro-ph/0405033, Phys. Rev. Lett **93**, 211301 (2004) [326, 330, 333, 345](#)
- [83] N. Mirabolfathi, *et al.*: AIP Conf. Proc. **605**, 517 (2002). [327, 331](#)
- [84] E. Simon, *et al.*: Nucl. Instrum. Meth. A **507**, 643 (2003); astro-ph/0212491 [326](#)
- [85] S. Ramo: in *Proceedings of the I.R.E.* **27**, 584 (1939). [328](#)
- [86] J. Llacer, E.E. Haller, R.C. Cordi: IEEE Trans. Nucl. Sci., **24**, 53 (1977). [328](#)
- [87] P.N. Luke, C.P. Cork, N.W. Madden, C.S. Rossington, M.F. Wesela: IEEE Trans. Nucl. Sci. **39**, 590 (1992). [328](#)
- [88] P.N. Luke, C.S. Rossington, M.F. Wesela: IEEE Trans. Nucl. Sci. **41**, 1074 (1994). [328](#)
- [89] T. Shutt *et al.*: Nucl. Instr. Meth. A **444**, 340 (2000). [328](#)
- [90] T. Shutt *et al.*: in *Proc. 9th Int. Workshop on Low Temperature Detectors*, AIP conference proceedings **605**, 513 (2001). [328](#)
- [91] B. Neganov and V. Trofimov: USSR patent No 1037771, Otkryтия i izobreteniya **146**, 215 (1985). [328](#)
- [92] P.N. Luke: J. Appl. Phys. **64**, 6858 (1988). [328](#)
- [93] N. Booth: Appl. Phys. Lett. **50**, 293 (1987) [329](#)
- [94] K. D. Irwin *et al.*: Appl. Phys. Lett. **66**, 1998 (1995). [329, 349](#)
- [95] R.P. Welty and J.M. Martinis: IEEE Trans. Appl. Superconduct. **3**, 2605 (1993). [329](#)
- [96] J. Hellmig *et al.*: Nucl. Instrum. Meth. A **444**, 308 (2000). [330](#)
- [97] M.J. Penn, B.L. Dougherty, B. Cabrera, R.M. Clarke: J. Appl. Phys. **79**, 8179 (1996). [332](#)
- [98] A. Broniatowski, *et al.*: in *Proceedings of the 10th International Workshop on Low temperature Detectors*, Genoa, 7-11 July 2003, Nucl. Instr. Meth. A **520**, 178 (2004). [332](#)
- [99] B. Censier, *et al.*: in *Proceedings of the 10th International Workshop on Low temperature Detectors*, Genoa, 7-11 July 2003, Nucl. Instr. Meth. A **520**, 156 (2004). [332](#)
- [100] A. Broniatowski, *et al.*: in *Low Temperature Detectors*, eds. F.S. Porter *et al.*, AIP Conference Proceedings **605**, 521 (2001). [333](#)
- [101] G. Chardin, *et al.*: in *Proceedings of the 10th International Workshop on Low temperature Detectors*, Genoa, 7-11 July 2003, Nucl. Instr. Meth. A **520**, 145 (2004). [333](#)
- [102] V. A. Kudryavtsev *et al.*: Phys. Lett. B **452**, 167 (1999). [336](#)
- [103] C. Bobin, *et al.*: Nucl. Instr. Meth. A **386**, 453 (1997). [337](#)
- [104] A. Alessandrello, *et al.*: Phys. Lett. B **420**, 109 (1998). [337](#)
- [105] S. Cebran, *et al.*: Phys. Lett. B **563**, 48 (2003). [337, 338](#)
- [106] <http://www.e15.physik.tu-muenchen.de/Tecnomusiq/Tecnomusiq.html> [339](#)
- [107] M. F. Weber, C. Stover, L. Gilbert, T. Nevitt, and A. Ouderkirk: Science **287**, 451 (2000). [340](#)
- [108] G. Angloher, *et al.*: CRESST collaboration, astro-ph/0408006 [340](#)
- [109] D.I. Bradley *et al.*: Phys. Rev. Lett. **75**, 1887 (1995). [342](#)

- [110] D. Santos: in *Sources and detection of Dark Matter and Dark Energy in the Universe*, (D. B. Cline, ed.), (Springer Berlin, 2001) [342](#)
- [111] H. Bernas, *et al.*: Phys. Lett. A **24**, 721 (1967). [343](#)
- [112] M. Abplanalp, *et al.*: Nucl. Instrum. and Meth. A **370**, 227 (1996). [343](#)
- [113] K. Borer, *et al.*: in *Proceedings of the 4th International Workshop on the Identification of Dark Matter* (IDM 02), York, England, eds. N.J.C. Spooner and V. Kudryavtsev, (World Scientific, Singapore, 2003), pp. 332-337 [343](#)
- [114] K. Miuchi, *et al.*: Astropart. Phys. **19**, 135 (2003); astro-ph/0204411. [343](#), [344](#)
- [115] J. Ellis and R.A. Flores: Phys. Lett. B **263**, 259 (1991). [343](#)
- [116] A. Habig: for the Super-Kamiokande Collaboration, hep-ex/0106024. [344](#)
- [117] E. Andres, *et al.*: Astropart. Phys. **13**, 1 (2000). [344](#)
- [118] M. Kamionkowski, K. Griest, G. Jungman, and B. Sadoulet: Phys. Rev. Lett. **74**, 5174 (1995). [344](#)
- [119] P. de Marcillac, *et al.*: in *Proceedings of the 10th International Workshop on Low temperature Detectors*, Genoa, 7-11 July 2003, Nucl. Instr. Meth. A **520**, 159 (2004). [344](#)
- [120] J. Rich and M. Spiro: Saclay report DPhPE-88-04 (1988) [344](#)
- [121] K.N. Buckland, M.J. Lehner, G.E. Masek, and M. Mojaver: Phys. Rev. Lett. **73**, 1067 (1994). [344](#)
- [122] R.E. Lanou: Nucl. Phys. B Proc. Suppl. **77**, 55 (1999). [344](#)
- [123] S.R. Bandler: *et al.*, Phys. Rev. Lett., 3169 **74** (1995). [344](#), [345](#)
- [124] J.I. Collar and F.T. Avignone III: Nucl. Instr. Methods B **95**, 349 (1995). [344](#)
- [125] M.J. Lehner, K.N. Buckland and G.E. Masek: Astropart. Phys. **8**, 43 (1997). [344](#)
- [126] D.P. Snowden-Ifft, E.S. Freeman and P.B. Price: Phys. Rev. Lett. **74**, 4133 (1995). [344](#)
- [127] D.P. Snowden-Ifft and A. J. Westphal: Phys. Rev. Lett. **78**, 1628 (1997). [344](#), [345](#)
- [128] D.P. Snowden-Ifft, C. J. Martoff, J. M. Burwell: Phys. Rev. D **61**, 101301 (2000). [344](#), [345](#)
- [129] G. Angloher, *et al.*: the CRESST Collaboration, astro-ph/0408006, submitted to Astropart. Phys. [345](#)
- [130] V. Sanglard: the EDELWEISS collaboration, astro-ph/0506537, to appear in Phys. Rev. D [345](#)
- [131] R. Bernabei *et al.*: Astropart. Phys. **4**, 45 (1995). [346](#)
- [132] H.V. Klapdor-Kleingrothaus: Nucl. Phys. **B110**, 364 (2002), and hep-ph/0206249. [346](#)
- [133] L. Baudis, *et al.*: Nucl. Instrum. Meth. A **481**, 149 (2002), hep-ex/0012022. [347](#)
- [134] L. De Braeckeleer: for the MAJORANA Collaboration, in *Proceedings of the Carolina Symposium on Neutrino Physics*, South Carolina, 10-12 Mar 2000, pp. 325-339. [347](#)
- [135] S. Pirro, *et al.*: Nucl. Instr. Meth. A **444**, 71 (2000). [347](#), [349](#)
- [136] C. Arnaboldi, *et al.*: CUORE Collaboration, Astropart. Phys. **20**, 91 (2003) and hep-ex/0302021. [347](#), [349](#)

- [137] Y. Ramachers, M. Hirsch, H.V. Klapdor-Kleingrothaus: Eur. Phys. J. A **3**, 93 (1998). [347](#)
- [138] F. Hasenbalg: Astropart. Phys. **9**, 339 (1998). [347](#)
- [139] P. Astone, *et al.*: Astropart. Phys. **7**, 231 (1997). [348](#)
- [140] G. Frossati: J. Low Temp. Phys. **101**, 81 (1995). [349](#)
- [141] H. Kraus: Supercond. Sci. Technol. **9**, 827 (1996). [349](#)
- [142] S. Marnieros, L. Berge, A. Juillard, L. Dumoulin: Phys. Rev. Lett. **84**, 2469 (2000); A. Juillard, PhD Thesis, Orsay, (1999), unpublished [349](#)
- [143] F. Gatti, G. Morelli, G. Testera, S. Vitale: Nucl. Instrum. Meth. A **370**, 609 (1996). [351](#)
- [144] B. Zeitnitz, G. Drexlin: Interdisciplinary Science Reviews (ISR) **18**, 313 (1993). [351](#)
- [145] J. Ellis, A. Ferstl, K.A. Olive: Phys.Lett. **B481**, 304 (2000). [352](#)

# Index

- activation (cosmogenic), 320
- alpha radioactivity, 325
- amorphous germanium, 328
- amorphous silicon, 328
- athermal, 331
- axial (interaction), 318
- baryonic, 313
- beta radioactivity, 325
- BGO, 336
- CaWO<sub>4</sub>, 336
- CDMS, 322
- charge regeneration, 332
- charge-phonon, 326
- Cooper pairs, 341
- cosmological constant, 314
- CRESST, 323
- CUORE, 347
- CUORICINO, 336
- Debye, 323
- diamagnetic, 343
- diamagnetic interaction, 343
- dilution cryostat, 335
- direct detection, 313
- discrimination, 319
- EDELWEISS, 322
- electron recoil, 319
- electrothermal feedback, 329
- fission, 349
- gamma radioactivity, 325
- germanium, 320
- granule (superconducting), 343
- <sup>3</sup>He, 342
- <sup>4</sup>He, 342
- HERON, 344
- implantation, 329, 335
- impurity, 332
- indirect detection, 317
- light-phonon, 337
- luminescence, 337
- MACHOs, 314
- Meissner effect, 343
- MIT, 327
- MSSM, 317
- muon (interactions), 330
- Neganov-Luke effect, 328
- neutralino, 317
- neutrino, 314
- neutron, 319
- NTD, 327
- nuclear recoil, 319
- phonon, 319
  - trapping, 329
- quasiparticles, 329
- quenching factor, 323
- radioactivity, 319
- radon, 319
- sapphire, 324
- scalar (interaction), 318
- scintillation, 321
- semiconductor, 332
- silicon, 329
- spallation, 349
- spin-dependent, 322

- spin-independent, 322
- SQUID, 326
- superfluid, 342
- supersymmetry, 313
- SUSY, 313
- TES, 324
- thin film sensor, 327
- tritium, 331
- WIMP, 313

# X-Ray Astronomy and Astrophysics

F.S. Porter, G.V. Brown, and J. Cottam

NASA/Goddard Space Flight Center, Greenbelt, MD 20771, USA

[porter@milkkyway.gsfc.nasa.gov](mailto:porter@milkkyway.gsfc.nasa.gov)

**Abstract.** The most compelling nature of X-ray astronomy is its richness and scale. Almost every observable object in the sky either naturally emits X-ray radiation or can be probed by X-ray absorption. Current X-ray observatories such as *Chandra* and *XMM-Newton* have considerably advanced our understanding of many of these systems by using dispersed X-ray spectrometers and imaging CCD cameras. However, it is the combination of these two techniques, a true broad-band, high spectral resolution, imaging spectrometer, that will drive the next revolution in X-ray astronomy. This is where Low Temperature Detectors can play a key role but also where the science will continuously challenge the technology. In this Chapter we will explore the constraints that both the science goals and the space environment place on the implementation of LTDs, and the solutions implemented in current missions such as the XQC and the XRS on *Astro-E2*. In addition we will see how the *NeXT*, *Constellation-X*, and *XEUS* missions will drive LTD instruments to a much larger scale. Finally, we will address scaling rules in current LTD detectors and where the LTD community needs to proceed to address both the science goals and expectations of the astrophysics community.

## 1 The Wealth and Breadth of the X-Ray Universe

X-rays are emitted by high-energy phenomena throughout the observable universe from the shock heating in stellar winds and supernova remnants, to the accretion processes in binary systems or in the nuclei of active galaxies, to the virilization of matter in intracluster gas. X-rays provide an excellent probe of the energetics and physical conditions in nearly all classes of astrophysical objects; the direct emission from these sources or the reprocessed spectra as the light interacts with the material along the line of sight are highly diagnostic and contain detailed spectroscopic signatures of the emitting and absorbing plasmas. Analysis of these spectra provides quantitative information on the physical conditions in these plasmas and ultimately allow us to study the physics of these different phenomena.

Over the past forty years since the first discovery of extra-solar X-ray sources [1], the field of X-ray astronomy has progressed rapidly. From the early 1960s to the late 1970s, X-ray detectors consisted primarily of proportional counters. The increasing sensitivity of these missions led to the detection of hundreds of X-ray sources. Although proportional counters are

very efficient photon counters, they have poor energy resolution. Other than the detection of a few bright spectral features, including the Fe K fluorescence line, spectroscopy was limited to basic comparisons between the global shapes of the spectra. Significant progress was made in the late 1970s and early 1980s when focusing optics became available. This led to orders of magnitude increase in sensitivity and hence in the number of detected X-ray sources. With focusing optics, dispersive spectrometers could be implemented, which provided several orders of magnitude increase in the spectral resolution. Unfortunately, the collecting area of these instruments was low, which limited their use to only the brightest sources. In the 1990s solid-state imaging spectrometers were launched with sufficient sensitivity to catalogue tens of thousands of sources from nearly all classes of astrophysical objects. Solid state imaging detectors also provided a significant improvement in spectral resolution over proportional counters. Discrete emission and absorption features with sufficient contrast could be identified, and basic imaging spectroscopy could be performed. However, because the resolving power of these instruments was only moderate, spectroscopic analysis required fitting often degenerate spectral models to the unresolved spectral features.

In the past few years, X-ray instruments have finally become available with sufficiently high throughput and spectral resolution to allow for quantitative X-ray spectroscopy of extra-solar objects. The first to fly are the diffraction grating spectrometers on-board NASA's *Chandra* X-ray Observatory [2] and ESA's *XMM-Newton* Observatory [3]. These spectrometers have revolutionized the field of X-ray astrophysics. Because they are dispersive spectrometers, they are excellent for point sources with soft X-ray spectra, but the spectral resolution degrades both with increasing energy and with increasing source extent. Cryogenic spectrometers, such as the XRS microcalorimeter that will shortly be launched as part of the joint NASA and ISAS/JAXA *Astro-E2* observatory, have resolving powers that increase with energy and that are independent of source extent. These instruments are critical to the progress of X-ray astrophysics. Not only will they fill the current need for high-resolution spectroscopy at high energies, but, as the technology develops, low-temperature detectors have the potential to finally provide true broad-band, high-resolution imaging spectroscopy of all types of sources.

In this chapter we will briefly discuss the X-ray spectroscopy that motivates the development of LTD detectors and the strengths of LTD detectors in the context of current spectroscopic instruments. We will then describe the development and use of current LTD instruments and the challenges of future missions.

## 2 High-Resolution X-Ray Spectroscopy

An X-ray spectrum from an astrophysical object provides excellent quantitative information about the emitting source and any absorbing plasmas

along the line of sight. The flux in a given emission line depends on the microphysical conditions in the plasma, such as the temperature and electron density, that determine the fraction of ions in each excited state, the rates of excitation and de-excitation, and the energy level populations. The shape, observed energy, and orbital phase-dependence of the spectral line depend on global properties such as the velocity distribution and geometry of the plasma. Quantitative analysis of the discrete spectral features can therefore be used to measure and map the conditions in these plasmas. In this section we will describe some of the spectroscopic diagnostics relevant to X-ray sources and the instrument resolving powers necessary to access them.

## 2.1 Ionization Mechanism

One of the most basic spectroscopic questions is the mechanism by which the plasma is ionized. The coronae of stars, the shocked gas of old supernova remnants, and even intracluster gas are collisionally ionized. The ions are mechanically heated by direct interactions with the surrounding free electrons, and they cool radiatively through bremsstrahlung emission, recombination, and line emission. The spectrum of a plasma in collisional ionization equilibrium (CIE) is essentially determined by the temperature of the plasma, which dictates the strengths of the line emission through the rates of excitation and recombination. The temperature of a CIE plasma is comparable to the ionization potential for observed ions. X-ray emission can therefore be observed from collisionally ionized plasmas with temperatures of  $0.1 \leq k_B T \leq 10$  keV. A second method of ionization is photoionization where the material is ionized by the absorption of photons from an external radiation field, and it cools by radiative recombination and electron cascade. The circumstellar material in accretion-powered binaries, stellar winds, and the clouds around active galactic nuclei are examples of photoionized plasmas. For a plasma in photoionization equilibrium (PIE) the emitted spectrum depends both on the plasma temperature and on the shape and intensity of the ionizing source, which determines the rates of ionization. PIE plasmas are characterized by the ionization parameter,  $\xi = L_x/n_e r^2$ , where  $L_x$  is the luminosity of the ionizing source,  $n_e$  is the electron density, and  $r$  is the radial distance to the ionizing source. Since a PIE plasma is highly over-ionized relative to a CIE plasma of the same local electron temperature, X-rays can be observed from photoionized plasmas with much lower temperatures. Excellent reviews of the physics of collisionally ionized and photoionized plasmas can be found in *Mewe* [4] and *Liedahl* [5] respectively.

There are many spectroscopic differences between collisionally ionized and photoionized plasmas, and it is fairly straightforward to distinguish them (Fig. 1). The simplest diagnostic is the presence of radiative recombination continua (RRC) features. When electrons with a Maxwellian distribution recombine onto an ion, photons with energies of  $\chi + k_B T$  are emitted, where  $\chi$  is the ionization potential. In photoionized plasmas the temperatures are

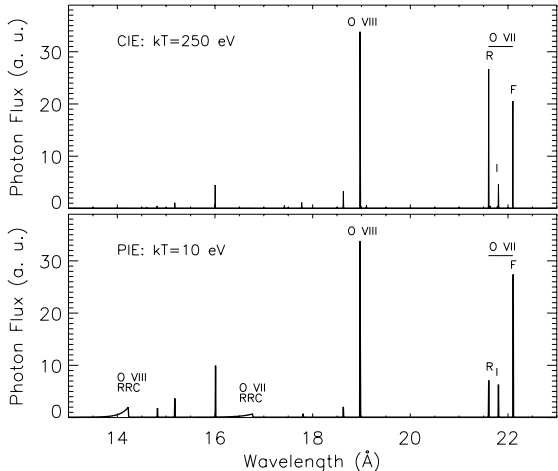


**Fig. 1.** Simulated oxygen emission spectra for a collisionally ionized plasma (*top*) and a photoionized plasma (*bottom*). The ratio of the O VII He-like lines and the presence or absence of RRC features are simple diagnostics of the ionization mechanism

lower than the ionization potential so the emitted photons, or RRC features, appear as narrow cusp-like features in the spectrum. In collisionally ionized plasmas, where the temperature is comparable to the ionization parameter, the RRC are too wide to be distinguished from the continuum emission.

Another simple diagnostic is the ratio of lines emitted by He-like ions, the resonance line, the intercombination lines, and the forbidden line. In a collisionally ionized plasma, where the energy levels are populated by direct excitation followed by cascade, the resonance line dominates the observed He-like emission. In a photoionized plasma, where the energy levels are populated by recombination and cascade from higher energy levels, the triplets are preferentially populated. The observed ratio of these lines,  $G = (i + f)/r$ , can be used to distinguish between a collisionally ionized and a photoionized plasma [6].

## 2.2 Temperature Structure

There are multiple spectral diagnostics that can be used to measure the temperature of a plasma. A simple diagnostic in photoionized plasmas comes from the RRCs. The widths of these features is a direct measure of the plasma temperature as  $\Delta E \sim k_B T$ . For collisionally ionized plasmas, the rate of ionization and the rate of recombination both depend on the temperature of the plasma. The ionization balance is therefore a unique function of the plasma temperature. In a photoionized plasma, the rate of ionization depends instead on the incident photon spectrum so the ionization balance is a more

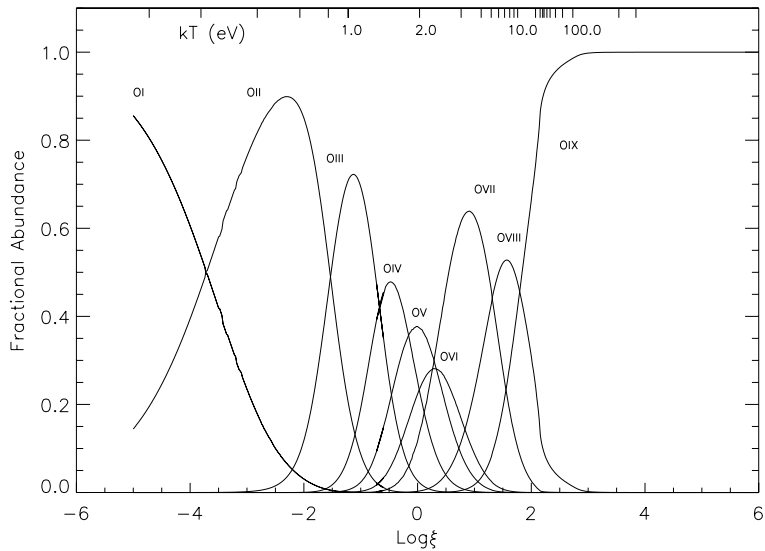


**Fig. 2.** Ionization balance for oxygen in a photoionized plasma ( $\Gamma = 2$ ) where  $\xi = L_x/n_e r^2$  is the ionization parameter. The relationship between the ionization parameter and the plasma temperature has been calculated using the XSTAR program [7]

complicated function. Figure 2 shows the ionization balance for oxygen in a photoionized plasma. The dependence on both temperature and ionization parameter are shown. This diagnostic is especially useful with sources like the cooling flows in clusters of galaxies where iron emission features can be detected from a range of ionization states. Measuring the observed line ratios for the different ions provides an excellent measure of the plasma temperature independent of the elemental abundances.

### 2.3 Density Structure

The ratio of lines in the He-like series depends additionally on the electron density. At sufficiently high electron densities, electron–ion collisions will excite electrons in the upper level of the forbidden transition to the upper level of the intercombination transitions as the rate of excitation becomes comparable to the rate of radiative decay. The line intensity of the intercombination features relative to the forbidden features,  $R = i/f$ , can therefore provide a measure of the electron density [6]. This is illustrated in Fig. 3. For most abundant elements (C, N, O, Ne, Mg, Si, S, and Fe) the critical densities are in the range of  $n_e = 10^8\text{--}10^{14}\text{ cm}^{-3}$ . Unfortunately, UV photons can also photo-excite the same transitions. If the UV flux at the excitation energy is sufficiently high it will compete with or mask the density effects. This can be

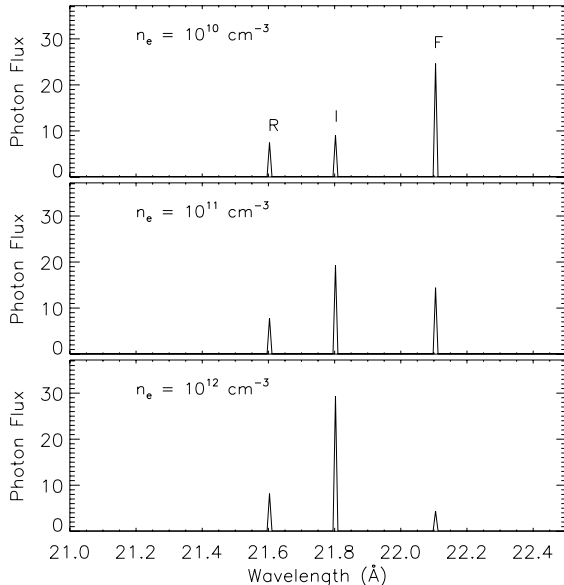


**Fig. 3.** Density diagnostics for the Oxygen He-like series in a  $k_B T = 10 \text{ eV}$  photoionized plasma. The two intercombination lines are not resolved at the resolution of the figure

the case in binary star systems where the photoionized winds from a massive star are illuminated by UV emission.

## 2.4 Velocity Structure

The velocity structure in the absorbing or emitting plasma will affect the shape and centroid of the spectral features. Bulk motion along the line of sight will Doppler-shift the line centroid by  $\Delta E/E_0 = v/c$ , where  $E_0$  is the nominal energy of the line transition and  $v$  is the velocity of the material. Velocity fields within the plasma produce features that appear broadened due to the integrated projected velocity distributions. The line shape is therefore a measure of the velocity fields.

## 2.5 Optical Depth

Material along the line of sight will attenuate the X-ray emission and generate discrete spectral features that are sensitive to the temperature, density and thickness of the absorbing material. The continuum absorption is described by  $F = F_0 e^{-\tau}$ , where  $F_0$  is the initial flux and  $\tau$  is the optical depth. The optical depth for a given ion, is described by  $\tau = n_i \sigma d$  where  $n_i$  is the ion density,  $\sigma$  is the scattering cross section, and  $d$  is the distance traversed. The scattering cross section,  $\sigma$ , decreases with increasing energy as

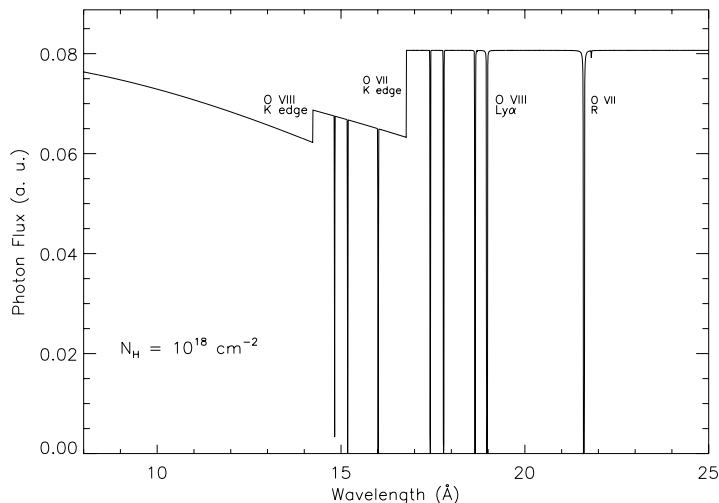


**Fig. 4.** A simplified absorption spectrum of oxygen. The absorption edges as well as the discrete absorption lines are visible

$\sigma(E) \sim \sigma(\chi)(E/\chi)^{-3}$  to produce the familiar edge feature in the continuum spectrum. The cross sections for discrete transitions are orders of magnitude larger than for continuum scattering. Discrete absorption features can therefore be used to probe material with a wide range of optical depths. A simplified absorption spectrum of oxygen is shown in Fig. 4. A plasma with thermal or turbulent velocities will absorb photons with a range of energies around the transition energy to produce absorption features that are broadened as  $\Delta E/E = \sqrt{(2k_B T/m_e c^2)}$  for thermal broadening and  $\Delta E/E = \nu_{\text{turb}}/c$  for turbulent broadening. Absorption spectroscopy is clearly extremely useful in characterizing astrophysical plasmas from the near-neutral material in the interstellar medium to the highly-ionized molecular clouds around active galactic nuclei.

## 2.6 Fluorescence Emission

When an inner-shell electron is ionized, the excited ion will stabilize through radiative decay, which is called fluorescence, or by ejecting an upper-level electron, which is called the Auger effect. The rate of decay by fluorescence emission depends on the energy of the transition and therefore scales with the atomic number as  $Z^4$ . The rate of Auger emission depends on the Coulomb interaction between the electrons and is therefore independent of atomic number. The fluorescence yield, which is the efficiency of fluorescence relative to Auger emission, is therefore low for all abundant elements except iron. Since iron is found in almost all types of astrophysical objects, iron fluorescence spectroscopy is an important diagnostic.

Fluorescence can occur in neutral to highly-ionized ions, so emission lines can be seen from material over a range of temperatures and ionization parameters. The ionization balance in the fluorescence emission can be used to determine the temperature structure in the emitting material. In practice, this is complicated by the fact that in near-neutral ions the inner-shell energy levels are not significantly affected by the screening of the outer electrons. The individual lines can therefore be difficult to distinguish. For example, Fe K $\alpha$  fluorescence emission lines from Fe I, to Fe XV are all within  $\sim 1 \times 10^{-3}$  Å of  $\lambda = 1.940$  Å [8]. Emission lines from more highly ionized iron are more easily separable.

## 2.7 Instrument Requirements

The resolving powers of the instruments limit which spectral diagnostics are accessible. At the most basic level, resolving the charge states of an element in order to measure the ionization balance requires separating the strongest lines, typically those of the H-like and He-like ions. The spacing between these lines scales with the atomic number roughly as  $\Delta E \sim 10Z$  and the line energies scale as  $E \sim 10Z^2$  [9] so a resolving power of  $\mathcal{R} = E/\Delta E \geq Z$  is required to separate these features. Measuring the plasma density requires separating the intercombination lines from the forbidden line in the He-like ions. The energy separation between these lines scales as  $\Delta E \sim 0.3Z^{4/3}$  [9] so resolving powers of  $\mathcal{R} \geq 14(Z - 1)$  are required. Measuring the width of an RRC in order to determine the temperature of a photoionized plasma requires a resolving power of  $\mathcal{R} \geq \chi/k_B T$ . Measuring Doppler shifts requires resolving powers of  $\mathcal{R} \geq c/v$  while measuring velocity widths requires resolving powers of  $\mathcal{R} \geq \sqrt{2}c/v$ . The resolving powers required for these spectroscopic diagnostics are summarized in Fig. 5. An excellent review of spectroscopic diagnostics, and the required instrumental resolving powers is given in Paerels [10]. In designing new spectrometers, or evaluating the usefulness of possible instrumentation, these resolution requirements must be taken into account.

## 3 Instrumentation for X-Ray Spectroscopy

X-ray spectrometers can be divided into two general categories, dispersive and non-dispersive. Dispersive spectrometers exploit the wave properties of light; they measure the wavelength of photons by deflection as they interact with discrete, periodic structures such as crystals or diffraction gratings. Non-dispersive spectrometers exploit the particle nature of photons; they convert photons into electrons, as in the case of proportional counters or charge coupled devices (CCDs), or into heat, as in the case of microcalorimeters. Dispersive and non-dispersive spectrometers have different strengths and limitations. Historically, non-dispersive spectrometers have been flown because of their efficiency, but their resolving powers are low. The recently launched

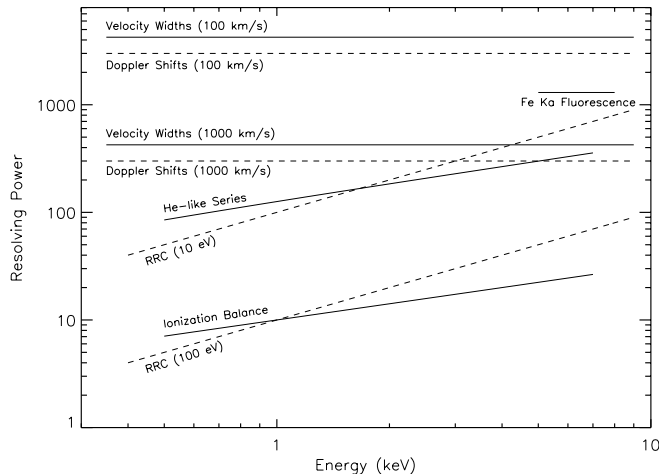


**Fig. 5.** Resolving power as a function of energy for the spectroscopic diagnostics described in Sect. 2

high-resolution instruments on both the *Chandra* and *XMM-Newton* observatories are dispersive spectrometers. Low temperature detectors offer the possibility of high-resolution in a non-dispersive spectrometer. In this section we will discuss these different types of instruments and describe the current applications of each.

### 3.1 Dispersive Spectrometers

Dispersive spectrometers operate on the principle of diffraction. The resolving power depends directly on the magnitude of the dispersion, which in turn depends on the spacing of the dispersive elements. In crystal spectrometers these elements are the lattice spacing of the crystals. In diffraction grating spectrometers the dispersive elements are the periodic grooves that are manufactured on or through a grating. Dispersive spectrometers require a narrow incident beam, since the angular width of the incident beam determines the blur in the dispersed beam that degrades the resolution of the instrument. Any spatial extent in the X-ray source also decreases the instrument resolving power. For most dispersive spectrometers, the resolution is nearly constant in wavelength. The resolving power therefore increases with increasing wavelength or decreasing energy. Dispersive spectrometers are optimal for soft X-ray point sources. Past high-resolution spectrometers have mostly employed transmission gratings and crystal spectrometers. These were successfully flown on the *EXOSAT* and *Einstein* Observatories [11, 12]. Transmission gratings are also used for the high-resolution spectrometers on-board *Chandra*. The *XMM-Newton* high-resolution spectrometer uses reflection gratings.

These two new high-resolution spectrometer are described in more detail below.

### 3.1.1 Chandra

The *Chandra* Observatory was launched in July 1999. It carries a high angular resolution telescope designed for arcsecond X-ray imaging. Two rings of transmission gratings are mounted on hinges that can be alternately rotated into the optical path behind the telescopes to create the High-Energy Transmission Grating Spectrometer (HETGS) [13] and the Low-Energy Transmission Grating Spectrometer (LETGS) [14]. These gratings intercept the focused X-ray beam and diffract the photons according to the equation,  $m\lambda = d(\sin \theta - \sin \chi)$  where  $m$  is the spectral order,  $d$  is the grating line spacing, and  $\theta$  and  $\chi$  are the incident and diffraction angles relative to the grating normal. The dispersed light is imaged at the focal plane by either the Advanced CCD Imaging Spectrometer (ACIS [15]) or the High Resolution Camera microchannel plate (HRC [16]). The intrinsic energy resolution of these focal plane detectors is used to separate the spatially overlapping spectral orders. The HETGS is composed of two types of grating elements, the High Energy Grating (HEG) and the Medium Energy Grating (MEG) that are spatially offset to form a shallow ‘X’ on the focal plane. The HEG has a wavelength resolution of  $\Delta\lambda_{\text{FWHM}} \sim 0.012 \text{ \AA}$ . It is optimized for the 1.2–15 Å band. The Medium Energy Grating (MEG) has a wavelength resolution of  $\Delta\lambda_{\text{FWHM}} \sim 0.023 \text{ \AA}$ . It extends the HETGS coverage to  $\sim 30 \text{ \AA}$ . The LETGS contains more widely spaced grating elements with a wavelength resolution of  $\Delta\lambda_{\text{FWHM}} \sim 0.05 \text{ \AA}$ . It is designed to cover the 1.2–175 Å wavelength band. The resolving power and the effective area of these instruments is shown in Fig. 6. The *Chandra* grating spectrometers provide extraordinary spectral resolution for bright point sources in the soft X-ray band. Spatially extended sources with angular extents of  $\Delta\theta = 1 \text{ arcs}$  degrade the instrument resolving power by a factor of  $\sim 3$ .

### 3.1.2 XMM-Newton

The *XMM-Newton* observatory, launched in December 1999, contains the Reflection Grating Spectrometer (RGS) [17], a high resolution dispersive spectrometer. The telescopes on the *XMM-Newton* are optimized for throughput and not angular resolution. The wide angular resolution ( $\Delta\theta \sim 15 \text{ arcs}$ ) of the *XMM-Newton* precludes the use of transmission gratings. Instead, the high-resolution RGS spectrometer employs reflection gratings. These disperse light according to  $m\lambda = d(\cos \beta - \cos \alpha)$ , where  $\alpha$  and  $\beta$  are the incident and dispersion angles with respect to the grating surface. For a telescope with an intrinsic angular resolution of  $\Delta\alpha$ , the grating resolving power is  $\mathcal{R} = (\cos \beta - \cos \alpha)/(\sin \alpha \Delta\alpha)$ . By going to grazing angles, the resolving

powers can be made large. There are two RGSs on-board the spacecraft. In each an array of 180 reflection gratings is permanently mounted to intercept the focused light emerging from the telescope mirrors. The gratings intercept approximately half the emerging light and disperse it onto offset arrays of CCDs. The remaining photons pass through the empty spaces in the grating arrays onto the European Photon Imaging Camera (EPIC [18]) for simultaneous broad-band imaging spectroscopy. The RGS has a wavelength resolution of  $\Delta\lambda_{\text{FWHM}} \sim 0.06 \text{ \AA}$  over the wavelength band of 5–35 Å. The properties of the RGS are shown in Fig. 6. The RGS provides high collecting areas and high resolving powers in the soft X-ray band making it ideal for studying lower flux sources. Because the resolving power depends less on the width of the telescope beam, sources with small spatial extents ( $\Delta\alpha \leq 0.5 \text{ arcmin}$ ) can still be studied without a significant reduction in the spectral resolution.

### 3.2 Non-Dispersive Spectrometers

Dispersive spectrometers have revolutionized the spectroscopy of point sources such as stars, X-ray binaries, and many active galactic nuclei, but high-resolution spectroscopy of most extended sources, such as supernova remnants and clusters of galaxies, and of high-energy spectral features has been very difficult. The HETGS spectrometer on *Chandra* covers the high energy band to 10 keV, but the resolving power degrades to  $\mathcal{R} \sim 100$  making quantitative spectroscopy difficult at high energies. The RGS on *XMM-Newton* has been used to measure spectral parameters of moderately extended sources. However using current dispersive spectrometers for extended sources is problematic at best and requires complex global modeling. Non-dispersive spectrometers are needed to obtain unambiguous diagnostic information for both extended sources and the high energy band above 2 keV.

Non-dispersive spectrometers operate by absorbing individual photons and converting their energy into recordable quantities, such as electrons or heat. The simplest non-dispersive spectrometers are gas-filled proportional counters. Incident photons ionize the absorbing gas, and cause cascades of electrons. The total number of freed electrons is proportional to the energy of the incident photon as  $N = E/W$ , where  $W$ , the work function, is equal to the ionization energy of the gas, typically  $\sim 30 \text{ eV}$ . This electron signal is then amplified, either by electronic bias or by gas scintillation and then read out as a pulse. The energy resolution of proportional counters depends on the statistical fluctuations in the number of electrons as well as the properties of the amplifying avalanche. The limit of a traditional proportional counter is  $\mathcal{R} \sim E^{1/2}$ . Gas scintillation proportional counters have 2 to 3 times better resolving powers because of the scintillation signal amplification. Proportional counters are the “work horses” of X-ray astronomy. They have flown repeatedly in X-ray missions beginning with the earliest extra-solar X-ray detector [1], through to currently orbiting observatories such as the Proportional Counter Array (PCA) on the *Rossi X-ray Timing Experiment (RXTE)* [19].

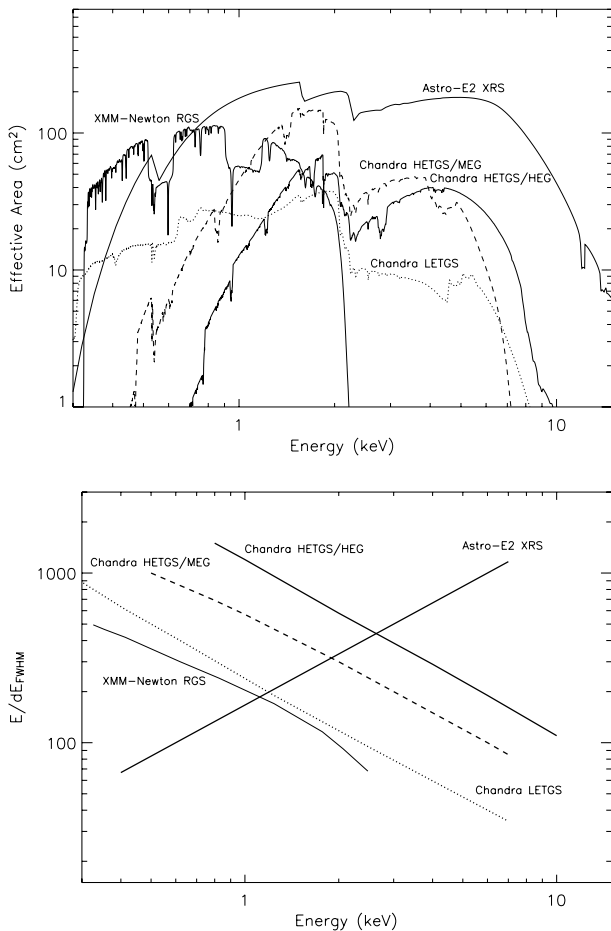


**Fig. 6.** The resolving power and effective area of the high-resolution spectrometers on-board the *Chandra*, *XMM-Newton*, and the *Astro-E2* Observatories. The values are plotted for the standard configurations of each instrument, and spectral order  $m = \pm 1$  for the *Chandra* gratings and  $m = -1$  for the *XMM-Newton* gratings

The development of solid-state spectrometers, and particularly charge coupled devices (CCDs) has significantly advanced non-dispersive spectroscopy. A CCD consists of a doped semiconducting material, usually silicon. When a photon is absorbed, freed electrons jump from the valance to the conduction band. The band gap for a solid state device is typically  $\sim 3$  eV so many more electrons are freed than in a proportional counter. A gate structure traps the ionized charge in localized “pixels” until it is electrically transferred off the silicon chip in a serial electronic readout. The energy resolution of a CCD is much higher than a proportional counter because of the smaller work function, the large charge collection and transfer efficiency, and

the development of low noise readout electronics. CCDs can have resolving powers of up to  $\mathcal{R} \sim 50$ . Although the spectral resolution is much lower than that of current dispersive spectrometers, the pixelation of CCDs (typically  $\sim 24\text{ }\mu\text{m}$ ) allows them to be used for imaging spectroscopy. X-ray CCDs were first flown on *ASCA* [20]. The *ASCA* detectors provided spectral imaging of a wide range of objects with sufficient resolution to uniquely identify bright emission and absorption features. X-ray CCDs are currently used on the *Chandra* X-ray Observatory as the Advanced CCD Imaging Spectrometer (ACIS [15]) and on the *XMM-Newton* Observatory as the European Photon Imaging Cameras (EPIC [18, 21]). X-ray CCDs have provided extraordinary X-ray images of the sky and within the limits of the spectral resolution, compelling imaging spectroscopy.

Since the energy resolution of non-dispersive spectrometers is roughly constant or increasing with energy, the resolving powers increase with increasing energy. The energy resolution is independent of source size making them ideal for studying spatially extended sources. However, in spite of these properties, the best CCD spectrometers still cannot compete with the spectral resolution of dispersive spectrometers.

### 3.3 The Niche for Low Temperature Detectors

Low temperature detectors (LTDs) have the potential to provide both high-resolution spectroscopy and imaging capabilities in the same instrument. An LTD array is intrinsically an imaging device, since the location of the X-ray in the focal plane is uniquely determined. Resolving powers of  $\mathcal{R} \sim 500$  to 2000 have been demonstrated over a broad energy band of 1 to 10 keV. An LTD is therefore a spatial-spectral imaging detector where every pixel in the focal plane array gives a complete high-resolution spectrum of the source. LTD instruments are non-dispersive. As such they provide resolving powers that are independent of the angular extent of the source. LTDs can therefore observe spatially extended objects with the same spectral resolution as point sources.

LTDs have additional benefits. Since they are not integrating detectors, they convey precise timing information for each photon, with high “pile-up” limits. LTDs can therefore be used for precision spectroscopy of rapidly varying sources such as X-ray binaries. LTDs are also broad-band spectrometers. They can be tuned to cover almost any spectral range from optical to gamma-ray energies with some tradeoff in the resolving power as the energy band is expanded. Most X-ray LTDs easily cover the full band from 0.1 to 10 keV with a single instrument. Finally, LTDs are very efficient photon detectors. The quantum efficiency is limited at energies below 1 keV by the infra-red blocking filters, and at the high energy end by the absorption cross sections of the absorbing material. However, across most of the 0.1 to 10 keV band the quantum efficiency is near unity.

Ultimately, LTDs are inherently complementary to the existing X-ray spectrometers. The energy resolution of the HETGS on *Chandra* is  $\Delta E_{\text{FWHM}} = 0.6 \text{ eV}$  at the He-like oxygen lines. This is an order of magnitude better than most LTDs at the same energy. The EPIC/MOS CCDs on *XMM-Newton* have 2.5 megapixels, each with spectral resolving power of  $\mathcal{R} \sim 50$ . LTDs are at least a decade away from achieving arrays of this scale. Although they cannot compete in either of these regions of phase space, LTDs uniquely offer high resolving powers at energies above 2 keV and the possibility for simultaneous high-resolution imaging spectroscopy of all types of astrophysical sources regardless of spatial extent. An ideal observatory would contain a full complement of instruments: a large field of view CCD imager, a high resolution dispersive spectrometer covering the region below 1 keV, and an LTD instrument with broad dynamic range, high resolving power, and precision timing. In fact most future X-ray observatories, including *Astro-E2*, *NeXT*, *XEUS* and *Constellation-X* will employ a mix of these instruments. As the next sections will describe, LTDs have a great deal to offer future X-ray observatories.

## 4 Ground Rules for Low Temperature Detectors in X-Ray Astronomy

X-ray astronomy fundamentally requires space-based instruments since the earth's atmosphere is opaque to all but the highest energy X-rays. While high altitude balloons allow access to X-rays with energies in excess of 20 keV, the rest of the X-ray band (0.1–10 keV) is completely inaccessible below about 100 km altitude. The lower energy band below 10 keV contains all the emission lines from the abundant astrophysical elements, and thus many of the diagnostic spectral features that motivate X-ray observations. X-ray observatories must therefore operate in space.

The ground rules for making LTDs usable for X-ray astronomy constrain how the instrument must be packaged for an orbiting observatory or suborbital rocket. This generally means that the instruments need to be compact, low-power and stable against launch vibration. The instrument must also be robust for long term operation in a space environment. The spaceflight requirements for LTD instruments affect everything from the cryogenic cooling to the room temperature electronics. In this section we will review these restrictions, how they affect the design of X-ray LTD instruments, and some of the methods used to overcome these obstacles.

### 4.1 Cryogenics

Most non-dispersive, high-resolution, X-ray detector systems, including microcalorimeters based on silicon, transition-edge, and magnetic thermistors,

operate at relatively low temperatures, usually below 0.1 K. Cryogenic systems on satellites have a long history and are typically complex, bulky, and expensive. The need for a sophisticated system to cool below 0.1 K drives a large part of the size and cost of an X-ray LTD instrument.

#### 4.1.1 Adiabatic Demagnetization Refrigerators

Temperatures below 0.1 K have been readily achieved on the ground for almost 80 years, first using Adiabatic Demagnetization Refrigerators (ADRs) and then with closed-cycle systems, such as dilution refrigerators. In addition, it has been possible for over 40 years to commercially purchase ADRs and dilution refrigerators for laboratory use. Starting in the mid-1960s, large commercial dilution refrigerators supplanted the adiabatic demagnetization refrigerator with the widespread availability of  $^3\text{He}$ . This is largely due to the much higher cooling capacity, continuous operation, and lower base temperatures that can be achieved with a dilution refrigerator. The move to space-borne instruments, however, limits the cooling options to what can be achieved in a fully-automated, zero-gravity, low-power system. The standard  $^3\text{He}$  recirculating dilution refrigerator with its large pumps and gas handling systems, and its reliance on gravity to maintain the phase separated region in the mixing chamber, is a poor match for spaceflight. Although substantial progress has been made in adapting the dilution refrigerator for space [22], all current and planned cryogenic X-ray missions use an ADR as the lowest temperature stage.

An ADR is basically an entropy pump and operates by cycling in the  $S, T$  (entropy, temperature) plane using an external magnetic field applied to a dilute spin system. The spin system can be made very dilute by using a heavily hydrated paramagnetic salt such as Ferric Ammonium Alum (FAA,  $\text{FeNH}_4(\text{SO}_4)_2 \cdot 12\text{H}_2\text{O}$ ). For FAA the entire magnetic moment of the molecule is in the 4d unpaired electron in the single iron atom. The rest of the material, including the 12 waters of hydration, simply serves to keep the dipoles far apart, suppressing the ordering temperature to below 30 mK and making it useful for magnetic cooling. A good introduction to ADRs can be found in Lounasmaa [23] and ADRs for spaceflight in Serlemitsos et al. [24].

The original ADRs used from the 1930s to the mid 1960s used bulky external water cooled magnets to cool very small magnetic samples suspended on silk threads in glass cryostats. At about the same time that ADRs were being replaced in the laboratory with dilution refrigerators, the key to modern and spaceflight ADRs, the compact, high-field superconducting magnet, was also becoming widely available. An ADR with a superconducting magnet turns out to be an excellent match for space cryogenic detectors; it requires no gas recirculation, no gravity, and is a fully solid-state system with no moving parts. It does, however, require a high current magnet and, in some cases, as in TES or magnetic microcalorimeters, a large amount of magnetic shielding. Unfortunately, the ADR, especially in a single stage design, also has

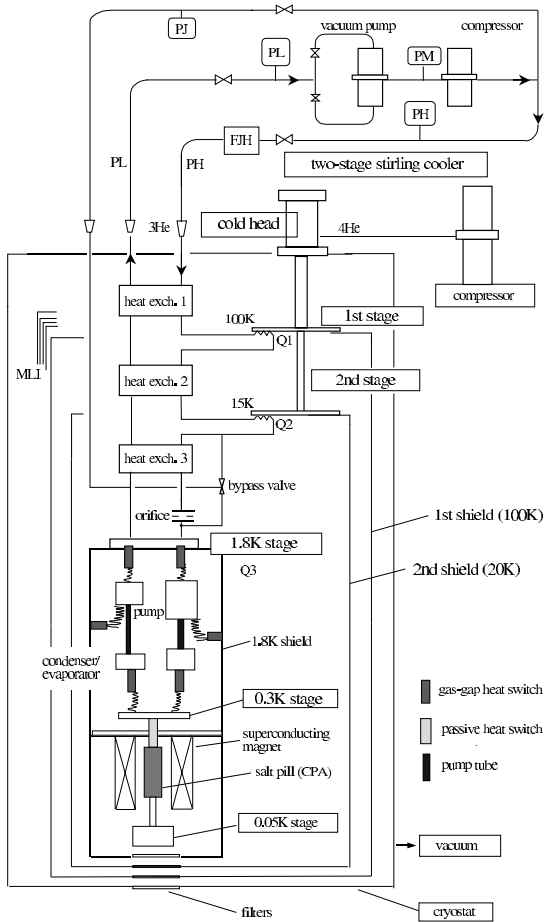
relatively low cooling power, typically a few microwatts, so careful cryogenic design is required. The first spaceflight ADRs have already been produced for the XQC and XRS instruments that are described in Sect. 6.

#### 4.1.2 Cryogens, Cryo-coolers, and Lifetime

In addition to the complex low temperature refrigerator, lifetime is the single biggest hurdle for cryogenic X-ray instruments in space. ADRs require a precooling stage as low as 1K to remove the cyclical heat of magnetization, to minimize radiative heating, and to intercept conductive heat on the ADR suspension system and wiring layer. The current X-ray LTD instruments use liquid cryogens as the precooling stage. The cryogen lifetime is limited, however, by the thermal conductance of the dewar structure, wiring, and dissipation due to the ADR and the detector system. Orbiting instruments generally must be launched with their entire stock of cryogens. When the cryogens are exhausted, the instrument ceases to function. Thus the lifetime of the instrument is limited by the mass and volume allocation for the instrument on the observatory. For reasonable lifetimes of a year or more, the instruments tend to be bulky and dominate the mass and volume budgets of the observatory.

One way of achieving a relatively long lifetime is to simply launch a large quantity of liquid helium. This was the approach used on *COBE* which included a massive 660 liter superfluid helium cryostat with a lifetime of about 10 months. Clearly, scaling the *COBE* system for a multi-year lifetime quickly becomes intractable. Another method is to use a fully closed-cycle mechanical refrigeration system such as that planned for *Constellation-X*. The lifetime of a mechanical system is only limited by the robustness of the mechanical cooler, and not by the consumption of any stored resource. Between these two extremes there is a large phase space for hybrid systems, such as that employed by the XRS instrument on *Astro-E2*. The XRS uses a three stage precooling system for the ADR including a cryo-cooler, a 120 liter solid neon cryogen tank, and a 32 l superfluid helium cryogen tank. A multistage cryogenic system allows for a much smaller cryostat than the *COBE* system for a longer lifetime.

Multi-stage cryogenic systems can give a long instrument lifetime. The XRS instrument, for example, achieves a lifetime of over three years on only 32 l of helium. However, at over 400 kg, the instrument dominates the *Astro-E2* spacecraft. This limits our ability to form partnerships on small-scale missions. In order to reduce the instrument's footprint we must minimize the use of heavy cryogens and move to cryogen-free, mechanical cooler based cryostats. The baseline for most future missions is a cryogen free design using some combination of mechanical cryo-coolers (Stirling, pulse-tube, etc...), sorption coolers, Joule–Thomson coolers, He-3 sorption coolers, and finally a one or more stage ADR. The exact mix of these components varies from mission to mission, and none of the instrument designs has yet been frozen.



Note: 100K shield and 20K shield are cooled by another two stirling coolers.

**Fig. 7.** A preliminary schematic design of the cryogen-free LTD instrument for the Japanese *NeXT* mission. The entire system weighs only 134 kg and its lifetime is only limited by the robustness of the coolers [28]

As an example, a preliminary cryogen-free design for the *NeXT* X-ray observatory is shown in Fig. 7. The design space for cryogenic systems thus seems large but there are also large constraints including the maturity of the technologies. Ultimately, a cryogen free, low power, low mass design is required if LTDs are to move from highly specialized, one-of-a-kind instruments that dominate a spacecraft to a ubiquitous system that is a ready choice for multi-instrument spacecraft. X-ray LTDs would then be an option not only for X-ray astronomy, but also for space plasma physics, and even possibly X-ray microanalysis instruments on future planetary landers.

## 4.2 Mass and Power

A spaceflight cryogenic X-ray instrument has serious mass and power constraints. For example, the M-V launch vehicle for the *Astro-E2* spacecraft has a launch capability of about 1800 kg to low earth orbit. The XRS instrument, not including its electronics and focusing optics, weighs over 400 kg. In comparison, the Pegasus launch vehicle used in NASA's small-explorer (SME) program, has a capability of about 400 kg into a 475 km circular orbit. Clearly LTD instruments are tightly mass constrained, and at least in their current form, incompatible with some launch opportunities.

The power budget of the spacecraft is similarly constrained. Spacecraft power is limited of course by the size of the solar panels, but also the significant mass of the batteries that operate the spacecraft when the sun is eclipsed. For example, the *Astro-E2* observatory has a total power budget of about 660 W for a power system that weighs a total of 147 kg. On a large multi-experiment observatory, an LTD instrument can only consume a small fraction of the available resources. The XRS instrument, for example, uses a total average power of 64 W and a peak power of 120 W during operation.

Large reductions in mass are possible but usually result in substantial increases in instrument power for cryogenic systems. The move to fully cryo-cooler based designs substantially increases the power consumption of the cryogenic instrument and also requires the addition of a radiator to dump the waste heat from the instrument. These added complexities, however, substantially shrink the mass of the instrument. The addition of the cryo-cooler to the XRS instrument consumes 35 W but lengthens the hold time of the solid Ne by 50%, a potential mass savings of 85 kg of Ne, not including the additional mass of the cryostat structure. The added mass of the XRS cooler is only 4.2 kg. Hybrid designs for a proposed SME X-ray mission have achieved predicted lifetimes of 2 years in less than 110 kg using a hybrid pulse-tube cooler/Ne/He/ADR design. *Constellation-X*, *XEUS*, and *NeXT* plan to go yet further, with totally cryogen-free designs. The *Constellation-X* requirement is for at least a 5 yr lifetime in under 100 kg with no consumables.

The cost for all of this savings in mass is power and efficiency. The cryo-coolers do not achieve even close to Carnot efficiency and this magnifies the problem. The efficiency of a Carnot cycle refrigerator is

$$\eta = \frac{T_1}{T_2 - T_1}, \quad (1)$$

where  $T_1$  is the base temperature and  $T_2$  is the higher reject temperature. Real systems achieve far less. The small (4.2 kg) *Astro-E2* cryo-cooler manufactured by Sumitomo Heavy Industries achieves about 8% of Carnot efficiency, giving 1 W of cooling power down to 80 K for a 35 W input. The lower temperature coolers planned for future missions do even worse. One design for *NeXT* would have 5 mW at 1.7 K for 180 W input giving about 0.5% of Carnot. Note, however that the 5 mW is about a factor of five more cooling

power than on the *Astro-E2* helium tank and with a lifetime only limited by the robustness of the cooler. The 1.7K cooler for *NeXT* has the additional advantage of only requiring a very simple single stage ADR. In this case one can trade power against the complexity of the lowest temperature stage. The *Constellation-X* baseline design includes only a 6K lowest temperature cryo-cooler stage requiring a complex 5 stage ADR and a custom high-temperature magnet system.

Finally, cryogenic X-ray detectors have relatively power-hungry electronics. Unlike integrating detectors, cryogenic X-ray instruments must process the entire X-ray pulse time-series, one event at a time. In addition, to achieve the highest resolution we must use a matched (optimal) filter. The optimal filter gives a 40% increase in the resolving power over using a shaping amplifier and a peak-hold-sample system such as is often used in nuclear instrumentation [25]. However, in order to calculate and then apply the optimal filter, one must process the entire X-ray event waveform using on-board processing. This requires fast digitizers, fast digital signal processors (DSPs), and a fair amount of on-board memory. On the XRS, the digital pulse processing electronics consumes about 25 W of peak power for 32 detector channels using a discrete DSP for each channel. Obviously this sort of system does not scale well to very large arrays.

### 4.3 Survivability: Mechanical Design and Analysis, Radiation Damage

A key requirement for space-based detector systems is, of course, survivability. The instruments must be tested and qualified to the maximum vibration loads expected during launch. The XRS on *Astro-E2* was tested to static loads of 25 g axial, and 9 g lateral, and random loads of 9  $g_{\text{rms}}$  axial and 3  $g_{\text{rms}}$  lateral. Sounding rocket experiments are tested to random vibration levels of 13  $g_{\text{rms}}$  and must, in addition, contend with the landing shocks of up to 200 g. This puts a heavy structural burden on cryogenic detector systems which must also require a great deal of internal thermal isolation.

Clearly, the spaceflight environment severely affects the design space for LTD instruments. The soft, cantilevered suspension systems that are adequate for laboratory cryostats are not acceptable for spaceflight. The instrument must be designed with careful staging of the resonant frequencies in the cryostat so that vibration on the outer shell of the instrument does not pump energy into high-Q resonances on the inner parts of the instrument including the detector system. For example, the XQC sounding rocket instrument sits on vibration isolation mounts that attach it to the rocket shell with a resonant frequency of about 30 Hz. The re-entrant shell He tank suspension has a resonant frequency of 130 Hz, and the tensioned ADR+detector system has a resonant frequency of 450 Hz [26]. This staged-resonance system results in a factor of almost 1000 isolation of the detector stage from rocket vibrations.

In addition, the detectors themselves have to be designed with resonant frequencies staged yet higher than the detector heat sink, typically in excess of 1 kHz. This is not a trivial task because the pixel suspension for microcalorimeters must also provide their thermal isolation. For XRS, the detector heat sink has a resonant frequency of about 350 Hz. The XRS detectors were then designed to have their first resonant mode at over 2 kHz [27]. As an added complication, the detector suspension has to be designed so that the static stress from differential thermal contraction is well below the yield strength of the materials.

The staged resonances necessary for survivability during launch also must serve to isolate the detector system from microphonic noise from spacecraft systems such as momentum wheels, and cryo-coolers. In the laboratory, detector systems are isolated from environmental vibration using soft damping systems. This becomes much more difficult on a spacecraft since soft damping systems would have to be locked during launch. In addition, a soft damping system would have to be carefully designed to avoid alignment errors with the X-ray focusing optics. Thus, space-borne detector systems must rely almost exclusively on the staged resonance system for isolation from microphonic interference to the detector signal.

Radiation damage is also a significant problem in space. The environment in near earth orbit is somewhat protected by the earth's magnetosphere, but the particle background is still considerable. Once beyond the magnetosphere, such as the 2nd Lagrange point (L2) orbit planned for *Constellation-X*, the observatory will receive the full force of the solar wind. Small-gate electronic components are heavily susceptible to damage from particle interactions. This limits the choice of components that are usable for an LTD instrument. The fast modern processors that one might use in the laboratory for event processing, are almost certainly not available in a radiation-hard version suitable for spaceflight. In addition, detector system components such as SQUIDs and the detectors themselves must be tested for radiation damage including long term effects such as activation. A full radiation analysis is usually required for a spaceflight instrument including radiation testing of all components. This issue must be confronted during the development of the detector system and not solely when it is adapted for spaceflight.

#### 4.4 Electronics

The electronic readout and analysis systems for LTD instruments are also heavily constrained in space. The electronics for LTD instruments typically consist of a cryogenic amplifier, a room temperature amplifier, a digital event processing system, an ADR controller, and possibly a cryo-cooler controller. As we have discussed these must conform to the mass and power constraints for a spaceborne observatory. In addition, low telemetry rates mean almost all event processing must occur on the spacecraft. All the electronics necessary

for an LTD instrument must be small, low power, and have low data rates commensurate with the finite telemetry bandwidth on a satellite observatory.

The electronic readout system for cryogenic detectors can vary considerably from field effect transistor (FET) front end amplifiers for silicon microcalorimeters, to superconducting quantum interference device (SQUID) readout of TES and magnetic microcalorimeters, to tuned oscillators for RF kinetic inductor detectors. There are, however, several commonalities that affect the system design. Once beyond the analog amplification, the digital processing is nearly identical.

The key building blocks for an LTD readout system include:

1. Wiring layer from the detectors to the first stage amplifiers and between the first stage amplifier and any additional cryogenic amplification stages.
2. Cryogenic amplification stages.
3. Cryogenic multiplexer electronics and/or bandpass filters for frequency division multiplexing.
4. Wiring layer to room temperature and staged heat sinks to minimize thermal conduction.
5. Room temperature analog electronics which include additional amplification, and control and feedback electronics for the cryogenic amplifiers.
6. Digital electronics which includes pulse reconstruction from the multiplexer (phase sensitive detection or time reconstruction), triggering, optimal filter generation and application, and event grading.
7. ADR temperature controller, including temperature diagnostics for the whole instrument.
8. Cryo-cooler controller.

There are also a large number of housekeeping functions that must be handled by the on-board electronics including temperature monitoring, noise characterization, detector and cryogenic amplifier diagnostics, and logic to handle off-nominal situations such as keeping the telemetry stream from saturating.

The XRS, for example, performs these tasks with separate analog and digital electronics boxes with a discrete amplifier and pulse processing chain for each pixel. Scaling to 1000+ channels, however, requires a completely different architecture. The wire count from the low temperature amplifiers, and to some extent, the room temperature analog electronics can benefit substantially from using cryogenic multiplexers. One design for *Constellation-X* uses time division multiplexing to read out 32 columns of 32 detectors, reading out the 32 rows in parallel and sampling the 32 columns in a round-robin fashion. This requires controlling and feeding back to only 32 SQUID amplifier chains at a time, growing the room temperature amplifier chain only as the number of Rows  $N$  rather than the number of channels  $N^2$ . The digital electronics, however, benefits from no such scaling.

In a multiplexed design, the digital electronics must, in addition to all of the pulse processing, perform the reconstruction necessary to separate the

multiplexed channels from each other. The digital electronics must reconstruct the data stream time series *per channel* in order to process the event stream. Unfortunately one cannot use a dedicated DSP for each channel as in the XRS because of both power and mass constraints.

A simple scaling of the XRS digital electronics from 32 to 1000 channels brings the peak power requirements to almost 1000 W. This is not possible for a space-borne observatory that may have a total power budget significantly less than this. There are additional issues of size, mass, and the 1000 W of waste heat. A solution is to move the event triggering to specialized logic that *precedes* the event processing. The triggering logic would be responsible for breaking the time series for each channel into an event stream with a channel tag that is then assigned to a free processor in a processor farm. The power for the pulse processing then scales with the *event rate* rather than the *number of channels*. Preliminary designs for *Constellation-X* have shown that it is possible to process  $10^4$  events/s in less than 80 W using 8 processors. When the event rate is low, some of the processors can even be put in a lower power state to further reduce the average power.

Scaling to 1000 channels appears to be an achievable task, especially using a cryogenic multiplexing scheme and a pulse-processing farm at room temperature. A 1000 channel detector system appears possible *in principle* but has not yet been achieved, and there are certainly significant design challenges left to be overcome. Even with these improvements the readout electronics for cryogenic detectors do not scale well making very large detector arrays extremely difficult.

## 4.5 Risk

Lastly we discuss some of the practical rather than technical constraints of using cryogenic detectors in space. Cryogenic detectors and their infrastructure are new and largely untested on space platforms. This is changing, especially with the launch of XRS in mid 2005. However, one must justify the *risk* of using unproven technology and the expense of its full development cost to traditionally conservative technical review panels in order to win approval for new missions. Risk, in the management definition, includes anything that can interfere with the success of the mission from an outright failure of the observatory, launch vehicle, or ground support equipment, to delayed development cycles, and overspent budgets.

In today's risk averse environment proposing new technology can be difficult. Demonstrating low risk must involve full system modeling for both short term instrument survivability as well as the long term viability in space, including effects such as radiation damage. Winning approval for new space instruments requires that these systems issues are addressed up-front, with viable full instrument designs, analysis, and demonstrations. This is at least as important as demonstrating the ultimate performance of the detector system itself. In a head-to-head competition, a low-risk proposal will almost

always win over an instrument with slightly higher performance but also higher perceived risk.

## 5 Current and Near-Term Missions

After almost two decades of development, X-ray LTD instruments are finally becoming a reality. Two such instruments have already been completed, the X-ray Quantum Calorimeter (XQC) sounding rocket, and the X-ray Spectrometer (XRS) on the US-Japanese *Astro-E2* observatory. In addition, there are several ambitious, large-scale observatories, *NeXT*, *Constellation-X*, and *XEUS*, that are currently in the planning stages. All of these missions include an X-ray LTD focal plane instrument.

In this section we describe, in detail, the XQC and XRS instruments as the first generation of X-ray LTD instruments. This includes some of the design parameters and challenges in implementing a cryogenic detector system for spaceflight. In the last section, we briefly discuss the three nearest term LTD missions. The requirements of the next generation missions provide huge challenges for the LTD community. Our success at designing and deploying kilopixel arrays for these new missions will govern whether and how low temperature X-ray detectors are carried into the future.

### 5.1 The X-Ray Quantum Calorimeter: The First LTD X-Ray Mission

#### 5.1.1 Introduction to the XQC

The X-ray Quantum Calorimeter ( XQC), a collaboration between the University of Wisconsin and NASA’s Goddard Space Flight Center, is the first space-borne cryogenic X-ray instrument. It had its maiden flight in December, 1995 and has flown a total of three times on a sub-orbital sounding rocket achieving an altitude of 240 km and a total flight time of about 15 min. Its primary purpose is to study the soft diffuse X-ray emission in the band from 0.03–1 keV with high spectral resolution. The large spatial extent and low surface brightness of the emission makes this a task uniquely suited to an LTD instrument.

The soft, diffuse X-ray background, first observed by proportional-counter based sounding rockets in the 1960’s, is the brightest X-ray object in the sky [29, 30]. The emitting source is currently believed to be a superposition of a number of physical processes including: thermal emission in the galactic halo, thermal emission in a region of nearby diffuse gas in the “local bubble”, charge exchange between the solar wind and geocoronal gas, charge exchange between the solar wind and the interstellar medium, and, thermal emission from the intergalactic medium. However, this is largely supposition since the individual components cannot be uniquely separated using the otherwise

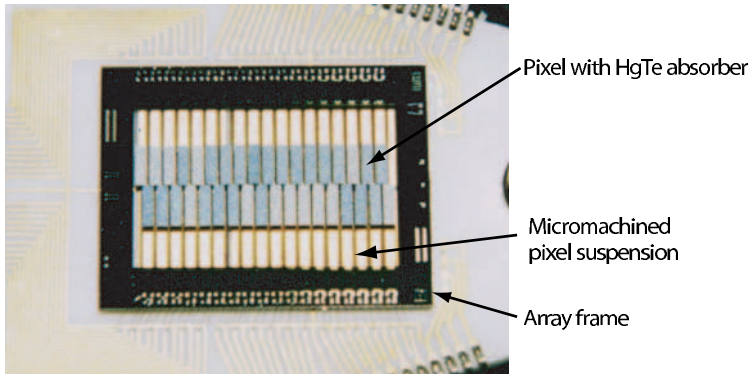


**Fig. 8.** The XQC  $2 \times 18$  microcalorimeter array

exquisite spatial maps compiled by the University of Wisconsin all sky survey [31] and the *ROSAT* all sky survey [32]. Detailed spectroscopy is required in order to break the degeneracy between the various emission mechanisms, to look, for example, for the specific spectral signature for thermal emission as opposed to charge exchange. A good review of the soft X-ray background can be found in *McCammon* and *Sanders* [33].

Although the Diffuse X-ray Spectrometer (DXS) instrument observed regions of the soft X-ray background in the low energy band from 0.15 to 0.284 keV with high resolution ( $\Delta E = 5\text{--}17\text{ eV}$ ), the results were difficult to interpret. This band includes the crowded L-shell emission from many abundant elements including Si, S, Mg, and Ar. Higher resolution is required to deconvolve the blended lines. The XQC experiment is designed to look at the larger spectral band from 0.03 to 1 keV. This contains the much less crowded 0.75 keV spectral band that includes the emission from O VII, O VIII, Ne IX and L-shell Fe as well as the Fe IX, X, XI emission around 70 eV. The XQC is designed to answer fundamental questions on the origin of the soft X-ray background, including the emission mechanism(s) and the composition and state of the emitting material.

### 5.1.2 The XQC Instrument

The XQC is launched on a Nike-Black Brant two stage sounding rocket. This is a short duration suborbital flight giving about 5 min of observing time above 100 km altitude where the atmosphere is thin enough for acceptable X-ray transmission in the low energy band. To acquire reasonable statistics in such a short flight, the XQC has a field of view that covers a full steradian on the sky. There is no spatial information other than the 1 sterad aperture stop. The observation is purely spectroscopic. A full description of the instrument can be found in *McCammon* et al. [34] and *Porter* et al. [35].

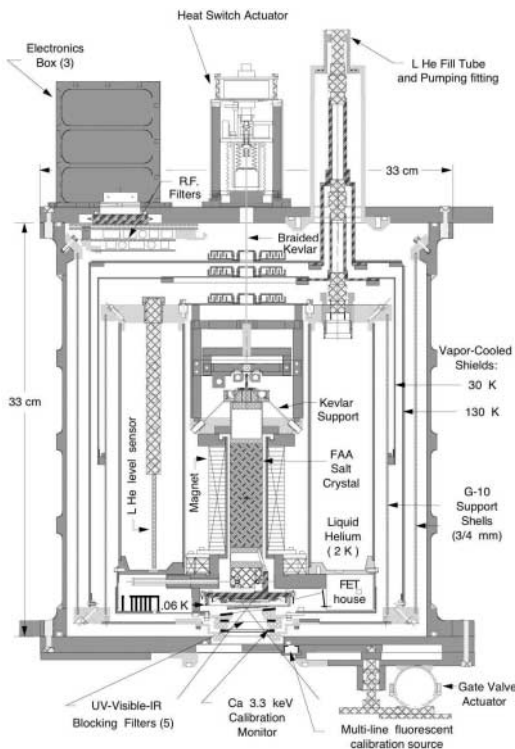


**Fig. 9.** A cross section of the X-ray Quantum Calorimeter (XQC) cryostat showing the helium tank, vapor cooled shields, ADR, and analog electronics. Reprinted from [34]

The XQC detector system is optimized for the largest possible detector area, with a high quantum efficiency only up to 1 keV. The detector consists of a 36 channel  $2 \times 18$  “bilinear” array of microcalorimeter detectors with doped silicon thermistors as shown in Fig. 8. These are large-area pixels compared to most X-ray microcalorimeter instruments, with  $1 \text{ mm}^2$  per pixel. The X-ray absorber is HgTe, a compromise material with a high quantum efficiency, a moderate Debye temperature of about 140 K, and most importantly, a high thermalization efficiency. Since the bandpass of the XQC only extends up to 1 keV, the absorber material is made very thin, around  $0.7 \mu\text{m}$ , deposited by molecular chemical vapor deposition (MoCVD) onto a silicon backing layer. This configuration minimizes the heat capacity of the absorber while supporting the thin absorber material. The absorbers are then epoxied onto silicon spacer blocks attached to the micro-machined, implanted silicon detector array.

The XQC contains all of the sub-systems needed for a long term cryogenic X-ray mission, in miniature form including a small 4 l liquid helium dewar

and a 50 g FAA salt pill in its adiabatic demagnetization refrigerator. The cryostat, shown in cross section in Fig. 9, is a two stage cryogenic system with a pumped volume of  $^4\text{He}$  at 1.6 K and a single stage Ferric Ammonium Alum (FAA) ADR [34]. The XQC uses a 50 g salt pill in a 40 kG NbTi superconducting magnet. The total heat load at the 60 mK operating temperature from radiation, wiring, and the Kevlar suspension system is below 1  $\mu\text{W}$  giving a hold time for the refrigerator of about 12 h on the ground. The four liter liquid helium bath is a single cryogen system with vapor cooled shields and a total parasitic heat load of 98 mW giving a 24 h hold time below 1.6 K. Since the flight time is only 15 minutes this is adequate for both pre-flight testing and for the heat input into the system during launch. The ADR is cycled on the ground about two hours before launch and holds at 60 mK (open loop during launch) until it lands on its parachute at the end of the flight. The XQC was and is a great success in demonstrating the key technologies required for cryogenic X-ray instruments in space.

The XQC electronics do not perform high-resolution pulse processing on the spacecraft. The detector electronics have hardware pulse triggering electronics, and telemeters down the entire waveform for each X-ray pulse for subsequent processing on the ground. This is possible because the XQC includes two 800 kb continuous telemetry channels allowing the X-ray event waveforms to be downlinked in real time. The system also includes a “quick look” system consisting of a shaping amplifier, a peak and hold system, and an ADC to give low resolution (between 15 and 20 eV FWHM) real time spectral information during the flight.

On the ground, the telemetry is received in real time. This allows in-flight monitoring of the quick-look spectral information and over 200 telemetered engineering parameters. Post-flight, the data is then optimally filtered, gain-drift corrected, and an energy scale added to produce an in-flight spectrum. Cosmic ray interactions in the detector are also filtered out to reduce the background signal. Figure 10 shows the final calibration spectrum taken on the ground, immediately preceding a launch in 1999. The preflight spectrum was integrated for 9000 seconds up to 4 minutes before launch with the instrument on the launch rail using an internal  $^{244}\text{Cm}$  alpha fluoresced multi-target X-ray source that produces a number of calibration lines below 1 keV. A  $^{41}\text{Ca}$  internal conversion X-ray source also continuously illuminates the array with 3.3 and 3.6 keV potassium K X-rays on the ground and during flight for gain-drift monitoring.

### 5.1.3 XQC Results and Future Plans

The XQC has flown three times since 1995. The most recent flight in March of 1999 yielded a high quality spectrum of a 1 sterad field of view centered on  $l = 90^\circ$ ,  $b = +60^\circ$  in galactic coordinates. This is a bright area in the soft X-ray sky near the north galactic pole that is otherwise devoid of bright, soft X-ray emitting objects. The instrument had a composite resolution of

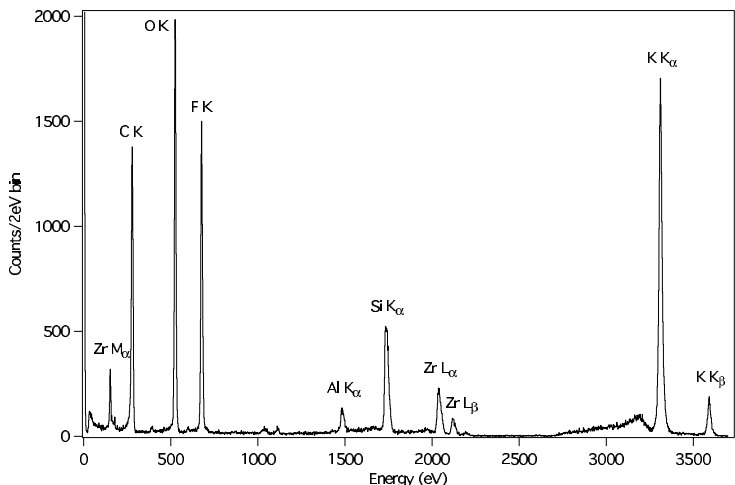


**Fig. 10.** XQC preflight calibration spectrum. The spectrum was integrated for 9000 s up to 4 min before launch with the instrument on the launch rail at White Sands Missile Range. Calibration sources were a  $^{244}\text{Cm}$  alpha fluoresced multi-target source and a  $^{41}\text{Ca}$  internal conversion source

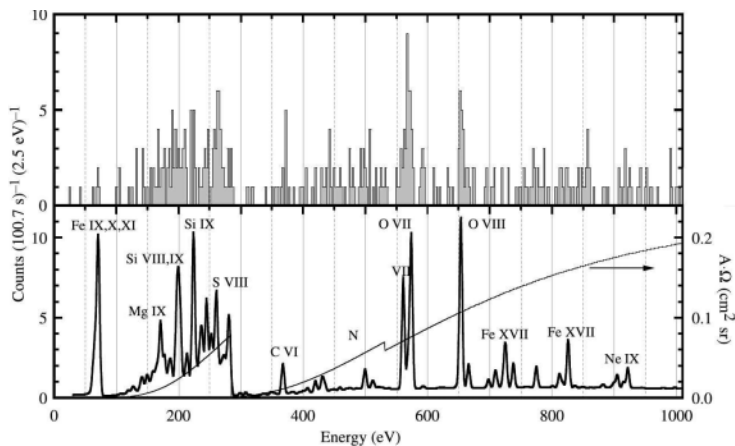


**Fig. 11.** (Top) Spectrum of the soft X-ray sky observed with the XQC instrument in March, 1999. (Bottom) A standard two component thermal model for the soft X-ray background folded through the XQC response function. The XQC throughput function is shown on the bottom panel, right hand axis. Reprinted from McCammon et al. [34]

$\sim 9$  eV across its spectral band. The in-flight spectrum is shown in Fig. 11. Emission lines from O VII, O VIII and C VI are clearly detected. A complete discussion of the results and their implications is contained in [34].

The XQC experiment is limited by the collecting area, even with a 1 sterad field of view. In addition, the 1 sterad field of view washes out the spatial detail shown in the UW and *ROSAT* all sky maps. The collecting area of the array needs to be increased to improve the statistics and to reduce the aperture to increase the spatial information. Higher spectral resolution is also needed, for example, to resolve the He-like oxygen K emission lines, and to look for the emission lines from Fe L-shell transitions which should be present in a 0.3 keV thermal plasma, even if the abundance of iron is largely depleted. The next rocket flight will consist of  $4\text{ mm}^2$  pixels, in a  $6 \times 6$  36 pixel array using the “deep implant” process used successfully for the XRS program. Operating at 50 mK a spectral resolution of less than 4 eV at  $E = 1\text{ keV}$  is expected with four times the collecting area of the current XQC experiment.

The long term solution is to fly a soft X-ray cryogenic detector system on an orbiting platform and to perform an all sky survey with high spectral resolution. In addition to resolving the local components of the soft X-ray background, an observatory of this type could observe the spatial distribution of the hot intergalactic medium which has important implications for cosmology. This has been proposed several times for NASA’s small and medium explorer program and has received high ratings for both the science and the technology readiness but has not yet been selected for flight.

## 5.2 The XRS on Astro-E2

### 5.2.1 Introduction to the XRS

The X-Ray Spectrometer (XRS) is a long term U.S.–Japanese collaboration to put a high-resolution, broad-band, non-dispersive X-ray spectrometer at the disposal of the astrophysics community. The instrument is part of the *Astro-E2* X-ray observatory to be launched in early 2005 on a Japanese M–V launch vehicle. The observatory, in addition to the XRS, contains four wide field CCD cameras, the X-ray Imaging Spectrometer (XIS), with a total of  $800\text{ cm}^2$  collecting area at 1 keV, and the Hard X-ray Detector (HXD) [36], with a bandpass from 10 keV to over 600 keV. Together this observatory will have both spectroscopy and imaging capabilities covering a very large dynamic range from 0.1 keV to 600 keV. The XRS provides high-resolution spectroscopy, the CCD cameras provide wide field imaging, and the HXD provides spectral information to very high energies. The observing program includes both a guaranteed time program and a large guest investigator program for the X-ray astrophysics community from 2005 to at least 2008 when the cryogens of the XRS are exhausted. The observatory will observe every major class of X-ray emitting object including supernova remnants, stellar coronae, active galaxies, galaxy clusters, X-ray binaries, comets, and the interstellar medium in our own and neighboring galaxies. The XRS instrument is the flagship instrument on the *Astro-E2* spacecraft and represents a culmination of the state-of-the-art in cryogenic X-ray instrumentation.

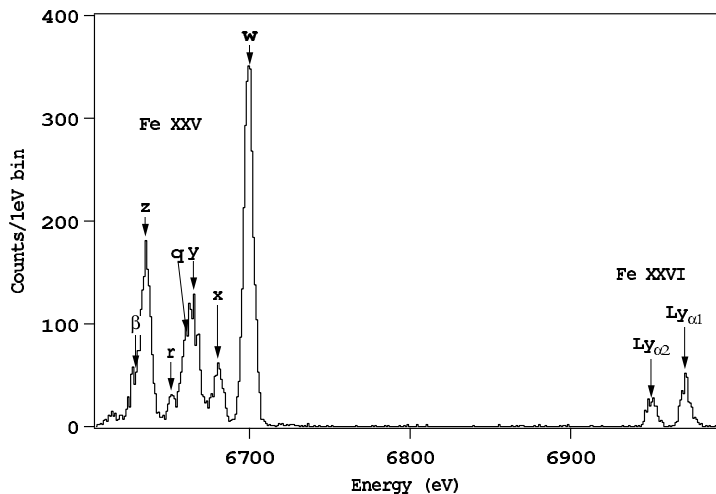


**Fig. 12.** X-ray spectrum of highly ionized He-like Fe XXV and H-like Fe XXVI taken with a laboratory XRS microcalorimeter array at the EBIT-I facility at Lawrence Livermore National Laboratory

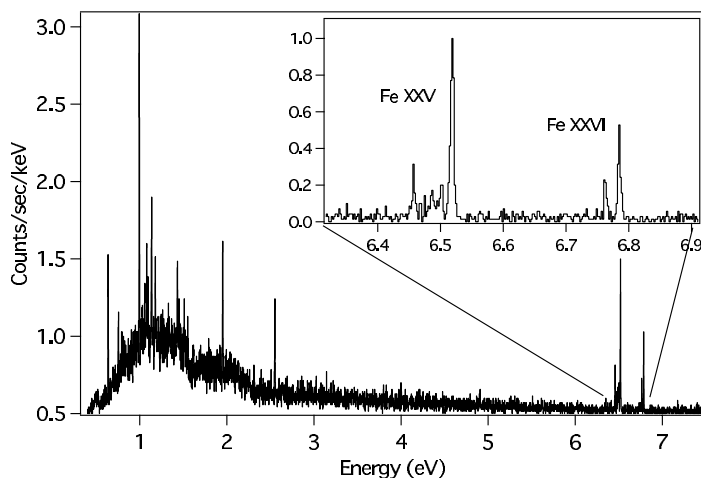


**Fig. 13.** A simulated X-ray spectrum of the Ophiucus cluster of galaxies using the X-ray Spectrometer (XRS) on the *Astro-E2* observatory. The simulation is for a 35 ks observation of the X-ray emitting cluster plasma with a temperature of  $11.6 \times 10^6$  K. Compare the *inset* to Fig. 12 that shows an actual XRS spectrum of highly ionized iron in the laboratory

The XRS complements the high resolution dispersive instruments on *Chandra* and *XMM-Newton*. The XRS has higher spectral resolution and more effective area above 2 keV than the RGS on *XMM-Newton* and the HETG on *Chandra* (see Fig. 6), and because it is non-dispersive its spectral resolution is not affected by the angular extent of the object. The XRS will observe extended sources such as supernova remnants and galaxy clusters, without degradation and without heroic tomographic measurements. The higher spectral resolution of the XRS above 2 keV makes the XRS uniquely suited for studying the K-shell emission from iron which is a crucial diagnostic for the study of X-ray emitting objects because it has a high abundance, a high fluorescent yield, and emits in a relatively uncrowded area of the X-ray spectrum. The XRS has the spectral resolution to largely deconvolve the He-like Fe XXV line emission, whose line ratios give an important temperature and density diagnostic of the emitting medium. The XRS can also separate the H-like Fe XXVI Ly $\alpha$  lines from the neighboring dielectronic recombination lines giving another important temperature diagnostic. As an example, Fig. 12 shows a spectrum of Fe XXV and XXVI produced in the laboratory using the EBIT-I electron beam ion trap. The spectrum was taken with a laboratory XRS instrument with a microcalorimeter array identical to the flight array. For comparison, a simulation of the predicted Fe K emission from a cluster of galaxies using the XRS flight instrument is shown in Fig. 13.

### 5.2.2 The XRS Cryogenic System

Figure 14 shows the completed XRS instrument prior to installation on the *Astro-E2* spacecraft. The XRS is the first X-ray LTD system designed for long term operation in space. As such, the design of the XRS conforms to all of the ground rules discussed in Sect. 4 and all future instruments will build on this experience. Here we review some of the characteristics of the XRS.

The XRS instrument is a four stage cryogenic system. The outer stage is a 35 W Stirling cycle cryo-cooler with 2 W of cooling power at 100 K. This is attached to the outermost of three vapor cooled shields which guard the second stage solid-neon cryogen tank. The solid neon system is a 120 liter toroidal tank containing 172 kg of solid neon cooled to below 17 K using liquid helium cooling coils on the ground and space pumping in orbit. This guards the third stage cooling system comprised of 321 of superfluid helium. The helium tank is suspended on tensioned carbon-fiber straps from a titanium support shell bolted to the solid neon tank. The 17 K guard plus careful control of radiative, conductive, and superfluid film flow heat leaks, keeps the parasitic load on the liquid helium to about 0.8 mW, an astonishing achievement compared to laboratory and earlier space based cryostats. When the additional heat load from operating the ADR is included, the total heat load on the liquid helium is around 1 mW. This gives a projected lifetime of 3.5 yr on orbit for the liquid helium. With the cryo-cooler running at 100% duty



**Fig. 14.** The XRS instrument during integration and testing prior to mounting on the *Astro-E2* spacecraft. The XRS is an LTD instrument with a four stage cryogenic system composed of a cryo-cooler, solid Ne tank, superfluid helium tank, and a single stage ADR. For scale, the XRS is about 1.2 m tall, and 1.0 m in diameter with a mass of about 400 kg including cryogens. The aperture of the instrument is at the *top of the figure*

cycle, the total cryogen lifetime is around 3 yr, after which the instrument is no longer operational.

The fourth stage of the XRS cryogenic system is a massive single stage ADR using 1000 g of paramagnetic (FAA) salt. The heat leak into the salt pill is dominated by the gas gap heat switch which dumps the cyclic heat of magnetization to the helium bath. The total heat load on the ADR is about  $5\mu\text{W}$  giving a 29 h hold time on the ground and about 24 h on orbit when cosmic ray heating of the ADR is included. The 32 pixel silicon microcalorimeter X-ray system only contributes about  $0.3\mu\text{W}$  to the total ADR heat load, largely from its separate suspension and wiring layer, the remaining heat load is solely from the accommodation of the refrigerator for spaceflight: its heavy Kevlar suspension, and gas-gap heat switch.

### 5.2.3 The XRS Detector System

The XRS instrument is based on a silicon microcalorimeter detector that is similar to the detectors used in the XQC but with important distinctions.

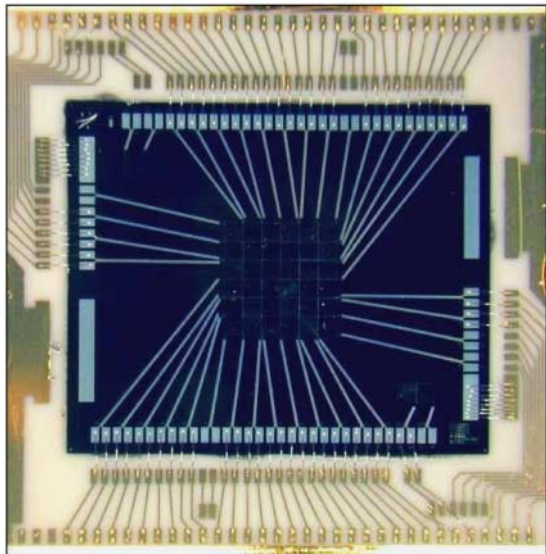


**Fig. 15.** The XRS microcalorimeter detector array. The array is close-packed in a  $6 \times 6$  geometry so the pixel suspension system is not visible underneath the HgTe absorbers. The pixels are 0.624 mm square on a 0.640 mm pitch giving a total array field of view of  $2.9 \times 2.9$  arcmin

The XRS detector array is a two dimensional square array organized in a  $6 \times 6$  geometry as shown in Fig. 15. There are also two calibration pixels situated in one corner of the detector dice. In the flight system, one of these is wired in place of an edge pixel in the main array. A collimated  $^{55}\text{Fe}$  source illuminates the calibration pixel which then provides continuous gain tracking for the detector array. The XRS detector array is a monolithic device, micro-machined out of a silicon-on-insulator (SOI) wafer using a deep reactive ion etching system. The pixels were designed [27] for resonant frequencies above 2 kHz, structural stability against differential contraction, and a thermal conductance of about  $4 \times 10^{-11} \text{ W/K}$  at 0.1 K. The resultant pixel design, shown in Fig. 16, was tested as a finite element model, and then modeled and tested in silicon before the array design was finalized.

The XRS thermistors are Mott-hopping conductivity, implanted silicon devices similar to the XQC. The goal is to form a large, uniformly implanted volume, where electrons are thermally assisted from one impurity site to another giving a strong variation in resistance of the device with temperature. In the XQC thermistors, a uniform impurity distribution with depth was attempted using 9 separate implantation doses at varying energies. These were then annealed to form a single uniform implant. Unfortunately, subsequent modeling showed that the implant density varied considerably with depth. This lead to a  $1/f$  noise [37] that gave a spectral resolution about 3 times



**Fig. 16.** The partially assembled XRS array. HgTe absorbers have not yet been attached to the pixels on the *lower left*. The pixel structure is micromachined from a single SOI wafer and one can see the pixel suspension structure and the circular mounting posts for the absorber at the edge of each pixel

worse than predicted. To overcome this problem, the XRS devices were made using a new “deep implantation” process where the phosphorus and boron impurities were implanted each with a single dose [27]. The impurities were then diffused throughout the  $1.5\text{ }\mu\text{m}$  thick SOI layer to form a uniform, well defined, and thick implanted thermistor. The result is about a factor of two improvement in spectral resolution over the XQC and the original XRS-1 system, both of which were fabricated using the old process.

The bare implanted silicon array is a poor X-ray thermalizer, and thus a separate X-ray absorber is needed [38]. The XRS, like the XQC, uses HgTe, a semi-metal, as an absorber material. An optimal X-ray absorber has a high stopping power (high  $Z$ , high density) and a low heat capacity. The high stopping power gives a high quantum efficiency in the smallest possible absorber volume, and the low heat capacity maximizes the spectral resolution. HgTe is a compromise material. While it has a high  $Z$  ( $Z_{\text{Hg}} = 80$ ,  $Z_{\text{Te}} = 52$ ) and density ( $\sim 8.2\text{ g/cm}^3$ ), it has a relatively low Debye temperature ( $\sim 140\text{ K}$ ) giving a heat capacity of  $\sim 0.1\text{ pJ/K}$  at  $70\text{ mK}$  for an XRS absorber. The benefit is that it thermalizes the X-ray interaction energy very efficiently, resulting in minimal, or non-existent, excess line broadening.

The energy resolution of the XRS instrument is about  $6\text{ eV}$  at  $6\text{ keV}$  and varies only weakly with energy. A spectrum of Mn  $K_{\alpha}$  from the completed flight instrument and Ga  $K_{\alpha}$  from ground calibration of the detector subsystem are shown in Fig. 17, and Fig. 18 respectively.

Equally important to the performance of the instrument is the instrument characterization. This is crucial to extracting the unknown spectrum of a cosmological source from the idiosyncrasies of the observing instrument. The

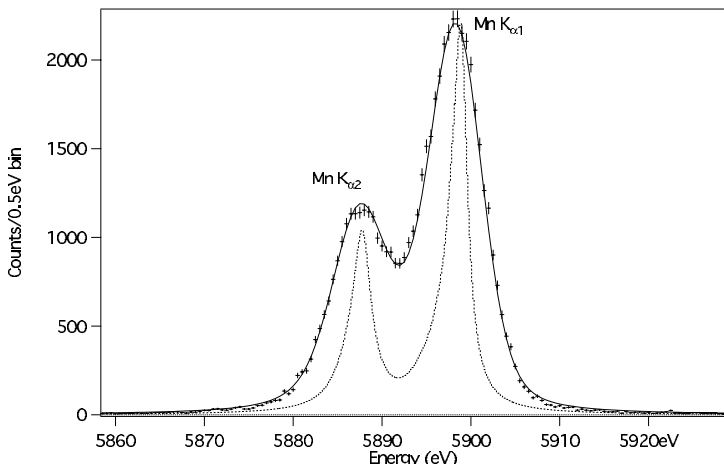


**Fig. 17.** Mn K $\alpha$  spectrum from an  $^{55}\text{Fe}$  internal conversion X-ray source taken with the XRS. The spectrum was taken with the XRS fully assembled and mounted on the XRS spacecraft with the cryo-cooler running at full power. In the spectrum the dashed line is the line model from Hölzer [39] and the solid line is a fit to the model with an instrumental resolution of 5.7 eV. The data is a summed composite from the XRS array

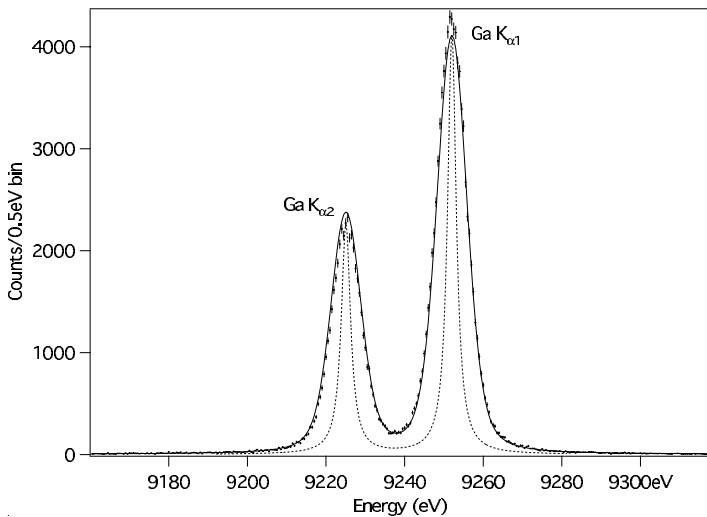


**Fig. 18.** An XRS spectrum of Ga K $\alpha$  from an X-ray fluoresced GaAs target during ground calibration at NASA/GSFC. The dashed line is a two Lorentzian line model and the solid line is a fit to the data with an instrumental width of 7 eV FWHM. The data is a summed composite for the XRS array

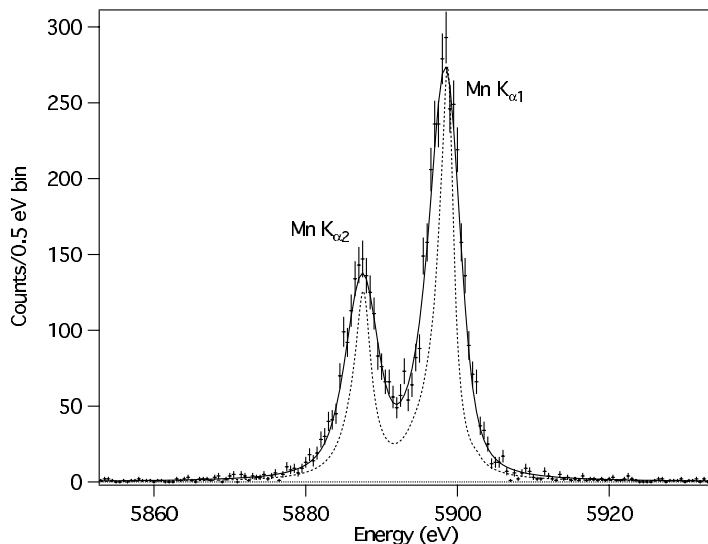


**Fig. 19.** A spectrum of Mn  $K_{\alpha}$  taken with a laboratory XRS microcalorimeter array with a 0.408 mm  $\times$  0.408 mm absorber. The instrumental width is 3.2 eV FWHM. The base temperature was 40 mK and the detector was biased to about 60 mK

instrument parameters such as quantum efficiency, resolution kernel, spectral redistribution function, gain scale, gain drift recovery, filter transmission, bore-sight alignment, timing accuracy, and imaging half-power diameter, for example, must all be modeled, measured carefully on the ground and in orbit, and then packaged in a manner usable by the observing community. Having a well characterized instrument is at least as important as having a high-performance instrument. The XRS has a detailed calibration program to characterize the instrument both on the ground and in-flight.

It is worth noting that the XRS is only a single example of an implanted silicon microcalorimeter instrument. It is a design constrained by the pixel dimensions, quantum efficiency, speed, and operating temperature of the instrument. The technology, however, is somewhat versatile in trading these parameters for each other. For example, in Fig. 19 we show the results for a similar array to the XRS flight array with smaller 408  $\mu$ m  $\times$  408  $\mu$ m absorbers operating at a 40 mK heat sink temperature. Here the resolution is improved to 3.2 eV FWHM at 5.9 keV with a 2.9 eV FWHM baseline resolution.

### 5.3 Future Missions

The XRS and XQC are a first, critical step for LTDs in X-ray astronomy. They are, however, merely a first step. The next set of observatories that will succeed *Chandra*, *XMM-Newton*, and *Astro-E2* will necessarily be more complex and put great demands on the cryogenic detector community if the

technology is to find a place on these observatories. Currently there are three major observatories that are in the planning stages and have a cryogenic X-ray instrument as part of the focal plane. These observatories must be significantly more powerful than the current observatories to be compelling investments for the scientific community and the government organizations that fund them.

Currently on the drawing board, roughly in order of launch schedule are the Japanese (ISAS/JAXA) *NeXT* mission, NASA's *Constellation-X*, and the European Space Agency's *XEUS*. National boundaries are routinely crossed in the construction of large observatories so that each of these missions will probably be constructed by large international consortiums. In addition, large observatories tend to change considerably from their early planning stages to their final launch configuration, sometimes merging, and sometimes separating into smaller payloads. Thus our discussion of these missions, should serve to illustrate the direction and challenges for the LTD community and not as a prediction of the final form any of these missions will take.

**Table 1.** Comparison of future large X-ray observatories showing some of the parameters important for low temperature detectors. The requirements shown are approximate, and for illustrative purposes only

	NeXT <sup>‡</sup>	Constellation-X <sup>#</sup>	XEUS <sup>§</sup>
Effective area (1 keV)	1000 cm <sup>2</sup>	15 000 cm <sup>2</sup>	60 000 cm <sup>2</sup>
Focal length	9 m	10 m	50 m
Half power dia.	30''	15''	5''
Spectral resolution	5 eV at 6 keV	2 eV at 1 keV 4 eV at 6 keV	2 eV at 1 keV 5 eV at 8 keV
Pixel size	0.5 mm	0.25 mm	1 mm
Operating temp.	< 100 mK	< 100 mK	< 100 mK
Array size	30 × 30	30 × 30	30 × 30
Field of view	5'	2.5'	1'
Cooler	cryogen-free	cryogen-free	cryogen-free

<sup>‡</sup>[www.astro.isas.jaxa.jp/future/NeXT](http://www.astro.isas.jaxa.jp/future/NeXT)

<sup>#</sup>[constellation-x.gsfc.nasa.gov](http://constellation-x.gsfc.nasa.gov)

<sup>§</sup>[www.rssd.esa.int/XEUS](http://www.rssd.esa.int/XEUS)

A summary of some of the characteristics of the three planned observatories are shown in Table 1. The general emphasis is on spectroscopy and very large collecting areas using very large X-ray optics. The *Constellation-X* mission, for example, will have almost 100 times more collecting area than the XRS. Similar expansions in capability are expected from the LTD community for these missions. The requirements in Table 1 include significant improvements in the detector design over the XRS in every respect: 30 times the pixel count, smaller pixel size, three times the spectral resolving power,

and a significantly higher throughput. This must all be accomplished in a smaller package and with a long lifetime, fully cryogen-free system.

The development work for these instruments drives nearly all progress in X-ray LTDs. There is little synergy with commercial applications so the entire development burden must be borne by future X-ray missions. Nearly all types of LTDs are still under consideration for the focal planes of these instruments including semiconductor, TES, and magnetic microcalorimeters, superconducting tunnel junctions, and kinetic inductor detectors. It is not clear which of these systems will actually make it into the final instruments, but what is clear is that this will not be a simple extension of the technology used in the XRS instrument. There must be a fundamental shift in development and assembly of cryogenic X-ray detectors. While the XQC and XRS are hand-assembled, and hand wired systems, this is not possible with 1000+ pixels and readout channels. Monolithic assembly techniques will be required. In addition, the cryogenic staging and complex wiring layers for 1000 discrete amplifier channels is probably not tractable in a compact instrument. A pixel multiplexing scheme is probably required. Several schemes are currently under consideration, including a time division multiplexed system [40] and a frequency division system [41]. In a time division multiplexer each channel in a column is sampled periodically in a round-robin fashion. In a frequency division multiplexed scheme each channel occupies its own part of the overall amplifier bandwidth.

Finally, future missions will require a low temperature refrigerator to cool the detectors to below 0.1 K. This must also interface with the base temperature and cooling power of the mechanical cryo-cooler. If the base temperature is more than a few degrees Kelvin, this will require a complex multi-stage ADR, using multiple refrigerants, magnets, and heat switches. In planning future LTD instruments it is important to remember that the “off” conductance of the heat switch sets the scale for the entire ADR as it sets the minimum cooling power that must be achieved by the ADR’s refrigerant. This in turn dictates the cycle time, the size of the magnet, and for magnetically sensitive detectors, the mass of the magnetic shielding. The XRS represents one point in this multi-dimensionally phase space, using the largest ADR refrigerant ever built to account for the high off-conductance of the gas gap heat switch. Future, compact instruments, including the next generation observatories discussed here, will need to find other designs that use much smaller refrigerants with smaller heat switches that have lower parasitic heat loads.

## 6 Laboratory Astrophysics and LTDs

The benefits provided to the astrophysics community by LTDs are not limited to sounding rocket experiments or X-ray observatories, but extend to ground-based measurements of astrophysically relevant X-ray spectra. For

these studies, engineering models and flight spare equipment are being retrofitted to operate in the laboratory. LTDs have become the highest resolution non-dispersive spectrometer available for laboratory studies of astrophysically relevant X-ray emission. Thus, the development of high resolution LTDs is multi-faceted, providing both the means for measuring spectra from extra-solar objects, and also the means for their reliable interpretation. Here we describe the use of LTDs for X-ray laboratory astrophysics.

## 6.1 Instruments for Laboratory Astrophysics: LTDs and Electron Beam Ion Traps

X-ray spectroscopy, as discussed in Sect. 2, provides the means for understanding the nature of non-terrestrial sources through a range of spectral diagnostics. The utility of these diagnostics requires knowledge of large sets of atomic data that describe the physics of the X-ray emission. Minimizing the uncertainty and establishing reliable error estimates associated with these data are paramount to their reliability and utility. Historically, testing of atomic data has been accomplished through a symbiotic relationship between theory and experiment: theoretical calculations produced large data sets, while experiments provided benchmarks to test and guide the theory. Because experiments often only covered a small portion of parameter space, testing entire atomic data bases was impossible. Over the past decade, however, more advanced experimental facilities have come online that are able to measure complete sets of atomic parameters in finite amounts of time. These facilities have the capacity to address specific problems facing the interpretation of astrophysical spectra. Experiments conducted specifically to address astrophysical problems are generally referred to as “laboratory astrophysics”. Laboratory astrophysics encompasses many different fields including the study of dust particles, optical spectra, UV spectra, and X-ray spectra [42]. In support of X-ray missions, laboratory X-ray astrophysics experiments are being conducted at several advanced facilities world-wide including, electron beam ion traps, heavy-ion storage rings, electron-cyclotron resonance facilities, and tokamaks. For a review of laboratory X-ray astrophysics see [43].

Low temperature detectors have been instrumental in laboratory astrophysics studies. Although LTDs have been tested earlier at LLNL [44] and some measurements at other facilities have been conducted [45, 46], it was not until the XRS/EBIT microcalorimeter spectrometer was installed on the LLNL EBIT-II in 2000 that LTDs have been routinely used as part of a laboratory astrophysics program [47, 48]. Here we give a brief description of the LLNL EBITs, the XRS/EBIT microcalorimeter spectrometer used at LLNL, and some examples of laboratory astrophysics measurements where the XRS/EBIT is used.

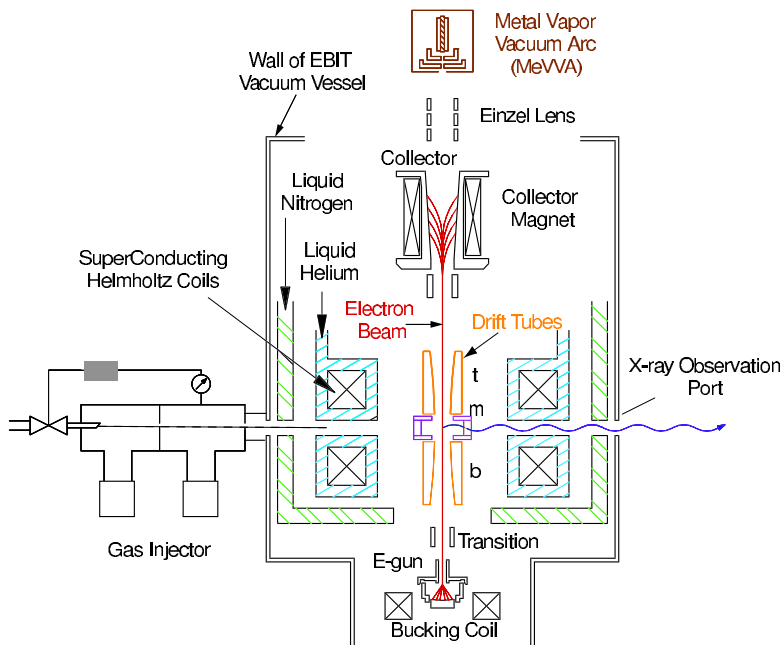


**Fig. 20.** Sketch of the layout of the Lawrence Livermore National Laboratory electron beam ion trap. Courtesy of Klaus Widmann

### 6.1.1 The Electron Beam Ion Trap

An electron beam ion trap (EBIT) is a device used to study the atomic physics governing the emission of radiation from highly-charged ions [49, 50, 51]. An EBIT consists of three major parts: a mono-energetic electron beam, an electrostatic trap, and a collector. The electron beam is used to create, excite, and trap ions in the radial direction. The electron beam travels from the electron gun, located near the bottom of EBIT, through the trap region and then terminates on the collector. The trap consists of three drift tubes that confine the ions electrostatically along a 2 cm portion of the electron beam. In the trap, the electron beam is compressed to a diameter of  $\sim 60 \mu\text{m}$  by the magnetic field created by a pair of superconducting Helmholtz coils. Figure 20 shows a sketch of all the major components of the EBIT.

Ions are injected into the trap using either a metal vapor vacuum arc (MeVVA), or a ballistic gas injector. The MeVVA uses an arc discharge to ablate low-charge-state ions from the cathode material. The ions are subsequently transferred electrostatically to the trap region. The ballistic gas injector uses differential pumping to inject a collimated stream of neutral material into the trap. Once the stream intersects the electron beam the neutral atoms and molecules are ionized and trapped. To avoid the accumulation

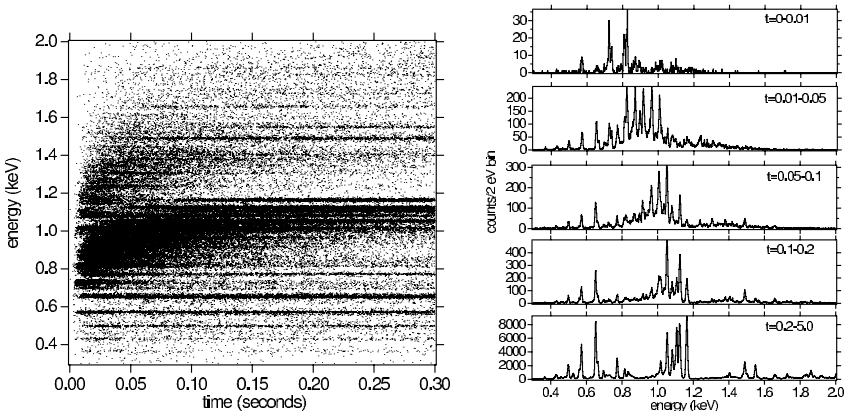


**Fig. 21.** Time resolved iron spectra emitted from the LLNL EBIT-II. The electron beam energy was 4.5 keV. The figure on the *left* shows the first 300 ms of a 5 s timing cycle. Equilibrium is achieved at  $\sim 200$  ms. The time selected spectra on the *right* demonstrate the evolving charge balance as a function of time

of background ions, the trap is emptied and replenished on a periodic timing cycle. A single cycle typically lasts a few seconds.

Once trapped, ions are ionized to the desired charge state by the mono-energetic electron beam. The time required for the trapped ions to reach equilibrium depends on the desired charge state and the conditions of the trap. Using time-resolved spectroscopy, it is possible to study the ionizing portion or the equilibrium portion independently. Without time resolution, measured spectra contain blends of ionization stages that can lead to confusing results. Figure 21 shows a time resolved spectrum of 10 000 phase-folded EBIT injection cycles with accompanying time-selected spectra. This figure shows the significant difference in ionization balance as a function of cycle time.

Access to the trap is granted through six axial ports directed towards the trap region. Five of these are used for spectroscopy, and the sixth is used for the gas injector. A seventh port looking down into the trap region houses the MeVVA. The electron beam enters through a port on the bottom. To reduce systematic errors and to provide high-resolution spectra over specific bandwidths, more than one spectrometer is used for each measurement. A typical arrangement of spectrometers attached to the LLNL EBIT is given in Fig. 22.

EBITs have operational parameters making them well suited for laboratory astrophysics. Because the electron beam is nearly mono-energetic with an energy spread of only 20–50 eV, it is possible to measure X-ray emission from nearly pure ion states, making it easy to identify lines from a specific charge state and to probe specific atomic processes. Typical electron densities in the trap are  $10^{10} \leq n_e \leq 10^{13} \text{ cm}^{-3}$  similar to those found in many astrophysical plasmas. The two EBITs, EBIT-I and Super-EBIT, currently

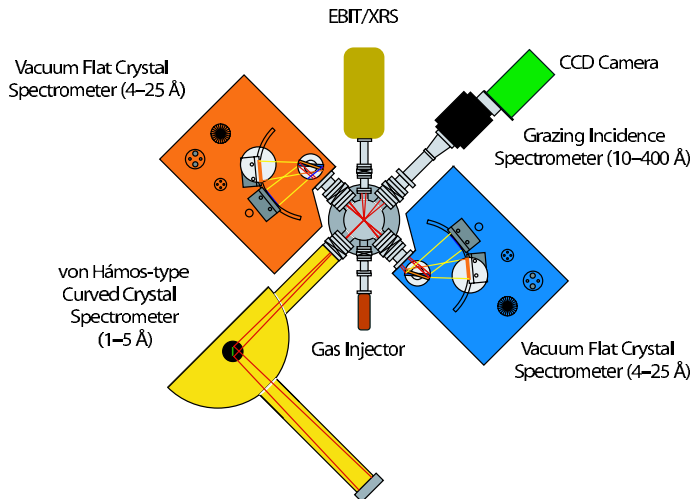


**Fig. 22.** Top down view of a typical spectrometer arrangement on the LLNL EBIT-I. In addition to the XRS/EBIT, are two flat crystal spectrometers, a curved crystal spectrometer, and a grazing-incidence spectrometer

operating at LLNL, have a combined operational electron beam energy range from below 100 eV to above 200 keV, making it possible to study all astrophysically relevant ions as well as truly high- $Z$ , highly-charged ions up to bare uranium,  $\text{U}^{92+}$ . The LLNL EBITs have also been used to produce spectra from Maxwellian plasmas [52] so that thermal plasmas in coronal equilibrium can be studied. In addition, by rapid switching of the electron beam energy, X-ray spectral signatures from photoionized plasmas can be produced [53].

### 6.1.2 The GSFC Microcalorimeter Detector For Laboratory Astrophysics

Two different NASA/GSFC microcalorimeter arrays have operated at the LLNL EBIT facility. The first was based on the *Astro-E1* design. The second array was assembled in the same fabrication run as the *Astro-E2* flight instrument. The *Astro-E1* array had a resolution of  $\sim 8$  eV below 1 keV and  $\sim 11.5$  eV at 6.7 keV. As stated in Sect. 5, the *Astro-E2* array has a resolution of 6 eV at 5.9 keV.

Both arrays utilize the same detector support system used in the *Astro-E2* flight instrument. The system has readout electronics for 32 channels, including pulse height and pulse shape analysis, pile-up detection, and noise analysis. The detector system time tags X-ray events to  $10\ \mu\text{s}$  precision using a GPS timing system to correlate the X-ray event times with the EBIT timing cycle. This makes it possible to perform detailed studies of both equilibrium and non-equilibrium plasmas.



**Fig. 23.** Photograph of the XRS/EBIT on LLNL's EBIT-I. Notice the pumping line on the back (*right side*) of the photograph. Read out electronics and thermometry can be seen in the background

The dewar system is a standard laboratory liquid helium cryostat adapted to accept a small ADR developed for the XQC described in Sect. 5. The typical hold time of the ADR is between 12 and 14 h at a control temperature of 60 mK. Temperature control of the detector assembly is achieved using commercial doped germanium thermometers read out by a high performance resistance bridge and a software PID controller. The PID controller provides live feedback to the superconducting magnet that controls the temperature of the ADR. At 60 mK, temperature control of  $\leq 1 \mu\text{K}$  RMS is consistently achieved. This cryostat accepts the *Astro-E2* engineering model detector assembly which is axially aligned with the X-ray port on the bottom of the cryostat, hence, the dewar is rotated horizontal when it is connected to one of the six axial X-ray ports on EBIT. The cryogen ports are offset so that the cryogens can be filled and the ADR can be operated while the dewar is horizontal. In this configuration the liquid helium bath is pumped to 1.5 K. Six liters of helium lasts 36–48 h. A photograph of the XRS/EBIT attached to EBIT-I is given in Fig. 23.

As in any low temperature detector, the array must be shielded from UV and thermal radiation, and photon-induced shot noise created by optical radiation. This is accomplished with four blocking filters, each made of  $\sim 1000 \text{ \AA}$  of polyimide coated with  $\sim 1000 \text{ \AA}$  of aluminum, each located at a different thermal interface. A fifth filter is used to separate the vacuum of the XRS/EBIT ( $\sim 10^{-8} \text{ Torr}$ ) from that of EBIT ( $\leq 10^{-11} \text{ Torr}$ ). This filter is mounted on a manual gate valve and is easily interchangeable. Typical materials for the vacuum isolation filter are parylene, beryllium, and polyimide. To ensure the integrity of the blocking filters and to account for any oxidation that may occur on the aluminum surfaces, the transmittance of

the blocking filters was measured as part of the *Astro-E2* filter calibration program [54, 55]. Once the XRS/EBIT is attached to EBIT and at its operating temperature, the condition of the filters is verified by illuminating the XRS/EBIT with a continuum of X-rays produced by an X-ray tube attached to the opposite viewport. Significant changes in absorption edge strengths, such as the oxygen edge or the aluminum edge, are indicative of a change in filter response.

## 6.2 Measurements Using the XRS/EBIT at the LLNL EBIT Facility

The XRS/EBIT has become a standard instrument used for a variety of experimental studies. For example, with the Maxwellian simulator mode [56], the XRS/EBIT has been used to measure spectral signatures of Maxwellian thermal plasmas. It has been used for transition rate measurements [57], and to measure X-ray emission from non-equilibrium ionizing plasmas. Described below are two examples of where the XRS/EBIT spectrometer provided new measurement capabilities: measuring absolute cross sections of Fe L-shell X-ray transition, and measuring X-ray emission from charge exchange in the study of cometary atmospheres.

### 6.2.1 Measuring Electron Impact Excitation Cross Sections of X-ray Transitions

As mentioned in Sect. 2, the line strengths of radiative transitions depend on several different atomic parameters and plasma conditions. One atomic parameter fundamental to the diagnostics of coronal plasmas is the radiative electron-impact excitation (EIE) cross section. EIE cross sections determine the strength of X-ray lines in collisional equilibrium. A multitude of calculated EIE cross sections are available, but because experimental data is sparse, many of the calculations remain unchecked. Measurements of the total excitation cross sections including non-radiative contributions, and low energy indirect excitation processes are measured using merged beam techniques [58, 59]. Also, cross sections of low charge states have been measured using crossed beams [60]. However, measurements at the LLNL EBIT are the only ones that provide EIE cross sections for radiative transitions in highly-charged ions for the direct interpretation of astrophysical spectra.

Using the LLNL EBITs, absolute EIE cross sections are measured by recording the X-ray emission from EIE and radiative recombination (RR) simultaneously. Then, by normalizing the emission from EIE to the well-known cross sections for RR, the EIE absolute cross section can be determined. For this technique to be successful, the RR and EIE spectral features corresponding to the same ion must be resolved. Otherwise, it is not possible to eliminate the electron beam-ion overlap integral that defines the emitting volume. For

astrophysically relevant X-ray emission, this is achieved by taking advantage of EBIT's narrow electron beam and the properties of the XRS/EBIT as described below.

Radiative recombination is the inverse process of photoionization and occurs when a free electron is captured by an ion into a bound state. In contrast to the RRC emitted from photoionized plasmas, RR radiation emitted from EBIT creates discrete spectral features whose energy is equal to the sum of the electron beam energy and the binding energy of the recombined state. The width of the RR feature emitted from EBIT is, therefore, equal to the beam width. The RR spectral features are very weak compared to direct excitation features because the cross sections for RR are  $\sim 1000$  times smaller.

The properties of radiative recombination create several requirements that must be met to measure the emission from RR and EIE simultaneously. First, the RR emission must be resolved. This can be problematic for several reasons. The finite Gaussian energy profile of the electron beam combined with the proximity of the ionization potentials of different ionic species makes it possible for neighboring ionization species to be present. Also present are ions of indigenous background gases. Thus, depending on the convolved width of the instrumental profile and the beam profile, blending of RR features from different ions may occur. Low resolution instruments that significantly broaden the RR features limit measurements to higher- $Z$  ions where differences in binding energies between the ions are larger. This requirement also means the spectrometer must have adequate time resolution to prevent the non-equilibrium portion of the timing cycle from contaminating the measurement.

The second and third major requirements are large bandwidth and large collection area. A large bandwidth is necessary because the accuracy of RR cross sections is better at high electron energies, and at these energies RR spectral features may appear at energies several keV above direct excitation features. A large collecting area is necessary in order to allow the detection of the weak RR features. This precludes the use of dispersive spectrometers because the reflection efficiencies of crystals and gratings are too small.

The first measurements of EIE cross sections at the LLNL EBIT facility used solid state detectors [62, 63, 64]. However, because of the low energy resolution of the detectors only the cross sections of K-shell transitions or high- $Z$  ions were measured. This problem is solved with the XRS/EBIT. The wide bandwidth, large collecting area, excellent time resolution, and  $\sim 10$  eV energy resolution made the measurement of absolute cross sections of Fe L-shell X-ray transitions possible for the first time.

Absolute cross sections of several Fe L-shell X-ray lines from Fe XVII–XXIV have been measured using the XRS/EBIT [61, 65, 66] including X-ray transitions in Fe XVII–XXIV. As an example, Fig. 24 shows the X-ray emission from Fe XVII measured by the XRS/EBIT at EBIT-I [61]. Notice the strong direct excitation line emission along with the relatively weak emis-

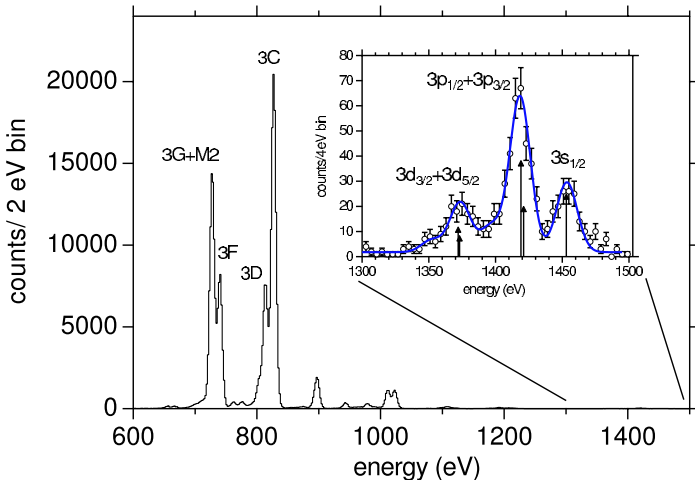


**Fig. 24.** Spectrum of Fe XVII measured by the XRS/EBIT microcalorimeter spectrometer. The *inset* shows the energy range containing the photons from radiative recombination. They represent the recombination into different fine structure components of Fe XVII. From the RR features, the electron beam energy is determined to be 964 eV with a FWHM of  $\sim 20$  eV. This figure is from Brown et al. [61]

sion from RR shown in the inset. The width of the electron beam for this measurements was  $\sim 20$  eV.

### 6.2.2 The Study of X-ray Emission Following Charge Exchange Recombination for Diagnosing Cometary Plasmas

In 1996 X-ray emission from comet Hyakutake was discovered in observations by *ROSAT*. Subsequently, X-ray emission from other Comets has been observed such as Linear C/1999 S4 and McNaught-Hartley [67]. The accepted mechanism for the X-ray radiation is charge exchange recombination (CEX). Charge exchange, in this case, is the radiationless transfer of a bound electron from a neutral atom in the comet to an upper level in an ion from the solar wind. The ion stabilizes radiatively by emitting an X-ray.

Just as in other realms of X-ray spectroscopy, the diagnostic utility of CEX X-ray emission relies on the accuracy of the atomic data used to interpret the spectra. Although studies of charge exchange have taken place for decades [68], most have focused on ion-neutral collisions with energies greater than 50 keV/amu. In contrast, the predicted interaction energy between cometary neutrals and solar wind ions is less than 3 keV/amu ( $\sim 800$  km/s) [69]. Theoretical models of charge exchange emission have made significant progress, especially since the discovery of cometary X-ray emission [70, 71], but they remain largely untested and incomplete.

Charge exchange following low-energy ion-neutral collisions for diagnosing solar wind-comet interactions is currently being studied at the electron cyclotron resonance (ECR) facility at NASA's Jet Propulsion Laboratory and at the EBIT facility at LLNL. At the ECR, ion-neutral collisions with interaction velocities of  $\sim 800$  km/s are being studied [72, 73], corresponding to the high-velocity solar-wind ions. The LLNL EBIT experiments are complementary, covering the low velocity range below 100 km/s corresponding to the velocities of solar wind ions in the inner region of a comet [74]. LTDs have played a significant role in the study of charge exchange emission at the LLNL EBIT.

X-ray emission following charge exchange recombination is studied at the LLNL EBIT facility using the magnetic trapping mode [75]. In this mode, instead of being trapped radially by the potential of the electron beam, the ions are trapped by the 3 T magnetic field produced by superconducting Helmholtz coils in the EBIT. Together with the electrostatic trapping by the drift tubes, this system acts like a Penning trap. Neutrals are either pulsed or continuously injected into the trap using the gas injector. When the electron beam is off, the ion cloud expands and it no longer acts as a slit for dispersive grating and crystal spectrometers. A non-dispersive spectrometer is therefore required.

High-purity germanium detectors with resolutions between 120 and 180 eV were used in the first charge exchange measurements at the LLNL EBIT [76, 77]. For these experiments, X-ray emission following charge exchange reactions between hydrogenic Ne, Ar, Kr, Xe, Au, U and neutral Ar, CO<sub>2</sub>, Ne, are measured. The results of these measurements demonstrated that for low energy collisions, X-ray emission from high- $n$  Rydberg states is unusually strong compared to those occurring after high-energy collisions. The figure of merit to determine the interaction energy is the ratio of the  $n \geq 3 \rightarrow 1$  transitions relative to the  $2 \rightarrow 1$  transitions, known as the hardness ratio. For low energy transitions the hardness ratio is high, and for high energy interactions the hardness ratio is low.

Using the XRS/EBIT at LLNL, X-ray emission from charge exchange between C<sup>5+</sup>, C<sup>6+</sup>, Ne<sup>8+</sup>, Ne<sup>9+</sup>, Ne<sup>10+</sup>, O<sup>7+</sup>, O<sup>8+</sup>, with neutral Ne, CO<sub>2</sub>, CH<sub>4</sub>, and alcohol, were all measured. Figure 25 shows the spectra measured after charge exchange occurs between O<sup>8+</sup> and either ethyl alcohol, methane, or carbon dioxide. The order of magnitude improvement in resolution compared to the germanium detector provides many new results. For example, strong line emission from the high- $n$  Rydberg transitions, and the spectral dependence on the neutral gas and different ion species is readily apparent. In addition, the significant contribution from double capture was discovered in these experiments [78]. Just as the name suggests, double capture occurs when two electrons are transferred to the ion as opposed to one. In Fig. 25, the signature of double capture is most apparent in the the spectrum of O<sup>8+</sup> interacting with alcohol. This results in strong emission from  $n = 3 \rightarrow 1$  and

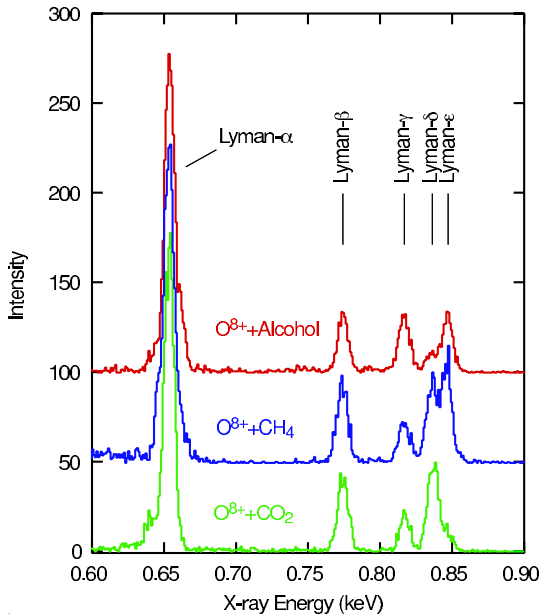


**Fig. 25.** Spectrum of X-ray emission produced after charge exchange between bare  $O^{8+}$  and different neutral gases using the XRS/EBIT. This demonstrates that it is possible to detect different gas constituents from a CEX spectrum and that contributions from double electron capture must be taken into account when modeling X-ray emission from charge exchange. This figure is reproduced from Beiersdorfer et al. [78]

$n = 4 \rightarrow 1$  transitions. This signature is unobservable at the resolution of a typical solid state detector.

Figure 26 shows the spectrum from the comet C/Linear 1999 S4 [79] observed with the *Chandra* ACIS CCDs. The lower panel shows the superposition of the spectra measured by the XRS/EBIT of helium-like and hydrogenic C, N, and O after charge exchange with  $CO_2$ . This comparison clearly shows the stark improvement in the spectral information provided by LTDs compared to solid state detectors. In addition, the laboratory data shown here were used to successfully fit the *Chandra* data demonstrating that charge exchange alone can account for all the X-ray flux emitted from a comet. Importantly, the laboratory data can be used to fit astrophysical spectra directly, with no reliance on theoretical databases [78].

The launch of *Astro-E2* in early 2005 will make possible the first high-resolution measurement of the cometary X-ray emission. Two observations are scheduled: the comet 9P/Temple on July 4, 2005, and comet 73P/Schwassmann-Wachmann 3 in 2006. The factor of nearly 20 improvement in spectral resolution compared to *Chandra* will surely present new insight into the physical processes taking place in the atmospheres of comets.

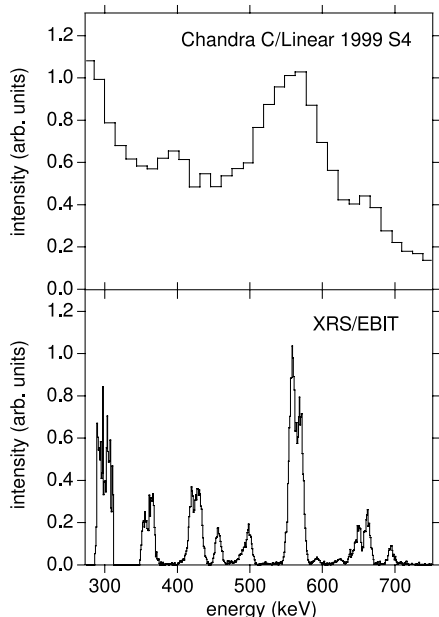


**Fig. 26.** X-ray emission spectrum measured from the comet C/Linear 1999 S4 using the *Chandra* ACIS-S and the charge exchange induced spectrum measured at LLNL EBIT-I using the XRS/EBIT. The XRS/EBIT spectrum is the superposition of six separate spectra of charge exchange induced emission from hydrogenic and helium-like C, N, and O. For a complete explanation of these data see *Beiersdorfer et al. [78]*

More importantly, because this emission is a diagnostic of the ionization balance, composition, and velocity of the solar wind ions, it can be used to remotely observe the properties of the solar wind throughout the solar system. *Astro-E2* will also observe other objects that show evidence for CEX emission, such as stellar winds, the galactic center, the galactic ridge, the cosmic X-ray background, and supernova remnants to name a few. The continued CEX studies in the laboratory will provide a significant contribution to the interpretation of these data.

## 7 Future Challenges

What astrophysicists want is an observatory with a large field of view, very fine spatial and spectral resolution, a very large effective area, and the ability to handle bright sources with precision timing. Future CCD instruments can and will provide the large field of view and fine spatial sampling in a single instrument, and future X-ray telescopes will provide the large collecting area. What is missing is the high spectral resolution and the ability to handle high

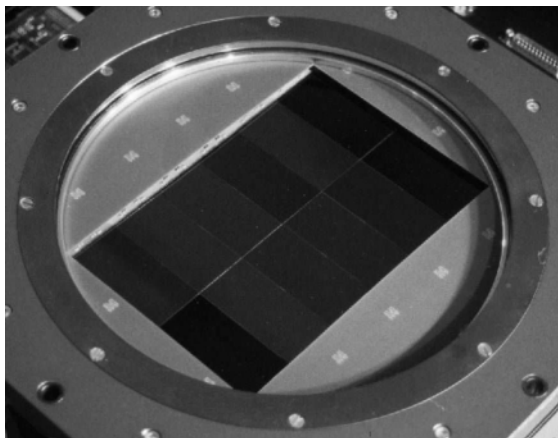


**Fig. 27.** An example of a large-scale CCD camera is the CFH12K CCD camera used at the focal plane of the Canada-France-Hawaii telescope on Mauna Kea in Hawaii. The CCD camera is  $12\,288 \times 8192$  pixels or over 100 megapixels. Reprinted from Cuillandre et al. [80]

count rates with precision timing. This is what the astrophysics community expects from low temperature detectors. The difficulty is that low temperature detectors are not CCDs. They don't scale the same way and present profoundly different challenges and problems in implementation.

The instrument scientist must face the very real problems of scaling todays  $\sim 30$  pixel arrays to the megapixel arrays needed for future instruments. This is a non-trivial task, and each order of magnitude expansion in the number of pixels brings daunting challenges to the detector design and instrument implementation.

## 7.1 Scaling Limits in Current LTD Technologies

Scaling today's small arrays of X-ray LTDs to large arrays that cover square centimeters or more of focal plane area present very real problems in detector and readout design. CCDs scale well because the packet of charge induced by an X-ray can be serially clocked out from the center of a large detector. Scaling CCDs to large area depends on developing high fabrication yields, producing 3 and 4 side abut-able sub arrays, and increasing the speed at which the induced charge can be clocked out of the array without loss. As an example, Fig. 27 shows the huge 100 megapixel CFH12K optical CCD camera operating on the Canada-France-Hawaii Telescope on Manua Kea. LTDs do not scale this way. There is no equivalent to the CCD charge transfer mechanism for LTDs where most devices operate calorimetrically. The heat induced by an X-ray interacting with an LTD cannot be "clocked out" of the LTD array.

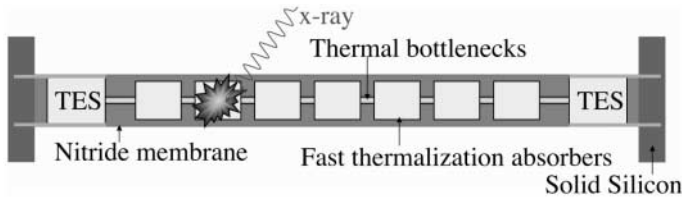


**Fig. 28.** A recent imaging microcalorimeter detector developed at NASA/GSFC [83]. The Position Sensitive TES (PoST) detector uses two TES thermometers to read out a linear array of pixelated absorbers. This allows a number of “effective pixels” to be read out using only two readout nodes

So how does one scale LTDs from the 32 pixel XRS to substantially more channels? One solution is to simply increase the number of readout channels. However, as in XRS, each readout node implies a low temperature amplifier (FET or SQUID) and a wiring layer that extends from the pixel to the low temperature amplifier and then to room temperature. People have envisioned, although not attempted, systems with up to 1000 discrete readout channels. The HAWC infrared instrument on the SOFIA airborne observatory uses 384 FET channels to read out an infrared bolometer array at 0.2K [81]. However, using such a brute force system for a large array of X-ray detectors with a base temperature of 0.05 K and in a space environment would present serious difficulties including the thermal staging of the FETs, the extremely complex wiring layer, and the very large number of discrete room temperature amplifiers.

To scale to very large arrays it is necessary to break the one-to-one correspondence between readout nodes and imaging elements on the detector array. One method, as we have discussed, involves a multiplexed row-column readout. This allows all the channels of one column of devices to be combined into one readout node. The number of readout nodes then only scales as the number of columns  $N$  in an  $N \times N$  array. The number of elements per column, however, is limited. The time and frequency division multiplexing schemes envisioned for *Constellation-X* and *XEUS* are limited by, among other things, the bandwidth of the low-temperature SQUID amplifier. In addition, the number of readout nodes is also limited by the power consumption at low temperatures, and the complexity of the wiring layer. A reasonable limit for scaling on these two axes would be of order 100 channels per readout node and of order 100 readout nodes per instrument. This is possible *in principle*, probably with some compromises in the detector speed, and gives a reasonable scaling limit for these two axes for the foreseeable future. However, the current requirements for *Constellation-X* and *XEUS* are an order of magnitude less with 32 columns and 32 readout nodes, and even this has not yet been demonstrated.

To reach megapixel scales, the number of channels must be increased using a fundamentally different approach. One method originally pioneered by

Krause in superconducting tunnel junctions [82] and recently demonstrated for TES based microcalorimeters [83] is to create LTDs with intrinsic spatial information. This allows one to divide up a discrete “pixel” into a larger number of “effective pixels” with some discriminating parameter to convey the location of the X-ray event within the “pixel”. An example of a position sensitive TES (PoST) microcalorimeter is shown in Fig. 28. In this configuration two readout nodes are used to locate the X-ray event in a linear array of segmented absorbers. The relationship between the event on the two readout nodes (relative timing, relative pulse shape, etc...) gives the position, and the sum the energy of the event. One could also envision this same type of scheme in two dimensions with four readout nodes locating the X-ray event in a plane of X-ray absorber(s). There are limitations to this scheme, however. In most cases the energy resolution degrades with the number of “effective pixels”. In addition, the pile up limits for each pixel do not increase as the pixel is subdivided into imaging elements. Thus the X-ray throughput per imaging element decreases as the number of imaging elements per “pixel” is increased. The benefit is, of course, another effective axis for increasing the pixel count. Figure 29 shows the increase in field of view of a *Constellation-X* instrument with the same number of multiplexed rows and columns (32 by 32) but with 10 imaging elements per node, giving  $10^4$  total imaging elements. The increased field of view drastically increases the observing efficiency of the observatory for extended objects and allows for the discovery of serendipitous sources within the larger observed field.

To continue with our scaling limits, we now have three axes: the number of readout nodes, the number of pixels per readout node, and the number of imaging elements per pixel. Again, reasonable limits for each axis are of order 100 giving an effective 1 megapixel imaging detector system, at least in theory, and with some compromises in spectral resolution and throughput. There are, however, immense implementation problems that we have not addressed including managing the heat produced in a close-packed array, developing the on-chip wiring layer, and producing high-yield, uniform device arrays. It will be interesting to see if this approach alone can yield a megapixel sized flight-qualified array with reasonable parameters.

To scale still further either requires additional compromises or a fundamental shift in how the device readout is accomplished. One possibility is to reduce the requirements on spectral resolution and combine pixels electrically in a row-column readout. Since the noise of the detectors is uncorrelated, the energy resolution will scale as the square root of the number of pixels combined per readout node. Thus one could increase the pixel count by an order of magnitude simply by combining channels, although with a factor of three lower spectral resolution.

The future for truly large scale LTDs probably lies in substantially increasing the number of multiplexed channels by significantly increasing the bandwidth of the connection between the low temperature amplifiers and the

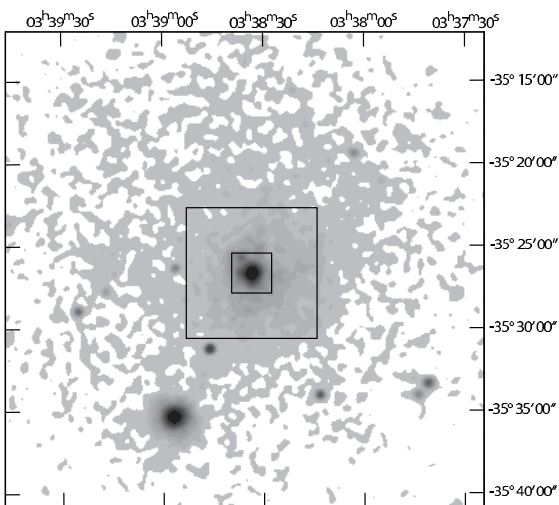


**Fig. 29.** A *ROSAT* image of NGC1399 a galaxy in the center of the Fornax cluster of galaxies. The *central square* denotes the standard *Constellation-X* field of view for a  $32 \times 32$  pixel detector array. The *outer square* shows the field of view using the same number of readout channels but using a position-sensitive detector array with 10 “effective pixels” per read-out node

room temperature electronics. Recently NIST-Boulder, has demonstrated a microwave SQUID frequency division multiplexing scheme [84] that could dramatically increase the number of multiplexed nodes per readout channel. Another important recent advance is the development of the microwave kinetic inductor detector [85]. The microwave kinetic inductor X-ray detector forms each detector into a microwave resonant circuit with very high  $Q$ . In principle, a very large number of channels with different resonant frequencies can then be combined on a single high bandwidth cable out of the cryostat. These or similar future developments are needed if we are to break out of the complex, and extremely limiting scaling rules for low temperature detectors.

## 7.2 Where Do We Go From Here? Future Missions, Dreams, and Challenges

The future of LTDs for X-ray astronomy is both exciting and daunting. The success of the XQC instrument and the imminent launch of the XRS are truly seminal moments for LTDs and for X-ray astronomy. This is the beginning of high-resolution spectroscopy with true spatial-spectral imaging. The next step, however, is truly daunting. There are huge technical challenges in developing the 1000+ pixel, high-resolution, high-throughput focal plane instruments for *NeXT*, *Constellation-X* and *XEUS*. These instruments, however, represent only the short-term challenges. To quote from the 2003

NASA/SEU (Structure and Evolution of the Universe) Road-map: “Thirty by thirty arrays of microcalorimeters are envisioned for *Constellation-X*, but such small array have very limited fields of view. Future missions will need much larger arrays” [86].

Future “vision” missions in NASA’s *Beyond Einstein* program include *MAXIM*, a microacrsecond X-ray interferometer, and *Generation-X*, a very large collecting area, 0.1 arcs X-ray observatory. Both of these missions will require very large format arrays of small 20 μm pixels. We as instrument scientists must look beyond our current challenges to come up with new ideas for large arrays. We as astrophysicists, however, must be mindful of the problems, challenges, and resources this development requires.

The ability of LTDs to gain and maintain a place on future missions will depend on our ability to innovate and keep pace with the requirements of ever more powerful X-ray observatories.

## References

- [1] R. Giacconi, H. Gursky, F. R. Paolini, B. B. Rossi: Phys. Rev. Lett. **9**, 439 (1962). [359](#), [369](#)
- [2] M. C. Weisskopf, B. Brinkman, C. Canizares, G. Garmire, S. Murray, L. P. Van Speybroeck: PASP **114**, 1 (2002). [360](#)
- [3] F. Jansen, D. Lumb, B. Altieri, J. Clavel, M. Ehle, C. Erd, *et al.*: A&A **365**, 1 (2001). [360](#)
- [4] R. Mewe: Atomic Physics of Hot Plasmas, in *X-Ray Spectroscopy in Astrophysics*, J. van Paradijs, J. A. M. Bleeker (Eds.) (Springer, Berlin 1999) p. 109. [361](#)
- [5] D. A. Liedahl: Spectral Properties of PIE and NIE Plasmas, in *X-Ray Spectroscopy in Astrophysics*, J. van Paradijs, J. A. M. Bleeker (Eds.) (Springer, Berlin 1999) p. 189. [361](#)
- [6] D. Porquet, J. Dubau: A&AS **143**, 495 (2000). [362](#), [363](#)
- [7] T. R. Kallman, J. H. Krolik: XSTAR-A Spectral Analysis Tool, HEASARC NASA/GSFC, Geenbelt, MD (1995). [363](#)
- [8] V. Decaux, P. Beiersdorfer, A. Ostereld, M. Chen, S. M. Kahn: ApJ **443**, 464 (1995). [366](#)
- [9] S. S. Holt: in *High Resolution X-Ray Spectroscopy of Cosmic Plasmas*, P. Gorenstein, M. Zombeck (Eds.) (Cambridge University Press, Cambridge, 1990) p. 346. [366](#)
- [10] F. Paerels: in *X-Ray Spectroscopy in Astrophysics*, J. van Paradijs, J. A. M. Bleeker (Eds.) (Springer, Berlin, 1999) p. 345 [366](#)
- [11] A. C. Brinkman, J. H. Dijkstra, W. F. P. A. L. Geerlings, F. A. van Rooijen, C. Timmerman, P. A. J. de Korte: ApOpt **19**, 1601 (1980). [367](#)
- [12] F. D. Seward, *et al.*: ApOpt **21**, 2012 (1982). [367](#)
- [13] T. H. Markert, C. R. Canizares, D. Dewey, M. McGuirk, C. S. Pak, M. L. Schattenburg: SPIE **2280**, 168 (1994). [368](#)
- [14] A. C. Brinkman, T. Gunsing, J. S. Kaastra, R. van der Meer, R. Mewe, F. B. Paerels, *et al.*: SPIE **4012**, 81 (2000). [368](#)

- [15] G. P. Garmire, M. W. Bautz, P. G. Ford, J. A. Nousek, G. R. Ricker: SPIE **4851**, 28 (1987). [368](#), [371](#)
- [16] S. S. Murray, G. K. Austin, J. H. Chappell, J. J. Gomes, A. T. Kenter, R. P. Kraft, *et al.*: SPIE **4012**, 68 (2000). [368](#)
- [17] J. W. den Herder, A. C. Brinkman, S. M. Kahn, G. Branduardi-Raymont, K. Thomsen, *et al.*: A&A **365**, L7-L17 (2001). [368](#)
- [18] M. J. L. Turner, A. Abbey, M. Arnaud, M. Balasini, M. Barbera, *et al.*: A&A **365**, L27 (2001). [369](#), [371](#)
- [19] K. Jahoda, J. H. Swank, A. B. Giles, M. J. Stark, T. Strohmayer, W. Zhang, E. H. Morgan: SPIE **2808**, 59 (1996). [369](#)
- [20] Y. Tanaka, H. Inoue, S. S. Holt: PASJ **46**, L37 (1994). [371](#)
- [21] L. Strueder, U. Briel, K. Dennerl, R. Hartmann, E. Kendziorra, N. Meidinger, *et al.*: A&A **365**, L18 (2001). [371](#)
- [22] P. R. Roach and B. P. M. Helvenstein: Cryogenics **39**, 1015 (1999). [373](#)
- [23] O. V. Lounasmaa: *Experimental principles and methods below 1K* (Academic Press, London, New York 1974). [373](#)
- [24] A. T. Serlemitsos, M. SanSebastian, E. Kunes: Cryogenics **32**, 117 (1992). [373](#)
- [25] A. E. Szymkowiak, R. L. Kelley, S. H. Moseley, C. K. Stahle: J. Low Temp. Phys. **93**, 281 (1993). [377](#)
- [26] W. Cui, R. Almy, S. Deiker, D. McCammon, J. Morgenthaler, W. T. Sanders, R. L. Kelley, F. E. Marshall, S. H. Moseley, C. K. Stahl, A. E. Szymkowiak: SPIE **2280**, 362 (1994). [377](#)
- [27] C. K. Stahle, C. A. Allen, K. R. Boyce, R. P. Brekosky, G. V. Brown, J. Cotttam, E. Figueroa-Feliciano, M. Galeazzi, J. D. Gygax, M. B. Jacobson, R. L. Kelley, L. Dahai, D. McCammon, R. A. McClanahan, S. H. Moseley, F. S. Porter, L. E. Rocks, W. T. Sanders, C. M. Stahle, A. E. Szymkowiak, J. E. Vaillancourt: SPIE **4851**, 1394 (2003). [378](#), [390](#), [391](#)
- [28] R. Fujimoto: personnel communication, NeXT Proposal Book (2003). [375](#)
- [29] C. S. Bowyer, G. B. Field, J. E. Mack: Nature **217**, 32 (1968). [381](#)
- [30] A. N. Bunner, P. L. Coleman, W. L. Kraushaar, D. McCammon, T. M. Palmieri: Nature **223**, 1222 (1969). [381](#)
- [31] D. McCammon, D.N. Burrows, W. T. Sanders, W. L. Kraushaar: ApJ **269**, 107 (1983). [382](#)
- [32] S. L. Snowden, R. Egger, M.J. Freyberg, D. McCammon, P. P. Plucinsky, W. T. Sanders, J.H.M.M. Schmitt, J. Trümper, W. Voges: ApJ **485**, 125 (1997). [382](#)
- [33] D. McCammon and W. T. Sanders: Ann. Rev. Ast. Astrophys. **28**, 657 (1990). [382](#)
- [34] D. McCammon, R. Almy, E. Apodaca, W. Bergmann Tiest, W. Cui, S. Deiker, M. Galeazzi, M. Juda, A. Lesser, T. Mihara, J. P. Morgenthaler, W. T. Sanders, J. Zhang, E. Figueroa-Feliciano, R. L. Kelley, S. H. Moseley, R. F. Mushotzky, F. S. Porter, C. K. Stahle, A. E. Szymkowiak: ApJ **576** 188 (2002). [382](#), [383](#), [384](#), [385](#)
- [35] F. S. Porter, R. Almy, E. Apodaca, E. Figueroa-Feliciano, M. Galeazzi, R. Kelley, D. McCammon, C. K. Stahle, A. E. Szymkowiak, W. T. Sanders: Nucl. Inst. and Meth. A **444**, 175 (2000). [382](#)
- [36] T. Kamae, H. Ezawa, Y. Fukazawa, H. Hirayama, E. Idesawa, N. Iyomoto, H. Kaneda, G. Kawaguti, M. Kokubun, H. Kubo, A. Kubota, K. Matsushita, K. Matsuzaki, K. Makishima, T. Mizuno, K. Nakazawa, S. Osone, H. Obayashi, Y.

- Saito, T. Tamura, M. Tanaka, M. Tashiro, J. Kataoka, T. Murakami, N. Ota, H. Ozawa, M. Sugizaki, K. Takizawa, T. Takahashi, K. Yamaoka, A. Yoshida, H. Ikeda, K. Tsukada, M. Nomachi: SPIE **314**, 2806 (1996). [386](#)
- [37] S. I. Han, R. Almy, E. Apodaca, W. Bergmann, S. Deiker, A. Lesser, D. McCammon, K. Rawlins, R. L. Kelley, S. H. Moseley, F. S. Porter, C. K. Stahle, A. E. Szymkowiak: SPIE **3445**, 640 (1998). [390](#)
- [38] R. L. Kelley, S. H. Moseley, C. K. Stahle, A. E. Szymkowiak, M. Juda, D. McCammon, J. Zhang: J. Low Temp. Phys. **93**, 225 (1993). [391](#)
- [39] G. Hölzer, M. Fritsch, M. Deutsch, J. Härtwig, E. Förster: Phys. Rev. A **56**, 4554 (1997). [392](#)
- [40] J. A. Chervenak, K. D. Irwin, E. N. Grossman, J. M. Martinis, C. D. Reintsema, M. E. Huber: Appl. Phys. Lett. **74**, 4043 (1999). [395](#)
- [41] J. van der Kuur, P.A.J. de Korte, H. F. C. Hoevers, M. Kivirana, H. Seppä: Appl. Phys. Lett. **81**, 4467 (2002). [395](#)
- [42] Rayleigh scattering, in: F. Salama (Ed.), NASA Lab. Astrophysics Workshop, Moffet Field, CA, 2002. [396](#)
- [43] P. Beiersdorfer: Astron. Astrophys. Rev. **41**, 343 (2003). [396](#)
- [44] M. LeGros, E. Silver, P. Beiersdorfer, J. R. C. López-Urrutia, K. Widmann, S. M. Kahn: Electron Beam Ion Trap Ann. Report, Lawrence Livermore National Laboratory, 1995, pp. 22–23, uCRL-ID-124429. [396](#)
- [45] M. Laming, I. Kink, E. Takacs, J. V. Porto, J. D. Gillaspy, E. H. Silver, H. W. Schnopper, S. R. Bandler, N. S. Brickhouse, S. S. Murray, M. Barbera, A. k. Bhatia, G. A. Doschek, N. Madden, D. Landis, J. Beeman, E. E. Haller: ApJ **545**, L161 (2000). [396](#)
- [46] E. Silver, H. Schnopper, S. Bandler, N. Brickhouse, S. Murray, N. Madden, D. Landis, J. Beeman, E. Haller, M. Barbera, G. Tucker, J. Gillapsy, E. Takacs, J. Porto, I. Kink: ApJ **541**, 495 (2000). [396](#)
- [47] F. S. Porter, M. D. Audley, P. Beiersdorfer, K. R. Boyce, R. P. Brekosky, G. V. Brown, K. C. Gendreau, J. Gygax, S. M. Kahn, R. L. Kelley, C. K. Stahle, A. E. Szymkowiak: SPIE **4140**, 407 (2000). [396](#)
- [48] F. S. Porter, P. Beiersdorfer, K. R. Boyce, G. V. Brown, H. Chen, R. L. Kelley, C. A. Kilbourne: Rev. Sci. Inst. **75**, 3772 (2004). [396](#)
- [49] M. Levine, R. Marrs, D. Knapp, M. Schneider: Phys. Scr. **T22**, 157 (1988). [397](#)
- [50] R. E. Marrs: Atomic, Molecular, and Optical Physics: charged particles, Vol. 29A of Experimental Methods in the Physical Sciences, Academic Press, Inc., San Diego, CA, 1995, chapter 14. Electron Beam Ion Traps. [397](#)
- [51] P. Beiersdorfer, G. V. Brown, J. C. Lopez-Urritia, V. Decaux, S. R. Elliott, D. Savin, A. J. Smith, G. Stefanelli, K. Widman, K. L. Wong: Hyperfine Inter. **99**, 203 (1996). [397](#)
- [52] D. W. Savin, B. Beck, P. Beiersdorfer, S. M. Kahn, G. V. Brown, M. F. Gu, D. A. Liedahl, J. H. Scofield: Phys. Scr. **T80**, 312 (1999). [399](#)
- [53] P. Beiersdorfer: in *X-ray and Inner-Shell Processes*, T. A. Carlson, M. O. Krause, S. T. Manson (Eds.), (AIP, Knoxville, TN, 1990) p. 648. [399](#)
- [54] M. D. Audley, R. Fujimoto, K. Mitsuda, K. Arnaud, K. C. Gendreau, K. R. Boyce, C. M. Fleetwood, R. L. Kelley, R. A. Keski-Kuhn, F. S. Porter, C. K. Stahle, A. E. Szymkowiak, J. L. Tveekrem, Y. Ishisaki, T. Mihara: in *Proceedings of a New Century of X-ray Astronomy*, H. Inoue and H. Kunieda (Eds.) (Astronomical Society of the Pacific, San Francisco, 2001), p. 516. [401](#)

- [55] M. D. Audley, K. A. Arnaud, K. C. Gendreau, K. R. Boyce, C. M. Fleetwood, R. L. Kelley, R. A. Keski-Kuha, F. S. Porter, C. K. Stahle, A. E. Szymkowiak, J. L. Tveekrem, R. Fujimoto, K. Mitsuda, Y. Ishisaki, T. Mihara: SPIE **3765**, 729 (1999). [401](#)
- [56] D. W. Savin, P. Beiersdorfer, S. M. Kahn, B. Beck, G. V. Brown, M. F. Gu, D. A. Liedahl, J. H. Scofield: Rev. Sci. Instr. **71**, 3362 (2000). [401](#)
- [57] E. Träbert: Can. J. Phys. **80**, 1481 (2002). [401](#)
- [58] E. K. Wahlin, J. S. Thompson, G. H. Dunn, R. A. Phaneuf, D. C. Gregory, A. C. H. Smith: Phys. Rev. Lett. **66**, 157 (1991). [401](#)
- [59] D. W. Savin, S. M. Kahn, G. Gwinner, M. Grieser, R. Repnow, G. Saathoff, D. Schwalm, A. Wolf, A. Müller, S. Schippers, P. A. Závodszky, M. H. Chen, T. W. Gorczyca, O. Zatsarinny, M. F. Gu: ApJS. **147**, 421 (2003). [401](#)
- [60] A. Chutjian: Phys. Rev. A **29**, 64 (1984). [401](#)
- [61] G. V. Brown, P. Beiersdorfer, H. Chen, K. Scofield, K. R. Boyce, R. L. Kelley, C. A. Kilbourne, F. S. Porter, A. E. Szymkowiak, S. M. Kahn: Phys. Rev. Lett., submitted. [402](#), [403](#)
- [62] K. Wong, P. Beiersdorfer, K. Reed, D. Vogel: Phys. Rev. A **51**, 1214 (1995). [402](#)
- [63] S. Chantrenne, P. Beiersdorfer, R. Cauble, M. Schneider: Phys. Rev. Lett. **69**, 265 (1992). [402](#)
- [64] R. Marrs, M. Levine, D. Knapp, J. Henderson: Phys. Rev. Lett. **60**, 1715 (1988). [402](#)
- [65] H. Chen, P. Beiersdorfer, G. V. Brown, K. C. Gendreau, K. R. Boyce, R. L. Kelley, F. S. Porter, C. K. Stahle, A. E. Szymkowiak, S. M. Kahn, J. Scofield: ApJ **567**, L169 (2002). [402](#)
- [66] H. Chen, P. Beiersdorfer, J. H. Scofield, G. V. Brown, K. R. Boyce, R. L. Kelley, C. A. Kilbourne, F. S. Porter, M. F. Gu, S. M. Kahn: ApJ **618**, 1086 (2005). [402](#)
- [67] V. A. Krasnopolsky: Icarus **167**, 417 (2003). [403](#)
- [68] H. R. Griem: in *Principles of Plasma Spectroscopy, 2nd Edition*, (Cambridge University Press, United Kingdom, 1997). [403](#)
- [69] D. J. McComas, S. J. Bame, B. L. Barraclough, W. C. Feldman, H. Funsten, J. T. Gosling, P. Riley, R. Skoug: Geophys. Res. Lett. **25**, 1 (1998). [403](#)
- [70] V. Kharchenko, A. Dalgarno: J. Geophys. Res. **105**, 18351 (2000). [403](#)
- [71] V. Kharchenko, M. Rigazio, A. Dalgarno, V. A. Krasnopolsky: ApJ **585** L73 (2003). [403](#)
- [72] J. B. Greenwood, I. D. Williams, S. J. Smith, A. Chutjian: ApJ **533**, L175 (2000). [404](#)
- [73] J. B. Greenwood, A. Chutjian, S. J. Smith: ApJ **529**, 605 (2000). [404](#)
- [74] V. A. Krasnopolsky: Icarus **128**, 368 (1997). [404](#)
- [75] P. Beiersdorfer, L. Schweikhard, J. C. López-Urrutia, K. Widmann: Rev. Sci. Inst. **67**, 3818 (1996). [404](#)
- [76] P. Beiersdorfer, C. M. Lisse, R. E. Olson, G. V. Brown, H. Chen: ApJ **549**, L147 (2001). [404](#)
- [77] P. Beiersdorfer, R. E. Olson, G. V. Brown, H. Chen, C. L. Harris, P. A. Neill, L. Schweikhard, S. B. Utter, K. Widmann: Phys. Rev. Lett. **85**, 5090 (2000). [404](#)

- [78] P. Beiersdorfer, K. R. Boyce, G. V. Brown, H. Chen, S. M. Kahn, R. L. Kelley, M. May, R. E. Olson, F. S. Porter, C. K. Stahle, W. A. Tillotson: Science **300**, 1558 (2003). [404](#), [405](#), [406](#)
- [79] C. M. Lisse and D. J. Christian and K. Dennerl and K. J. Meech and R. Petre and H. A. Weaver and S. J. Wolk: Science **292**, 1343 (2000). [405](#)
- [80] J. C. Cuillandre, G. A. Luppino, B. M. Starr, S. Isani: SPIE **4008**, 1010 (2000). [407](#)
- [81] D. A. Harper, C. A. Allen, M. J. Amato, T. J. Ames, A. E. Bartels, S. C. Casey, R. J. Derro, R. Evans, I. Gatley, S. J. Heimsath, A. Hermida, M. Jhabvala, J. H. Kastner, R. F. Loewenstein, S. H. Moseley, R. J. Pernic, T. S. Rennick, H. E. Rhody, D. Sandford, R. A. Shafer, P. J. Shirron, G. M. Voellmer, S. Wang, J. Wirth: SPIE, **4014**, 43 (2000). [408](#)
- [82] H. Kraus, F. von Feilitzsch, J. Jochum, R. L. Mössbauer, T. Peterreins, F. Pröbst: Phys. Lett. B, **231**, 195 (1989). [409](#)
- [83] E. Figeroa-Feliciano: Nucl. Inst. and Meth. A, **520**, 496 (2004). [408](#), [409](#)
- [84] K. D. Irwin, K. W. Lehnert: Appl. Phys. Lett., **85**, 2107 (2004). [410](#)
- [85] P. K. Day, H. G. Leduc, B. A. Mazin, A. Vayonakis, J. Zmuidzinas: Nature, **425**, 817 (2003). [410](#)
- [86] NASA/SEU 2003 Roadmap: *Beyond Einstein: From the Big Bang to Black Holes*, <http://universe.gsfc.nasa.gov/be/roadmap.html>. [411](#)

# Index

- ACIS, 368, 371, 405, 406  
ADR, 373, 374, 376–379, 383, 384, 388, 389, 395, 400  
Astro-E, 399  
Astro-E2, 359, 360, 370, 372, 374, 376, 377, 381, 386–389, 393, 399, 405, 406  
Beyond Einstein, 411  
CCD, 359, 366, 368–372, 386, 405–407  
CFH12K, 407  
Chandra, 359, 360, 367–372, 388, 393, 405, 406  
charge exchange, 381, 382, 401, 403–406  
COBE, 374  
comet, 386, 401, 403–406  
Constellation-X, 359, 374, 376–381, 394, 408–411  
cryo-cooler, 374, 376–379, 388, 389, 392, 395  
deep implant, 386, 391  
dielectronic recombination, 388  
diffraction grating, 360, 366, 367  
direct excitation, 362, 402  
EBIT, 387, 388, 396–402, 404, 406  
Einstein, 367  
electron-impact excitation (EIE), 401, 402  
EPIC, 369, 371, 372  
EXOSAT, 367  
field effect transistor (FET), 379, 408  
Generation-X, 411  
HETG, 368, 369, 372, 388  
HgTe, 383, 390, 391  
HXD, 386  
LETG, 368  
MAXIM, 411  
Maxwellian distribution, 361, 399, 401  
microcalorimeter, 360, 366, 372, 373, 378, 379, 382, 383, 387–390, 393, 395, 396, 399, 403, 408, 409, 411  
multiplexer, 379, 395  
NeXT, 359, 372, 375–377, 381, 394, 410  
photoionization equilibrium (PIE), 361  
Position Sensitive TES (PoST), 408, 409  
proportional counters, 359, 360, 366, 369, 370, 381  
radiative recombination, 361, 362, 366, 401–403  
reflection grating, 367–369  
RGS, 368, 369, 388  
ROSAT, 382, 386, 403, 410  
RXTE, 369  
Super-EBIT, 398  
superconducting quantum interference device (SQUID), 378, 379, 408, 410  
TES, 373, 379, 395, 408, 409  
transmission grating, 367, 368  
X-ray absorber, 390, 391, 393, 408  
X-ray absorber, 383, 391, 393, 409  
XEUS, 359, 372, 376, 381, 394, 408, 410  
XIS, 386

- XMM-Newton, 359, 360, 367–372, 388, 393  
XQC, 359, 374, 377, 381–386, 389–391, 393, 395, 400, 410
- XRS, 359, 360, 374, 376–381, 386–395, 408, 410  
XRS/EBIT, 396, 399–406

# Optical/UV Astrophysics Applications of Cryogenic Detectors

B. Cabrera and R. W. Romani

Physics Department, Stanford University, Stanford, CA 94305-4060  
[cabrera@stanford.edu](mailto:cabrera@stanford.edu)

**Abstract.** Since the laboratory demonstrations of optical photon detection with STJs in 1993 [1], and with TESs in 1998 [2], there has been steady progress on the utilization of energy-resolving cryogenic detectors for astrophysical observations in the near-IR through UV. These detectors provide the unique and powerful possibility of simultaneously time-stamping, energy-resolving, and imaging each photon. Prime applications include studies of compact rapid time variable sources, and studies of faint sources where maximum utilization must be made of each photon to extract information on redshift and source characteristics. To date observations of the Crab pulsar have been made with TES and with STJ detectors, as well as a number of other sources including accretion-powered systems with white dwarf, black hole and neutron star primaries. The greatest scientific potential for these instruments will be seen when they are placed above most or all of the atmosphere. A series of applications are on the horizon, beginning with large ground-based telescopes, high altitude (SOFIA - Stratospheric Observatory for IR Astronomy, balloon) observations, and finally explorer class satellites. In this paper we summarize the scientific case for these instruments, the status of the technology, and recent observations.

## 1 Introduction

Several groups are developing superconducting tunnel junction (STJ) and transition-edge sensor (TES) instruments for novel IR-optical-UV photon detectors that should have a revolutionary impact on a range of fields requiring faint object spectrophotometry. These efforts have met with remarkable success. They have produced and characterized first-generation devices, developed systems for astrophysical observations, made the first scientific measurements, and have planned a number of modifications that should greatly increase the power of second-generation detectors. Here we summarize the recent advances with these STJ and TES devices, focusing on our own TES work, but referring to recent progress by the STJ groups, and highlighting common experimental challenges. We start by describing the scientific advantages of this broad-band time- and energy- resolving detector technology for faint object spectrophotometry, and then proceed to a description of TES and STJ instruments.

The frontiers of astrophysics are advanced by spectral measurements of the very faintest sources. A typical astrophysical source is a glowing hot body of size  $R$  with temperature  $T$ , at distance  $D$ , where the photon flux scales as  $(R/D)^2 T^3$ . So faint sources are small, distant, cool or some combination of the above. To study these objects, in which the physics is encoded in the spectral energy distribution (SED) and its variability, we need to wrest maximum information from every photon collected. For example, TES devices detect photons with high efficiency over the range  $\approx 0.1 - 10\text{ eV}$  ( $\approx 10 - 0.1\text{ }\mu\text{m}$ ), provide their energy to  $\approx 0.1\text{ eV}$  accuracy, and determine the arrival time to sub-microsecond precision. These properties can greatly advance a number of faint object studies. These capabilities are particularly well suited to the small  $R$  domain: compact objects emit over a wide energy range, often non-thermally, have spectra dominated by broad features (spectral energy breaks and velocity- and pressure- broadened lines), and exhibit variability on timescales  $\sim R/c$  extending well below 1 ms for stellar mass objects. The first astrophysical applications have been focused on neutron stars, accreting black holes, and white dwarf systems. Because redshifts are often very uncertain, distant sources must also be studied over a wide energy range. Since many high  $z$  sources have strong spectral lines and breaks, these detectors are also suited to certain photon-starved applications in the large  $D$  domain. With the substantial IR sensitivity of these TES and STJ devices, studies of low  $T$  objects can also be of interest, although IR array technology is now sufficiently advanced that cool object studies may be best pursued with other devices.

We discuss several important science programs for these novel detectors in Sect. 5. In addition, because of the novelty of this  $0.1 - 10\text{ eV}$  instrument, we expect that many unanticipated applications will likely be found. To set the scope of these programs, however, we discuss two possibilities: (1) the measurement of the time-resolved SED of a galactic compact object in the  $0.1 - 10\text{ eV}$  range with maximal sensitivity, and (2) imaging spectrophotometry of very faint extragalactic sources, e.g. interacting galaxies and AGN. To access this broad energy range we must, of course, be in a space (or near-space balloon) environment. There, a maximally sensitive observation for a given telescope aperture requires minimizing the background. To observe point sources at near optimum sensitivity we therefore require that individual pixels be matched to the diffraction-limited point-spread-function (PSF) near the UV limit of the system and the size of the array,  $30 \times 30$  to  $100 \times 100$ , matched to the spatial PSF at the IR end of the observed band. Thus, the optimal detector will have a size of a few  $\times (\lambda_{\max}/\lambda_{\min})$  to allow optimal PSF-limited source detection across the full energy range. Such an array would be well suited for balloon and explorer class programs whose primary mission is the high speed, broad-band spectrophotometry of compact objects and other point sources. Furthermore, from a balloon or space platform, such arrays would also provide the opportunity for spatially resolved spectral studies of extraordinarily faint extended sources in a wider field mode. Note that, for

the  $\approx 0.7 - 4$  eV ground-based application, the array criterion is achievable with the existing  $6 \times 6$  TES array and the  $10 \times 12$  STJ array technology already in hand.

The ESA (European Space Agency) has a well established imaging STJ program. They have operated S-Cam 2, the second prototype of a cryogenic camera for ground-based astronomy, based on a  $6 \times 6$  array of Ta/Al STJs. It is an improved version of S-Cam 1, which was tested on the William Herschel Telescope in La Palma (Canary Islands) in early 1999. S-Cam 2 has since been used on two successful observing campaigns on the same telescope in December 1999 and April 2000. More recently, the ESA group has built a  $10 \times 12$  array with Ta/Al STJs with optimized IR rejection filters. Other recent efforts include small telescope astronomical observations with a Nb/Al STJ detector [3].

In the near-term, a strong motivator for progress with these arrays is found in ground-based tests accessing a fraction ( $< 1$  decade) of the device energy range. On a longer term, if this calorimetric detector technology can be scaled to high pixel count arrays, a wide range of astrophysical observations will become possible. To this end, research must address arraying solutions amenable to such extension.

One challenge will be dealing with the enormous data rate that such a photon resolving technology provides. A combination of device pulse fall times and amplifier properties limit the read rates in current TES array designs to  $\approx 30$  kHz/channel. Our program at Stanford in collaboration with NIST Boulder (National Institute for Standards and Technology) has as a development goal a kilopixel array of  $32 \times 32$  pixels. The approach to this array is staged. We are presently working with ‘brute force’ arrays of  $6 \times 6$  and  $8 \times 8$  pixels, each pixel having a separate read channel. These arrays are being instrumented in a configuration suitable for high data rate observations from a balloon or ground-based platform. The  $10 \times 12$  pixel ESA STJ array provides similar capabilities. To extend to  $32 \times 32$  we can explore adaptation of present TES multiplexing schemes to the optical regime. Both STJ and TES groups are also exploring position-sensitive (DROID) pixel devices for alternative approaches to large pixel count. These larger format cameras will, of necessity, have serious count-rate limitations. The extended arrays will be of interest for future long duration balloon (LDB) and space-based observations.

## 2 Optical STJ and TES Sensors

An ideal photon detector would absorb each photon while providing maximal information, including x-y image position, arrival time, energy, and polarization. For the past fifteen years, such energy dispersive detectors operating below 0.1 K have been available in the X-ray band, where the combination of high resolving power (now  $R \approx 2500$  at 6 keV, see Chapter by Irwin and Hilton) and high efficiency ( $\approx 100\%$  at 6 keV) make them the detectors of

choice for the next generation of X-ray satellite missions such as Constellation X. These detectors are based on STJs (see Chapter by *Lerch and Zehnder*), on microcalorimeters, which use semiconducting thermisters (see Chapter by *McCammon* and Chapter by *Porter, Brown and Cottam*) and more recently on TESs (see Chapter by *Irwin and Hilton*).

Over the past decade, the STJ and TES cryogenic technologies have been extended to access longer wavelengths in the UV, visible, and near IR. These detectors count single photons, while time-stamping to better than 0.1  $\mu$ s and energy resolving with an attainable  $R \approx 100$  ( $500 \text{ nm}/\lambda$ ) $^{1/2}$ . The same single photon counting cryogenic technologies thus scale from the near IR to the far UV and on up to X-rays. In fact, these are also the detectors of choice, operated in bolometric mode, for far-IR/mm observations in the next generation of CMB satellites such as Planck and in ground based IR cameras such as SCUBA. In the visible through UV, the detectors have an absorption efficiency above 50% and with coatings, in principle, can approach 100% from the near IR through the UV (see Sect. 4.4).

**Table 1.** Fundamental resolutions for TES and STJ photon detectors

TES	STJ or $L_K$
$\Delta E_{\text{FWHM}} = 2.355 \sqrt{4k_B T_c^2 C \sqrt{n/2/\alpha}}$	$\Delta E_{\text{FWHM}} \approx 2.355 \sqrt{E \epsilon_0 (F + G)}$
$n = 5$ electron-phonon coupling $T_e \approx T_c$ and $E_{\text{sat}} \approx T_c C/\alpha$	$\epsilon_0 \approx 1.7$ $\Delta \approx 1.7(1.76k_B T_c) \approx 3k_B T_c$ $F \approx 0.2$ is Fano factor $G \approx 0 - 2$ (back tunneling noise)
$\Delta E_{\text{FWHM}} \approx 2.355 \sqrt{6.4k_B T_c E_{\text{sat}}}$	$\Delta E_{\text{FWHM}} \approx 2.355 \sqrt{0.6k_B T_c E}$
$\Delta E_{\text{FWHM}} \approx 24 \text{ meV} \sqrt{\frac{E_{\text{sat}}}{2.5 \text{ eV}}} \sqrt{\frac{T_c}{70 \text{ mK}}}$	$\Delta E_{\text{FWHM}} \approx 26 \text{ meV} \sqrt{\frac{E}{2.5 \text{ eV}}} \sqrt{\frac{T_c}{1 \text{ K}}}$
$R_{\text{TES}} \approx 103 \sqrt{\frac{E_{\text{sat}}}{2.5 \text{ eV}}} \sqrt{\frac{70 \text{ mK}}{T_c}}$	$R_{\text{STJ}} \approx 96 \sqrt{\frac{E}{2.5 \text{ eV}}} \sqrt{\frac{1 \text{ K}}{T_c}}$ with $G = 0$

As discussed in Chapter by *Lerch and Zehnder*, STJs can be analyzed in a similar manner to semiconductor diode detectors since the signal is proportional to the number of electron-like excitations produced by the photon. The difference is that the energy per excitation is less than 1 meV, twice the energy gap of the superconductor, rather than about 1 eV, the gap of the semiconductor. This difference provides an improvement in the fundamental resolution by a factor of  $\approx 30$  from the counting statistics on the number of excitations. TESs, on the other hand, are calorimeters which actually measure the temperature rise in an isolated heat capacity to determine the photon energy. Their fundamental resolution is determined by, and proportional to, the

square root of the transition temperature of the superconductor. As shown in Table 1, the comparison of fundamental resolution between TESs and STJs results in remarkably similar numbers. The noise from the counting statistics for the STJs, where the unit energy gap is given by  $1.76 \times k_B T_c$ , ends up nearly identical to the noise from the thermodynamic fluctuations of the TESs with the same energy scale given by  $k_B T_c$ . The one difference is that for a given STJ detector, the energy resolution is proportional to the square root of the photon energy, so that  $\Delta E_{\text{FWHM}} \propto \sqrt{E_\gamma}$ , whereas for a given TES detector, the energy resolution is a constant given by the device saturation energy, so that  $\Delta E_{\text{FWHM}} \propto \sqrt{E_{\text{sat}}}$ . Note also that if the back-tunneling coefficient  $G \approx 1$ , the resolving power  $R$  is reduced by a factor of  $\approx 2.5$  compared to the value shown in Table 1 where optimistically  $G$  is set to zero.

So ultimately the choice between STJ and TES will come down to the answers to three questions about which technology: (1) most closely approaches the fundamental energy resolution limits, (2) provides the highest manufacturing yield and ease of operation, and most importantly, (3) can instrument the largest pixel arrays. With respect to the first question, both technologies have attained  $\approx 0.15$  eV FWHM near 1 eV ( $1.24 \mu\text{m}$ ) and improvements of a factor of 2 or 3 are expected, and both technologies have demonstrated counting rates above 10 kHz per pixel. With respect to the second question, the critical fabrication issue for TESs is the control of  $T_c$ , which is more straightforward than the control of the tunneling barrier for STJ, but not a major advantage. Both technologies will want to operate below 100 mK, but the cryogenic X-ray and CMB missions are already working hard on satellite cryogenic systems capable of reaching this temperature range. With respect to the third question, currently the TES technology has an advantage because a time-domain multiplexing technique has been demonstrated which takes advantage of the low noise provided by a SQUID-readout (see Chapter by *Irwin and Hilton*). Recently, an interesting frequency domain multiplexing scheme has been suggested which utilizes a new low noise amplifier called the rf SET (single electron transistor) [4]. Also, a new readout scheme based on kinetic inductance in superconductors has the same fundamental resolution limits as STJs, but has an attractive frequency-domain multiplexing scheme which utilizes existing GHz room temperature electronics [5]. Ultimately, large arrays will provide the broadest science reach and the technology allowing the most straightforward path to large arrays will be chosen.

We note that because of their broadband nature, these detectors are not intrinsically solar blind, and so do not easily replace the need for micro-channel plate (MCP) detectors with dispersive optics for UV spectroscopy on or near bright optical sources. The filters required to make them solar blind, such as Woods filters of MgF with Na layers, have proven difficult to make with high throughput efficiency. However, lower backgrounds than those provided by MCPs may be possible with STJ or TES instruments and may offset the filter efficiency losses for some applications.

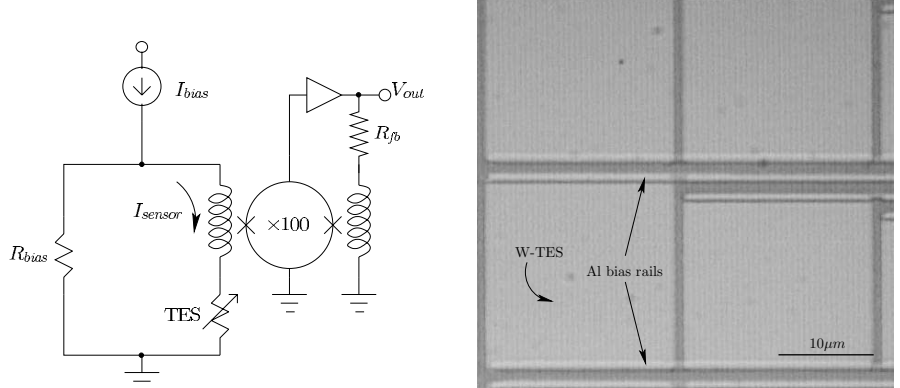


**Fig. 1.** The electrical circuit (*left*) of the ETF-TES showing voltage bias scheme and SQUID current readout. A photograph (*right*) of a W TES sensor array with Al rails (common ground rail)

## 2.1 The Superconducting Transition Edge Sensor

In the TES electrical schematic and sensor photo shown in Fig. 1, photons are absorbed directly into a thin superconducting metal film and cause a temperature rise of the electron system in the film. This metal film is biased in temperature within its superconducting to normal transition and the temperature rise results in a resistance increase. The device operation and performance are detailed in [2].

The fundamental resolution [6] is given by

$$\Delta E_{FWHM} = 2.355 \sqrt{4k_B T^2 \sqrt{n/2}/\alpha}, \quad (1)$$

where \$T\$ and \$C\$ are the temperature and heat capacity of the electron system (very near \$T\_c\$), respectively, \$n = 5\$ for electron-phonon limited conductance, and \$\alpha = (\mathrm{dln} R / \mathrm{dln} T)\_{V=\text{const}}\$. This resolution is independent of energy in the limit of a small temperature excursion around \$T\_c\$; however, the optimum detector design gives

$$\Delta E_{FWHM} \approx 2.355 \sqrt{4\sqrt{n/2} k_B T_c E_{sat}}, \quad (2)$$

with \$E\_{sat} \approx CT\_c/\alpha\$, which scales as \$\sqrt{T\_c}\$. For example, for \$T\_c = 80 \text{ mK}\$ and \$E\_{sat} = 10 \text{ eV}\$ we obtain \$\Delta E\_{FWHM} \approx 0.05 \text{ eV}\$. This intrinsic resolution is limited by thermodynamic fluctuations. The W TES sensors are intrinsically fast, with a pulse rise-time constant of \$\approx 0.3 \text{ } \mu\text{s}\$ and pulse fall-time constant of \$\approx 10 \text{ } \mu\text{s}\$.

To complete the estimate of detector resolution, we must determine what fraction of the initial photo electron energy is captured in the electron system. Although the electron system is thermally isolated from the phonon

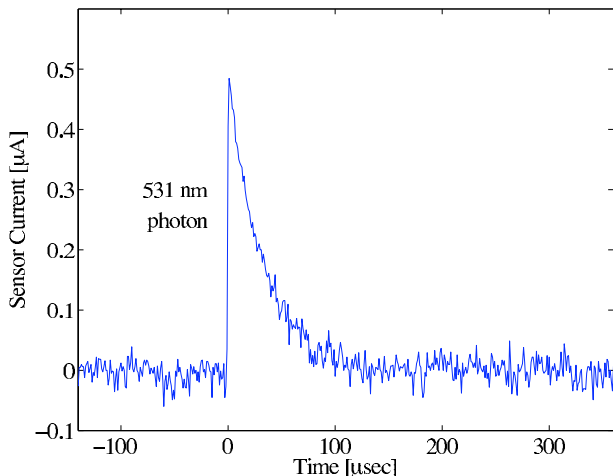


**Fig. 2.** Pulse from single photon

system near  $T_c$ , during the initial cascade process many high-energy athermal phonons are produced, and many escape the film before interacting again with the electron system. Monte Carlo simulations of these cascades in aluminum and niobium suggest that slightly more than half of the initial energy is lost from the film. Using the absolute calibration of the electrothermal feedback integral, we obtain an energy efficiency of 42% for these sensors. We are now exploring the use of SiN membranes to increase this efficiency to near 100%. Thus, with the present efficiency factor, the predicted resolution becomes  $\Delta E_{\text{FWHM,obs}} = 0.088 \text{ eV}$ . For comparison, our best resolution to date is 0.12 eV FWHM. A single-photon pulse is shown in Fig. 2.

In Fig. 3 we have combined 22 spectra from 800 nm to 360 nm in 20 nm steps. Filters were used to suppress the out of band flux scattered by the grating. As seen in Fig. 3, there are well-defined central peaks that increase slightly in full width half maximum from 0.15 eV to 0.17 eV. These spectra also show a second step feature at about one half of the energy of the primary peak. This feature is due to photons which interact with the voltage bias rails rather than the central part of the sensor, for which about half of the energy escapes before being trapped in the sensor region. We have shown that by collimating the fiber output onto the middle of the sensor, we suppress these rail hits.

There is also a low energy feature seen in Fig. 3 near 0.5 eV (2.5  $\mu\text{m}$ ) due to thermal photons. This feature does not move with the monochromator setting. The spectra for the highest incident photon energies are identical with the background spectra with the fiber blocked at the dewar bulkhead because there are very few photons at those energies coming from the lamp. We thus attribute this peak near bin 50 to infrared photons from the room

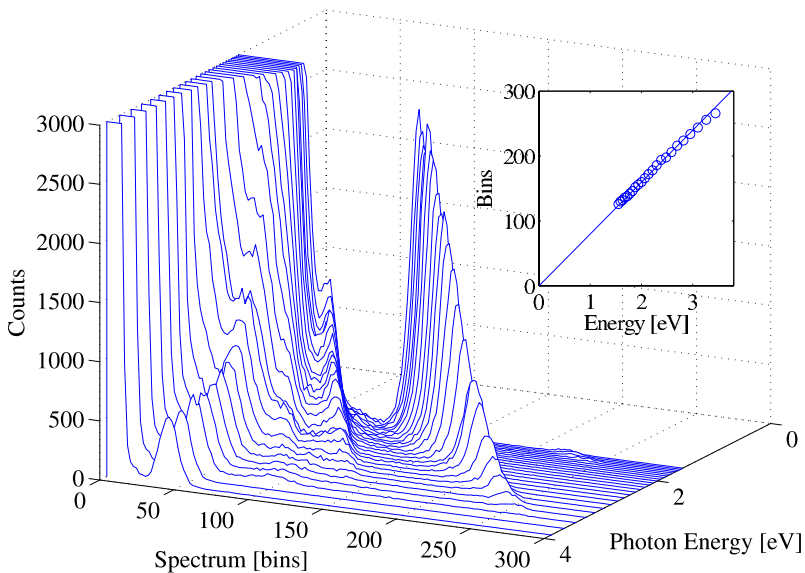


**Fig. 3.** Array of calibration spectra from 360 nm to 800 nm in 20 nm steps, showing the linearity (also see *insert*), rail hits, and thermal background. The electronics noise wall is at 0.25 eV (5  $\mu\text{m}$ ), and the spectra are cut off at 3000 counts. The resolution is 0.15 eV FWHM at 800 nm and degrades to 0.17 eV FWHM at 360 nm

temperature end of the fiber. It is seen as a peak because the lower energy photons are suppressed by the infrared cutoff of the fiber. The Fig. 3 inset shows the linearity between the primary peak position in the spectra and the incident photon energy.

A very useful calibration technique is to inject heat pulses directly into the TES sensor. The injected energy can be increased in a controlled manner and signal averaging can improve the diagnostic resolution. In Fig. 4, we show a sequence of heat pulse averages (each trace is the average of 1000 pulses) from 0.5 eV to 8 eV photon-equivalent energy. The saturation effects start near 4 eV, but the energy is accurately measured above this saturation by integrating the area under the pulse. This integral is directly proportional to energy (see Fig. 4 *inset*). As discussed in Sect. 2.2, we are working on techniques for analyzing these pulses near and into saturation to obtain the best energy resolution possible.

In summary, the TES has a fundamental resolution equal to or better than that of any other calorimetric technology operated at the same temperature, count rate, and heat capacity. Additional benefits include temperature self-biasing, self-calibration, insensitivity to temperature fluctuations and film non-uniformities, improved linearity, and suppression of electrical noise. The fundamental limit of these detectors is difficult to achieve; however, careful designs allow us to approach the optimal performance.

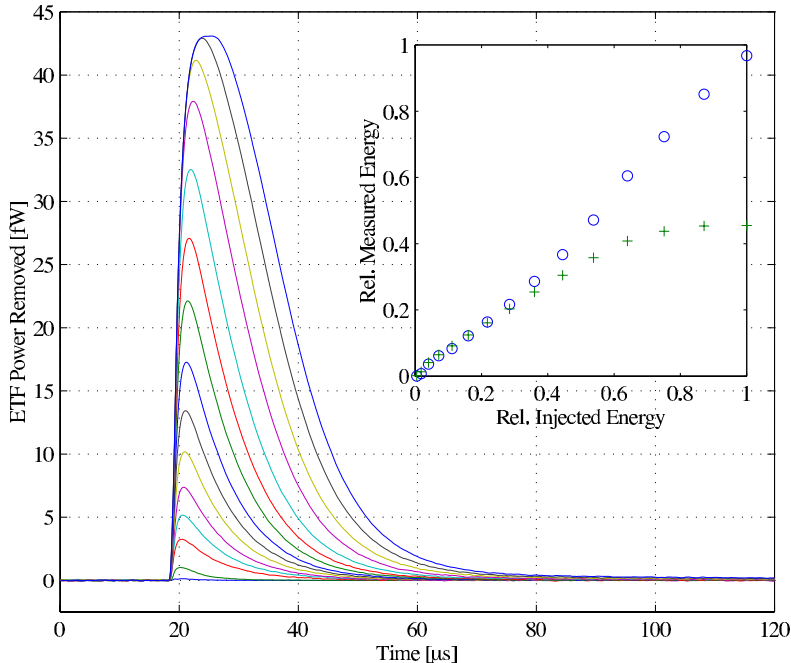


**Fig. 4.** Heat pulse calibrations into a  $25\text{ }\mu\text{m}$  TES from  $0.5\text{ eV}$  to  $8\text{ eV}$  photon equivalent. Each trace is the average of 1000 pulses and shows amplitude saturation at  $4\text{ eV}$ , however, the true energy is still recovered by integrating the area under the pulse. The decay time constants are  $\approx 8\text{ }\mu\text{s}$ . Flattening of the pulses is apparent for the highest energies, with a saturation power of  $\approx 43\text{ fW}$ . The *inset* shows the sensor linearity for peak-height (+) and pulse integral ( $\circ$ )

## 2.2 Optimal Filter Analysis for Nonlinear TES Response

As can be seen from the heat pulse data (Fig. 4), as the energy of a pulse approaches saturation and beyond, the shape of the pulse changes significantly. That means that the standard optimal filter analysis technique, often called a Wiener filter, fails when the pulse energy is beyond the small signal limit ( $E \ll E_{\text{sat}}$ ). In addition, as we shall see momentarily, the Wiener filter assumption of stationary noise is also violated. There exists a generalization of the Wiener filter for nonlinear pulses with non-stationary noise, which is optimum in the least squares sense [7]. For the best signal to noise, we want to operate very near the saturation energy since the resolution improves with lower  $E_{\text{sat}}$  proportional to  $\sqrt{E_{\text{sat}}}$ .

To investigate this analysis tool we simulated an optical TES with  $E_{\text{sat}} \approx 1\text{ eV}$ . In Fig. 5 we show the results of a thermal and electrical model which includes the Johnson noise of the resistor and the transport noise in the thermal link. For the thermal and electrical equations we use

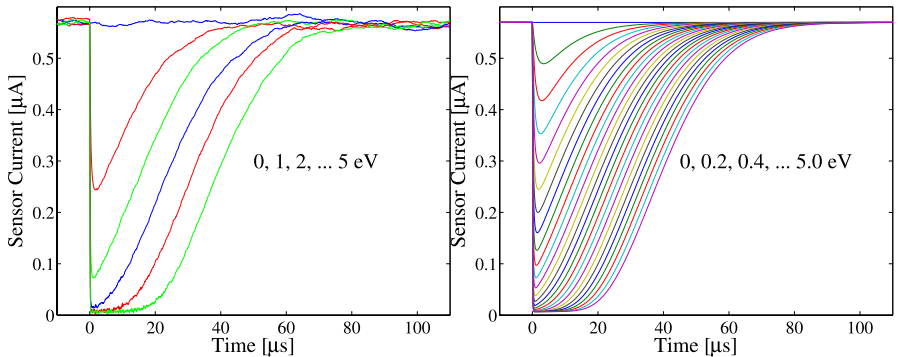


**Fig. 5.** Heat pulse (*left*) and template (*right*) simulation where we have set  $E_{\text{sat}} \approx 1 \text{ eV}$ . Johnson and phonon TES noise terms are added accurately and we assume that SQUID noise is negligible since it is typically an order of magnitude smaller than the sensor noise

$$C \frac{dT_e}{dt} = I_s^2 R_W - \Sigma (T_e^5 - T_{\text{ph}}^5) + E_0 \delta(t - t_0) + P_{\text{nyq}} + I_s V_{\text{nyq}}, \quad (3)$$

$$R_s(I_b - I_s) - V_{\text{nyq}} + V_{R_s R_p \text{nyq}} = I_s R_W - L \frac{dI_s}{dt} \quad (4)$$

where  $C$  is the heat capacity of the TES which we assume to be constant,  $T_e$  and  $T_{\text{ph}}$  are the electron and phonon system temperatures in the TES,  $I_s$  is the current flowing through the TES,  $R_W$  is the temperature-&-current dependent resistance of the TES,  $\Sigma$  is the electron-phonon coupling constant in W,  $E_0$  is the absorbed photon energy, and  $P_{\text{nyq}}$  and  $V_{\text{nyq}}$  are the phonon and electrical (Johnson) Nyquist noises (Fig. 1 *left*). The additional terms in the coupled electrical equation include  $R_s$  the shunt resistor,  $I_b$  the bias current, and  $L$  the SQUID input coil inductance. Note that the noise along the simulated pulses is not constant. In particular when the TES is near or into saturation the Johnson noise is suppressed. Thus the Wiener filter of stationary noise is clearly violated. We will handle the nonlinear aspect of the changing pulse shape by obtaining 256 pulse shapes with no noise from 0 to 5.10 eV in 0.02 eV steps (Fig. 5 *right*).

Next, we construct the template array from  $M^i = \langle S^i \rangle$  by averaging many individual pulse vectors of the same energy. The noise vector is then given by  $D^i = S^i - M^i$  and the covariance matrix is constructed as  $V^{ij} = \langle D^i D^j \rangle$ . The weighting matrix  $W = \text{inv}(V)$  is also calculated and we form the  $\chi^2$  as [8]

$$\chi^2 = (S^i - M^i)^T \cdot W^{ij} \cdot (S^j - M^j) \quad (5)$$

where we calculate a weighting matrix for each pulse template. Then for each event, the optimal estimate for the energy in the least squares sense is the one with the minimum  $\chi^2$  value.

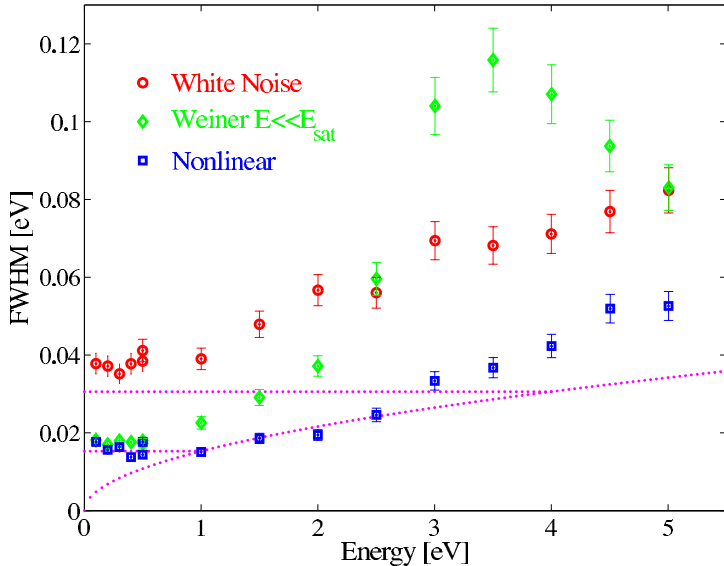


**Fig. 6.** Comparison of optimal filter analysis using standard Wiener filter based on quiescent noise, white noise filter and optimal nonlinear and non-stationary filter

Figure 6 shows the results of this simulations. For each energy at 0, 1, 2, 3, 4, and 5 eV, weighting matrices were calculated from 1000 pulses and then again from 4000 pulses for comparison. We then generated 200 pulses at each of 0.1, 0.2, 0.3, 0.4, and 0.5 eV and continuing more coarsely spaced at 1.0, 1.5, 2.0, 2.5, 3.0, 3.5, 4.0, 4.5, and 5.0 eV. For each set of pulses, we calculated the FWHM using three estimates: (a) the full non-stationary noise weighting matrices using interpolation for energies between the coarse grid at 1 eV spacing, (b) a white noise filter where the weighting matrix is replaced by the identity matrix, and (c) the Wiener filter using the weighting matrix for 0 eV at all energies. Note that for all three calculations we used the nonlinear templates. In Fig. 6 we also show two horizontal dotted lines. The lower line corresponds to the small signal limit for this TES heat capacity calculated analytically [6]. Note that both the Wiener filter estimates and the full non-stationary estimates are in good agreement below 0.5 eV, and that the white noise filter results are worse by more than a factor of 2. The upper horizontal dotted line corresponds to the small signal limit for a heat capacity four times larger, as would be required to maintain the small signal limit up to 2.5 eV. The non-stationary analysis follows the dotted curve ( $\propto \sqrt{E_{\text{sat}}}$ ) to  $\approx 2.5$  eV and then deviates upward. We suspect that finer time binning would result in better performance between  $\approx 2.5 - 5.0$  eV. Still, the message is clear: the best energy resolution for a particular application requires running the TES near and into saturation and provides a factor of two improvement in the

FWHM. Finally, note that the Wiener filter is considerably worse than even the white noise filter for pulses near and into saturation.

## 3 Fiber-Optic-Coupled TES Spectrophotometer

### 3.1 Operation of Four-Pixel Fiber-Optic TES Spectrophotometer

To demonstrate the ability of TES devices to provide new and astronomically interesting data, we have fiber-coupled detectors to a number of small telescopes and made some simple demonstration observations. Indeed, we reported on the first astronomical optical observations with an energy-resolving detector (coupled to a commercial 0.2 m telescope) in [9]. This use was followed by Crab observations at the Stanford 0.6 m teaching observatory [10] that demonstrated a unique new capability of simultaneous near-IR through near-UV time-tagged photon detection. Finally, our Stanford-NIST collaboration completed a successful observing campaign at the 2.7 m Harlan J. Smith Telescope at McDonald Observatory. For these observations a four-pixel sub-array of the  $6 \times 6$  array (shown in Fig. 1) was read out by a prototype four-channel digital SQUID feedback system [11, 12]. The NIST-developed readout system was capable of handling event rates well in excess of the 30 k-cts/s per pixel produced by the TES devices. Over the 7-night 2.7 m observing run, more than 100 million photons were energy-resolved, time-tagged to within 100 ns of UTC, and logged to disk for later analysis. The astronomical significance of these data is discussed in Sect. 3.2.

The cryogenic system used for these observations was a small dilution refrigerator and was quite limited in that it did not allow direct imaging. All input to the four-pixel detector array was via fiber-optic coupling. Fiber coupling is convenient from the perspective of IR background filtering, however it is more difficult to obtain high-efficiency light coupling to the cryogenic devices. As shown in Fig. 7, with no fiber losses the tungsten TES pixels have a raw absorptivity (i.e. quantum efficiency or QE) of nearly 50% across the optical/near-UV band. Ideally, the fiber absorption provides long-wavelength filtering while maintaining good transmission in the optical band. In practice, however, the fiber losses are exacerbated by fiber-to-fiber coupling,  $f$ -ratio reducers, and fiber-to-detector focusing (discussed below). For the 0.6 m/ $f$ 3.5 telescope observations, the plate scale was small enough to allow direct 50  $\mu$ m fiber coupling to the pixels and we achieved a peak on-sky efficiency of  $\approx 20\%$ . For the 2.7 m observations, a fiber optic taper and focusing system were needed to bring the light to the four active pixels. This optical train significantly reduced the system efficiency. Figure 8 shows our achieved telescope-to-detector efficiency as a function of photon energy. The majority of the losses came from a faulty fiber-to-fiber coupler

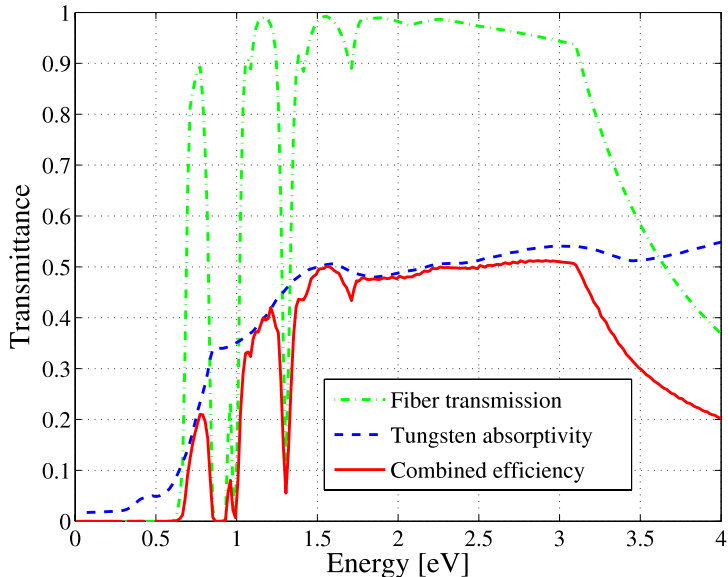


**Fig. 7.** Bare tungsten absorptivity, high OH “wet” fiber optic transmission, and the combined raw efficiency

at room temperature, and from geometric losses in focusing the output of the fiber to our small detectors. Our coupling efficiency improves dramatically by moving to a direct imaging system (see Sect. 4.2). This also, of course, provides major advances for source acquisition and photometric stability.

We used 400  $\mu\text{m}$  diameter fibers for adequate sky coverage at the telescope, together with a 400  $\mu\text{m}$  to 200  $\mu\text{m}$  tapered section. Coupling the 200  $\mu\text{m}$  fiber to our  $\approx 40 \times 40 \mu\text{m}^2$  array of pixels required a cold-optics focusing solution. Figure 9 shows a diagram and photograph of the fiber-to-detector coupling method used for these observing demonstrations. The fiber was cleaved, polished, and then inserted into a custom-made aluminum ferrule. This ferrule fit tightly on a 1.8 mm diameter Gradient-Index rod lens that collimated the fiber output. The resulting beam was focused by a 1 mm diameter ball lens onto the four devices with a factor of two in light loss. The entire lens assembly was attached to the Si substrate via small drops of epoxy at the end of long thin legs. These legs helped minimize the thermally induced stresses on the glue joints.

As described in Sect. 2.1, a TES device outputs a pulse with an integral proportional to the absorbed photon energy [6]. The pulse integrals may be binned to form an energy spectrum of the incoming light, obtaining  $R = 17$  at 2.5 eV (500 nm). The devices used in the initial fiber-coupled observations have no substrate or bias-line masking which allows a significant fraction

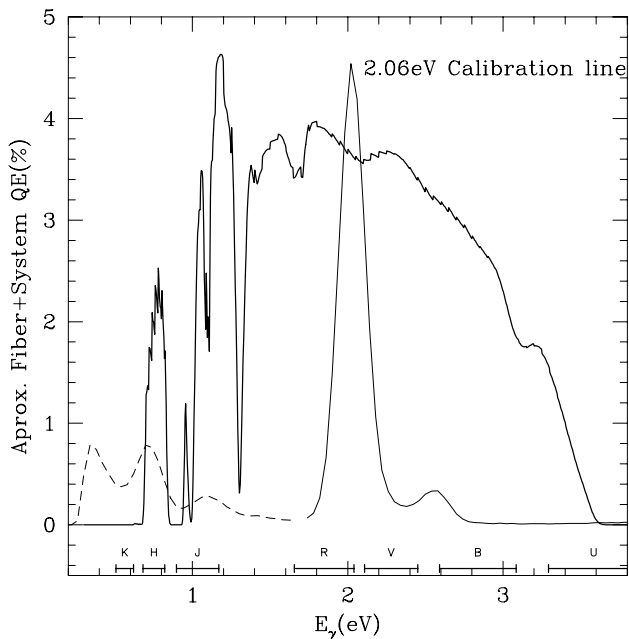


**Fig. 8.** Estimated total quantum efficiency of our system (fiber+detector) at the back end of the telescope. For comparison, the count spectrum is shown for a setting of 2.06 eV on a grating monochromator. The low energy events (*dashed line*) include a rising continuum due to Si substrate events, as well as an IR H-band peak from the warm optics and lamp

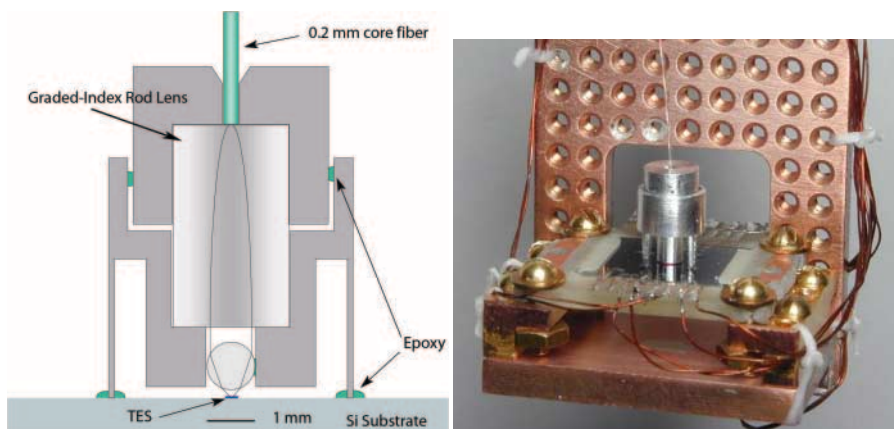


**Fig. 9.** (left) Diagram of a machined Al optics mount for coupling a  $200 \mu\text{m}^2$  fiber to a small ( $40 \times 40 \mu\text{m}$ ) set of four TES pixels. (right) Photograph of the assembly mounted on the sample stage of the dilution refrigerator

( $\approx 10\%$ ) of the incoming light to fall on non-optimal portions of the array. These ‘rail’ and ‘substrate’ photons cause high- and low-energy artifact peaks off the main ‘direct-hit’ event peak. This is illustrated in Fig. 8 where the small high-energy peak caused by rail-hit events is clearly seen. The next generation of TES array (detailed in Sect. 4.2) are designed to have a significant reduction in artifact events and thus a much cleaner energy point-spread function (PSF).

### 3.2 Crab Pulsar and Other Observations at McDonald 2.7 m

We conducted several nights of astronomical observations in February 2000 to gauge the performance of our first generation fiber-fed TES array system. These test observations served to focus attention on the challenges of delivering photons to the TES array and provided the first end-to-end test of the sensor and data analysis system.

We used calibrated photon sources and absolute power meters to demonstrate a total efficiency at 850 nm of 10% for light from a 200  $\mu\text{m}$ -core fiber at the top of the cryostat. Observations of astronomical spectrophotometric standards allowed us to measure the full QE of the system, including losses incurred from the fiber train and reducing optics (Fig. 8). The peak estimated QE was 4% with significant sensitivity extending from the ultraviolet (U band) into the infrared (astronomical H band). We have identified avoidable sources of loss that should provide over 5-fold increase in the system QE.

During this run, we observed a number of compact object sources, from isolated spin-powered pulsars to accreting white dwarf systems. The primary target used to tune and calibrate the system was the relatively bright Crab pulsar, which provided  $> 1 \text{ kHz}$  count rates. Phase-resolved spectrophotometry from an hour of these observations (Fig. 10) is analyzed in [13]. These data show, for the first time, rapid changes in the optical/IR spectrum through the pulse profile (Fig. 11). At X-ray and gamma-ray energies, the Crab pulsar shows spectral variations with a similar phase structure and the spectral energy distribution of these changes can be used to constrain the properties of the synchrotron-emitting particle population in the pulsar magnetosphere. These data are more fully described in [13]. We also searched for pulse-to-pulse variation in the pulsar emission, searched for non-Poisson photon correlations, and conducted exploratory spectrophotopolarimetry, measuring the energy dependence of the polarization sweep of the Crab pulsar emission.

Observations of other compact object systems, such as the LMXB Her X-1 and several accreting white dwarf (polar) systems also showed our sensitivity to rapid spectral variations. In the polar ST LMi, for example, we detect emission lines from the accretion stream and abrupt spectral changes as the white dwarf hot spot goes into eclipse. Observations of very faint pulsar targets, such as Geminga (Fig. 12), were used to explore the limits of

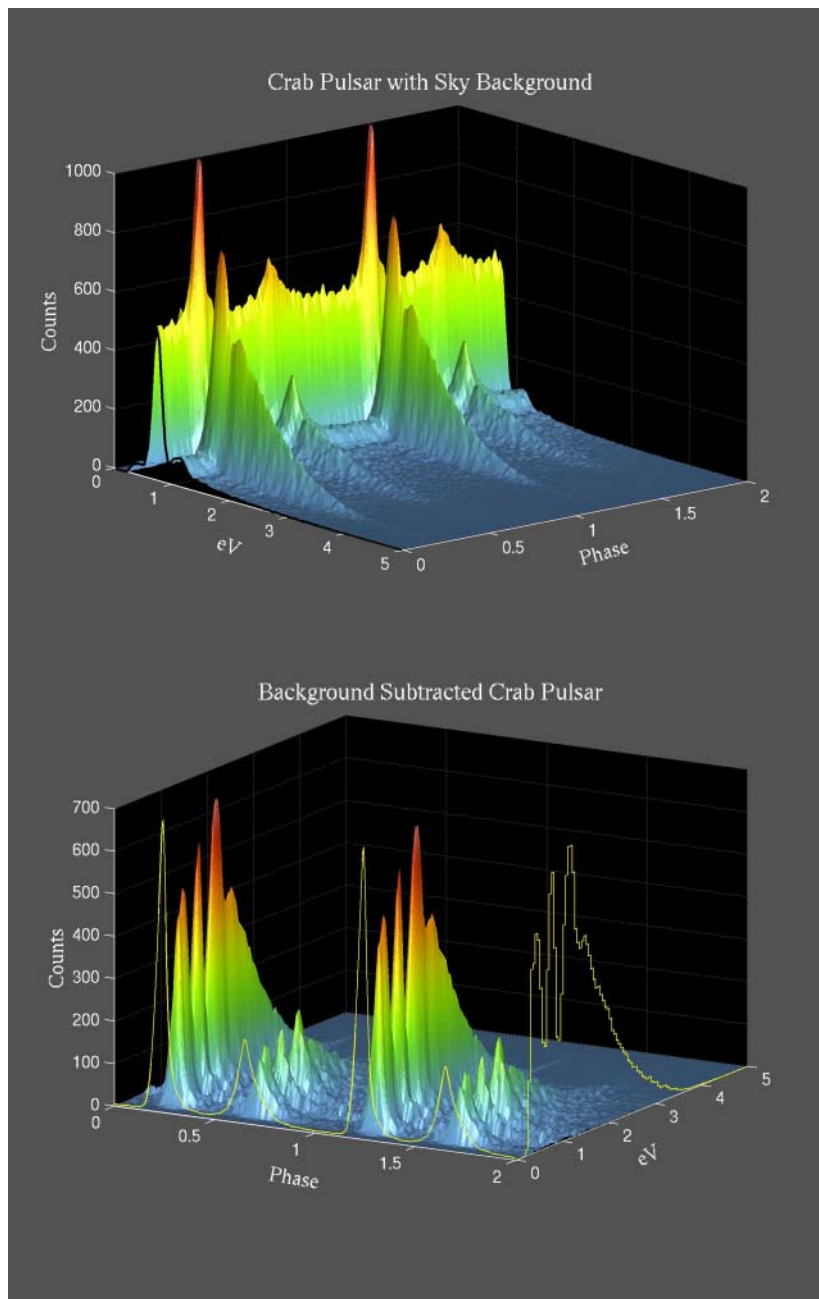


**Fig. 10.** Two-dimensional histograms showing photon energy versus Crab pulsar phase, for all photons (*upper*) where the thermal background increase is evident, and for Crab photons (*lower*) where the Crab off phase interval between 0–0.2 was used to subtract the background

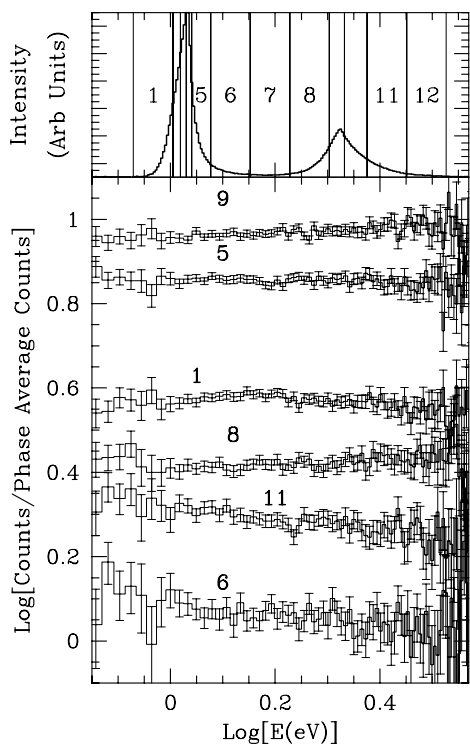


**Fig. 11.** Calibrated phase spectra for selected phase bins based on 3500 s of Crab 2.7 m data. These spectra extend into the near IR, and show for the first time subtle changes in the spectral index and breaks, which vary rapidly through the peaks of the Crab pulse profile

the sensitivity and stability of the TES system. These data are of appreciable scientific interest, showing new phenomena and demonstrating that the TES system outperforms more conventional fast photometers, even on substantially larger telescopes. Perhaps more importantly, the data serve to emphasize how important it is to move to a full focal plane imaging solution. The improved faint object extraction and spectrophotometry afforded by imaging has therefore driven the design of the next stage of the optical TES project.

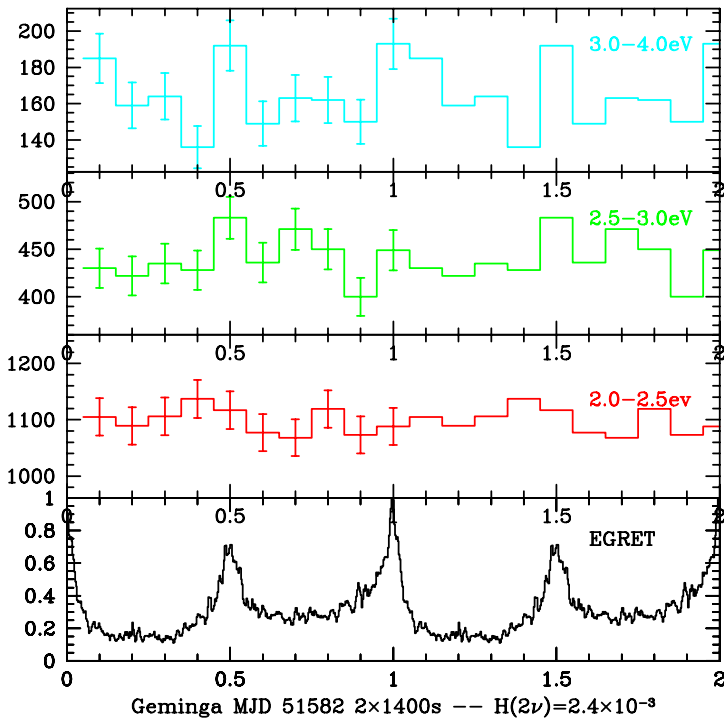


**Fig. 12.** Folded light curves in three energy ranges from 2.7 m test observations of the Geminga pulsar. Evidence for pulsation ( $\approx 3\sigma$  from an H test) appears above 2.5 eV (roughly, the U, B bands). Support for this tentative detection comes from the alignment of the peaks in pulse phase with the gamma-ray emission as determined from our absolute photon timing and the accurate high-energy ephemeris. The EGRET  $> 100$  MeV light curve is shown in the bottom panel for comparison. The apparent pulse flux is in reasonable agreement with the HST observed DC flux  $B \approx 26$ . Given that the only previous optical pulsed detection is a 3 sigma result from many hours of MAMA integration at the 6 m BAT, even this low significance detection with our small telescope and fiber-fed prototype is remarkable

## 4 Imaging STJ and TES Arrays

### 4.1 ESA S-Cam Instruments and Observations

The first implementation of an imaging solution came from the ESA group which has a well-established effort to build cameras using STJ sensor arrays [14]. The first instrument, S-Cam 1, featured a  $6 \times 6$  imaging array of diamond shaped pixels, each  $25 \mu\text{m}$  on a side with  $4 \mu\text{m}$  gaps, deposited on the backside of a sapphire substrate (see Fig. 13 left). S-Cam 1 achieved a resolving power of  $R \approx 5$  at 500 nm and was tested at the William Herschel 4.2 m telescope in early 1999. It was found to be limited by infrared leakage. A second generation S-Cam 2 improved performance to  $R \approx 8$  at 500 nm [15]. Also

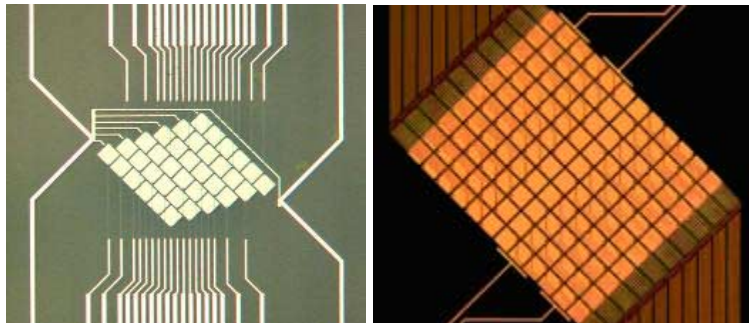


**Fig. 13.** Two designs of ESA of S-Cam instruments (*left*) S-Cam 1 & 2 were  $6 \times 6$  arrays and (*right*) S-Cam 3 is a  $10 \times 12$  array. Each pixel has a sensitive area of  $33 \times 33 \mu\text{m}^2$  with  $4 \mu\text{m}$  gaps between the pixels. (from [14] © ESA)

$6 \times 6$  arrays, S-Cam 2 detectors were made of a Ta-Al-AlO<sub>x</sub>-Al-Ta multilayer deposited on a  $520 \mu\text{m}$  thick sapphire substrate. The light shines through the substrate allowing the surface to be used for wiring without obstructing the optical sensing area. The detectors were operated at  $350 \text{ mK}$  and each pixel was read out individually with a FET amplifier. The thick Al layer provided a higher responsivity than the S-Cam 1 generation and the IR blocking filters were also improved (see Sect. 4.5) [15, 16, 17, 18]. The camera used a Schott KG2 filter at  $12 \text{ K}$ , a Schott KG5 filter at  $2 \text{ K}$ , and the sapphire substrate was maintained at  $0.32 \text{ K}$ .

A series of observations have been undertaken with the S-Cam 2 instrument at the  $4.2 \text{ m}$  telescope. As for the TES observations, the Crab pulsar was one of the first targets [19, 20]. Good light curves were obtained in several colors, although the spectral range, energy resolution and S/N were inadequate to show phase-resolved spectral variations. Other astronomical detections have been published, including high-speed energy-resolved STJ photometry of the eclipsing binary UZ For [21], direct determination of quasar redshifts using the STJ-supplied colors [22] including targets as faint as  $V \approx 21$ , STJ observations of the  $V \approx 15$  eclipsing polar HU Aqr [23], and estimation of bright star temperatures from STJ colors [24]. To date these observations only address relatively bright targets at quite modest efficiency, so the results would be easily obtained on smaller telescopes with conventional techniques. However, these pioneering observations are very important in illustrating the sort of analyses that should be possible on very faint time variable sources, when high efficiency, higher-resolution cryogenic imaging spectrophotometers are available.

ESA is now using S-Cam 3, an imaging  $10 \times 12$  STJ array and has obtained  $R \approx 8-11$  at  $500 \text{ nm}$  with this instrument (see Fig. 13 right). Each pixel is  $33 \times 33 \mu\text{m}^2$  with  $4 \mu\text{m}$  gaps between pixels for a fill factor of 76%. The larger area per pixel and the larger pixel count have increased the field of view at

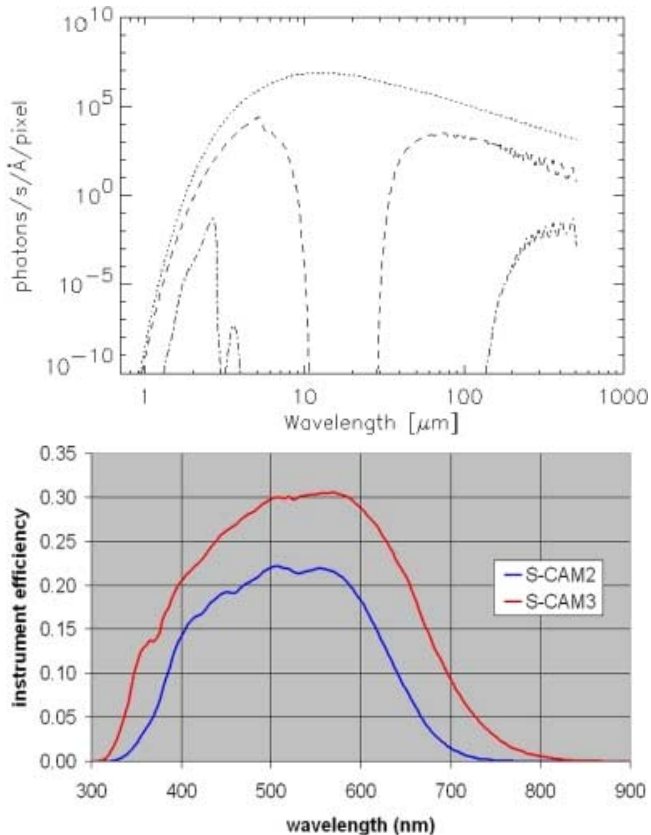


**Fig. 14.** The IR loading (*top*) has been a problem for both STJ and TES imaging cameras. Combinations of IR blocking filters are used to obtain the useful efficiency (*bottom*) in the optical. (from [14] © ESA)

the William Herschel 4.2 m telescope from  $4'' \times 4''$  for S-Cam 2 to  $11'' \times 9''$  for S-Cam 3, with a pixel scale of  $0.8''$ . As we discuss further in Sect. 4.5, the rejection of thermal infrared photons is very important as these detectors are sensitive to wavelengths out to  $1000\text{ }\mu\text{m}$ . Fig. 14 (*top*) shows the blackbody spectrum from 300K radiation (*dotted*), the spectrum passing through the sapphire substrate (*dashed*), and finally the spectrum passing through the filters (*dot-dash*). For this improved rejection of IR radiation, KG5 used with the S-Cam 2 was replaced with two BK7 filters, each 9.5 mm thick with one at 4K and the other at 0.3K. These reduced the IR loading by more than one order of magnitude. The bandpass from  $330 - 745\text{ nm}$  is shown in Fig. 14 (*bottom*) and reaches 30% efficiency at 500 nm, up from the values obtained with S-Cam 2.

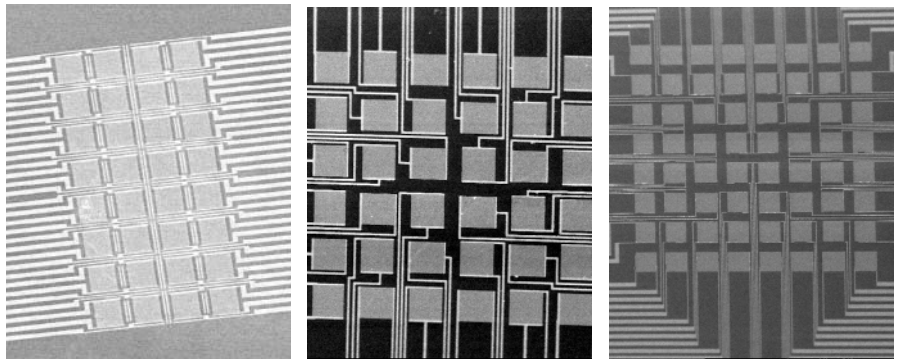


**Fig. 15.** Three generations of TES imaging arrays, starting with  $4 \times 8$  array, then  $6 \times 6$  array, and finally the  $8 \times 8$  array. Each pixel has a sensitive area of  $24 \times 24 \mu\text{m}^2$  and the array has  $36 \times 36 \mu\text{m}$  center-to-center spacing. The space between pixels is covered with reflection mask (shown in Fig. 17)

The S-Cam 3 instrument was first used for observations during July, 2004 at the WHT 4.2 m at La Palma, Spain. The observation targets were objects with large temporal and large spectral variability. The ESA group is in the process of analyzing these data.

## 4.2 Imaging Array with TESs

Our TES imaging array instruments have also gone through three generations of laboratory testing, but have not yet been used for observations. The first shown in Fig. 15 (*left*) was a  $4 \times 8$  array of  $24 \times 24 \mu\text{m}^2$ W pixels with  $12 \mu\text{m}$  gaps [11, 12]. All detectors use the same 35 nm thick W films for the sensitive areas. All wiring to each pixel is carried in the gaps between pixels, and as we discuss in Sect. 4.3 our reflection mask prevents photons from hitting the gaps and reflects nearly all such photons back into the sensitive pixel area. The second generation was a  $6 \times 6$  square array with the same pixel and gap dimensions (see Fig. 15 *center*). Our 32-channel electronics readout system is connected to all but the four corner pixels in this square array.

We have performed many tests with the  $6 \times 6$  and  $4 \times 8$  arrays; some are described below. As shown in Fig. 16, we have also demonstrated similar energy resolution to our fiber-coupled system with  $\Delta E_{\text{FWHM}} = 0.19 \text{ eV}$ , giving  $R = 13$  at  $2.5 \text{ eV}$  (500 nm). As discussed in Sect. 4.5, the IR loading on the imaging arrays degrades their performance and is the key issue which needs to be resolved before we can fully utilize the intrinsic energy resolution of present and future TES instruments. In anticipation of doubling our readout electronics from 32 channels to 64 channels, we have also fabricated and are testing the third generation  $8 \times 8$  imaging array with the same pixel dimensions (Fig. 15 *right*).

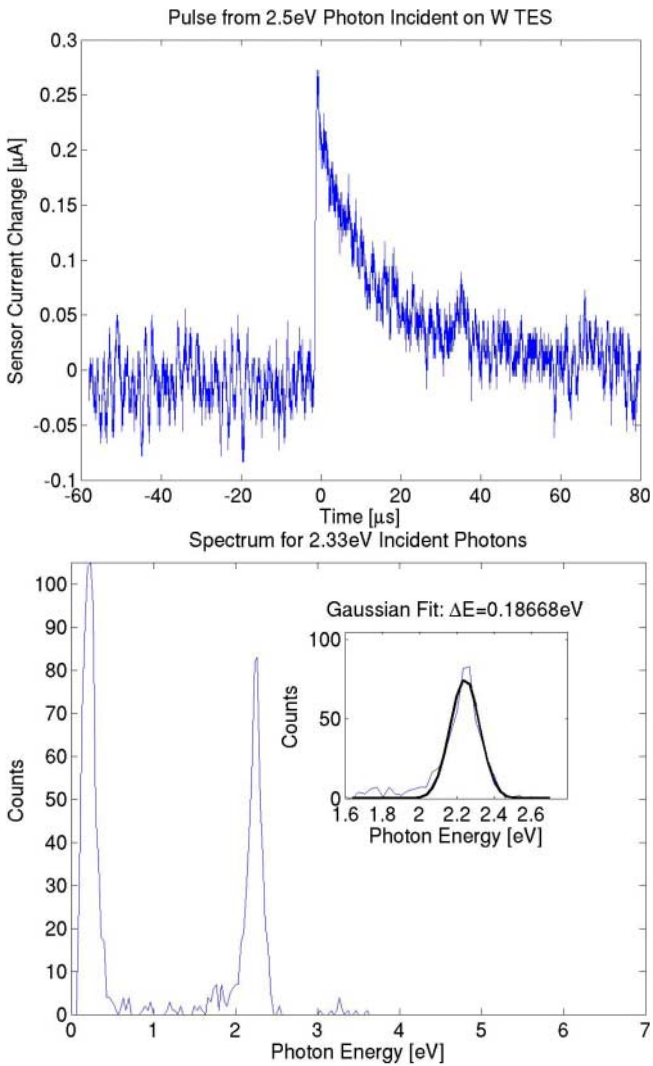


**Fig. 16.** (top) Pulse from single photon. (bottom) Calibration spectra from a 532 nm laser. The resolution (inset) is 0.19 eV FWHM, or  $R = 13$  at 2.5 eV (500 nm)

#### 4.3 Reflection Masking

As can be seen from Fig. 15, for simple planar configurations with no crossover wiring, as the number of pixels in an array is increased a larger amount of the focal-plane area is taken up by the electrical rails. There are a number of ways to maintain high fill factors. These include the fabrication of thinner wires by e-beam lithography, utilization of buried wiring layers, bump bonding from the sensor wafer to a second wiring wafer, incorporation of SiN-membrane

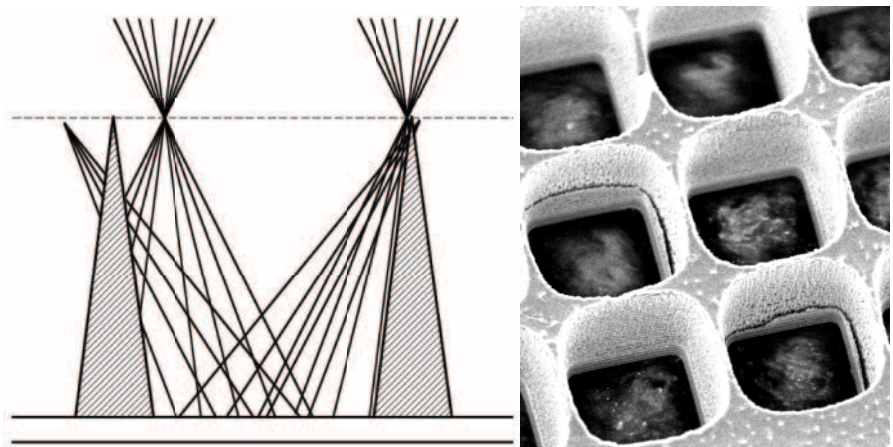


**Fig. 17.** Schematic (*left*) showing the image plane at the top of the mask and the reflected rays which avoid the rails. An SEM (*right*) of 36  $\mu\text{m}$  center-to-center by 60  $\mu\text{m}$  thick reflection mask, which is not yet coated with Al

shadow masks, and reflection mask technology. The latter option has a number of advantages; we have developed the reflection mask shown in Fig. 17. For this mask, a Si wafer is thinned to about 60  $\mu\text{m}$  and then etched using reactive ion etching to obtain the sloped edge profile. Finally, the Si is coated with aluminum, which has a near unity grazing reflection coefficient. The effective fill factor is  $\approx 92\%$  for this reflection mask and improved designs can approach unity. Beyond making a more astronomically useful instrument, these reflection masks are an invaluable tool when characterizing an array. They simplify spectral data (by removing artifacts from photons interacting with the voltage bias rails and/or substrate), allow a given focal plane area to be covered with smaller TES pixels (giving decreased heat capacity and improved energy resolution) and make it much easier to confine incident radiation to one pixel, allowing for effective probes of cross-talk and position-dependence.

#### 4.4 Anti-reflection Coatings

Metal films such as tungsten have quantum efficiencies (QE) around 50% over the optical band, dropping to  $\approx 10\%$  in the mid-IR [25]. To improve the QE over a much wider band it is necessary to utilize an absorber coating over the TES spectrophotometers. We must pick a system that does not dominate the heat capacity of the detector, nor degrade the superconducting properties of the TES. Our collaborators at NIST have developed a combination mirror,  $\lambda/4$  layer, and anti-reflection coating to achieve 97% efficiency at 1550 nm at room temperature. While this demonstration is for a different target wavelength, a simplified version has achieved  $\approx 80\%$  absorption at 795 nm on

cold tungsten TESs, indicating that near-unity quantum efficiency is within reach [26].

We have also investigated a surface coating of Au-black, produced when Au is evaporated directly onto the surface of the TES spectrophotometer in  $\approx 1$  torr of an inert gas such as Ar or  $N_2$ . With this recipe, efficiencies  $> 99\%$  have been achieved over the entire band from 2 nm to 10  $\mu\text{m}$  [27], with a film thickness of  $\approx 50$  nm. The results of our first test showed that the photons were absorbed by the Au-black with very high efficiency, but pulses were not observed in the TES devices. Either the energy down-conversion was too efficient within the Au-black film and the thermal phonons did not couple to the W electrons, or the thermalization time constant was greater than  $\approx 100 \mu\text{s}$ . We are planning follow-up studies with a Au metal layer between the Au-black and the W TES with no oxide layer present, thus avoiding a barrier for electron transport. In addition, we will try W-black coatings and Cu-black to see if they provide a more satisfactory absorber with QE approaching 100% for the TES devices.

#### 4.5 IR Blocking Filters

Infrared cutoff filters are critical for the successful deployment of TES spectrophotometers. Their importance cannot be underestimated, and several research groups have cited long-standing difficulties solving this problem (Fig. 7b in [28]). Since the thermal IR background increases rapidly for wavelengths above 2  $\mu\text{m}$ , blocking filters are needed to prevent low energy (long wavelength) photons from degrading the spectral resolution or even saturating the TES pixels. So far, several strategies have been explored – fiber optics, heat absorbing filters, plastics, and grid filters. The first fiber optic coupled instruments [10] used carefully chosen high-OH (so-called “wet”) fiber optics, where the passivation of UV absorbing centers strongly absorb IR beyond 1.7  $\mu\text{m}$  while allowing transmission through the atmospheric band pass to about 350 nm. Five meters of wet fiber, coiled and thermally coupled to 4 K, sufficiently reduces the IR background in the fiber coupled system (see results in Sect. 3.2). Single-mode fibers have also been used to couple TES detectors with excellent results for quantum cryptography applications [29, 30].

As we have moved to an imaging instrument [11, 12], we have spent appreciable time exploring IR filtering options. A coherent wet fiber bundle remains a fall-back filter option; however, this solution has substantial cost in throughput, limits the future UV capability, and significantly constrains the optical design. We are therefore working toward monolithic imaging filter solutions. This issue is complex, as filtering IR is a multi-faceted problem. Shorter wavelength photons (1 – 10  $\mu\text{m}$ ) and longer wavelength (10 – 100  $\mu\text{m}$ ) photons couple to the system differently and must be filtered independently. For our initial trials, we used standard heat-absorbing filters such as KG3 glass, with the filters thermally anchored to 77 K and 4 K. This approach has also been tried by the ESA STJ (S-Cam) team [24]. We have, however, found

this solution to be highly inadequate. Heat absorbing glass limits the band-pass to  $0.75 - 0.35\text{ }\mu\text{m}$ . More importantly, the substantial near-IR ( $\approx 2.7\text{ }\mu\text{m}$ ) and far-IR ( $> 30\text{ }\mu\text{m}$ ) leaks of these glasses allow large IR photon and radiative heating rates onto the detector. The result is substantially degraded energy resolution. We have recently been developing a combination solution of plastic absorber, crystalline sapphire, and metal grid filter that promises much better thermal isolation and detector response from  $1.7\text{ }\mu\text{m}$  out to  $< 0.3\text{ }\mu\text{m}$ . Suppression of the far-IR flux is particularly difficult and may be best solved with reflective grid filters in the stack. Commercial grids are available (e.g.  $2.5\text{ }\mu\text{m}$  bars on a  $12.5\text{ }\mu\text{m}$  pitch) but custom grids will be required for a high transmission filtering scheme. Simulations done with measured filter parameters agree well with detected radiation transmitted through the stack.

## 4.6 The Path to Larger Arrays and Multiplexing

Even a 32-channel TES system is quite useful for ground-based demonstrations, since the atmospheric dispersion and guiding errors for point sources are completely contained within the array and nearby background subtraction is possible. This is also demonstrated by the S-CAM1 and S-CAM2 36-channel observations. For the TES system, the extension to an  $8 \times 8$ , or 64 pixel, imaging system is relatively straightforward, with each pixel connected to its own SQUID array amplifier and room-temperature DFB (digital feedback) processing card. Even this modest growth in pixel count should ease the use of the instrument and improve its functionality for astronomical observations of point sources. This 64 channel system will be suitable for initial mission designs such as configuration A & B<sub>0</sub> in Table 2. The S-Cam 3 120 pixel format offers similar advantages. However, it seems difficult to push such ‘brute force’ solutions much beyond the few hundred pixel level, as the complexity and heat load costs of the individual read channels becomes prohibitive.

Eventually, for larger format arrays, it will become necessary to develop some form of multiplexed readout. A potential TES solution is to multiplex the SQUID electronics readout of many individual pixels. Recently, a SQUID multiplexing system has been demonstrated at NIST [31]. The SQUID MUX circuit was originally developed at NIST as part of a collaborative program with GSFC to build infrared-submillimeter TES bolometer arrays. With proper implementation, it may be possible to read out many TES pixels with one output channel with little degradation in signal to noise.

The SQUID multiplexer circuit is shown in Fig. 18. In this circuit, each TES element in a proposed  $20 \times 20$  array is read out by a single first-stage SQUID amplifier. The bias lines of each 20-element column of SQUIDs are connected in series. The total signal across the entire column is monitored by a 100-SQUID series array. The bias voltage is applied to the first-stage SQUIDs, one row at a time, through address lines which are connected to each column. At any one time, the bias voltage is only applied to one row

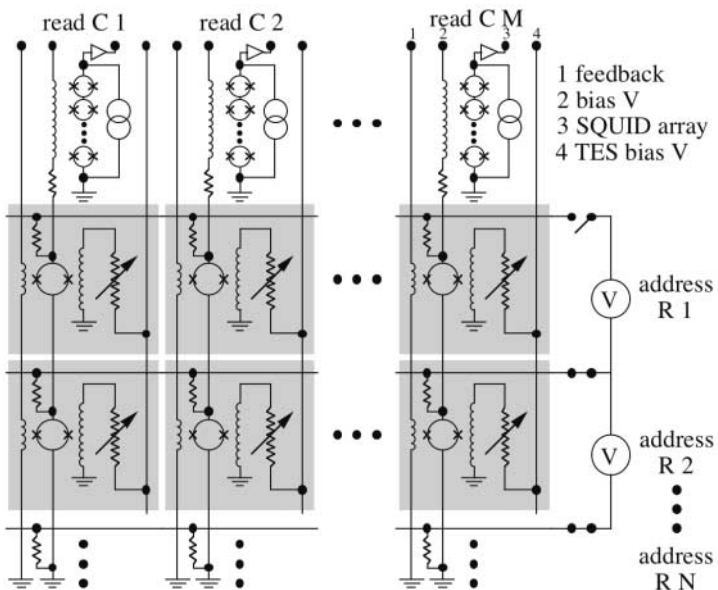


**Fig. 18.** Schematic of multiplexing scheme for reading an  $M \times N$  element array. Each row is turned on in sequence and sampled. The cycle time through the whole array must be fast compared to the  $L/R$  time constant of the TESs

of the first-stage SQUIDS in each column, leaving the others in their superconducting, or 'off' state. Since the SQUIDS outside of the addressed row are superconducting, they contribute no signal or noise to the readout, and dissipate no power. As the address bias is switched from row to row, the vector of SQUID outputs sequentially provides a measurement of the current flowing through the transition-edge sensors in each row of the array. In order to increase the linearity and dynamic range, each time a first-stage SQUID is sampled, a signal is applied to the common flux modulation coil for its column to return the SQUID to a constant flux bias. With the one dimension of multiplexing, the number of wires scales as the number of elements on a side of the array instead of the number of microcalorimeters ( $2N$  versus  $N^2$ ).

The application of this SQUID MUX to optical photon detectors needs further advances. Though a demonstration has been performed on slow IR bolometers and is being actively pursued for X-ray devices, the demands on the multiplexing system for optical detectors are more challenging. For instance, a typical IR bolometer operated in a DC read-out mode may be sampled as few as 100 times per second for adequate measurement. An X-ray TES with a signal pulse duration of  $\approx 100\ \mu\text{s}$  may be sampled at 100 kHz for adequate sampling of the pulse shape. However, the optical devices have a fast rise ( $\approx 0.3\ \mu\text{s}$ ) and fall ( $\approx 5\ \mu\text{s}$ ) which must be sampled no slower than  $\approx 1\ \text{MHz}$ . Thus the multiplexing system must be able to handle high

( $\approx 20$  MHz) switching and sampling rates to adequately reproduce the pulses from a modest array ( $\approx 20 \times 20$  pixels). A significant limitation to high-speed multiplexed readout is the speed of the SQUID feedback system. Phase delays in the cryostat wiring and feedback electronics prevent stable SQUID feedback faster than  $\approx 10$  MHz with present systems. Though SQUID feedback is a convenient method for linearizing the pre-amplifier response, it is not a necessary component for optical TES device read-out. Running the front-end SQUID amplifiers in an open-loop (no feedback) mode may allow operation up into the 20 – 30 MHz range. Device and SQUID linearization would be accomplished together in post-processing using system calibrations.

An alternate approach which has had some success for X-ray detectors (for example see Chapter by *Lerch and Zehnder* and Chapter by *Porter, Brown, and Cottam*) is to instrument both ends of narrow and long absorber with STJs [32] or TESs [33]. Photons absorbed along the length of the absorber have both energy and position determined by the sum and difference of the outputs from the two ends. In addition, the ESA group is building S-Cam 4 with  $3 \times 30$  DROIDs (Distributed Read Out Imaging Detectors) [34], each with a length-to-width ratio of 10. The array covers  $1 \times 1$  arcmin with 900 effective pixels read out with 180 STJs. The problem with these schemes is that for most applications even the small single pixels are often rate limited at 10 m class telescopes, so covering a larger field of view in one structure will only make the rate problem worse. The DROID read-out also inevitably decreases the energy resolution and produces ‘analog’ pixelation in one dimension. On the other hand, for X-ray applications where photon rates are much lower these schemes are very attractive.

The viability of these schemes, both multiplexing and position sensitivity, will be explored by several groups as a possible path to larger arrays. In this process, we should strike a balance between technological advances and demonstrations that field-test instruments and highlight the scientific advantages of both.

## 5 Development Goals for Cryogenic Spectrophotometers

### 5.1 Optical Configurations

If the challenges of efficient direct imaging solutions can be adequately addressed, cryogenic spectrophotometers should be useful in a variety of configurations. In the near-future brute force arrays are likely to remain at the  $\approx 100$  pixel scale. As has already been shown, such small arrays can be very useful for point source applications. Split arrays with polarizing fore-optics can also be used to produce imaging dual linear spectrophotopolarimeters. As arrays are pushed to the few kilo-pixel level other options become attractive. For example, linear pixel arrays can be used as order-sorting detectors in an echelle spectrograph, and ESA [35] has described a concept for an  $R \approx 8000$

near-IR/visible spectrograph with a 5000 pixel STJ linear array detecting spectral orders 1-6. One very attractive feature of cryogenic detectors is the intrinsic sensitivity to a very large (more than a decade) wavelength range. Careful attention to the optical design is needed to preserve useful signals over such a wide band. The opportunities (and challenges) will, of course, be even greater in a space environment with access to the UV. Ultimately high pixel count ( $\geq$ Megapixel) arrays could provide very exciting opportunities for survey science and cosmology. Clearly such applications will require major advances in multiplex technology. We next note some attractive science applications, focusing on near future ( $10^2 - 10^3$  pixel) formats and then describe some mission concepts that would employ such arrays in a space environment.

## 5.2 Astrophysics Science Goals

A very natural application for TES or STJ array instruments is the fast spectrophotometry of compact objects, such as spin-powered pulsars. As is common in all wavebands, initial proving observations will continue to target the Crab pulsar. However, efficient imaging systems should provide phase-resolved spectroscopy to much fainter magnitudes. A dozen or so pulsar targets, and many more accretion powered compact objects are accessible if the instrument is sensitive at magnitude  $m \approx 25$ . Particularly important for this science is good sensitivity over a broad near-IR to near-UV spectral range.

Pulse phase spectroscopy of the  $m \approx 25$  counterparts of the older ( $10^4 - 10^6$  y) spin-powered pulsars [36], can provide detections of both the magnetospheric synchrotron spectrum and the thermal surface emission. Ground based observations will already provide significant sensitivity, but the wider spectral range available from a high altitude (e.g. ULD - Ultra Long Duration balloon or SOFIA) or space (e.g. explorer-class mission) platform allows even better discrimination of the models. In Fig. 19 we show background-subtracted simulations of spectra from two phase bins from a nearby young neutron star (e.g. PSR B0656+14). Observations of a variety of objects should be possible, including nearby millisecond pulsars and possibly pulsar-induced heating of planets (PSR B1257+12 [37]), disks or companions.

Other compact object observations are also quite attractive. Even with small ( $\leq 100$  pixel) imaging systems, the improved background measurements, reduced aperture losses, and optimal extraction of the image in the presence of chromatic atmospheric dispersion, all allow greatly improved point source spectrophotometry and variability studies. Magnetic CVs and LMXBs are attractive systems for spectrophotopolarimetry since their broad, often polarized, spectral features showing short time-scale variability provide an ideal match to the cryogenic spectrophotometer capabilities. Rapid fluctuations in accreting neutron star and black hole binaries can also be used to study the dynamics of the accretion flow. Pulsing XRB, such as Her X-1 can be studied

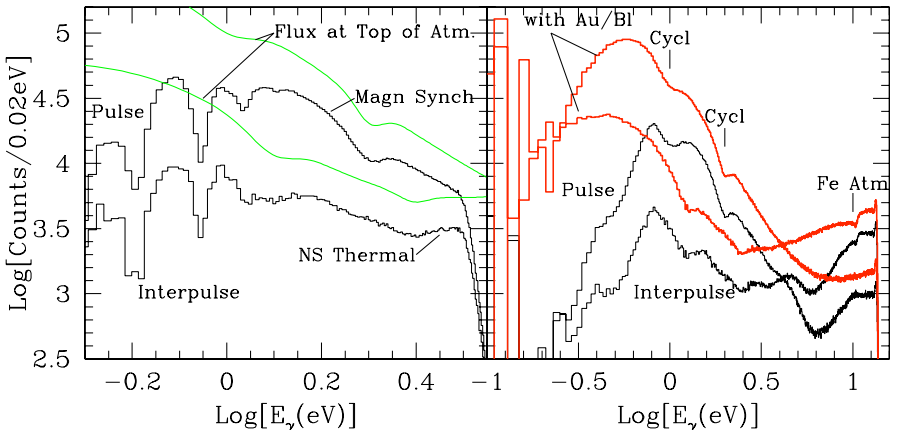


**Fig. 19.** Simulated TES spectra for a nearby young ( $\approx 10^5$  y) pulsar such as PSR B0656+14, with a magnitude  $m_V = 25$ . *Left:* 600 s exposure with a 4 m telescope from a good ground-based site (1" seeing), showing the background-subtracted count spectrum from a bare W TES. Spectra from two pulse phases are shown, indicating the varying magnetospheric emission that dominates at low energies and the higher energy contribution from the hot neutron star surface. The *solid curves* show the model spectra at the top of the atmosphere. *Right:* Simulated TES array observations of the same pulsar model, with a 3600 s exposure from an orbiting, cool, 1 m telescope. In the spectra from two pulse phases, one sees varying features in both the magnetospheric synchrotron emission and the flux from the magnetic atmosphere on the neutron star surface [38]. The *upper curves* show the increased QE obtained by adding a passive absorber, such as Au/Black. The increased noise at long wavelengths arises from the background in the growing source aperture that remains diffraction-limited

through the sweep of the ionizing X-ray beam across the disk and companion. In black hole systems there is the exciting possibility of using fluctuation analysis of the high excitation lines, such as the Bowen fluorescence HeII 4686 and the C/N blend to probe disk kinematics and photon propagation near the innermost stable orbit, where GR effects should be strong. It should be noted, however, that in contrast to the spin powered pulsars, the rapid sub-s variations in accreting sources tend to have small amplitudes. High count-rate data acquisition systems will be important to obtain the high dynamic range measurements needed to probe such fluctuations.

With high sensitivity imaging modes, observations of the spectra and structure of faint high- $z$  sources also become interesting. Fig. 20 (after [10]) shows sample TES spectra from a moderate integration (10 h) with a small aperture (1 m) space mission. Galaxies and galaxy components can clearly be studied to very faint magnitudes. Since the field is relatively small, targeted observations will be most common. Example extragalactic programs include studying faint interacting galaxies, studying low luminosity Seyferts

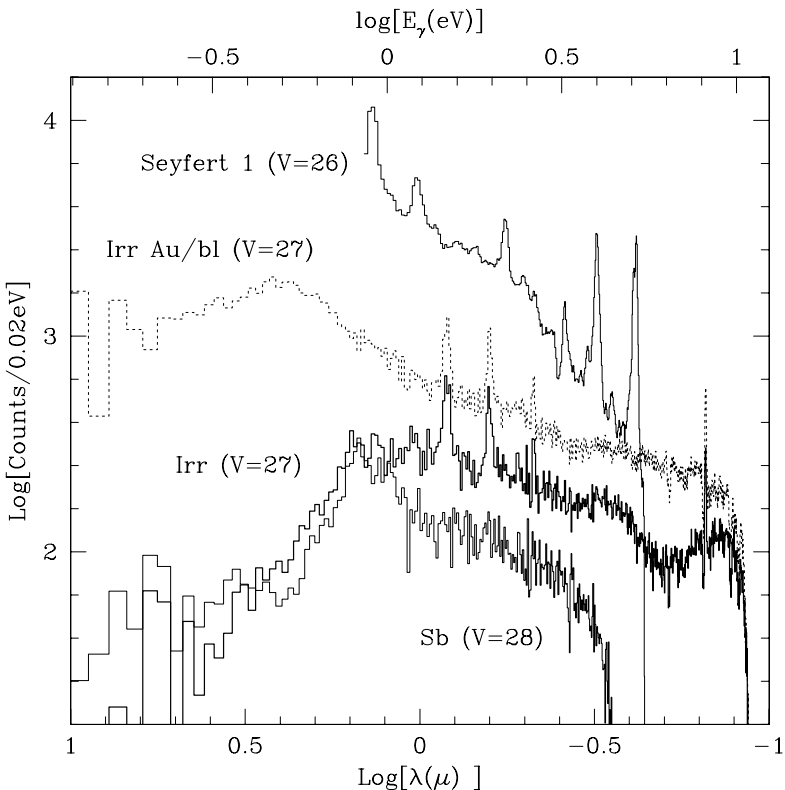


**Fig. 20.** Simulated background subtracted spectra from one  $0.1''$  region of a TES array on a 1 m-aperture space telescope. Passively cooled optics, zodiacal background from moderate ecliptic latitude, 0.05 eV resolution and 10 h exposure are assumed. Sample synthetic spectra [43] show a portion of an Sb galaxy ( $M = 10^9 M_\odot$ ,  $z = 2$ ) a low mass irregular galaxy ( $M = 1.5 \times 10^9 M_\odot$ , age = 30 My,  $z = 0.25$ ) and a low luminosity Seyfert 1 nucleus (scaled from NGC5548;  $V = 26$ ,  $z = 1$ ). The dashed line shows the increased S/N expected from coating the bare W with Au-black. Continuum breaks and a number of lines are well detected; broad (e.g., AGN) lines are resolved in the blue

at high- $z$ , mapping the emission line regions of nearby active galaxies, and studying the star formation rate, disk structure and dust formation in young galaxies. Observations of faint lensed galaxies may be used to probe the mass distribution of compact groups and high- $z$  clusters. TES and STJ-type resolution, sensitivity and broad wavelength coverage are also well suited to studies of high- $z$  supernovae [39, 40] and their host galaxy environments. There are also exciting opportunities for the study of the fading counterparts and host galaxies of GRB [41, 42].

### 5.3 Design of Future Missions

Although interesting ground-based applications clearly exist, the real power of cryogenic detectors awaits applications above the bulk of the atmosphere. Increasing the maximum accessible energy range from  $\approx 3.5\text{ eV}$  to  $\geq 10\text{ eV}$  triples the number of accessible spectral bins. Even more importantly, space or sub-orbital platforms offer dramatically reduced background rates, eliminating atmospheric emission and decreasing thermal emission with cool optics. The prospects are certainly heady for such cryogenic spectrophotometers in a low background environment, since the energy-resolved photon counting provides essentially noise-free measurements over a decade or more of energy.

Motivated by this prospect an ambitious early effort was made to design an STJ spectrophotometer for HST (e.g., work by *Kahn* and *Griffiths*, as described in [44]). Even the arrays in hand can, however, be interesting for long-duration balloon and orbital (e.g. explorer-class) applications. Of course, optimal use of the limited TES array format, maximal wavelength coverage, filtering and count-rate management place significant optical design constraints. The background filtering needs from space in particular are quite different to those for ground-based observations – we will wish to open up a wider IR range, but may also wish to exclude geocoronal Ly $\alpha$ . There are also complex infrastructure issues dealing with the practical limits of cryogenic technology (adiabatic demagnetization refrigerator + expendables versus closed cycle systems), optical design (aperture efficiency, emissivity, shielding and cooling), and platform limitations (source acquisition and tracking, on-board processing, power, telemetry, etc.). Happily, many of these issues are being independently addressed by other proposed space missions (e.g. the Planck mission cryogenic systems).

**Table 2.** Characteristic imaging spectrophotometer designs

	A	B <sub>0</sub>	B <sub>1</sub>	B <sub>2</sub>	C <sub>1</sub>	C <sub>2</sub>
max rate (kHz/pixel)	30	30	1	1	1	1
arcs/pixel	0.5	0.18	0.04	1.4	0.025	1.4
field (arcs)	4	1.4	1.3	43	0.8	43
array size (pixels)	$8 \times 8$	$8 \times 8$	$32 \times 32$	$32 \times 32$	$32 \times 32$	$32 \times 32$
wavelength range ( $\mu\text{m}$ )	0.3–1.7	0.2–2.5	0.2–5.1	0.2–4.0	0.1–15	0.1–15
energy range (eV)	0.7–4.0	0.5–6.2	0.2–6.2	0.3–6.2	0.1–12	0.1–12
mv,min ( $\nu^{-1}$ )	16	14	15	18	14	18

A = 4 m,  $f/3$ , 0.9 clear, 0.1 emis, 0 °C

B<sub>0</sub> = 1 m,  $f/95$ , 0.9 clear, 0.03 emis, -50 °C

B<sub>1</sub> = 1 m,  $f/170$ , 0.9 clear, 0.03 emis, -50 °C

B<sub>2</sub> = 1 m,  $f/5$ , 0.03 emis, -50 °C

C<sub>1</sub> = 1 m,  $f/270$ , 0.03 emis, 50 K

C<sub>2</sub> = 1 m,  $f/5$ , 0.03 emis, 50K

Even without considering such detailed design issues, some interesting insight can be drawn from considering present and near-future arrays. Table 2 lists some example format and capabilities of TES imaging systems, assuming 36  $\mu\text{m}$  pitch square arrays, with bare W absorption and a reflection mask. ‘A’ describes ground-based 4 m-class telescope applications (assuming a near-IR to near-UV transmitting filter stack). ‘B’ describes arrays with a 1 m class low-emissivity cool optical systems on a high-altitude balloon platform while ‘C’ describes a similar telescope on a space platform with cold optics. For the  $8 \times 8$  arrays, we assume a ‘brute force’ readout with one data chain channel per pixel. This approach allows high data rates and relatively bright minimum point source magnitudes ( $m_V$ ). For B and C we list two configurations (1) a diffraction-matched, optimal sensitivity mode and (2) a wider field imaging mode. For each of these concepts, the rapidly rising IR background count rate limits the red extension of the observed pass-band. To set the stage, the long wavelength cutoff (in  $\mu\text{m}$ ), achieved with heat absorbing filters, for each configuration above indicates where the background provides a substantial fraction of the channel saturation count rate. Limiting magnitudes and area coverage are also listed. The platforms and optical configurations are in the footnotes.

## 6 Conclusions

On the five to ten year timescale, we expect TES arrays in the  $32 \times 32$  range with some multiplexing and STJ arrays utilizing one FET per pixel. These instruments will make interesting ground-based and long duration balloon observations and should be considered for explorer-class space missions. An interesting intermediate step to larger arrays would be a  $1024 \times 1024$  array in which any 256 pixels could be addressed and read out continuously, much like a programmable multi-fiber spectrometer. The redshifts of a faint field such as the Hubble deep field (HDF) could then be rapidly determined. Such an instrument would explore many of the fabrication issues for larger arrays, including buried wiring layers and high efficiency. Long linear arrays for order-sorting spectrographs can be manufactured with present single layer lithography, but will need fairly advanced multiplexing schemes to achieve a useful pixel count. Such multiplexing capabilities are not yet in hand, but a number of interesting ideas are being developed. In addition to the SQUID-based time-domain multiplexing, these include frequency-domain multiplexing with rf SET (single-electron transistors) amplifiers for STJs and a new kinetic inductance readout scheme.

On this timescale, the cleanest applications for TES or STJ detectors will remain study of fast time variable sources such as pulsars, and neutron star & black hole binaries. Already, these point-source spectrophotometers have been used in ground-based observations of the Crab pulsar as well as several

white dwarf, neutron star & black hole binaries. In addition the high efficiency of cryogenic detectors over a broad band make them good candidates for photon starved applications such as faint galaxies, where direct redshift measurements would be possible to  $V \approx 28$  with 10 m class telescopes. An interesting application may very well be a combined X-ray and optical-UV mission, where the cryogenics would already be provided for the X-ray detectors and simultaneous observations of point-like compact or faint objects would substantially advance the science. It is again important to note that the X-ray and CMB satellite missions where cryogenic detectors must be used will provide a space-qualified infrastructure for cooling and electronics.

In the long term, we can hope that that superconducting detectors, like the Superconducting Tunneling Junctions and the Transition Edge Sensors, will revolutionize space astrophysics in the optical/UV by providing simultaneous broad-band imaging with low noise and high QE, photon time-tagging and low resolution spectroscopy. Wide-ranging success, however, depends on major progress in increasing array size. Clearly Megapixel-class arrays are needed for these devices to have a major impact on many areas of astrophysics and cosmology.

## Acknowledgements

The authors wish to acknowledge the many contributions of Stanford and NIST Boulder research staff described in this paper. These include J. Burney, T.J. Bay, J. Barral, J.P. Castle, A. Tomada, P. Brink, S.W. Nam, A.J. Miller and D. Rosenberg. The Stanford devices described in this paper were fabricated in the Stanford Nanofabrication Facility. The Stanford/NIST program is supported in part by NASA Grants NAG5-3775, NAG5-9087, NAG5-11439 and NAG5-13344.

## References

- [1] N. Rando, A. Peacock, M.C.V. Perryman, P. Hubner, A. Vandordrecht, P. Videler, and J. Lumley: *J. Low Temp. Phys.*, **93**, 659 (1993). [417](#)
- [2] B. Cabrera, R.M. Clarke, P. Cooling, A.J. Miller, S.W. Nam, and R.W. Romani: *Appl. Phys. Lett.* **73**, 735 (1998). [417](#), [422](#)
- [3] S. Shiki, H. Sato, Y. Takizawa, M. Kurakado, and H.M. Shimizu: *Publ. Astron. Soc. Jap.* **56**, 19L (2004). [419](#)
- [4] T.R. Stevenson, F.A. Pellerano, C.M. Stahle, K. Aidala and R.J. Schoelkopf: *Appl. Phys. Lett.* **80**, 3012 (2002). [421](#)
- [5] P.K. Day, H.G. LeDuc, B.A. Mazin, A. Vayonakis, J. Zmuidzinas: *Nature* **425**, 817 (2003). [421](#)
- [6] K.D. Irwin: *Appl. Phys. Lett.* **66**, 1998 (1995). [422](#), [427](#), [429](#)
- [7] D.J. Fixsen, S.H. Moseley, B. Cabrera, E. Figueroa-Feliciano: *Nucl. Instr. and Meth. A* **520**, 555 (2004). [425](#)

- [8] D.J. Fixsen, S.H. Moseley, B. Cabrera, E. Figueroa-Feliciano: *LTD9, Ninth International Workshop on Low Temperature Detectors*, (eds. F.S. Porter, D. McCammon, M. Galezaai and C.K. Stahle), AIP Conference Proceedings **605**, 339 (2002). [426](#)
- [9] R.W. Romani, B. Cabrera, E. Figueroa, A.J. Miller, and S. W. Nam: Bull. Am. Astron. Soc. **193**, 1112 (1998). [428](#)
- [10] R.W. Romani, A.J. Miller, B. Cabrera, E. Figueroa-Feliciano, and S.W. Nam: Astrophys. J. **521**, L153 (1999). [428, 440, 445](#)
- [11] T.J. Bay, J.A. Burney, P.L. Brink, B. Cabrera, J.P. Castle, R. W. Romani, A. Tomada, B.A. Young, S.W. Nam, A.J. Miller, J.M. Martinis, T. Kenny, and E. Wang: *Proceedings of SPIE Vol. 5209 Materials for Infrared Detectors III*, (eds. R. E. Longshore, S. Sivananthan), (SPIE, Bellingham, WA, 2003). [428, 437, 440](#)
- [12] J. Burney, T.J. Bay, P.L. Brink, B. Cabrera, J.P. Castle, R.W. Romani, A. Tomada, S.W. Nam, A.J. Miller, J.M. Martinis, E. Wang, T. Kenny, and B. Young: Nucl. Instr. and Meth. A **520**, 533 (2004). [428, 437, 440](#)
- [13] R.W. Romani, A.J. Miller, B. Cabrera, S.W. Nam, J.M. Martinis: Astrophys. J. **563**, 221 (2001). [431](#)
- [14] Website for S-Cam 1, 2 & 3:  
<http://sci.esa.int/science-e/www/object/index.cfm?fobjectid=33541> [434, 435, 436](#)
- [15] N. Rando, J. Verveer, S. Andersson, P. Verhoeve, A. Peacock, A. Reynolds, M.A.C. Perryman, F. Favata: Rev. Sci. Instr. **71**, 4582 (2000). [434, 435](#)
- [16] N. Rando, S. Andersson, B. Collaudin, F. Favata, P. Gondoin, A. Peacock, M. Perryman, J. Verveer, P. Verhoeve, D.J. Goldie: IEEE Transactions on Applied Superconductivity **10**, 1617 (2000). [435](#)
- [17] N. Rando, P. Verhoeve, P. Gondoin, B. Collaudin, J. Verveer, M. Bavdaz, A. Peacock: Nucl. Instr. and Meth. A **444**, 457 (2000). [435](#)
- [18] N. Rando, A. Peacock, F. Favata, M. Perryman: Exp. Astron. **10**, 499 (2000). [435](#)
- [19] M.A.C. Perryman, F. Favata, A. Peacock, N. Rando, B.G. Taylor: Astron. Astrophys. **346**, L30 (1999). [435](#)
- [20] N. Rando, S. Andersson, B. Collaudin, F. Favata, P. Gondoin, A. Peacock, M.A.C. Perryman, J. Verveer, P. Verhoeve, D.J. Goldie: Nucl. Instr. and Meth. A **444**, 441 (2000). [435](#)
- [21] M.A.C. Perryman, M. Cropper, G. Ramsay, F. Favata, A. Peacock, N. Rando, A. Reynolds: Mon. Not. R. Astron. Soc. **324** 899 (2001). [435](#)
- [22] J.H.J. De Bruijne, A.P. Reynolds, A.M.C. Perryman, A. Peacock, F. Favata, N. Rando, D. Martin, P. Verhoeve, N. Christlieb: Astron. Astrophys. **381**, L57 (2002). [435](#)
- [23] C.M. Bridge, M. Cropper, G. Ramsay, M.A.C. Perryman, J.H.J. de Bruijne, F. Favata, A. Peacock, N. Rando, A.P. Reynolds: Mon. Not. R. Astron. Soc. **336**, 1129 (2002). [435](#)
- [24] A.P. Reynolds, J.H.J. de Bruijne, M.A.C. Perryman, A. Peacock, C.M. Bridge: Astron. Astrophys. **400**, 1209 (2003). [435, 440](#)
- [25] E.D. Palik: “*Handbook of Optical Constants of Solids*”, (Academic Press, London 1985), p.12-127. [439](#)

- [26] D. Rosenberg, S. Nam, A.J. Miller, A. Salminen, E. Grossman, R.E. Schwall, and J.M. Martinis: Nucl. Instr. and Meth. A **520**, 537 (2004). **440**
- [27] L. Harris: J. of Op. Soc. Am. **46**, 160 (1956). **440**
- [28] G. Brammertz, A. Peacock, P. Verhoeve, A. Kozorezov, R. den Hartog, N. Rando, R. Venn: *LTD9, Ninth International Workshop on Low Temperature Detectors*, (eds. F.S. Porter, D. McCammon, M. Galezaai and C.K. Stahle), AIP Conference Proceedings **605**, 59 (2002). **440**
- [29] S. Nam, A. J. Miller, and D. Rosenberg: Nucl. Instr. and Meth. A **520**, 523 (2004). **440**
- [30] D. Rosenberg, A.E. Lita, A.J. Miller, S. Nam, R. Schwall: IEEE Trans. Appl. Supercond., in press (2005). **440**
- [31] J. A. Chervanek, K.D. Irwin, E.N. Grossman, J.M. Martinins, C.D. Reintsema, and M.E. Huber: Appl. Phys. Lett., **74**, 4043 (1999). **441**
- [32] C.M. Wilson, K. Segall, L. Frunzio, L. Li, D.E. Prober, D. Schiminovich, B. Mazin, C. Martin, R. Vasquez: Nucl. Instr. and Meth. A **444**, 449 (2000). **443**
- [33] E. Figueroa-Feliciano: PhD thesis, Stanford University, 2001. **443**
- [34] R. den Hartog, A. Kozorezov, D. Martin, G. Brammertz, P. Verhoeve, A. Peacock, F. Scholze, D.J. Goldie: *AIP Conference Proceedings* **605**, 11 (2002). **443**
- [35] M. Cropper, M. Barlow, M.A.C. Perryman, K. Horne, R. Bingham, M. Page, P. Guttridge, A. Smith, A. Peacock, D. Walker, P. Charles: Mon. Not. R. Astron. Soc. **344**, 33 (2003). **443**
- [36] A. Shearer, R.M. Redfern, G. Gorman, R. Butler, A. Golden, P. O'Kane, G.M. Beskin, S.I. Neizvestny, V.V. Neustroev, V.L. Plokhotnichenko, M. Cullum: *Astrophys. J. Lett.* **487**, L181 (1997). **444**
- [37] A. Wolszczan: *Science* **264**, 538 (1994). **444**
- [38] M. Rajagopal, R.W. Romani, and M.C. Miller: *Astrophys. J.* **479**, 347 (1997). **445**
- [39] S. Perlmutter, G. Aldering, G. Goldhaber, R.A. Knop, P. Nugent, P.G. Castro, S. Deustua, S. Fabbro, A. Goobar, D.E. Groom, I.M. Hook, A.G. Kim, M.Y. Kim, J.C. Lee, N.J. Nunes, R. Pain, C.R. Pennypacker, R. Quimby, C. Lidman, R.S. Ellis, M. Irwin, R.G. McMahon, P. Ruiz-Lapuente, N. Walton, B. Schaefer, B.J. Boyle, A.V. Filippenko, T. Matheson, A.S. Fruchter, N. Panagia, H.J.M. Newberg, and W.J. Couch: *Astrophys. J.* **517**, 565 (1999). **446**
- [40] A.G. Riess, P. Nugent, A.V. Filippenko, R.P. Kirshner, S. Perlmutter: *Astrophys. J.* **504**, 935 (1998). **446**
- [41] K.C. Walker, B.E. Schaefer, and E.E. Fenimore: *Astrophys. J.* **537**, 264 (2000). **446**
- [42] P. Meszaros, and M.J. Rees: *Astrophys. J. Lett.* **502**, L105 (1998). **446**
- [43] M. Fioc, and B. Rocca-Volmerange: *Astron. Astrophys.* **326**, 950 (1997). **446**
- [44] P. Jakobsen: *Ultraviolet-Optical Space Astronomy Beyond HST*, (eds. J.A. Morse M.J. Shull, A.L. Kinney), *Astron. Soc. Pac. Conf. Ser.* **164**, 397 (1999). **447**

# Index

- anti-reflection coating, 438
- black hole, 418, 445, 449
- CMB, 420, 421, 449
- covariance matrix, 427
- crab pulsar, 431–434
- DROID, 419, 443
- energy-resolved, 428, 435, 447
- fiber optic, 429, 440
- fill factor, 436, 438
- frequency-division multiplexing, 421, 449
- HST, 447
- imaging arrays, 437–443
- IR astronomy, 417–449
- IR cutoff, 424
- IR filters, 441
- Johnson noise, 426
- kinetic inductance, 421, 449
- McDonald Observatory, 428, 431–434
- neutron star, 444, 445, 449
- Nyquist noise, 426
- optical STJ and TES, 419–428
- optimal filter, 425
- photon detectors, 417
- Poisson correlations, 433
- pulsar, 431–434
- pulse template, 427
- quantum efficiency, 428, 439
- reflection mask, 437, 438
- resolving power, 419
- rf SET, 421
- S-Cam, 435–437
- SCUBA, 420
- spectrophotometer, 428–434, 444
- spectrophotometry, 417, 428–434, 444
- spectrophotopolarimeters, 444
- STJ array, 419, 436, 444, 448
- TES, 417, 422–428
  - arrays, 435–443
- thermal emission, 447
- thermal photons, 424
- time-division multiplexing, 421, 449
- time-resolved, 418
- ULD balloon, 444
- UV astronomy, 417–449
- weighting matrix, 427
- white dwarf, 418, 431, 433, 449
- white noise, 425, 428
- Wiener filter, 425–427
- William Herschel Telescope, 419, 435
- Woods filters, 421

# Beta Decay Experiments

E. Fiorini

Dipartimento G.P.S. Occhialini dell'Universita' di Milano Bicocca and Sezione di Milano, Piazza della Scienza 3, 20126 Milano (Italy)  
[ettore.fiorini@mib.infn.it](mailto:ettore.fiorini@mib.infn.it)

**Abstract.** One of the main problems to be studied with cryogenic detectors is the search for a finite value of the neutrino mass. In fact recent experiments on neutrino oscillations have shown that the mass difference between neutrinos of different flavours is different from zero. This stimulates searches on the absolute value of the neutrino mass, which can be very effectively performed with cryogenic detectors. One option is the precise determination of the spectrum of single beta decays, which has been so far mainly obtained by measuring the energy spectrum of decay electrons. Experiments carried out with the bolometric technique are complementary, since they allow measuring the total energy released by the decay into the detector, including for instance the energy spent into excitation of atomic or molecular excited levels. The spectra of beta decays with low transition energy allows also to investigate the crystal structure with Beta Environmental Fine Structure (BEFS). Cryogenic detectors are very promising to study processes like electron capture also in view of experiments on solar neutrinos. Another way to investigate the absolute value of neutrino mass is neutrinoless double beta decay, whose existence would imply not only lepton number violation, but also a non vanishing mass for the neutrino. While searches on single beta decays are carried out with microcalorimeters, double beta decay experiments require large mass detectors, installed underground in order to avoid the cosmic ray background. Unlike conventional techniques they allow a wide choice of nuclear candidates for double beta decay. The use of cryogenic detectors in searches on weak interactions are by no means limited to these two subjects. Many rare decays can be investigated in order to obtain important results in low energy nuclear physics and in other fields like geochronology or even material science.

## 1 Introduction

Beta decay experiments carried out with cryogenic detectors are going to give important contributions to our understanding of fundamental problems in nuclear, subnuclear and astro-particle physics. The main interest is presently stimulated by the unresolved problem of the neutrino mass, whose absolute value can hopefully be determined in cryogenic single and double beta decay experiments.

It would be however quite incomplete to limit ourselves only to these very important problems. The flexibility of the technique of low temperature detectors is very promising in searches of rare nuclear events, which, among

other things, could offer help in geochronology. In a total different field, the study of low energy beta decays with these detectors has been already fruitful to solid state physics and material science and could yield important and perhaps unexpected results in the near future.

## 2 The Neutrino Mass

The problem of the absolute value of the finite mass of at least one type of neutrino, is presently one of the hottest topic of fundamental physics. The present *standard model* which unifies the theories of weak and electromagnetic interactions predicts the existence of the electron, muon and tau leptons with the corresponding neutrinos  $\nu_e$ ,  $\nu_\mu$ , and  $\nu_\tau$ . Each of these three leptons and the corresponding neutrinos are characterized by a specific quantum number named *flavor*. The *lepton* quantum number of all these leptons is equal to +1, while that of the corresponding six anti-lepton is equal to -1. The standard model predicts that both lepton and flavour numbers are conserved and that as a consequence the neutrino mass is equal to zero. On the contrary most of the Gran Unified Theories (GUT) which attempt to include in a single frame the strong interactions with the already unified weak and electromagnetic ones, predict that the neutrinos have a mass different from zero. The same would be obviously true also for the antineutrinos whose mass, according to CPT conservation, should be equal to that of the corresponding partners. A way to test this exciting problem are the experiments on *neutrino oscillations* suggested more than forty years by Bruno Pontecorvo and collaborators. As an example, the electron neutrinos produced by nuclear fusion inside the Sun passing through this star or in their long travel from the Sun to Earth would partially transform themselves in muon or tau neutrinos. This would indicate that the flavor number is not conserved and that the square of the difference of the mass of neutrinos of two different flavors is different from zero. Beautiful experiments without accelerators carried out recently have unambiguously proved than not only solar [1, 2], but also atmospheric [3] and reactor [4] neutrino oscillate and that therefore the mass of at least one of the neutrinos of the three flavors is different from zero. It becomes therefore essential to devote efforts to experiments capable to measure the absolute value of the neutrino mass.

This problem plays an important role in astrophysics, since the mass of the neutrinos has an important impact in the development of the expansion of the Universe from the Big Bang. Very precise measurements have been performed in these last years on the anisotropy of the microwave background left in the Universe since when, about 300 000 years after the Big Bang, electromagnetic radiation de-coupled from matter. An upper, model dependent, limit on the sum of the mass of the neutrinos of the three flavors can be set from these measurements. The beautiful results on the full sky microwave maps by the WMAP experiment [5] together with those of the 2dF Galaxy

Redshifts Survey, constraint to 0.7 eV the maximum value for the sum of the masses of the neutrinos of the three flavors.

The role played by cryogenic experiments on single and double decay and their impact on this subject will be considered.

### 3 Single Beta Decay

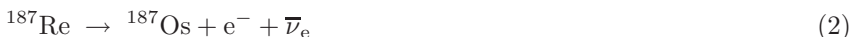
#### 3.1 Determination of the Antineutrino Mass

The most sensitive experiments on the direct measurement of the neutrino mass refer in reality to the mass of the electron *antineutrino* which, in the generally accepted CPT conservation law, should be equal to that of its *neutrino* counterpart. No evidence for a neutrino different from zero has been obtained. The best constraints have been reached so far, with electron spectroscopy, on the decay



whose transition energy is of  $\sim 18.6$  keV only. Recent values obtained by the Mainz and Troitsk experiments [6] have set an upper limit of 2.2 eV for the mass of the electron antineutrino. The KATRIN experiment, due to operate in 2007, should reach a sensitivity of 0.35 or perhaps 0.2 eV. We would like to note that these experiments enable to determine only the *electron* energy. A different and totally complementary approach is based on the use of low temperature thermal detectors [7, 8, 9].

Referring to the direct measurement of the neutrino mass the complementarity of this approach with respect to spectrometers lies on the fact that bolometers measure the *entire* energy delivered to the detector and not the electron energy only. They are therefore also sensitive to decays leading to excited states, as long as these states de-excite in time. Experiments are being carried out on the first forbidden unique decay:



which is particularly promising [11] due to its low transition energy ( $\sim 2.5$  keV). In addition, the large isotopic abundance of  $^{187}\text{Re}$  (62.8%) allows the use of absorbers made with natural rhenium. We note also that a precise direct measurement of the half lifetime of this decay ( $\sim 43$  Gy) is of great interest in geochronology, for the determination of the age of minerals and meteorites from their Re–Os abundance [12].

Experiments on this decay have been initiated in Genoa [13, 14], and are presently being carried out also by the Milan group [15]. The Genoa approach is based on the use of absorbers of polycrystalline rhenium and Neutron Transmutation Doped (NTD) thermistors. In order to avoid the superconductivity of rhenium the Milan group has adopted  $\text{AgReO}_4$  absorbers

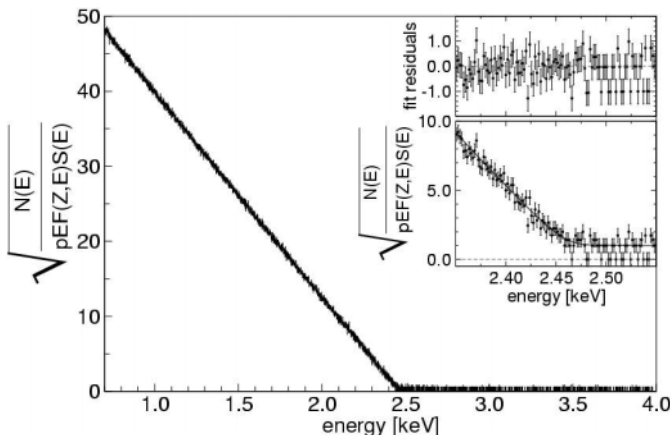


**Fig. 1.** Curie plot of the bolometric experiment by the Milan group

(where incidentally the expected BEFS, to be considered later, is lower) and both NTD and Si:P thermistors.

High statistics calorimetric measurements have been recently performed by this group with arrays of silver perrhenate ( $\text{AgReO}_4$ ) crystals operated at low temperature. The crystals have masses between 250 and 350  $\mu\text{g}$  and their average FWHM energy resolution, constantly monitored by means of fluorescence X-rays, is of 28.3 eV at the  $\beta$  end-point. The Curie plot is shown in Fig. 1 with an end-point energy of  $2466.1 \pm 0.8_{\text{stat}} \pm 1.5_{\text{syst}}$  eV, while the half lifetime of the decay is found to be  $43.2 \pm 0.2_{\text{stat}} \pm 0.1_{\text{syst}}$  Gy. These values are the most precise obtained so far for  $^{187}\text{Re}$ . From the fit of the Curie plot one can deduce at 90% C.L. an upper limit for  $m_{\bar{\nu}_e}$  of 15.3 eV.

The Genoa group has also searched, with negative results, the possible evidence for the existence of heavy neutrinos with masses in the range 50–1000 eV from their measurements on  $^{187}\text{Re}$  decay [17].

Plans to substantially improve these limits are in progress both in Genoa and in Milan. Those of the Genoa group are mainly based on the use of transition edge sensors (TES). Those in Milan, in collaboration with the NASA-Wisconsin and with the Berkeley group, are based on the increase on the number of crystals with large arrays constructed by micro-machining and on reduction of the rise time with the correspondent increase of the mass of the single crystals. The same group, in collaboration with the group of the Brown and Heidelberg Universities, is considering also to strongly reduce the rise time of the  $\text{AgReO}_4$  bolometers (e.g. to a few microseconds) with magnetic sensors.

### 3.2 The BEFS Effect

An important result in the field of material science has been the experimental detection [16], by the Genoa group of oscillations in the  $\beta$  particle spectrum,

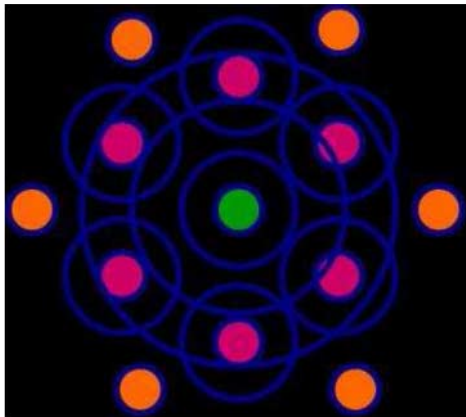


**Fig. 2.** The BEFS effect. Courtesy Flavio Gatti

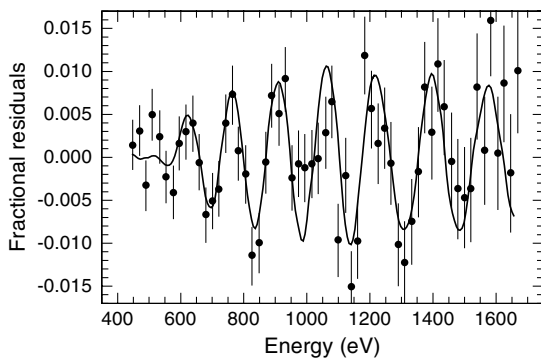


**Fig. 3.** The BEFS effect found for rhenium by the Genova group

due to the interaction of the emitted electron with its local crystal environment (Fig. 2).

This Beta Environmental Fine Structure (BEFS) is analogous, but complementary, to the well known Extended X-ray Absorption Fine Structure (EXAFS) [18, 19]. The result of the Genoa group for metallic polycrystalline rhenium and Neutron Transition Doped (NTD) thermistors [16] is shown in Fig. 3.

In the Milan experiment with  $\text{AgReO}_4$  the effect is expected to be much reduced (by an order of magnitude) because of the minor packing factor of  $\text{AgReO}_4$  with respect to metallic rhenium [19]. Despite that, the BEFS structure has also been seen by the Milan group recently (Fig. 4). The theoretical comparison between these two results will be of considerable interest to investigate the structure of these two crystals and the possible different percentage of the S and P waves contributing to the decay.

### 3.3 Measurements of the Antineutrino Mass

Even if CPT conservation prevents difference between the particle and antiparticle mass, many experiments have been carried out on the mass of the

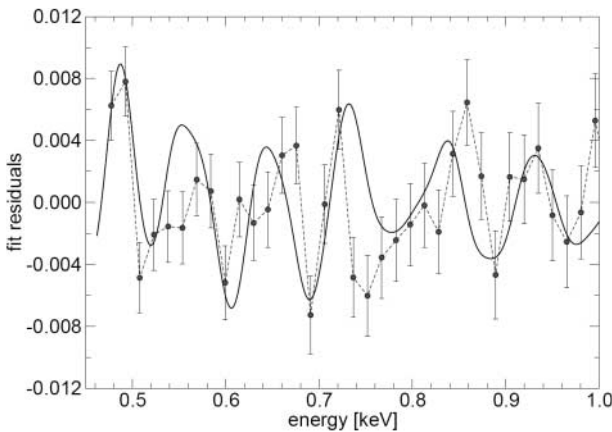


**Fig. 4.** The BEFS effect found for AgReO<sub>4</sub> by the Milan group

electron *neutrino* with limits less stringent than for its antiparticle. They are either based on the measurement of the photon spectrum in radiative Electron Capture (EC) or on the different rates of EC to the various atomic levels of the daughter atoms which depend obviously on the neutrino mass. This last approach has been adopted by the Genoa group [20] for the decay



The four MI, MII, NI, NII lines are resolved in this promising preliminary experiment.

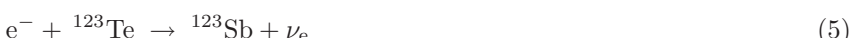
Among the other *thermal* results I would like to quote the evidence against the 17 keV neutrino by the Oxford group [21] and the measurements of the decay of polarized tritium nuclei performed in Leuven [22].

### 3.4 Searches for Rare Beta Decays

The forth forbidden unique transition



has been studied underground by the Milan–Kiev collaboration [23] with crystals of CdWO<sub>4</sub> of 58 and 144 g. The values of the transition energy (318.5 keV) and of the lifetime  $(9 \pm 1) \times 10^{15}$  yr, are the best in the literature. The spectrum of this decay has been obtained for the first time. The electron capture process



leading to the K level of <sup>123</sup>Sb has been investigated by the Milano group [26]. They were worried that the value of the lifetime quoted in the literature ( $1.3 \times$

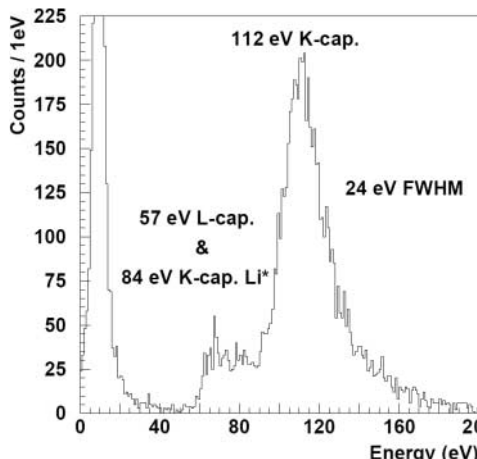


Fig. 5. Spectrum of  ${}^7\text{Be}$  measured by the Genoa group

$10^{13}$  yr) could imply a serious pile-up in their double beta decay experiment with large  $\text{TeO}_2$  bolometers. Four detectors of  $\text{TeO}_2$  of 340 g each were operated underground in coincidence and anti-coincidence. It was thus found that in previous experiments the excitation K line at 27 keV of tellurium was wrongly taken as the 30.5 keV EC line of  ${}^{123}\text{Te}$ . Unlike what had been indicated in these searches there is now no clear evidence of the peak at 30.5 keV, where the observed counts are  $17 \pm 12$  and therefore no evidence for K electron capture of  ${}^{123}\text{Te}$ . In particular, by applying a maximum likelihood analysis to the data, one can set a 90% C.L. lower limit  $\tau_{1/2} < 5 \times 10^{19}$  yr, more than six orders of magnitude larger than the previous reported *evidence!*

### 3.5 Cryogenic Detectors and Solar Neutrinos

Experiments on the interactions of solar neutrinos in large arrays of thermal detectors have been proposed and look technical feasible, even if very expensive [24]. A less ambitious approach is the *thermal* detection of the radioactive nuclei produced by these interactions. The Genoa–Moscow collaboration [25] has proposed an experiment to detect the reaction:



where the produced nucleus undergoes electron capture with a lifetime of 53 d. Previous planned experiments on this reaction were based on the detection of X-rays from EC of  ${}^7\text{Be}$  on a 320 keV excited level of  ${}^7\text{Li}$ , which occurs however with a branching ratio of 10% only. K electron capture to the ground state would deliver an energy of 112 eV, hard to be revealed with any conventional detector. Using a bolometer with an absorber of Be and later of  $\text{BeO}$  the Genoa group was able to separate the 112 keV line from a line at  $\sim 75$  eV.

The spectrum of  ${}^7\text{Be}$  by the Genoa group reported in Fig. 5 shows the peak at 112 keV due to the sum of the 29 eV recoil from electron capture to the 320 keV excited state and the 57 eV signal expected from L electron capture to the ground state.

Another thermal approach to the detection of the products of solar neutrinos is being pursued by the Garching group who is participating in the Gallium Neutrino Observatory (GNO) experiment. The reaction in this case is:



where  ${}^{71}\text{Ge}$  undergoes electron capture with a lifetime of 11.4 d and the production of L and K lines at 1.3 and 10.4 keV, respectively. The corresponding signals are presently measured with proportional counters. The Garching group has, however, fabricated a  $4\pi$  low temperature detector of  ${}^{71}\text{Ge}$  with a much better resolution and 100% efficiency.

## 4 Double Beta Decay

Negative double beta decay (DBD) [27, 28] (we will not consider here the other double beta processes) occurs in principle in three different channels



The two neutrino process (8) is allowed by the standard model and has been detected in the following ten nuclei  ${}^{48}\text{Ca}$ ,  ${}^{76}\text{Ge}$ ,  ${}^{82}\text{Se}$ ,  ${}^{96}\text{Zr}$ ,  ${}^{100}\text{Mo}$ ,  ${}^{116}\text{Cd}$ ,  ${}^{128}\text{Te}$ ,  ${}^{130}\text{Te}$ ,  ${}^{150}\text{Nd}$ , and  ${}^{238}\text{U}$ . In this channel the sum of the two electron energies is shared by the two emitted antineutrinos.

The lepton violating process (10) consists in the emission of one or more massless Goldstone particles  $\chi$ , named majorons, which also share its or their energies with the two electrons.

In the so called *neutrinoless* double beta decay (9) the sum spectrum of the two electron energy should show a peak corresponding to the full transition energy. In addition its rate should be strongly favored with respect to the process (8). As a consequence neutrinoless double beta decay is a powerful tool to test lepton number conservation.

Neutrinoless double beta decay can be induced by a massive majorana neutrino and/or by the presence of right handed currents. By neglecting these latter ones we can express the inverse of the half lifetime with the formula

$$[T_{\beta\beta}^{0\nu}]^{-1} = C_{mm} \langle m_{0\nu} \rangle^2, \quad (11)$$

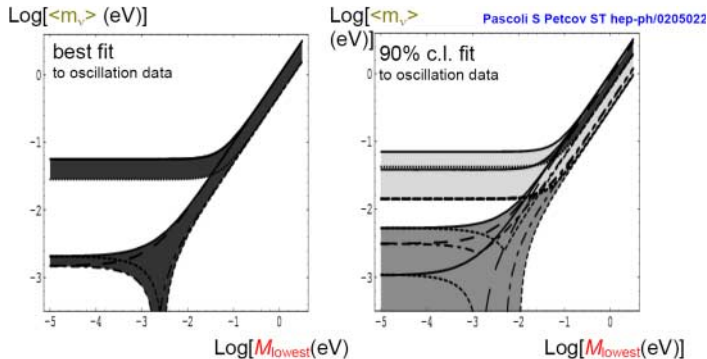


**Fig. 6.** Expectations of the effective neutrino masses in neutrinoless double beta decay

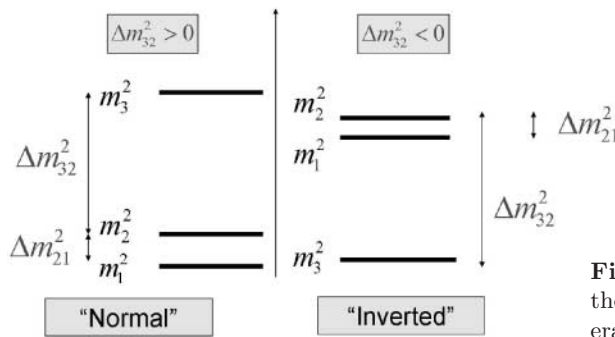


**Fig. 7.** Neutrino masses in the normal and inverted hierarchies

where  $m_\nu$  is the effective neutrino mass and the term  $C_{mm}$  depends on the available transition energy and on the nuclear matrix elements of the specific nucleus. The calculation of these latter is quite difficult. An obvious consequence is the need to investigate neutrinoless double beta decays in various nuclei. There is another reason, even more important for an experimentalist. The radioactive background produces a very large number of peaks which sometimes cannot be easily attributed to a specific radioactive source. Should therefore a peak corresponding to neutrinoless double beta decay be found in a specific nucleus, the peak at different energy indicating the same decay in a different nucleus would be the only way to unambiguously prove this result.

The importance of neutrinoless double beta decay has been strongly emphasized by the recent results on neutrino oscillations [29]. Without going into details, we could indicate that the effective majorana neutrino mass could be of a few meV or of a few tens of meV (Fig. 6a,b) under the hypothesis of normal and inverted hierarchies, respectively (Fig. 7).

## 4.1 Experimental Approaches and Present Experimental Status

Double beta decay can be investigated with indirect methods like the geochemical ones, where an abnormal isotopic abundance of the nucleus ( $A, Z + 2$ ) is searched for in a rock containing the father nucleus ( $A, Z$ ). The results have definitely proved the existence of double beta decay, but cannot directly discriminate between the various decay channels: neutrinoless, two neutrino or majoron decays, and even decays to excited levels. The possibility that some of the double decay products, when in form of gas, could have been lost during these geological times is excluded by most of the authors. In addition we can say that, with the exception of that of  $^{128}\text{Te}$ , all these decays were confirmed with direct methods. In particular the two neutrino double beta decay of  $\text{Te}^{130}$  has been recently directly detected by the cryogenic experiment of the Milan group [31]. Similar problems, but lower sensitivity, affect also the radiochemical experiments where a large mass of an ( $A, Z$ ) double beta active nucleus is stored underground for a reasonable time and then searched for the presence of the nucleus ( $A, Z + 2$ ).

Direct methods to detect double beta decay are based on two different approaches. In the so called *source  $\neq$  detector* approach: the double beta decay material is inserted, normally in form of thin layers, inside the detector. This approach is very appropriate for research on two neutrino double beta decay, where it has led to excellent results. For the detection of the sharp peak corresponding to neutrinoless double beta decay the resolution can be limited by auto absorption of a part of the electron energy inside the source. We note that, if the resolution is poor, a contribution in the region of the neutrinoless peak can come from the tail of the continuous spectrum due to the two neutrino channel.

The so-called *source = detector* or *calorimetric* approach [30]: the detector itself is made of a material containing the double beta active nucleus. Detectors like  $\text{CaF}_2$  and  $\text{CdWO}_4$  scintillators, Ge diodes, Xe ionization, proportional and TPC chambers have been amply used. A special role are going to play in this approach massive thermal detectors which can exploit the ample choice of materials with good thermal properties and favorable double beta decay nuclear candidates. The most promising ones are shown in Table 1.

All these compounds have been tested as thermal detectors for double beta decay with the following results:

- Crystals of  $\text{CaF}_2$  have been tested and a *scintillating bolometer* was fabricated [32] where heat and scintillation were recorded simultaneously. This approach is very interesting since the background at 4272 keV, definitely above the region of the  $\gamma$  background, is dominated by degraded  $\alpha$  particles. This background would be strongly reduced if a *coincidence* between heat and scintillation (limited for  $\alpha$  particles, but large for electrons) is applied.

**Table 1.** Thermal candidates for double beta decay

Compound	Isotopic abundance (%)	Transition energy (keV)
$^{48}\text{CaF}_2$	0.0187	4 272
$^{76}\text{Ge}$	7.44	2 038.7
$^{100}\text{MoPbO}_4$	9.63	3 034
$^{116}\text{CdWO}_4$	7.49	2 804
$^{130}\text{TeO}_2$	34	2 528
$^{150}\text{NdF}_2$	5.64	3 368
$^{150}\text{NdGaO}_3$	5.64	3 368

- Crystals of germanium have been already operated as thermal detectors, as can be seen in the Dark Matter chapter of this book, and their resolution has been found to be similar or superior to that of Ge diodes.
- Crystals of MoPbO<sub>4</sub> and CdWO<sub>4</sub> have been successfully operated both as scintillators and thermal detectors.
- Massive crystals of TeO<sub>2</sub> are the only ones presently widely used for double beta decay research, as will be reported later. They exploit the high natural abundance of  $^{130}\text{Te}$ , which allows to avoid the very expensive enrichment procedure.
- Crystals of NdF<sub>2</sub> and NdGaO<sub>3</sub> have been cooled down to 70 and 40 mK, respectively, and they will be tested in Milan to see if they could operate as detectors for double beta decay.

The only experiments carried out so far with thermal detectors are those performed with natural TeO<sub>2</sub> in the Gran Sasso Laboratory by the Milano Group and presently by the CUORICINO collaboration.

No evidence of neutrinoless double beta decay has been reported so far with the exception of a positive results on  $^{76}\text{Ge}$  by *Klapdor-Kleingrothaus et al. [33]* who indicate a lifetime of  $\approx 1.5 \times 10^{25}$  yr corresponding to an effective majorana neutrino effective mass of  $\approx 0.4\text{ eV}$ . This results is, however, confuted by other papers [34, 35].

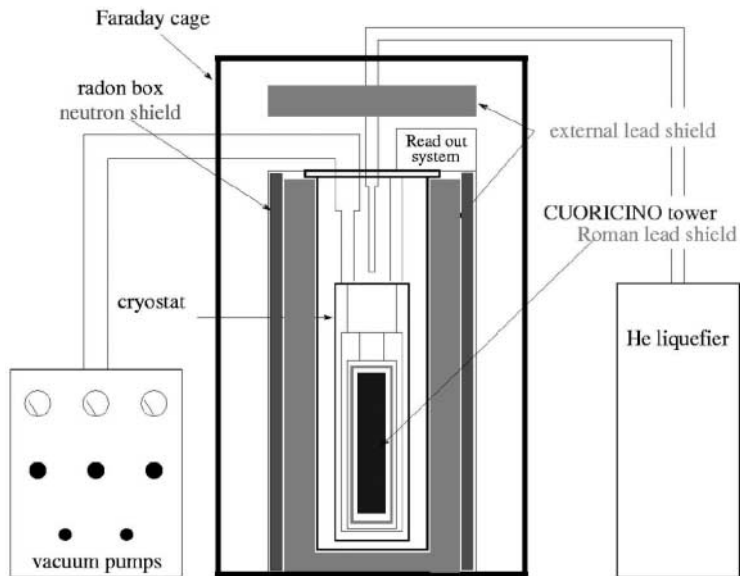
The present limits for neutrinoless double beta decay [27, 28] are reported in Table 2.

## 4.2 The Future

Two new experiments are already running: NEMO III based on the *source  $\neq$  detector* approach and the cryogenic experiment CUORICINO [36] which is the first step towards the much larger experimental setup CUORE. It consists (Fig. 8) of a massive array of TeO<sub>2</sub> crystals (Fig. 9) to search for double beta decay of  $^{130}\text{Te}$ . The absorbers are thermally coupled with NTD thermistors with a resistance of  $\sim 100\text{ M}\Omega$ . The temperature increase of the bolometer is 300  $\mu\text{V}$  for a delivered energy of 1 MeV. CUORICINO contains 44 crystals of

**Table 2.** Present results on neutrinoless double beta decay with lower limits for the lifetime and upper limits for the effective neutrino mass

Compound	$\Delta E$ (keV)	$\tau$ (s)	$m_\nu$ (eV)
$^{48}\text{Ca}$	4 272	$1.8 \times 10^{22}$	6–40
$^{76}\text{Ge}$	2 038.7	$(1.9 \times 10^{25}–1.6 \times 10^{25})$	$(0.34–1.14)–(0.40–1.35)$
$^{82}\text{Se}$	2 992	$2.7 \times 10^{22}$ (68% c.l.)	4.7–14.4
$^{96}\text{Zr}$	3 351	$1.3 \times 10^{21}$	$\approx 29$
$^{100}\text{Mo}$	3 134	$6 \times 10^{22}$	2–46
$^{116}\text{Cd}$	2 804	$1.7 \times 10^{23}$	2–2.1
$^{128}\text{Te}$	867	$7.7 \times 10^{24}$	0.72–1.5
$^{130}\text{Te}$	2 528	$5.5 \times 10^{23}$	0.4–2
$^{136}\text{Xe}$	2 469	$5.5 \times 10^{23}$	1.2–3
$^{150}\text{Nd}$	3 368	$1.4 \times 10^{21}$	17–31

**Fig. 8.** Cuoricino setup

$5 \times 5 \times 5 \text{ cm}^3$ , and 18 crystals of  $3 \times 3 \times 6 \text{ cm}^3$  with a total mass of  $\sim 40 \text{ kg}$ . Two of the  $3 \times 3 \times 6 \text{ cm}^3$  are enriched to 82.3%  $^{128}\text{Te}$  and other two to 75%  $^{130}\text{Te}$ .

No evidence has been found so far for neutrinoless DBD of the  $^{130}\text{Te}$  (Fig. 10) setting at 90% C.L. a lower limit of  $5.5 \times 10^{23} \text{ yr}$  for neutrinoless DBD of  $^{130}\text{Te}$ . According to the various calculations of the nuclear matrix elements this limit is equivalent to a constraint ranging from 0.37 to 1.9 eV in the  $m_\nu$ , the most constraining one after those on the  $^{76}\text{Ge}$  decay.

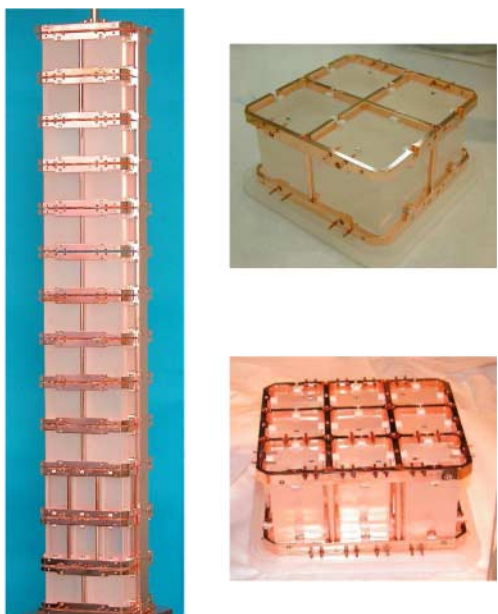


Fig. 9. The CUORICINO tower and crystals

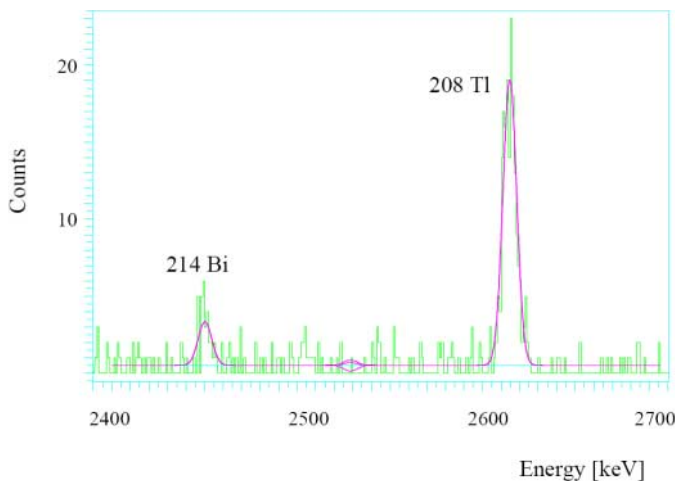


Fig. 10. Preliminary results of the CUORICINO experiment

**Table 3.** Future experiments for neutrinoless DBD

Experiment	Nucleus	Detector	$\tau_{1/2}$ (s)	$m_\nu$ (eV)
NEMO III (op.)	$^{100}\text{Mo}$	Tracking	$4 \times 10^{24}$	0.23 –0.98
CUORICINO (op.)	$^{130}\text{Te}$	Bolometer	$1.5 \times 10^{25}$	0.09 –0.63
CUORE	$^{130}\text{Te}$	Bolometer	$7 \times 10^{26}$	0.014–0.09
EXO	$^{136}\text{Xe}$	TPC	$8 \times 10^{26}$	0.055–0.12
GENIUS	$^{76}\text{Ge}$	Diodes in LN	$1 \times 10^{28}$	0.010–0.050
Majorana	$^{76}\text{Ge}$	Diodes in LN	$4 \times 10^{27}$	0.2 –0.07
MOON	$^{100}\text{Mo}$	34 tons Mo + scinti.	$1 \times 10^{27}$	0.014–0.057
DCBA	$^{150}\text{Nd}$	Tracking	$2 \times 10^{25}$	0.035–0.055
CAMEO	$^{116}\text{Cd}$	CdWO–4 scinti.	$\approx 1 \times 10^{26}$	0.053–0.24
COBRA	$^{116}\text{Cd}$	CdTe Diodes	$1 \times 10^{26}$	0.5 –2
CANDLES	$^{48}\text{Ca}$	CaF <sub>2</sub> in liq.scinti.	$1 \times 10^{26}$	0.15 –0.26
GSO	$^{160}\text{Gd}$	Cd <sub>2</sub> SiO–5 scinti.	$2 \times 10^{26}$	0.038–0.17
Xe	$^{136}\text{Xe}$	Liquid scinti.	$5 \times 10^{26}$	0.066–0.16
Xe	$^{136}\text{Xe}$	Liquid xenon	$3 \times 10^{26}$	0.086–0.25

#### 4.2.1 Future Experiments to Search for Neutrinoless Double Beta Decay

A list of future planned experiments [27, 28] is reported in Table 3. Hopes to reach the indications from neutrino oscillation results seem indeed justified.

It can be seen that only two of them are based on the cryogenic technique: the already running CUORICINO and CUORE.

CUORE, for Cryogenic Underground Observatory for Rare Events, is an extension [31] of the presently running CUORICINO setup. It will consist of a cubic (Figs. 11, 12) array of 1000 crystals of natural TeO<sub>2</sub> of  $5 \times 5 \times 5 \text{ cm}^3$  with a total active mass of  $\approx 760 \text{ kg}$ . These detectors have been tested already in CUORICINO and have reached a FWHM resolution of  $\approx 1 \text{ keV}$  and  $3.2 \text{ keV}$  at 46 keV and 5.6 MeV, respectively. Due to the flexibility of the thermal detectors other crystals as those reported in Table 1 can be considered.

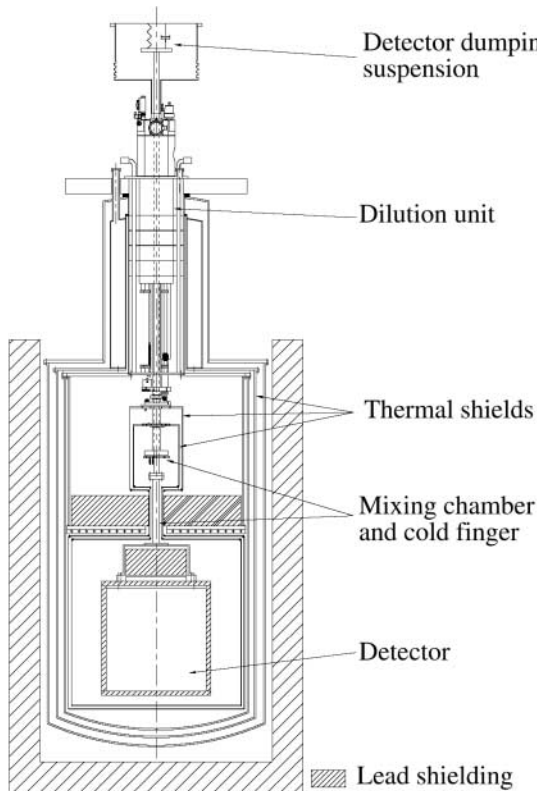


Fig. 11. Cryostat for CUORE

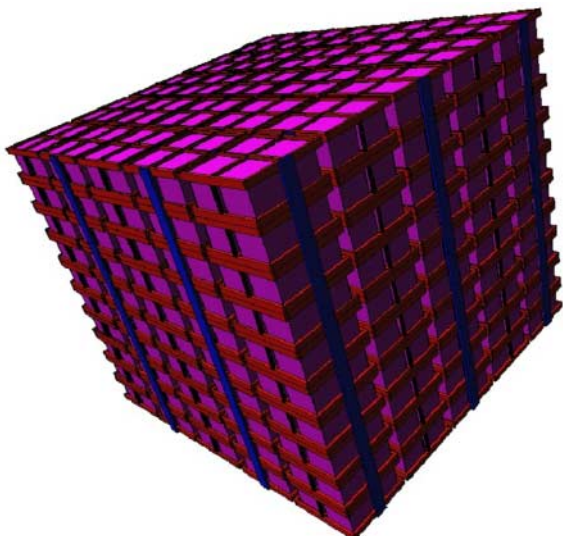


Fig. 12. CUORE

## References

- [1] Q.R. Ahmad et al.: Phys. Rev. Lett. **89**, 001302 (2002) (and references therein) and Q.R. Ahmad et al., arXiv:nucl-ex/0309004 **454**
- [2] Y. Fukuda et al.: Phys. Rev. Lett. **86**, 5656 (2001) (and references therein); and M.B.Smy et al., arXiv:hep-ex/0309011 **454**
- [3] T. Kajita and Y. Totsuka: Rev. Mod. Phys. **73**, 85 (2001) (and references therein) **454**
- [4] K. Eguchi et al.: Phys. Rev. Lett. **90**, 011802 (2003) **454**
- [5] O.Elgaroy et al.: Phys. Rev. Lett. **89** 061301 (2002) **454**
- [6] V.M.Lobashov: Nucl. Phys. A**719**, 153 (2003)(and references therein) **455**
- [7] E.Fiorini and T. Niinikosky: Nucl. Instrum and Meth. **224**, 83 (1984) **455**
- [8] D.Twerenbold: Rep. on Prog. in Phys. **59**, 349 (1996) **455**
- [9] N.Booth, B. Cabrera and E.Fiorini: Ann. Rev. of Nucl. Sci. **46**, 471 (1996) **455**
- [10] See Proceeding of LTD-10 Workshop on Low temperature Detectors, (ed. F. Gatti), Genoa July 9-15, 2003
- [11] S. Vitale: INFN internal report, INFN/BE-85/2 1985 **455**
- [12] M. F. Horan, M. I. Smoliar, and R. J. Waker: Geoch. and Cosmoch. Acta **62** 545 (1998) (and references therein) **455**
- [13] M.Galeazzi et al.: Phys. Rev. C **63**, 014302 (2001) (and references therein) **455**
- [14] F.Gatti: Nucl.Phys.B. (Proc.Suppl.) **91**, 293 (2001) **455**
- [15] C. Arnaboldi et al.: Phys. Rev. Lett. **91**, 161802 (2003) **455**
- [16] F.Gatti et al.: Nature **397**, 137 (1999) **456**, **457**
- [17] M.Galeazzi et al: Phys. Rev. Lett. **86** 1971 (2001) **456**
- [18] S.E. Koonin: Nature **354**, 468 (1991) **457**
- [19] G.Benedek et al.: Nucl. Instrum. and Meth. A **426**, 147 (1999) **457**
- [20] F. Gatti et al.: Phys. Lett. B **398**, 415 (1997) **458**
- [21] R.J. Gaitskell et al.: Phys. Lett. B **370**, 163 (1996) **458**
- [22] P. de Moor et al.: Proc. of LTD-7, 27 July- 2 August 1997, Munich / Germany, ed. by S. Cooper, page 181 **458**
- [23] A. Alessandrello et al.: Nucl. Phys. B (Proc.Suppl) **35**, 394 (1994) **458**
- [24] A. Alessandrello et al: Astrop. Phys. **3**, 239 (1995) 239 (and references therein) **459**
- [25] M. Galeazzi et al.: Phys. Lett. B **398**, 187 (1997) **459**
- [26] A. Alessandrello et al.: Phys. Rev. C **67**, 014323 (2003) **458**
- [27] S. Elliott and J. Engel: J. Phys. C: Nucl. Part. Phys. **30**, R183 (2004) **460**, **463**, **466**
- [28] V.I.Tretyak and Yu.G.Zdesenko: At. and Nuclear Data Tables **80**, 83 (2002) **460**, **463**, **466**
- [29] S.Pascoli, S.T. Petkov and W.Rodejohann: Phys. Lett. B **558** 141 (2003) (and references therein) **461**
- [30] G.F. dell'Antonio and E.Fiorini: Suppl. Nuovo Cimento **17**, 132 (1960) **462**
- [31] C.Arnaboldi et al.: Phys. Lett. B **557**, 167 (2003) **462**, **466**
- [32] A. Alessandrello et al: Phys. Lett. B**420**, 109 (1998)(and references therein) **462**
- [33] H. Klapdor Kleingrothaus et al.: Mod. Phys. Lett. A**16**, 2409 (2001) **463**

- [34] F. Feruglio et al.: Nucl. Phys. C **637**, 345 (2002) [463](#)
- [35] C. Aalseth et al.: Mod. Phys. Lett. A**17**, 1475 (2002) [463](#)
- [36] C. Arnaboldi et al: First results on neutrinoless double beta decay of  $^{130}\text{Te}$  in the calorimetric CUORICINO experiment, Phys. Lett. B, submitted [463](#)

# Heavy Ion Physics

P. Egelhof<sup>1,2</sup> and S. Kraft-Bermuth<sup>1,2</sup>

<sup>1</sup> Gesellschaft für Schwerionenforschung, Planckstrasse 1,  
D 64291 Darmstadt, Germany

<sup>2</sup> Institut für Physik, Johannes Gutenberg Universität Mainz, Staudingerweg 7,  
D 55128 Mainz, Germany  
[P.Egelhof@gsi.de](mailto:P.Egelhof@gsi.de)

**Abstract.** Calorimetric low temperature detectors have the potential to become powerful tools for applications in many fields of heavy ion physics. A brief overview of heavy ion physics at present and at the next generation heavy ion facilities is given with a special emphasis on the conditions for heavy ion detection and the potential advantage of cryogenic detectors for applications in heavy ion physics.

Two types of calorimetric low temperature detectors for the detection of energetic heavy ions have been developed and their response to the impact of heavy ions was investigated systematically for a wide range of energies ( $E = 0.1\text{--}360 \text{ MeV/amu}$ ) and ion species ( ${}^4\text{He} \dots {}^{238}\text{U}$ ). Excellent results with respect to energy resolution,  $\Delta E/E$  ranging from 1 to  $5 \times 10^{-3}$  even for the heaviest ions, and other basic detector properties such as energy linearity with no indication of a pulse height defect, energy threshold, detection efficiency and radiation hardness have been obtained, representing a considerable improvement as compared to conventional heavy ion detectors based on ionization. With the achieved performance, calorimetric low temperature detectors bear a large potential for applications in various fields of basic and applied heavy ion research. A brief overview of a few prominent examples, such as high resolution nuclear spectroscopy, high resolution nuclear mass determination, which may be favourably used for identification of superheavy elements or in direct reaction experiments with radioactive beams, as well as background discrimination in accelerator mass spectrometry, is given, and first results are presented. For instance, the use of cryogenic detectors allowed to improve the sensitivity in trace analysis of  ${}^{236}\text{U}$  by one order of magnitude and to determine the up to date smallest isotope ratio of  ${}^{236}\text{U}/{}^{238}\text{U} = 6.1 \times 10^{-12}$  in a sample of natural uranium.

Besides the detection of heavy ions, the concept of cryogenic detectors also provides considerable advantage for X-ray spectroscopy in atomic physics with highly charged heavy ions. Such detectors are to be used in near future for sensitive tests of quantum electrodynamics in very strong electromagnetic fields by a precise determination of the 1s Lamb shift in hydrogen-like heavy ions. The status of development of a high-resolution, and highly efficient detector for hard X-rays is reported, the performance of which is with  $\Delta E/E = 1.1 \times 10^{-3}$  for  $E_\gamma = 60 \text{ keV}$  close to fulfill the demands of the Lamb shift experiment.

## 1 Introduction

The success of experimental physics and the quality of experimentally determined results generally depend on the quality of the available detection

systems with respect to energy resolution, detection threshold, detection efficiency, granularity, etc. Consequently, the search for improved detection techniques is always a basic part of research activities in all disciplines of physics. When focusing on atomic, nuclear, particle and astrophysics, detectors for radiation – covering photons from the visible light via X-rays to hard  $\gamma$ -rays, and particles such as  $\alpha$ - or  $\beta$ -radiation, light and heavy ions in a wide range of energies, and various exotic particles – will be important.

Whereas most of the standard methods for detection of radiation are based on ionization, the concept of cryogenic detectors, where photons or particles are detected independent of ionization processes, opens completely new and promising perspectives for radiation detectors. A large variety of detection concepts for cryogenic detectors has been investigated over the years by numerous research groups all over the world for many applications in different fields of physics, and excellent results have been reported [1, 2]. Attempts to develop cryogenic detectors for applications in heavy ion physics were started about 15 years ago at the University of Mainz, Germany, and at GSI Darmstadt, Germany, and have meanwhile succeeded to obtain interesting and promising results, which have recently lead to a first application in experiments. The aim of the present contribution is to give an overview of heavy ion physics with a special emphasis on the potential applications of cryogenic detectors and the requirements for such detection schemes, to discuss the status of the development and the performance of such detectors for a number of topics of interest, and to present the first results which have been achieved.

An overview of the heavy ion facilities, presently existing and planned for the future project FAIR, at GSI Darmstadt, which is chosen exemplarily as one of the leading centers for heavy ion physics worldwide, is displayed in Fig. 1 (for details see [3, 4]). Some of the specialities of that facility (at present and in the future) are, among many others:

- the production and acceleration of intense beams of all ion species from hydrogen to uranium with a wide range of kinetic energies starting around the Coulomb barrier ( $E \approx 3\text{--}10\text{ MeV/amu}$ ) up to relativistic energies ( $E \approx 100\text{--}2000\text{ MeV/amu}$ ) or even higher at the future facility FAIR;
- the production of isotopically clean intense beams of radioactive ions by in-flight separation in the fragment separators FRS and SFRS, and their use for nuclear structure and nuclear astrophysics investigations on nuclei located far outside the valley of stability in the chart of nuclides;
- the storage of stable as well as radioactive ion beams in storage rings and their cooling to highest phase space densities, then reaching excellent beam qualities with energy spreads of  $\Delta E/E \leq 10^{-4}\text{--}10^{-6}$ ;
- the separation, detection and unique identification of very rare isotopes, such as, e.g., in the search for superheavy elements [5, 6] (with event rates down to  $\leq 1/\text{week}$ ), and in accelerator mass spectrometry [7, 8] where small isotope ratios down to  $10^{-16}$  are to be measured;

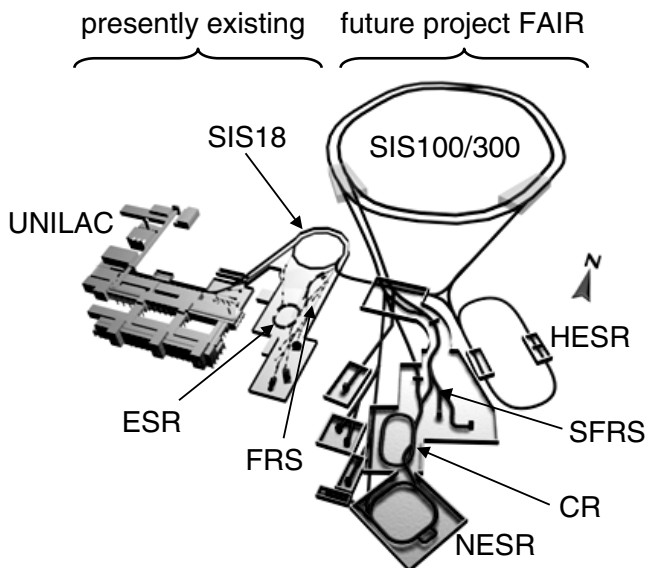


**Fig. 1.** Schematic view of the existing GSI facility (*left*) with the linear accelerator UNILAC, the heavy ion synchrotron SIS18, the fragment separator FRS and the experimental storage ring ESR, and the future project FAIR (*right*) with the double ring synchrotron SIS100/300, the high energy antiproton storage ring HESR, the superconducting fragment separator SFDR, the collector ring CR and the new experimental storage ring NESR

- the production and storage of highly charged, bare or hydrogen- and helium-like very heavy ions and their use for atomic physics experiments.

As compared to the present GSI facilities, the performance at the future facility FAIR will improve the experimental conditions with respect to beam intensities, luminosities and variety of potential applications by orders of magnitude. With such or similar performance at the GSI facilities as well as at the present and future facilities worldwide, extended physics programs addressing a wide spectrum of physics questions are currently running or will be started in near future. As will be discussed below in more detail, for some future investigations of considerable interest, detectors with highest energy resolution and/or highest detection efficiency and low detection threshold are required, reaching a performance not obtained with conventional detection systems currently available. For example, heavy ion detectors with an energy resolution of the order of  $\Delta E/E \leq 10^{-3}$  are required:

- for high-resolution nuclear spectroscopy with cooled heavy ion beams available from storage rings;
- for mass identification via combined energy/time-of-flight detection for reaction products in direct reaction and  $\gamma$ -spectroscopy experiments with

radioactive beams. Such experiments, performed in inverse kinematics, require an event by event identification of the beam-like reaction products [4];

- for a unique background-free and highly efficient mass determination – again via combined energy/time-of-flight techniques – for the identification of superheavy elements;
- for a highly efficient and background-free identification of rare isotopes in accelerator mass spectrometry [7, 8] via a high-resolution total energy measurement. Hereby, high detection efficiency for very slow heavy ions ( $E \leq 0.1$  MeV/amu) is also very important.

Whereas conventional heavy ion detectors, such as semiconductor detectors and ionization chambers, which operate on a charge collection principle, provide relative energy resolutions for the heaviest ions of only about  $\Delta E/E \geq (1\text{--}5) \times 10^{-2}$ , and have relatively high detection thresholds for slow very heavy ions, the concept of cryogenic detectors promises, due to its different operation principle, considerable advantage over conventional detectors with respect to energy resolution, detection efficiency, energy threshold and radiation hardness. High-resolution magnet spectrographs are capable of achieving a relative resolution as good as  $10^{-3}$  or better, but at the cost of very limited solid angle and thus detection efficiency, and charge state ambiguities, especially for slow heavy ions.

Besides heavy ion detectors, also photon detectors are important for heavy ion physics. Highly charged stored heavy ions, interacting with an internal target, provide a source of characteristic hard X-rays ( $E \leq 100$  keV) which need to be detected with highest energy resolution, not reached by conventional semiconductor detectors, to obtain the necessary spectroscopic information for sensitive tests of Quantum ElectroDynamics (QED) and other topics of interest in atomic physics [4, 10, 11].

In summary, it turns out that cryogenic detectors for heavy ions and hard X-rays have the potential to be powerful tools for atomic and nuclear physics experiments at heavy ion accelerators, and are worth to be considered and further developed in the future.

The present contribution is organized in the following way: After experimental conditions in heavy ion physics and requirements for cryogenic heavy ion detectors are considered in Sect. 2, detector design and detector performance will be discussed in Sect. 3. Section 4 contains examples for potential applications and first results on experiments with cryogenic detectors in heavy ion physics. In Sect. 5 layout and performance of detectors for hard X-rays, which are applied in atomic physics experiments with highly charged heavy ions, are discussed.

## 2 Experimental Conditions and Specific Requirements for Cryogenic Heavy Ion Detectors

When constructing cryogenic detectors for energetic heavy ions, it has to be realized that the conditions and detector parameters with respect to absorber size, incident energy, energy resolution, amount of radiation damage, etc., are different by orders of magnitude from those of most other applications of such detectors [1, 2]. As already discussed in Sect. 1, the typical incident kinetic energies of the heavy ions to be detected in the various applications range from energies well below the Coulomb barrier ( $E \leq 0.1\text{--}1\text{ MeV/amu}$ ) via energies around the Coulomb barrier ( $E \approx 3\text{--}10\text{ MeV/amu}$ ) up to relativistic energies ( $E \geq 100\text{--}2000\text{ MeV/amu}$ ), thus corresponding to total energies of  $E \approx 10\text{--}20\text{ MeV}$  up to some hundred GeV. Despite the relatively large total energies, the high specific energy loss of heavy ions in matter leads to comparably small ranges ( $2\text{ }\mu\text{m}\text{--}15\text{ mm}$  in most cases, except for light relativistic ions, see also Table 1), thus allowing relatively small absorber volumes. If quantitatively compared to the case of photons, electrons or protons, etc., it turns out that, due to the characteristic energy loss processes, the energy deposit per range in matter is for heavy ions by orders of magnitude higher. This specific feature makes calorimetric low temperature detectors, which reach their highest sensitivities for small absorber sizes, attractive for the detection of heavy ions. Due to the relatively high incident energies, already operating temperatures around 1.5 K will allow sufficient sensitivity of calorimetric detectors for heavy ions, thus reducing the demands on low temperature technology.

**Table 1.** Range of various heavy ions in sapphire for energies between 0.1 and 500 MeV/amu (calculated using the program TRIM [12])

E (MeV/amu)	Range ( $\mu\text{m}$ ) for			
	$^{20}\text{Ne}$	$^{40}\text{Ar}$	$^{132}\text{Xe}$	$^{238}\text{U}$
0.1	1.4	1.6	2.7	2.7
1	6	7	10	12
10	94	72	57	62
100	4 760	2 980	1 230	945
500	70 820	43 780	15 920	8 080

After having fixed the conditions for heavy ion detection, we may address the question of what can be the potential advantages of cryogenic detectors for heavy ions, and where are the limitations. Due to their operation principle the potential advantage of calorimetric low temperature detectors over conventional ionization detectors – such as semiconductor detectors or ionization chambers, etc. – are:

- the smaller energy gap  $\omega$  for the creation of an elementary excitation, leading to a better counting statistics: Whereas the energy gap for producing an electron-ion pair in a conventional semiconductor detector is of the order of a few eV, the excitation energy of thermal phonons is of the order of  $\omega \leq 10^{-3}\text{--}10^{-4}$  eV. This results in a potentially better energy resolution and lower energy threshold, both decreasing with  $\sqrt{\omega}$ . It should be noted, however, that for the relatively large incident energies of heavy ions this effect is of minor importance, except for the lowest total energies of  $E \leq 10$  MeV;
- the more complete energy detection: For ionization detectors, considerable losses in the ionization signal up to 60–80% appear due to direct phonon creation and charge recombination (the latter effect is especially dominating for very heavy ions due to the extremely high charge densities) and result in a substantial pulse height deficit. In contrast, for calorimetric detectors principally the whole deposited energy, besides small losses (see below), is finally transferred into heat after the decay of the initial electronic excitations;
- the lower detection threshold due to the absence of dead layers and entrance windows, which are unavoidable in conventional ionization detectors and therefore result, especially for very slow heavy ions, in limitations in detection efficiency and energy resolution due to energy loss straggling effects;
- the flexibility in the choice of the absorber material: As compared to semiconductor detectors, a much wider variety of materials is expected to fulfill the conditions for absorber materials of calorimetric detectors. The absorber material may therefore be optimized with respect to radiation hardness and other criteria. The short lifetimes caused by radiation damage, mainly due to lattice damage by nuclear stopping, is one of the basic limitations of semiconductor detectors when detecting high count rates of very heavy ions.

The fundamental limit on the energy resolution of a calorimetric detector is given by thermodynamic fluctuations of the energy content in the absorber (also called phonon noise) and the Johnson noise of the thermistor [13, 14]. For the detectors discussed in Sect. 3, these contributions are as low as 10–100 keV. An overview on practical limitations of energy resolution due to various effects is given in [14]. For the special case of cryogenic heavy ion detection, where the slowing down and stopping mechanisms considerably affect the lattice structure of the absorber, we expect that the limit of intrinsic resolution will be determined by the solid state properties of the absorber material. Theoretical predictions for the energy resolution of cryogenic detectors for some selected cases of ion species and absorber material are given in [15, 16]. It is found that statistical fluctuations of that amount of energy, which finally does not contribute to the thermal signal, will determine the intrinsic limit of energy resolution. Such loss processes are

due to the creation of local lattice defects, so-called “Frenkel pairs” which give rise to phonon trapping, the creation of long living metastable electronic states with lifetimes much longer than the thermal time constant of the detector, the stored energy consequently not contributing to the thermal signal, the creation of photons which escape from the absorber volume, etc. Unfortunately, there is presently not much known about the quantitative contribution of these effects to the energy resolution. For the special case of calorimetric detection of 25 MeV Br ions in a diamond absorber, a relative energy resolution of  $\Delta E/E = 2.5 \times 10^{-3}$  is predicted in [15]. Qualitatively it is expected that the effects discussed above contribute most for very slow and very heavy ions for which nuclear stopping is dominant, whereas for faster ions ( $E \geq 0.1\text{--}0.2\,\text{MeV/amu}$ ) electronic stopping contributes most to the specific energy loss (see also [12, 16]).

For the future, systematic investigation of the energy resolution of calorimetric low temperature detectors for various ion species, incident energies and absorber materials may provide more quantitative information, not only on properties of the detectors, but, vice versa, also on the solid state properties of the absorber materials (see also Sect. 3).

### 3 Design and Performance of Calorimetric Low Temperature Detectors for Energetic Heavy Ions

The principles of cryogenic detectors, based on semiconductor thermistors as well as on Transition Edge Sensors (TES), are discussed in detail in the contributions by *McCammon* and *Irwin* et al., respectively [9, 17], to this volume. We shall therefore not repeat this discussion, but focus in this section on the technical details and realization of such detectors for the special case of detection of energetic heavy ions.

#### 3.1 Detector Design

Within the last 15 years, two types of calorimetric detectors for heavy ions with different thermometers, one on the basis of a semiconducting germanium thermistor, and the other on the basis of a superconducting phase transition thermometer, have been developed. A detailed discussion of the layout and the preparation of these detectors may be found in [16, 18, 19, 20, 21, 22, 23, 24].

##### 3.1.1 Calorimetric Detectors Based on Semiconductor Thermistors

The first type of calorimeter is prepared on the basis of a germanium thermistor. It consists of a  $3 \times 1 \times 0.5\,\text{mm}^3$  germanium crystal, heavily doped and compensated with indium ( $2 \times 10^{17}\,\text{atoms/cm}^3$ ) and antimony

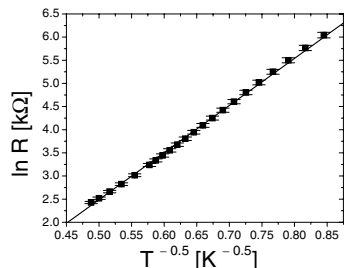
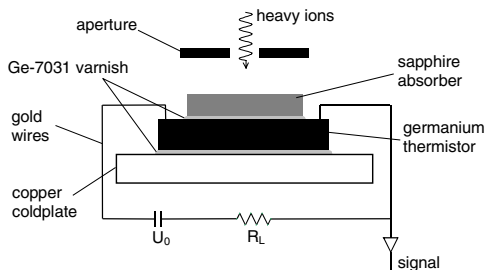


**Fig. 2.** The setup of a calorimetric heavy ion detector with a semiconducting germanium thermistor is schematically displayed on the *left side* (for details see text). The corresponding  $R(T)$  characteristics is shown on the *right side*. The *solid line* represents a fit to the data using the modified Mott equation [9]

( $1 \times 10^{17}$  atoms/cm $^3$ ). For such compensated semiconductors, conduction is realized mainly by the so-called “phonon assisted hopping conductivity” [9]. Consequently, the  $R(T)$  characteristics is well described by the modified Mott equation  $R(T) = R_0 \exp(T_0/T)^{1/2}$  with the parameters  $R_0 = 69\Omega$  and  $T_0 = 106\text{ K}$  (see solid line in Fig. 2, right side), determined by the semiconductors material properties. At a typical operating temperature around  $T = 1.7\text{ K}$ , the resistance is  $R = 200\text{ k}\Omega$  with a  $dR/dT = -0.48\text{ M}\Omega/\text{K}$ , corresponding to a thermistor sensitivity  $\alpha = (1/R)(dR/dT) = -2.4\text{ K}^{-1}$ .

A schematic view of the detector setup is displayed in Fig. 2 (left side). The germanium crystal is glued onto a copper coldplate with GE-7031 varnish. The electrical contacts are realized by thermal pressure bonding with gold wires of  $25\mu\text{m}$  in diameter. As absorber a sapphire crystal ( $2 \times 1 \times 0.33\text{ mm}^3$ ) is glued with GE-7031 varnish onto the germanium thermistor. Sapphire is a suitable absorber material because of its low heat capacity, the Debye temperature amounting to  $\Theta_D = 1025\text{ K}$ . The thermistor is biased by a battery through a load resistor ( $R_L = 10\text{ M}\Omega$ ). The voltage signal due to the impact of an incident ion is read out by conventional pulse electronics, namely a voltage sensitive preamplifier (bandwidth: 1 kHz–10 kHz, gain: 1000–10 000) and a shaping amplifier (shaping time: 25–200  $\mu\text{s}$ ).

To adapt such detectors to very low ion energies, detectors with smaller heat capacities were also developed. For these detectors, the germanium thermistor has dimensions of only  $0.5 \times 0.5 \times 0.5\text{ mm}^3$  and the sapphire absorber of  $3 \times 3 \times 0.05\text{ mm}^3$ , respectively. With this setup, the heat capacity and also the thermal coupling to the heat sink are reduced by about one order of magnitude, thus allowing higher sensitivity for low energetic heavy ions [16].

### 3.1.2 Calorimetric Detectors Based on Aluminum Transition Edge Sensors

The second type of calorimeter consists of a superconducting thin aluminum film, which is operated in the region of the phase transition between the

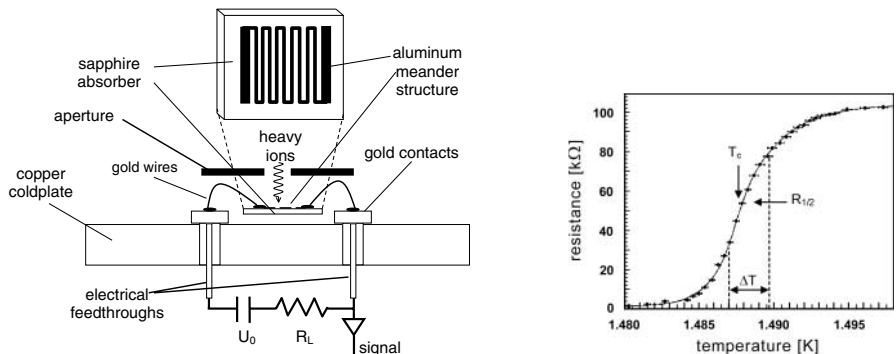


**Fig. 3.** The setup of a calorimetric heavy ion detector with a superconducting aluminum TES calorimeter is schematically displayed on the *left side*. The corresponding  $R(T)$  characteristics is shown on the *right side* (for details see text)

super- and the normalconducting state, and again a sapphire absorber. The setup, shown schematically in Fig. 3 (left side), is similar to the one for the germanium calorimeter (Fig. 2), the main difference being that the aluminum thermistor is evaporated as a thin film on the surface of the sapphire substrate. The thickness of the aluminum film of about 10 nm is adjusted to provide a narrow transition width for high sensitivity. In order to match the resistance of the microstrip to conventional preamplifiers, the aluminum film is patterned in a meander-like structure by photolithographic techniques<sup>1</sup>. It consists of 51 connected strips of 10  $\mu\text{m}$  width and 1 mm length each [21]. A typical observed  $R(T)$  characteristics is displayed in Fig. 3 (right side). The phase transition appears at a temperature of  $T_c = 1.488 \text{ K}$  with a width of  $\Delta T = 2.9 \text{ mK}$  and an impedance of  $R(T_c) = 52 \text{ k}\Omega$ , yielding a sensitivity of  $\alpha(T_c) = (1/R)(dR/dT) = 404 \text{ K}^{-1}$ . In contrast to the germanium calorimeters discussed above, the detectors with aluminum thermistors are not glued onto the copper coldplate, but supported only by the gold wires of 25  $\mu\text{m}$  diameter, which realize the electrical contact.

For both types of calorimeters the absorber thickness is adjusted to the individual experimental conditions. Especially for the case of relativistic heavy ions where the standard absorber thickness of 330  $\mu\text{m}$  is not sufficient to stop the ions, additional sapphire absorbers are glued onto the sapphire substrate. These detectors are fixed by specially shaped copper support structures in order to minimize thermal contact to the environment.

<sup>1</sup> Photolithography is provided by K. Haberle et al., Institut für Halbleitertechnik, Technische Universität Darmstadt, Schlossgartenstrasse 8, D 64289 Darmstadt, Germany

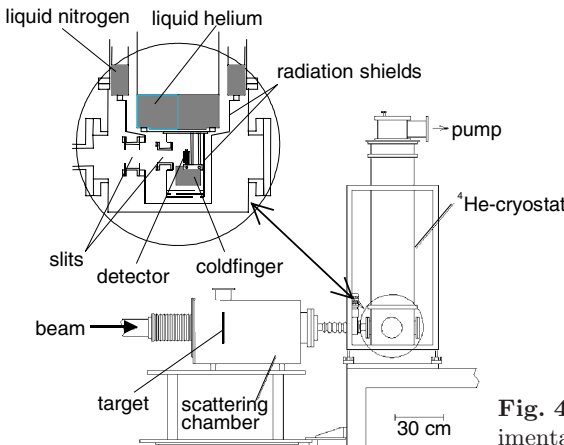


**Fig. 4.** Schematic view of the experimental setup for heavy ion detection (for details see text)

### 3.2 Detector Performance

In several measurements, the detectors discussed in the previous section were tested with various heavy ion beams ( ${}^{13}\text{C}$  ...  ${}^{238}\text{U}$ ) at various energies ranging from 0.1 MeV/amu up to 360 MeV/amu, and their response to the impact of heavy ion beams and their performance were systematically investigated. For both types of detectors excellent results have been obtained. In the following, a brief overview on the most prominent results is given (for a more detailed discussion see [16, 18, 19, 20, 21, 22, 23, 24, 25]).

Whereas measurements at higher energies ( $E = 5\text{--}360\text{ MeV/amu}$ ) were done at GSI with heavy ion beams from the UNILAC accelerator and from the synchrotron SIS18 (see Fig. 1), experiments at lower energies ( $E = 0.1 - 1\text{ MeV/amu}$ ) were performed at the VERA facility located at the university of Vienna, Austria [26]. The experimental setup used for most of the measurements is shown in Fig. 4. A pumped  ${}^4\text{He}$  window cryostat, operated at temperatures between 1.2 K and 4.2 K, is used to cool down the detectors to their operating temperature. The detectors are mounted on a cold finger (see insert in Fig. 4) which is temperature regulated by an electronic control circuit. A temperature stability of about  $10\text{ }\mu\text{K}$  was achieved in the earlier measurements. With recent improvements in temperature regulation, a temperature stability of  $\leq 1\text{ }\mu\text{K}$  is reached (see [16] for details). To improve the performance, a new cryostat was designed recently, especially adjusted to the needs of heavy ion research, providing considerably higher cooling power and allowing for a larger detector solid angle. For the measurements, the cryostat is connected to a scattering chamber or directly to the beamline at one of the accelerator facilities discussed above. Both scattering chamber and cryostat, are mounted on a movable arm, allowing the detectors

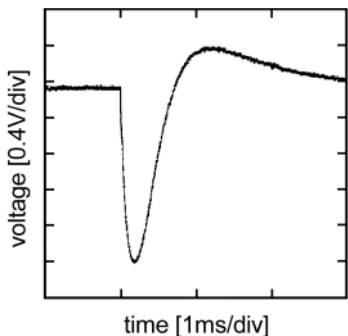


**Fig. 5.** Preamplifier signal due to the impact of a 11.4 MeV/amu  $^{136}\text{Xe}$  ion onto the germanium calorimeter

to be irradiated either by Rutherford-scattered ions from thin target foils, or by the direct beam at reduced intensity.

In Fig. 5, a preamplifier signal for the impact of a 11.4 MeV/amu  $^{136}\text{Xe}$  ion onto the germanium calorimeter is displayed. From the observed pulse height a temperature rise of the calorimeter of  $\Delta T = 9.5\text{ mK}$  at an operating temperature of  $T = 1.7\text{ K}$  was obtained. The decay time of about  $\tau = 250\text{ }\mu\text{s}$  is determined by the thermal coupling to the heat sink and allows for count rates up to about 0.5–1 kHz. An energy spectrum calorimeter for 11.6 MeV/amu  $^{209}\text{Bi}$  ions, again taken with the germanium calorimeter [19], is displayed in Fig. 6. The baseline noise was determined with a pulser, which was coupled to the preamplifier, to be  $\Delta E = 2.2\text{ MeV}$ . For the incident  $^{209}\text{Bi}$  ions a clean spectrum showing a narrow Gaussian peak with a width of  $\Delta E = 4.3\text{ MeV}$  was obtained, which corresponds to a relative energy resolution of  $\Delta E/E = 1.8 \times 10^{-3}$ . This result already represents a considerable improvement as compared to conventional ionization detectors, in particular for such very heavy ions. For the detectors with aluminum transition edge sensors similar results were obtained [20, 21, 22, 23]. For example, for 4.8 MeV/amu  $^{58}\text{Ni}$  ions an energy resolution of  $\Delta E/E = 1.6 \times 10^{-3}$  was achieved.

In further test measurements the detectors were also irradiated with relativistic heavy ions, provided from the heavy ion synchrotron SIS18 (see Fig. 1). For 100 MeV/amu  $^{20}\text{Ne}$  ions a relative energy resolution of  $1.9 \times 10^{-3}$  was obtained [23] (see also Fig. 11), again representing for these high energies a considerable improvement as compared to conventional detectors. Of special interest was a comparison, where data were taken [22] with two detectors of the same type, but with different absorber sizes ( $V = 6\text{ mm}^3$  and  $V = 121\text{ mm}^3$ ). In spite of the large difference in heat capacity, the energy resolution obtained was comparable. This indicates that the resolution in this case was not limited by the sensitivity of the detector, and provides perspectives for the design of large solid angle detector systems.

When summarizing all the results obtained at energies above  $E = 5\text{ MeV/amu}$ , it turns out that the relative energy resolutions of  $(1.6\text{--}1.9) \times 10^{-3}$  are very similar, independent on the ion species, the ion energy, the type

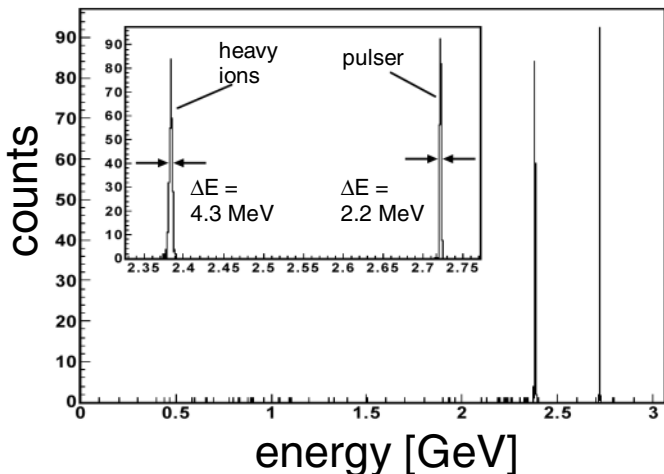


**Fig. 6.** Energy spectrum obtained with the germanium calorimeter for 11.6 MeV/amu  $^{209}\text{Bi}$  ions. The *insert* shows the peaks due to the heavy ions and due to a pulser on an expanded scale. The relative energy resolution achieved is  $\Delta E/E = 1.8 \times 10^{-3}$

of detector and the absorber size. These findings indicate that the present limitation in energy resolution is not determined by the intrinsic detector resolution due to sensitivity, thermal or electronic noise contributions, heat capacity, statistics of the energy loss processes, etc. (see Sect. 2), but most probably by the quality of the heavy ion beams from the UNILAC and SIS18 accelerators, namely the energy spread of these beams, which is expected to be of the order of  $\Delta E/E \approx (1-2) \times 10^{-3}$ . Consequently, in one further experiment [23] the detectors were tested with a cooled heavy ion beam, extracted from the storage ring ESR (see Fig. 1). The energy spread of the beam was determined from Schottky spectra of the circulating beam to be better than  $\Delta E/E = 2.4 \times 10^{-4}$ . The resulting energy spectrum, obtained for the aluminum TES calorimeter, is displayed in Fig. 7. For a 360 MeV/amu  $^{238}\text{U}$  beam a relative energy resolution of  $\Delta E/E = 1.1 \times 10^{-3}$  was achieved, which represents the up to date best result for heavy ions.

For some potential applications (see Sect. 4), high resolution detectors for relatively low ion energies of  $E \leq 1$  MeV/amu are needed. Therefore, the response of calorimetric detectors to the impact of very low energetic heavy ions was recently studied [16] using  $^{13}\text{C}$ ,  $^{197}\text{Au}$  and  $^{238}\text{U}$  beams at various incident energies ranging from total energies of  $E = 10$  MeV to  $E = 60$  MeV, corresponding to  $0.1 \leq E \leq 1$  MeV/amu. In addition, data for 5.5 MeV  $\alpha$ -particles provided by a  $^{239}\text{Pu}/^{241}\text{Am}/^{244}\text{Cm}$  source, mounted inside the cryostat, were taken. As the lowest energy provided by the UNILAC accelerator at GSI is around 3 MeV/amu, these investigations were performed at the

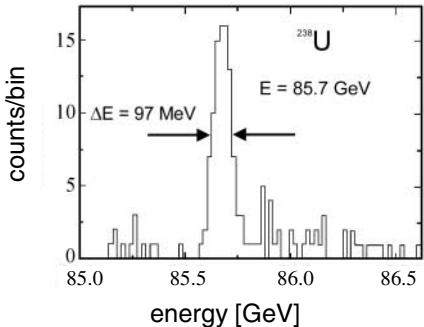


**Fig. 7.** Energy spectrum obtained with the aluminum TES calorimeter for a cooled  $^{238}\text{U}$  beam with  $E = 360 \text{ MeV}/\text{amu}$  which was extracted from the ESR storage ring at GSI Darmstadt. The obtained relative energy resolution is  $\Delta E/E = 1.1 \times 10^{-3}$

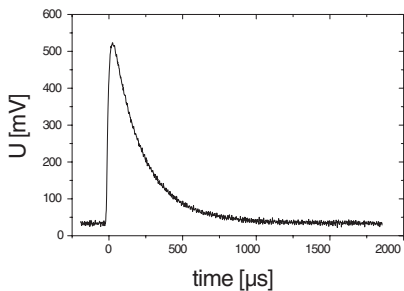


**Fig. 8.** Preamplifier signal (*left side*) and energy spectrum (*right side*) for  $^{238}\text{U}$  ions at  $E = 17.39 \text{ MeV}$  obtained with the aluminum TES calorimeter. The relative energy resolution achieved is  $\Delta E/E = 4.6 \times 10^{-3}$

3 MV Tandem accelerator of the VERA facility at the university of Vienna, Austria [26]. This facility is discussed in detail in Sect. 4.3, where also the experimental arrangement is displayed in Fig. 17. The present measurements took advantage of the excellent beam qualities provided by this facility, the energy spread being of the order of  $\Delta E/E \leq 10^{-4}$ , and the fact that changing from one ion species to another is a fast and relatively easy operation which facilitates systematic investigations with various ion species at various energies.

All measurements were performed with the aluminum TES calorimeter, because these detectors provide higher sensitivities for low energies as compared to the germanium calorimeters (see Sect. 3.1). A preamplifier signal for the impact of a  $^{238}\text{U}$  ion with  $E = 17.39 \text{ MeV}$  is displayed in Fig. 8 (left side). The relatively short thermal decay time of  $\tau = 206 \mu\text{s}$  allows for count rates up to about 0.5–1 kHz. The corresponding energy spectrum is displayed in Fig. 8 (right side). The solid line is the result of a fit with a Gaussian to the data resulting in a width of  $\Delta E = 80 \text{ keV}$ , corresponding to a relative energy resolution of  $\Delta E/E = 4.6 \times 10^{-3}$  which represents the best result

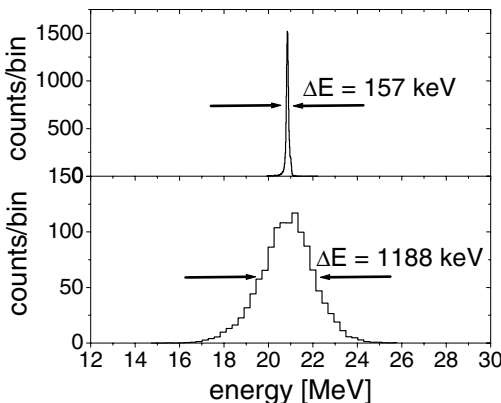


**Fig. 9.** Energy spectra for  $^{238}\text{U}$  ions at  $E = 20.85$  MeV taken under identical experimental conditions with an aluminum TES calorimeter (*upper part*) and a conventional silicon surface barrier detector (*lower part*). The relative energy resolution achieved is  $\Delta E/E = 7.5 \times 10^{-3}$  for the calorimetric detector, and  $\Delta E/E = 57 \times 10^{-3}$  for the silicon detector, respectively

obtained at energies below 1 MeV/amu at present. The shoulder on the low energy side is due to scattering of ions from the entrance slits.

As compared to conventional ionization detectors, the present result represents a considerable improvement in energy resolution, especially at these relatively low ion energies. For a direct comparison, a conventional silicon surface barrier detector was mounted at the same beamline (see Fig. 17) and could be moved in front of the calorimetric detector, thus allowing measurements under practically identical experimental conditions. The result of such a measurement for  $^{238}\text{U}$  ions at  $E = 20.85$  MeV is displayed in Fig. 9. It turns out that the relative energy resolution of the calorimetric detector of  $\Delta E/E = 7.5 \times 10^{-3}$  is about one order of magnitude better than the resolution of  $\Delta E/E = 57 \times 10^{-3}$  achieved with the silicon detector. Furthermore, a relatively fast decrease of the energy resolution of the silicon detector throughout several hours of measuring time was observed, most probably due to radiation damage, whereas the calorimetric detector showed no evidence of such behaviour even after irradiation with integrated ion doses as high as  $10^9$  ions/cm $^2$ .

Results of a systematic study on the energy resolution obtained for all ions and energies investigated are summarized in Fig. 10 (left side). At low energies ( $E < 20$  MeV), an increase of  $\Delta E/E$  for  $\alpha$ -particles and  $^{13}\text{C}$  is observed. This behaviour may be explained by a lack of sensitivity of the present detectors due to their relatively large heat capacity, and could be improved in future by using substantially thinner absorbers as compared to  $d = 330\text{ }\mu\text{m}$  in the present setup. For energies  $E \geq 20$  MeV, the relative energy resolution is approximately constant, independent of ion species and incident energy. The

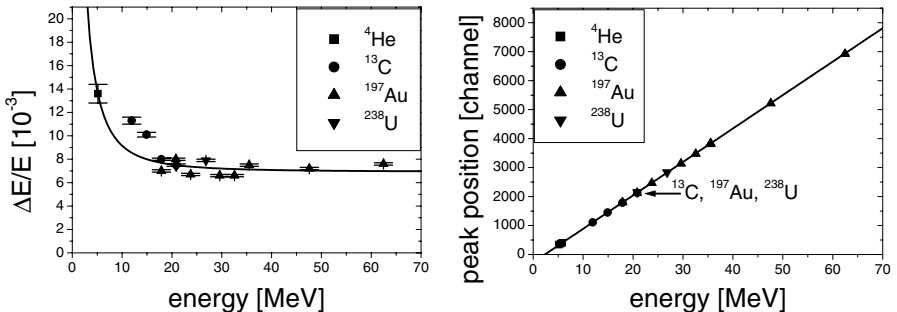


**Fig. 10.** Summary of a systematic study of the detector performance for various ions and energies: relative energy resolution (*left side*) and linearity of energy response (*right side*) obtained for various ions ( $^4\text{He}$ ,  $^{13}\text{C}$ ,  $^{197}\text{Au}$ ,  $^{238}\text{U}$ ) in an energy range of  $E = 5\text{--}70\text{ MeV}$ . All measurements were performed with an aluminum TES calorimeter as described in Sect. 3.1.2. The *solid lines* represent fits to the data (for discussion see text)

solid line is the result of a fit to the data using the ansatz:

$$\frac{\Delta E}{E} = \frac{1}{E} \sqrt{\Delta E_{\text{BLN}}^2 + (\beta E)^2}. \quad (1)$$

Hereby,  $\Delta E_{\text{BLN}}$  represents the contribution of the baseline noise which is supposed to limit the signal-to-noise-ratio for low energies and describes the increase in relative energy resolution for  $E < 20\text{ MeV}$ . For the higher energies, the term  $\Delta E \sim E$  dominates,  $\beta$  being a proportional constant. This term is most probably due to intrinsic detector properties. It can, e.g., be caused by a position dependence of the detector response function due to incomplete thermalization of the whole absorber [27]. Further detailed investigation of the energy deposition processes will be necessary for a full understanding of the obtained detector performance.

Figure 10 (right side) summarizes the results on the linearity of detector response. A perfectly linear behaviour as a function of energy was obtained over the entire range of ions from  $^4\text{He}$  to  $^{238}\text{U}$ . The solid line represents a linear fit to the data. Even more remarkable, the peak positions for the three different ions  $^{13}\text{C}$ ,  $^{197}\text{Au}$ ,  $^{238}\text{U}$  at the same energy agree within 0.1%, showing no evidence of a pulse height defect. In contrast, for the conventional silicon detector a considerable pulse height defect of 70 % was observed when comparing the peak position of  $^{13}\text{C}$  to that of  $^{238}\text{U}$  [16]. Besides the good energy resolution, we consider the non-existence of a pulse height defect for calorimetric detectors to be a considerable advantage over ionization detectors, important for many applications (see Sect. 4). Furthermore, this result allows to set an upper limit on the existence of  $Z$ -dependent energy loss processes, like creation of Frenkel pairs etc. (see Sect. 2) and on their contribution to the energy resolution.

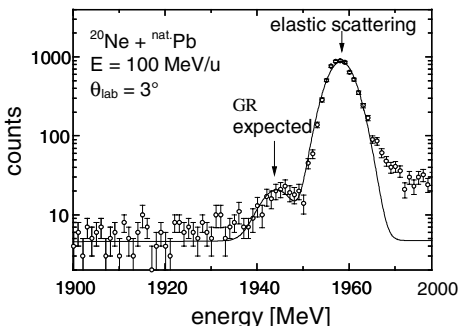


**Fig. 11.** Energy spectra obtained with an aluminum TES calorimeter for scattering of a 100 MeV/amu  $^{20}\text{Ne}$  beam from a lead target. The bump due to the excitation of the giant resonance in lead is indicated by the label *GR*. The solid line represents the result of Gaussian fits to the data

## 4 Applications of Calorimetric Low Temperature Detectors for Heavy Ions and First Results

Based on the excellent results already obtained for the performance of cryogenic heavy ion detectors (see previous section), such detectors bear the potential to be powerful tools for heavy ion physics. In the following, a brief overview on applications, including a few selected examples where also first results were obtained, is presented.

### 4.1 High Resolution Nuclear Spectroscopy

The investigation of direct reactions, such as elastic and inelastic scattering, few-nucleon transfer reactions, charge exchange reactions, etc., is a well known tool in nuclear physics to obtain information on nuclear structure [4]. Heavy ion detectors, which detect the scattered particles or the reaction products after the nucleus–nucleus interaction, need to have sufficient energy resolution to separate elastic from inelastic reaction channels, or to identify specific reaction channels. The availability of high-quality heavy ion beams, cooled in storage rings to highest phase space densities with a relative energy spread as good as  $\Delta E/E \leq 10^{-4}$ – $10^{-6}$ , and of high resolution detectors opens new possibilities in that field.

As an example, a scattering experiment [23], performed with a relativistic heavy ion beam from the SIS18 synchrotron at GSI (see Fig. 1), representing the first application of a cryogenic detector in nuclear structure physics, is discussed. The excitation of the giant resonance, which is a collective vibrational mode of nucleons in nuclei [28], was investigated for the lead nucleus by separating inelastically from elastically scattered ions in the spectrum for scattering of 100 MeV/amu  $^{20}\text{Ne}$  ions from a lead target. Since a beam particle which has excited a giant resonance in a target nucleus essentially loses an amount of kinetic energy corresponding to the excitation energy, the excitation of the resonance can be detected in the total energy spectrum of the scattered  $^{20}\text{Ne}$  projectiles. In contrast to standard detection techniques [28], where all decay products of the giant resonance have to be

detected for a missing-mass reconstruction, thus requiring a rather extended and complicated experimental setup, the present method allows a relatively simple setup, but requires high energy resolution. In Fig. 11 the measured energy spectrum for  $^{20}\text{Ne}$  ions, scattered from a lead target at a scattering angle of  $\Theta_{lab} = 3^\circ$ , is displayed. Below the elastic peak, a bump appears which is attributed to the excitation of the giant dipole resonance in the lead nuclei. The positions and the intensities of the two peaks were extracted by Gaussian fits. The resulting excitation probability of 1.7(3)% and excitation energy of 14.0(1.2) MeV are within errors in good agreement with theoretical predictions (for details see [23]).

In future it is planned to continue such investigations, the excitation of single giant resonances of different multipolarities, and especially of higher order modes, so called multiphonon giant resonances, being of particular interest [29, 30].

## 4.2 High Resolution Mass Determination for Identification of Superheavy Elements and Reaction Products from Direct Reactions with Radioactive Beams

The direct in-flight mass determination of nuclides produced in heavy-ion induced reactions is an important task, required in many fields of heavy ion physics, and is in many cases mandatory for a unique identification of rare isotopes and an unambiguous interpretation of experimental data. As the required relative mass resolution for resolving neighbouring masses scales with the nuclear mass  $M$  according to  $1/M$ , such a task turns out to be most challenging for the heaviest particle-stable isotopes under investigation.

Due to their excellent energy resolution and energy linearity because of the absence of a pulse height defect (see Sect. 3.2) and their radiation hardness, calorimetric low temperature detectors may in future be favourably used for such purposes. The idea is to replace the standard  $B\varrho/\text{TOF}$  method, where an isotope mass  $M = p/v$  is determined by a magnetic rigidity ( $B\varrho$ ) measurement of the momentum  $p$  and a Time-Of-Flight (TOF) measurement of the velocity  $v$ , by an energy/TOF determination of the mass via  $M = 2E/v^2$ . The advantage of this method is that ambiguities due to multiple charge states, as appearing in the  $B\varrho/\text{TOF}$  method for not fully stripped ions, do not exist, and moreover, no solid angle limiting magnetic spectrometers are needed. However, since mass resolution for  $E/\text{TOF}$  measurements is determined by  $\Delta M/M = [(\Delta E/E)^2 + 2(\Delta v/v)^2]^{1/2}$ , it is obvious that the separation of masses up to the heaviest isotopes ( $M \approx 300$  amu) will require a relative energy resolution of at least  $\Delta E/E \leq 3 \times 10^{-3}$ , presently obtainable only with calorimetric low temperature detectors. The determination of the ion velocity with a relative resolution of the order of  $\Delta v/v \leq 1 \times 10^{-3}$  is possible with standard TOF techniques [25, 31, 39] by using fast channelplate detectors and applying, especially for the case of very slow heavy ions, ultra-thin carbon foils [32] to keep energy-loss straggling on a tolerable level.

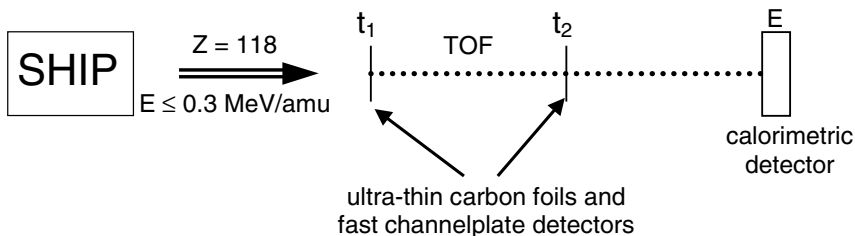
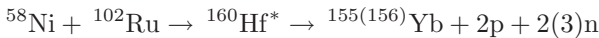


**Fig. 12.** Scheme of a setup proposed for the identification of superheavy elements with  $Z > 112$ . The mass of the superheavy nucleus, separated from other reaction products by the heavy ion separator SHIP [5], is determined by a combined  $E$ /TOF determination. Besides the superheavy nucleus, its decay products are additionally to be detected time-resolved in the calorimetric detector.

One prominent example where such a detection system could be favourably employed in future is the research on superheavy elements. An overview of this research field and of its recent progress at GSI Darmstadt and worldwide is given in [5, 6]. At GSI Darmstadt, elements with  $Z = 107\text{--}112$  have been successfully synthesized and unambiguously identified within the last two decades. The elements Bh ( $Z = 107$ ), Hs ( $Z = 108$ ), Mt ( $Z = 109$ ), Ds ( $Z = 110$ ) and Rg ( $Z = 111$ ) have already been named. As discussed in more detail in [5, 6], the superheavy elements have been produced by cold fusion heavy ion reactions at relatively low incident energies around  $1\text{--}5$  MeV/amu, and the resulting fusion products (with energies of  $E = 0.1\text{--}1$  MeV/amu) are separated in the heavy ion separator SHIP and transported to a conventional silicon semiconductor detector where the heavy isotope and its  $\alpha$ -decays are detected time-resolved. The production cross sections are as low as  $10^{-10} - 10^{-13}$  barn, corresponding to production rates down to 1/week or even less, thus demanding for a highly efficient event characterization for each single event [5, 6]. For the superheavy elements with  $Z \leq 112$ , this was possible by identifying the complete  $\alpha$ -decay chain leading to an already known decay chain, and therefore allowing to unambiguously identify the isotope even for one single event. Indications of the existence of superheavy elements with  $Z = 113, 114, 116$  and  $118$  have been reported from heavy ion research centers at Dubna, Russia [33, 34] and RIKEN, Japan [35]. However, for superheavy elements with  $Z > 112$ , the situation is essentially different, as the isotopes produced are most likely to decay by spontaneous fission instead of feeding known  $\alpha$ -decay chains, and therefore the identification method discussed above for  $Z \leq 112$  is not applicable any more.

To overcome this problem, it was recently proposed [24] to use an  $E$ /TOF detection system (Fig. 12) with a high resolution calorimetric detector that would allow a mass identification of the superheavy nuclide produced, and in addition a precise determination of the total kinetic energy of the fission products. In a series of test experiments [16, 25] performed recently at the heavy ion separator SHIP at GSI and at the VERA facility in Vienna (see

Sect. 4.3), it was demonstrated that the proposed detection scheme fulfills the requirements for a successful future application in superheavy element research. At the SHIP separator, fusion products from the reaction



and their  $\alpha$ -decays were detected time-resolved in an aluminium TES calorimeter with aluminum thermistor (as described in Sect. 3). It turned out [16] that the dynamic range of the detector was sufficient to detect the heavy ion and its correlated  $\alpha$ -decays, and it was possible to identify the isotopes  $^{155}\text{Yb}$  and  $^{156}\text{Yb}$  via their  $\alpha$ -decays chains. The best  $\alpha$ -resolution achieved with such detectors is  $\Delta E = 32\text{ keV}$  and therefore also sufficient for the demands of the proposed experiment.

In another test experiment performed at the VERA facility, direct in-flight mass identification of  $^{206,208}\text{Pb}$  isotopes at energies slightly below  $0.1\text{ MeV/amu}$ , close to the energy expected for superheavy elements, was tested (for details of the experimental setup see [25]). The experimental method was demonstrated to principally work, but with the not optimal energy resolution of the calorimetric detector of only  $\Delta E/E = 9.8 \times 10^{-3}$  under the experimental conditions of this test run and a time resolution of  $\Delta t/t = 1.4 \times 10^{-3}$ , the resulting mass resolution of  $\Delta M/M = 11.0 \times 10^{-3}$  allowed to separate only partly the isotopes  $^{206}\text{Pb}$  and  $^{208}\text{Pb}$  (see Fig. 13). With the nowadays reached energy resolution of the order of  $\Delta E/E = (2\text{--}5) \times 10^{-3}$ , a mass resolution of  $\Delta M/M = (2\text{--}5) \times 10^{-3}$  should be achievable.

As a next step towards a cryogenic detection system for application in superheavy element research, a detector array with an active area of  $3 \times 8\text{ cm}^2$ , consisting of 96 pixels with  $5 \times 5\text{ mm}^2$  pixel size and design values of a position resolution of  $\Delta x = 5\text{ mm}$ , an  $\alpha$ -resolution of  $\Delta E = 30\text{ keV}$ , a heavy ion energy resolution of  $\Delta E/E \leq 3 \times 10^{-3}$  and a rate capability of  $300\text{ s}^{-1}$  per pixel is currently under design and construction. The design of a prototype array consisting of  $2 \times 5$  detector pixels of aluminium TES calorimeters is displayed in Fig. 14.

A second example for application of cryogenic detectors to be briefly discussed concerns nuclear structure investigations on nuclei far off stability. With the availability of intense isotopically pure secondary beams of radioactive nuclei (see also Sect. 1), such investigations are most favourably performed by using the method of inverse kinematics which is sketched schematically in Fig. 15 for the example of a one-neutron ( $d,p$ ) transfer reaction. In order to study the structure of the radioactive projectile nucleus, a direct reaction is initiated by the radioactive beam hitting a  $^2\text{H}$  target, and the target-like reaction products are to be detected in coincidence with the beam-like reaction products. Such investigations are of high interest at present and even more at the second generation future radioactive beam facilities (see Sect. 1), as many questions of nuclear structure and nuclear astrophysics – e.g., on the isospin dependence of nuclear structure, the mechanisms of nu-

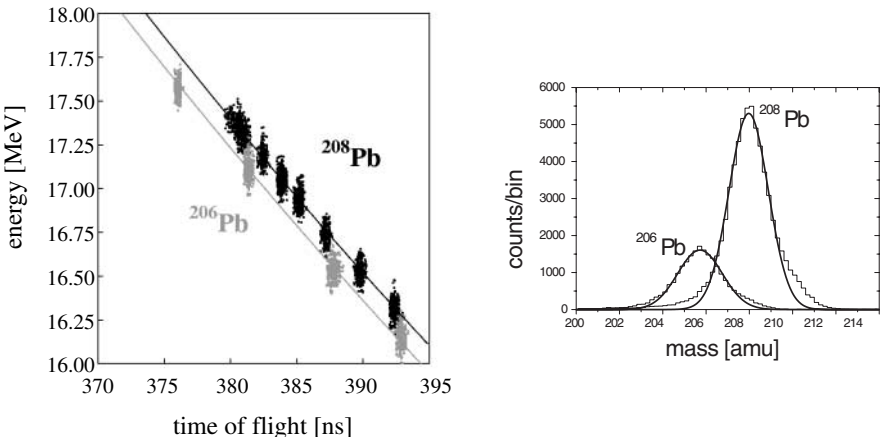


**Fig. 13.** Results of a test experiment for isotope identification by a combined  $E/\text{TOF}$  measurement. The energy versus time-of-flight correlation is shown on the *left side* for the isotopes  $^{206}\text{Pb}$  and  $^{208}\text{Pb}$  at several energies slightly below 0.1 MeV/amu. The *solid lines* represent fits to the data according to the expected kinematic correlation. The corresponding mass spectrum is displayed on the *right side*. A relative mass resolution of  $\Delta M/M = 11.0 \times 10^{-3}$  is achieved

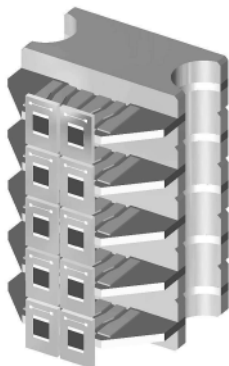


**Fig. 14.** Design of a prototype array consisting of  $2 \times 5$  detector pixels of aluminum TES calorimeters

cleosynthesis in stars and supernovae, etc. – may be addressed (see [3, 4, 36] for an overview).

The experimental technique (see Fig. 15) requires, among others, an unambiguous mass identification of the beam-like reaction products, which, especially for very slow heavy radioactive beams, is not provided by standard detection techniques. The application of cryogenic detectors for mass identification via the  $E/\text{TOF}$  method as discussed before is therefore of high interest for future radioactive beam facilities

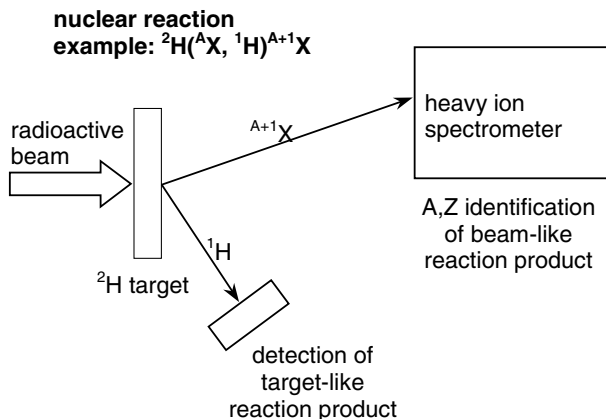


**Fig. 15.** Sketch of a typical experimental setup for the investigation of heavy-ion induced direct reactions with radioactive beams in inverse kinematics. For the identification of the beam-like reaction product, high-resolution cryogenic detectors may favourably be used

like SPIRAL II at GANIL, France [37], and FAIR at GSI Darmstadt, Germany [3, 4].

## 4.3 Accelerator Mass Spectrometry

### 4.3.1 Cryogenic Detectors in Accelerator Mass Spectrometry

For many fields of basic and applied research in nuclear physics and astrophysics, solid state physics, material analysis, nuclear chemistry, biology, life sciences, etc., a precise knowledge of the isotopic composition of a material sample is of high interest. **Accelerator Mass Spectrometry (AMS)** is a well established method for the determination of very small isotope ratios with high sensitivity. Preselected by a conventional “low energy” mass spectrometer, the ions of interest are injected into an accelerator. After acceleration, the ion beam passes an additional “high energy” mass spectrometer which usually consists of several filters for nuclear mass and charge, well adjustable to the individual experimental conditions for specific cases (see [7, 8] for a detailed overview on the experimental technique and its applications). As compared to conventional mass spectrometry, the use of accelerated ion beams and “high energy filters” provides substantial advantage in the quality of isotope separation and suppression of background from neighbouring isotopes, isobars and molecular ions, and therefore allows an enhancement in sensitivity by many orders of magnitude. With such performance, the precise determination of isotope ratios down to a level of  $10^{-10}$ – $10^{-16}$ , by far not reached with conventional techniques, becomes possible with AMS and thus enables

to address interesting applications in trace analysis, radionuclide dating, cosmochronology and many others, radiocarbon dating representing the most prominent example.

Within the last 10 years, very heavy elements like uranium and plutonium have become more and more interesting for AMS applications, e.g. in biological research or reactor safety. However, AMS of such very heavy nuclides bears new and more involved challenges:

- For very heavy ions, the discrimination of neighboring isotopes, which have always a small but finite probability to leak – due to multiple charge exchange processes – through the high energy filters, becomes more demanding. As the mass resolving power required scales linearly with the nuclear mass  $M$ , high resolution energy and/or time-of-flight detectors are necessary to separate the different isotopes.
- Most AMS facilities nowadays use tandem accelerators with 3–5 MV terminal voltage, resulting in typical ion energies as low as 0.1–1 MeV/amu for very heavy ions when selecting charge states with maximum transmission. Moreover, the present trend is to use, for cost reduction purposes, even smaller accelerators with correspondingly lower terminal voltage and thus lower ion energies. The detection of such slow heavy ions with high resolution, low threshold and high detection efficiency, most important for very rare isotopes, is a challenging task, and in many cases beyond the limits of the performance of standard detection techniques (see Sect. 2).

With the performance of cryogenic heavy ion detectors (as discussed in Sect. 3.2), such detectors have the potential to considerably improve the experimental conditions for AMS applications with very heavy ions. Due to their excellent energy resolution for slow heavy ions, they are capable of separating neighbouring masses by their high energy resolving power alone, and are therefore very suitable to replace conventional  $E/TOF$  detection systems in AMS measurements. Together with their low detection threshold and their radiation hardness, this leads to substantially improved detection efficiency and long-time stability, especially important for the detection of very rare isotopes. Consequently, as discussed in the next section, cryogenic heavy ion detectors were recently applied for the first time in an AMS experiment addressing a question of basic physics interest [16, 38].

#### 4.3.2 First Application of Cryogenic Detectors in AMS for Trace Analysis of $^{236}\text{U}$

One of the heaviest nuclides of interest for AMS is  $^{236}\text{U}$ . Being produced in nature by the capture of thermal neutrons in the reaction  $^{235}\text{U}(\text{n}, \gamma)^{236}\text{U}$  and having a half-life of 23.4 million years, the relative abundance of  $^{236}\text{U}$  provides an excellent neutron flux monitor integrated over geological timescales [26, 39]. Besides other applications, e.g., in reactor safety,  $^{236}\text{U}$  is therefore most

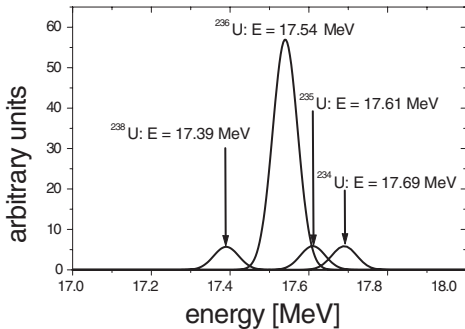


**Fig. 16.** Simulation of the background situation for the AMS measurement of  $^{236}\text{U}$ . The ratio of  $^{236}\text{U} : ^{234,235,238}\text{U}$  is assumed to be 10:1, the energy resolution to be  $\Delta E/E = 4.6 \times 10^{-3}$

interesting for geology research. Its isotopic ratio with respect to the long lived isotope  $^{238}\text{U}$  can be used to determine the neutron flux that samples of natural uranium ore have been exposed to in their geological history. This could be used to prove the existence of an enhanced neutron flux due to natural “reactor-like” conditions in the past. A prominent example is the uranium mine in Oklo, West Africa [40], where nuclear fission of  $^{235}\text{U}$  is believed to have occurred under specific geological conditions. However, in natural uranium ore, the isotope ratio is of the order of  $^{236}\text{U}/^{238}\text{U} = 10^{-10} - 10^{-14}$ , depending on the samples history and surroundings, and therefore an ultra-high sensitivity for the detection of  $^{236}\text{U}$  is required for such kind of investigations.

Under typical experimental conditions, e.g., at the VERA AMS facility at the university of Vienna, Austria, background in AMS measurements for very heavy ions is mainly due to neighbouring isotopes which have, due to various charge exchange processes, the same magnetic rigidity  $ME/q^2$  ( $M$  being the mass and  $q$  the charge state of the ion) and therefore pass through the “high energy” magnetic analyzer and, after additional charge exchange, also through the electrostatic analyzer (see [26] for a detailed discussion). The background situation expected for the case of 17.54 MeV  $^{236}\text{U}^{5+}$  ions is displayed in Fig. 16. Since standard energy detectors, (e.g., ionization chambers etc.) do not provide sufficient energy resolution to resolve these background peaks, in the previous measurements [26, 39] TOF spectrometers combined with ionization chambers were used. The level of sensitivity reached for the  $^{236}\text{U}/^{238}\text{U}$  ratio was limited to  $6 \times 10^{-11}$ , mainly due to the limited detection efficiency of only 20% and/or the poor energy resolution of the ionization chamber. The aim of the present experiment was therefore to replace the conventional detection system by a calorimetric low temperature detector to increase the sensitivity, and to precisely determine the  $^{236}\text{U}/^{238}\text{U}$  ratio for various samples of natural uranium in order to establish an improved material standard.

The experiment was performed at the “Vienna Environmental Research Accelerator (VERA)” in Vienna, Austria. This 3 MV tandem accelerator is

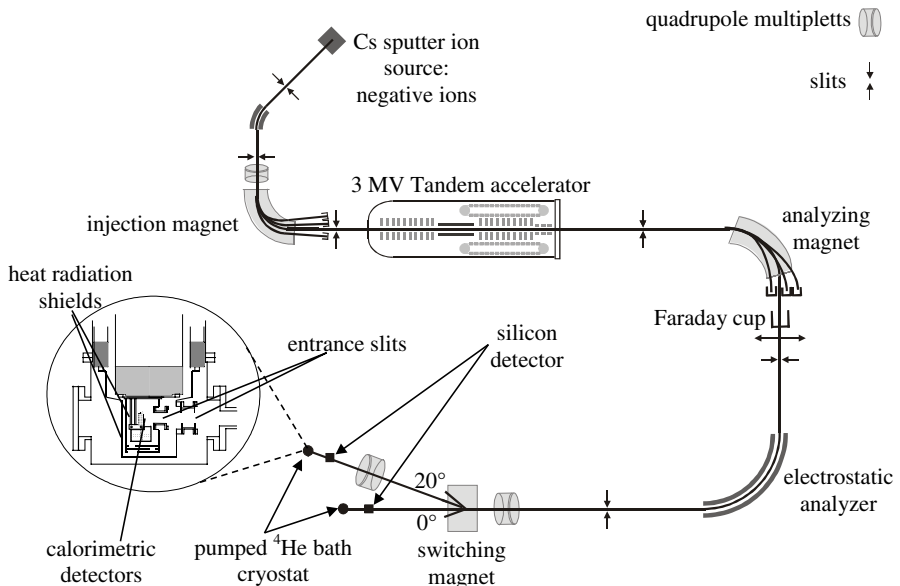


**Fig. 17.** The experimental setup for the AMS experiment at the Vienna Environmental Research Accelerator VERA. For the systematic investigations of detector performance discussed in Sect. 3.2, the superconducting aluminum TES calorimeters were mounted at the  $0^\circ$ -beamline, for the AMS measurements at the  $20^\circ$ -beamline. For a detailed discussion see text and [16, 25, 38]

part of a dedicated AMS setup for all ions ranging from beryllium up to uranium [26]. The experimental setup is schematically displayed in Fig. 17 (see [16, 38] for details). For the AMS measurements, the accelerator provides  $\text{U}^{5+}$  beams with  $E \approx 17.5$  MeV. The analyzing magnet and the electrostatic analyzer form a high energy mass spectrometer with a mass resolution of  $\Delta M/M = 1.8 \times 10^{-3}$ , principally sufficient to separate  ${}^{236}\text{U}$  from its neighbouring isotopes  ${}^{234}\text{U}$ ,  ${}^{235}\text{U}$  and  ${}^{238}\text{U}$ . However, due to multiple charge exchange processes with the residual gas in the beamline (as discussed before), these isotopes can pass the mass spectrometer and reach the detector at the end of the beamline, where the  ${}^{236}\text{U}$  ions are detected. The cryostat which houses the aluminum TES calorimeters as described in Sect. 3.1 was attached directly to the VERA  $20^\circ$ -beamline. For the determination of the isotope ratio, the radioisotope  ${}^{236}\text{U}$  was detected in the calorimetric detector, while the beam current of the “stable”  ${}^{238}\text{U}$  was measured in a Faraday cup situated directly behind the analyzing magnet, which was moved in and out of the beam frequently throughout the measuring cycles. Cooled slits at the entrance of the cryostat were used to minimize thermal irradiation from the surroundings. Typical count rates ranged from  $10 \text{ s}^{-1}$  down to  $10^{-2} \text{ s}^{-1}$  for the sample with the lowest  ${}^{236}\text{U}$  abundance.

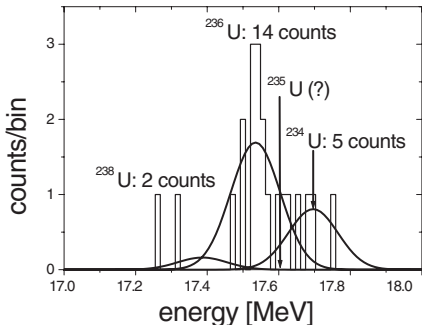


**Fig. 18.** Energy spectrum obtained with the aluminum TES calorimeter for the AMS measurement of the  $^{236}\text{U}/^{238}\text{U}$  isotope ratio in a sample from natural uranium. The isotope ratio was determined to be  $^{236}\text{U}/^{238}\text{U} = (6.1 \pm 2.1) \times 10^{-12}$

For the very first AMS measurement performed with a cryogenic detector, the results of which are presented here, the detector performance under running conditions was unfortunately worse as compared to the results presented in Sect. 3.2, but already with a resolution of  $\Delta E/E = 9.1 \times 10^{-3}$ , essential parts of the background from  $^{234}\text{U}$  and  $^{238}\text{U}$  could be separated, whereas a possible contribution of  $^{235}\text{U}$  is still included in the  $^{236}\text{U}$  count rate (see also Fig. 18). Several samples of natural uranium were investigated (see [16, 38] for a detailed discussion). Uranium ore from the mine ‘‘Joachimsthal’’, processed and stored before 1918 and therefore not contaminated by nuclear bomb fallout, is very suitable as a material standard in AMS if its  $^{236}\text{U}/^{238}\text{U}$  isotope ratio is known precisely. Within errors, the present result of  $^{236}\text{U}/^{238}\text{U} = (3.89 \pm 0.35) \times 10^{-11}$  is in agreement with previous measurements [39]. Statistical as well as systematical errors were considerably reduced, mainly due to an improvement in detection efficiency from 20% to 65%.

With the increase in sensitivity obtained, it was possible for the first time to investigate one sample of uranium extracted from spring water from Bad Gastein, Austria, for which an isotope ratio of  $^{236}\text{U}/^{238}\text{U} \leq 10^{-12}$  was expected. Fig. 18 shows the energy spectrum obtained. Due to the rather complicated sample preparation and the low uranium concentration in the water, the amount of sample material was limited, and only one measurement of 20 minutes duration could be performed. The isotope ratio was determined to be  $^{236}\text{U}/^{238}\text{U} = (6.1 \pm 2.1) \times 10^{-12}$ . This represents the smallest isotope ratio determined for  $^{236}\text{U}/^{238}\text{U}$  up to now. As compared to the measurements with a conventional setup [39], sensitivity was enhanced by one order of magnitude. Increasing the active detector area and realizing the best resolution achieved under AMS experiment conditions (see Sect. 3.2) will allow to further increase the sensitivity and to measure even smaller isotope ratios.

## 5 Cryogenic Detectors for Hard X-rays and their Application in Atomic Physics with Highly Charged Heavy Ions

Besides the detection of heavy ions, the concept of cryogenic detectors also provides considerable advantage for X-ray spectroscopy in heavy ion physics. Whereas the worldwide activities on cryogenic heavy ion detectors are still very scarce, a lot of activities with various motivations and potential applications for X-ray detectors exist [17, 41]. Most of these developments are restricted to the energy range  $E_\gamma \leq 10\text{ keV}$ . However, relativistic heavy ion beams, available e.g., at GSI Darmstadt (Sect. 1), allow to prepare highly stripped ion beams of very heavy ions with correspondingly high electronic transition energies of the order of  $E_\gamma = 50\text{--}100\text{ keV}$ . Consequently, there is a demand for high resolution detectors for such “hard” X-rays.

### 5.1 Lamb Shift Measurements on Hydrogen-like Heavy Ions

About fifty years ago, it became evident that for small distances between electric charges the classical Coulomb interaction potential is not completely correct. The accurate experimental test of the theoretical predictions of quantum electrodynamics (QED), then developed, on corrections to the classical Coulomb interaction is still – at least for high- $Z$  systems – one of the outstanding and most challenging problems of atomic physics. In the hydrogen atom, or in hydrogen-like ions, the QED corrections give rise to the so-called Lamb shift, which is a small deviation of the binding energies from those predicted by the relativistic Dirac–Coulomb theory (see Fig. 19). Whereas in light systems, where QED predictions were confirmed to high accuracy [42] and the higher-order contributions are almost negligible, they increase strongly with higher  $Z$ . On the other hand, the theoretical predictions of QED, which are usually performed in series expansions in  $Z\alpha$  ( $\alpha$  being the fine structure constant), become most critical for the heaviest systems, where  $Z\alpha$  approaches values close to unity. Therefore, an accurate determination of the Lamb shift in hydrogen-like very heavy ions represents one of the most sensitive tests of QED in strong electromagnetic fields, not accessible otherwise [11, 43, 44].

The level scheme of the hydrogen-like  $\text{U}^{91+}$  ion is displayed in Fig. 19. The binding energy of the 1s-energy level is about  $-132\text{ keV}$ , thus yielding transition energies for the Lyman- $\alpha$  lines of about  $100\text{ keV}$ . The 1s Lamb shift is predicted to be about  $466\text{ eV}$  [45]. Besides the QED contributions of self energy ( $\approx 80\%$ ) and vacuum polarization ( $\approx 20\%$ ), the effect of finite nuclear size ( $\approx 40\%$ ) also contributes considerably to this value. Therefore, apart from the experimental uncertainties, the accuracy on the QED test will be finally limited by the uncertainties on the finite nuclear size effects, estimated for  ${}^{238}\text{U}$  to be about  $0.1\text{ eV}$  [44, 45]. This provides the Lamb shift experiments

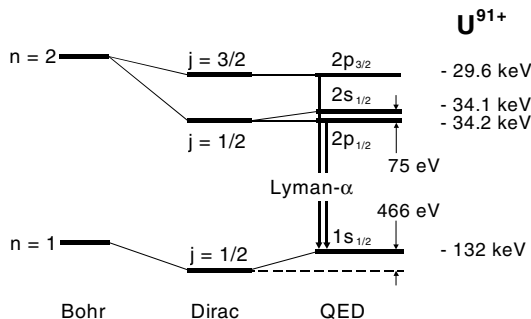


**Fig. 19.** Level scheme for hydrogen-like  $\text{U}^{91+}$  according to various atomic models. The numbers on the right indicate the electronic binding energies

also with the potential to deduce nuclear charge radii by testing QED in one isotope with a well known nuclear structure, and by investigating the Lamb shift for the corresponding chain of isotopes, which may in the future also be extended to unstable isotopes.

To determine the 1s Lamb shift of heavy ions the transition energies of the Lyman- $\alpha$  transitions are to be measured with high accuracy and compared to theoretical predictions from the Dirac theory. Such experiments are performed at the experimental storage ring (ESR) of GSI Darmstadt [44, 45] (see also Fig. 20). A beam of bare  $\text{U}^{92+}$  ions is injected, stored and cooled in the ESR and interacts with an internal gas-jet target. This may lead to the capture of one electron and to the population of a 2p state, which promptly decays to the 1s state. The emitted Lyman- $\alpha$  X-rays are detected by X-ray detectors surrounding the internal target in coincidence with the charge exchanged  $\text{U}^{91+}$  ions. The latest experimental results on the  $Z = 79$  and  $Z = 92$  systems are compared with theoretical predictions in [45]. The experimental results agree well with the theoretical predictions and provide already a test of QED for the high- $Z$  domain on the level of 3%. However, the experimental errors ( $\pm 13 \text{ eV}$ ) are about one order of magnitude larger than the theoretical ones ( $\pm 1 \text{ eV}$ ). Thus, the experimental accuracy has to be improved considerably for a more stringent test of QED and/or for the determination of precise nuclear charge radii.

One major contribution to the experimental error is the poor energy resolution of  $\Delta E \geq 500 \text{ eV}$  obtained with germanium detectors, which must be improved to at least  $\Delta E \leq 50\text{--}100 \text{ eV}$  in order to reach an absolute accuracy of about  $\delta E = \pm 1 \text{ eV}$  in the determination of the center of gravity of the transition energy. Consequently, it was first proposed in 1995 [46] to apply the concept of calorimetric low temperature detectors for improving the experimental conditions in Lamb shift experiments. As compared to the alternative concept of using crystal spectrometers [47], which also provide excellent energy resolution but suffer from poor overall detection efficiency, cryogenic detectors represent a good compromise between good energy resolution and still reasonable detection efficiency (for details see [46]). Very recently it was also proposed [48] to study the 2s Lamb shift in the Balmer series using calorimetric detectors covering the lower energy range of  $E_\gamma \leq 10 \text{ keV}$ .

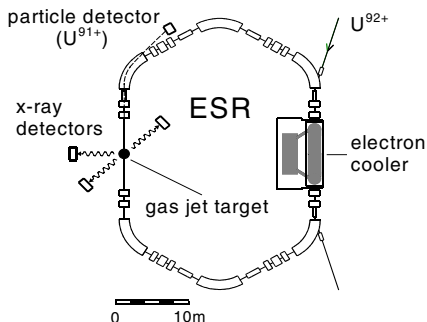


**Fig. 20.** Experimental setup for Lamb shift measurements on hydrogen-like very heavy ions at the internal gas-jet target of the storage ring ESR at GSI Darmstadt

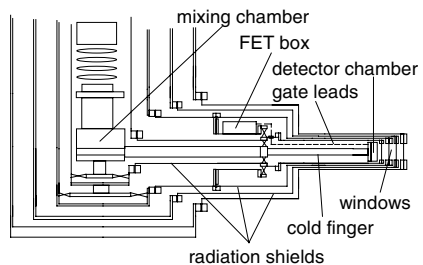


**Fig. 21.** Layout of the detector side arm of the  ${}^3\text{He}/{}^4\text{He}$  dilution refrigerator especially designed for the Lamb shift experiment (for details see text)

## 5.2 Development of Calorimetric Low Temperature Detectors for Hard X-rays and First Results

The detection of X-rays with calorimetric low temperature detectors is discussed in detail in the contribution of Porter et al. [41] for the region of soft X-rays with  $E_\gamma \leq 10 \text{ keV}$ . To meet the experimental conditions required by the 1s Lamb shift experiment discussed in the previous section, the calorimetric detector should have a relative energy resolution of  $\Delta E/E \leq 1 \times 10^{-3}$  for  $E_\gamma = 50\text{--}100 \text{ keV}$  and a total detection efficiency (including detector solid angle) of  $\geq 10^{-6}\text{--}10^{-5}$ , which may be reached with a photopeak efficiency of  $\geq 30\%$  and an active detector area of  $\geq 50 \text{ mm}^2$ . The detector modules for the present experiment are designed on the basis of silicon microcalorimeters which were developed by the Goddard/Wisconsin groups for astrophysical applications [41, 49]. The detector pixels consist of silicon thermistors, made from a wafer of silicon containing an implanted thermistor and of X-ray absorbers glued on the top of the thermistors by means of an epoxy varnish. Thermistor arrays [49], consisting of 36 pixels each, are provided from the collaborating group from the Goddard Space Flight Center.

For the Lamb shift measurement, the experimental setup was optimized with respect to energy resolution and detection efficiency for hard X-rays at the experimental area of the storage ring ESR (for details see [50, 51, 52]). The final detector concept foresees three calorimeter arrays, the active area of one pixel being about  $0.5 \text{ mm}^2$ . In order to reach sufficient photopeak efficiency, the absorber should be a high-Z material and have a volume of at least  $V \geq 0.5 \text{ mm}^2 \times 40 \mu\text{m}$ . Additional requirements are low heat capacity as well as rapid and complete thermalization. Absorber materials under investigation are Sn, HgTe and Pb. To obtain a reasonable detection solid angle, the detector arrays have to be located as close as possible to the interaction zone

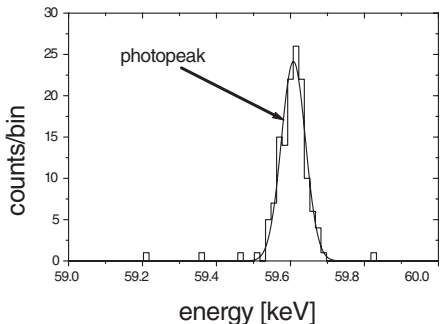


**Fig. 22.** Energy spectrum observed with a calorimetric low temperature detector with a  $0.2 \text{ mm}^2 \times 47 \mu\text{m}$  Pb absorber for 59.6 keV photons. The solid line represents a Gaussian fit to the data. For the photopeak, an energy resolution of  $\Delta E = 65 \text{ eV}$  is obtained

at the internal target of the ESR. To realize this concept a special  ${}^3\text{He}/{}^4\text{He}$  dilution refrigerator with a side arm which fits to the internal target geometry was designed in cooperation with Oxford Instruments. A schematic view of the layout of the system is displayed in Fig. 21. The detector arrays are mounted on the cold finger at the end of the side arm and can be irradiated through a system of aluminum-coated mylar windows. In order to suppress low-frequency microphonics, the first amplifier stage is positioned close to the detectors inside the side arm of the cryostat. The cryostat is prepared to read out a total of 100 detector channels. In agreement with the specifications, the cryostat reaches a base temperature of 11.5 mK, and a cooling power of  $400 \mu\text{W}$  at 11.5 mK. The operating temperature of the detectors can be chosen between  $T = 50 \text{ mK}$  and  $T = 100 \text{ mK}$ .

The detector performance presently achieved is already close to fulfill the demands of the Lamb shift experiment. The best results were obtained with Sn and Pb as absorber materials. The energy spectrum obtained for a detector with a  $0.2 \text{ mm}^2 \times 47 \mu\text{m}$  Pb absorber for 59.6 keV photons, provided by an  ${}^{241}\text{Am}$  source, is displayed in Fig. 22. For the photopeak at 59.6 keV, an energy resolution of  $\Delta E = 65 \text{ eV}$  is obtained. This result may be compared to the theoretical limit of the energy resolution for a conventional semiconductor detector which is about  $\Delta E \approx 380 \text{ eV}$  for 60 keV photons.

Very recently, a prototype array consisting of 8 pixels with a total active area of  $2.9 \text{ mm}^2$  was installed at the ESR storage ring and is presently subject to tests under realistic experimental conditions. Covering a total solid angle of  $1.9 \times 10^{-5} \text{ sr}$ , an overall  $K_\alpha$  detection efficiency of  $2 \times 10^{-7}$ , corresponding to a count rate of 15/h under realistic experimental conditions is expected, and an average energy resolution of  $\Delta E = 75\text{--}150 \text{ keV}$  is obtained.

With respect to atomic physics investigations at the future GSI facility FAIR (see Sect. 1), we expect that the concept of cryogenic detectors will play a major role for X-ray spectroscopy on stored and trapped heavy ions. So within the SPARC project [53], it was proposed to build up highly efficient arrays of calorimetric detectors covering a major part of the available solid angle. For this purpose, besides micro-calorimeters on the basis of semiconductor thermistors or transition edge sensors, as used nowadays, the concept

of magnetic calorimeters [54] may be a promising detector concept for such investigations.

## Acknowledgements

The authors are indebted to D. Ackermann, R. Golser, W. Henning, F.P. Hessberger, S. Hofmann, H.-J. Kluge, W. Kutschera, D. Mc Cammon, G. Münzenberg, H. J. Meier, K. W. Shepard, C. K. Stahle, P. Steier and T. Stöhlker for many helpful and stimulating discussions. The experimental results presented in this article were obtained in close collaboration with V. A. Andrianov, A. Bleile, W. Böhmer, R. Golser, W. Henning, A. v. Kienlin, A. Kiseleva, O. Kiselev, G. Kraus, W. Kutschera, U. Liebisch, H. J. Meier, J. P. Meier, A. Priller, O. Sebastian, A. Shrivastava, P. Steier, C. Vockenhuber, M. Weber and A. Weinbach.

## References

- [1] Proceedings of the 10th International Workshop on Low Temperature Detectors LTD10, F. Gatti (ed.), Nucl. Instr. Meth. A **520** (2004) **470**, **473**
- [2] Cryogenic Particle Detection, C. Enss (ed.), Topics Appl. Phys. **99** (2005) **470**, **473**
- [3] W. F. Henning: Nucl. Instr. Meth. B **214**, 211 (2004) **470**, **488**, **489**
- [4] Conceptual Design Report: An international accelerator facility for beams of ions and antiprotons, H. H. Gutbrod *et al.* (eds.), GSI Darmstadt, Germany (2001), [http://www.gsi.de/zukunftsprojekt/veroeffentlichungen\\_e.html](http://www.gsi.de/zukunftsprojekt/veroeffentlichungen_e.html) **470**, **472**, **484**, **488**, **489**
- [5] S. Hofmann and G. Münzenberg: Rev. Mod. Phys. **72**, 733 (2000) **470**, **486**
- [6] S. Hofmann: J. Nucl. Rad. Sc. **4**, R1 (2003) **470**, **486**
- [7] W. Kutschera and M. Paul: Ann. Rev. Nucl. Part. Sci. **40**, 411 (1990) **470**, **472**, **489**
- [8] W. Kutschera: in Experimental Nuclear Physics in Europe, ENPE 99: Facing the Next Millennium, B. Rubio *et al.* (eds.), AIP Conference Proceedings **495**, 407 (1999) **470**, **472**, **489**
- [9] D. Mc Cammon: in Cryogenic Particle Detection, C. Enss (ed.), Topics Appl. Phys. **99**, 35 (2005) **475**, **476**
- [10] Atomic Physics with Heavy Ions, H. F. Beyer, V. P. Shevelko (eds.), Springer, Berlin (1999) **472**
- [11] T. Stöhlker: Physica Scripta T **73**, 29 (1997) **472**, **494**
- [12] J. F. Ziegler, J. P. Biersack and U. Litmark: The stopping and range of ions in solids, Pergamon Press, New York (1985) **473**, **475**
- [13] S. H. Moseley and J. C. Mather: J. Appl. Phys. **56**, 1257 (1984) **474**
- [14] D. McCammon: in Cryogenic Particle Detection, C. Enss (ed.), Topics Appl. Phys. **99**, 1 (2005) **474**
- [15] H. H. Andersen: Nucl. Instr. Meth. B **15**, 722 (1986) **474**, **475**
- [16] S. Kraft-Bermuth: PhD thesis, Johannes Gutenberg Universität, Mainz (2004) **474**, **475**, **476**, **478**, **480**, **483**, **486**, **487**, **490**, **492**, **493**

- [17] K. D. Irwin, G. C. Hilton: in *Cryogenic Particle Detection*, C. Enss (ed.), *Topics Appl. Phys.* **99**, 63 (2005) [475](#), [494](#)
- [18] A. v. Kienlin: PhD thesis, Johannes Gutenberg Universität, Mainz (1993) [475](#), [478](#)
- [19] A. v. Kienlin, F. Azgui, W. Böhmer, K. Djotni, P. Egelhof, W. Henning, G. Kraus, J. Meier and K. W. Shepard: *Nucl. Instr. Meth. A* **368**, 815 (1996) [475](#), [478](#), [479](#)
- [20] J. Meier, P. Egelhof, C. Fischer, A. Himmler, G. Kirchner, A. v. Kienlin, G. Kraus, W. Henning and K. W. Shepard: *J. Low Temp. Phys.* **93**, 231 (1993) [475](#), [478](#), [479](#)
- [21] J. Meier: PhD thesis, Johannes Gutenberg Universität, Mainz (1994) [475](#), [477](#), [478](#), [479](#)
- [22] J. Meier, L. Chulkov, P. Egelhof, C. Fischer, W. Henning, A. v. Kienlin, G. Kirchner, G. Kraus and A. Weinbach: *Nucl. Instr. Meth. A* **370**, 259 (1996) [475](#), [478](#), [479](#)
- [23] H. J. Meier, P. Egelhof, W. Henning, A. v. Kienlin, G. Kraus and A. Weinbach: *Nucl. Phys. A* **626**, 451c (1997) [475](#), [478](#), [479](#), [480](#), [484](#), [485](#)
- [24] P. Egelhof: *Advances in Solid State Physics* **39**, 61 (1999) [475](#), [478](#), [486](#)
- [25] S. Kraft, A. Bleile, P. Egelhof, R. Golser, O. Kiselev, W. Kutschera, V. Liechtenstein, H. J. Meier, A. Priller, A. Shrivastava, P. Steier, C. Vockenhuber and M. Weber: in *Low Temperature Detectors*, F.S. Porter, D. Mc Cammon, M. Galeazzi, C.K. Stahle (Eds.), AIP Conference Proceedings **605**, 405 (2002) [478](#), [485](#), [486](#), [487](#), [492](#)
- [26] C. Vockenhuber, I. Ahmad, R. Golser, W. Kutschera, V. Liechtenstein, A. Priller, P. Steier and S. Winkler: *Int. J. Mass. Spectr.* **223-224**, 713 (2003) [478](#), [481](#), [490](#), [491](#), [492](#)
- [27] V. A. Andrianov, A. Bleile, P. Egelhof, S. Kraft, A. Kiseleva, O. Kiselev, H. J. Meier and J. P. Meier: *Nucl. Instr. Meth. A* **520**, 84 (2004) [483](#)
- [28] M. N. Harakeh and A. van der Woude: *Giant Resonances*, Clarendon Press, Oxford (2001) [484](#)
- [29] T. Aumann, P. F. Bortignon and H. Emling: *Annu. Rev. Nucl. Part. Sci.* **48**, 351 (1998) [485](#)
- [30] H. Emling: *Prog. Part. Nucl. Phys.* **33**, 729 (1994) [485](#)
- [31] W. H. Trzaska, V. Lyapin, T. Alanko, M. Mutterer, J. Räisänen, G. Tjurin and M. Wojdyr: *Nucl. Instr. Meth. B* **195**, 147 (2002) [485](#)
- [32] V. Liechtenstein, T. M. Ivkova, E. D. Olshanski, R. Repnow, J. Levin, R. Hellborg, P. Persson and T. Schenkel: *Nucl. Instr. Meth. A* **480**, 185 (2002) [485](#)
- [33] Y. T. Oganessian, V. K. Utyonkov, Y. V. Lobanov, F. S. Abdullin, A. N. Polyakov, I. V. Shirokovsky, Y. T. Tsyanov, G. G. Gulbekian, S. L. Bogomolov, B. N. Gikal, A. N. Mezentsev, S. Iliev, V. G. Subbotin, A. M. Sukhov, A. A. Voinov, G. V. Buklanov, K. Subotic, M. G. Itkis, K. J. Moody, J. F. Wild, N. J. Stoyer, M. A. Stoyer, R. W. Lougheed, C. A. Laue, J. B. Patin, D. A. Shaughnessy and J. M. Kenneally: in *Proceedings of the Fourth Tegernsee International Conference on Particle Physics Beyond the Standard Model, BEYOND 2003*, H.-V. Klapdor-Kleingrothaus (ed.), Springer, Berlin, 1091 (2004) [486](#)

- [34] Y. T. Oganessian, V. K. Utyonkov, Y. V. Lobanov, F. S. Abdullin, A. N. Polyakov, I. V. Shirokovsky, Y. S. Tsyanov, G. G. Gulbekian, S. L. Bogomolov, B. N. Gikal, A. N. Mezentsev, S. Iliev, V. G. Subbotin, A. M. Sukhov, A. A. Voinov, G. V. Buklanov, K. Subotic, V. I. Zagrebaev, M. G. Itkis, J. B. Patin, K. J. Moody, J. F. Wild, M. A. Stoyer, N. J. Stoyer, D. A. Shaughnessy, J. M. Kenneally and R. W. Lougheed: Phys. Rev. C **69**, 054607 (2004) 486
- [35] K. Morita, K. Morimoto, D. Kaji, T. Akiyama, S. Goto, H. Haba, E. Ideguchi, R. Kanungo, K. Katori, H. Koura, H. Kudo, T. Ohnshi, A. Ozawa, T. Suda, K. Sueki, H. Xu, T. Yamaguchi, A. Yoneda, A. Yoshida and Y. Zhao: J. Phys. Soc. Jpn. **73**, 2593 (2004) 486
- [36] P. Egelhof, O. Kisselev, G. Münzenberg, S. R. Neumaier and H. Weick: Physica Scripta **T104**, 151 (2003) 488
- [37] <http://www.ganil.fr/spiral/> 489
- [38] S. Kraft, V. Andrianov, A. Bleile, P. Egelhof, R. Golser, A. Kiseleva, O. Kiselev, W. Kutschera, J. P. Meier, A. Priller, A. Shrivastava, P. Steier and C. Vockenhuber: Nucl. Instr. Meth. A **520**, 63 (2004) 490, 492, 493
- [39] P. Steier, R. Golser, W. Kutschera, A. Priller, A. Valenta, C. Vockenhuber and V. Liechtenstein: Nucl. Instr. Meth. B **188**, 283 (2002) 485, 490, 491, 493
- [40] C. A. Cowen: Scientific American **235**, 36 (1976) 491
- [41] F. S. Porter, G. V. Brown and J. Cottom: in Cryogenic Particle Detection, C. Enss (ed.), Topics Appl. Phys. **99**, 361 (2005) 494, 496
- [42] M. Weitz, F. Schmidt-Kaler and T. W. Hänsch: Phys. Rev. Lett. **68**, 1120 (1992) 494
- [43] T. Stöhlker, T. Beier, H. F. Beyer, T. Kühl and W. Quint: Tests of Strong Field QED – The Physics of Multiply and Highly Charged Ions, Kluwer Academic Publishers (2003) 494
- [44] P. M. Mohr, G. Plunien, G. Soff: Phys. Rep. **293**, 227 (1998) 494, 495
- [45] T. Stöhlker, P. H. Mokler, F. Bosch, R. W. Dunford, F. Franzke, O. Klepper, C. Kozhuharov, T. Ludziejewski, F. Nolden, H. Reich, P. Rymuza, Z. Stachura, M. Steck, P. Swiat and A. Warczak: Phys. Rev. Lett. **85**, 3109 (2000), and references therein 494, 495
- [46] P. Egelhof, H. F. Beyer, D. McCammon, F. v. Feilitzsch, A. v. Kienlin, H.-J. Kluge, D. Liesen, J. Meier, S. H. Moseley and T. Stöhlker: Nucl. Instr. Meth. A **370**, 263 (1996) 495
- [47] H. F. Beyer, T. Stöhlker, D. Banas, D. Liesen, D. Protic, K. Beckert, P. Beller, J. Bojowald, F. Bosch, E. Förster, B. Franzke, A. Gumberidze, S. Hagmann, J. Hoszowska, P. Indelicato, O. Klepper, H.-J. Kluge, S. König, C. Kozhuharov, X. Ma, B. Manil, I. Mohos, A. Orsic-Muthig, F. Nolden, U. Popp, A. Simionovici, D. Sierpowski, U. Spillmann, Z. Stachura, M. Steck, S. Tachenov, M. Trassinelli, A. Warczak, O. Wehrhan and E. Ziegler: Spectrochimica Acta **59**, 1535 (2004) 495
- [48] E. Silver, H. Schnopper, G. Austin, R. Ingram, G. Guth, S. Murray, N. Madden, D. Landis, J. Beeman, E. E. Haller and T. Stöhlker: Nucl. Instr. Meth. A **520**, 60 (2004) 495
- [49] C. K. Stahle, R. L. Kelley, D. McCammon, S. H. Moseley and A. E. Szymkowiak: Nucl. Instr. Meth. A **370**, 173 (1996) 496

- [50] H. J. Meier, P. Egelhof, S. Han, H.-J. Kluge, D. McCammon, T. Mihara, S. H. Moseley and C. K. Stahle: in Proc. of the 7th Int. Workshop on Low Temperature Detectors LTD7, Munich, S. Cooper (ed.), MPI of Physics, Munich, 213 (1997) 496
- [51] A. Bleile, P. Egelhof, H.-J. Kluge, U. Liebisch, D. McCammon, H. J. Meier, O. Sebastián, C. K. Stahle and M. Weber: Nucl. Instr. Meth. A **444**, 488 (2000) 496
- [52] A. Bleile, P. Egelhof, S. Kraft, D. McCammon, H. J. Meier, A. Shrivastava, C. K. Stahle and M. Weber: in Low Temperature Detectors, F.S. Porter *et al.* (eds.), AIP Conference Proceedings **605**, 409 (2002) 496
- [53] [http://www.gsi.de/zukunftsprojekt/experimente/sparc/index\\_e.html](http://www.gsi.de/zukunftsprojekt/experimente/sparc/index_e.html) 497
- [54] A. Fleischmann, C. Enss and G. M. Seidel: in Cryogenic Particle Detection, C. Enss (ed.), Topics Appl. Phys. **99**, 151 (2005) 498

# Index

- Abrikosov–Gor’kov pair breaking, 109  
absorber, 3, 112–117  
absorber loss, 235, 250  
accelerator mass spectrometry, 489  
ACIS, 368, 371, 405, 406  
activation (cosmogenic), 320  
adiabatic demagnetization refrigerator, 278  
ADR, 278, 373, 374, 376–379, 383, 384, 388, 389, 395, 400  
AlGaAs, 293  
alpha radioactivity, 325  
amorphous germanium, 328  
amorphous silicon, 328  
amplifier noise, 14  
anti-reflection coating, 439  
array, 121–141, 253, 254  
Astro-E, 399  
Astro-E2, 359, 360, 370, 372, 374, 376, 377, 381, 386–389, 393, 399, 405, 406  
athermal, 331  
athermal electrons, 161  
Au:Er, 155–163  
electron configuration, 155  
heat capacity, 156  
magnetic susceptibility, 155  
magnetisation, 157, 159  
response time, 160  
axial (interaction), 318  
back-tunneling, 218, 219, 235, 240, 252, 253  
baryonic, 313  
 $\text{BaTiO}_3$ , 291, 300–302  
BCS theory, 66  
beta radioactivity, 325  
Beyond Einstein, 411  
BGO, 336  
Bi absorber, 111  
bias circuit, 8  
bias power, 20  
bilayers  
    Mo/Cu, 101  
black hole, 418, 444, 448  
BN, 309  
bolometer, 3, 63, 240  
branching ratio, 2  
Brillouin function, 157  
bulk micromachining, 123  
calorimeter  
    basic linear theory, 2–7, 29  
    ideal, 3  
cancellation, 236  
capacitance, 22  
carbon, 285  
 $\text{CaWO}_4$ , 336  
CCD, 359, 366, 368–372, 386, 405–407  
CDMS, 322  
cerium magnesium nitrate, 153  
CFH12K, 407  
Chandra, 359, 360, 367–372, 388, 393, 405, 406  
charge division, 247  
charge exchange, 381, 382, 401, 403–406  
charge regeneration, 332  
charge sensitive amplifier, 240  
charge-phonon, 326  
chemical shift, 297  
closed-loop gain, 9, 86  
CMB, 420, 421, 449  
COBE, 374  
coherence length, 66  
comet, 386, 401, 403–406  
complex admittance, 95

- complex impedance, 71  
 Constellation-X, 359, 374, 376–381, 394, 408–411  
 contacts, 36  
 Cooper pairs, 66, 217, 341  
 cosmological constant, 314  
 Coulomb gap, 37  
 count rate, 287  
     microcalorimeter, 289  
     Si-EDS, 288  
     WDS, 288  
 covariance matrix, 426  
 crab pulsar, 431–433  
 CRESST, 323  
 critical density, 36  
 cryo-cooler, 374, 376–379, 388, 389, 392, 395  
 CUORE, 347  
 CUORICINO, 336  
 Curie constant, 156  
 Curie-Weiss relation, 197  
 current output, 25, 27  
 current-biased, 7  
 current-referred noise, 96  
 de Gennes factor, 154  
 Debye, 323  
 deep implant, 386, 391  
 deep reactive ion etching (DRIE), 123  
 defect review, 305  
 detector response, 7  
 diamagnetic, 343  
 diamagnetic interaction, 343  
 dielectronic recombination, 388  
 diffraction, 274  
 diffraction grating, 360, 366, 367  
 diffusion, 229  
 dilution cryostat, 335  
 direct detection, 313  
 direct excitation, 362, 402  
 dirty limit, 67  
 discrimination, 319  
 disordered system, 36  
 distributed readout, 247  
 doping, 40  
     ion-implanting, 42  
     neutron transmutation doping (NTD), 40  
 DROID, 419, 443  
 dual circuit transformation, 25  
 duality, 26  
 dynamic resistance, 77  
 EBIT, 387, 388, 396–402, 404, 406  
 EDELWEISS, 322  
 EDS, 271, 275  
 efficiency  
     geometric, 284  
 Einstein, 367  
 electric field effects, 45  
 electrical nonlinearities, 44–52  
 electron probe microanalysis, 267  
 electron range, 298  
 electron recoil, 319  
 electron–phonon  
     coupling, 76, 110  
     time constant, 50  
 electron-impact excitation (EIE), 401, 402  
 electron-phonon  
     decoupling, 69, 111  
 electronic heat capacity, 50  
 electrothermal feedback, 9–11, 19, 30, 329  
     external, 22  
 energy dispersive X-ray spectrometer, 271  
 energy fluctuations, 193  
 energy linearity, 289  
 energy resolution, 21  
     first look, 3  
     optimal filtering, 15  
 energy-resolved, 428, 435, 447  
 EPIC, 369, 371, 372  
 EPMA, 267  
     applications, 291  
 erbium isotope, 161  
 ETF, 9  
 excess noise  
     TES, 98  
     thermistors, 52  
 excess quasiparticles, 219  
 EXOSAT, 367  
 $F_{\text{LINK}}$ , 12  
 fabrication, 237, 239  
 fall time, 80  
 feedback

- external, 22
- feedback factor, 10
- FET, 256
- fiber optic, 428, 440
- field effect transistor (FET), 379, 408
- fill factor, 435, 438, 439
- Fiske, 238, 240, 254
- fission, 349
- fluctuations, 235
- flux noise, 170
- Fourier transforms, 16
- frequency-division multiplexing, 129, 421, 448
- gain, 9
- gamma radioactivity, 325
- gamma-ray spectroscopy, 211
- generalized responsivity matrix, 82
- Generation-X, 411
- germanium, 48, 57, 320
- Ginzburg–Landau Parameter, 67
- Ginzburg–Landau theory, 66
- granule (superconducting), 343
- $^3\text{He}$ , 342
- $^4\text{He}$ , 342
- heat sink, 2
- heavy ion physics, 470–498
- HERON, 344
- HETG, 368, 369, 372, 388
- HgTe, 383, 390, 391
- high electron-mobility transistor (HEMT), 138
- high-frequency phonons, 161
- hopping conduction, 36–40
  - nearest neighbor hopping, 36
  - variable range hopping, 36
- hot electron bolometer, 56
- hot electron model, 46, 49
- HST, 447
- HXD, 386
- hydrogen-like heavy ions, 494
- hyperfine contribution, 161
- ideal X-ray spectrometer, 281
- imaging arrays, 437–443
- implantation, 329, 335
- impurity, 332
- indirect detection, 317
- inductance, 22
- interface, 231
- internal fluctuation noise, 26, 99
- internal time constant, 26
- ion-implanting, 42
- IR astronomy, 417–449
- IR cutoff, 424
- IR filters, 440
- IR radiation, 240
- Johnson noise, 12, 88, 90, 96, 425, 426
- Josephson, 218
- Kammerlingh Onnes, 63
- kinetic equation, 222
- kinetic inductance, 421, 448
- kinetic inductance thermometer, 32
- Korringa relation, 161
- Kosterlitz–Thouless transition, 67
- Kosterlitz–Thouless transition, 103
- Kramers doublet, 155
- Lamb shift, 494
- Langevin equations, 88
- layered sample, 304
- LETG, 368
- light-phonon, 337
- limits of detection, 273, 292
- linearity correction
  - microcalorimeter, 289
- load impedance, 22
- load resistor, 96
- load resistor noise, 13
- London penetration depth, 66
- loop gain, 9, 77
- Lorenz number, 69
- low voltage microanalysis, 298
- luminescence, 337
- LVSEM, 298
- MACHOs, 314
- magnetic calorimeter, 151–214
  - cylinder geometry, 174–179
  - energy resolution, 190–199
  - meander geometry, 179–186
  - optimization, 165–186
  - X-ray spectroscopy, 202–207
- magnetic calorimeters, 32
- magnetic dipole-dipole interaction, 158

- magnetic field sensitivity, 56  
 magnetic Johnson noise, 186–190  
 manganese oxide, 206  
 Markovian noise processes, 88  
 MAXIM, 411  
 Maxwellian distribution, 361, 399, 401  
 McDonald Observatory, 428, 431–433  
 mean-field approximation, 158  
 Meissner effect, 343  
 membrane, 110  
 metal oxides, 35  
 metal-insulator transition, 36  
 metallic manganese, 206  
 metrology applications, 209  
 microcalorimeter, 360, 366, 372, 373, 378, 379, 382, 383, 387–390, 393, 395, 396, 399, 403, 408, 409, 411  
 efficiency, 286  
 microcalorimeter array, 310  
 microcalorimeter EDS, 278  
 microelectromechanical systems, 110  
 micromachined thermal supports, 110  
 microwave SQUID multiplexers, 137  
 minimum mass fraction, 293  
 MIT, 327  
 MMC, 151–214  
     cylinder geometry, 174–179  
     energy resolution, 190–199  
     meander geometry, 179–186  
     optimization, 165–186  
     X-ray spectroscopy, 202–207  
 MSSM, 317  
 multiplexer, 379, 395  
 multiplexing  
     SQUID noise, 131  
 muon (interactions), 330  
  
 natural linewidth, 283  
 nearest neighbor hopping, 36  
 Neganov-Luke effect, 328  
 negative electrothermal feedback, 85  
 NEP, 11, 18, 195  
 neutralino, 317  
 neutrino, 314  
 neutron, 319  
 neutron star, 444, 448, 449  
 neutron transmutation doping (NTD), 40  
 NeXT, 359, 372, 375–377, 381, 394, 410  
 NIS junctions, 33  
 noise, 11–15  
     amplifier noise, 14  
     Johnson noise, 12–13  
     load resistor noise, 13–14  
     photon noise, 15  
     thermodynamic fluctuations, 11–12  
     thermometer noise, 15  
      $1/f$  noise, 52  
     noise correlations, 30  
     noise equivalent power, 11  
     noise sources, 18  
     nonlinear Markov fluctuation-dissipation relations, 94  
     nonlinear regime, 29  
     nonlinear thermal conductance, 95  
     nonlinearity, 23, 93  
     NTD, 327  
     nuclear recoil, 319  
     nuclear spectroscopy, 484  
     nuclear spin, 161  
     Nyquist noise, 88, 426  
     Nyquist theorem, 130  
  
     open-loop gain, 86  
     optical STJ and TES, 419–428  
     optimal filter, 425  
     optimal filtering, 15–18  
         energy resolution, 15  
     optimization, 18, 56  
     overvoltage, 300  
  
     pair breaking, 226  
     paramagnetic thermometer, 32  
     particle analysis, 305  
     peak interference, 272, 295  
     peak-to-background, 295  
     phonon, 217, 219, 224, 225, 319  
         losses, 226  
         noise, 88  
         trapping, 222, 226, 329  
     photoionization equilibrium (PIE), 361  
     photon detectors, 417  
     photon noise, 15  
     pileup, 30  
     planar gradiometer, 171  
     Poisson correlations, 431  
     Position Sensitive TES (PoST), 408, 409

- power responsivity, 7–11, 70  
 power-referred noise, 96  
 power-to-current responsivity, 80, 96  
 proportional counters, 359, 360, 366, 369, 370, 381  
 proximity bilayers, 108  
 proximity effect, 219, 230, 242, 250, 252  
 pulsar, 431–433  
 pulse template, 426  
 pulse-tube cryocooler, 307  
 pyro-electric thermometer, 33  
 qualitative analysis, 291  
 quantum efficiency, 428, 440  
 quasiparticles, 69, 217, 218, 224, 329 losses, 226, 241  
 quenching factor, 323  
 radiative recombination, 361, 362, 366, 401–403  
 radioactivity, 319  
 radionuclide dating, 490  
 radon, 319  
 readout, 239, 251, 253, 256  
 recombination, 226  
 reflection grating, 367–369  
 reflection mask, 437, 439  
 relaxation, 222  
 resolution, 282  
 resolving power, 419  
 responsivity, 219, 227, 240, 243–245  
 rf SET, 421  
 RGS, 368, 369, 388  
 rise time, 80  
 RKKY exchange interaction, 154, 157  
 ROSAT, 382, 386, 403, 410  
 Rothwarf-Taylor, 224, 227, 253  
 RXTE, 369  
 S-Cam, 434–437  
 sapphire, 324  
 saturation, 30  
 saturation power, 104  
 scalar (interaction), 318  
 scaling, 163  
 scanning electron microscope, 269  
 Schottky anomaly, 156, 159  
 scintillation, 321  
 SCUBA, 420  
 self-biasing, 85  
 self-calibration, 85  
 self-inductance MMC, 207  
 SEM, 269 low voltage, 298  
 semiconductor, 332  
 series-array-SQUID, 74  
 Si<sub>3</sub>N<sub>4</sub> membranes, 111  
 Si-EDS, 271 limitations, 272  
 resolution, 272  
 WDS, TES comparison, 277  
 silicon, 48, 57, 329  
 silicon nitride, 76  
 spallation, 349  
 spectral artifacts, 290  
 spectral density, 11  
 spectrometer efficiency, 283  
 spectrophotometer, 428–433, 443–444  
 spectrophotometry, 417, 428–433, 443–444  
 spectrophotopolarimeters, 443  
 spin glass state, 156  
 spin-dependent, 322  
 spin-electron, 161  
 spin-exchange, 50  
 spin-independent, 322  
 spin-spin interaction, 38  
 SQUID, 71, 240, 326  
 SQUID noise, 131  
 SrBi<sub>2</sub>Ta<sub>2</sub>O<sub>9</sub>, 309  
 STJ array, 419, 435, 444, 448  
 stray capacitance, 22  
 stray inductance, 22  
 Super-EBIT, 398  
 superconducting quantum interference device (SQUID), 378, 379, 408, 410  
 superconducting transition-edge sensor, 63–142  
 small signal theory, 70–71  
 theory, 65–105  
 supercurrent, 219  
 superfluid, 342  
 superheavy elements, 485  
 supersymmetry, 313  
 surface micromachining, 127  
 SUSY, 313

- TES, 63–142, 278, 324, 373, 379, 395, 408, 409, 417, 422–428  
array fabrication, 122  
arrays, 121, 434–443  
bilayers, 108  
current-biased, 86  
electrical response, 71  
elemental superconductors, 107  
excess noise, 98  
frequency-division multiplexing, 129  
low-frequency FDM, 135  
low-frequency TDM, 132  
magnetically doped superconductors, 109  
microwave SQUID multiplexers, 137  
multiplexed readout, 128  
optical-photon calorimeters, 118  
proximity-coupled, 108  
saturation power, 104  
single-pixel implementation, 105  
small signal theory, 70–71  
stability, 83  
theory, 65–105  
thermal response, 71  
time-division multiplexing, 129  
voltage-biased, 86  
WDS, Si-EDS comparison, 277  
X-ray calorimeters, 119  
TFN, 88  
thermal circuit, 8  
thermal conductance, 110  
Si<sub>3</sub>N<sub>4</sub> membranes, 118  
thermal conductivity, 12  
electron-phonon, 46  
thermal differential equation, 75  
thermal emission, 447  
thermal ionization, 36  
thermal link, 2  
thermal photons, 423  
thermal–electrical analogies, 7  
thermalization noise, 28  
theristor, 5  
thermocouples, 35  
thermodynamic fluctuation noise, 4, 11, 88  
thermometer noise, 15  
Thevenin-equivalent circuit, 74  
Thevenin-equivalent load resistor, 85  
thin film sensor, 327  
time constant, 50  
time-division multiplexing, 129, 421, 448  
time-resolved, 418  
TiN, 301, 303  
trace analysis, 490  
trace detection, 296  
trace element, 304  
transmission grating, 367, 368  
trapping, 233  
trapping rate, 229  
tritium, 331  
tunnel barrier, 237  
tunneling, 218, 227, 228  
type I superconductors, 67  
type II superconductors, 67  
ULD balloon, 444  
useful bandwidth, 5  
UV astronomy, 417–449  
variable range hopping, 36  
voltage output, 25  
voltage-biased, 7  
vortex pairs, 103  
wavelength dispersive X-ray spectrometry, 274  
WDS, 274, 275  
diffractors, 275  
resolution, 274  
scanning, 274  
Si-EDS, TES comparison, 277  
weighting matrix, 426  
white dwarf, 418, 431, 449  
white noise, 425, 428  
Wiedemann–Franz law, 110  
Wiedemann–Franz thermal conductance, 68  
Wiener filter, 425–427  
William Herschel Telescope, 419, 434  
WIMP, 313  
Woods filters, 421  
WSi<sub>2</sub>, 292, 304  
X-ray absorber, 390, 391, 393, 408  
X-ray optic, 287  
X-ray absorber, 383, 391, 393, 409

- XEUS, 359, 372, 376, 381, 394, 408, 410  
XIS, 386  
XMM-Newton, 359, 360, 367–372, 388,  
393  
XQC, 359, 374, 377, 381–386, 389–391,  
393, 395, 400, 410  
XRS, 359, 360, 374, 376–381, 386–395,  
408, 410  
XRS/EBIT, 396, 399–406  
 $\text{YBa}_2\text{Cu}_3\text{O}_7$ , 273, 275, 283  
zero-frequency responsivity, 82

